



Sponsors: Korea Science and Technology Foundation, U.S. National Science Foundation, Brain Korea 21



SUNDAY, AUGUST 5

7:00pm **Reception**, Levis Faculty Center, 2nd Floor

MONDAY, AUGUST 6

Beckman Institute Auditorium

8:45am **Opening Session**

Welcome and Introductions Dan Abrams
 Opening Remarks Sung Pil Chang, Neil Hawkins, Chang Ho Park, T-John Kim

9:15am *State of the Art in Earthquake Engineering in Korea* Sung Pil Chang

9:45am *Consequence-Based Engineering Approach to Reduction of Risk in Moderate Seismic Zones* Dan Abrams

10:15am Break

10:45am **Technical Session 1: Ground Motions**

A Research Plan Leading to Probabilistic Seismic Hazard Maps for Korea Robert Herrmann

Prediction of Strong Ground Motions in Southern Korea Chang Eob Baag

Modeling Site Amplification of Ground Motions Youssef Hashash

12:00pm LUNCH

1:25pm **Technical Session 2: Building Design and Assessment for Moderate Seismicity**

Seismic Performance Evaluation of Structures under Multi-directional Loading Jae Kwan Kim

Seismic Resistance of Low Ductility Structures Amr Elnashai

Displacement-Based Design and Assessment of Structural Walls Sung Gul Hong

Modeling Fragility of Essential Facility Structures Y.K. Wen

Structural Damage Detection in Time Domain from Measured Acceleration during Earthquake Hae Sung Lee

3:30pm Break

4:00pm **Technical Session 3: Building Components and Response Modification**

Seismic Performance of Reinforced Concrete Columns Depending on Longitudinal Reinforcement Details Jae Hoon Lee

Seismic Performance of Reinforced Concrete Beam-Column Connections and Frames James LaFave

Effect of Directionality of Reinforcing Bars on RC Members in Cyclic Shear Hong Gun Park

Response Modification for Low-Rise Buildings James Craig

Vertical Distribution of Seismic Loads for Base-Isolated Building Structures Dong Guen Lee

6:05pm Close for Day

7:30pm **Seminar Banquet**, Illini Union Room A



Sponsors: Korea Science and Technology Foundation, U.S. National Science Foundation, Brain Korea 21



TUESDAY, AUGUST 7

Beckman Institute Auditorium

8:30am	<p>Technical Session 4: Bridge Components</p> <p><i>Analytical Study on Inelastic Behavior and Ductility Capacity of Reinforced Concrete Bridge Columns Subjected to Seismic Load</i> Hyun Mock Shin</p> <p><i>Performance of Rehabilitated Reinforced Concrete Bridge Columns</i> Neil Hawkins</p> <p><i>Seismic Performance Evaluation of RC Bridge Piers with Limited Ductility by Pseudo Dynamic Test</i> Young Soo Chung</p>
10:00am	Break
10:30am	<p>Technical Session 5: Assessment of Bridge Systems</p> <p><i>Design Considerations on Seismic Isolation of Bridges in Low and Moderate Seismic Regions</i> Hyun Moo Koh</p> <p><i>Seismic Analysis of Major Bridges in America</i> Jamshid Ghaboussi</p> <p><i>Dynamic Behavior Analyses of Bridges under Bi-directional Seismic Excitations</i> Sang Hyo Kim</p> <p><i>Seismic Evaluation of a Steel Truss Railway Bridge</i> Doug Foutch</p>
12:15pm	LUNCH, Newmark Civil Engineering Laboratory Crane Bay
2:00pm	<p>Technical Session 6: Lifeline Structures</p> <p><i>Seismic Response of Geotechnical Port & Harbor Structures under Shaking Table Tests</i> Myoung Mo Kim</p> <p><i>Seismic Design and Analysis of Underground Structures</i> Youssef Hashash</p> <p><i>Seismic Response Analysis of Jointed Buried Pipeline Network</i> Moon Kyum Kim</p> <p><i>Key Parameters Governing the Performance of Soft Tunnel Coating for Seismic Isolation</i> Dae Sang Kim</p> <p><i>Scenario Analysis on Economic Impacts of Transportation Network Changes Under Unscheduled Events</i> Jong Sung Lee</p>
4:00pm	Break
4:20pm	Discussion of Workshop Resolutions
5:40pm	Adjourn
	Dinner Open



WEDNESDAY, AUGUST 8
KEERC-MAE STUDENT PRESENTATIONS
 5602 Beckman Institute

8:30am	Welcome and Introductions	
8:45am	Session S1: Geotechnical Issues and Response of Dams	
	<i>Evaluation of Dynamic Pile Group Effect by Shaking Table Tests</i>	Ik Soo Ha
	<i>Nonlinear Wave Propagation in the Mississippi Embayment</i>	Duhee Park
	<i>Shaking Table Test of Small-Scale Model of a Concrete Gravity Dam</i>	Jin Ho Lee
9:45am	Session S2: Bridge Structures	
	<i>Simplified Nonlinear Design Model for URM in-plane Wall Response</i>	Joonam Park
	<i>Cost Effectiveness Evaluation of Seismically Isolated Bridges</i>	Daegi Hahm
10:30am	Break	
10:50am	<i>Fatigue Strength of Stud Shear Connection in Full-Depth Precast Concrete Deck Bridge</i>	Hyung Geun Ryu
	<i>Nonlinear Embankment Contribution to the Seismic Response of Short Bridges</i>	Mehmet Inel
11:50am	LUNCH	
1:20pm	Session S3: Building Structures	
	<i>Seismic Assessment of Existing Unreinforced Masonry Buildings</i>	Sang-Cheol Kim
	<i>Structural Damage Assessment from Modal Data using a System Identification Algorithm with Regularization Techniques</i>	Joo Sung Kang
	<i>Utility Software for Earthquake Engineering</i>	Erich Bretz
	<i>Displacement Based Seismic Design of Asymmetric-Plan Buildings</i>	Bong Ho Cho
	<i>Seismic Rehabilitation of Unreinforced Masonry Shear Walls</i>	Omer Erbay
3:00pm	Break	
3:20pm	<i>Ductility Confinement of RC Shear Walls</i>	Su Min Kang
	<i>Flexural Behavior of Retrofitted Masonry Piers</i>	Jaret Lynch
	<i>Unified Constitutive Model for RC Planar Members under Cyclic Load</i>	Jae Yo Kim
	<i>Dynamic Stability of Unreinforced Masonry Bearing Walls</i>	Can Simsir
4:40pm	Adjourn	



KEERC-MAE Joint Seminar on
Risk Mitigation for Regions of Moderate Seismicity
University of Illinois at Urbana-Champaign, August 5-8, 2001



Sponsors: Korea Science and Technology Foundation, U.S. National Science Foundation, Brain Korea 21



State of the Art in Earthquake Engineering in Korea

Sung-Pil CHANG¹

¹ *Director, Korea Earthquake Engineering Research Center
Professor of School of Civil, Urban, Geosystem Engineering, Seoul National University
email: changsp@plaza.snu.ac.kr*

ABSTRACT: Since the establishment of Earthquake Engineering Society of Korea (EESK) in 1996 and Korea Earthquake Engineering Research Center (KEERC) in 1997, the earthquake engineering researches have been activated as numerous as they are needed in the early stage toward the hazard mitigation in Korea. Currently over 20 research projects focusing on moderate and low seismicity are being performed intensively by KEERC researchers. The center has been hosted for 4 international symposiums, 17 workshops and seminars. Research outputs of the KEERC will contribute to establish earthquake resilient country at the national level and to provide technical information regarding the moderate seismicity with international researchers who have common concern. In addition, the KEERC Information Service (KEERCIS) has worked on compiling earthquake engineering information targeting on the ultimate objective of technology transfer to the interesting people worldwide.

KEYWORDS: KEERC, EESK, ANCER, earthquake, KEERCIS

INTRODUCTION

There were two earthquake events at Ssange-Sa in 1936 and Hong-Sung in 1978. The magnitude of both earthquakes was estimated to be 5.0 that were not big enough to warn Korean to prepare against for hazardous seismic disasters. However, the devastating Hyogoken-Nanbu earthquake occurred in Japan in 1995 caused mental shock waves that awakened the public concern about the possible earthquake disaster in Korea. The historical records of seismic events in Korea, especially from 16th to 17th century, showed that the possibility of disastrous seismic hazards could not be ignored any longer. The largest historic earthquake in Korea is estimated to be around 6.5 or a little bigger in magnitude. From the lesson of this earthquake most seismologists pointed out that a disastrous earthquake might occur at any time soon. Consequently, more intensive activities on earthquake engineering research were set out in Korea. The government began to realize that preparatory measures had to be implemented at national level. The consensus among the design engineers and researchers resulted in the foundation of the Earthquake Engineering Society of Korea (EESK) in November 28, 1996. The core members of EESK in joint with other researchers made a proposal to establish an earthquake engineering research center to the Korea Science and Engineering Foundation (KOSEF). After long review process, the proposal was finally approved by KOSEF. The Korea Earthquake Engineering Research Center (KEERC) is nominated as an engineering research center by KOSEF. KEERC began to receive fund from KOSEF since June 1, 1997 for the period of 9 years. The mission of KEERC is to perform integrated researches and disseminate the results for the mitigation of earthquake hazards. Currently, EESK and KEERC are two main organizations active in the field of earthquake engineering research in Korea.

OVERVIEW OF KEERC

Organization and Vision of KEERC

The Korea Earthquake Engineering Research Center headquartered at Seoul National University was founded to help establish earthquake resilient communities throughout Korea with the grant from KOSEF. The support of KOSEF will last for 9 years. The primary goal of the center is to contribute to the mitigation of earthquake hazards through researches in the area of seismic hazard evaluation, seismic analysis and design technology and social preparedness. The center is composed of two divisions: research and support and has three committees: steering committee, advisory committee, and evaluation committee. During the first period of 3 years, the research division was subdivided into 6 research groups: Seismic Hazard and Ground Motion, Geotechnical Engineering, Buildings, Infra Systems, Seismic Risk Management and Innovative Seismic Design. Each group performs one integrated project that consists of several research topics.

The KEERC vision is to be a national center for research, education, and industrial interaction in the domain of earthquake engineering. The salient aspects of this vision include the functioning as a national hub for the exchange of ideas explored and results produced in other centers and institutions involved in this area; as an effective collaborator with industry for the development of new and practical technology; and as an educational environment that fosters multidisciplinary research. Toward the KEERC vision, the strategic research plan the KEERC has been refined periodically at the end of every 3 years. After the first period of 3 years, the existing strategic research plan developed in 1997 when the center was established was systematically examined and refined further to achieve the global research vision of KEERC.

The refinement has been made on the following concerns: a) the reorganization of the existing researches in accordance with the emphasis of the KEERC vision for upcoming period; b) the development of a knowledge base system for integrating and accumulating earthquake engineering information obtained through researches of our center and other cooperative institutions; and The 4 broad research themes were appeared as needed: (1) Ground Motion and Geotechnical Engineering; (2) Seismic Design and Analysis; (3) Seismic Assessment and Upgrading; and (4) Seismic Risk, Reliability, and Economics. And all the research projects of KEERC will be centered to the Knowledge Base System. Such a centralization of research clusters is to synthesize the research outcome into an integrated knowledge base system. It is thereby expected that the research results be implemented effectively and transferred easily to cross-disciplinary researchers, industry, government, and the public. This activity has been performed under the special project of the KEERC.

ONGOING RESEARCH PROGRAM OF KEERC

Currently over 20 research projects focusing on moderate and low seismicity are being performed intensively by KEERC researchers. The center has been hosted for 4 international symposiums, 17 workshops and seminars. Research projects are composed of four broad groups as follows.

□ Group I: Ground Motion and Geotechnical Engineering

Toward the first step to prepare for earthquake hazard mitigation, the estimation of characteristics of strong ground motions in Korea must be elicited. For example, predictions of the peak ground acceleration and response spectra as a function of earthquake magnitude and hypocentral distance are of paramount importance for the assessment of earthquake hazard on buildings and infra structures. The lack of strong ground motion data in Korea, however, makes it difficult to establish empirical relations among ground motions, earthquake magnitudes, and hypocentral distance. Moreover, high-frequency ground motions contain much complexities and uncertainties of earthquake source, wave propagation, and site effect, which could not be modeled by deterministic method. To obtain the most credible outline of seismic hazard in Korea, the following 5 projects are being performed actively.

- Stochastic and deterministic prediction of ground motions in southern Korea
- Ground Motions of Korean Earthquakes
- Evaluation of Dynamic Properties of Korean Subsoil for Seismic Design
- Liquefaction Hazard Zonation in Port and Harbor
- Numerical analysis and model test for seismic design of geotechnical structures in port and harbor

□ **Group II: Seismic Design and Analysis**

The most realistic implementation of hazard mitigation for new structures may be accomplished by designing seismic resistant structures using the corresponding structural analysis techniques. The seismic design hazard in Korea obtained at the time of proposal of new seismic design code, many researchers are working on the various subjects ranged from the detailing of members, to the dynamic analysis of structures including buildings and bridges, and to the soil-structure interaction. The research outcomes will contribute to provide researchers in similar domain with useful information on moderate seismicity and further enhance the current design practice of Korea. This group has the following 6 different research projects.

- The Development of 3 Dimensional Nonlinear Analysis and Earthquake Resistant Design Method for Building Structures
- Study on Nonlinear Dynamic Behavior of Coupled Soil-Structure Systems Focused on the Boundary and Material Nonlinearity
- A Study on Nonlinear Dynamic finite Element Analysis of Reinforced Concrete Structures and Seismic Assessment
- Reinforcement Details and Design Strength of Bridge Columns in Moderate Seismicity Region
- Analytical Modeling and Design Method for Rib-Reinforced Seismic Steel Moment Connection
- Design Technology for Earthquake Response Control System

□ **Group III: Seismic Assessment and Upgrading**

Not only new structures but also existing structures must have the earthquake-resisting capacity. For the existing structures such as bridges, buildings and dams, the evaluation of the seismic performance of the structures is the first step to be taken. For existing structures lacking of earthquake-resisting capacity, the deficiencies found through the assessment must be upgraded appropriately for the remaining duration of its life cycle. The following research topics will address the issues raised mostly around existing buildings.

- Pseudo-Dynamic Tests of Concrete-Filled Steel Columns
- Research for Seismic Assessment and Enhancement of Retrofitted RC Bridges
- Dynamics Strut-and-Tie Model for Earthquake Resistant Structural Concrete
- Determination of Damping ratio and Seismic Assessment of a structure by System Identification Technique in Time Domain
- Development for a reliability estimation Method and Prediction Technique for the Bridge System under Seismic Excitations in the Korean Peninsula

□ **Group IV: Seismic Risk, Reliability, and Economics**

The assessment of the expected damage level is very important in preparing seismic hazard mitigation programs. The possibility of collapse varies depending on the location and degree of the damage, which might result in massive loss of human lives or economic loss. The researchers of this group consider rather global view on the risk assessment than on structures themselves. Also, the research about tsunami inundation is included because Korea is a peninsular whose boundary is surrounded mostly by seas. The outcome of the research work will enable to assess the degree of damage level of structures but also other sources of earthquake induced disasters. The research topics of this group include the followings.

- Earthquake Hazard Prediction in Korea
- Tsunami Inundation Mapping for the east Korean coast
- Development of Seismic Fragility Assessment Technology Considering Characteristics of Korean Database
- Development of Simplified Seismic Design Method for Underground Structures considering Soil-Structure Interaction
- Development of Nondestructive Testing Techniques Using radar for Concrete Structures Damage by Earthquake
- Development of real-time seismic damage assessment system for large structures

KEERC INFORMATION SERVICE (KEERCIS)

KEERC is in a unique position to develop a framework that can be served as a catalyst to bring together the various groups (researchers, industry people, government, and public) to work together. A new cluster "Knowledge Base System" has been formed recently to provide an integrated information over the multidisciplinary domain related to earthquake engineering especially for moderate and low seismic zones. During the 1 year after this project was set out, the necessary infra software was equipped but still in the preliminary stage and will be evolved toward a worldwide knowledge base system which international information is merged into and extracted from. To develop and implement the Knowledge Base System, the environment of a KEERC-centered network must be established first and then the specialized and detailed software will be implemented upon the built-in network environment. There are two layers, each of which is a national kernel and an international kernel respectively. In the national kernel all the KEERC researchers and facilities and other related national institutions and organizations are interconnected to the KEERC server system. In the

international kernel the international research centers which have made and are developing cooperative research agreements with KEERC. When the Knowledge Base System based on the KEERC-centered network has been established, this will be utilized enormously, which further accelerates the achievement of KEERC vision and objectives. For example, electronic communications between KEERC headquarters and KEERC researchers are possible. Especially protection-requested communication will be made through a password-protected web site on which the KEERC Committee can process a RFP and also manage KEERC researches more efficiently.

INTERNATIONAL COOPERATIVE RESEARCH

The KEERC has been hosted for 4 international symposiums, 17 workshops and seminars. Through these international academic activities, many researchers coming from U.S.A, Japan, China, and Chinese Taipei attended the 17 workshops and seminars.

On August in 1998, the 1st symposium was held with the title of “new development in the earthquake hazard mitigation technology for moderate seismicity regions”. The 2nd symposium on “seismic hazards and ground motion in the region of moderate seismicity” was held on November of the same year. The 3rd international symposium on seismic isolation, passive energy dissipation and active control of vibrations of structures was held at the Cheju island in 1999. And very recently the 4th international symposium on earthquake engineering for the moderate seismicity regions, was held on February in 2001.

After that symposium an Asian-Pacific Network of Centers for Earthquake Engineering (ANCER) was established with the founding members of Korea Earthquake Engineering Center, Institute of Engineering Mechanics of China Seismological Bureau, Multidisciplinary Center for Earthquake Engineering Research of USA, Mid-America Earthquake Center of USA, Pacific Earthquake Engineering Research Center of USA, Disaster Prevention Research Institute of Japan, and Center for Research on Earthquake Engineering of Chinese Taipei.

Recently, the KEERC has a chance to apply for the fund for the international cooperative projects at the KOSEF. It supports \$770,000 per year for the projects. The KEERC and KOSEF have the same relationship as the MAE and NSF. Concerning about the projects, prior consultations between researchers of both countries are needed and the researchers should follow the procedures to apply for research plan to each country until the end of September. The research plan is independently evaluated at each country and mutual agreements are needed. Using the relationship, we could perform more international cooperative researches between KEERC and MAE in the future.

CONCLUDING REMARKS

The KEERC and EESK directed many fundamental researches in earthquake engineering over the past few years but there still much remains to be accomplished. The research in earthquake engineering in Korea will be continuously upgraded to reduce the potential loss of life and facilities due to earthquakes. The KEERC and EESK work with all members of the earthquake engineering community, including practicing engineers and other design professionals, policy makers, public officials in Korea as well as international collaborative partners. Especially KEERCIS is expected to play a major role in sharing the information earthquake engineering worldwide.

Recently, the KEERC has actively performed international activities such as symposiums, workshops, and seminars. At the 4th international symposium, on February in 2001, Asian-Pacific Network of Centers (ANCER) for Earthquake Engineering was established with other earthquake engineering research centers.

In addition, using the relationships between KEERC and KOSEF and MAE and NSF, the KEERC and MAE could perform more international cooperative research projects.

RERERENCES

1. Kiehwa Lee, "*Earthquakes of Korea*," Proceedings of 1996 Symposium on Seismology in East Asia, Daejon, 1996, Korea, pp. 5-12.
2. Myung-Soon Jun, "*Earthquake Data In and Out the Korean Peninsula during 1905-1942*," Proceedings of 1996 Symposium on Seismology in East Asia, Daejon, Korea, 1996, pp. 87-92.
3. J. B. Kyung et al., "*Paleoseismological Approach in the Southeastern Part of the Korean Peninsula*," Proceedings of 1996 Symposium on Seismology in East Asia, Daejon, Korea, 1996, pp. 38-47.



KEERC-MAE Joint Seminar on
Risk Mitigation for Regions of Moderate Seismicity
University of Illinois at Urbana-Champaign, August 5-8, 2001



Sponsors: Korea Science and Technology Foundation, U.S. National Science Foundation, Brain Korea 21



Consequence-Based Engineering Approach to Reduction of Risk in Moderate Seismic Zones

Daniel P. ABRAMS¹

¹ *Hanson Engineers Professor of Civil and Environmental Engineering and
Director of Mid-America Earthquake Center, University of Illinois at Urbana-Champaign
1245 Newmark Laboratory, 205 N. Mathews, Urbana, Illinois, USA
email: d-abrams@uiuc.edu*

ABSTRACT: Consequence-Based Engineering is a new paradigm for reducing risks attributable to future earthquakes. Development of this paradigm is a central unifying goal of the Mid-America Earthquake Center. System-level research programs of the Center are described in this paper in terms of meeting this goal. Vision and mission statements for the Center are given followed by a discussion of how Consequence-Based Engineering can be used to reduce risk for the infrequent earthquakes that are common in the moderate seismic zone of Mid-America. This discussion provides an introduction to the three core research thrust areas of the Center for the purposes of identifying potential areas of collaboration with the Korean Earthquake Engineering Research Center.

KEYWORDS: moderate earthquakes, engineering, risk reduction, consequences, seismology, uncertainty, societal response, economics, loss

INTRODUCTION

Seismic Hazards in Mid-America

Earthquakes in the central and eastern parts of the United States can be equally as intense as those that occur more frequently along plate boundaries on the west coast. The New Madrid earthquake sequence between November of 1811 and February 1812 included three major earthquakes ranging in magnitude from 7.6 to 8.3. These intraplate earthquakes occur within stable continental regions, and as a result, must be modeled with different geophysical models than used to represent mechanisms in interplate earthquakes. They also pose different challenges to mitigation and loss-reduction efforts as a result of other unique physical, technical, social, economic and political problems that are germane to this region of the country. Earthquake energy is known to attenuate across longer distances in the eastern half of the country because of the presence of clay and alluvium deposits, and tend not to have the directivity attributes of earthquakes in California. As a result, a repeat of one of the New Madrid earthquakes could affect the built environment in seventeen states, be felt on the eastern seaboard, and significantly disrupt transportation and utility networks from coast to coast. Added to this the high vulnerability of construction to earthquake-induced loadings, the high population density, and the reliance of the nation's economy on functional infrastructure systems in Mid-America¹, the loss potential for a repeat of the 1812 earthquake is extremely high at approximately \$200 billion. This loss estimate is four times larger than the sum of losses from the 1989 Loma Prieta, 1994 Northridge and 2001 Nisqually earthquakes. A further complexity arises from the poor sense of earthquake awareness from the general public to critical decision makers, and as a result, their reluctance to invest in safe seismic practices.

Problems related to the infrequent, but high consequence nature of earthquakes in Mid-America need to be addressed. In fact, a new engineering approach is needed to design and rehabilitate the built environment in such a way to economically minimize potential losses to property, businesses and public health across a community, a national network linking communities or other system on concern. In the past, structural engineering research has been focused predominately on response and behavior of individual structures. Design and analysis methods have been developed on the premise of estimating seismic response for a *single* building, bridge, lifeline or other type of structure. Though new performance-based methods are a major step forward towards loss reduction, their context is limited to an isolated structure, rather than a system of the built environment within a specified region.

¹ According to the 1993 Commodity Flow Survey (CFS) by the Bureau of the Census, U.S. Department of Commerce, \$2.01 trillion, or 33% of total U.S. commodities, originate, pass through, or arrive within the New Madrid Seismic Zone.

Consequence-Based Engineering – a New Paradigm in Earthquake Engineering

Research at the MAE Center is directed towards a common theme and new engineering approach for reducing losses from infrequent, high-consequence events. This new approach is known as *Consequence-Based Engineering* and differs from current engineering methods because design or rehabilitation of the built environment is based on reducing potential losses across a system having greater horizons than an individual building, bridge or other structure. A working definition of this new paradigm is given below.

“Consequence-based engineering is a new paradigm for seismic risk reduction across regions or systems that incorporates identification of uncertainty in all components of seismic risk modeling and quantifies the risk to societal systems and subsystems by working with policy-makers and decision-makers to ultimately develop risk reduction strategies and implement mitigation actions.”

Consequence-Based Engineering (CBE) is a methodology that prescribes mitigation action plans that will minimize losses across a specific socio-economic environment. New technologies, needed to support the development of CBE, include improved methods to: (a) identify and inventory the specific system, (b) characterize probable seismic hazard and response of the built environment, (c) assess seismic risk and (d) establish mitigation priorities. The goals and subsequent strategic research plan for the Center are specifically directed at development of these new Consequence-Based Engineering approaches to earthquake-loss reduction.

Though technologies developed through the MAE Center are pertinent to earthquakes and construction in the eastern and central United States, work of the Center establishes a new and unique framework for Consequence-Based Engineering that can be extended to other parts of the world with similar seismic exposures, or to other locations with similar infrequent, high-consequence threats due to other natural and man-made hazards.

STRATEGIC RESEARCH PLANNING

MAE Center Vision and Mission

Over the last year, the Mid-America Earthquake Center has developed a new strategic plan of research for the next five years. As part of this plan, its vision and mission statements have been revised to more specifically express the intentions of the Center leadership. The following vision statement is used to set the stage for the plan and drive the needs for the research of the Center.

Vision: *Through systems-driven research, education and outreach, the MAE Center is developing innovative solutions to mitigate impacts of earthquakes through quantification of seismic risk across regions and networks, and works proactively with decision and policy makers, stakeholders and practitioners to develop advanced knowledge and applicable technologies necessary to diminish effects of future earthquakes.*

The Center's mission follows from its vision statement and articulates the direction of the Center's research towards development of the Consequence-Based Engineering paradigm through its research thrust areas on regional damage synthesis, network vulnerability and engineering provisions.

***Mission:** The mission of the MAE Center is to develop through research, and disseminate through education and outreach, new engineering approaches necessary to minimize consequences of future earthquakes across hazard-prone regions, including but not limited to, the eastern and central United States. Correlated interdisciplinary research synthesizing damage across regions, estimating seismic vulnerability across regional and national networks, and improving current engineering practices, forms the core research needed to develop such consequence-based approaches, and to support stakeholder interests in risk assessment and seismic engineering.*

Based on these vision and mission statements, a set of goals and objectives were developed from which coordinated research thrust areas and projects are formulated.

Systems-Driven Research Plan

General research categories are shown on the three-plane chart (Figure 1) to illustrate the systems-driven nature of the research and the balance between systems integration, enabling technologies and fundamental knowledge. All research is directed towards long-range development of the Consequence-Based Engineering paradigm. Because CBE considers risk quantification for societal systems, Center research polarized towards development of the paradigm is inclusive of needs of the social-economic environment. Systems integration research shown on the top plane includes an integrating project on development of a CBE framework that links research needs of the paradigm development to research of the core and stakeholder thrust areas. Closely associated with this framework project is a project on uncertainty modeling that provides an ability to reflect key problem uncertainties in future selection and funding of projects. Other systems integration activities include the overall thrust efforts on synthesizing damage across regions and modeling vulnerability of networks, as well as a capstone project that uses advanced information technologies for visualization of synthesized damage and loss across regional systems.

Research on the enabling technology plane includes advanced technologies for more rapid and accurate inventories of the built environment across regions or networks, new computational methods for estimating seismic response of the built environment (for purposes of regional damage synthesis, or engineering of individual structures), new modeling approaches to assess vulnerability of systems and components, new engineering techniques to improve seismic safety and performance of new and existing construction, updated hazard maps dictating revised seismic demand forces for construction in Mid-America, code revisions that will result in safer and more economical construction, and new synthetic ground motions for response analyses. Needs for fundamental knowledge is driven by both system-level research as well as enabling technology research and includes basic social science studies of organizational

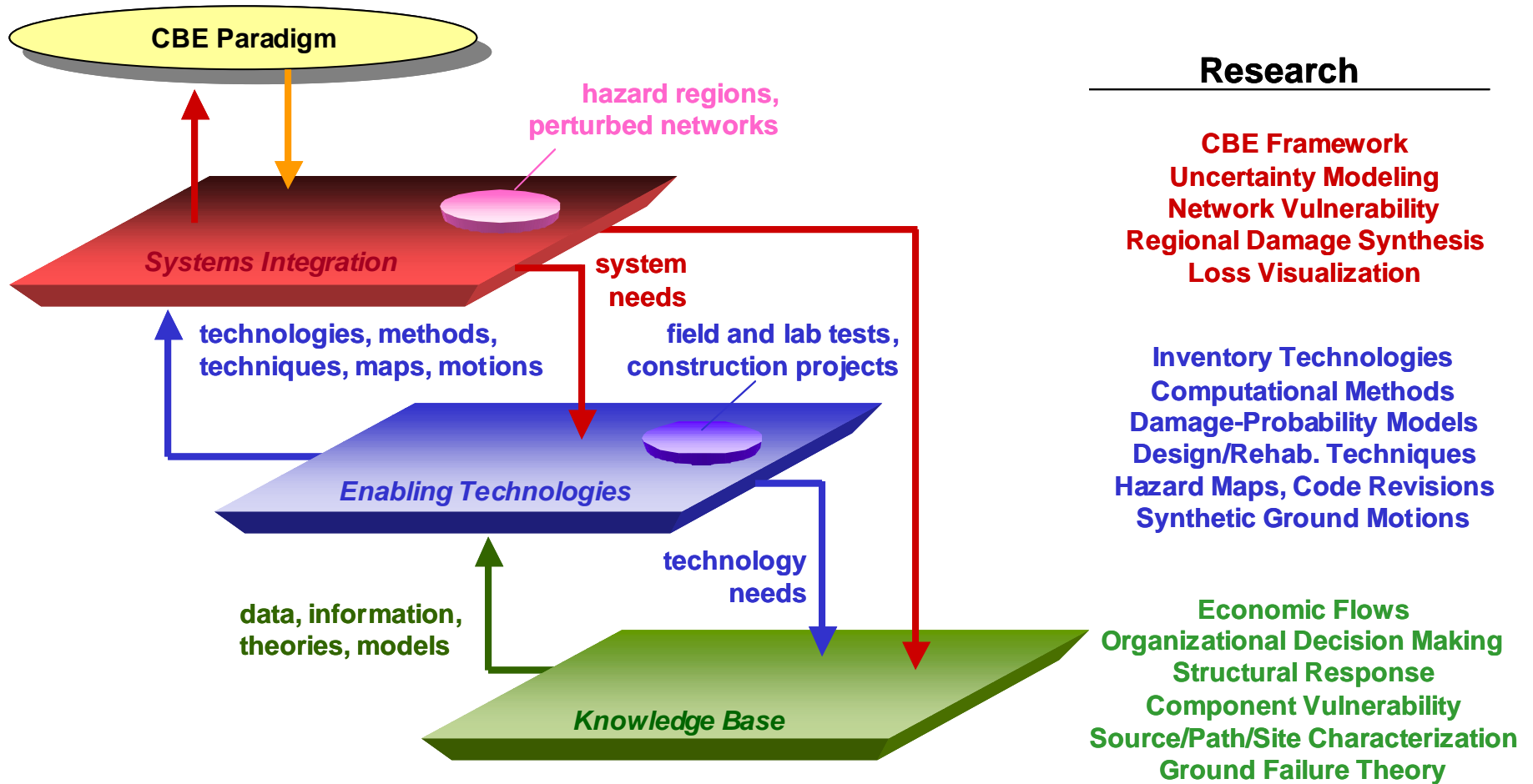


Fig. 1 Systems approach to research planning

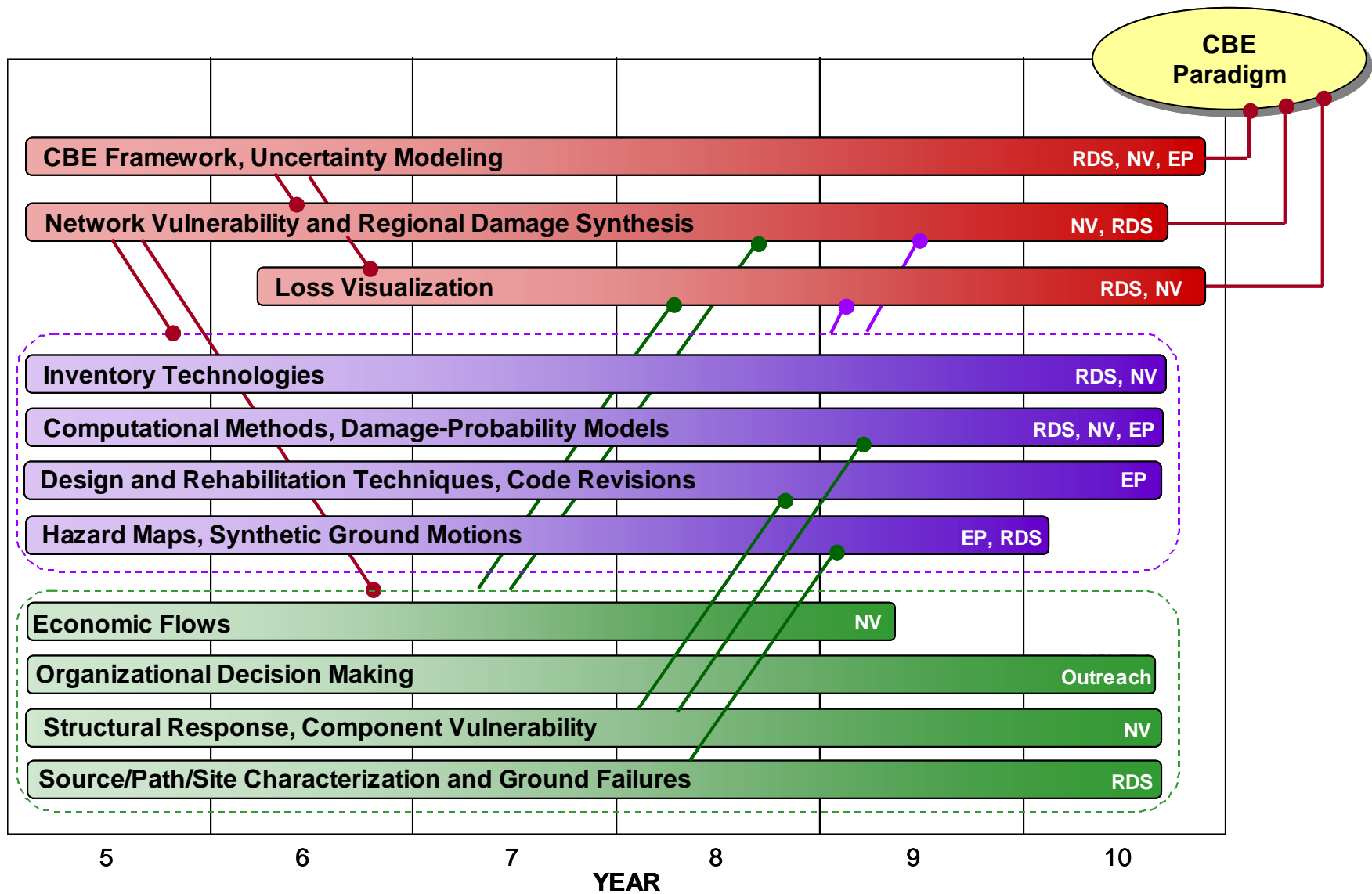


Fig. 2 Interdependency of research towards development of Consequence-Based Engineering paradigm

decision making, dynamic response of structural systems and behavior of components and materials, and the basic nature of ground motions and ground failures including liquefaction.

The coherency of the research plan is further illustrated in Figure 2 where project groupings for the three planes are shown on a timeline through the tenth year of the Center. Projects on CBE framework development and uncertainty modeling drive the Center research in an obvious top-down manner in such a way that results of the core research thrusts and the capstone project on loss visualization will feed into necessary development of the CBE paradigm.

Research Thrust Areas

Core research thrust areas as noted in Figure 3 provide the organization for systems-level research needed to better define seismic hazards, response and vulnerability of the built environment, losses to human life and economies, and societal response. The first core thrust area is termed *Regional Damage Synthesis* and develops technologies needed to simulate seismic response of the built environment across regions of interest, and includes research to simulate ground motions, response of construction and response of societal groups. The second core program, *Network Vulnerability*, develops modeling tools needed to assess economic losses across various types of regional or national networks ranging from transportation to power and pipeline networks. The third core program, *Engineering Provisions*, researches and develops new improvements in engineering methods for constructing new structures, and rehabilitating existing ones, to resist earthquakes of the kind anticipated to occur in Mid-America.

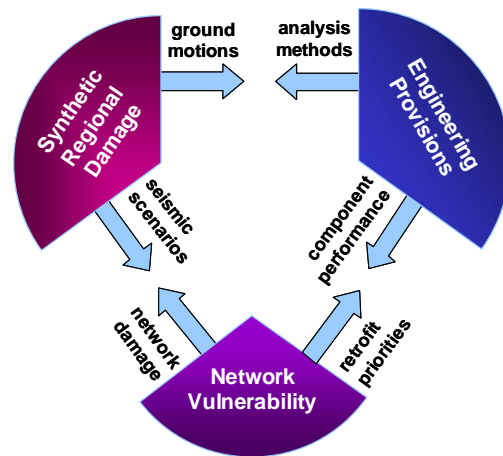


Fig. 3 Core research thrust areas

Stakeholder research thrusts serve to apply core research results to earthquake hazards mitigation across relevant systems of interest. These stakeholder thrust areas yield products and outcomes that impact the marketplace and environment specific to any stakeholder group. As noted with the triangularly shaped areas in Figure 4, the first four stakeholder research thrust areas include a diverse portfolio of interests in the public and private sectors including insurance, construction industries, transportation and owners of large building stocks. These four areas have been selected to make the optimal impact on earthquake mitigation in the eastern and central United States. Work of the transportation group applies to national networks spanning the entire focus region while work of the building owners and construction industries group focuses on systems of construction over regions of interest. The fourth stakeholder thrust area on insurance transfers technology and knowledge of the Center's core research to enhanced knowledge of earthquake risks that will influence premium and

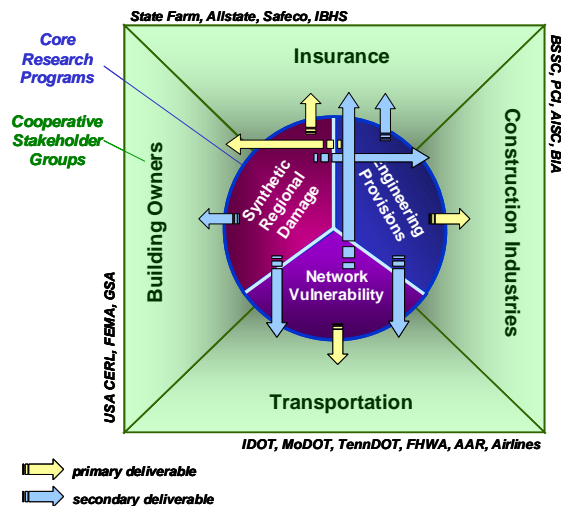


Fig. 4 Integration of core research and stakeholder research

deductible rates offered in the near future. Also, the insurance group best follows the model of an industry cooperative (as this industry has done in the past through the Institute of Business and Home Safety) to pool its resources to research and solve common problems.

Interdisciplinarity of Research

The Center believes that the objective of seismic risk mitigation can only be achieved through the integrated deployment of expertise in diverse disciplines. In particular, the new thrust area in Regional Damage Synthesis is reflective of the Center internalizing this core value within its strategic planning process. Projects in formerly isolated disciplines ranging from urban planning, earth sciences, computer science, social science, economics, structural engineering and geotechnical engineering are being worked on by cross-disciplinary teams to yield system-wide results that will be of use by a variety of disciplines. Interdisciplinarity is even more vivid with the Network Vulnerability thrust area that combines best practices and new developments in optimization, structural response, economic modeling, and systems engineering, and will add in the near future site response and liquefaction susceptibility.

Modeling Uncertainty

Uncertainty is a common feature inherent in each of the three core thrust areas. Regional damage synthesis, network vulnerability and code provisions each deal with the same chain of events, from the seismic source to excitation to damage and loss. Uncertainties in each element of the chain, as well as the linkage between any two elements, are modeled within the framework. To account for uncertainty and its propagation through the chain, statistics of each element, structural response, damage, loss and regression analyses are used. Because of the large number of random variables and analyses involved, development of an efficient methodology for representing uncertainty at all levels of the research program is necessary.

A simulation-based procedure is being developed to consider uncertainty using uniform-hazard ground motions based on seismicity of the region and available ground motion models.

This procedure can be used to capture effects of uncertainty from source to structural response. Development of the uncertainty framework will include identification and quantification of sources of uncertainty in each of the elements and links in the three thrust areas, and incorporation of the uncertainty in performance/loss estimates. Critical uncertainties need to be examined including occurrence rates and size of large seismic events, attenuation relations and site conditions associated with ground motions in Mid-America.

CONCLUSIONS

This paper has presented a brief summary of research for the Mid-America Earthquake Center that is directed towards development of a new paradigm for earthquake engineering known as Consequence Based Engineering. Core and stakeholder research thrust areas have been described that coordinate systems-level research towards this goal. This presentation has been made in the hope that these concepts and research projects will stimulate ideas regarding potential collaboration between the MAE Center and KEERC on common problems related to engineering methods for the constructed environment in moderate earthquake zones. Additional information on the Center's research, education and outreach programs can be found on their website (<http://mae.ce.uiuc.edu>).

ACKNOWLEDGMENTS

The Mid-America Earthquake Center is supported by the National Science Foundation through the Earthquake Engineering Research Centers Program under award number EEC-9701785.



KEERC-MAE Joint Seminar on
Risk Mitigation for Regions of Moderate Seismicity
University of Illinois at Urbana-Champaign, August 5-8, 2001



Sponsors: Korea Science and Technology Foundation, U.S. National Science Foundation, Brain Korea 21



A Research Plan Leading to Probabilistic Seismic Hazard Maps for Korea

Robert B. HERRMANN¹, and Kiehwa LEE²

¹ *Professor of Geophysics, Saint Louis University
Macelwane Hall, 3507 Laclede Avenue, St. Louis, MO 63103, USA
email: rbh@eas.slu.edu*

² *Professor of Geophysics, Department of Geological Sciences, Seoul National University
Seoul 151-742, Republic of Korea
email: kihwalee@plaza.snu.ac.kr*

ABSTRACT: Probabilistic seismic hazard maps can be prepared for Korea. The procedure requires quantifying seismicity rates and locations, maximum magnitudes and ground motion scaling. Given past work on seismicity, the future task is to convert this information into spatial activity rates. In addition work on a quantitative estimate of ground motion is required. It may be possible to generate prototype maps in as few as two years.

KEYWORDS: seismicity, probabilistic seismic hazard maps, ground motion scaling, maximum magnitude

INTRODUCTION

Seismic hazard maps are a tool for design and regulation. If much is known about the earthquake process, site-specific deterministic estimates can be made of the expected ground motion. If there are uncertainty about the earthquake process and the ground motion attenuation relations, probabilistic seismic hazard analysis is a tool for quantifying those uncertainties.

As a modern industrial society Korea should be concerned about the effect of earthquakes on its infrastructure and should strive for a logical framework for making decisions about seismic hazard and aseismic design. It is time to begin the development of probabilistic seismic hazard maps for the nation.

REQUIREMENTS FOR PROBABILISTIC SEISMIC HAZARD MAPS

Seismic hazard analysis requires the following questions to be answered:

- where do earthquake occur?
- how often to the recur?
- how big can they be?
- what is the ground motion at the site for a given sized earthquake?

The response to these questions is easily obtained. In some cases the answers will only be approximate until new data and research are performed. In other cases, we may never know the answer, e.g., for the maximum earthquake size, but we are still required to provide the best possible set of design parameters.

LESSONS FROM THE EASTERN UNITED STATES

Although it may seem that seismic hazard is well understood in the United States, vast portions of the country in the eastern and central United States are known to have an earthquake problem which is poorly quantified because of the infrequency of large earthquakes. Thus the important parameters of maximum magnitudes and ground motion scaling for large earthquakes are poorly defined. On the other hand significant progress has been accomplished during the 1990's and hopefully the quantitative assessment of earthquake hazard is converging.

The procedure used in generating the 1996 NEHRP (National Earthquake Hazard Reduction Program) maps is described in a series of papers [1,2,3]. The 1996 maps were the result of a lengthy consensus building process that involved meetings of geologists, seismologists, statisticians and engineers so that the lack of knowledge in the input parameters could be quantified. The 1996 NEHRP maps form the basis for current design in the United States and are being upgraded on a biennial schedule.

The important lesson for Korea is that a framework for hazard map generation and review was established, a framework that is capable of accepting new knowledge as it becomes available.

APPLICATION TO KOREA

Given the requirements for seismic probabilistic seismic hazard analysis, what is the status of current knowledge for Korea and what must be learned?

Seismicity

Significant work has been performed in compiling an earthquake catalog for Korea. These catalogs cover the historical record as well as the more modern period of the past 100 years. Figure 1 presents the locations of known earthquakes as obtained from two catalogs: the historical catalog compiled by one of the authors and the modern catalog obtained from KMA.

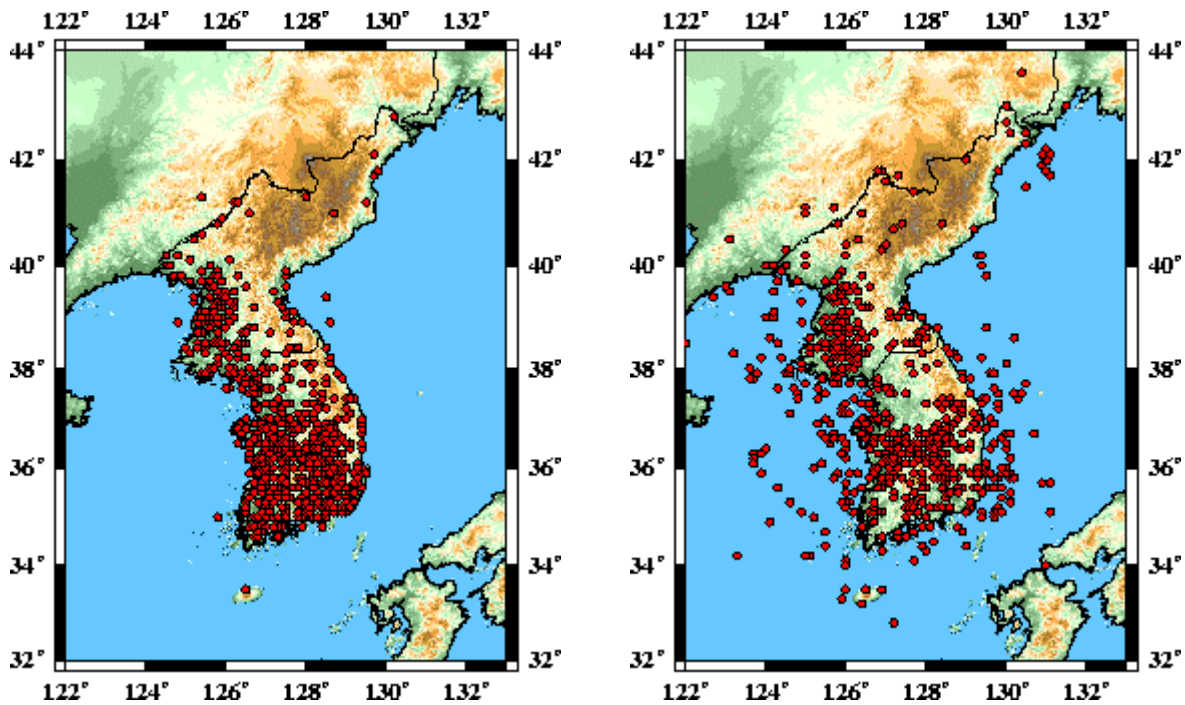


Figure 1 Seismicity patterns in Korea: historical record from 0 – 1905 CE (left), modern record from 1905 – 2000 (right). Earthquake magnitudes are not indicated.

The questions to be addressed are the assignment of earthquake magnitude to the historical events for which only intensity is known. This requires in turn the evaluation of the magnitude scale. The modern seismicity pattern is similar to the historical pattern, but, as expected, is better defined spatially. The pattern is not uniformly distributed through the peninsula.

The objective of the seismicity studies will be to define the earthquake activity rates as a function of magnitude and location and also the maximum expected earthquake.

Ground motion scaling

Ground motion scaling is a more difficult problem. Fortunately the ground motions are the composite effect of the earthquake source, wave propagation and the local site condition. Source scaling in Korea is a major unknown, but perhaps the scaling of earthquakes in the same geological province, the northeast China platform, can be applied to Korea.

The wave propagation characteristics within the Peninsula can be constrained by weak-motion seismic waveform data from the current seismic stations in Korea. Figure 2 shows the current KMA stations in the southern part of the peninsula. At the current rate of activity, of about 50 small earthquake per year, and the expectation of at least one $M \sim 4$ earthquake during the next 5 years, sufficient data will be acquired to constrain geometrical spreading and Q . The combination of modern waveform modeling techniques and the occurrence of the $M \sim 4$, will permit the development of a moment-magnitude scale for the peninsula.

SUMMARY

Probabilistic seismic hazard maps can be constructed for Korea. This task will require cooperation and input of geologists, seismologists and engineers. Research can be initiated now to gather the data required to accomplish this task.

REFERENCES

1. Frankel, A., "Mapping Seismic Hazard in the Central and Eastern United States", *Seismol. Res. Letters*, Vol 66, No. 4, pp 8-21.
2. Frankel, A., C. Mueller, T. Barnhard, D. Perkins, E. V. Leyendecker, N. Dickman, S. Hanson and M. Hopper, "National Seismic Hazard Maps: Documentation June 1996", *U. S. Geological Survey Open-File Report 96-532*, 70 pp.
3. Wheeler, R. L., and A. Frankel, "Geology in the 1996 USGS Seismic-hazard Maps, Central and Eastern United States," *Seismol. Res. Letters*, Vol 71, N. 2, pp 273-282.

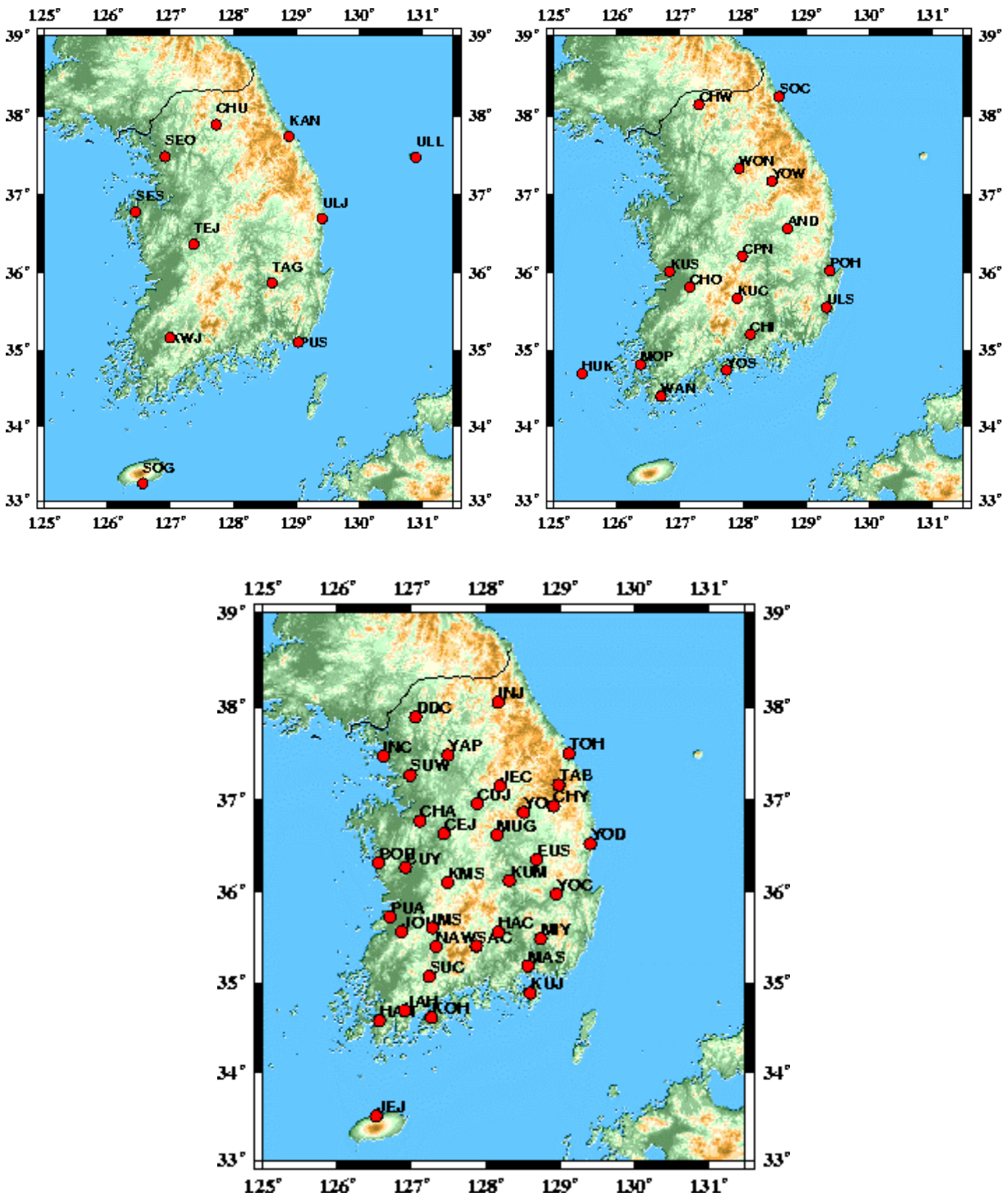


Figure 2 Current distribution of KMA stations in Korea: STS-2 broadband sensors (upper left), short periods sensors (upper right) and Episensor strong motion sensors (bottom)



Prediction of Strong Ground Motions in Southern Korea

Chang-Eob BAAG¹

¹ Professor, School of Earth and Environmental Sciences, Seoul National University
San 56-1, Sillim-dong, Gwanak-gu, Seoul 151-742, Korea
email: baagce@snu.ac.kr

ABSTRACT: Seismic parameters for computation of ground motions in Southern Korea are obtained from recently recorded data, and site-independent regional and site-dependent local strong ground motions are predicted using efficient computational techniques. For the computation of ground motions, we devised an efficient procedure to compute site-independent κ_q and dependent κ_s values separately. The first step of this procedure is to use the coda normalization method for computation of site independent Q or corresponding κ_q value. The next step is the computation of κ_s values for each site separately using the given κ_q value. For computation of ground motions the empirical Green's function (EGF) is modified to account for the depth and distance variations of subevents on a finite fault plane. The original empirical Green's function is deconvolved by the theoretical Green's function corresponding to the source depth and epicentral distance and then convolved with the theoretical Green's function corresponding to the subevent at different locations on the fault plane. The theoretical Green's function in layered medium is computed using wavenumber integration technique. The site independent ground motions in southern Korea and site dependent ground motions at seismic stations in southeastern local area were properly simulated using stochastic simulation method for finite fault model and modified empirical Green's function method in layered medium, respectively. The proposed method and procedures for estimation of site dependent seismic parameters and ground motions could be efficiently used in the low and moderate seismicity regions

KEYWORDS: Site-dependent kappa value, Stress drop, Strong ground motion, Modified empirical Green's function, Layered velocity structure, Stochastic simulation, southern Korea.

INTRODUCTION

The Korean Peninsula is classified as an intraplate region with moderate seismicity. During the period of two thousand years from AD 2, about 2000 earthquakes were reported in the Korean Peninsula. Definition of the terms, "historical" and "instrumental" for earthquakes in Korea is based on the date of installation of a modern seismograph in Incheon during the year 1905. Earthquakes occurred in or after this year are called instrumental or instrumentally-recorded earthquake, even though the number of stations is small and the quality of recording is poor in early dates, especially before the year 1978. In some documents, the style of descriptions of earthquake occurrence is similar to those of historical time. On the other hand, earthquakes occurring during the time of AD 2 - 1904 are called historical earthquakes. In the historical time, there were about 50 earthquakes for which damages and loss of lives were reported. In the 20th century, about 20 earthquakes with magnitudes equal to or greater than 4.5 have occurred in the Peninsula. The seismic activity in some periods of historical time, especially in the 16th and 17th centuries was very high. On the other hand, there have been no significantly large, damaging earthquakes in the 20th century, in which instrumental recordings are available. Thus the seismicity of Korea is characterized by moderate seismicity with long return period of large earthquakes. Since the year 1978, a few seismic networks with small number of stations have been operated. Korea has only a few years of accelerogram recording history. Since relatively low seismic activity in the 20th century compared to previous time, there has been no instrumentally recorded strong motion data. Therefore, we need to predict strong ground motions using the information on the source parameter and wave propagation constants and using efficient computational methods.

Strong ground motions can be computed provided that information on the seismic parameters such as seismic moment, corner frequency of the source spectrum, stress drop, and propagation constants. We try to devise efficient techniques to compute strong ground motions in low or moderate seismicity regions such as Korea. We propose a new procedure to compute site-independent κ_q and dependent κ_s values separately. This procedure is to use the coda normalization method (Frankel et al., 1990) for the computation of site independent Q or corresponding κ_q value as the first step followed by next step, the computation of κ_s values for each site separately using the given κ_q value. Once these seismic parameters are obtained, we can compute ground motions using several methods. In the conventional EGF method (example: Frankel, 1995) for the estimation of ground motion, the accelerogram called EGF recorded by an event at a fixed source depth is used as a component wave common to all subevents on the fault plane. However, the subevent generated near the surface will produce different waveforms from those of events at depth. Therefore, we convert the prototype EGF to the EGFs appropriate to the wave path of subevents using theoretical Green's function in layered medium. The original empirical Green's function is deconvolved with the theoretical Green's function corresponding to the source depth and epicenter distance and then convolved with the theoretical Green's function corresponding to the subevent at different source depth and epicentral distance. The theoretical Green's function in layered medium is computed using wavenumber integration technique. The site independent ground motions in southern Korea and site dependent ground motions at seismic stations in southeastern local area were

simulated using stochastic simulation method for finite fault model and modified empirical Green's method in layered medium, respectively.

ESTIMATION OF SITE DEPENDENT SEISMIC PARAMETERS

The propagation constant κ consists of site-specific κ_s and attenuation part $\kappa_q R$ where κ_q is related to the quality factor Q and R is the hypocenter distance. Usually, the kappa value is obtained by measuring the slope of acceleration spectrum. We used 50 seismograms from 11 stations recorded by 16 earthquakes in southeastern Korea in the period from January 4th of 1999 to April 16th of 2001 (Table 1, Fig. 1). Computed kappa values were plotted in the distance range. However, it is difficult to fit the computed values to a linear curve due to scattering of points of values. This fact implies the computed kappa values are highly contaminated by the site effect of stations. We need to devise a new procedure to compute site-independent κ_q and dependent κ_s values separately. The first step of this procedure is to use the coda normalization method (Frankel, 1990) for the computation of site independent Q or corresponding κ_q value. This is done by normalization of the S wave spectrum by that of the coda wave, which leads to cancellation of the site amplification effect common to both waves. Values of the ratio for frequency points of spectrum from 11 stations are inverted to get the quality factor Q value of 2023. This value corresponds to the κ_q value of 0.0001413 which indicates the slope of linear curve in the κ - R relation. The next step is the computation of κ_s values for each site separately using the given κ_q value of 0.0001413 (Fig.2). The result of computation shows variation of κ_s values from -0.01087 at the GKP station to 0.03588 at the UJA station (Table 2, Fig. 3).

The computed κ values at each station are used to convert the data spectrum to the source spectrum in which the propagation and site effects are removed. The source spectra of the three small-to-medium-sized earthquakes of the year 1999 were obtained by conversion of the recorded data. The earthquakes are the April 24 event with the moment magnitude 3.1, June 2 event with 3.8, and the September 12 event with 3.4 (Table 3, Fig. 4). Epicenters of the three events are almost the same near the city Gyeongju (Fig. 5). The low frequency spectral levels, corner frequencies, and stress drops of the events are computed from the source spectra using Andrews' spectral integration method (Andrews, 1986; Snoke, 1987). The computed stress drops of the three events are 48, 44, and 99 bars, respectively (Fig. 6). The average value of the stress drop obtained with weighting factor based on the number of data is 78 bars.

ESTIMATION OF GROUND MOTIONS BASED ON EMPIRICAL GREEN'S FUNCTION METHOD MODIFIED FOR THE PATH EFFECTS IN LAYERED STRUCTURE

The empirical Green's function in engineering seismology is the recording of ground motion at a specific site caused by a small earthquake on a causative fault of a possible large earthquake. The EGF contains site response, scattered waves and path effects of the waves. Scaled EGFs from subevents at all the subfaults on a finite fault are summed to get simulated synthetic seismogram for a large earthquake. However, the summation of the small event responses cannot produce the low frequency contents of a large earthquake. In order to compensate this low frequency problem in the method, a relative slip velocity function is convolved with the EGF sum. In the conventional EGF method (example: Frankel, 1995) for the estimation of ground motion, the accelerogram recorded by an event at a fixed source depth is used as a component wave common to all subevents on the fault plane. However, the subevent generated near the surface will produce different waveforms from those of events at depth. Therefore, we need a procedure to convert the prototype EGF to the EGFs appropriate to the depths and epicentral distances of corresponding subevents. We propose a method to avoid the problem by using theoretical Green's function in layered medium (Fig. 7). The original empirical Green's function is deconvolved with the theoretical Green's function corresponding to the source depth and epicenter distance and then convolved with the theoretical Green's function corresponding to the subevent at different source depth and epicenter distance. The theoretical Green's function in layered medium is computed using wavenumber integration technique. The crustal structure of Chang and Baag (2001) is used for the layered medium. For the prototype empirical Green's function, accelerograms recorded at stations by the June 2, 1999 Gyeongju earthquake were used. Simulated strong ground motions at each station for magnitude 7.0 earthquakes show variation of waveforms depending on the site effects (Fig. 8).

COMPARISON OF THE SIMULATED SITE-DEPENDENT LOCAL GROUND MOTIONS WITH SITE-INDEPENDENT REGIONAL ESTIMATIONS BY STOCHASTIC SIMULATIONS

In order to estimate the source parameters and propagation constants in regional area of southern Korea, data set 64 event-station pairs for the κ value estimation and 40 event-station pairs for the estimation of the stress drop was used. The κ value was computed by conventional spectral slope method (Anderson and Hugh, 1984). Data highly contaminated by site effects were eliminated from the analysis in order to get seismic parameters corresponding to site-independent regional property. The computed values of κ_q and stress drop are 0.000147 and 65 bars, respectively. These values for southern Korea are not far from the local values 0.0001413 and 78 bars for the southeastern Korea. Strong ground motions at distances up to 500 km of regional area in southern Korea were computed for earthquake magnitudes from 4 to 7 using the site independent seismic parameters (Fig. 9). The site dependent strong ground motions corresponding to seismic stations spread at distances up to 200 km were also

computed for earthquake magnitude 7 using the site dependent local seismic parameter. In comparison of these two types of ground motions for magnitude 7 event, the trends of the ground motion curves in distance are similar, but there are significant deviations depending on sites due to the local site effects (Fig. 9).

CONCLUSION

The site independent ground motions in southern Korea and site dependent ground motions at seismic stations in southeastern local area were properly simulated using stochastic simulation method for finite fault model and modified empirical Green's method in layered medium, respectively. In order to reduce scatters in computed source parameter and propagation constant values, the quantity of data should be accumulated.

The proposed method and procedures for estimation of site dependent seismic parameters and ground motions could be efficiently used in the low and moderate seismicity regions.

REFERENCES

1. Anderson, J., and Hough, S., "A model for the shape of the Fourier amplitude spectrum of acceleration at high frequencies", *Bull. Seism. Soc. Am.*, 74, 1998, pp. 1969-1993.
2. Andrews, D. J., "Objective determination of source parameters and similarity of earthquakes of different size", in *Proc. 5th Maurice Ewing Symp. Earthquake Source Mechanics*, S. Das, J. Boatwright, and C. H. Scholtz, Editors, American Geophysical Union, Washington, D.C., 1986, pp. 259-267.
3. Chang, S. J., and Baag, C.-E., "*Crustal velocity structure in southeastern Korea from broadband seismic data*", in preparation.
4. Frankel, A., " *Simulating strong motions of large earthquakes using recordings of small earthquakes; The Loma Prieta mainshock as a test case* " , *Bull. Seism. Soc. Am.*, Vol.85, No. 4, 1995, pp.1144-1160.
5. Frankel, A., McGarr, A., Bicknell, J., Mori, J., Seeber, L., and Cranswick, E. " *Attenuation of high-frequency shear waves in the crust; measurements from New York state, South Africa, and southern California* " , *J. Geophys. Res.*, Vol. 95, 1990, 441-17447.
6. Snoke, A., "Stable determination of (Brune) stress drops", *Bull. Seism. Soc. Am.*, 77, 1987, pp. 530-538.

Table 1 List of events used for estimations of site-dependent spectral decay constant κ .

Year	Month	Day	Lat. (°N)	Lon. (°E)	Mag.	Year	Month	Day	Lat. (°N)	Lon. (°E)	Mag.
1999	01	24	37	128.8	3.3	2000	04	15	36.6	128.3	2.3
1999	04	07	37.2	128.9	3.3	2000	05	09	35.2	128.1	2.3
1999	04	24	35.85	129.27	3.1	2000	05	19	36.3	128.5	2.7
1999	06	02	35.85	129.27	3.8	2000	08	06	36.3	128.4	2.2
1999	09	12	35.85	129.26	3.4	2000	09	23	35.6	128.4	2.4
1999	12	20	36	128.4	2.5	2000	10	08	37.3	128.8	2.6
1999	12	27	36.8	128.2	3.0	2001	02	14	36	128.2	2.2
2000	02	21	35.8	128.2	2.1	2001	04	16	35.9	129.7	2.2

Table 2 Computed site-dependent κ values at stations.

Station	WSA	WSB	WSC	WSN	KRA	KRB	KOR	UJA	TAG	GKP	PUS
κ	0.02647	0.01337	0.01732	0.02885	0.03300	0.01513	0.02577	0.03588	0.002665	0.01087	0.01302

Table 3 Source orientations of the three 1999 Gyeongju earthquakes.

Event	Latitude	Longitude	Depth (km)	Strike (°)		Dip (°)		Rake (°)	
1999-04-24	35.8467°N	129.2665°E	6.76	155	11	15	78	55	99
1999-06-02	35.8467°N	129.2672°E	6.80	140	10	20	80	45	105
1999-09-12	35.8522°N	129.2578°E	6.93	100	10	80	85	10	175

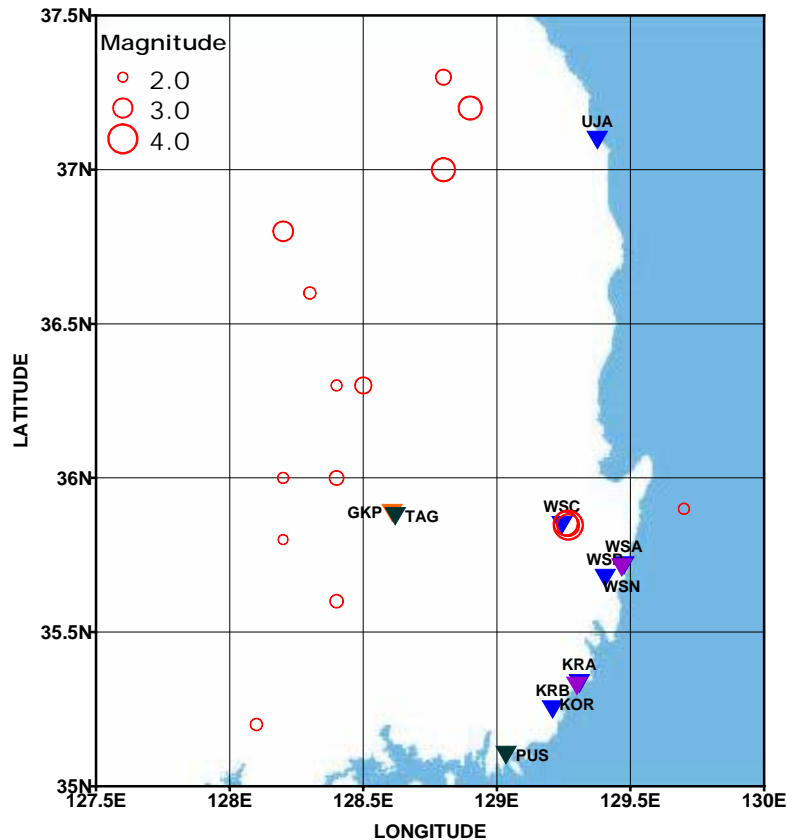


Figure 1 Distribution of epicenters and stations used for the estimation of spectral decay constant κ .

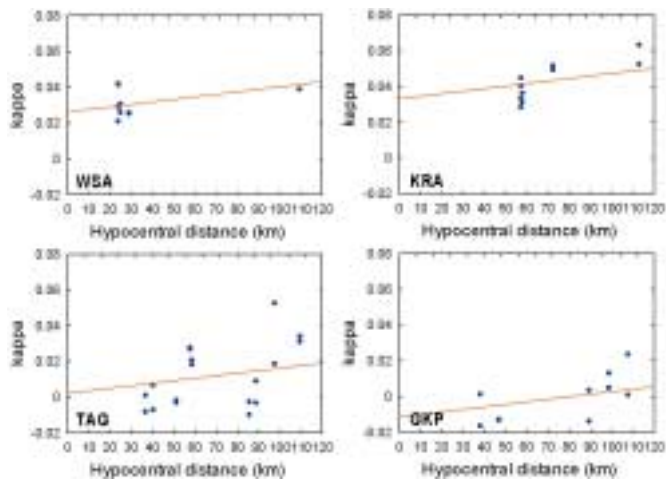


Figure 2 Example for determination of site-dependent κ_s value at each station for a fixed κ_f value.

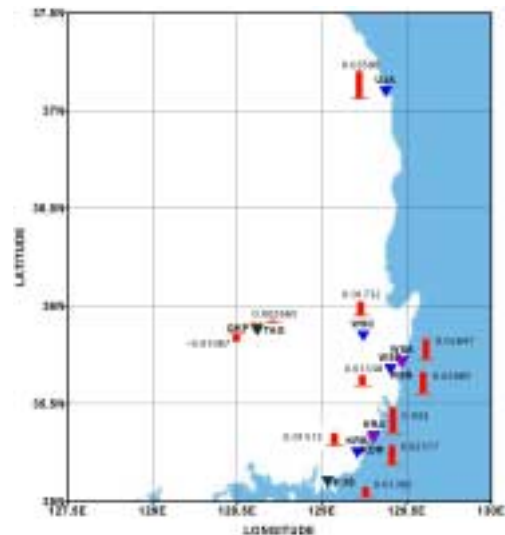


Figure 3 Distribution of site-dependent κ_s value.

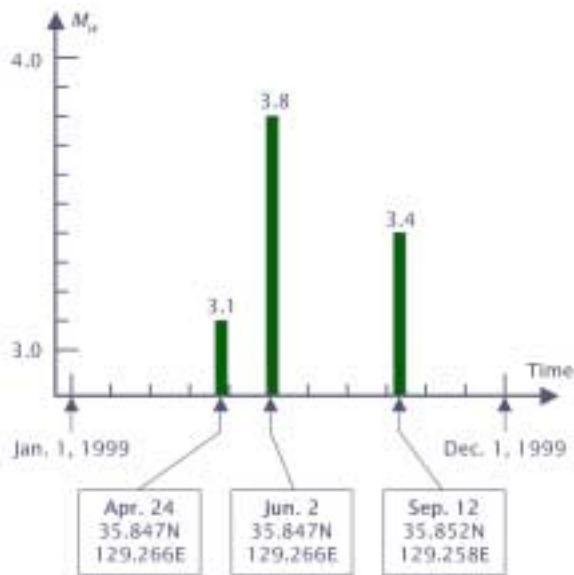


Figure 4 Temporal variation of magnitude of the three 1999 Gyeongju earthquakes.

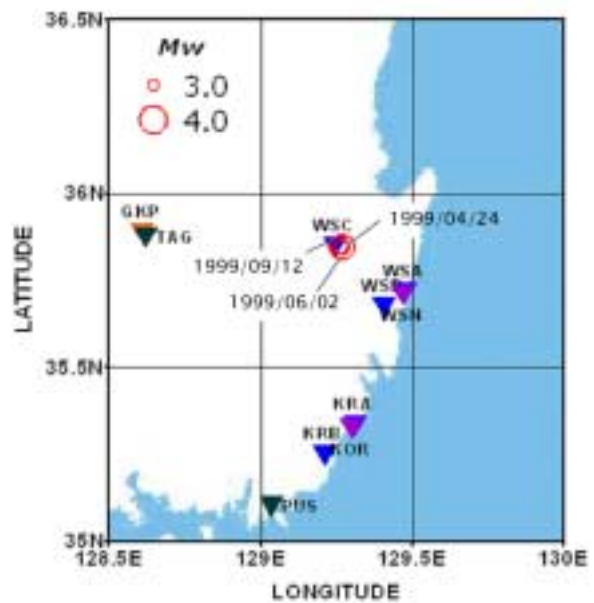


Figure 5 Locations of the three 1999 Gyeongju earthquakes and seismic stations.

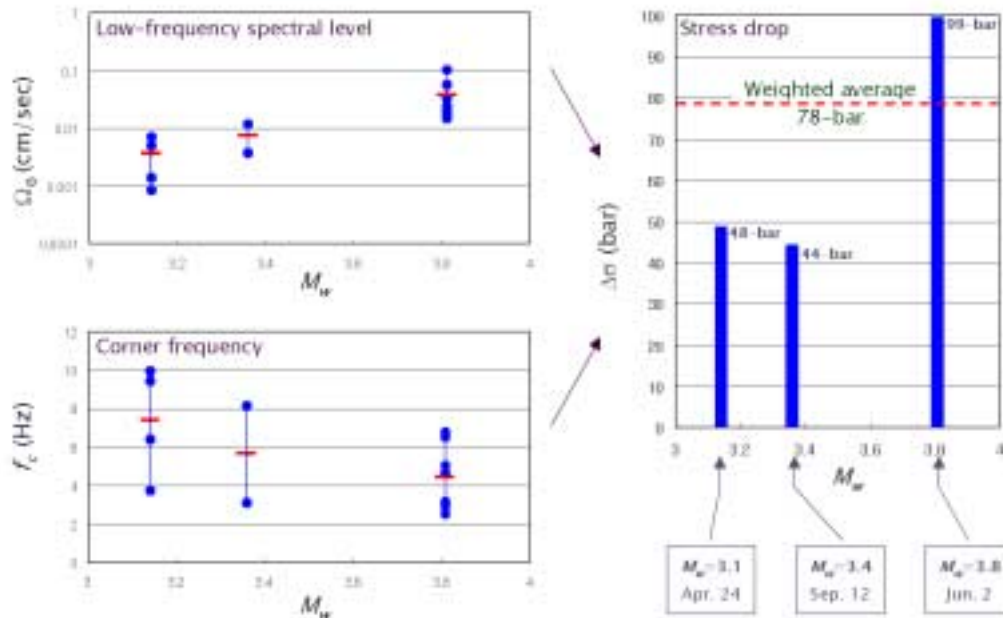


Figure 6 Computed source parameters of the three 1999 Gyeongju earthquakes.

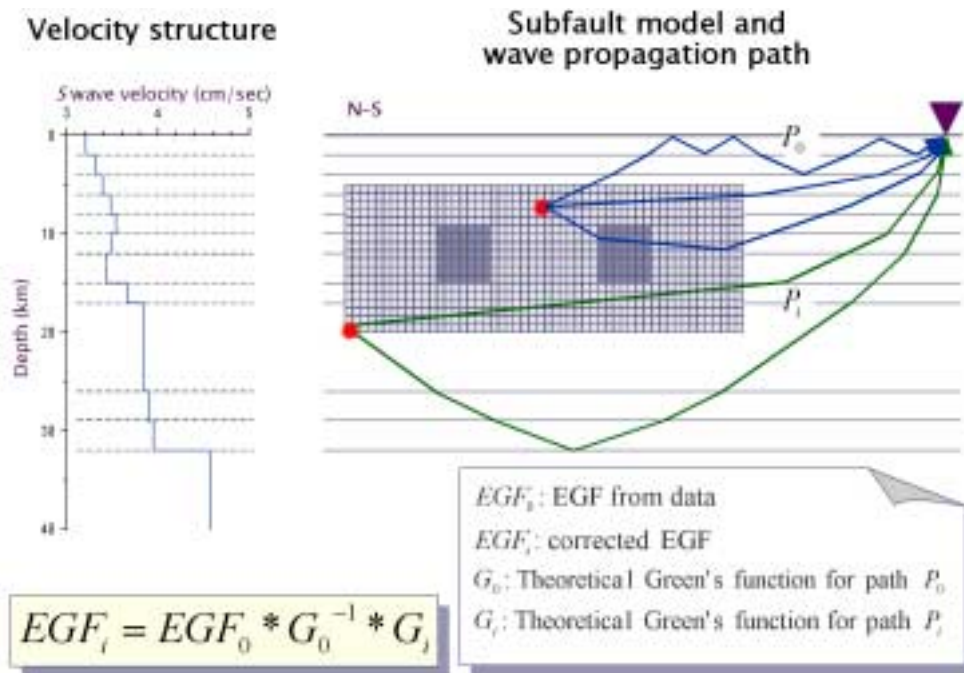


Figure 7 Schematic diagram for the concept of the path correction of the EGF in layered structure.

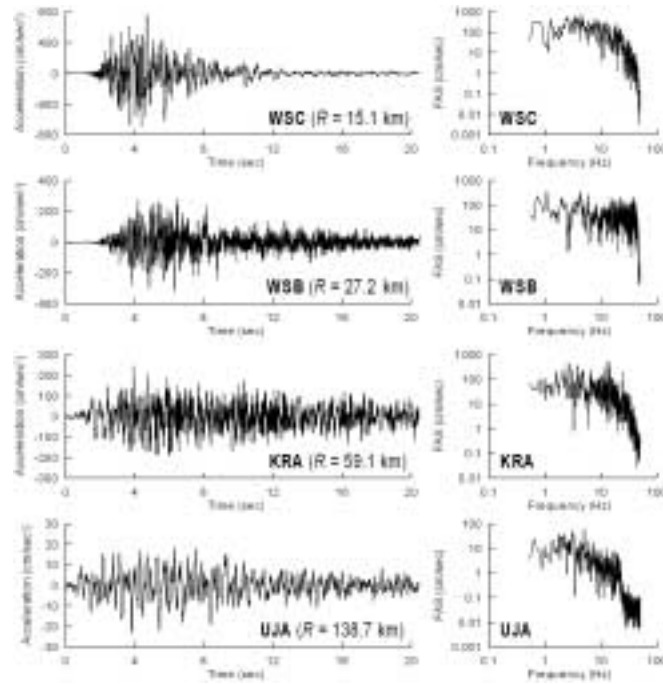


Figure 8 Synthetic seismograms obtained using path-corrected EGFs of the 1999/06/02 Gyeongju earthquake.

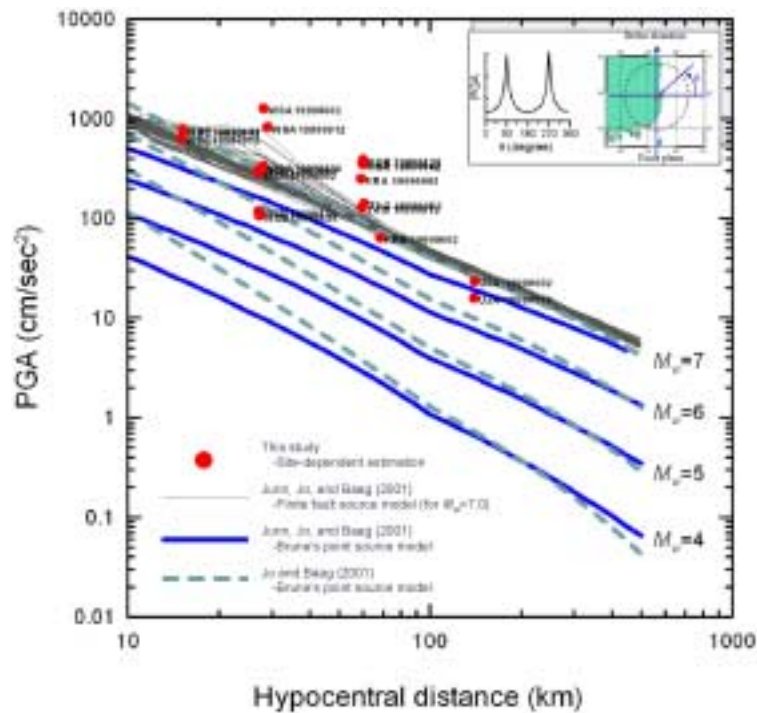


Figure 9 Comparison of the simulated site-dependent local ground motions with regional estimations obtained by stochastic simulations.



KEERC-MAE Joint Seminar on
Risk Mitigation for Regions of Moderate Seismicity
University of Illinois at Urbana-Champaign, August 5-8, 2001



Sponsors: Korea Science and Technology Foundation, U.S. National Science Foundation, Brain Korea 21



Modeling Site Amplification of Ground Motion

Youssef M. A. HASHASH¹ and Duhee PARK²

¹ *Assistant Professor, University of Illinois at Urbana-Champaign,
205 N. Mathews Avenue, Urbana, Illinois, USA
email: hashash@uiuc.edu*

² *Graduate Research Assistant, University of Illinois at Urbana-Champaign,
2216 Newmark Laboratory, 205 N. Mathews Avenue, Urbana, Illinois, USA
email: dpark1@uiuc.edu*

ABSTRACT : This paper summarizes the development of a new non-linear one-dimensional site response analysis model for vertical propagation of horizontal shear waves in deep soil deposits. The new soil model accounts for the influence of large confining pressures on strain dependent modulus degradation and damping of soil. In addition, new formulation is introduced for the viscous damping matrix. Details of the new model, DEEPSOIL, can be found in [1].

The new model is used to estimate ground motion amplification and attenuation for three soil columns 100 m, 500 m and 1000 m thick, representative of soil thickness variability within the Mississippi Embayment. The new model shows that some high frequency components of ground motion, usually filtered out using conventional wave propagation methods, are transmitted through these deep deposits. Spectral amplification factors of deep deposits are greater than unity and can be as large as 5 in the longer period range of 2-10 sec. Preliminary evaluation of model results show that computed surface response spectra in the period range of 0.5-2 sec are larger than the 1997 NEHRP recommended design response spectrum.

KEY WORDS: Site response, deep deposit, frequency content, nonlinear, amplification, confining pressure, viscous damping

INTRODUCTION

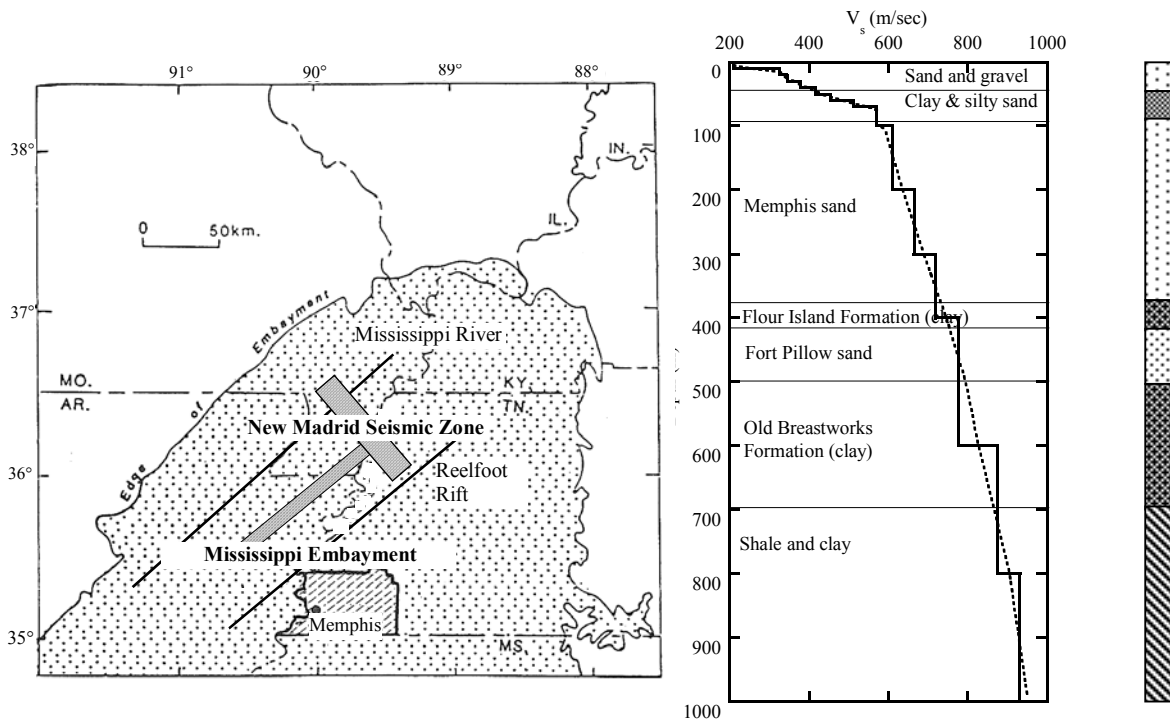
Earthquakes in the New Madrid Seismic Zone (NMSZ) are characterized as low probability, high consequence events. Estimate of ground motion characteristics in the NMSZ is required to assess the seismic vulnerability of structures and the susceptibility of soils to liquefaction. The presence of very deep (up to 1000 m) unconsolidated deposits in the Mississippi Embayment has an important, though poorly understood effect on the propagation of seismic waves.

In the absence of strong motion records, numerical models can be used to develop an understanding of wave propagation characteristics of the Mississippi Embayment. This paper proposes a new one-dimensional, non-linear wave propagation model to account for the effect of very high confining pressures encountered in the Embayment. The model development is based in part on recent data regarding cyclic response of soils under high confining pressures. A series of analyses are presented to illustrate the influence of deep deposits on the amplitude and frequency content of propagated weak and strong ground motions.

THE MISSISSIPPI EMBAYMENT AND NEW MADRID SEISMIC ZONE

The Mississippi Embayment is a syncline or a trough-like depression that plunges southward along an axis that approximates the course of the Mississippi River. The Paleozoic rock forms the bedrock floor of the Mississippi Embayment and is located about 1000 m below Memphis and Shelby County, which is near the central part of the Mississippi Embayment. The presence of thick unconsolidated deposits adds significant uncertainty regarding the nature of seismic ground motion propagation and attenuation in the Embayment. The effect of soil deposits on propagated ground motion is well documented in other parts of the world (e.g. Mexico City, [2]). However, limited information is available regarding wave propagation through very thick deposits (up to 1000 m) such as those found in the Mississippi Embayment.

The geologic layers can be considered nearly horizontal. Analysis of wave propagation through these deposits is approximated as one-dimensional vertical propagation of horizontal shear waves. Three profiles, 1000 m, 500 m, and 100 m deep, shown in **Figure 1**, are selected to represent the range of soil depths encountered in the Embayment ([3],[4]). The 1000 m profile is representative of conditions in the Memphis, Shelby County area while the 100 m profile represents conditions south of the St. Louis Area. The selected shear wave velocity profile is based on a combination of surface information and a few deep wells as compiled by Romero et al. [5]. The density of the soil (ρ) in the columns is assumed to be 1.98 kg/m^3 .



V_s and soil profile at Memphis, TN

Figure 1 Mississippi Embayment and shear wave velocity profiles used in the analysis

ONE-DIMENSIONAL WAVE PROPAGATION IN SOIL DEPOSITS

One-dimensional site response analysis is used to solve the problem of vertical propagation of horizontal shear waves (SH waves) through a horizontally layered soil deposit. Horizontal soil layer behavior is approximated as a Kelvin-Voigt solid whereby constant elastic shear moduli and viscous damping characterize soil properties. Solution of wave propagation equations is performed in the frequency domain. Seed, Idriss and co-workers introduced the equivalent linear approximation method to capture non-linear cyclic response of soil. Modulus degradation and damping curves are then used to obtain revised values of shear modulus and damping.

The equivalent linear approach is computationally easy to use and implement. However, it does not capture the full range of cyclic behavior of soil, including modulus degradation due to number of loading cycles, permanent (residual) straining of soil and excess pore pressure generation. Non-linear analysis is used to capture these important aspects of soil behavior. In this approach, equations of motion and equilibrium are solved in discrete time increments in the time domain. A constitutive model is used to represent soil behavior.

In this approach, equations of motion and equilibrium are solved in discrete time increments in the time domain. The required mass, damping and stiffness matrices M , C , K in this non-linear model are assembled from the incremental properties of the layers, which in turn are obtained from a constitutive model that describes the non-linear behavior of the soil.

NON-LINEAR PRESSURE DEPENDENT CYCLIC SOIL MODEL

The constitutive model used in the analysis is based on modified hyperbolic model [6]. In this model, there is no coupling between confining pressure and shear stiffness. The model is extended in this paper to capture the influence of confining pressure on modulus degradation and damping.

Effect of Confining Pressure on Shear Modulus and Damping

Laird and Stokoe [7] performed resonant column and torsional shear tests at strain levels up to 10^{-3} and confining pressures up to 3.5 MPa using remolded sand specimens, as well as undisturbed specimens of sand, silty sand, silt, lean clay, and fat clay. Low and high amplitude cyclic torsional shear and resonant column tests were used to determine the effect of strain amplitude and confinement on shear modulus and damping curves. In this paper, only results from remolded sand specimens (washed mortar sand) are used. Figure 2 plots the extrapolated modulus degradation curve to an effective stress of 10000 kPa (equivalent to a depth of 1000 m, with the water table at ground surface).

A new formulation for the reference strain is introduced to capture the influence of confining pressure on modulus degradation and damping ratio. Figure 2 shows that using the new formulation; the model can capture the variation in shear modulus measured in laboratory experiments by Laird and Stokoe [7].

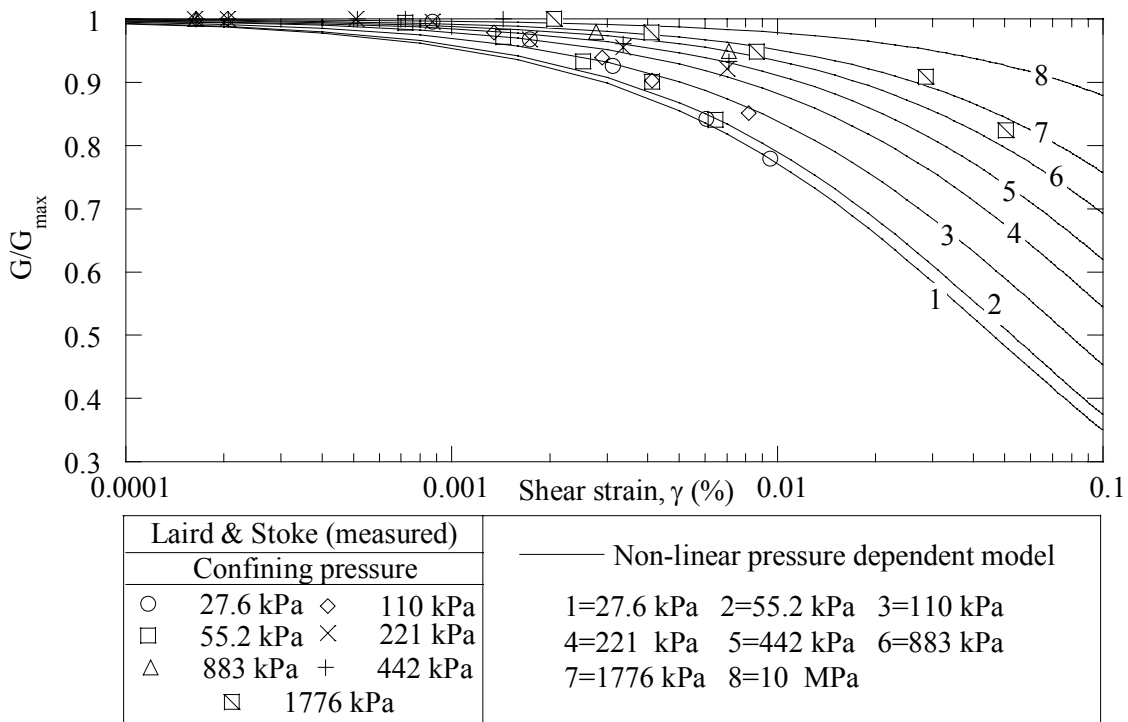


Figure 2 Influence of confining pressure on normalized shear modulus degradation curves in the proposed nonlinear model. Data of Laird and Stokoe shown for comparison

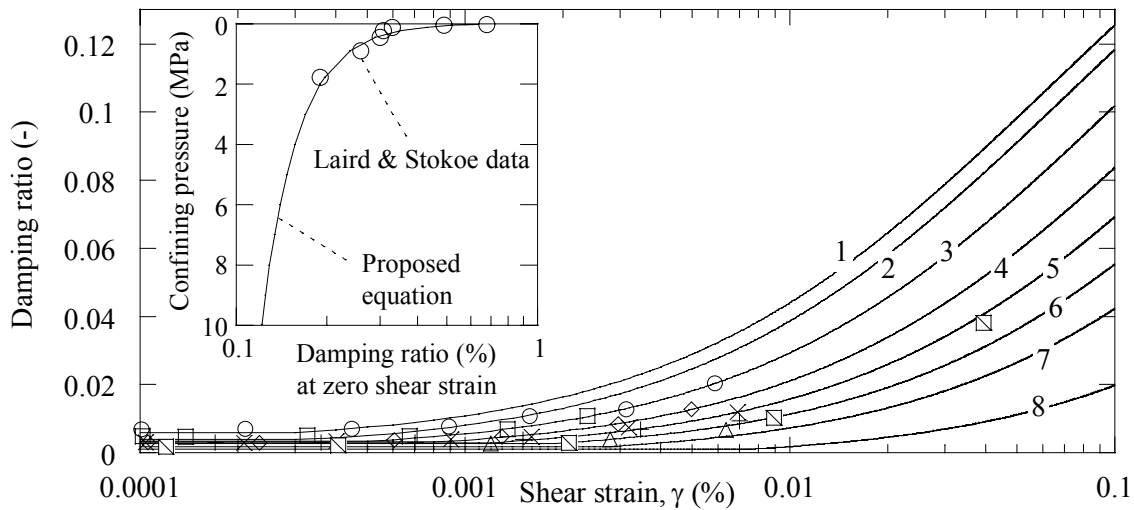


Figure 3 Influence of confining pressure on damping ratio curves in proposed nonlinear model. Data of Laird and Stokoe shown for comparison. Legend shown in Figure 2

Hysteretic damping of the soil model defined by Matasovic [8] can capture damping at strains larger than 10^{-4} to 10^{-2} %, depending on the value of reference strain. However, the hyperbolic model is nearly linear at small strains (less than 10^{-4} to 10^{-2} %) with practically no damping, which can cause unrealistic resonance during wave propagation. The model described by Matasovic [6] incorporates additional damping to the dynamic equation in the form of [C] matrix, using the values of the equivalent damping ratio ξ obtained from the damping ratio curves at small strains (**Figure 3**).

Laird & Stokoe data show a dependency of very small strain soil damping on confining pressure. A new pressure dependent small strain damping is proposed in this paper to describe the dependency of zero strain equivalent damping ratio on confining pressure.

Figure 3 shows a comparison between the small strain damping and Laird & Stokoe data. Figure 3 includes plots of the total damping ratio equal to hysteretic plus small strain damping. The proposed equation captures measured damping at very small strains, as shown in the inset. Total damping curves fall within range of measured data but do not provide an exact fit.

Effect of Viscous Damping Formulation

In a non-linear soil model, soil damping is captured through hysteretic loading-unloading cycles in the soil model. The use of the damping matrix [C] may become unnecessary. The damping matrix may be used as a mathematical convenience or to include damping at very small strains where response of many constitutive models is nearly linear elastic.

[C] is assumed to be independent of strain level and therefore, the effect of hysteretic damping induced by nonlinear soil behavior can be separated from (but added to) viscous damping. The [C] matrix is a combination of the mass matrix and the stiffness matrix. In conventional site response analysis, small strain viscous damping effects are assumed proportional only to the stiffness of the soil layers and that only 1st mode determines the damping matrix. While it is a reasonable assumption in short soil columns, it cannot be applied to thick columns resulting in over-estimation of the damping matrix. It can seriously underestimate the response by filtering out a significant portion of high frequency component.

INFLUENCE OF CONFINING PRESSURE AND NEW VISCOUS DAMPING FORMULATION

The influence of confining pressure on 1-D site response is demonstrated through comparisons of analyses using non-linear, confining pressure-dependent (NLPD) and independent (NLPI) soil models. The difference between the two models can be observed by examining the surface response spectra shown in Figure 4. For a soil thickness of 1000 m, the influence of the confining pressure is very pronounced. Short period spectral accelerations are much larger for the NLPD model compared to the NLPI model. For both models, motion amplification is computed at a period of about $T=5.0$ seconds which corresponds to the theoretical characteristic site period for the 1000 m soil column. Similar observations can be made for the 500 m column. For the 100 m column, response spectra are also similar for $T>0.9$ sec. However, for shorter periods the NLPD model spectral acceleration is larger than that of the NLPI model. The influence of pressure-dependent behavior is still significant for the 100 m thick column.

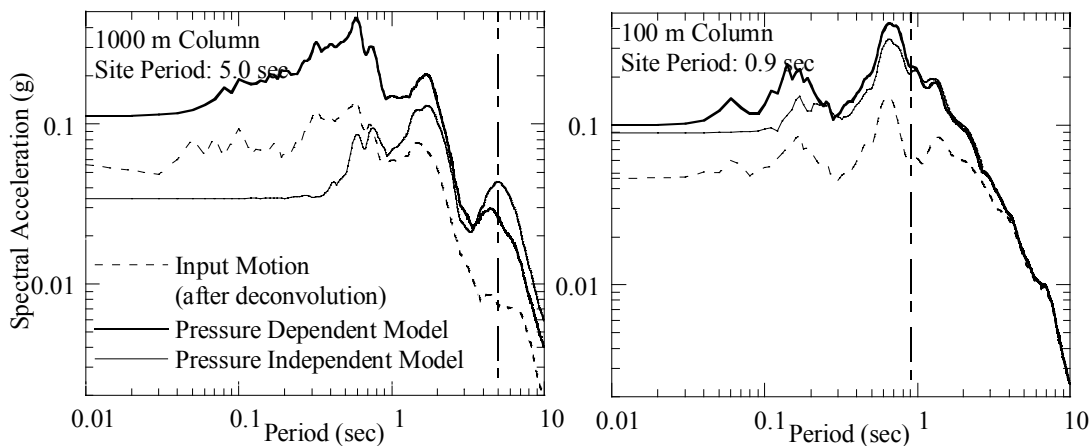


Figure 4 Comparison of surface response spectra, with 5% damping using pressure dependent and pressure independent soil models. Input time series is recordings at Yerba Buena Island during Loma Prieta Earthquake. Note the overall higher spectral acceleration in the pressure dependent model analyses (dark solid lines) compared to pressure independent analyses (light solid lines)

VERIFICATION OF THE MODEL

The new model was verified using ground motion records at Treasure Island-Yerba Buena during the Loma Prieta earthquake (1989). Verification was also done using several records in the Mississippi Embayment during the Warm Springs Earthquake (1999). The computed responses agreed well with those recorded.

RANGE OF COMPUTED SPECTRAL AMPLIFICATION FACTORS IN EMBAYMENT

A measure of the effect of deep soil deposits on propagated ground motion is the spectral amplification factor. The spectral amplification factor is defined as the ratio of surface spectral acceleration to input motion spectral acceleration for a given period or frequency. 13 Input ground motion time series have been selected to include a range of earthquake events at rock outcrop and synthetic time series using the program SMSIM [8] and parameters for the NMSZ (Frankel et al., 1996). The peak accelerations, a_{\max} , range from 0.0073 g to 1.16 g. Three soil columns, 100 m, 500 m and 1000 m thick, shown in Figure 1 are used in the analyses. The non-linear, confining pressure-dependent (NLPD) soil model proposed in this paper is used in most analyses.

Figure 5 plots Fourier amplitude spectral amplification factors for the 1000 m soil column analyses. The plots include spectra for thirteen time series selected for the parameter study, using the NLPD model. It is not possible to distinguish individual spectra in these plots. However, it is possible to establish ranges of amplification factors that can be interpreted from these analyses. Most time series results fall within a well-defined band. The amplification factor has a peak at approximately 0.2 Hz, which corresponds to the characteristic site period. Other peaks are observed that correspond to higher order natural frequencies of the soil column. A gray trend line is sketched through the data, which shows the general change of amplification factor with frequency. In the frequency range 0.1 to 4 Hz the amplification factor is greater than unity and can be up to a value of 5. At higher frequencies, the amplification factor is less than one. This interpretation represents the general trend, but as Figure 5 shows, there are numerous exceptions.

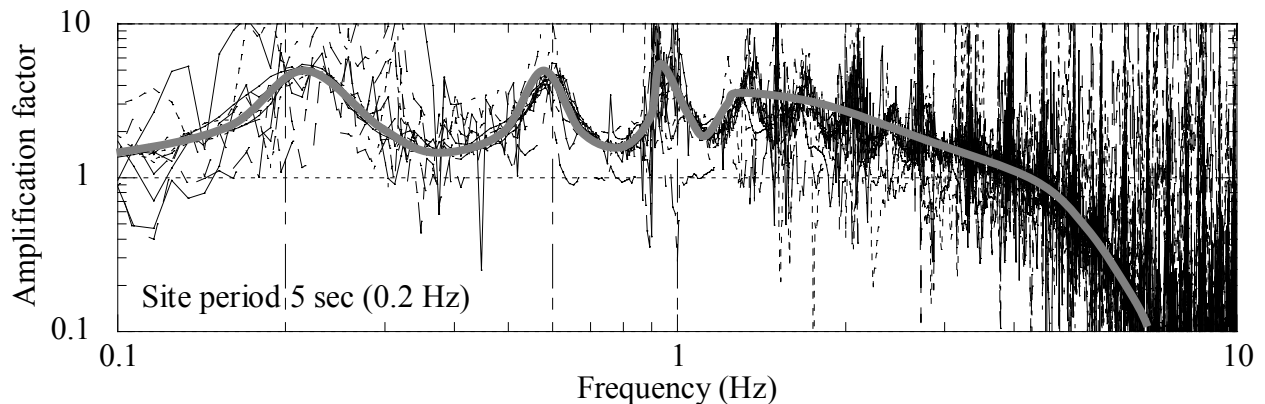


Figure 5 Ratio of computed surface to input Fourier amplitude spectra for all ground motions using pressure dependent model and 1000 m soil column. The gray line shows the general trend for the data sets. The peaks correspond to the site natural frequencies

Figure 6 plots Fourier amplitude spectral amplification factors for the 500 m soil column analyses. The plot shows that the amplification factor has peaks at the deposit natural frequencies. The amplification factor exceeds unity over a frequency range of 0.1 to 5 Hz. Higher frequency amplification factors are generally less than unity.

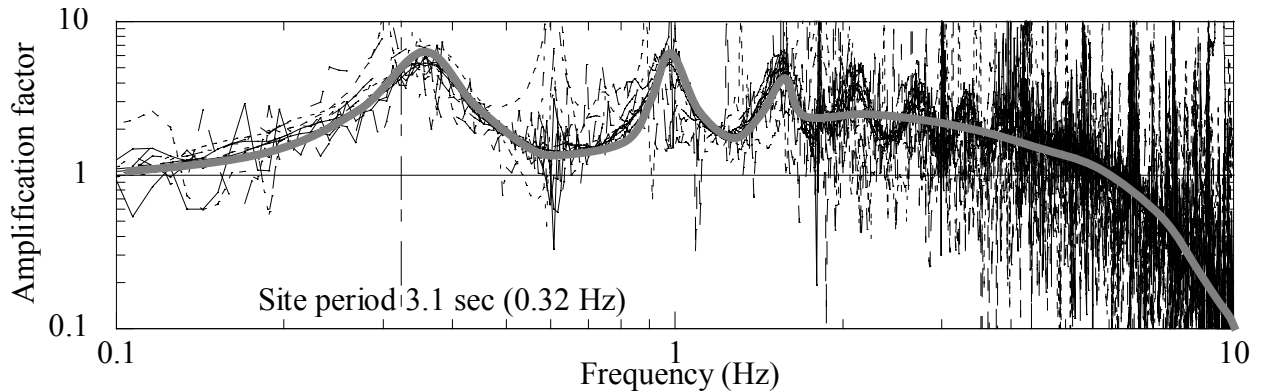


Figure 6 Ratio of computed surface to input Fourier amplitude spectra for all ground motions using pressure dependent model and 500 m soil column. The gray line shows the general trend for the data sets. The peaks correspond to the site natural frequencies

Figure 7 plots Fourier amplitude spectral amplification factors for the 100 m soil column analyses. The plot shows that there is significantly less amplification of ground motion at low frequency (long periods) compared to 1000 m and 500 m soil columns. The plot shows that greater amplification of high frequency components is computed compared to deeper soil profiles.

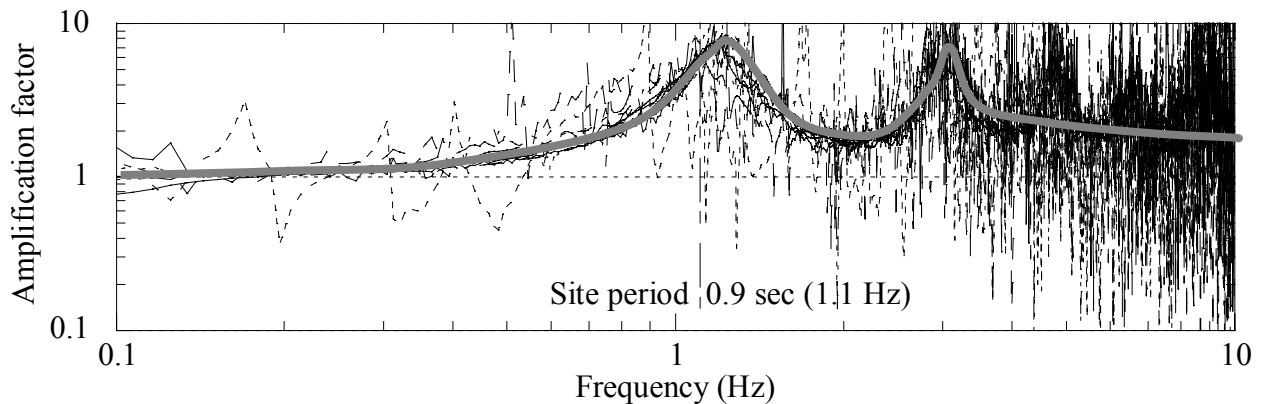


Figure 7 Ratio of computed surface to input Fourier amplitude spectra for all ground motions using pressure dependent model and 100m soil column. The gray line shows the general trend for the data sets. The peaks correspond to the site natural frequencies

Amplification factor plots show that for deeper soil columns there is greater amplification of low frequency (long period) components. The analyses for the three soil columns show that amplification factors at short periods/high frequency generally increase with decreasing soil deposit thickness. The fundamental frequency of the site and higher order natural frequencies influence the amplification factor. The deposit natural frequencies are related to the shear wave velocity of the site. It is necessary to obtain more extensive measurements of shear wave velocity profiles at depth at various locations within the Embayment.

COMPARISON WITH SELECTED NEHRP RESPONSE SPECTRUM FOR NMSZ

Response spectra from the present analyses (NLPD only) are compared with response spectra proposed in the NEHRP Recommended Provisions of 1997 (FEMA 302). The NEHRP response spectrum is developed for Site Class D (Stiff Soil). The soil column defined in **Figure 1** and used in the analyses falls within the NEHRP Site Class D. NEHRP spectral accelerations are obtained from Maps 13 & 14, Maximum Considered Earthquake Ground Motion for the New Madrid Area. Maximum values of spectral parameters in NMSZ $S_a(0.2 \text{ sec})=3.69 \text{ g}$ and $S_a(1 \text{ sec})=1.23 \text{ g}$ at the B-C boundary are used.

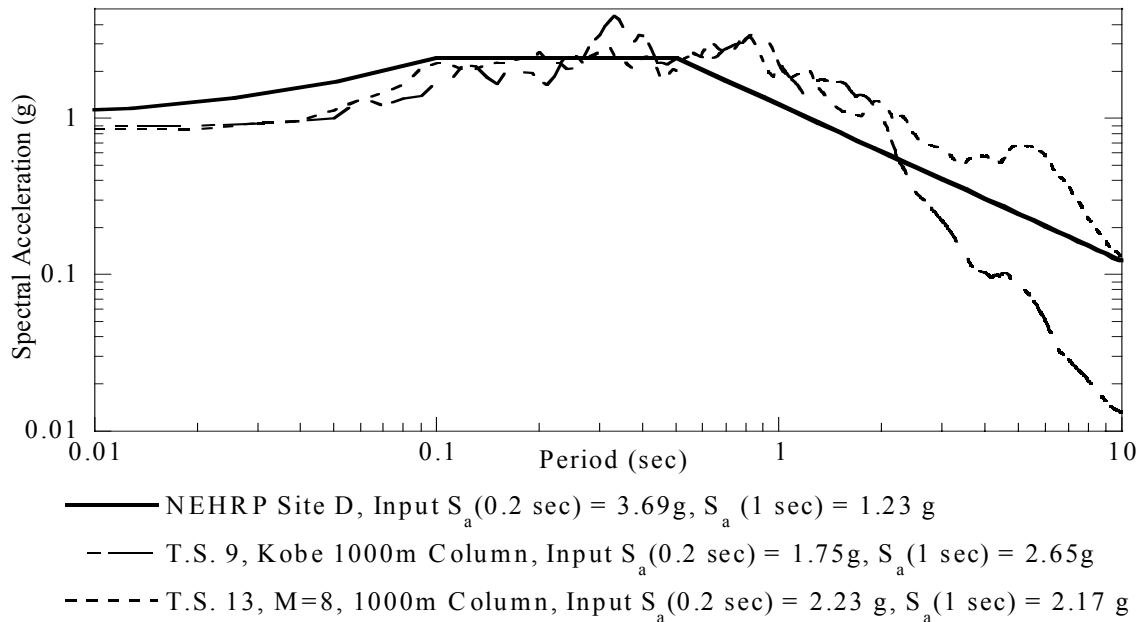


Figure 8 Comparison of computed surface response spectra with the maximum NEHRP recommended spectrum for the NMSZ. At periods greater than 0.7 sec, computed spectra exceed NEHRP spectra

Figure 8 shows a plot of surface response spectrum for NEHRP Site Class D and for a 1000 m soil column using the proposed model and input motion from Kobe earthquake (station JMA NS) and synthetic ground motion from SMSIM (M = 8, R = 20km). Both of the time series have spectral parameters less than those used in developing NEHRP spectrum. The computed response in the proposed model gives spectral accelerations larger than those for NEHRP Site Class D at periods longer than 0.3 sec. A detailed study is planned to re-examine NEHRP

spectral values systematically within the Mississippi Embayment using the new proposed model to represent the underlying soil column.

CONCLUSIONS AND FUTURE WORK

Analyses presented in this paper show the importance of the influence of confining pressure on seismic site response analysis. The analyses show that:

- Significant portions of high frequency components of ground motion are propagated through deep soil deposits.
- Propagation of seismic waves through very deep deposits result in the development of long period ground motion.
- Spectral amplitudes of propagated ground motions are higher than what would be obtained using conventional wave propagation analyses. Therefore estimates of ground motion that are derived from paleo-liquefaction features should consider the higher propagated ground motions.

The paper presents preliminary results of ongoing model development. Further work is underway to improve model calibration.

ACKNOWLEDGEMENTS

This work was supported primarily by the Earthquake Engineering Research Centers Program of the National Science Foundation under Award Number EEC-9701785; the Mid-America Earthquake Center. The authors gratefully acknowledge this support.

REFERENCES

1. Hashash, Y.M.A., and Park, D. (2001), "Non-linear one-dimensional seismic ground motion propagation in the Mississippi Embayment," *Engineering Geology*
2. Stone, W. C., Yokel, F. Y., Celebi, M., Hanks, T. and Leyendecker, E. V. (1987). "Engineering aspects of the September 19,1985 Mexico earthquake." NBS Building Science Series 165, National Bureau of Standards, Washington, D.C., 207 p.
3. Ng, K. W., Chang, T. S., and Hwang H. (1989). "Subsurface conditions of Memphis and Shelby County." Technical Report NCEER-89-0021, National Center for Earthquake Engineering Research, State University of New York at Buffalo, Buffalo, NY.
4. VanArsdale, R. B., Williams, R. A., Schweig III, E. S., Shedlock, K. M., Kanter, L. R. and King, K. W. (1994). "Preliminary seismic reflection study of Crowley's Ridge, Northeast Arkansas." U.S. Geological Survey Professional Paper 1538-A-C, United States Government Printing Office, Washington.
5. Romero, S. and Hebler, G. and Rix, G. J., (2001), "Recommended reference profile for Memphis, Tennessee." <http://mae.ce.uiuc.edu/Research/GT-1/RRP.htm>. *Engineering Geology*.

6. Matasovic, N. (1993). "Seismic response of composite horizontally-layered soil deposits." Ph. D. Thesis, Department of civil engineering, University of California at Los Angeles.
7. Laird, J. P. and Stokoe, K. H. (1993). "Dynamic properties of remolded and undisturbed soil samples test at high confining pressure." Geotechnical Engineering Report GR93-6, Electrical Power Research Institute.
8. Boore, D. M. (2000). "SMSIM – Fortran programs for simulating ground motions from earthquakes: Version 1.87." User Manual, V 1.0, U.S. Geological Survey Open-File Report 96-80-A, 73 pp.



KEERC-MAE Joint Seminar on
Risk Mitigation for Regions of Moderate Seismicity
University of Illinois at Urbana-Champaign, August 5-8, 2001



Sponsors: Korea Science and Technology Foundation, U.S. National Science Foundation, Brain Korea 21



Seismic Performance Evaluation of Structures Under Multi-Directional Loading

Jae Kwan KIM¹, Ick Hyun KIM² and Jae Ho LEE³

¹Associate Professor, Department of Civil Engineering, Seoul National University
San 56-1, Shillim-dong, Kwanak-ku, Seoul 151-742, KOREA
email: jkwankim@plaza.snu.ac.kr

²Assistant Professor, Department of Civil & Environmental Engineering, University of Ulsan
San 29, Muger 2-dong Namgu, Ulsan, 689-749, KOREA
email: ickhyunkim@lycos.co.kr

³Graduate Student, Department of Civil Engineering, Seoul National University
San 56-1, Shillim-dong, Kwanak-ku, Seoul 151-742, KOREA
email: over1@snu.ac.kr

ABSTRACT: The seismic capacity of columns usually has been tested in uniaxial loading condition. The seismic performance used to be evaluated under the same assumption. Since the real earthquake motion is multi-directional, the effects of multi-directional excitation on the seismic capacity of structures need to be carefully examined. In this paper, a frequency dependent alternate biaxial cyclic loading test is proposed as an evaluation method of seismic capacity under multi-directional excitation. Four test specimens were made and tested to study the degradation of strength, stiffness and ductility under biaxial loading condition. A capacity spectrum procedure is proposed for the evaluation of seismic performance under multi-directional excitation. The capacity is obtained using frequency dependent alternate biaxial cyclic loading test. The orthogonal effect is taken into account by increasing the demand.

KEYWORDS: Biaxial Loading, Cyclic Loading Test, Capacity, Degradation, Capacity Spectrum, Demand Spectrum, Seismic Performance

INTRODUCTION

Columns such as bridge piers and vents will experience multi-directional cyclic loading during a strong earthquake. However, in practice, the seismic capacity of columns used to be studied under the uniaxial loading condition. In previous studies, the strength degradation and ductility reduction was observed in biaxial or multidirectional loading conditions [1-3]. It appears that the seismic capacity of a column could be overestimated if it is obtained solely based on the uniaxial loading test results. Presently applications of pushover analysis method and capacity spectrum method seems to be limited to the unidirectional applications [4].

So far there has not been proposed a simple yet reliable evaluation procedure of the seismic capacity of structures under the bi-axial loading conditions. More over there is no reliable method that can take into account the orthogonal effect in nonlinear analysis procedure. Multi-directional pseudo-dynamic test can be a method that can handle this situation. But it appears to be costly and not readily be applicable. Hence a very simple but yet reliable and practical method is in order for the evaluation of seismic capacity and performance under the multi-directional loading condition.

These observations motivated the present work. The first objective of this work is to propose an alternative procedure for the evaluation of the seismic capacity of structures under multi-directional horizontal earthquake loading. To support the premises, four specimens of rectangular section were tested under four distinct loading patterns.

CONCEPT OF FREQUENCY DEPENDENT ALTERNATE BIAXIAL CYCLIC LOADING TEST

A structure tends to vibrate in its first mode with corresponding fundamental period within elastic range. Under the biaxial excitation, the same will be true in each principal axis direction. Then the ratio of number of cycles experienced by the structure in each direction will be proportional to the ratio of natural frequency. Even when the load-displacement relation is nonlinear, it will be reasonable to assume that the ratio of cycles will be approximately equal to the ratio in elastic vibration for the structure designed optimally.

Figure 1 shows a rectangular structure with bi-symmetric elastic properties. It can be modeled as SDOF system. The load-displacement relation in each direction is assumed being elastic-perfectly plastic. Natural periods of vibration in elastic range can be expressed as follows:

$$T_x = 2\pi \sqrt{\frac{M}{K_{ex}}} \quad (1)$$

$$T_y = 2\pi \sqrt{\frac{M}{K_{ey}}} \quad (2)$$

Then, the following relation may approximate the ratio of vibration cycles:

$$RVC = \left(\frac{T_d}{T_y} \right) / \left(\frac{T_d}{T_x} \right) = \frac{T_x}{T_y} = \sqrt{\frac{K_{ey}}{K_{ex}}} \quad (3)$$

If the displacement is large then the response will enter into plastic range. In this case, one may assume that the response reaches the maximum ductility in each direction proportionally. Then, the ratio of vibration cycles can be approximated as follows:

$$T_x = 2\pi \sqrt{\frac{M}{K_{ex} / \mu_x}} \quad (4)$$

$$T_y = 2\pi \sqrt{\frac{M}{K_{ey} / \mu_y}} \quad (5)$$

$$RVC = \frac{2\pi \sqrt{\mu_x}}{2\pi \sqrt{\mu_y}} \cdot \sqrt{\frac{K_{ey}}{K_{ex}}} = \sqrt{\frac{\mu_x}{\mu_y}} \cdot \sqrt{\frac{K_{ey}}{K_{ex}}} \quad (6)$$

The above argument can be substantiated by the following examples. A bi-symmetric structure has natural periods in two directions $T_x=0.96$ and $T_y=0.32$, respectively. This structure is excited by bi-directional ground motion as shown in Figure 2. The relative displacement time histories are presented in Figure 3. The ratio of vibration is found to be the same as the natural frequency ratio as expected. The next example is an elasto-plastic model. The maximum ductility is assumed to be 5 in both axes. The effective periods at ultimate displacement is specified to be $T_x=1.82$ and $T_y=0.6$, respectively. When this model is subjected to the biaxial excitation given in Figure 4, the response histories in Figure 5 are obtained. Counting the number of peaks, the ratio of vibration cycles is found to be approximately 3 as predicted by the formula (6).

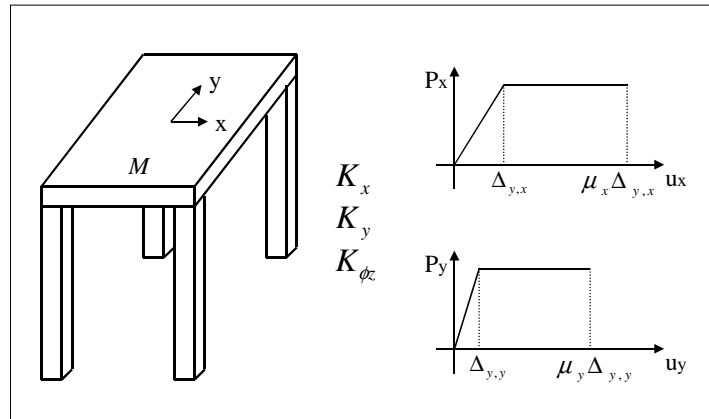


Figure 1 Rectangular bi-symmetric structure

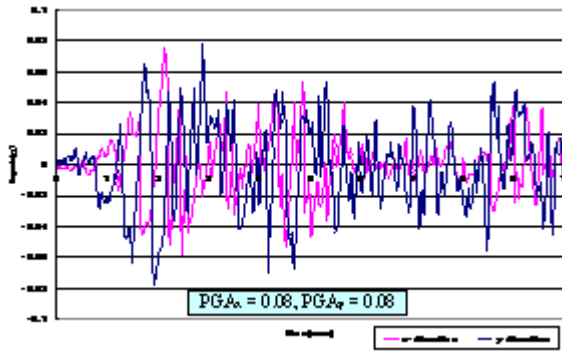


Figure 2 Ground acceleration for elastic response

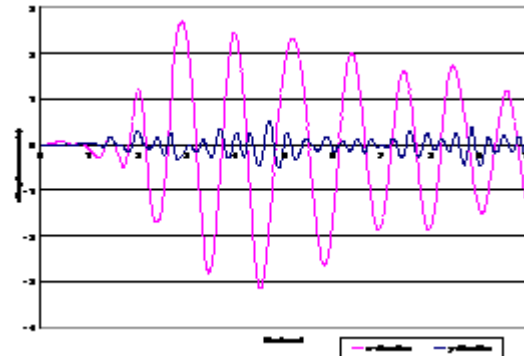


Figure 3 Relative displacement of elastic response

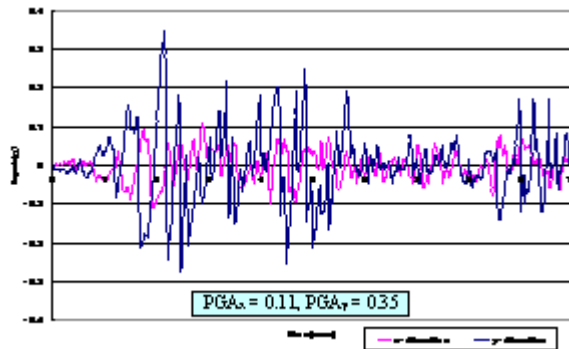


Figure 4 Ground acceleration for inelastic response

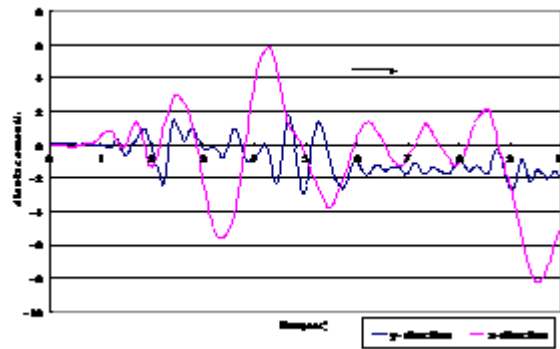


Figure 5 Relative displacement of inelastic response

The above observation leads to the concept of frequency dependant alternate cyclic loading test as a method that can be used for the evaluation of capacity under multi-directional excitation. Since the structure vibrates maintaining the frequency ratio almost constant between two principal axes, the degradation in strength, stiffness and ductility can be captured by a biaxial load pattern that takes into account the frequency characteristics reasonably well.

The cyclic loading sequence in uniaxial directional test should be determined considering the following factors in order to represent the actual capacity in real earthquake:

1. Duration, intensity and frequency contents of ground motion
2. Vibration characteristics of the structure

The characteristics of load sequence includes the following features:

1. Increment of load level
2. The number of cycles at each level

In this paper a quite simple load pattern is proposed for the biaxial loading test as shown in Figure 6. The load sequence will be decided in each direction. But the load will be applied alternatively in each axis direction. In one axis direction the number of load cycles will be applied at each level. The load will be applied in other axis direction up to the predetermined number of cycles. Then the same process will be repeated at the next load level.

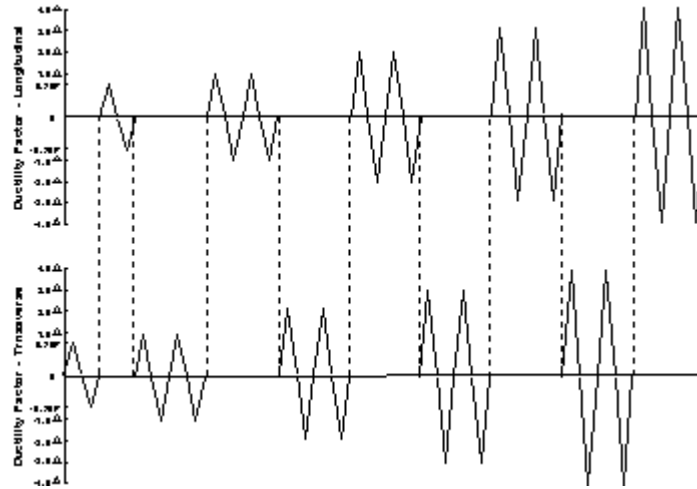


Figure 6 Simple alternate biaxial loading pattern

EXAMPLES OF FREQUENCY DEPENDENT ALTERNATE BIAxIAL CYCLIC LOADING TEST

Four test specimens of rectangular section were made for this purpose. Two specimens were tested under uniaxial loading condition: one in longitudinal direction and the other transverse direction. One of the remaining specimens was subjected to the alternate biaxial loading. The side view and plan view of the column are provided in Figure 7. The last one was subjected to the alternate biaxial loading but the number of cycles was determined considering the ratio of natural frequencies in two orthogonal principal directions. The periods of the structure is assumed to be 1.6 Sec in longitudinal direction and 0.8 Sec in transverse direction. The load cycle ratio is determined to be 2. The load pattern used for the biaxial loading test is given in Figure 8.

Strength degradation and ductility reduction was observed in biaxial loading conditions compared with uniaxial loading. Their rates were found to be more rapid in the loading pattern that was determined considering the difference in natural frequencies. It is also observed that energy absorption capacity deteriorate most rapidly in frequency dependent biaxial cycle loading pattern. The hysteresis loops are provided in Figure 9. Their envelopes in longitudinal and transverse directions compared in Figure 10(a) and (b), respectively. The test results are summarized in Table 1. It appears that frequency dependent biaxial loading condition is more severe than simple alternate biaxial cyclic loading.

Strength degradation and ductility reduction was observed in biaxial loading conditions compared with uniaxial loading. Their rates were found to be more rapid in the loading pattern that was determined considering the difference in natural frequencies. It is also observed that energy absorption capacity deteriorate most rapidly in frequency dependent biaxial cycle loading pattern. The hysteresis loops are provided in Figure 9. Their envelopes in longitudinal and transverse directions compared in Figure 10(a) and (b), respectively. The test results are summarized in Table 1. It appears that frequency dependent biaxial loading condition is more severe than simple alternate biaxial cyclic loading.

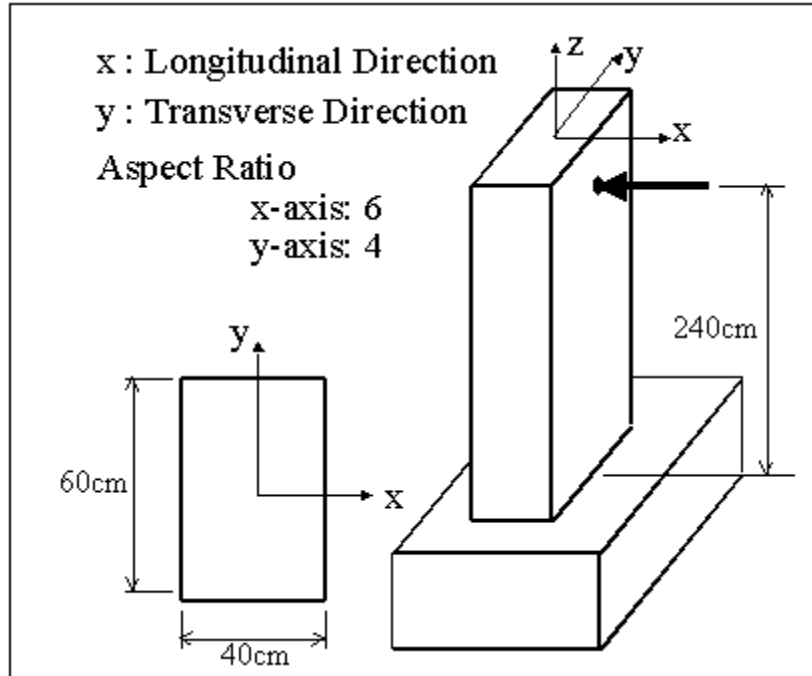


Figure 7 The shape and plan view of the column specimen

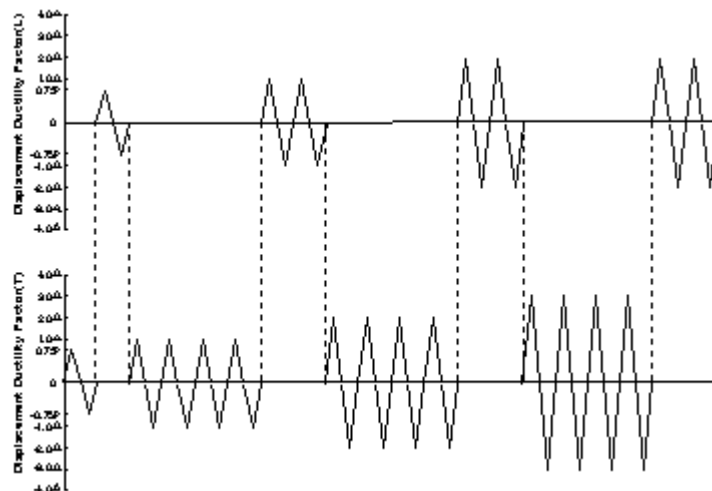


Figure 8 Frequency dependent alternate biaxial loading pattern

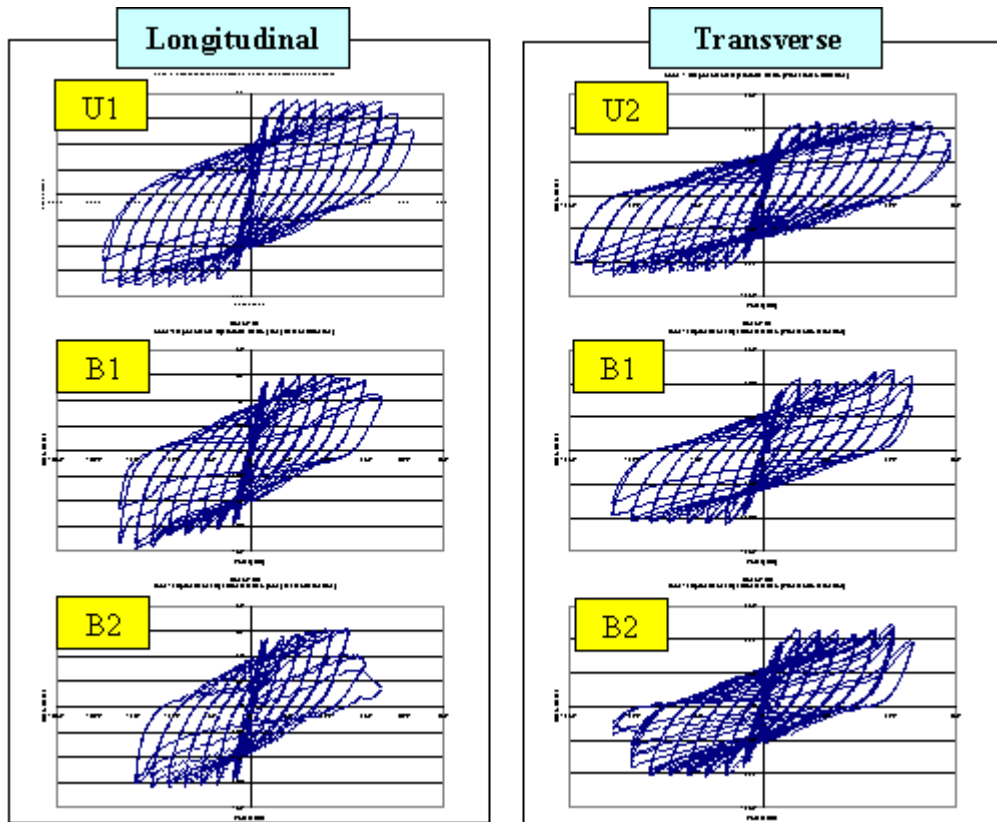
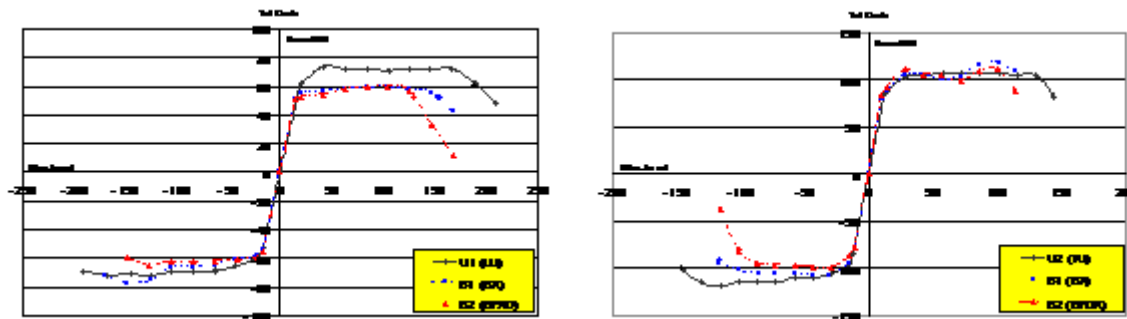


Figure 9 Load-displacement hysteresis loops



(a) Longitudinal Direction

(b) Transverse Direction

Figure 10 Load-displacement envelope curve

Table 1 Test results

Specimen		P_{max} (kN)	Normalized P_{max} (%)	μ_{max}	μ_f	Normalized Absorbed Energy at $\mu=7$
Longitudinal direction	U1	72.3	100	6	9	1.00
	B1	66.8	92.4	7	7.5	0.79
	B2	61.5	85.1	5	6.5	0.56
Transverse direction	U2	112.3	100	8	10	1.00
	B1	111.0	98.8	6	8	0.85
	B2	101.2	90.1	6	7	0.70

PERFORMANCE EVALUATION USING FREQUENCY DEPENDENT ALTERNATE BIAxIAL CYCLIC LOADING TEST

As mentioned in the introduction, seismic performance can be evaluated using capacity spectrum method. The capacity may be estimated using the frequency dependent alternate biaxial cyclic load test. But the remaining problem is the demand spectrum. In order to take into account the orthogonal effect, the simplest way is to increase the demand spectrum by certain amount. If the response is in elastic range, the increment in demand spectrum can be determined based on SRSS method or 100% and 30% rule. But if the response is beyond elastic range the problem is not that simple. The authors think that the amount of increase will be less than that of elastic response but this fact needs additional study.

If the increment in demand is given, then seismic performance can be evaluated in each principal axis direction as shown in Figure 11. The axis that renders lower intensity of demand will be assumed as governing the performance.

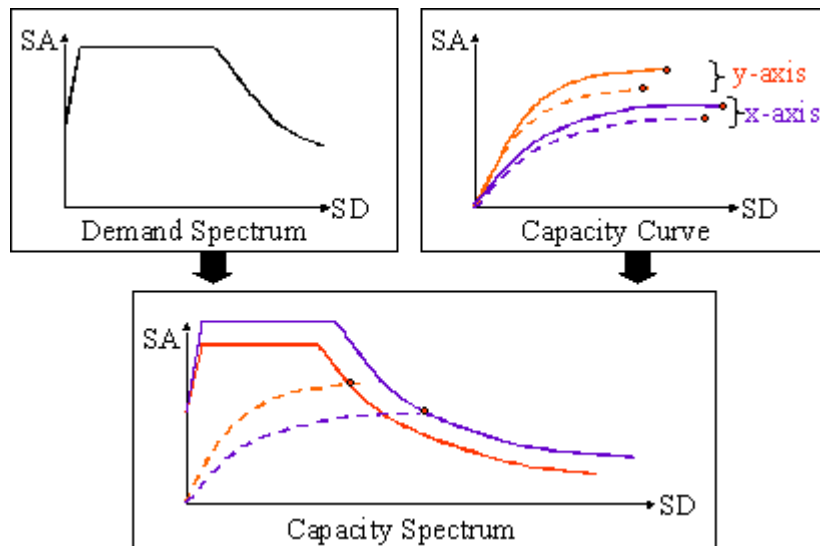


Figure 11 Evaluation of Seismic performance

CONCLUSION

A frequency dependent alternate biaxial cyclic loading test is proposed. It takes into two-dimensional vibration characteristics along with degradation of strength, stiffness and ductility in multi-directional loading condition.

A seismic performance evaluation procedure is proposed for the multi-directional loading condition. Capacity spectrum method is employed to this end. The capacity curves obtained using frequency dependant alternate biaxial cyclic loading test are converted into capacity spectra and compared with demand spectra in ADRS framework. Yet the amount of increase in demand needs further study.

ACKNOWLEDGMENT

This work was supported (in part) by the Korea Science and Engineering Foundation (KOSEF) through the Korea Earthquake Engineering Research Center (KEERC) at the Seoul National University (SNU) under Grant No. 2000G0202 and the Brain Korea 21 Project in 2001. And this work was partly supported by the Daelim Industrial Co., Ltd. The tests were performed at the Hyundai Institute of Construction Technology. Their kind support is greatly acknowledged.

REFERENCES

1. S.S Low and J.P. Moehle, *Experimental Study of Reinforced Concrete Columns Subjected to Multi-Axial Cyclic Loading*, Earthquake Engineering Research Center, UCB/EERC-87/14, California, Berkeley, Sep. 1987.
2. Y. Wong, T. Paulay and M.J.N. Priestley, "Response of Circular Reinforced Concrete Columns to Multi-Directional Seismic Attack", *ACI Structural Journal*, Vol. 90 No. 2, Mar-Apr, 1993, pp. 180-191.
3. S.N. Bousias, G. Verzeletti and M.N. Fardis, "Load-Path Effects in Column Biaxial Bending with Axial Force", *Journal of Engineering Mechanics*, Vol.121, No.5, May, 1995, pp. 596-605.
4. ATC, *Seismic Evaluation and Retrofit of Concrete Buildings*, Vol. 1, ATC-40, Applied Technology Council and California Seismic Safety Commission, California, Nov. 1996.



KEERC-MAE Joint Seminar on
Risk Mitigation for Regions of Moderate Seismicity
University of Illinois at Urbana-Champaign, August 5-8, 2001



Sponsors: Korea Science and Technology Foundation, U.S. National Science Foundation, Brain Korea 21



Seismic Resistance of Low Ductility Structures

A.S.Elnashai¹, and A.M.Mwafy²

¹ *Professor of Civil Engineering, University of Illinois at Urbana-Champaign
2129e Newmark Laboratory, 205 N. Mathews, Urbana, Illinois, USA
email: aelnash@uiuc.edu*

² *Ass.Professor, Department of Civil Engineering, Zagazig University, Egypt*

ABSTRACT: In this paper, the energy absorption capacity and ductility of reinforced concrete structures with minimum seismic detailing are examined. A sample of structure is designed to a modern code that has separate provisions for high, medium and low ductility classes. The sample, comprising 3 structural types with four structures in each type, is subjected to a number of code-compatible and natural earthquake records. Comprehensive assessment of these structures, 8 moment resisting frame buildings and four frame-wall buildings, using a number of yield and ultimate limit states, indicates that well-designed RC structures with minimum detailing provisions may exhibit appreciable levels of ductility, energy absorption capacity and therefore seismic resistance in the inelastic range. Moreover, the essential role played by overstrength in protecting structures in earthquake zones is confirmed.

KEYWORDS: Seismic resistance, reinforced concrete, ductility, response modification factors, overstrength.

INTRODUCTION

Issues of mitigating seismic risk in areas of low and moderate exposure have come to the fore in recent years. This is due to the relentlessly high toll exacted by small and medium earthquakes on vulnerable and unprepared communities. On the other hand, the culture of earthquake resistant design is controlled by research and development work in high seismicity areas of the world. This imposes certain requirements on moderate and low seismicity areas that render adopting seismic design procedures an issue of economic significance. Against this backdrop, concerted efforts have been dedicated in recent years to studying problems of hazard and vulnerability for moderate/frequent and large/infrequent earthquakes, both of which, from a probabilistic standpoint, lead to low levels of design earthquake motion for a given lifetime of a structure (e.g. the EU project Safety Assessment for Earthquake Risk Reduction 'SAFERR', see www.saferr.net).

The unintentional seismic resistance of non-seismically designed structures could be used to reduce seismic design requirements, or waive it completely, for some classes of structure. Moreover, the seismic resistance of low ductility (by design) structures could reduce the economic impact of imposing statutory seismic design. To quantify the latter, a set of structures was designed and analysed using advanced inelastic dynamic assessment procedures. The structural configurations, modelling approach, limit states, input motions and results are briefly presented below. The basic approach was to compare the response modification factor (supply) and ductility capacity of a number of nominally identical structures but with different detailing levels, namely low, medium and high ductility classes according to the European code Eurocode 8, as described below.

ANALYTICAL MODELS AND ASSESSMENT PROCEDURE

Building Configuration

Three types of building were designed by the University of Patras (Greece) group for the purposes of calibration studies of the seismic resistance of code-designed reinforced concrete buildings. The four types are 12 storey irregular frames (IF class), 8 storey regular frames (RF class) and 8 storey frame-wall buildings (FW class). Within each class there are four structures with two design ground accelerations and three ductility (detailing and capacity design protection) levels. The ductility class-design acceleration pairs considered are: high-0.3g (H030), medium-0.3g (M030), medium-0.15g (M015) and low-0.15g (L015). The amount of concrete and steel for each structure in the sample and the design response modification factors are given in Table 1.

Table 1 Characteristics of the Studied RC Frames

Reference	Concrete (m ³)	Steel					R _{code}
		Total (ton)	Beam/Col. or Walls (%)	Longitudinal/Transverse (%)			
				Beams	Col. & walls	Total	
IF-H030	414	81.88	35/65	74/26	59/41	64/36	4.00
IF-M030	414	80.12	40/60	84/16	74/26	78/22	3.00
IF-M015	362	52.73	39/61	77/23	71/29	73/27	3.00
IF-L015	362	54.61	43/57	88/12	76/24	81/19	2.00
RF-H030	712	126.0	36/64	74/26	58/42	64/36	5.00
RF-M030	682	117.0	42/58	84/16	72/28	78/22	3.75
RF-M015	643	94.37	32/68	78/21	72/28	74/26	3.75
RF-L015	643	97.17	37/63	89/11	76/24	80/20	2.50
FW-H030	310	65.74	22/78	76/24	42/58	50/50	3.50
FW-M030	310	68.53	25/75	85/15	49/51	58/42	2.625
FW-M015	224	38.58	23/77	76/24	42/58	50/50	2.625
FW-L015	224	44.48	24/76	86/14	48/52	57/43	1.75

Limit States

The limit states considered are, for yield LS are: (i) yield of tensile reinforcement, (ii) global yield displacement of an equivalent SDOF system. For the ultimate limit state, the criteria selected are: (i) rupture of reinforcing bars, (ii) concrete critical strain, (iii) stability index violation and (iv) exceeding an interstorey drift limit. These were selected after exhaustive studies of available limit states and also exploratory analyses to eliminate limit states that are never observed in analytical assessment. More details are available in other publications by the authors.

Modelling Approach

An overlay approach was employed, whereby the 3D structure is reduced to a layered 2D structure by modelling all external and internal frames, but coupling the beam-column connection nodes to take account of the different stiffness and strength characteristics of the frames. Detailed fibre analysis was undertaken of all members, with springs used to model the behaviour of beam-column connections and rigid members inserted to insure that the beam critical section is captured in the model.

Selection and Scaling of Input Motion

A total of six records were used in the analysis. These comprise four records generated to match the code spectrum used in design, which is Eurocode 8 alongside two natural records selected to have significant amplification in a broad frequency band and high vertical motion. The latter consideration lead to the selection of records within ~20 km from the source. The two records were scaled using the concept of velocity spectral intensity proposed by Housner, with a period range dictated by the elastic and inelastic periods of the structure.

Sample Results

The number of inelastic dynamic analyses performed for this study is about 900, for the various configurations, the eight records and the different scaling levels required to achieve the limit states for all criteria defined above. Table 2 gives resistance and deformation quantities for the 12 frames when subjected to the four code-compatible record (average values) at the design acceleration and twice the design. The results are presented as ratios for the two ductility classes to highlight the possible differences in response due to the different levels of detailing rigour and application of capacity design principles. It is clear that the cost of applying the medium ductility class requirements, which would be more onerous than Low and less than High, is not warranted, since the response parameters are quite similar, especially for deformational quantities.

Table 2 Response Parameters at Design and Designx2

	Gr.	Reference	Max.Top Disp.	Max. ID	Max. Base Shear	Inelastic Period
<i>Intensity 1.0</i>	1	IF-030 (H / M)	1.22	1.32	0.88	1.16
		IF-015 (M / L)	0.94	1.01	1.05	1.05
	2	RF-030 (H / M)	0.96	1.05	0.99	1.05
		RF-015 (M / L)	0.98	1.03	0.88	0.96
	3	FW-030 (H / M)	0.88	0.88	0.87	1.05
		FW-015 (M / L)	0.87	0.86	0.87	1.05
<i>Intensity 2.0</i>	1	IF-030 (H / M)	1.06	1.16	0.90	1.04
		IF-015 (M / L)	0.87	0.98	0.81	1.16
	2	RF-030 (H / M)	0.98	1.05	0.94	0.96
		RF-015 (M / L)	0.97	1.03	0.91	1.08
	3	FW-030 (H / M)	1.03	0.99	0.86	1.01
		FW-015 (M / L)	1.10	1.02	0.86	1.08

The response modification factors (behavior factors in European practice) for all buildings and all records are shown in Table 3. It is noted that the ratio between the design value and the capacity (supply) value is high, with a minimum of 1.72 and a maximum of 4.89. It is further noted that for the moment resisting frames, structures designed with minimum ductility capacity requirements (denoted L) exhibit reliable seismic response with response modification factors in the region of twice the design value. This indicates that low ductility structures may still be feasible for seismic resistance.

Table 3 Response Modification Factors (Supply) for All Records

Reference	$R'_{c,ay}$ Average for four art. records			$R'_{c,ay}$ Average for two nat. records (H)			$R'_{c,ay}$ Average for two nat. records (H+V)			R_{code}	$R'_{c,ay}$ (average) / R_{code}		
	L	G	F	L	G	F	L	G	F		L	G	F
	IF-H030	8.91	5.57	8.91	8.27	5.35	8.27	9.75	5.89		9.39	4.00	2.24
IF-M030	8.43	4.85	8.43	4.96	3.97	4.96	5.05	4.83	5.05	3.00	2.05	1.52	2.05
IF-M015	10.04	6.81	10.04	15.22	8.81	14.23	12.53	8.91	12.53	3.00	4.20	2.73	4.09
IF-L015	4.25	4.77	4.25	3.52	5.68	3.52	3.69	6.31	3.69	2.00	1.91	2.79	1.91
RF-H030	6.50	5.11	6.50	13.11	8.16	13.11	13.21	7.10	13.21	5.00	2.19	1.36	2.19
RF-M030	5.75	3.93	7.28	11.76	5.23	14.58	11.13	4.90	12.85	3.75	2.54	1.25	2.54
RF-M015	10.23	7.88	10.23	9.33	6.93	9.33	8.39	6.95	8.39	3.75	2.48	1.93	2.48
RF-L015	3.92	5.59	3.92	6.41	6.25	6.41	6.22	6.13	6.22	2.50	2.21	2.40	2.21
FW-H030	7.22	20.66	7.22	5.47	8.69	5.47	5.83	8.50	5.83	3.50	1.76	3.61	1.76
FW-M030	4.59	16.04	4.59	4.46	6.81	4.46	4.54	6.68	4.54	2.63	1.72	3.74	1.72
FW-M015	9.64	13.21	9.64	5.39	8.43	5.39	4.95	9.12	4.95	2.63	2.53	3.90	2.53
FW-L015	9.59	10.32	9.59	4.59	7.59	4.59	4.33	7.76	4.33	1.75	3.52	4.89	3.52

$$R'_{c,ay} = (a_{g(collapse)} / a_{g(actual\ yield)}) \cdot \Omega_d$$

L: Local criteria are employed to calculate $R'_{c,ay}$

G: Global criteria are used

F: First observed yield and collapse are employed to calculate $R'_{c,ay}$

General Observations

The following observations were made during the course of the study:

- Yield occurs at a lower level of excitation for structures designed to higher level of ductility since they are assigned lower longitudinal reinforcement. The lowest PGA causing yield is observed for the –M015 buildings, whilst the highest intensity is for the –M030 buildings.
- The margin of safety, expressed by the ratio of collapse-to-design PGA, decreases with increasing ductility level. However, the higher supply-to-demand force reduction factors observed for buildings designed to higher ductility levels confirm the enhanced performance and justifies the rigorous capacity design provisions imposed on these buildings.
- Beams in buildings designed to ductility level ‘Low’ are vulnerable to shear failure. This is manifested in the low force reduction factors ‘supply’ evaluated for these buildings.
- Buildings designed to lower PGA show better performance and higher force reduction factor ‘supply’ due to their higher reserve strength.

The results of this study therefore strongly supports the application of sound engineering design alongside minimum seismic provisions in moderate and low seismic hazard areas. This leads to safe and economic design solutions.



KEERC-MAE Joint Seminar on
Risk Mitigation for Regions of Moderate Seismicity
University of Illinois at Urbana-Champaign, August 5-8, 2001



Sponsors: Korea Science and Technology Foundation, U.S. National Science Foundation, Brain Korea 21



Displacement-Based Design and Assessment of Structural Walls

Sung-Gul HONG¹ and Bong-Ho CHO²

¹ *Assistant Professor, Department of Architecture, Seoul National University
Shinlim Dong, Kwank Gu, Seoul, Korea
email: sglhong@snu.ac.kr*

² *Graduate Student, Department of Architecture, Seoul National University
Shinlim Dong, Kwank Gu, Seoul, Korea
email: cho525@snu.ac.kr*

ABSTRACT: As one of likely future promising seismic design methods, the displacement-based design is reviewed in this paper to incorporate performance based design concepts. The displacement-based design is applied to the design of structural walls for purpose of their rational dimensioning and detailing in regions of moderate seismicity. Various stories, wall length, and seismic zones are selected for comparison of the force-based design and the direct displacement based design of walls with end boundaries unconfined. The plastic hinge rotation capacity for walls with unconfined boundaries is determined from experimental data. Comparison shows that the design base shears from the direct displacement-based design method are lower than those from force-based design method in the regions of moderate seismicity. This study extends the direct displacement-based design concepts to the seismic assessment of existing structural walls with assumption of a likely failure mechanism. The application shows the seismic demand is determined by a target displacement and determination of performance point.

KEYWORDS: Displacement-based Design, Structural Walls, Unconfined Boundary, Plastic Hinges.

INTRODUCTION

The framework proposed by SEAOC in Vision 2000 [16] appropriately addressed all aspects of the performance-based engineering including structural and non-structural design, construction quality assurance and maintenance of building integrity throughout its life cycle. The performance-based design concepts involve the definition of multiple target performance levels subjected to ground motion of specified intensity. These design concepts need new future design methods such as displacement-based design, energy-based design, and consequence-based design rather than traditional force-based design. The shift of the basis for earthquake-resistant design from strength to displacement has been an important issue since desired performances are directly expressed in terms of damage levels that are strain-dependant [12,16,17].

In the current force-based method, global displacement and local ductility demands are end results of the design method [3,7,9,11]. The force-based design employs structural response modification factors as simple relations between elastic and inelastic responses and assumes that strength is independent of stiffness. By contrast, displacement-based design method uses displacement and/or deformation as the basis for the design procedure and strength and stiffness are not variables in the procedure [9,10,13].

Seismic assessment of an existing structure is much more complex task than the design of a new structure. The seismic evaluation of existing buildings compares their capacity against earthquake demand at specific site and concerns the potential earthquake-caused risk to building systems and components that are closely related to human life safety. The purpose of detailed assessment is to identify the particular weaknesses and deficiencies for retrofitting. For this reason there has been a worldwide shift from rapid visual screening evaluation and compliance with the provisions of current seismic design codes to fundamental assessment procedure based on comparison of the inelastic deformation demands with the corresponding deformation capacities. The so-called capacity spectrum method with non-linear static analysis procedure [1] is one of rational tool that plays a central role among all documents developing a new generation of design and retrofitting procedure to incorporate performance-based engineering concepts. A controversial part of the capacity spectrum method is the use of elastic spectra with equivalent damping concepts to consider inelastic behavior for the determination of seismic demand. In order to overcome the deficiencies of the original capacity spectrum method, Bertero, Reinhorn and Fajfar proposed the capacity spectrum method based on inelastic demand spectra [5].

This paper reviews the procedure for direct-displacement based design and applies the method to the design of cantilever wall structures with unconfined boundaries in the regions of moderate and high seismicity. In the second part of the paper, the seismic evaluation of existing walls of unconfined edge boundaries is proposed by use of direct-displacement design concepts. The method proposed by researchers such as Priestley for displacement-based assessment has been implemented for this purpose.

DIRECT-DISPLACEMENT-BASED DESIGN FOR WALL STRUCTURES

The main concept of the method, based on Priestley, is that a structure is designed for a specified target displacement. According to Appendix I of SEAOC Blue Book [17] that is proposed by Priestley and co-workers [8,12] the following procedures are recommended;

Step 1) Define multi-earthquake hazard for selected performance objective. The performance objective assigns the corresponding performance level to each hazard.

Step 2) Select an appropriate maximum inelastic displacement. In case of cantilever type structure such as structural walls, the plastic hinge angle is defined as

$$\theta_u = \theta_p + \theta_y = (\phi_u - \phi_y)l_p + \frac{\phi_y h_w}{2} = \phi_p l_p + \frac{\phi_y h_w}{2} \quad (1)$$

where the plastic hinge length $l_p = \max\left[(0.2l_w + 0.03h_n), (0.054h_n + 0.022f_y d_b)\right]$, θ_y =yield angle and ϕ_p = plastic curvature. Then, the displacement at i-th story is calculated as follows;

$$\Delta_i = \Delta_p + \Delta_y = \theta_p \left(h_i - \frac{l_p}{2} \right) + \frac{1}{3} \phi_y h_i^2 \quad (2)$$

In this step the determination of yield and ultimate curvature for the collapse prevention performance level is necessary. It is reasonable to use a constant value $2\varepsilon_y / l_w$ as the yield curvature as recommended by Priestley even though the yield curvature of structural walls varies to some extent with the degree of axial forces and longitudinal reinforcement ratio. Then, equation (3) is rewritten as

$$\Delta_i = \frac{1}{3} \frac{2\varepsilon_y}{l_w} h_i^2 + \theta_p \left(h_i - \frac{l_p}{2} \right) \quad (3)$$

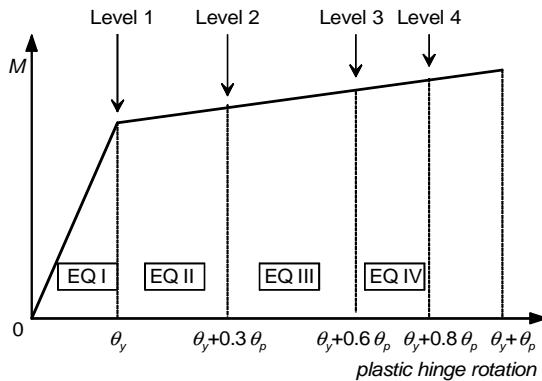


Figure 1 Performance-level to plastic hinge rotation relation[17]

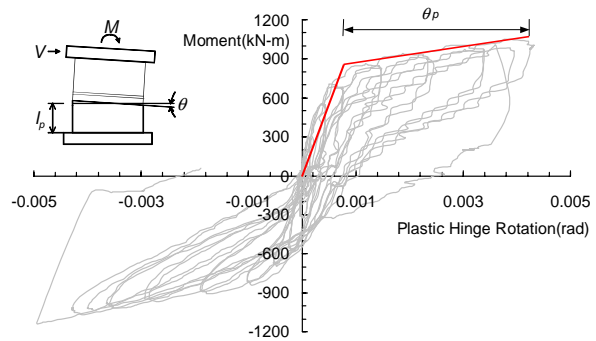


Figure 2 Plastic hinge rotation of unconfined wall[6]

The equivalent SDOF displacement is estimated by the substitute structure method [15] and the resulting values are considered as the target displacement;

$$\Delta_T = \frac{\sum m_i \Delta_i^2}{\sum m_i \Delta_i} \quad (4)$$

where m_i = story mass.

Step 3) Choose an appropriate value of effective structural damping.

The damping relationship is derived considering the effect of ductility on damping and is related to the hysteretic energy absorbed. An appropriate damping value dependent on structural systems includes both hysteretic damping and the traditional 5 percent viscous damping. The target displacement is modified with consideration of effective damping including viscous and hysteretic damping;

$$\Delta_{T,\xi} = \Delta_{T,5\%} \sqrt{\frac{7}{2 + 100\xi_e}} \quad (5)$$

where the effective damping $\xi_e = 0.05 + 0.7(1 - 1/\mu) / \pi$.

Step 4) Determine effective period and stiffness.

The effective period is determined by entering the displacement response spectrum curve (DRS) with Δ_T and reading across DRS curve based on appropriate system damping and down to T_{eff} . The effective stiffness at each selected performance level is determined from the following equation.

$$K_e = 4\pi^2 M_e / T_{eff}^2 \quad (6)$$

where the effective mass $M_e = \sum m_i \Delta_i / \Delta_{T,\xi}$.

Step 5) Determine required strength.

The base shear can be determined based on the effective stiffness and target displacement;

$$V_B = \Delta_{T,\xi} K_e \quad (7)$$

and thereby story shear is distributed and analyzed to calculate member forces for design. In the following the procedure is applied to design of walls.

The design base shear forces obtained by force-based design and DBD procedure are compared for 12, 16, and 20 story buildings with 4.8 m and 7.2 m of wall lengths and the 180 mm of thickness. The longitudinal reinforcements were provided with a 0.45 % reinforcement ratio distributed uniformly along the wall length with 1.4 % concentrated reinforcement in two equal groups at a distance of $0.1l_w$ from each end of the wall. The axial load ratios are varied with 0.09, 0.12, and 0.15 as higher stories. Earthquake levels for regions of high and moderate

seismicity are selected as UBC Zone 3 [7] and Zone 1 of Korea [4], respectively. The EPA's are equal to 0.45g and 0.18g for ground condition Sc. The target displacement depends on the performance level. The collapse prevention level for both cases is selected in this study. A likely plastic hinge location for slender cantilever walls is assumed at the bottom of the walls. The rotation angle of plastic hinges is chosen for the target displacement parameter instead of the top displacement used in most cases.

The maximum angle of plastic hinges depends on the degree of confinement in edge boundaries, axial forces, and shear forces. Assuming compatibility of deformation along the wall cross section, the ultimate curvature can be expressed as a function of the extreme concrete strain and neutral axis depth;

$$\phi_u = \varepsilon_{cu} / c_u = \varepsilon_{cu} / \alpha l_w \quad (8)$$

Note that UBC [7] sets concrete compression strain limit as $\varepsilon_{cu} = 0.015$ and the inter-story drift ratio criteria govern the design. According to Kowalsky, ε_{cu} of UBC is too large [9]. The ultimate curvature of walls with unconfined edge boundaries is obtained by UCFyber program [2] with setting of the extreme fiber compressive strain of 0.004. Priestley [14] recommended the use of the ultimate curvature $\phi_u l_w = 0.072 \pm 10\%$ for confined reinforcement corresponding to approximately double the value of $\varepsilon_{cu} = 0.004$ for $\alpha = 0.1$. Figures 3 and 4 show the decrease of the ultimate curvature as the increases of wall length and the axial force ratio. It is shown that the theoretical results are lower than the ultimate curvature of the experimental results.

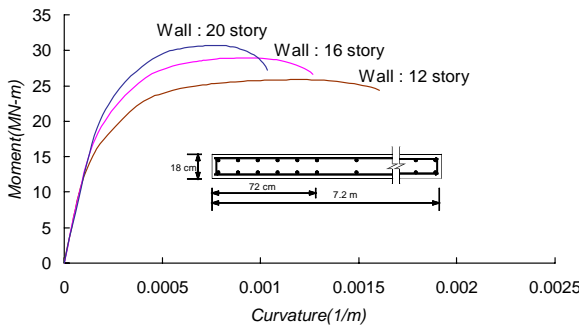


Fig. 3 Moment-curvature relation of 7.2m length walls

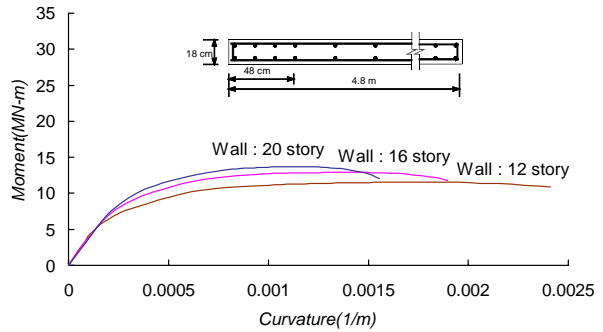


Fig. 4 Moment-curvature relation of 4.8m length walls

In this study the target plastic hinge rotation for the collapse prevention level is set as $\theta_T = \theta_y + 0.8(\theta_u - \theta_y)$. That is $\theta_p = 0.8(\phi_u - \phi_y)l_p$. Substitution of this into Eq. (3) and (4) yields the target displacement for the collapse prevention performance level as column (b) of Table 1. Then, the procedures for DDB are followed to obtain the design base shears. Another set of design base shears for the identical walls are calculated by the conventional force-based design method with R=3.0. Figure 5 shows the comparison of base shears from two methods.

Table 1 Design results by displacement and force based design

Walls		Displacement -Based Design						Force-Based Design			
		(a) θ_p (rad)	(b) Δ_T (m)	(c) ξ_e	(d) T_e (sec)	(e) K_e (kN/m)	(f) V_B (kN)	(g) V_B / W	(h) T_e (sec)	(i) V_B (kN)	(j) V_B / W
Korea zone I	K-4.8-12	0.0026	0.159	0.117	3.56	1025	163	0.033	1.18	235	0.046
	K-4.8-16	0.0022	0.247	0.098	5.12	633	121	0.018	1.58	271	0.040
	K-4.8-20	0.0020	0.359	0.087	7.11	402	81	0.010	1.97	303	0.036
	K-7.2-12	0.0022	0.116	0.128	2.69	1815	209	0.042	0.96	259	0.051
	K-7.2-16	0.0018	0.175	0.105	3.74	1200	209	0.032	1.29	300	0.044
	K-7.2-20	0.0014	0.245	0.088	4.86	860	173	0.021	1.61	335	0.040
UBC zone III	U-4.8-12	0.0026	0.159	0.117	1.42	6115	972	0.205	1.18	580	0.115
	U-4.8-16	0.0022	0.247	0.098	2.05	3739	924	0.148	1.58	669	0.010
	U-4.8-20	0.0020	0.359	0.087	2.84	2360	848	0.109	1.97	749	0.090
	U-7.2-12	0.0022	0.116	0.128	1.07	10943	1265	0.264	0.96	641	0.127
	U-7.2-16	0.0018	0.175	0.105	1.49	7150	1249	0.198	1.29	740	0.110
	U-7.2-20	0.0014	0.245	0.088	1.94	5.98	1247	0.159	1.61	828	0.098

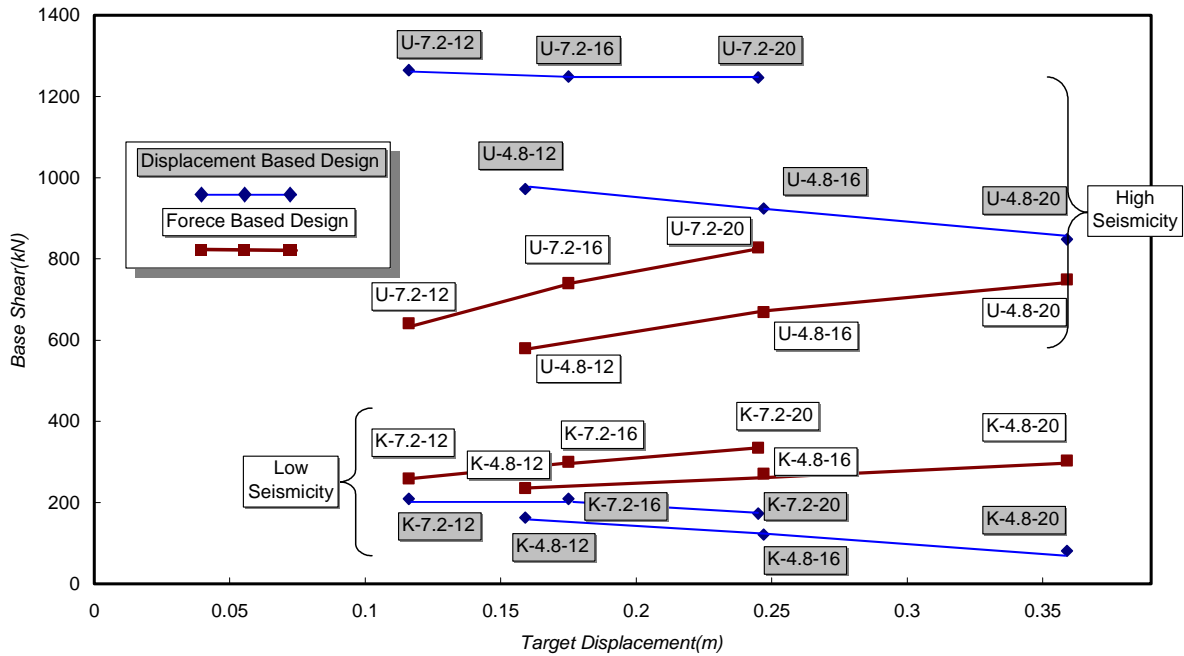


Figure 5 Comparison of base shears

As Priestley pointed out [13, 14], the required base shear by the direct displacement based design decreases more than those by the force-based design depending on different levels of seismicity. Higher story walls by DBD result in smaller base shears meanwhile higher story walls by FBD larger base shears. The DBD may account for the effect of the length of walls that have been neglected by the force-based design method.

DIRECT DIPLACEMENT-BASED ASSESSMENT

So-called capacity spectrum method is one of rational method for seismic assessment of existing structures. By means of graphical presentation, it compares the capacity of a structure with the demand of earthquake motion on the structure. The capacity of the structure is represented by a base shear-displacement curve obtained by pushover analysis. This method determines the performance point as the intersection of demand spectrum and capacity spectrum where the demand spectrum curve should consider inelastic behavior.

Displacement-based assessment procedure for the case of reinforced concrete buildings proposed by Priestley and Calvi [13] needs to estimate structural displacement capacity with plastic rotation capacities after classification of story-sway mechanisms and structural displacement demand from code displacement spectra. The method results in a single set of the base shear based on the probable post-elastic mechanism and corresponding story drift as the capacity of structure under consideration. Then, this procedure finally compares the displacement capacity and the displacement demand. This method is simple to judge acceptance of seismic capacity but not enough to give information for retrofitting in case of deficiency. To supplement this method this study uses the concept of the direct displacement-based design approach to construct a continuous demand spectrum curve for consideration of inelastic deformation of structures depending on required various performance levels.

The following procedures are suggested for the determination of demand spectrum curves;

Step 1) Likely locations of plastic hinges and failure mechanisms are identified throughout the structure by the capacity design method.

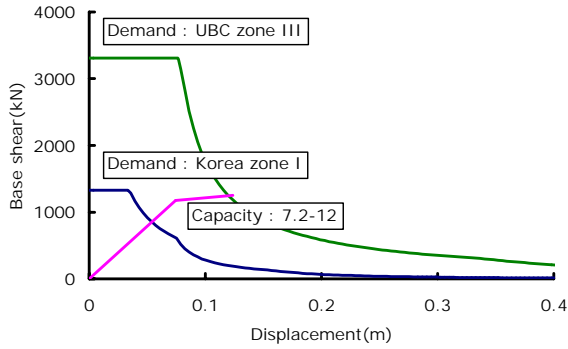
Step 2) A deformation model for the structure is made to estimate elastic, yield and inelastic displacements with the calculation of member plastic hinge capacities

Step 3) For given target displacements the required corresponding base shears are calculated. In this stage, all of the subsequent procedures are performed in the same way as the direct-displacement based design method.

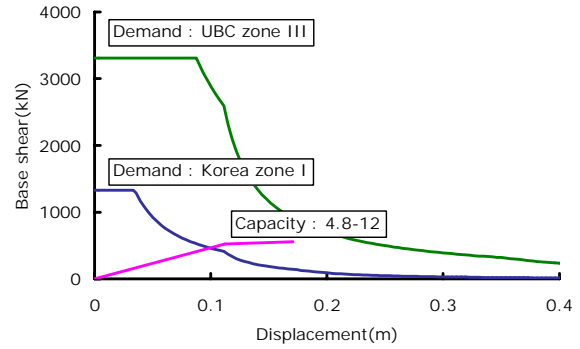
Step 4) Find the intersection point with the capacity curve obtained from a pushover analysis or a limit analysis based on a probable failure mechanism.

Figure 6 shows a set of curves for demands and capacities of walls with different lengths and stories in two seismic zones. Most walls of unconfined boundaries in UBC Zone 3 are not satisfactory for collapse prevention performance level except for U-7.2-12 wall. By contrast

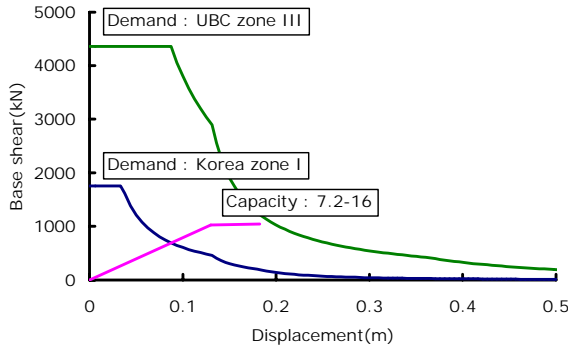
seismic capacity of walls with unconfined edge boundaries in region of moderate seismicity such as Korea shows sufficient strength and ductility.



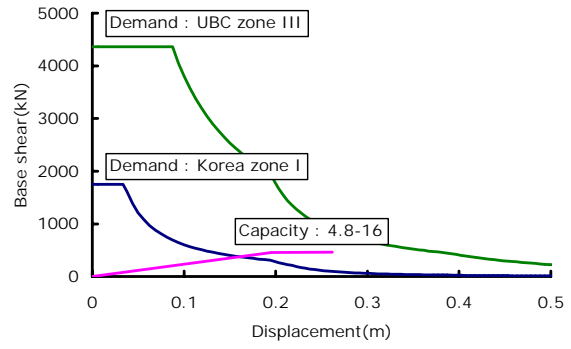
(a) 12-7.2



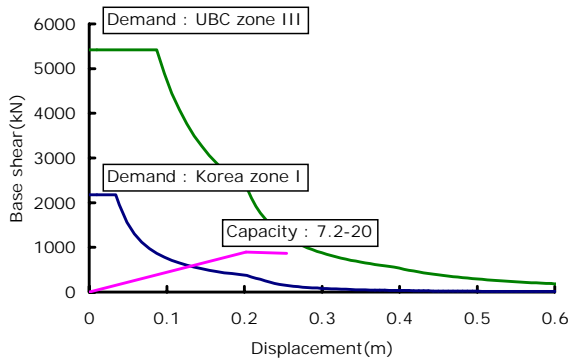
(b) 12-4.8



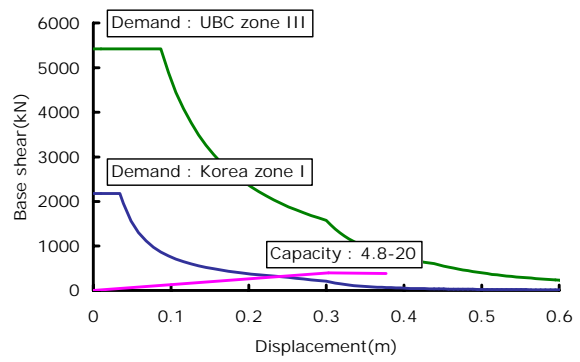
(c) 16-7.2



(d) 16-4.8



(e) 20-7.2



(f) 20-4.8

Figure 6 Assessment results in two seismic zones (story-1w)

CONCLUSION

As one of rational design methods for implementation of the performance-based design concepts the direct displacement-based design has been reviewed in this study and has been applied to the design of isolated walls with unconfined edge boundaries. The comparison with the force-based design has shown that DBD can be a rational tool for seismic design in the region of moderate seismicity that does not require strict bar detailing for ductility. For the force-based design, the required base shears are reduced with the higher story walls (reduction of stiffness) due to the use of constant force reduction factors and the reduced response acceleration (increase of T). In contrast, the required base shear based on displacement-based design increases with the higher story walls due to reduced ductility and effective damping with larger elastic deformation.

The extension application of the direct displacement design concept to a seismic assessment has been proposed. A continuous demand curve by the displacement-based design concept may provide a retrofit design guideline that considers strength and/or stiffness upgrading with deformability enhancement. The assessment has shown that the resulting performances of walls with unconfined edge boundaries have sufficient strength and ductility.

ACKNOWLEDGMENTS

This work was partially supported by grant No. 1999-1-310-002-3 from the Basic Research Program of the Korea Science & Engineering Foundation and the Brain Korea 21 Project. Opinions, findings and conclusions in this paper are those of the authors and do not necessarily represent those of the sponsors.

REFERENCES

1. ATC, "ATC 40: Seismic Evaluation and Retrofit of Concrete Buildings" California Seismic Safety Commission, 1996
2. Chadwel, C., "UCFYBER : Cross Section Analysis Software for Structural Engineers," University of California, Berkeley, 1999
3. Chandler, A. M. and Mendis, P.A., "Performance of Reinforced Concrete Frames using Force and Displacement based Seismic Assessment Methods," Engineering Structures 22 352-363, 2000
4. EESK , " A Study on the Seismic Design Criteria, Vol. 1 & 2" Ministry of Construction and Transportation, Dec. 1997
5. Fajfar, P. , " Capacity Spectrum Method based on Inelastic Demand Spectra," Earthquake Engineering and Structural Dynamics, 28, 979-993, 1999

6. Hong, S-G, Cho, B-H, Kang, S-M, and Park, H-G., "Ductility of Slender R/C wall structures," EESK Proceedings, 2000. 3.
7. International Conference of Building Officials, "Uniform Building Code," Whittier, California, 1997
8. Kowalsky, M.J., Priestley, M.J.N., and Macrae, G. A., "Displacement-Based Design of RC Bridge Columns in Seismic Regions", Earthquake Engineering and Structural Dynamics, Vol. 24, 1995
9. Kowalsky, M.J., "RC Structural Walls designed according to UBC and Displacement-based Method," Journal of Structural Engineering, ASCE, Vol. 127, No. 5, May, 2001
10. Medhekar, M. S. and Kennedy, D. J. L., "Displacement-Based Seismic Design-Theory," Engineering Structures 22, 2000
11. Paulay, T., and Priestley, M.J.N., " Seismic Design of Reinforced Concrete and Masonry Buildings," Wiley Inter-science, 1992
12. Priestley, M.J.N., "Performance Based Seismic Design," State of the Art, 12th World Conference of Earthquake Engineering, Auckland, New Zealand, 2000
13. Priestley, M.J.N. and Calvi, G.M., "Concepts and Procedures for Direct Displacement-based Design and Assessment, "Seismic Design Methodologies for the Next Generation of Codes, Balkema, Rotterdam, 1997
14. Priestley, M.J.N. and Kowalsky, M.J., " Aspects of Drift and Ductility Capacity of Rectangular Cantilever Structural Walls, " Bulletin, New Zealand Society for Earthquake Engineering, Vol. 33, 1998
15. Shibata, A. and Sozen, M.A., "Substitute-Structure Method for Seismic Design in R/C", Journal of the Structural Division, ASCE, 102(6), 1976.
16. SEAOC Vision 2000 Committee, " Performance Based Seismic Engineering," Report, Sacramento, California, 1995
17. SEAOC, "Guidelines for performance-based seismic engineering," SEAOC Blue Book, 1999



KEERC-MAE Joint Seminar on
Risk Mitigation for Regions of Moderate Seismicity
University of Illinois at Urbana-Champaign, August 5-8, 2001



Sponsors: Korea Science and Technology Foundation, U.S. National Science Foundation, Brain Korea 21



Modeling Fragility of Essential Facility Structures

Y. K. WEN¹, and K. W. LIAO²

¹ *Professor of Civil Engineering, University of Illinois at Urbana-Champaign
3129 Newmark Laboratory, 205 N. Mathews, Urbana, Illinois, USA
email: y-wen@uiuc.edu*

² *Research Assistant, University of Illinois at Urbana-Champaign
3106 Newmark Laboratory, 205 N. Mathews, Urbana, Illinois, USA
email: kliao@uiuc.edu*

ABSTRACT: Mid-America is a region where infrequent moderate to large earthquakes have occurred in the past and may occur again in the future. Almost all the essential facilities such as fire stations, police stations, and hospitals whose functionality after an earthquake is crucial have not been designed for seismic forces. The vulnerability of such structures is therefore a serious concern. In view of the large uncertainty and scarce data of recorded ground motions of engineering interest and past performance of such structures during earthquakes, the performance evaluation requires numerical analysis of response of such structures under synthetic ground motions that reflect the seismicity of the region. Such a study has been carried out for a class of essential facility buildings represented by un-reinforced masonry (URM) buildings in Carbondale Illinois. The seismic hazard is captured by suits of simulated uniform hazard ground motions corresponding to a given probability of exceedance. The nonlinear response behaviors of the URM buildings are modeled by finite element. Response time histories are calculated and probabilistic performance curves are obtained which can be used in evaluating the adequacy of the performance of the buildings, loss estimate and effectiveness of retrofit.

KEYWORDS: ground motions, simulation, essential facilities, fragility, nonlinear restoring force, uncertainty, probability, performance, masonry buildings.

INTRODUCTION

Although Mid-America is not a high seismic region, moderate to large such as the 1812 New Madrid events have occurred in the past and have a recurrence period of 500 years or less according to the most recent estimates. The threat of such damaging events and serious consequences is real and has not been considered in structural design in general in this region. The central issue is obviously the large uncertainty associated with the future excitations as well as the structural behavior under such excitations since very little data are available. Under such circumstances, simulation of ground motions and structural responses according to the best of our knowledge is necessary for evaluation of structural performance and estimation of loss. A study of the performance of essential facilities in Mid-America is carried out following this approach. The emphasis is on proper modeling of the uncertainties in the various elements from source, path, ground motions, to structural response, and their propagation in this chain of events. The results can be used in damage and loss evaluation as well as justification of retrofit. It is an on-going research. The methodology and findings thus far are summarized in the following. Details can be found in Wu and Wen (2000) and Wen and Liao (2001).

MODELING OF GROUND MOTIONS

Due to the lack of data of ground motion of engineering interest, ground motions are modeled by method of simulation. The uncertainties in occurrence time, source location, magnitude, attenuation, and soil amplification are modeled by random variables and simulated based on regional seismicity information and most up-to-date random vibration-based ground motion models. Both point-source and finite-source models are used which allow incorporation of some of the important near source effects of large events. The method can be used for fast simulation of large number of ground motions for a given site and from which suites of uniform hazard ground motions (corresponding to a given probability of exceedance) are selected and used for structural response analysis. The uniform hazard ground motions represent events of various magnitudes, distance, and attenuation. Their frequency and intensity are such that the median elastic or inelastic response of the structure gives an accurate estimate of the demand on structure for a given probability of exceedance. In other words, the suite of ten ground motions allows one to evaluate the structural response of small probability of exceedance that normally required much larger number (thousands) of structural response analyses. Figure 1 shows samples of the 2% in 50 years ground motions generated for Carbondale, Illinois. More details of the method and results of can be found in Wen and Wu (2001).

MODELING OF STRUCTURES

A site visit of the essential facilities of Carbondale, Illinois was carried out and information of the structural configuration and construction details was obtained. A fire station and a police

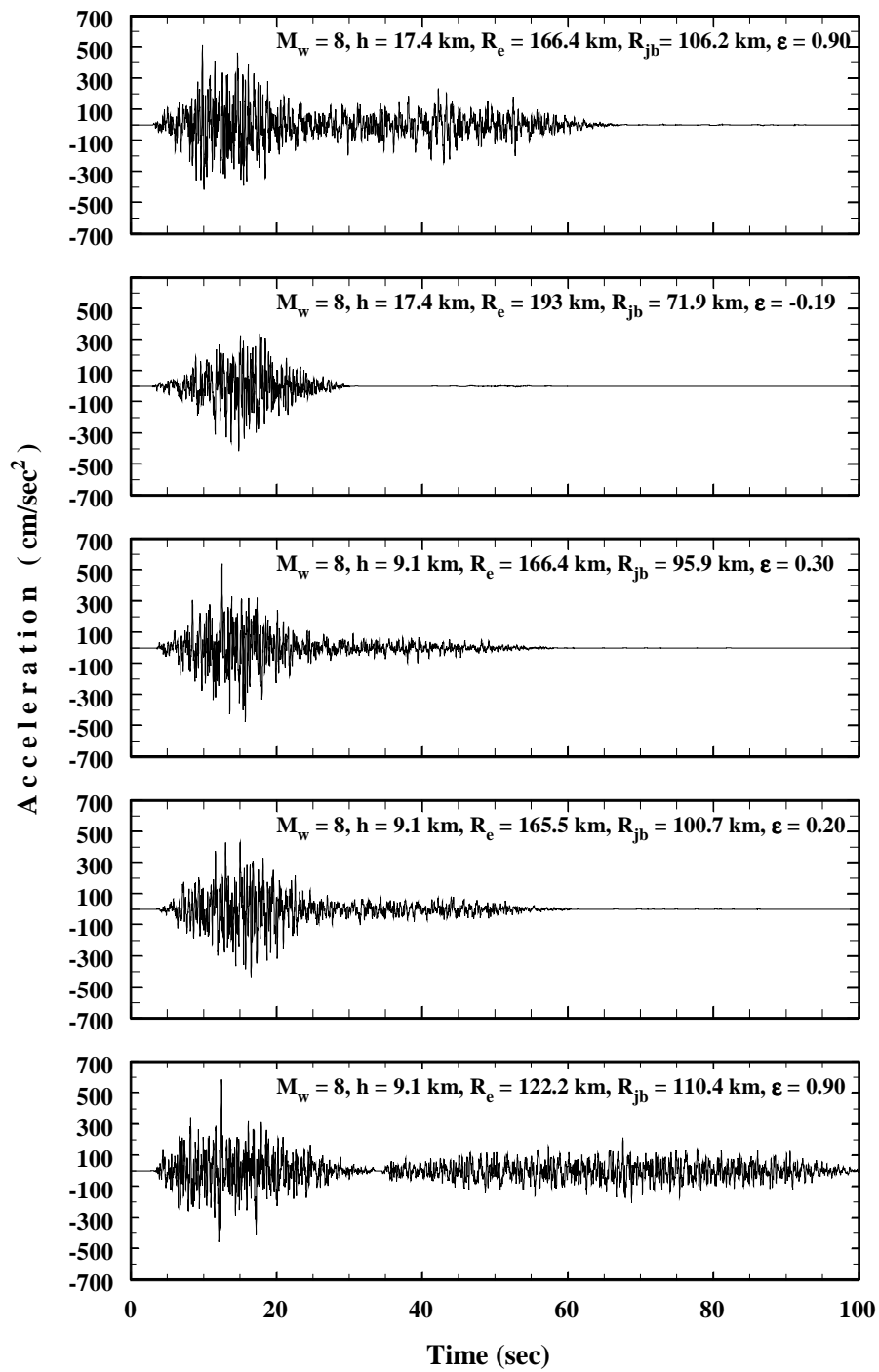


Figure 1 Samples of Simulated 2% in 50 Years Ground Motions at Carbondale Illinois



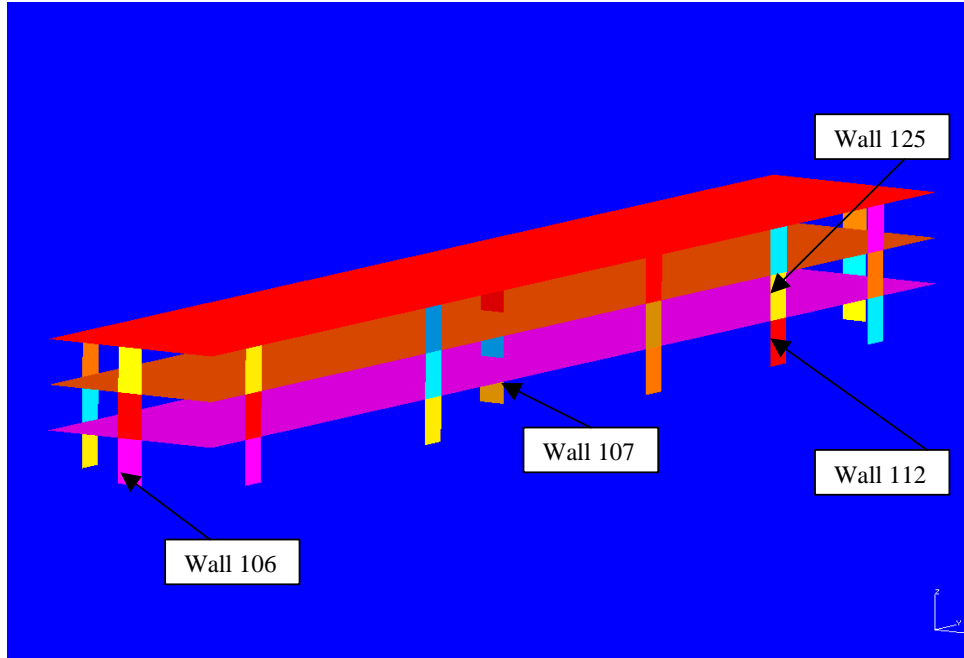
Figure 2 Carbondale Police Station (left) and Fire Station (right)

station, both 1960 un-reinforced masonry structures, were studied (Figure 2). The police station is three-story with a plane dimension of 35 ft by 230 ft and a height of 27 ft. The fire station is 60ft by 60 ft one-story building of a height of 16 ft. The thickness of the walls is 12 in. A finite element model based on ABAQUS was developed following the method by White and Kim (2001) for URM structures which has been verified by comparison with recorded structural response during the Loma-Prieta earthquake. The finite element models of these two structures are shown in Figure 3. The elastic modulus and the Poisson ratio for the walls are 515 ksi and 0.25. The stiffness for each wall was calculated according to the dimensions of the piers. The mass was calculated according to the sum of the weight of the slabs, the walls and fraction of the live load. The mass was lumped at the center of each diaphragm, and at the intersection of the central axes of walls and diaphragms. The diaphragms of the fire station were assumed to have shear modulus of 32500 lb/in^2 whereas those of the police station 1500000 lb/in^2 according to the material and structure of the actual construction. The diaphragms are assumed to be rigidly connected to the walls. The fundamental frequencies in the two horizontal directions are shown in Figure 3. The strength of the walls is modeled according to four different failure modes, i.e. diagonal tension, bed-joint sliding, toe crushing and rocking. Table 3 shows a typical example of the lateral strength calculation of Wall 106 (first floor end wall, see Figure 3) of the police station. For dynamic response analysis, it was assumed that when elastic limit is exceeded and the failure mode with the lowest strength prevails. The most common failure modes were sliding and rocking.

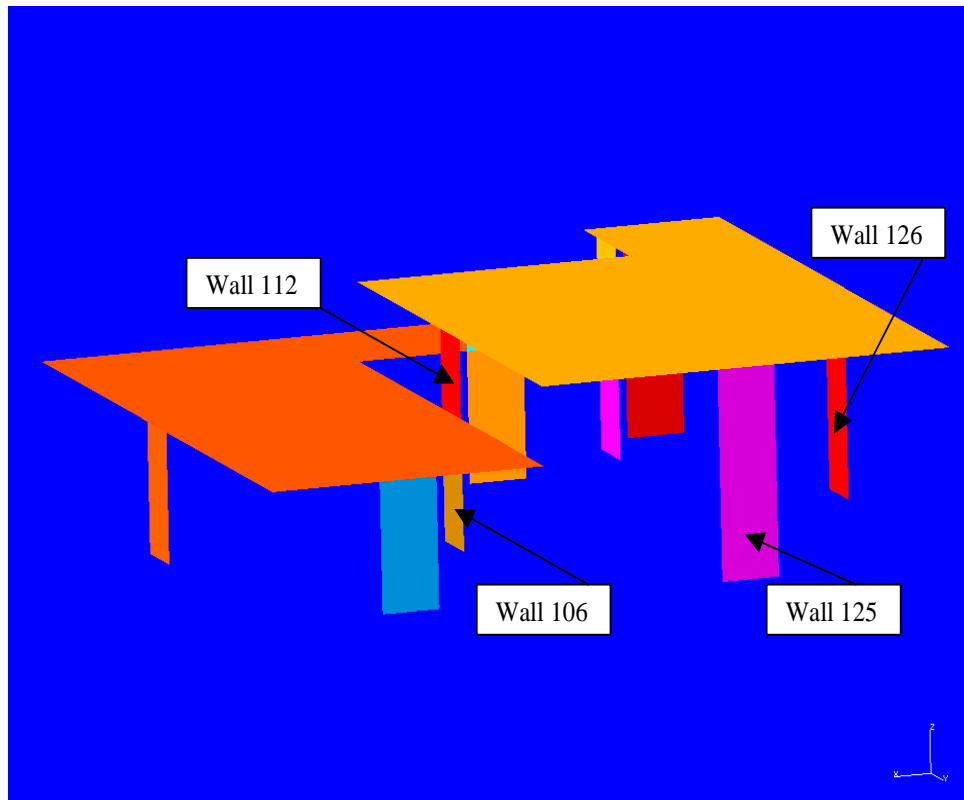
STRUCTURAL RESPONSE

Structural response time histories were calculated for each of the ten uniform-hazard ground motions. Figure 4 shows example of the time history and force-displacement (with bed-joint

sliding) of the response of Wall 112 of the fire station under a 2% in 50 years earthquake ground motion. Figure 5 shows the responses with rocking of Wall 112 of the police station under a 2% in



Police station. Period: $T_x=0.4$ sec. $T_y=0.15$ sec.



Fire station. Period: $T_x=0.59$ sec. $T_v=0.41$ sec.

Figure 3 Finite Element Models for the Police Station (top) and Fire Station (bottom)

Table 3 The Strength Calculation of Wall 106 of Police Station.

Wall 106	(Unit: kips)			
Pier No.	Bed-joint sliding	Rocking	Diagonal Tension	Toe Compressive
1	45.36	49.00	93.92	53.22
2	45.36	49.00	93.92	53.22
Total	90.72	98.00	187.83	106.44

50 years ground motion. The different energy dissipation characteristics of the two failure modes are obvious. The response analyses were carried out for each of the uniform hazard ground motions and for both 10% and 2 % in 50 years hazards. The drift ratio (in %) statistics are shown in Table 4 for the fire station and Table 5 for the police station. The median response represents the demand on the structures corresponding to a given probability of exceedance. It is seen that there are large differences among the response of the walls. For the fire station, Wall 125 models the gate of the station for fire trucks. It has small stiffness and the response is almost all elastic and reaches large amplitude. Wall 126 and 122 are the sidewalls, which provide most of the lateral resistance. They become inelastic and fail in bed-joint sliding mode. For the police station, it has only three lateral resisting walls (e.g.106, 107) in the transverse (X) direction. This is the weak axis and the drift responses are approximately three times larger than those in the longitudinal (Y) direction. Also the force demand at the wall/diaphragm interface is very high, especially for the 2% in 50 years ground motion. For example, the force demand at top of Wall 106 of the police station is 90,000 lb under the 2% in 50 years ground motions. Site visit inspection showed that there is very little constraints at the interface for the police station. The indication is that collapse of the structure is quite likely.

PROBABILISTIC PERFORMANCE EVALUATION

Because of the uncertainty in the demand and the capacity of the structures, the performance needs to be described in probabilistic terms. Commonly used performance criteria are occurrence rate (or probability) of specified structural limit state being exceeded over specified period of time, e.g. per year or over 50 years of structure's lifetime. The performance of the two essential structures can be described in terms of the drift response statistics under the uniform hazard ground motions. The median response is an accurate measure of this demand corresponding to a given probability of exceedance, which captures the effects of uncertainty of the seismic hazards. The uncertainty in the structural capacity against a given structural limit state, e.g. incipient collapse can be incorporated via a capacity uncertainty correction factor applied to the median response (Wen and Foutch 1997).

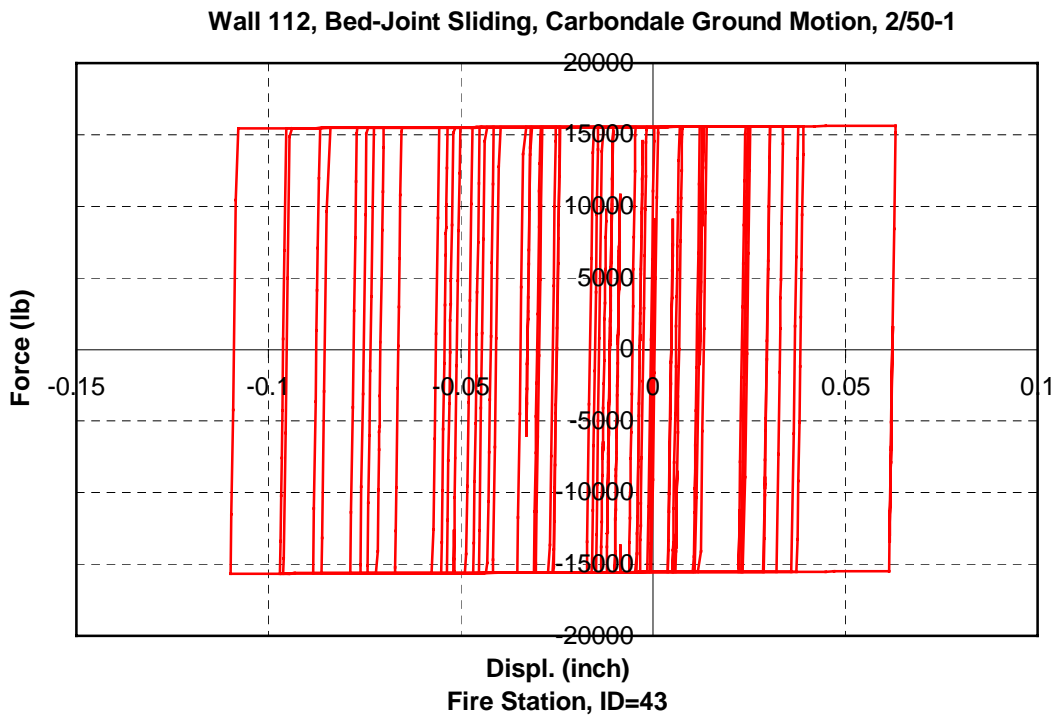
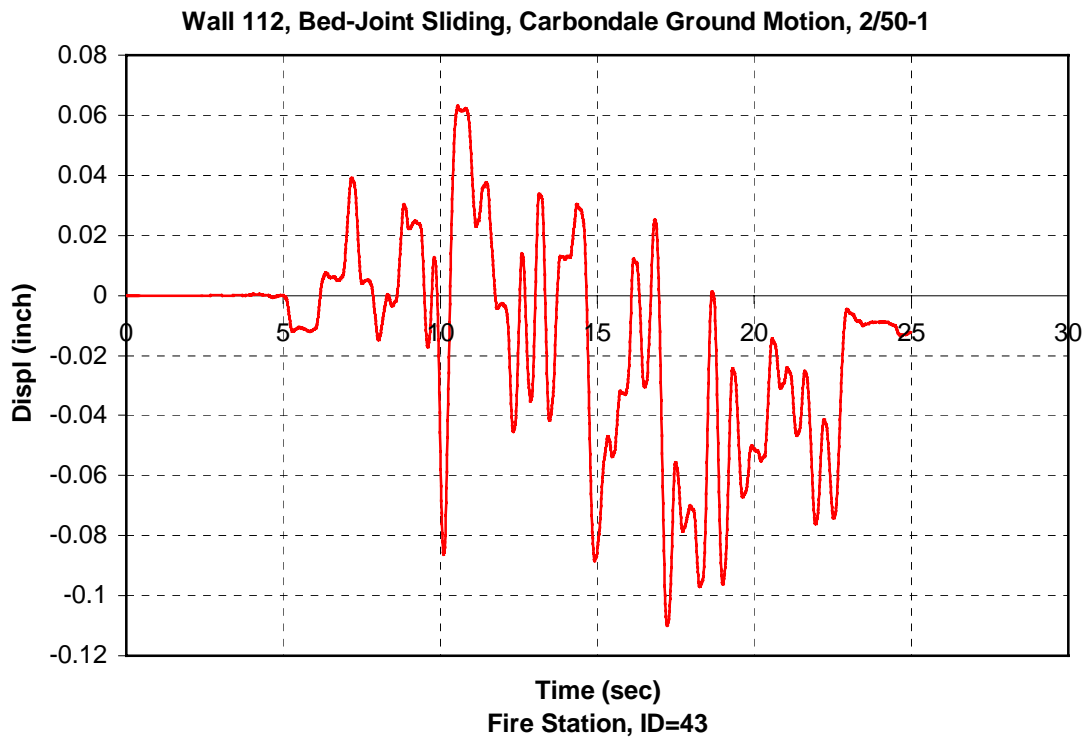


Figure 4 Time History Response and Fore-Displacement Relationship (Bed-Joint Sliding) of Wall 112, Fire Station under a 2% in 50 Years Ground Motion

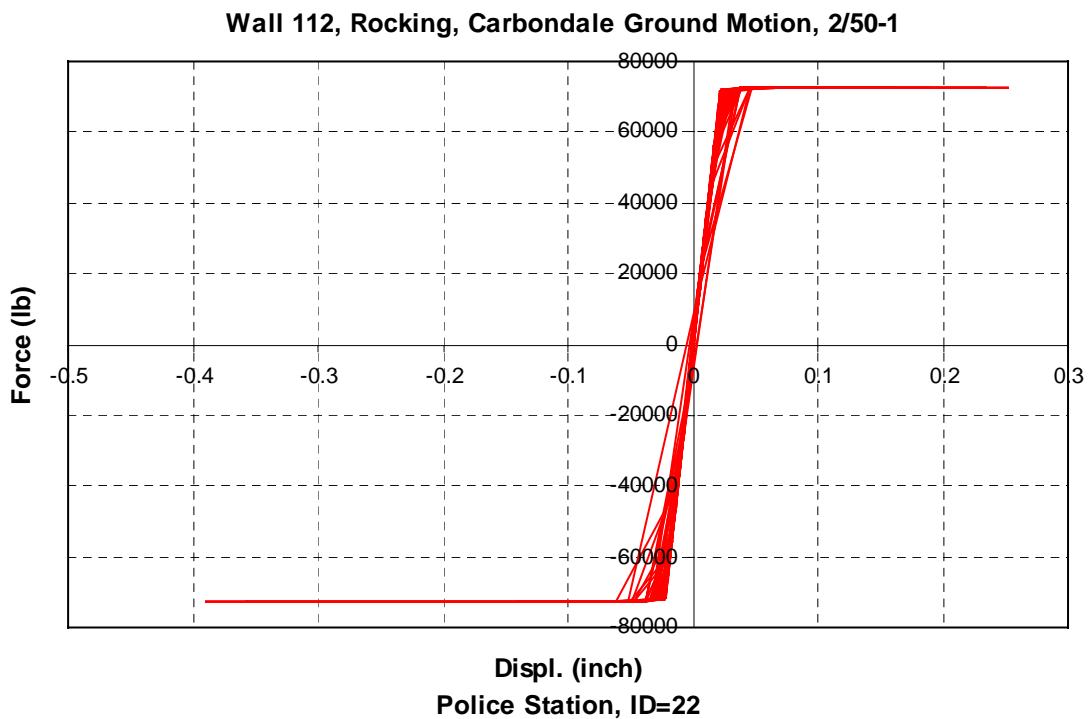
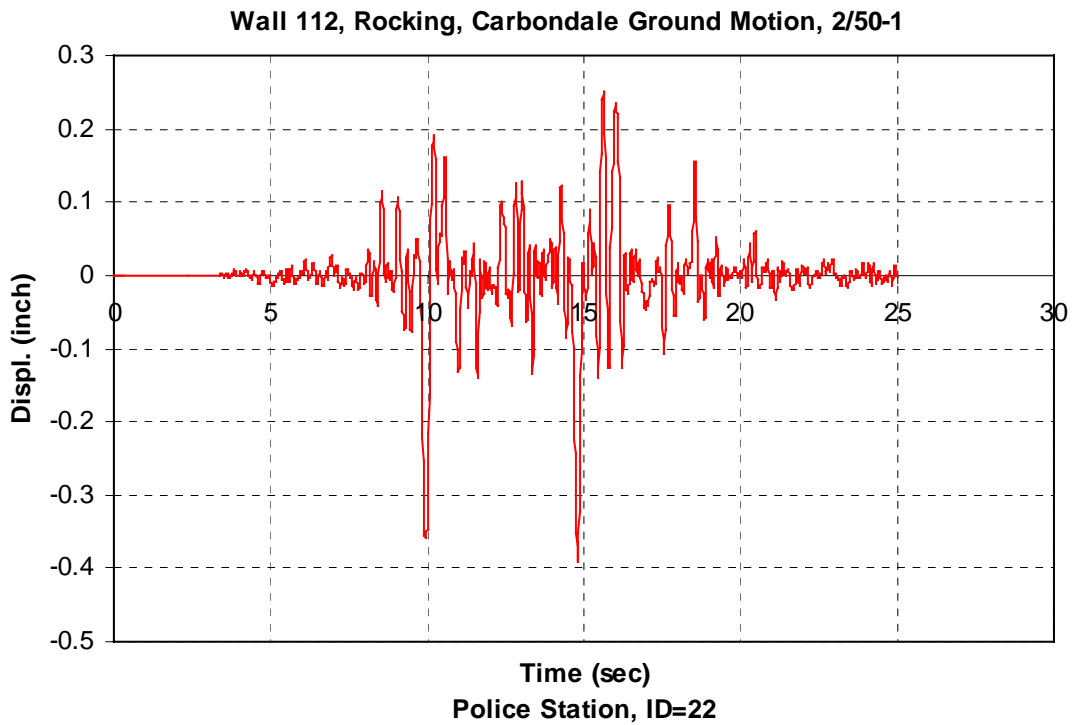


Figure 5 Time History and Force-Displacement Relationship (Rocking) of Wall 112 Police Station under a 2% in 50 Years Ground Motions

Table 4 The Median and Coefficient of Variation (COV) of Drift Ratio (%) of Selected Walls of the Fire Station

WALL	10/50		2/50	
	Med. (%)	COV	Med. (%)	COV
WALL 106	0.0060	0.4549	0.1118	0.3537
WALL 112	0.0066	0.7429	0.1687	0.2443
WALL 125	0.3001	0.1767	1.2899	0.1915
WALL 126	0.0052	0.2124	0.0243	0.1812

Table 5 The Media and Coefficient of Variation (COV) of Drift Ratio (%) of Selected Walls of the Police Station

WALL	10/50		2/50	
	Med. (%)	COV	Med. (%)	COV
WALL 107	0.1414	0.4369	1.2965	0.2934
WALL 112	0.0255	0.7942	0.3151	0.4947
WALL 125	0.0195	0.2171	0.0608	0.8177
WALL 106	0.1097	0.6231	0.9639	0.3673

The correction factor is given by

$$C = 1 + \frac{1}{2} S \delta^2$$

in which S is a sensitivity coefficient depending on the seismic hazard curve and δ is the coefficient of variation of the structure capacity. A coefficient of variation of 50% was assumed in this study and the sensitivity coefficient of 1.15 was found for seismic hazard at Carbondale IL for the 2% in 50 years hazard, yielding a correction factor of approximately 1.2. The median responses multiplied by the correction factor at the two probability levels then allow one to determine the probabilistic performance curve using a lognormal fit. The probabilistic performance curves are obtained for each structural element of the two buildings. Figure 6 shows the performance curve of Wall 125 (gate) of the fire station. The sample responses (\square) to the uniform hazard motions and the median point (O) are shown. The performance curves with and without consideration of the system capacity uncertainty are shown by solid and dashed lines. It is seen that in spite of the large uncertainty assumed for the capacity the results are not sensitive to the assumption due to the dominance of the uncertainty in the seismic hazard in Mid-America. The performance curve of Wall 107 of the police station is shown in Figure 7. It is one of the first floor lateral load-resisting elements along the weak axis. Large drift ratios indicate that the wall would be seriously damaged.

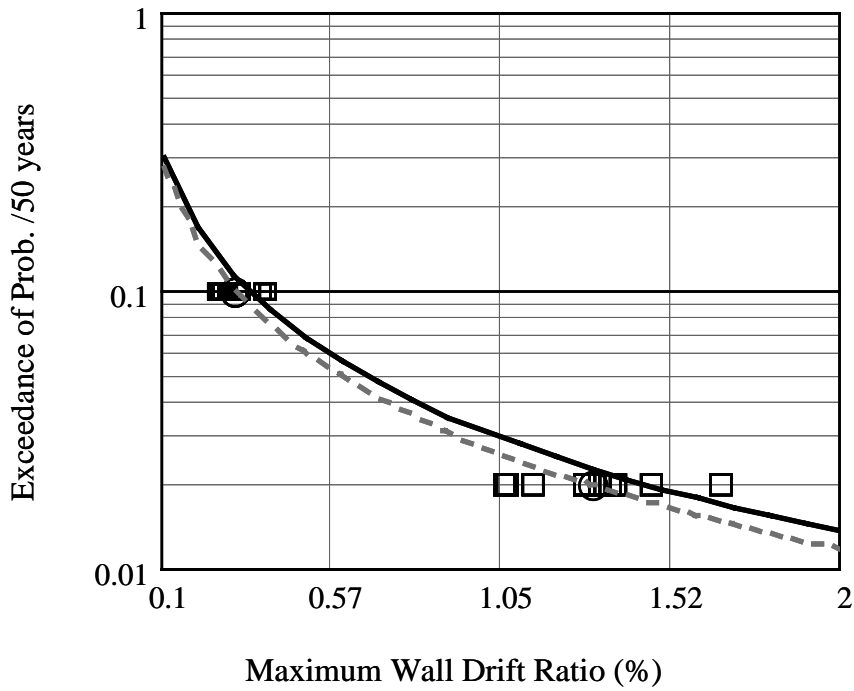


Figure 6 Probabilistic Performance Curve of Wall 125 of the Fire Station.
 (response \square , median \circ , solid line includes capacity uncertainty)

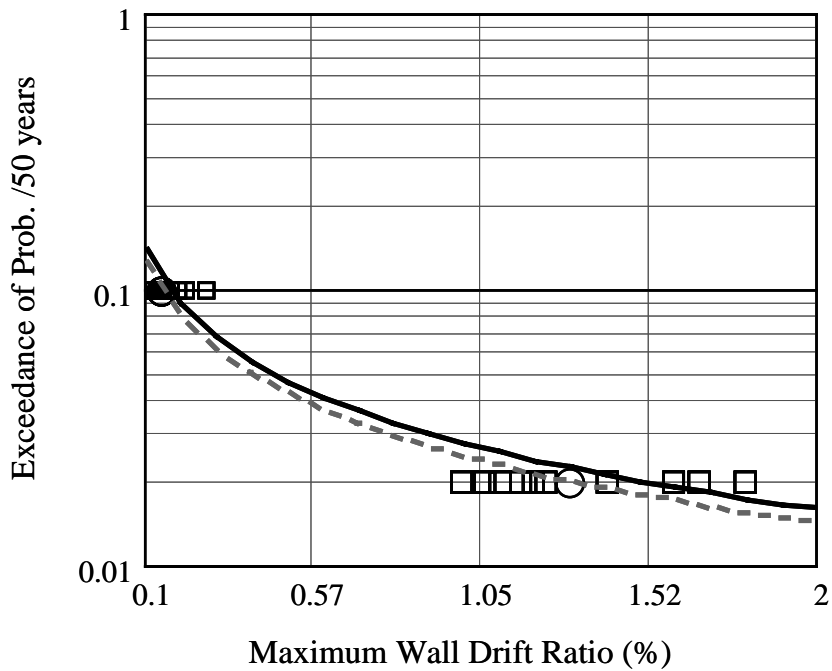


Figure 7 Probabilistic Performance Curve of Wall 107 of the Police Station.
 (response \square , median \circ , solid line includes capacity uncertainty)

The probabilistic performance curves of the structural elements generally indicate that the two essential facility buildings do not have adequate resistance for protection of the structures against serious structural limit states including collapse during the next 50 years. The risks of such serious structural limit states and large consequences are significant that retrofit or replacement of the structure may be necessary. The structural response can be converted into damage and loss measures and the performance curves provide information necessary for evaluation of probability and expected value of loss and reduction of expected loss through retrofit or replacement of the structures.

SUMMARY AND CONCLUSIONS

In view of the scarcity of ground motion and structural performance records in Mid-America, a method of evaluation of the vulnerability of essential facility buildings based on simulation is presented. Uniform-hazard ground motions were generated according to regional seismicity and latest ground motion models in which large uncertainty inherent in seismic hazards were properly considered. The response of the police station and the fire station at Carbondale Illinois, both 1960 un-reinforced masonry buildings not designed for seismic forces, were studied. The nonlinear structural response behavior was modeled by finite-element. Uncertainty in the structural capacity was also considered. Response time histories were obtained and from which probabilistic performance curves for each structural element and structure as a whole were obtained. The results show that the displacement and force demands on the structural are quite large that serious structural limit states including collapse are likely to occur during a 2% in 50 years event. The probabilistic performance curves of the structural elements show that the risk of serious damage and large consequence are significant that retrofit or replacement of the structure may be necessary. The performance curves also provide information necessary for evaluation of expected loss and loss reduction through retrofit or replacement of the structures.

ACKNOWLEDGMENTS

This study is supported primarily by the Earthquake Engineering Research Centers Program of National Science Foundation under Award Number EEC-9701785 through Mid-America Earthquake Center. The authors are grateful to D. W. White and S. C. Kim for their help in developing the nonlinear finite element models.

REFERENCES

1. Wen, Y. K., Song, S-H and Liao, K. W. “ Fragility of Retrofitted Essential Facilities” Report to Mid-America Earthquake Center, under preparation.
2. Wen Y. K. and Wu, C.-L. “ Uniform Hazard Ground Motions for Mid-America Cities”, *Earthquake Spectra*, May, 2001, pp 359-384.
3. White, D. W. and Kim, S-C ”Analysis of Gilroy Fire House under Loma Prieta and Carbondale Earthquake Motions”, Georgia Institute of Technology, Atlanta, Georgia, April 2001.
4. Wen, Y. K. and Foutch, D. A., Proposed Statistical and Reliability Framework for Comparing and Evaluating Predictive Models for Evaluation and Design, and Critical Issues in Developing Such Framework, *SAC Joint Venture Report No. SAC/BD-97/03*,1997.



KEERC-MAE Joint Seminar on
Risk Mitigation for Regions of Moderate Seismicity
University of Illinois at Urbana-Champaign, August 5-8, 2001



Sponsors: Korea Science and Technology Foundation, U.S. National Science Foundation, Brain Korea 21



Structural Damage Detection in Time Domain from Measured Acceleration During Earthquake

Joo Sung KANG¹, Inho YEO² and Hae Sung LEE³

¹ Graduate Student, Seoul National University
School of Civil, Urban and Geosystem Eng., Shillim-dong, Kwanak-gu, Seoul 151-742, Korea
email: jskang94@plaza1.snu.ac.kr

² Senior Researcher, Highway Management Corporation
Research Institute, Ichon 467-860, Korea
email: ihyeo@himan.co.kr

³ Associate Professor, Seoul National University
School of Civil, Urban and Geosystem Eng., Shillim-dong, Kwanak-gu, Seoul 151-742, Korea
email: chslee@plaza.snu.ac.kr

ABSTRACT: This paper introduces an algorithm for the parameter estimation scheme based on system identification (SI) in time domain. Acceleration data measured by dynamic tests are used as the measured responses. The least squared errors of the difference between calculated acceleration and measured acceleration are adopted as an error function. Damping parameters as well as stiffness properties of a structure are considered as system parameters. The Rayleigh damping is adopted for the SI. A regularization technique is applied to alleviate the ill-posed characteristics of SI problems. A new regularization function suitable to the time domain is proposed. The regularization factor is determined by the geometric mean scheme (GMS). First order of sensitivity of acceleration is obtained by direct differentiation of the equation of motion. The validity of the proposed method is demonstrated by numerical examples.

KEYWORDS: parameter estimation, system identification, time domain, regularization, geometric mean scheme, least square error, measured acceleration, inverse problem

INTRODUCTION

The modal analysis approaches have been widely adopted to identify structural properties using measured acceleration. The modal analysis approaches suffer from drawbacks caused by insensitiveness of modal data to changes of structural properties. In addition, the damping properties of structures cannot be estimated by the modal analysis. To overcome the drawbacks of the modal analysis approaches, this paper presents a system identification scheme to determine structural properties such as stiffness and damping parameters of structures using measured acceleration data. The proposed algorithm is based on the minimization of an error function with respect to the structural parameters. The error function is defined as the time integral of the least squared errors between the measured acceleration and the calculated acceleration by a mathematical model.

A system identification problem is a type of inverse problems, which are usually ill-posed. An ill-posed problem is characterized by the non-uniqueness and instability of solutions. The regularization technique has been employed to overcome the ill-posedness of inverse heat transfer problems and inverse elasticity problems. In the regularization technique, a predefined regularization function is added to the error function to impose constraints on the admissible solutions of a given inverse problem. This paper introduces a new regularization function that is defined as the L_2 norm of the time derivative of system parameters. To determine the regularization factor, which has crucial effect on the solution of the SI scheme, the geometric mean scheme is adopted.

The validity and effectiveness of the proposed method are demonstrated with several numerical examples. The numerically generated data with noises are utilized as measured acceleration. Detailed discussions on the numerical behaviors of the proposed method are presented.

PARAMETER ESTIMATION SCHEME IN TIME DOMAIN

The discretized equation of motion of a given structure is obtained by the finite element method as follows.

$$\mathbf{M}\mathbf{a} + \mathbf{C}(\mathbf{x})\mathbf{v} + \mathbf{K}(\mathbf{x})\mathbf{u} = \mathbf{P}(t) \quad (1)$$

where \mathbf{x} and \mathbf{P} are a system parameter vector and a load vector, and \mathbf{M} , \mathbf{C} and \mathbf{K} represent the mass, damping and stiffness matrix of the structure, respectively. \mathbf{a} , \mathbf{v} and \mathbf{u} are the acceleration, velocity and displacement of the structure, respectively. Newmark β -method is used to integrate the equation of motion (1).

It is assumed for damage detection that accelerations of a given structure are measured from a dynamic test at some discrete observation points, and that the stiffness properties and damping properties during the test do not change. The unknown system parameters of a structure

including stiffness and damping properties are identified through minimizing least squared errors between computed and measured acceleration.

$$\Pi_E(t) = \text{Min}_x \frac{1}{2} \int_0^t \|\tilde{\mathbf{a}}(\mathbf{x}) - \bar{\mathbf{a}}\|^2 dt \quad \text{subject to } \mathbf{R}(\mathbf{x}) \leq 0 \quad (2)$$

where $\tilde{\mathbf{a}}$, $\bar{\mathbf{a}}$ and \mathbf{R} are the calculated acceleration and the measured acceleration at observation points and constraint vector, respectively, with $\|\cdot\|$ representing the Euclidean norm of a vector. Linear constraints are used to set physically significant upper and lower bounds of the system parameters. The minimization problem defined in Eq. (2) is a constrained nonlinear optimization problem because the acceleration vector $\tilde{\mathbf{a}}$ is a nonlinear implicit function of the system parameters \mathbf{x} .

The parameter estimation defined by a minimization problem as Eq. (2) is a type of ill-posed inverse problems. Ill-posed problems suffer from three instabilities: nonexistence of solution, non-uniqueness of solution and discontinuity of solutions when measured data are polluted by noises. Because of the instabilities, the optimization problem given in Eq. (2) may yield meaningless solutions or diverge in optimization process. Attempts have been made to overcome instabilities of inverse problems merely by imposing upper and lower limits on the system parameters. However, it has been demonstrated by several researchers that the constraints on the system parameters are not sufficient to guarantee physically meaningful and numerically stable solutions of inverse problems [1].

The regularization technique proposed by Tikhonov is considered as a more rigorous way to overcome the ill-posedness of inverse problems. In the regularization technique, the original object function is modified by adding a positive definite regularization function [2,3]. Various regularization functions are used for different types of inverse problems. The following regularization function is adopted for the parameter estimation in time domain.

$$\Pi_R(t) = \frac{\lambda}{2} \int_0^t \left\| \frac{d\mathbf{x}}{dt} \right\|^2 dt \quad (3)$$

where λ is the regularization factor. By adding the regularization function to the error function, the regularized parameter estimation scheme is defined as follows.

$$\text{Min}_x \Pi(t) = \frac{1}{2} \int_0^t \|\tilde{\mathbf{a}}(\mathbf{x}) - \bar{\mathbf{a}}\|^2 dt + \frac{\lambda}{2} \int_0^t \left\| \frac{d\mathbf{x}}{dt} \right\|^2 dt \quad \text{subject to } \mathbf{R}(\mathbf{x}) \leq 0 \quad (4)$$

The regularization function defined in Eq. (3) represents the variance of system parameters in time. Since the system parameters are assumed to be invariant in time, the regularization function vanishes in case the SI yields exact solution. However, the ill-posedness of a inverse problem and noises in measurements generally lead to severe oscillations of the solution of Eq. (2) in time. The regularization function added in Eq. (4) becomes smaller as the rates of

changes of the system parameters decrease, and thus prevents the system parameters from arbitrary changes in time during optimization.

The regularization effect in parameter estimation process is determined by the regularization factor. The regularization effect vanishes for a small regularization factor while the regularization function has a dominant effect over the error function during the optimization process for a large regularization factor. In either case, the optimization problem is unable to estimate correct system parameters due to instabilities or excessive regularization effects on the system parameters. Therefore, selection of a proper regularization factor is very crucial to obtain meaningful solutions of system identification problems. The geometric mean scheme proposed (GMS) by Park is adopted in this study to determine the optimal regularization factor [4]. In the GMS, the optimal regularization factor is defined as the geometric mean between the maximum singular value and the minimum singular value of the Gauss-Newton hessian matrix of the discretized error function given in Eq. (2).

$$\lambda_{opt} = \sqrt{S_{max} \cdot S_{min}} \quad (5)$$

where λ_{opt} , S_{max} , S_{min} denote regularization factor, maximum singular value and minimum singular value which is greater than zero, respectively. The singular values of any given matrix can be obtained by using the singular value decomposition [5]. The sensitivity of the computed acceleration required in the optimization process is obtained by the direct differentiation of the equation of motion (1).

DAMPING MODEL

It is a difficult task to model damping properties of real structures. In fact, existing damping models cannot describe actual damping characteristics exactly, and are approximations of real damping phenomena to some extents. Since the damping has an important effect on dynamic responses of a structure, the damping properties should be considered properly in the parameter estimation scheme. In most of previous studies on the parameter estimation, the damping properties of a structure are assumed as known properties, and only stiffness properties are identified. However, the damping properties are not known a priori and should be included in system parameters in the SI.

Among various classical damping models, the modal damping and the Rayleigh damping are the most frequently adopted model. In the modal damping, a damping matrix is constructed by using generalized modal masses and mode shapes [6].

$$\mathbf{C} = \mathbf{M} \left(\sum_{n=1}^N \frac{2\zeta_n \omega_n}{M_n} \boldsymbol{\phi}_n \boldsymbol{\phi}_n^T \right) \mathbf{M} \quad (6)$$

where N , M_n , ζ_n , $\boldsymbol{\phi}_n$ and ω_n denote the number of the degrees of freedom (DOF), n -th generalized modal mass, modal damping ratio for n -th mode, the n -th mode shape and n -th

mode frequency, respectively. In Rayleigh damping, a damping matrix is represented by a linear combination of the mass matrix and stiffness matrix.

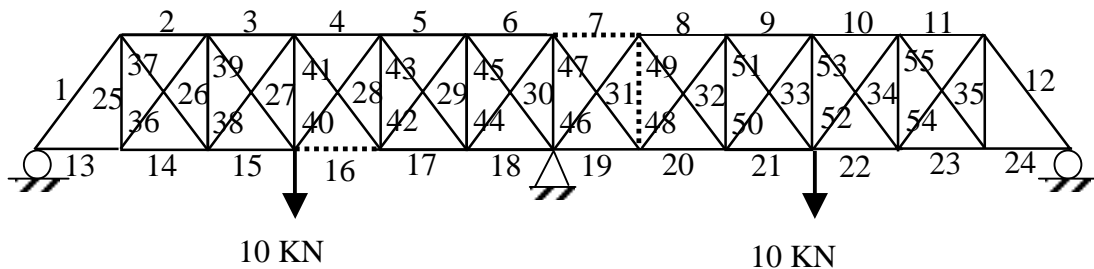
$$\mathbf{C} = a_0\mathbf{M} + a_1\mathbf{K} \quad (7)$$

The damping coefficients of the Rayleigh damping can be determined when any two modal damping ratios and the corresponding modal frequencies are specified.

In case the modal damping is employed in the parameter estimation, the number of the system parameters associated with the damping is equal to that of the total number of DOFs, which increases the total number of unknowns in the optimization problem given in Eq. (4). Since neither modal damping nor Rayleigh damping can describe actual damping exactly, and the modal damping requires more unknowns than the Rayleigh damping in the parameter estimation, this study employs the Rayleigh damping for the SI. The Rayleigh damping yields a linear fit to the exact damping of a structure.

EXAMPLE

The validity of the proposed time domain SI is examined through a simulation study with a two-span continuous truss shown in Figure 1. Typical material properties of steel (Young's modulus = 210 GPa, Specific mass = 7.85Kg/m³) are used for all members. The cross sectional area of each member (top member, bottom member, vertical member and diagonal member) is given in Figure 1. The natural frequencies of the truss range from 6.6 Hz to 114.7 Hz.



Member	Area(cm ²)	Member	Area(cm ²)
Top	112.5	Vertical	62.5
Bottom	93.6	Diagonal	75.0

Figure 1 2-span continuous truss

Damage of the truss is simulated with 40%, 50% and 34 % reductions in the sectional areas of member 7, 16 and 31, respectively. The damaged members are depicted by dotted lines in Figure 1. It is assumed that accelerations are measured from a free vibration induced by a sudden release of applied loads of 10KN shown in Figure 1. The measured accelerations are generated by the finite element model used in SI. The measurement errors are simulated by adding 8% random noise generated from a uniform probability function to acceleration calculated by the finite element model. The observation points are located at 12 bottom nodes of the truss. Both x - and y - component of acceleration are measured in the time period from 0 sec to 0.2 sec with the interval of 1/200 sec. The modal damping is employed for the calculation of measured acceleration while Rayleigh damping is adopted for the SI. The modal damping ratios for the calculation of measured acceleration are shown in Figure 4.

In case either the regularization scheme or damping estimation is not included in the SI, the optimization procedure does not converge or converges to meaningless solutions. Therefore, only the results with the regularization scheme and damping estimation are presented here. Figure 2 illustrates the variation of the identified stiffness properties of the damaged members with time. Although rather large measurement noise of 8% is presented, the proposed method is able to identify accurately the severity of damage of each damaged member. The identified stiffness properties of all members at the final time step are shown in Figure 3. Since stiffness properties of the damaged members reduce prominently compared with the oscillation magnitude of the other members, the damaged members are clearly assured. Figure 4 shows the exact modal damping ratios used for the calculation of measured accelerations together with identified modal damping ratios by the Rayleigh damping. The initial modal damping ratio calculated by the assumed Rayleigh damping coefficient is also drawn in the same figure. The identified Rayleigh damping well approximates the real modal damping.

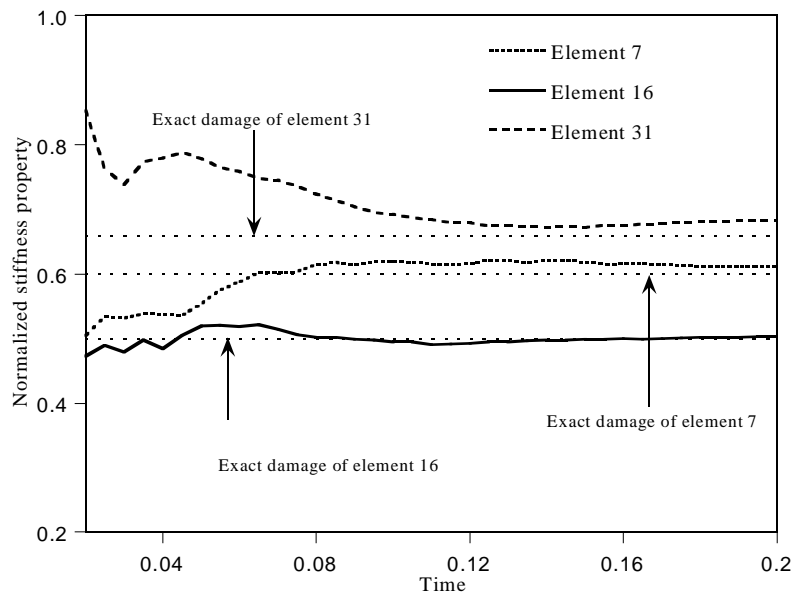


Figure 2 Variation of estimated stiffness properties of damaged members with time

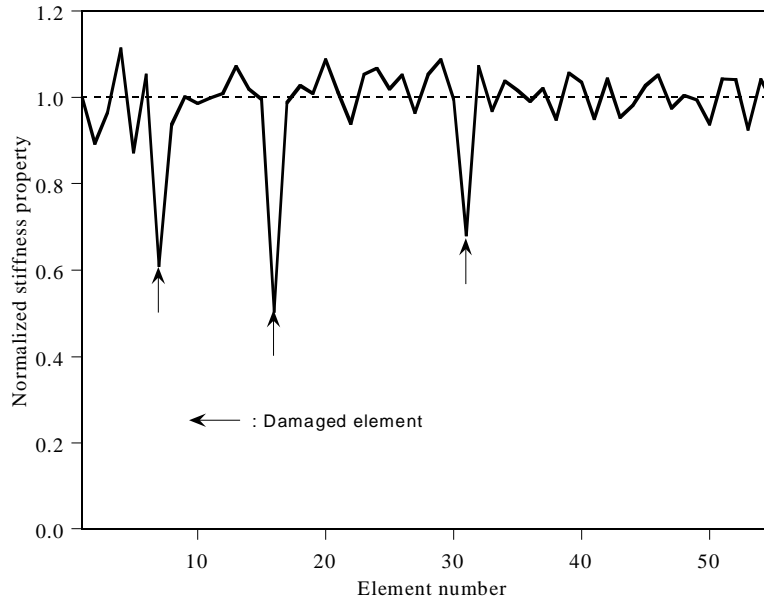


Figure 3 Estimated stiffness properties at the final time step

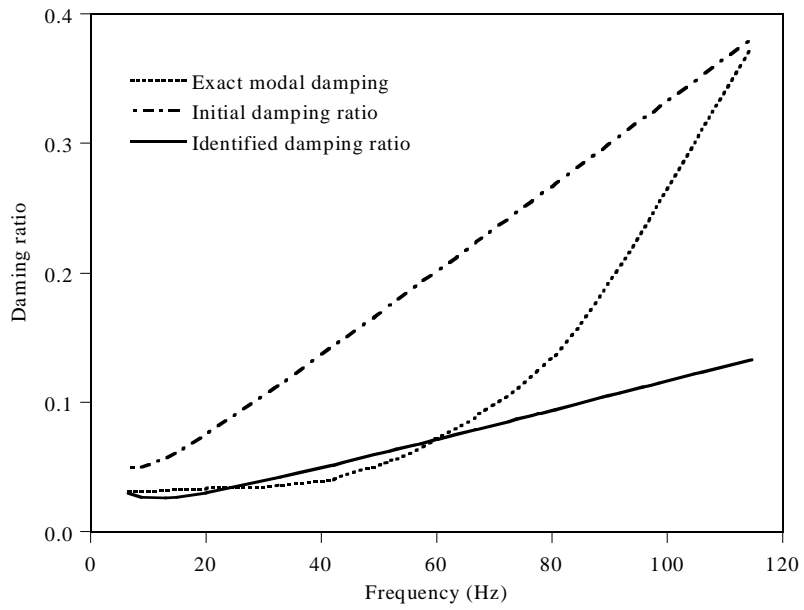


Figure 4 Estimated damping ratio

CONCLUSION

A time domain SI using measured acceleration data is proposed. The least squared errors of the difference between calculated acceleration and measured acceleration is adopted as an error function. The Tikhonov regularization technique is employed to alleviate the ill-posedness of the inverse problem in SI. The GMS is utilized to determine the optimal regularization factor. The Rayleigh damping is used to estimate the damping characteristics of a structure. The system parameters include the damping coefficients of the Rayleigh damping as well as the stiffness parameters of a structure.

In most previous study, the damping characteristics of a structure are assumed as known values. It is confirmed that the damping characteristics should be adjusted properly according to measured acceleration data. Although it is not possible to form the exact damping matrix of a structure, it is very important to approximate the damping matrix to the real damping matrix as close as possible. The proposed method can estimate the stiffness properties accurately even though the damping characteristics are approximated by Rayleigh damping. The final solution converges to the exact solution even for noise-polluted data. It is believed the proposed method provides a very powerful engineering tool to identify dynamic characteristics of structures and to detect damage in structures based on measured acceleration.

REFERENCES

1. Neuman, S.P., and Yakowitz, S., "A statistical approach to the inverse problem of aquifer Hydrology," *Water Resources Research*, Vol. 15(4), 1979, pp. 845-860.
2. Bui, H.D., *Inverse problems in the mechanics of materials: An introduction*, CRC Press, Boca Raton, 1994.
3. Hansen, P.C., *Rank-deficient and Discrete Ill-Posed Problems: Numerical Aspects of Linear Inversion*. SIAM: Philadelphia, 1998.
4. Park, H.W., Shin, S.B. and Lee, H.S., "Determination of Optimal Regularization Factor for System Identification of Linear Elastic Continua with the Tikhonov Function," *International Journal for Numerical Methods in Engineering*, Vol. 51, No.10, 2001, pp.1211-1230.
5. Golub, G.H. and Van Loan C.F., *Matrix Computations* (3rd edition). The Johns Hopkins University Press: London, 1996.
6. Chopra A.K., *Dynamics of Structures (theory and applications to earthquake engineering)*, Prentice Hall, 1995.



KEERC-MAE Joint Seminar on
Risk Mitigation for Regions of Moderate Seismicity
University of Illinois at Urbana-Champaign, August 5-8, 2001



Sponsors: Korea Science and Technology Foundation, U.S. National Science Foundation, Brain Korea 21



Seismic Performance of Reinforced Concrete Columns Depending on Longitudinal Reinforcement Details

Jae-Hoon LEE¹

¹Associate Professor, Dept. of Civil Engineering, Yeungnam University
214-1 Dae-Dong, Kyungsan City, KyungPuk 712-749, KOREA
email : jholee@yu.ac.kr

SUMMARY: Structural behavior of reinforced concrete column under seismic loading is significantly influenced by longitudinal reinforcement details. It may be preferable to use continuous longitudinal reinforcement for plastic hinge region of the column. However, longitudinal reinforcement connection within plastic hinge region is practically unavoidable in the case of large size bridge columns. This paper deals with experimental behavior of spirally reinforced bridge columns with various types of longitudinal reinforcement connection details. Eight column specimens with aspect ratio of 3.5 were tested under simulated earthquake loading. Variables of the experiment were longitudinal reinforcement connection details, transverse steel spacing, and axial load level. Ultimate drift, displacement ductility, and failure behavior are investigated and discussed.

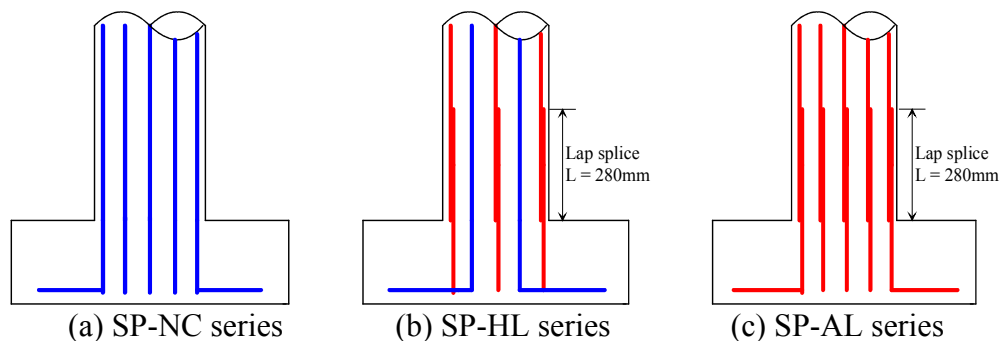
KEYWORDS: columns, seismic performance test, longitudinal reinforcement, connection detail, failure, ductility.

INTRODUCTION

There were severe damages of reinforced concrete bridge columns by shear failure and/or bond failure due to inappropriate lap splices of longitudinal reinforcement in San Fernando earthquake(1972), Whittier earthquake(1987), Loma Prieta earthquake(1989), and Kobe earthquake(1995). Therefore, the most seismic design specifications do not permit the lap-splices of longitudinal reinforcement within plastic hinges for the regions of high seismic risk. Current Korean seismic bridge design specifications have no special provisions that prohibit lap-splices of longitudinal reinforcement, since Korean peninsula is in moderate seismicity region. Nevertheless, the most Korean bridge engineers try to use continuous longitudinal reinforcement for plastic hinge region of the column, since it has been thought that the lap splices of longitudinal reinforcement are not desirable for seismic performance. However, longitudinal steel connection is practically unavoidable especially in the case of large size bridge columns. The objective of this paper is to investigate the seismic performance of spirally reinforced concrete columns with various types of longitudinal reinforcement connection details.

EXPERIMENTAL PROGRAM

The experimental program consisted of 18 spirally reinforced concrete column specimens with or without longitudinal reinforcement connection. Each column had a 400mm diameter cross-section and 1,600 mm height. The shear span was 1,400mm so that the aspect ratio should be 3.5. Reinforcement of D16 (diameter of 16 mm) was used for longitudinal steel with 5 types of connection details: 1) continuous, 2) half of reinforcements lap spliced, 3) all reinforcements lap spliced, 4) all reinforcements mechanically connected, 5) combination of lap splice and mechanical connection. The lap splice length was 280 mm, which was 12.6 times the longitudinal bar diameter and 0.7 times the cross sectional diameter. Reinforcement of D10 (diameter of 10 mm) was used for transverse steel with 2 types of spacing: 1) 80 mm for specimens of SP-HLS series, 2) 200 mm for the rest of the specimens. Spacing of 80 mm was equivalent to 5 times the longitudinal bar diameter, 8.4 times the transverse bar diameter, and volumetric steel ratio of 0.0099. Spacing of 200 mm was equivalent to 12.6 times the longitudinal bar diameter, 21 times the transverse bar diameter, and volumetric steel ratio of 0.004. Details and variables of the column specimens are shown in Fig. 1 and Table 1.



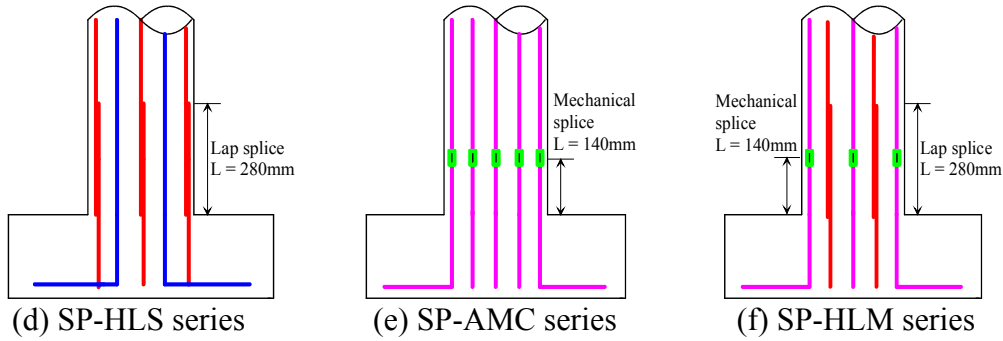


Figure 1 Longitudinal reinforcement details

Table 1 Test specimens

Series	No	Specimen	Longitudinal steel details	Spacing of transverse steel	Longitudinal steel ratio
NC	1	SP-NC-10	No connection	200 mm	$\rho_g = 1.26\%$ (8-D16)
	2	SP-NC-20			
	3	SP-NC-30			
HL	4	SP-HL-10	Half re-bars lap spliced	200 mm	
	5	SP-HL-20			
	6	SP-HL-30			
AL	7	SP-AL-10	All re-bars lap spliced	200 mm	
	8	SP-AL-20			
	9	SP-AL-30			
HLS	10	SP-HLS-10	Half re-bars lap spliced	60 mm	
	11	SP-HLS-20			
	12	SP-HLS-30			
AMC	13	SP-AMC-10	All re-bars mechanically connected	200 mm	
	14	SP-AMC-20			
	15	SP-AMC-30			
HLM	16	SP-HLM-10	lap splices + mechanical connection	200 mm	
	17	SP-HLM-20			
	18	SP-HLM-30			

Material tests were carried out to determine the actual strength of concrete and reinforcing steel. The average compressive strength of concrete was 30 MPa, which was obtained by compression test of 100 x 200 mm cylinders. The yield strength of the reinforcement was measured to be 338 MPa for the longitudinal steel (D16) and 367 MPa for the transverse steel (D10). The test was carried out under constant axial compression and incrementally increasing lateral deformation reversals. The axial load ratio ($P / f_{cu} A_g$) varied between 0.1 and 0.3. Fig. 2 illustrates test setup and lateral loading pattern.

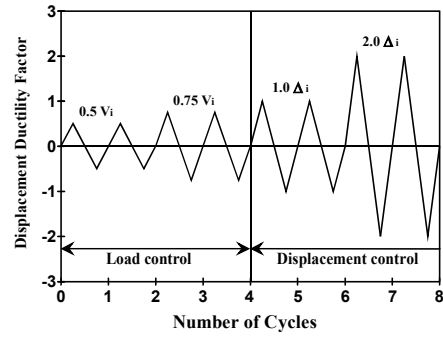


Figure 2 Test setup and lateral loading pattern

OBSERVED BEHAVIOR and TEST RESULTS

All the specimens showed similar behavior up to yield displacement. The first flexural crack occurred at 200 mm above the column base and the second flexural cracks developed at the construction joint between footing and column. Concrete cover under compressive stress started to spall at the displacement stage of $2 \Delta_y$. The longitudinal reinforcement in the plastic hinge region buckled at the displacement stage of $5 \sim 6 \Delta_y$. Reduction of lateral load resistance occurred due to stiffness deterioration. It was observed that the buckling and fracture of the longitudinal reinforcement were different by connection details.

Fig. 3 shows lateral load-displacement relationships of SP-NC-20, SP-HL-20, and SP-AL-20 specimens. Pinching is observed in the specimen of lap-spliced longitudinal reinforcement.

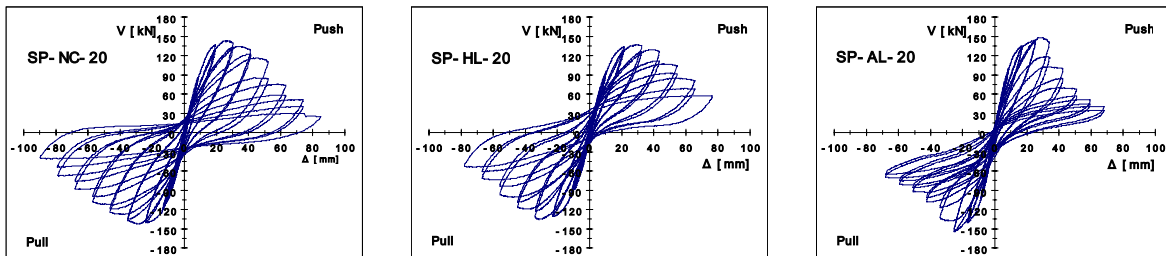


Figure 3 Lateral load-displacement relationships

Load-displacement envelope curves under the axial load ratio of 0.2 are shown in Fig.4. The envelope of HL specimen with 50% of longitudinal reinforcement lap spliced is close to that of NC specimen with continuous longitudinal reinforcement. The specimen AL with the entire longitudinal reinforcement lap spliced shows relatively abrupt strength degradation after maximum lateral force reaches. The specimen HLS with relatively larger transverse steel shows less strength degradation. The specimen AMC with the entire longitudinal reinforcement mechanically connected shows sustained strength after maximum lateral force.

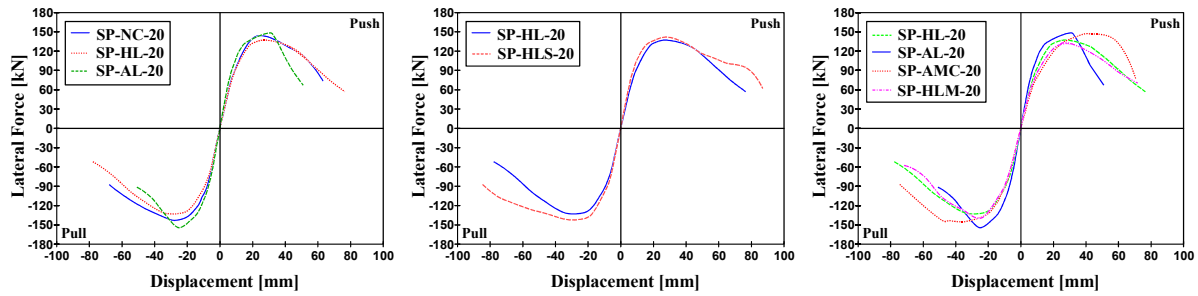


Figure 4 Envelope curves

Fig. 5 shows displacement ductility based on experimentally obtained yield displacement of each specimen. All the series show decreased displacement ductility as the axial load ratio increases. The specimens NC with continuous longitudinal reinforcement show at least 4.5 of displacement ductility, even though they are confined by small amount of transverse reinforcement. The displacement ductility of specimens with lap splices are less than those of NC specimens. AMC specimens with the entire longitudinal reinforcement mechanically connected show less displacement ductility than NC specimens, but higher than HL and HLM specimens

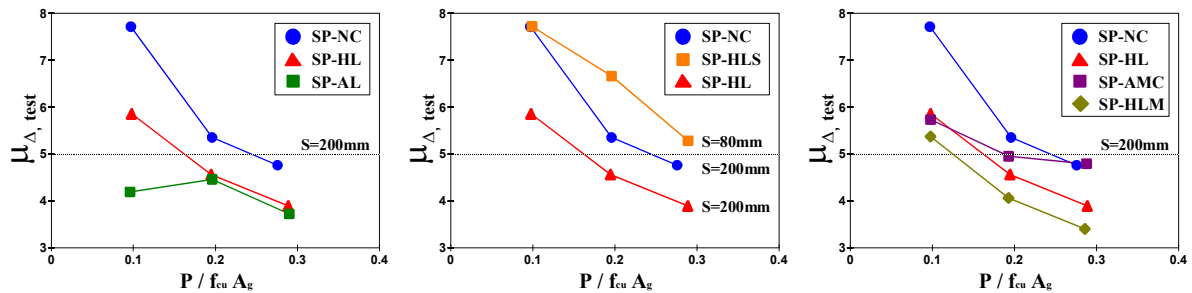


Figure 5 Displacement ductility

CONCLUSIONS

1. The specimens with the entire longitudinal reinforcement lap spliced showed relatively abrupt strength degradation and lower ductility than the other specimens.
2. The specimens with combination of lap splices and continuous longitudinal reinforcement showed less ductility than the specimens of which entire longitudinal reinforcement are continuous. However, those specimens with increased transverse steel amount showed greater ductility than the specimens with lightly confined continuous longitudinal reinforcement.
3. The specimens with the entire longitudinal reinforcement mechanically connected showed less displacement ductility than the specimens with continuous longitudinal reinforcement, but higher than the specimens with lap spliced longitudinal reinforcement.

REFERENCES

1. Ministry of Construction & Transportation, Korean Society of Civil Engineers, *Standard Specification of Highway Bridges*, 2000.
2. AASHTO, *Standard Specifications for Highway Bridges*. American Association of State Highway and Transportation Officials. 16-th edition, Washington, D.C. 1995.
3. ACI Committee 318, *Building Code Requirements for Structural Concrete (318-99) and Commentary (318R-99)*. American Concrete Institute, Farmington Hill, Michigan, 1999.
4. Paulay, T., and Priestley, M. J. N., *Seismic Design of Reinforced Concrete and Masonry Buildings*, John Wiley & Sons, Inc., New York, 1992.
5. Priestley, M. J. N., Seible, F., and Calvi, G. M., *Seismic Design and Retrofit of Bridges*, John Wiley & Sons, New York, USA, 1996.



KEERC-MAE Joint Seminar on
Risk Mitigation for Regions of Moderate Seismicity
University of Illinois at Urbana-Champaign, August 5-8, 2001



Sponsors: Korea Science and Technology Foundation, U.S. National Science Foundation, Brain Korea 21



Seismic Performance of Reinforced Concrete Beam-Column Connections and Frames

James M. LaFAVE¹, and Denise L. WELSH²

¹ Assistant Professor of Civil Engineering, University of Illinois at Urbana-Champaign
3108 Newmark Laboratory, 205 N. Mathews Ave., Urbana, Illinois 61801 USA
e-mail: jlafave@uiuc.edu

² Graduate Fellow, Department of Civil & Environmental Engineering
University of Illinois at Urbana-Champaign
3139 Newmark Laboratory, 205 N. Mathews Ave., Urbana, Illinois 61801 USA
e-mail: dwelsh@uiuc.edu

ABSTRACT: This paper summarizes the current seismic design approach required by the American Concrete Institute (ACI) *Building Code Requirements for Structural Concrete* (ACI 318-99) for proportioning beam-column connections in monolithic reinforced concrete frame structures. Important aspects of reinforced concrete beam-column connection design for earthquake-resistance include: confinement of the joint core, connection shear, reinforcement anchorage at the connection, and flexure at the connection. A new code provision related to tension slab participation effects on flexure at the connection is described. Nonlinear DRAIN-2DX pushover analyses of a recently designed and constructed reinforced concrete frame case study building (both including and neglecting slab participation) have been performed. It appears that the new code provision may have some unintended consequences on the relative proportions of reinforced concrete beams and columns that are ultimately selected for a particular frame. Additional analyses are still underway.

KEYWORDS: reinforced concrete, beam-column connections, seismic design, slab participation, joint shear, pushover analysis

INTRODUCTION

Low and moderate rise reinforced concrete (R/C) frame structures are common in seismically active regions of the world, providing economical buildings for a wide variety of end uses. If properly designed and detailed, R/C frame structures can perform quite well when subjected to strong earthquake ground motions. The members (beams and columns) of an R/C frame structure that may be subjected to earthquake loading are typically proportioned using lateral forces from a building code static design procedure. The lateral design forces specified in such codes are usually less than those that would correspond to a linear elastic response of the building to a strong earthquake ground motion. Therefore, the structure will be forced to absorb and dissipate energy by responding inelastically when subjected to a strong earthquake. This means that an R/C frame that is part of a lateral load resisting system must be able to undergo cyclic deformations into the inelastic range without any significant loss in strength.

The most common seismic design philosophy used in R/C frame structures is the so-called “strong column – weak beam” approach. This approach attempts to ensure that plastic hinges occur in the beams rather than in the columns during an earthquake. This is preferred because column plastic hinging would likely be accompanied by large lateral displacements and could lead to irreparable permanent sway in a structure or even a weak column story failure mechanism leading to collapse. Properly detailed R/C beam plastic hinge zones are capable of absorbing large amounts of energy while still maintaining their flexural and shear strengths. Beam-column connections must be designed to allow these beam plastic hinges to properly dissipate energy without a significant loss of connection strength or stiffness. In summary, if an R/C beam-column connection is designed so beam plastic hinging can occur without column plastic hinging, connection shear failure, or loss of reinforcing bar anchorage, then it is likely that the connection region will perform adequately when the structure is subjected to a strong earthquake ground motion.

This paper summarizes the current design approach required by Chapter 21 (“Special Provisions for Seismic Design”) of the American Concrete Institute (ACI) *Building Code Requirements for Structural Concrete* (ACI 318-99) [2] for proportioning beam-column connections in monolithic R/C frame structures. Then, an ongoing research project examining the effects of slab participation on R/C beam-column connections as well as on R/C frames is described.

DESIGN OF BEAM-COLUMN CONNECTIONS PER ACI 318-99

There are four key elements in the design of R/C beam-column connections per ACI 318-99. These are: 1) confinement of the joint core, 2) connection shear, 3) reinforcement anchorage at the connection, and 4) flexure at the connection. Each of these is briefly described below, along with a summary of current ACI 318-99 design provisions related thereto.

Confinement of the Joint Core

The column core in an R/C beam-column connection (known as the joint core) must be properly confined for the connection to perform adequately in a strong earthquake. Confinement permits the joint core to anchor beam reinforcement, transfer shear forces, and transmit the column axial load. Confinement of the joint core is related to the amount and spacing of longitudinal and transverse column reinforcement in the connection, as well as to the presence of transverse beams at the connection.

In order to ensure adequate confinement of the joint core, ACI 318-99 requires a minimum amount and a maximum spacing (typically 100 to 150 mm (4 to 6 in.)) of transverse reinforcement through the joint and into the adjacent column. The minimum amount of transverse reinforcement is in part a function of the confinement provided by transverse members framing in to the connection, while the maximum spacing of transverse reinforcement is in part a function of the distance between crossties or legs of overlapping hoops (which is of course a function of the spacing of the column longitudinal reinforcement).

Connection Shear

R/C beam-column connections must be designed to resist horizontal and vertical shears that result from flexural tension and compression forces and shear forces from the beams and columns framing into the joint. The ability of a beam-column connection to resist cyclic shear forces is influenced by many factors, such as transverse reinforcement, longitudinal reinforcement, transverse beams, concrete strength, and column axial load. The forces in a beam-column connection during a large lateral displacement of an R/C frame structure are as shown in Figure 1. The horizontal shear in the connection (V_u) is related to the flexural forces in the beams and the shear in the columns as:

$$V_u = (A_{s1} + A_{s2}) \alpha f_y - V_{c1} \quad (1)$$

where f_y is the nominal yield stress of the reinforcing steel, α is a stress multiplier, A_{s1} and A_{s2} are the areas of beam top and bottom reinforcement, and V_{c1} is the shear force in the column. The yield stress multiplier (α) can account for the possibility of increased steel stress resulting from strain hardening and/or a mean-to-nominal yield strength ratio greater than unity. The value of α is taken as 1.25 in ACI 318-99. V_{c1} may be estimated by equilibrium using the beam plastic hinge moments and shears and assuming the column contraflexure points to be at approximately mid-height when the frame is subjected to severe lateral deformation.

The ACI 318-99 provisions for connection shear strength assume a diagonal concrete compression strut joint failure mechanism and therefore simply relate the shear strength of the connection to the compressive strength of the concrete and the dimensions of the joint core, assuming that the joint core is properly confined per the requirements described in the previous section. The design shear strength (ϕV_n) prescribed by ACI 318-99 for an R/C beam-column connection is:

$$\phi V_n = \gamma \sqrt{f'_c} A_j \quad (2)$$

where γ is a factor that depends on the level of confinement provided to the four faces of the joint by the adjacent framing members, f'_c is the concrete design compressive strength, and A_j is the effective area of the joint (see Figure 2).

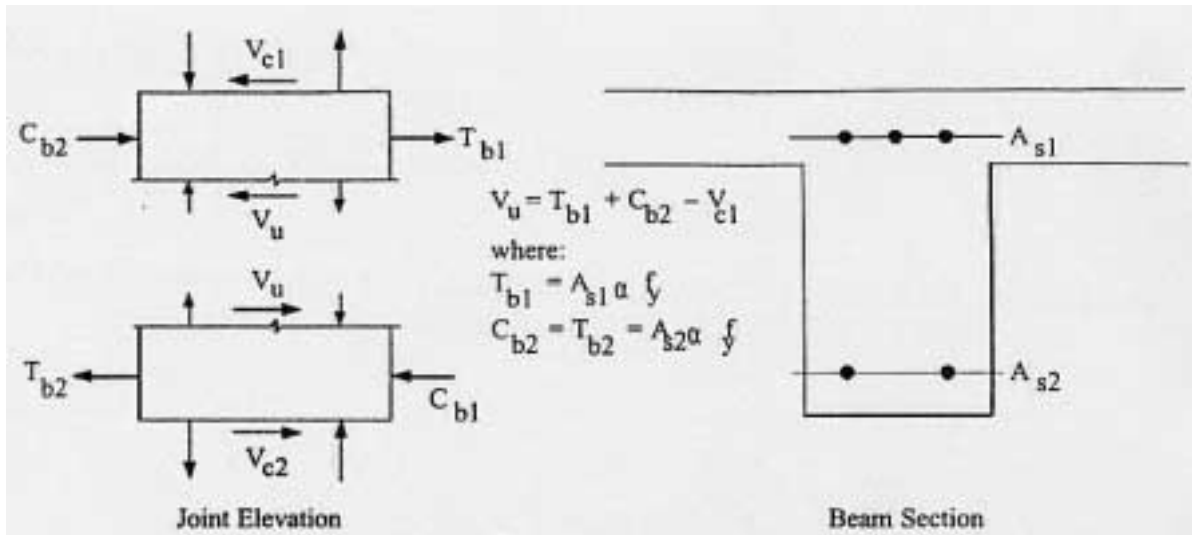


Figure 1 Forces in an R/C beam-column connection [3]

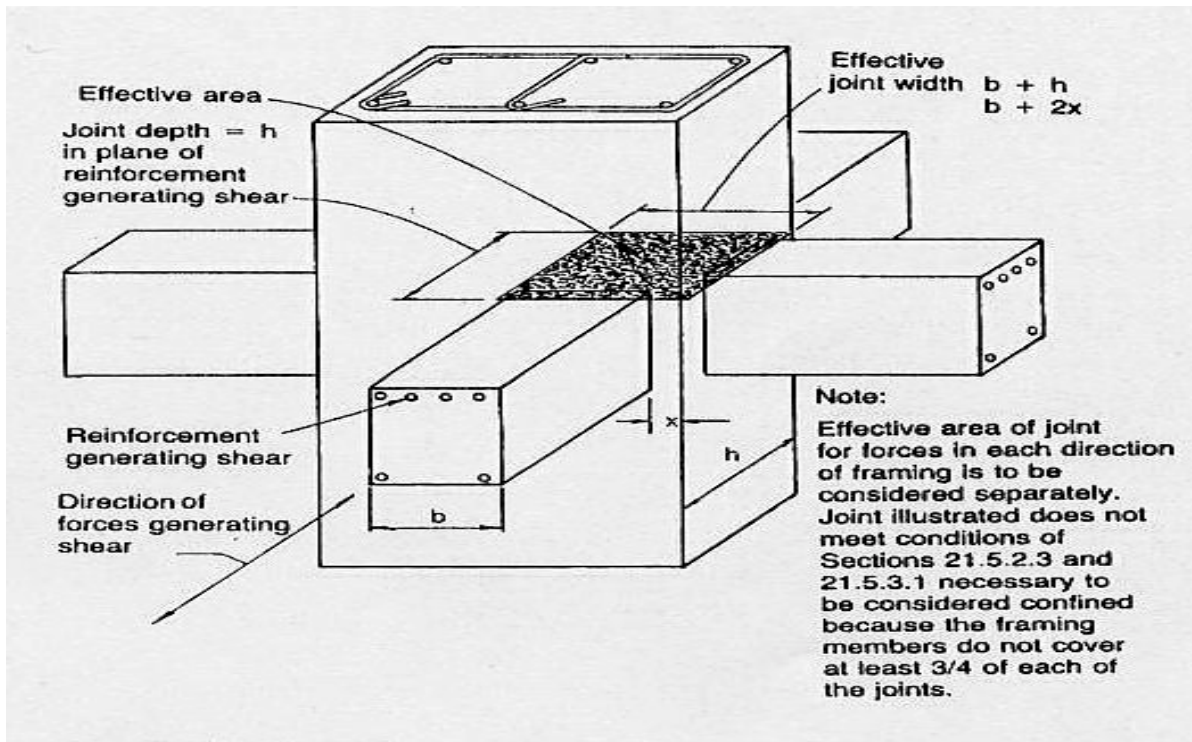


Figure 2 Effective area of an R/C joint for shear [2]

Reinforcement Anchorage at the Connection

Anchorage is an important consideration for beam and column reinforcement passing through an R/C beam-column connection and for beam reinforcement that terminates in a connection. Loss of reinforcing steel anchorage in a connection during cyclic loading can lead to a decrease in overall frame strength and stiffness. Slippage of reinforcement in the connection is related to the reinforcement bond stress and anchorage length, as well as to the level of shear stress and degree of confinement in the joint core. To minimize slip of beam bars through the joints of R/C beam-column connections, ACI 318-99 limits:

$$h_c / d_{b(bm)} \geq 20 \quad (3)$$

where h_c is the depth of the column and $d_{b(bm)}$ is the diameter of the beam reinforcement passing through the column. ACI 318-99 also prescribes minimum development lengths of beam bars terminating in connections and recommends that such bars have a standard 90-degree hook anchored within the joint core.

Flexure at the Connection

To reduce the likelihood of column hinging in R/C frame structures, ACI 318-99 requires:

$$\sum M_c / \sum M_g \geq 1.2 \quad (4)$$

where $\sum M_c$ is the sum of the moment capacities (at the faces of the joint) corresponding to the nominal flexural strength of the columns framing into the connection, and $\sum M_g$ is the sum of the moment capacities (at the faces of the joint) corresponding to the nominal flexural strength of the girders (beams) framing into the connection. The column flexural strengths should be calculated for the factored axial force, consistent with the direction of lateral forces considered, resulting in the lowest flexural strength. For the first time ever, ACI 318-99 requires that $\sum M_g$ be computed including the contribution to flexural strength of an assumed effective slab width (b_e) when the slab is in tension at the face of the joint in T-beam construction (see Figure 3).

SLAB PARTICIPATION EFFECTS IN R/C BEAM-COLUMN CONNECTIONS

In many R/C structures, slab contributions to the negative bending moment capacity in beam-column-slab frames can be quite significant. This was first demonstrated almost twenty years ago in a static lateral load test of a large-scale seven-story R/C building in Japan as part of a U.S.-Japan cooperative research program [8]. The maximum base shear measured in that test was considerably more than had been predicted, and a major source of the discrepancy was found to be the contribution of slab reinforcement adding to the flexural capacity of the beams.

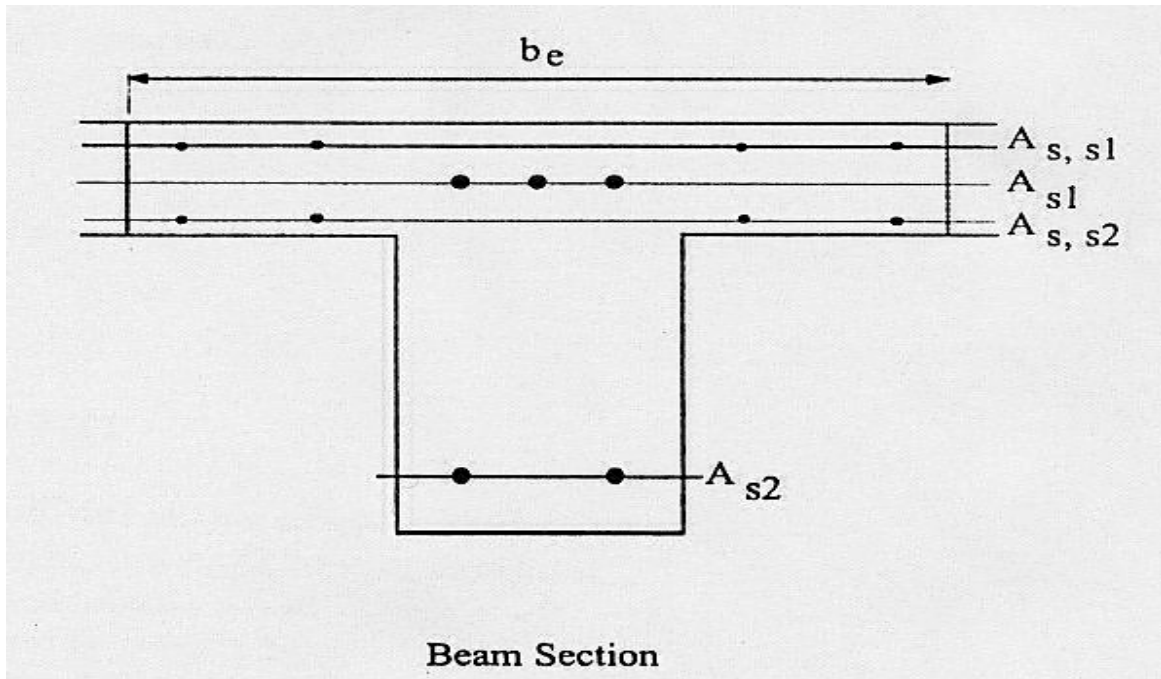


Figure 3 Effective slab width (b_e) of a T-beam with slab in tension

In the last decade, many researchers have explored the amount of slab participation occurring at R/C beam-column-slab connections, as well as the possible effects of slab participation on the overall behavior of R/C frames subjected to lateral loads [4,6]. The most significant effects of slab participation occur when slab reinforcement adds to the negative moment (tension on top) capacity of beams by increasing the amount of available tension reinforcement. This increase in beam flexural strength can have an overall effect on: frame ultimate failure mechanisms, connection shear behavior, base shear of a structure, shear and bending moment magnitude and distribution in beams, and torsion in transverse spandrel beams.

Slab Participation per ACI 318-99

As indicated above, ACI 318-99 for the first time recognizes some of the effect of slab participation on performance of R/C frames subjected to lateral earthquake loads. For purposes of checking flexure at a connection, the $\sum M_g$ must be computed including the contribution to flexural strength of an assumed effective slab width when the slab is in tension at the face of the joint. However, this contribution of slab reinforcement in tension is still neglected per ACI 318-99 for purposes of other design checks such as those related to connection shear and beam shear.

ACI 318-99 indicates that the effective width of floor slab in tension (b_e) for beams in negative bending should not exceed one-quarter of the span length of the beam. The effective overhanging flange width on each side of the beam web should also not exceed eight times the slab thickness or one-half the clear distance to the next beam web. For edge beams with a slab

on one side only, the effective overhanging flange width should not exceed one-twelfth the span length of the beam, six times the slab thickness, or one-half the clear distance to the next beam web. These values are simply the ones that have always been used in ACI 318 for the effective slab width of T-beams with the slab in compression. Research on R/C beam-column-slab connections under lateral loading has indicated that using these values of negative moment effective slab width gives reasonable estimates of beam negative moment strengths at interstory drifts of approximately 2% [6].

R/C Frame Building Case Study on Slab Participation

Description of the Case Study Building

An existing R/C frame building was selected to investigate the effects of slab participation on the design and performance of R/C frames under lateral loads. The building is a modern medical research facility located in the vicinity of Seattle, Washington and has been in service since the early 1990s. The structure consists of below-ground levels for parking, a first floor at ground level, and a second floor, third floor, and roof level above ground; the above-ground floor levels are used for offices and research. The below-ground floor levels consist of R/C spread footings, foundation walls, floor slabs on grade, columns, beams, and elevated two-way floor slabs. In addition to being designed to resist gravity loads, key columns below ground have been designed and detailed to resist any lateral loads imparted on them by the above-ground floors in an earthquake. The above-ground floors consist of R/C beams, columns, two-way floor slabs, and drop panels. The overall height of the building is approximately 16 m (53 ft) above ground.

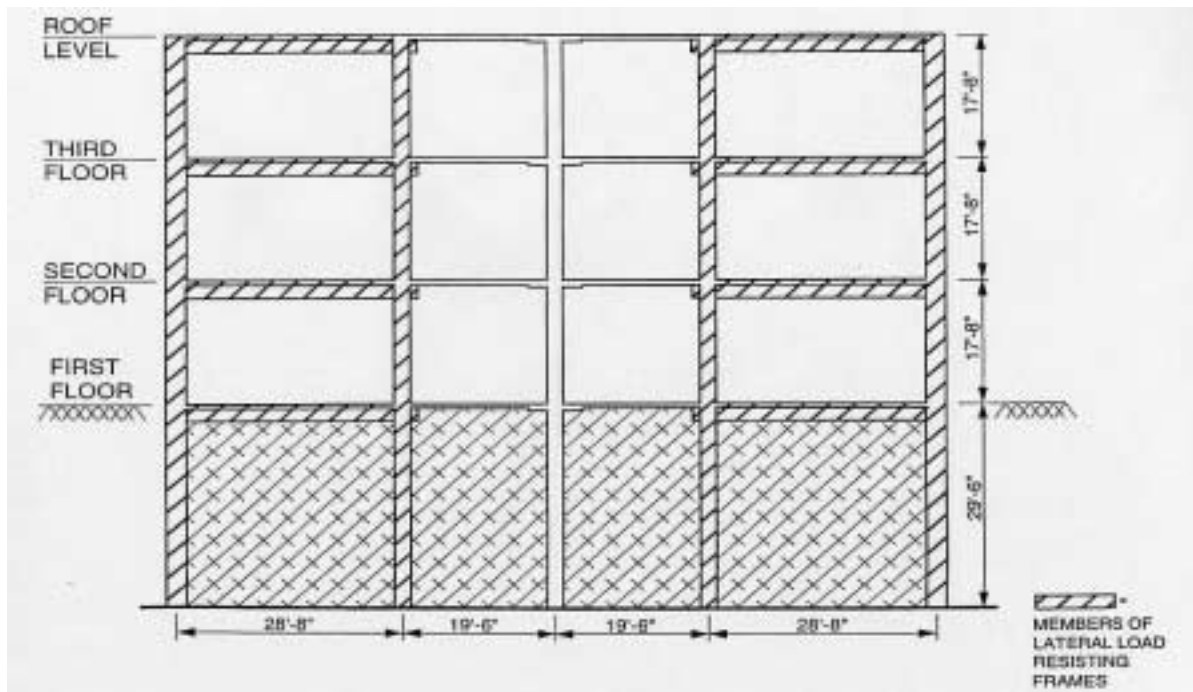


Figure 4 Elevation of a typical R/C frame in the case study building [5]

Figure 4 is an elevation view of a typical R/C frame in the east-west direction of the case study building, with those members designed to resist lateral load (in addition to gravity load) clearly indicated. Figure 5 shows a partial floor plan of the existing structure. Beams in the east-west lateral load resisting frames are 762 mm (30 in.) square, and the slab is a two-way floor slab, 203 mm (8 in.) thick. Interior columns in the east-west lateral load resisting frames are 610 mm (24 in.) square with 8-#10 (32 mm dia.) reinforcing bars, and exterior columns in the lateral load resisting frames are 762 mm x 610 mm (30 in. x 24 in.), bending about the strong axis, with 8-#9 (29 mm dia.) reinforcing bars. Beam and slab sections at the second floor of the structure, indicating the layout of the reinforcement, are shown in Figure 6. Beam and slab reinforcement at the other floor levels is similar.

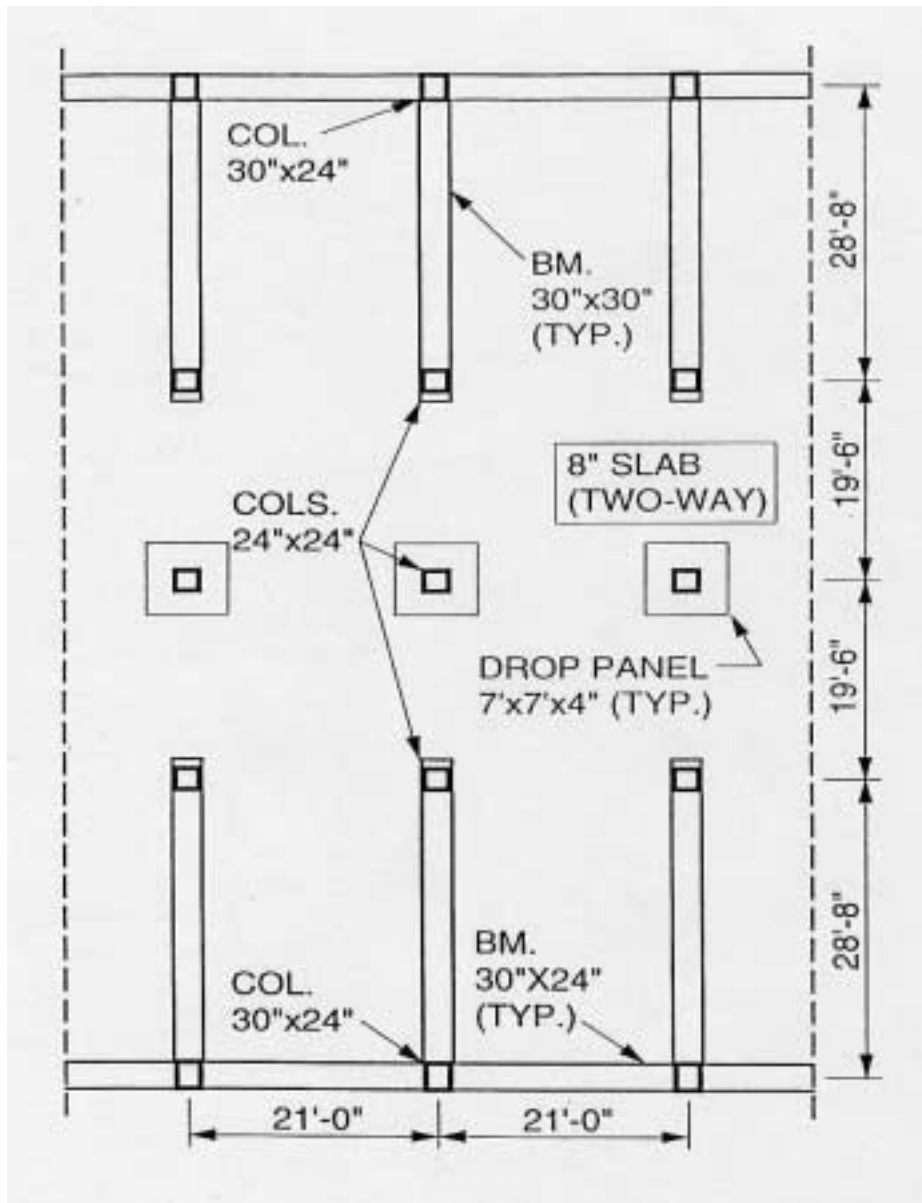


Figure 5 Partial plan of the R/C case study building [5]

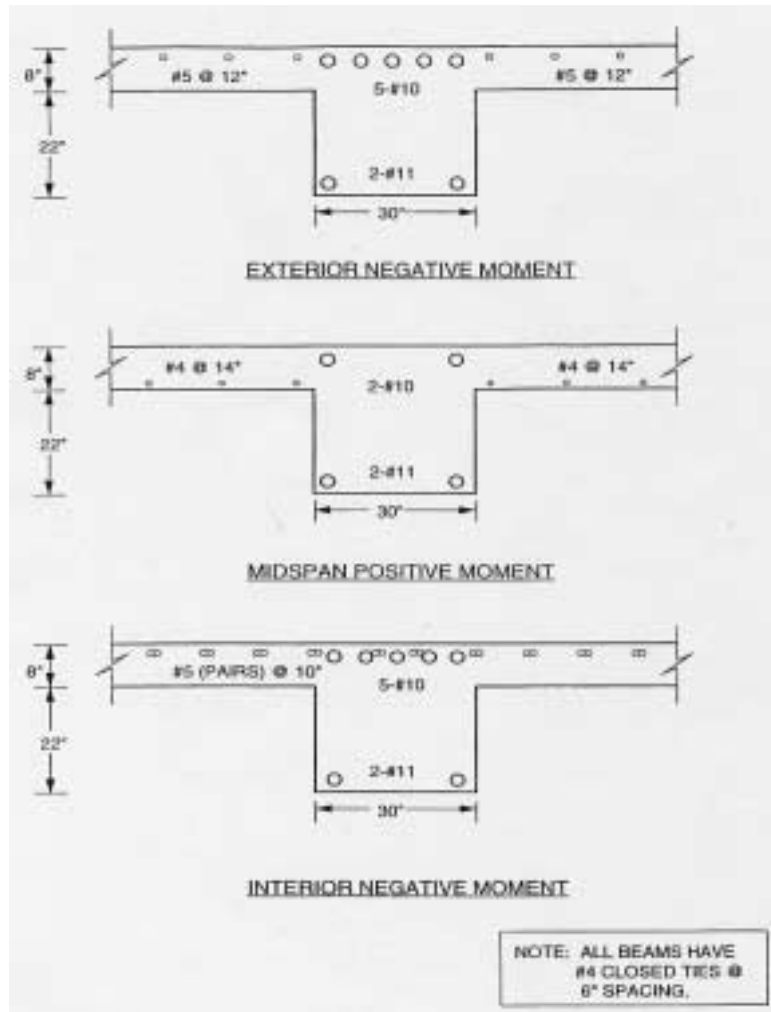


Figure 6 R/C beam and slab sections at the second floor of the case study building [5]

Evaluation of the Case Study Building

The design of the case study structure is generally in conformance with ACI 318-95 [1], the predecessor to ACI 318-99. With respect to beam-column connections, ACI 318-95 did not require any consideration of slab participation effects, so all of the slab reinforcement noted in Figure 6 was most likely neglected in the design of the lateral load resisting frames for this structure. Ignoring the possible effects of slab participation, all of the design values of $\sum M_c / \sum M_g$ for this frame are greater than 1.2, and all of the design horizontal connection shear forces (V_u) are less than the design joint shear strengths (ϕV_n) as well. If the current provisions of ACI 318-99 (including slab participation) are applied to these frames, the design values of $\sum M_c / \sum M_g$ at the interior beam-column connections of the frame are substantially less than 1.2 (and even less than unity). If slab participation were to be included in the connection shear check (*not* required even by ACI 318-99), the design horizontal connection shear forces at the interior connections would be far in excess of the permitted design joint shear strengths as well.

Analytical models of the lateral load resisting frames from the case study building have been created using the two-dimensional inelastic frame analysis program DRAIN-2DX. [7] To date, two models of the existing structure (one neglecting slab participation and one including slab participation) have been generated. They have been subjected to static pushover analyses to shed light on the lateral load-displacement behavior when the frames are loaded into the inelastic range and to determine the overall lateral strength and likely plastic hinging patterns. During the pushover analyses, the frame models were subjected to monotonically increasing lateral load profiles of an inverted triangular shape.

Throughout the static pushover analyses, the model with floor slab participation had more column plastic hinging than the model without floor slab participation, whereas the model without floor slab participation had more beam plastic hinging than the model with floor slab participation. The failure mechanism for the model with floor slab participation was a two-story mechanism controlled by column plastic hinges at the first and third floor levels along with beam plastic hinges and additional column plastic hinges at the second floor level. The failure mechanism for the model without floor slab participation was simply a three-story mechanism controlled by column plastic hinges at the first floor level and beam plastic hinges at the second, third, and roof levels. Therefore, this lateral load resisting frame that was designed with the intent of having “strong column – weak beam” behavior under lateral load would in fact have very different behavior in the real structure due to substantial slab participation. This is clearly the motivation behind requiring the consideration of slab participation in ACI 318-99.

In addition to all of the column plastic hinging that occurred in the frame including slab participation, the interior beam-column connections of this frame experienced joint shears as much as 20% in excess of the design values currently permitted by ACI 318-99, a result that might have been predicted had slab participation been considered in designing for joint shear under lateral load. However, even in ACI 318-99, this is currently not required. Furthermore, the most likely way in which the case study building would be redesigned to come in conformance with ACI 318-99 would be to increase the size of the reinforcing bars in the columns so that $\sum M_c / \sum M_g$ would be greater than 1.2. This would likely solve the problem of column plastic hinging and lead to overall frame performance dominated by beam plastic hinging. However, by strengthening the structure, the actual horizontal connection shear forces would increase even further, so the new code provision in ACI 318-99 of including slab participation in some checks but not in others might actually lead to frames that go from having their capacity dictated by column hinging to having their ultimate capacity dictated by joint shear distress. This is likely not an intended consequence. Additional analyses of this case study building are currently underway.

CONCLUSION

Beam-column connections are important components in R/C frames, and their proper design and detailing is essential to the overall seismic performance of R/C structures. Care must be taken when introducing new design provisions into building codes to ensure that these design provisions have the intended consequences on structural behavior.

REFERENCES

1. ACI Committee 318, *Building Code Requirements for Structural Concrete (ACI 318-95)*, American Concrete Institute, Farmington Hills, Michigan, 1995.
2. ACI Committee 318, *Building Code Requirements for Structural Concrete (ACI 318-99)*, American Concrete Institute, Farmington Hills, Michigan, 1999.
3. ACI-ASCE Committee 352, *Recommendations for Design of Beam-Column Joints in Monolithic Reinforced Concrete Structures (ACI 352R-91)*, American Concrete Institute, Detroit, Michigan, 1991.
4. French, C. W., and Moehle, J. P., "Effect of Floor Slab on Behavior of Slab-Beam-Column Connections," *Design of Beam-Column Joints for Seismic Resistance (SP-123)*, American Concrete Institute, Detroit, Michigan, 1991, pp. 225-258.
5. Goodell, A. R., "Seismic Performance of Reinforced Concrete Frame Buildings with and without Floor Slab Participation," *M.S. Thesis*, University of Massachusetts, Amherst, Massachusetts, September 1999.
6. Pantazopoulou, S. J., and French, C. W., "Slab Participation in Practical Earthquake Design of Reinforced Concrete Frames," *ACI Structural Journal*, Vol. 98, No. 4, July-Aug. 2001, pp. 479-489.
7. Prakash, V., Powell, G. H., and Campbell, S., "DRAIN-2DX Base Program and User Guide," *Report No. UCB/SEMM-93/17*, Department of Civil Engineering, University of California, Berkeley, California, 1993.
8. U. S. Members of JTCC (Joint Technical Coordinating Committee) Group on Reinforced Concrete Building Structures, "U.S.-Japan Research: Seismic Design Implications," *Journal of Structural Engineering*, Vol. 114, No. 9, 1988, pp. 2000-2016.



KEERC-MAE Joint Seminar on
Risk Mitigation for Regions of Moderate Seismicity
University of Illinois at Urbana-Champaign, August 5-8, 2001



Sponsors: Korea Science and Technology Foundation, U.S. National Science Foundation, Brain Korea 21



Effect of Directionality of Reinforcing Bars on RC Planar Members in Cyclic Shear

Honggun PARK¹, and Jae Yo KIM²

¹ Assistant Professor, Department of Architectural Engineering, Seoul National University
San 56-1 Shinlim-Dong Kwanak-Gu, Seoul, Korea
email: hgpark@gong.snu.ac.kr

² Graduate Student, Department of Architectural Engineering, Seoul National University
San 56-1 Shinlim-Dong Kwanak-Gu, Seoul, Korea
email: beholder@snu.ac.kr

ABSTRACT: For reinforced concrete planar members subjected to cyclic shear, the load-carrying capacity depends on the orientation of the reinforcing steel bar relatively to the orientation of the tensile crack. In this study, the variations of strength, ductility, and energy dissipation with the directionality of reinforcing steel bars were studied by investigating the existing experiments and by performing numerical analyses. Through this study, it was found that for describing cyclic behavior of reinforced concrete, it is required to consider the behavior of reinforcing steel bar independently in every tensile crack orientation. As a result of the study, an improved material model was proposed to estimate the strength and energy dissipation of the shear panels.

KEYWORDS: Cyclic load, Energy dissipation, Reinforced concrete, Shear panel, Tensile crack

INTRODUCTION

In the reinforced concrete planar members subjected to cyclic loads such as beams, shear walls, and beam-column joints, degradation of the stiffness and strength occurs due to tensile cracking of concrete and induces early crushing of concrete and pinching effect. Generally, the orientations of the reinforcing steel bars(re-bars) are not orthogonal but diagonal to tensile crack orientations. Based on the previous Earthquakes and experimental studies, it has been reported that the members with such general arrangement of re-bars are vulnerable to cyclic shear. Therefore, the re-bars orthogonal to tensile cracks which is so-called 'diagonal reinforcement' are frequently used for the vulnerable members such as connecting beams for coupled shear walls. It has been well known that the strength and ductility of such members are superior to those reinforced with horizontal and vertical bars.

PREVIOUS STUDIES

Sittipunt and Wood [5,8] performed shear wall tests to study the effect of the orientation of re-bars on the overall behavior. The web of W1 is reinforced typically with horizontal and vertical bars, and on the other hand, W3 is diagonally reinforced. Fig. 1 presents the cyclic behaviors of W1 and W3. As shown in the figures, the main difference between W1 and W3 is the characteristics of the unloading/reloading curves: W1 shows severe pinching while W3 shows stable cyclic behavior. Also, the failure mechanisms are different: The failure of W1 was initiated from the web crushing, while W3 failed in the boundary elements.

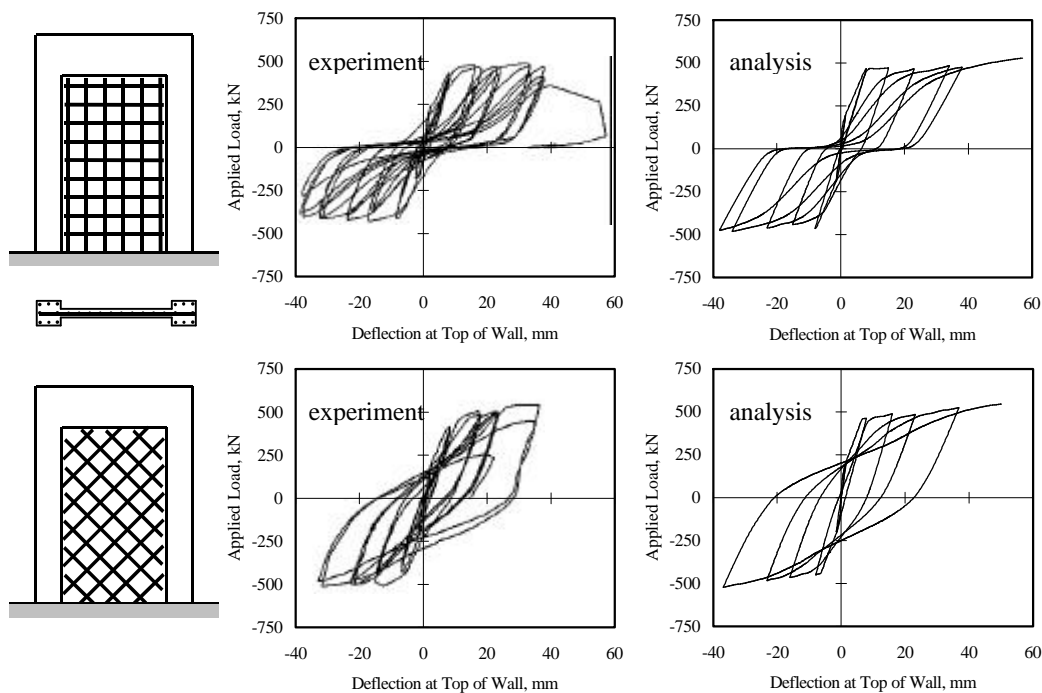


Fig. 1 Shear Walls Tested by Wood and Sittipunt [8]

Table 1 Properties of Shear Panels Tested by Ohmori et al. [2] and Stevens et al. [6]

Specimen	Panel Dimensions, mm	Concrete Compressive Strength, MPa	Reinforcement	
			Yield Strength, MPa	Reinforcement Ratio percent
SR05	2500×2500×140	30.4	398	$\rho_x = \rho_y = 0.51$
SR10	2500×2500×140	36.6	398	$\rho_x = \rho_y = 1.02$
SR14	2500×2500×140	29.3	398	$\rho_x = \rho_y = 1.36$
SR17	2500×2500×140	28.7	398	$\rho_x = \rho_y = 1.70$
SR20	2500×2500×140	28.7	398	$\rho_x = \rho_y = 2.04$
SE8	1524×1524×285	37.0	X dir. :492, Y dir. :479	$\rho_x = 2.94, \rho_y = 0.98$
SE9	1524×1524×285	44.2	422	$\rho_x = \rho_y = 2.94$
SE10	1524×1524×285	34.0	X dir. :422, Y dir. :479	$\rho_x = 2.94, \rho_y = 0.98$

In Fig. 1, the numerical analyses present similar trend to the experimental results. For these numerical analyses, the material model developed by Park and Kim [4] was used.

Ohmori et al.[2] and Stevens et al.[6] performed experiments for shear panels subjected to cyclic shear. The dimensions and material properties for the specimens are presented in Table 1. SR series were subjected to pure shear and reinforced isotropically. While SE series were subjected to pure shear or a combination of biaxial compression and shear, and were reinforced isotropically or anisotropically. Commonly for all the shear panels, the re-bars were oriented at exactly or about 45 degrees from the tensile crack orientations.

Fig. 2 shows the shear stress-strain relations. As expected, the shear panels present severe pinching. Fig. 3 shows the stress-strain relations of concrete and re-bar. Since the stress-strain relations cannot be directly measured from the experiment, the following methods are used for obtaining the relations: The stress-strain relation of the re-bar that can be easily expected is assumed. From the experimental results, the average strain in the direction of the re-bars is obtained, and the stress is calculated with the assumed stress-strain relation. Then the stress of concrete is calculated by extracting the stress of the re-bar from the overall stress of the shear panel. Therefore it cannot be assured that the stress-strain relations of concrete and re-bar present the actual behaviors.

Fig. 4 shows the numerical analysis for SR10. The numerical results show similar trend though not exactly the same. In comparison of Fig. 2 and 4, the strengths are equivalent and the overall behaviors are similar, but the unloading/reloading curves are quite different. The experiment shows more complicated behavior and the larger capacity of energy dissipation. For the purpose of investigating the effect of the orientation of the re-bars, SR10 remodeled with re-bars arranged at the orthogonal to the tensile crack directions was numerically analyzed. Fig. 5 shows the results. As expected, the remodeled panel presents stable behavior and large energy dissipation.

The observations on the previous experiments and numerical analyses can be summarized as follows:

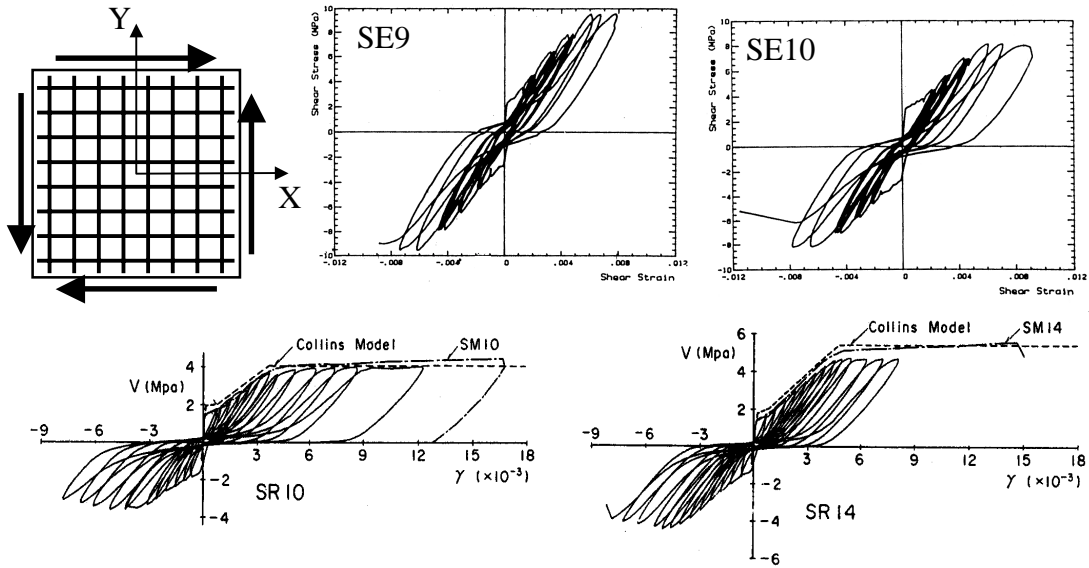


Figure 2 Test Results of Shear Panels (Shear Stress-Strain Relations)

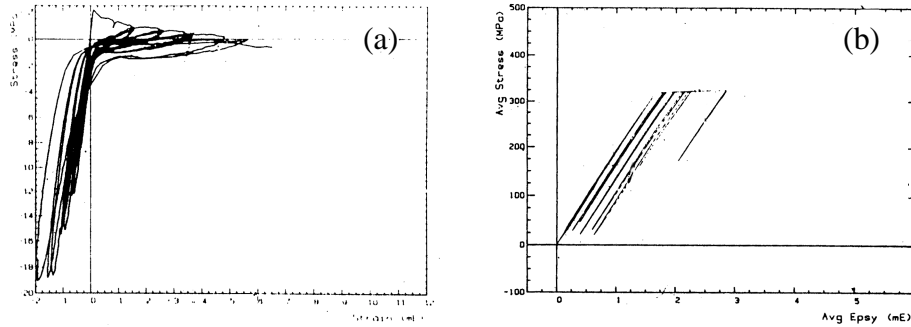


Figure 3 Test Results of SE9 : (a) Principal Stress-Strain Relations of Concrete; and (b) Stress-Strain Relations of Reinforcing Steel

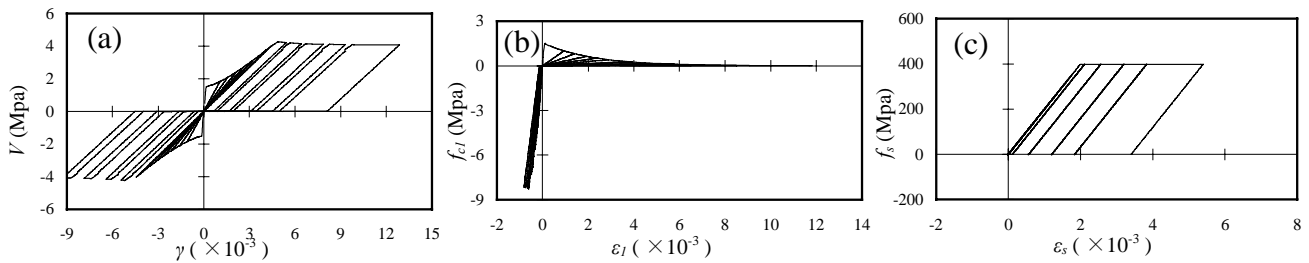


Figure 4 Numerical Results of SR10 : (a) Shear Stress-Strain Relation; (b) Principal Stress-Strain Relation of Concrete; and (c) Stress-Strain Relation of Reinforcing Steel

1) Energy dissipation

From the comparison of Fig. 3 and 5, in the panels with re-bars orthogonal to the tensile cracks, the re-bars experience full cyclic histories, and the panels have enhanced capacity of energy dissipation. On the other hand, in the panels with re-bars diagonal to the tensile cracks, the re-bars do not experience the full cyclic histories, and the strain and stress remain in tension.

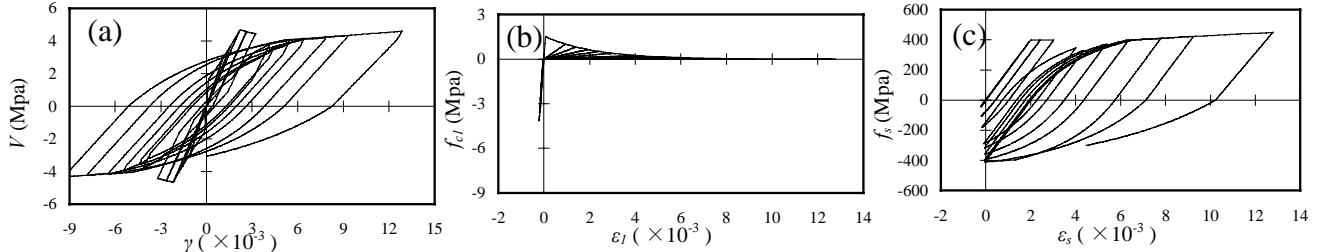


Figure 5 Numerical Results of SR10 with Different Arrangement of Reinforcing Steel Bar : (a) Shear Stress-Strain Relation; (b) Principal Stress-Strain Relation of Concrete; and (c) Stress-Strain Relation of Reinforcing Steel

This is the primary reason of the pinching reducing energy dissipation. However, the experiments show that the panels still dissipate considerable energy. According to the experimental results in Fig. 3, the concrete has considerable compressive stress at large tensile strain, i.e. before the tensile cracks do not close. The previous studies[1,2,3,6] simulated the compressive stress to describe the energy dissipation.

1) Load-carrying capacity

In Fig. 2, the dotted lines shows the numerical analyses for the shear panels subjected to monotonic shear, using the material model suggested by Vecchio and Collins [7]. The Collins model is a general approach using average stress-strain relations of concrete and re-bars, and is sufficiently accurate for monotonic load. However, the numerical analyses overestimate the load-carry capacity of the panel under cyclic shear, except for SR5 and SR10 with low reinforcement ratios. This means that the effective yield stresses of the re-bars were reduced in case of cyclic load. Table 2 compares the experimental and predicted strengths of the shear panels. In the previous studies, any definite explanation for the decrease in the load-carrying capacity has not been given yet.

Table 2 Comparison of Experimental and Predicted Strengths of Shear Panels

	Shear Strength (Mpa)		T_s , Predicted	ΔT_s , Decrement in Tensile Resistance (4) = (2) - (1)
	V_{exp} , Experiment (1)	V_{pre} , Prediction (Collins Model) (2)	Tensile Resistance of Re-bar ($\sum \rho_s F_y \cos^2 \theta$) (3) = (2)	
SR10	4.02	4.06	4.06	0.04
SR14	4.70	5.41	5.41	0.71
SR17	6.10	6.77	6.77	0.67
SR20	6.82	8.12	8.12	1.30
SE8	5.50	6.20	6.20	0.70
SE9	9.60	12.4	12.4	2.80
SE10	8.20	10.2	6.8 ¹⁾	1.33 ²⁾

¹⁾ (3) = (2)×2/3 ²⁾ (4) = ((2) - (1))×2/3

Table 3 Comparison of Concrete Strengths of Shear Panels

		SE8	SE9	SE10	SR05	SR10	SR14	SR17	SR20
$\frac{f_{c2}}{f_c'}$	Experiment (1)	0.31	0.42	0.48	0.17	0.22	0.32	0.43	0.44
	$\left(0.8 - 0.34 \frac{e_1}{e_{c0}}\right)^{-1}$ (2)	0.42	0.62	0.52	0.31	0.35	0.46	0.52	0.61
f_c' (MPa)		37.0	44.2	34.0	30.4	36.6	29.3	28.7	31.2
$[(2) - (1)] f_c'$, MPa (percent)		4.07 (11)	8.84 (20)	1.36 (4)	4.26 (14)	4.76 (13)	4.10 (14)	2.58 (9)	5.30 (17)
$T_s = \sum r f_y \cos^2 q$		6.20	12.4	6.80	2.03	4.06	5.41	6.77	8.12

3) Ductility

Though the load-carrying capacity depends on the yield stress of the re-bars, the failure of the shear panel occurs due to concrete crushing. For the shear panels with re-bars diagonal to the tensile cracks, the reduction in the ductility is primarily due to two causes: From the comparison of Fig. 4(b) and 5(b), the concrete is subjected to compressive stress two times larger than the concrete with re-bars orthogonal to tensile cracks. The re-bars diagonal to tensile cracks develop tensile forces, and by the internal equilibrium, the tensile forces induce compressive forces to the concrete in addition to the externally applied compressive force (Table 4(1)). Second, the concrete strength is reduced due to the coexisting tensile cracks[7]. Moreover, the cyclic loads reduce the concrete strength further. Table 3 compares the compressive strengths of the experiments and the Collins Model [7] which was based on the panel tests under monotonic shear. As presented in the table, the concrete strength under cyclic shear decreases by 4 to 20 percents of the cylinder strength, compared with the panels under monotonic shear.

BEHAVIOR OF RE-BARS IN INDIVIDUAL CRACK ORIENTATION

Fig. 6 shows the idealized cracked concretes with different arrangements of the re-bars. For the re-bars orthogonal to the tensile cracks in Fig. 6(a), the tensile strain of the re-bars in the tensile crack A decreases as the tensile crack closes, while the strain of the re-bars in B increases as the tensile crack opens. As far as the stresses are concerned, the re-bar in A develops a compressive stress far before A closes, since the re-bar has a tensile plastic strain through the previous cyclic history. Of course, the compressive stress is transferred to the concrete by the bond. Therefore, the re-bars experience the full cyclic history, and the reinforced concrete can develop large energy dissipation that is equivalent to that of the bare steel bars (See Fig. 5).

Fig. 6(b) shows the cracked concrete with re-bars diagonal to the tensile cracks. Although the re-bars in tensile cracks A' and B' are continuously connected, the parts in A' and B' experience independent cyclic histories, due to the bond developed by the concrete.

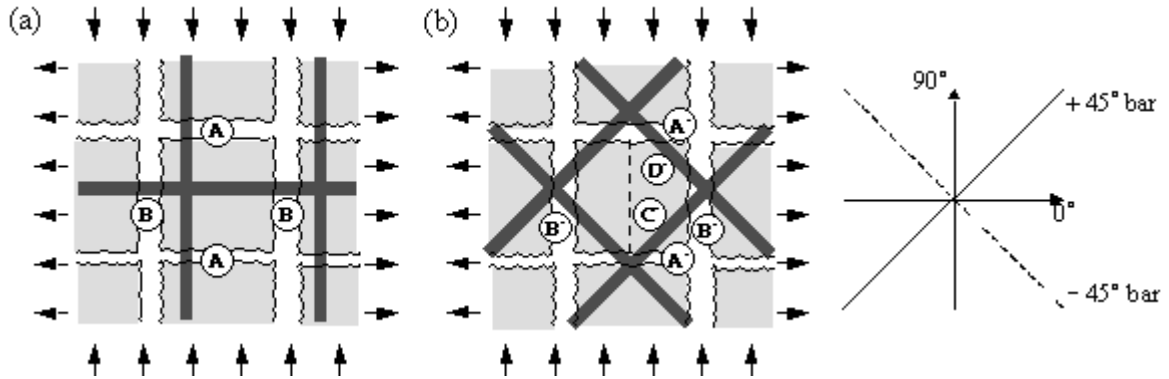


Figure 6 Idealization of Reinforced Concrete under Cyclic Shear

Table 4 Mohr Circles for Stresses of Re-bars and Concrete

		Re-bar in Opening Crack		Re-bar in Closing Crack		Concrete	Overall Stress
		-45° bar	+45° bar	-45° bar	+45° bar		
Monotonic Load (1)				-	-		
Cyclic Load	Before Complete Closing of Crack (2)						
	After Complete Closing of Crack (3)						

Note: $F_t = \rho f_y$, and $F_c = \beta \rho f_y$

Therefore, the behavior of the panel may be the same as that with the orthogonal re-bars in Fig. 6(a). However, as presented in the severe pinching in Fig. 2, obviously, the diagonal re-bars do not experience such full cyclic histories. In Fig. 6(b), the compressive forces of the re-bars in the closing crack A' induce a compressive stress in the transverse direction, and also a tensile stress in the longitudinal direction. If the tensile stress increases large enough to induce the additional transverse crack C', the tensile resistance of the concrete loses and the re-bars in the transverse crack should take the tensile stress. Under further loading, the strain of the re-bars in A' is affected by the opening transverse crack C' as well as the closing longitudinal crack, and the compressive stress does not increase significantly until the longitudinal crack closes completely. According to the experiments in Fig. 3, the compressive force of the re-bars is limited approximately to the tensile cracking stress of concrete.

IMPROVEMENT IN MATERIAL MODEL

The discussions presented above indicate that the behavior of the shear panels is affected by the cyclic behavior of the re-bars in opening and closing tensile cracks. Based on the discussions, the following improvement is needed in estimating the behavior of shear panels:

1) **Load-carrying capacity**

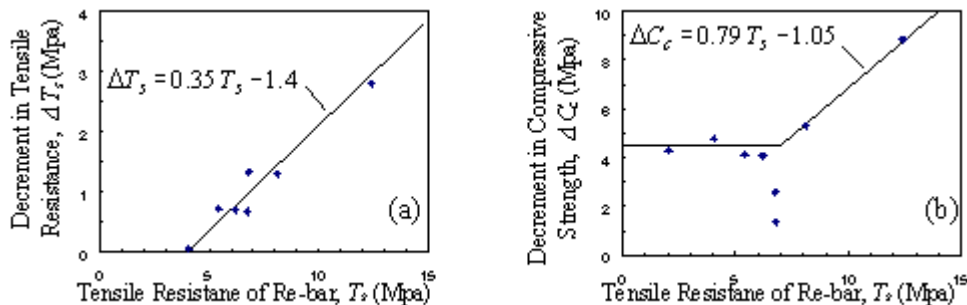
The compressive stress of the re-bars developed in the closing cracks reduces the load-carrying capacity by the two mechanisms. In Fig. 6(b), the bond stresses due to the compressive stress of the re-bar in A' as well as the tensile stress of the re-bar in B' are concentrated in the corner of the cracked concrete D'. The loss of the bond reduces the number of re-bars that are effective in resisting cyclic shears.

Table 4 presents the Mohr circles for the stresses of concrete and re-bars in cyclic pure shear. The re-bars in the closing cracks develop compressive stresses before complete closing of the crack. The compressive stress induces a tensile stress to concrete by internal equilibrium. However, since concrete is vulnerable to tensile cracking, the tensile stress is resisted by the re-bars in opening cracks. After complete closing of the cracks, the stresses of the re-bars in the closed crack is transferred directly to concrete by bond and friction. But, the residual compressive stress of the re-bars developed before closing of the crack equilibrates with the tensile stress of the re-bars in opening cracks. Therefore, the maximum tensile stress of the re-bar that is effective in resisting the applied force is reduced by the tensile stress required for the internal equilibrium, $\Delta T_s = F_c = \beta p f_y$. For the shear panels with the low reinforcement ratio that is not enough to induce additional tensile cracking, the maximum tensile stress of the re-bar is equivalent to the yield stress.

Fig. 7 shows the relations of the predicted tensile resistance of re-bars and the decrement of the resistance which are directly related to the decrement in the shear strength of the panels. As shown in the figure, the decrement is correlated with the tensile resistance of re-bars.

2) **Ductility**

Since the failure occurs due to the compressive crushing of concrete, reduction in ductility is directly related to the decrease in concrete strength. There are several factors affecting the concrete strength: The bond failure reduces the area of concrete available to resist compressive force.



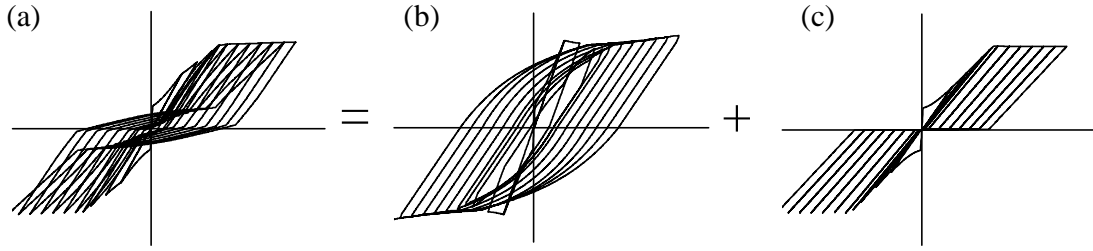


Fig. 8 Proposed Model for Energy Dissipation

(Fig. 6D); The additional compressive stress is required for the internal equilibrium with the residual compressive stress of re-bars (Table 4(3)); And, the bond stress due to the compressive stress of re-bars induces a local failure due to the stress-concentration. All the causes are related to the tensile resistance of re-bars. Fig. 7 shows the relationship of the decrements in the ultimate compressive stress of concrete to the tensile resistance of re-bars.

3) Energy dissipation

The previous studies [1,2,3,6] used the material model simply simulating the experimental results shown in Fig. 3: The strains and stresses of the re-bars are always in tension during the cyclic loading; and the concrete shows compressive stresses at large tensile strains. However, the stress-strain relations of the re-bars and concrete are based on the assumption of the average strain, and therefore the previous material models do not address the actual stress-strain relations of the re-bars in opening and closing cracks. The concrete is obviously in compression before closing of the tensile crack. But since the compressive stress is originally developed by the re-bars in the closing crack, the behavioral characteristics of the re-bars should be addressed to describe the actual behavior.

According to the experimental results, the compressive stress of the re-bars in the closing crack is limited approximately to the tensile cracking stress of concrete. This can be interpreted as that a portion of the re-bars developing the compressive stress experiences the cyclic history while the other portion do not. With this interpretation, the overall cyclic behavior of the shear panels in Fig. 8(a) can be idealized with the combinations of Fig. 8(b) and (c). Based on the experiments, the portion of re-bars experiencing cyclic history, \mathbf{a} is defined as

$$\mathbf{a} = f'_t / (\mathbf{r}_s f_y \cos^2 \mathbf{q}_i) \leq 0.25 \quad (1)$$

\mathbf{r}_s = reinforcement ratio; f_y = yield stress of re-bar; f'_t = tensile cracking stress of concrete; and \mathbf{q}_i = orientation of re-bar from the orthogonal to i th tensile crack direction. The other portion of the re-bar, $(1 - \mathbf{a})\mathbf{r}_s$ do not experience the full cyclic history, and the corresponding stress is defined with the average strain calculated in the orientation of the re-bar.

On the other hand, the stress of the re-bar $\mathbf{a}\mathbf{r}_s$ is defined in the individual crack orientation. Instead of using the average strain, the strain of the re-bar \mathbf{e}_{si} is defined with the strain in the

orthogonal to the crack direction: $\varepsilon_{si} = \varepsilon_{ni} \cos^2 \theta_i$, where ε_{ni} = strain in the orthogonal to i th crack orientation. The stress of the re-bar σ_{si} is defined by the function of ε_{si} . If the stress of the re-bar is expressed in the orthogonal to the crack orientation,

$$\sigma_{ni} = \sigma_{si} \cos^2 \theta_i; \quad \sigma_{ti} = \sigma_{si} \sin^2 \theta_i; \quad \text{and} \quad \tau_i = \sigma_{si} \sin \theta_i \cos \theta_i \quad (2)$$

Since the tensile stress σ_{ti} is internally equilibrated with concrete or re-bars in tension, the tensile stress should not be accounted for in resisting the applied force: $\sigma_{ti} = 0$. Fig. 9 and 10 compare the experiments, the proposed model, and Maekawa's model[1]. The figures show that the proposed model relatively agree with the experiments.

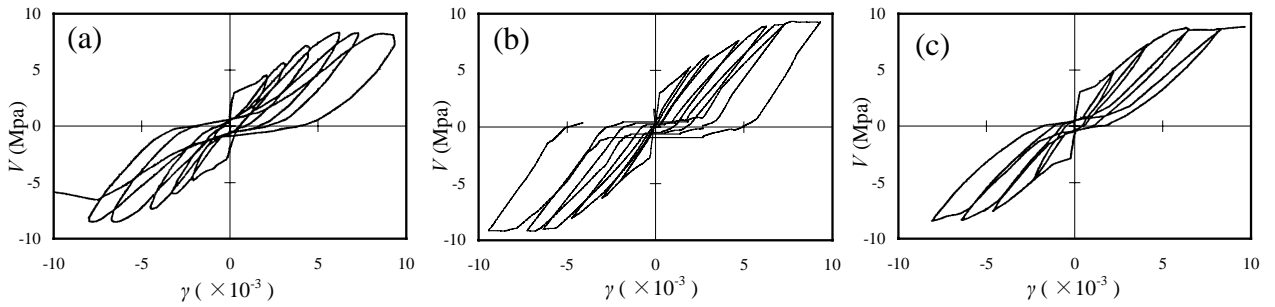


Figure 9 Comparison of Experiment and Numerical Analysis (SE10) :

(a) Experiment; (b) Proposed Model ; and (c) Maekawa's Model

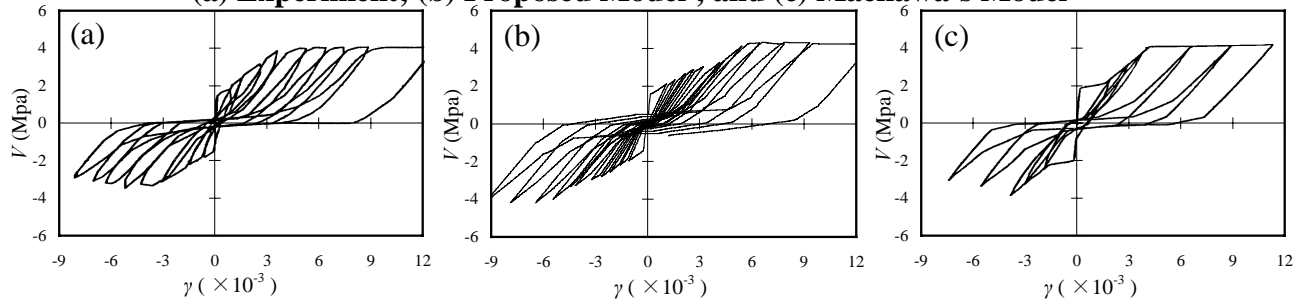


Figure 10 Comparison of Experiment and Numerical Analysis (SR10) :

(a) Experiment; (b) Proposed Model ; and (c) Maekawa's Model

CONCLUSIONS

The reinforced concrete planar members with the re-bars arranged diagonal to the tensile crack orientations are vulnerable to shear. Moreover, cyclic load significantly reduces the strength and ductility, compared with monotonic load, and also significantly reduces the capacity of energy dissipation. By investigating the existing experiments and by performing numerical analyses, it was found that the cyclic behavior of the re-bars in individual crack orientation and the internal stress-strain relations developed by the cyclic behavior need to be addressed to describe actual behavior of the members. Based on the investigation, the decrements of the strength and ductility were estimated, and a material model was proposed to describe the cyclic behavior of shear panels.

ACKNOWLEDGMENTS

The research presented herein has been carried out with the financial assistance of the Major Field in Brain Korea 21, and the authors are sincerely grateful to the authorities for their support.

REFERENCES

1. Fukuura, N. and Maekawa, K., “ Multi-directional crack model for in-plane reinforced concrete under reversed cyclic actions – 4way fixed crack formulation and verification,” *Computational Modelling of Concrete Structures, Balkema, Rotterdam*, 1998, pp.143-152.
2. Ohmori, N., Takahashi, T., Inoue, H., Kurihara, K. and Watanabe, S., “Experimental Studies on Nonlinear Behaviors of Reinforced Concrete Panels Subjected to Cyclic in-Plane Shear,” *Transaction. Architectural Institute of Japan*. Vol. 403, 1989, pp.105-118.
3. Okamura, H. and Maekawa, K., *Nonlinear Analysis and Constitutive Models of Reinforced Concrete*, Tokyo: Gihodo-Shuppan Co., 1991.
4. Park, H. and Kim, J. Y., “Unified Constitutive Model for Planar Members in Cyclic Shear,” *KEERC-MAE Joint Seminar*, 2001.
5. Sittipunt, C. and Wood, S. L., “Influence of Web Reinforcement on the Cyclic Response of Structural Walls,” *ACI Structural Journal*, Vol.92, No.6, 1995, pp.745-767.
6. Stevens, N. J., Uzumeri, S. M. and Collins, M. P., ”Reinforced Concrete Subjected to Reversed Cyclic Shear-Experiments and Constitutive model,” *ACI Structural Journal*, Vol. 88, No. 2, 1991, pp.135-146.
7. Vecchio, F. J., and Collins, M. P. “The modified compression-field theory for reinforced concrete elements subjected to shear.” *ACI Structural Journal*, Vol.86, No.2, 1986, pp.219-231.
8. Wood, S. L., and Sittipunt, C., “ Development of Reinforcement Details to Improve The Cyclic Response of Slender Structural Walls”, *WCEE*, Auckland, New Zealand, 2000, pp.1770.



KEERC-MAE Joint Seminar on
Risk Mitigation for Regions of Moderate Seismicity
University of Illinois at Urbana-Champaign, August 5-8, 2001



Sponsors: Korea Science and Technology Foundation, U.S. National Science Foundation, Brain Korea 21



Response Modification for Low-Rise Buildings

Peeranan TOWASHIRAPORN¹, James I. CRAIG², and Barry J. GOODNO³

¹ *Graduate Research Assistant, Georgia Institute of Technology
790 Atlantic Dr., Atlanta, Georgia, 30332 USA
email: gt0087d@prism.gatech.edu*

² *Professor of Aerospace Engineering, Georgia Institute of Technology
270 Ferst Dr., Atlanta, Georgia, 30332 USA
email: james.craig@aerospace.gatech.edu*

³ *Professor of Civil Engineering, Georgia Institute of Technology
790 Atlantic Dr., Atlanta, Georgia, 30332 USA
email: barry.goodno@ce.gatech.edu*

ABSTRACT: Passive energy dissipation (PED) devices can be an effective means for seismic response modification of unreinforced masonry (URM) buildings with flexible floor diaphragms commonly used in Mid America. A key characteristic of earthquakes in this region is the long-recurrence interval, and metallic hysteretic devices are attractive for seismic protection systems under these conditions because they are passive devices and offer good long-term reliability, modest cost and relatively simple design. Two simple rehabilitation schemes are proposed in this paper. The devices are activated using either the relative displacement between the flexible floor diaphragms and the in-plane walls or between the diaphragm and the ground. The amount of energy dissipated through the PED devices is used as a design criterion. When the optimally designed devices are incorporated, reductions as high as 48% in maximum displacement and can be achieved.

KEYWORDS: response modification, unreinforced masonry, rehabilitation, low-rise, passive control, energy dissipation, hysteretic damper, diaphragm.

INTRODUCTION

Essential facilities are those buildings and structures such as firehouses, police stations, emergency management offices and hospitals that must remain fully operational following a major earthquake. As such they must be designed or rehabilitated to meet the highest performance levels (e.g., FEMA Level 1 for structural and nonstructural elements [4]). In Mid America, which is a focus for the research being carried out in the Mid America Earthquake (MAE) Center, nearly one third of the current essential facilities are constructed from unreinforced masonry (URM), and most of these are one or two stories in height [5]. URM is one of the most vulnerable building materials in earthquake-prone regions, and essentially all such structures, if unrehabilitated, present serious risks to life safety, if not outright collapse.

The focus for this paper, which was prepared under research project ST-4 at the MAE Center, is response modification for essential facilities to maintain fully operational capabilities in a major regional earthquake. Since over 30% of the essential facilities are of URM construction, we focused our research on rehabilitation of this type of structural system with particular attention to one and two story buildings typical of firehouses and police stations. Rehabilitation of structures is a complex process and detailed procedures are available [4] to guide this effort. Objectives usually include a combination of both strengthening to address major structural weaknesses (increase seismic capacity) as well as response modification to reduce seismic demand. We are addressing the latter but as apart of a comprehensive rehabilitation strategy that could also include strengthening.

Under seismic loading, URM structures are usually considered to be quite stiff, especially for loads that act in the plane of the walls. While the initial response is largely elastic, the URM material behaves in a very brittle manner. Walls subjected to inplane loadings (called inplane walls or IPW's here) can fail through combinations of shear cracking, bed-joint fracture and slip, pier rocking, and toe crushing, and the post-failure behavior can exhibit varying degrees of hysteretic behavior. Walls subjected to out-of-plane loads (called out-of-plane walls or OPW's here) exhibit little or no strength and are vulnerable to outright failure and collapse unless significant compressive preloads are present.

Given the general lack of ductility in URM structures, the most common rehabilitation approach is to first consider strengthening to address the most serious IPW weaknesses and to prevent collapse of OPW elements. There is considerable literature on methods for strengthening URM, and a number of commercial approaches have been developed and are available. At least one MAE Center project is addressing strengthening of URM walls [1]

In addition to walls, there are a number of other components in URM buildings, and these can combine to create more complicated structural systems. One major component in most URM buildings dating before the mid-20th century is a flexible floor and/or roof diaphragm that in many designs is connected to load bearing URM walls with little or no regard for lateral loading and overall structural continuity. Rehabilitation of such buildings must consider not only securing these diaphragm-wall connections but also stiffening the diaphragms themselves. In this case, the objectives involve both strengthening and response modification so that improved (reduced) diaphragm flexibility reduces out-of-plane loads on URM walls and helps stabilize their out-of-plane behavior.

The vast majority of floor diaphragms in URM structures in Mid America are constructed of wood in varying configurations, and Project ST-8 [2] at the MAE Center is investigating the behavior of such diaphragms and their rehabilitation in laboratory testing. This work clearly identifies the very low stiffnesses that typical wooden diaphragms exhibit, and it also reveals the relatively modest increases in stiffness that can be achieved with the common rehabilitation approaches such as re-nailing and adding additional decking layers.

This paper describes how passive response modification could be employed to reduce the response of flexible floor diaphragms and thereby reduce their demand on the OPW's while providing lateral support for these vulnerable walls. Normally, passive response modification is not considered for URM structures due to their very stiff characteristics with relatively little deformation available to activate typical passive energy dissipators (PED's). Response modification can be achieved using simple PED's because the typical diaphragms are flexible enough to activate these devices. Our preliminary research shows that this can be an effective means for seismic response modification for certain kinds of low-rise URM buildings in the Mid-America region. Specifically, for one or two story structures with flexible floor and roof diaphragms and with fairly regular floor plans, the application of PED's can significantly reduce displacement responses and improve fragility. This paper summarizes preliminary analysis and design studies carried out at Georgia Tech for several possible PED configurations that might be applied and evaluated in testing of a full-scale URM building under MAE Center project ST-11 at Georgia Tech and a half-scale model under project ST-22 (being carried out jointly at U.S. Army-CERL).

POTENTIAL REHABILITATION SCHEMES

A key characteristic of earthquakes in this region is the long-recurrence interval. Metallic hysteretic PED's are attractive for seismic protection systems under these conditions because they offer good long-term reliability, modest cost and relatively simple design. The PED considered in this study is a simple ductile metal flexural device based on designs studied in previous work [10, 11], but the results could easily be extended to other metallic hysteretic designs. Previous studies by the research team and others show that such devices, even those fabricated from mild steel, are capable of developing large and stable hysteresis loops under cyclic loads and are capable of providing good and predictable energy dissipation [8].

Normally, PED's are not considered for URM applications because it is difficult to realize sufficient deformation in these relatively stiff structures to activate typical devices. However, the flexibility of the floor diaphragm and its interaction with the walls in a building with fairly regular floor plan may provide sufficient deformation to activate inelastic deformation, and hence an energy dissipation mechanism, in such passive devices. For example, preliminary analysis of the full-scale 2-story ST-11 model (24 ft square floor plan) shows that the relative displacement between the center of the floor diaphragm and the top of the in-plane wall is in the order of 6 times greater than that between the diaphragm center and the out-of-plane wall. This suggests the possible use of PED's, perhaps in connection with floor stiffening, to reduce this flexibility and therefore stabilize the out-of-plane walls. As a result, the devices considered in this study are activated using the flexibility in the floor diaphragm.

One configuration makes use of relative displacement between a flexible floor diaphragm and the in-plane walls. Another potential configuration is to utilize the relative displacement between the center of the flexible diaphragm and the ground. These implementations are called Type 1 and Type 2 rehabilitation schemes, respectively. Other schemes that would involve use of other kinds of PED's (e.g., viscous) or schemes that might involve application of much stiffer PED's to reduce the in-plane response of URM walls are not considered in this paper.

Type 1 Rehabilitation Scheme

The concept behind the Type 1 rehabilitation scheme is to utilize the differential displacement between the flexible floor (or roof) diaphragm and the much stiffer in-plane walls to activate the hysteretic devices. Actual application could be in a number of forms involving either distributed deformation or transfer (via braces or link beams) to a localized device. The implementation of the devices using a link beam and localized PED is shown in Fig. 1a. For this illustration, it is assumed that the device will respond only to seismic input in a direction perpendicular to the link beam. A relatively stiff beam is used to connect between two in-plane walls. The PED is then attached between the middle of the box beam and center of the diaphragm. Provided that the lateral stiffness (and possibly the torsional stiffness for eccentric connections) of the link beam is relatively high, the displacement at the middle of the box beam is comparable to that of the in-plane wall. The PED then sustains relative displacement between center of the diaphragm and the in-plane walls, and energy dissipation is developed when the device deforms inelastically.

Type 2 Rehabilitation Scheme

Because of the flexibility of the diaphragm, high differential displacement between the center of the diaphragm and the ground is expected. The Type 2 scheme makes use of this differential movement directly to trigger inelastic deformation and, consequently, energy dissipation in a PED connected between the floor diaphragm and the ground. Second floor implementation may be less effective, but definitely is possible. In order to capture this differential displacement, a simple K-brace frame is used to support the PED relative to the floor diaphragm. A very stiff k-brace system is desirable in such scheme, and it seems reasonable to think that such a design could be incorporated in a rehabilitation project. Fig. 1b illustrates the application of a Type 2 rehabilitation scheme in unreinforced masonry building. In this illustration it is assumed that the device will respond to seismic input in the direction of the k-brace plane.

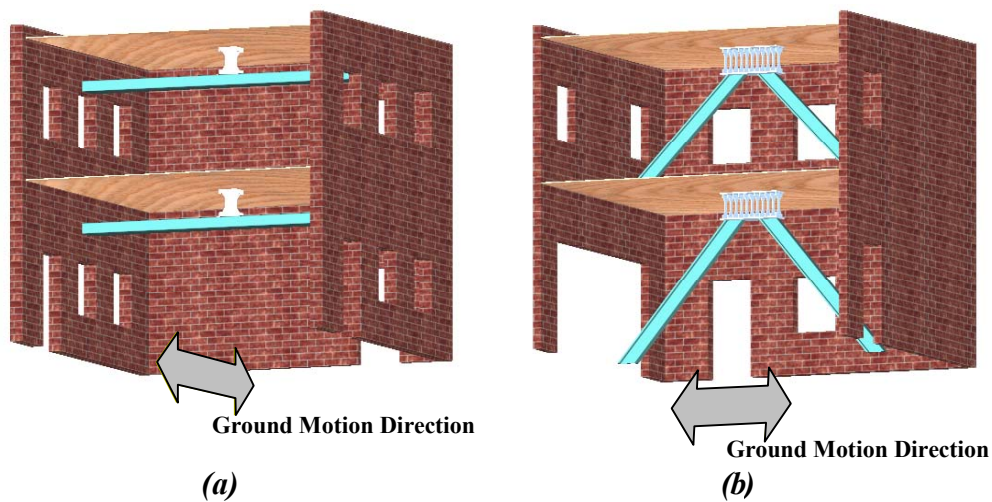


Fig. 1 Rehabilitation schemes, (a) Type 1, and (b) Type 2

DESIGN MODEL

A key part of the present study is the development of suitable analysis models for the target building. Related research has used DRAIN-2dx [12] to construct 2D models of frame structures with nonlinear behavior. While DRAIN-2dx does not have a straightforward means to model URM structures, it does include a versatile, zero-length spring element with a variety of possible nonlinear behaviors. As will be described below, this simple nonlinear spring element can be used to develop basic nonlinear “design” models for simple URM structures with flexible floor diaphragms [9].

A DRAIN-2dx design model has been developed to capture the behavior of the ST-11 test structure. The model is constructed using the DRAIN TYPE 04 zero-length nonlinear spring following the approach described in Ref. [9]. This results in what is basically a one-dimensional (1D) model of zero-length springs connected between a number of coincident nodes. Fig. 2 shows configuration of this simple spring model in which the zero-length springs and nodes are separated in order to show the model topology. The two springs at the bottom of the figure represent the in-plane wall (IPW) stiffness, the out-of-plane wall (OPW) stiffness, while the other two springs represent the diaphragm shear stiffness, and the diaphragm axial stiffness. The masses of the in-plane wall, out-of-plane wall, and diaphragm are lumped at the nodes indicated.

The elastic stiffnesses and masses used for each component and derived from the building design for the ST-11 full-scale building model are shown in Table 1. While nonlinear IPW behavior could be incorporated following Ref. [9], it is not included in the present study because we are assuming that URM strengthening has also been done to preclude localized failure and to achieve FEMA Level 1 (“immediate occupancy”) performance.

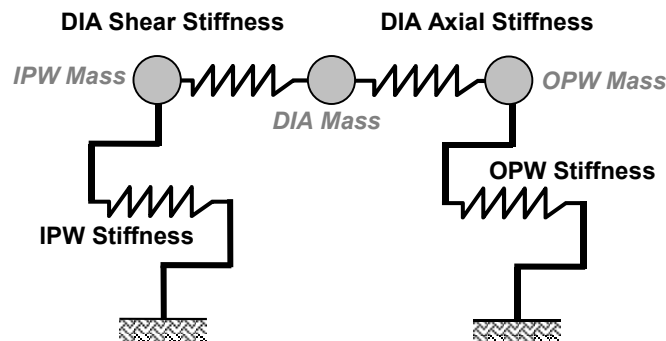


Fig. 2 Simple DRAIN linear-elastic spring model for ST-11 test structure

A similar lumped-parameter ABAQUS model developed by the ST-11 and ST-5 research teams is used to verify our DRAIN design model [7]. The same selected representative ground acceleration is applied to both the DRAIN spring model and the reference ABAQUS model. As can be seen from Table 2, the peak displacement responses for both models are almost identical.

Table 1 Properties of the DRAIN model

IPW Stiffness (k/in)	664
OPW Stiffness (k/in)	29.4
DIA Shear Stiffness (k/in)	15.6
DIA Axial Stiffness (k/in)	65.3
IPW Mass (k-sec ² /in)	0.134
OPW Mass (k-sec ² /in)	0.167
DIA Mass (k-sec ² /in)	0.0186

Table 2 Comparison between the results from DRAIN and ABAQUS models

	DRAIN Model	ABAQUS Model
Fundamental Period (sec)	0.412	0.412
Max Displ of node 2 - IPW (in.)	0.029	0.026
Max Displ of node 3 - DIA (in.)	0.407	0.393
Max Displ of node 4 - OPW (in.)	0.453	0.451

As noted, these preliminary results are based on elastic behavior of the in-plane walls, and this implies that URM strengthening measures have been taken as part of the rehabilitation process (or that the walls are strong enough to sustain the loads without failure). This restriction will be relaxed in a subsequent phase of this study, and the effect of nonlinear in-plane wall response will be examined.

A basic well-designed hysteretic metallic PED can be represented by an elasto-plastic force-displacement model with hysteresis. This kind of behavior is easily modeled using the DRAIN-2dx TYPE 04 nonlinear zero-length spring element. As a result, it is a relatively simple matter to introduce the PED into the building model simply by adding another TYPE 04 spring in the appropriate place(s). For a Type 1 PED design, this spring is introduced between the in-plane wall and diaphragm masses as shown in

- a. For the Type 2 PED design, the spring is introduced between the diaphragm mass and the ground as shown in a.

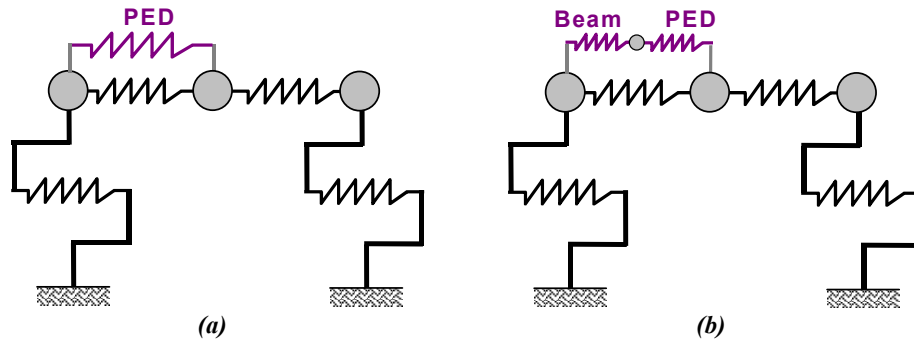


Fig. 3 DRAIN models for structure with Type 1 rehabilitation scheme, (a) with infinitely stiff link beam, (b) consider link beam stiffness

The stiffness of the link beam used with the Type 1 design or the stiffness of the brace used to support the Type 2 design will clearly reduce the available differential displacement across the PED and therefore reduce its potential performance capability. This non-ideal behavior can be taken into account in the DRAIN-2dx models by introducing a linear-elastic spring connected in series with the PED. The incorporation of a separate spring to model the finite stiffness of the link beam is shown in

b and a similar topology for the Type 2 braces is shown in b.

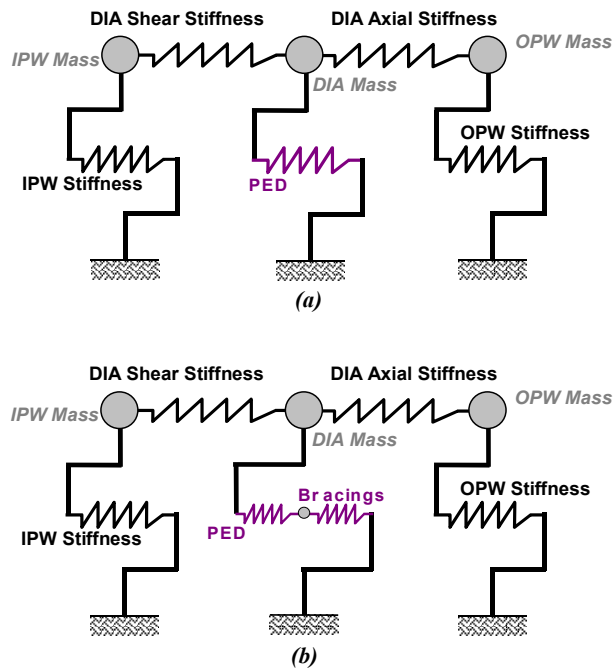


Fig. 4 DRAIN models for structure with Type 2 rehabilitation scheme, (a) with infinitely stiff braces, (b) consider braces stiffness

DESIGN CRITERIA FOR PED

The PED itself is designed using an energy-based formulation derived from earlier research [6, 11, 13]. In this approach, the best design for the PED is defined as the design that maximizes the ratio of energy dissipated in the PED (or PED's if multiple devices are used) to the total amount of input seismic energy. An energy-based approach has the advantage of responding to the overall behavior of the structure but at the expense of requiring more complicated analysis steps compared to, for example, using a simple force or point deformation criterion. The design process can easily be cast into the form of a simple nonlinear optimization process with the energy ratio as the objective function and appropriate constraints added for the maximum PED force, stiffness and dynamic ductility, for example.

- the ductility demand on any of the PED's should not exceed an allowable value defined for each particular energy dissipator (e.g. based on laboratory tests);
- PED physical geometry and fabrication constraints (these were not explicitly considered in the present study).

The design variables for the present optimization process are direct properties of the PED, and they include, (a) the elastic stiffness, and (b) the yield capacity of the metallic devices. The use of only 2 design variables makes it somewhat easier to graphically describe the design space since a simple Cartesian 3D surface or a 2D contour plot can be used to describe the objective function, and the constraints can be readily superposed. It should be noted that for more complicated cases involving more design variables, a numerical optimization procedure could also be employed to compute the design parameters directly. However, in most cases little or no information about the design space itself is revealed. For the present study, a grid of values of the objective (energy ratio) and constraint (dynamic ductility demand) functions were computed and plotted as superposed contour plots.

PED Design Results (Type 1 Scheme)

A number of test cases are investigated using the Type 1 PED model subjected to reference ground accelerations for Carbondale, IL. The ranges of yield load and initial stiffness of the PED's are varied from 1.0 to 3.0 kips and from 5 to 60 kips/in, respectively. The resulting contour plot is shown in **Fig. 4**. The contour lines for the energy ratio are shown as solid lines while the contour lines for the plastic ductility demand are shown as dashed lines.

From the plot in **Fig. 4**, the objective function is well-behaved and optimal solutions will lie to the right side of the figure. If the dynamic ductility is considered as a constraint in order to represent the finite deformation capacity of the devices (before fracture), the optimal solutions can be limited by the superposed dashed curves. For example, optimal solutions for a ductility constraint of 20 would lie along the constraint curve for increasingly higher stiffnesses and yield forces. While this is logical behavior, one cannot simply increase these design variables without eventually overloading the PED (or turning the whole PED subsystem into additional structural stiffening). Rather, constraints must be placed on the maximum practical yield force and possibly on the device initial stiffness. Assuming that the PED yield force is limited to a practical value of 1.5 kips such as might be representative of a tapered flexural device, the optimal designs will have an initial (elastic) stiffnesses of 20 and

35 kips/in for dynamic ductility constraints of 10 and 20, respectively. The objective contours indicate that by adding these PED's into the existing structure, from 27-35% of the input seismic energy can be dissipated, depending on dynamic ductility constraints (i.e., reliability) assumed for devices.

Table 3 presents the maximum displacement at the top of in-plane (IPW), out-of-plane (OPW) walls, and the diaphragm (DIA). It can be seen that as high as 39% reduction in the maximum displacement can be obtained when an appropriate passive rehabilitation system is applied.

PED Design Results (Type 2 Scheme)

A similar approach can be applied to the design of a Type 2 scheme. The only difference is in where and how the PED is introduced into the building model. The PED yield load and the initial (elastic) stiffness of the device varies from 1.0 to 5.0 kips and from 50 to 150 kips/in, respectively. The optimal designs for typical metallic flexural PED's can be seen to range from approximately 2.5 kips (yield load) with 75 k/in (stiffness) for a so-called, Design #1 and 2.0 kips (yield load) with 100 k/in (stiffness) for a so-called, Design #2. By adding these PED's into an existing structure, more than 35% of the input seismic energy to the test structure can be dissipated through the devices. As much as a 48% reduction in the maximum displacement is obtained from the analyses.

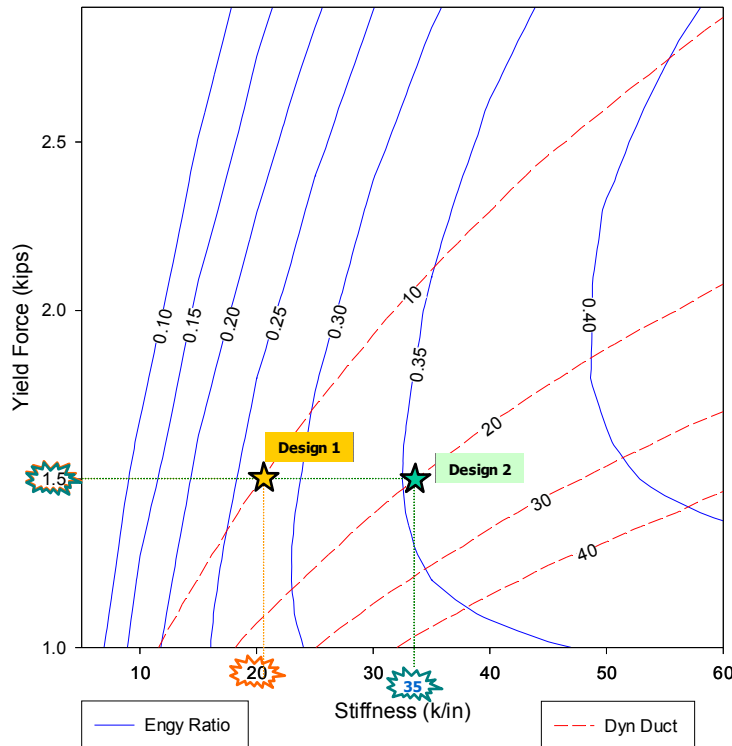


Fig. 4 Contour plots of the energy ratio and the dynamic ductility demand for Type 1 rehabilitation scheme

Table 3 Comparison in maximum displacements (Type 1)

	Max Displacement (in.)		% Reduction
	Existing	Rehabilitated	
<i>Top IPW</i>	0.029	0.027	8
<i>Top OPW</i>	0.453	0.298	34
<i>Center DIA</i>	0.407	0.247	39

DISCUSSION

The key result is the reduction in OPW displacements with its implications for improved performance of this vulnerable component. More comprehensive studies reported for project ST-4 [13] show that both Type 1 and 2 schemes provide similar performance. These results also show that the effectiveness of this approach is reduced when the diaphragm stiffness for shear mode deformation is more than about 8% of the in-plane wall stiffness, but this is well above the stiffnesses of typical unrehabilitated floor and roof diaphragms. The studies also show that the PED effectiveness decreases, as expected, when the flexibility of the structure supporting the PED increases. Finally, it is possible that PED's could also be applied in parallel with the IPW's to improve their performance (rather than rely on strengthening alone). However, this would require very stiff PED designs similar, for example, to the toggle bracing concepts developed by Constantinou [3].

CONCLUSIONS

These results verify that incorporation of a properly designed passive energy dissipator (PED) in the rehabilitation of certain kinds of URM structures could minimize energy dissipation demand in the main structure, reduce seismic responses, and lessen possible damage. Given the inherently stiff nature of URM structures, this approach can only be applied in cases where sufficient deformation can be developed, for example in a flexible floor or roof diaphragm, to fully activate typical metallic hysteretic dampers considered in this study. The primary benefit of this kind of response modification is a significant reduction in out-of-plane wall deformation induced by a flexible floor diaphragm. Thus the use of a PED as outlined in this study could be considered as a part of a rehabilitation scheme that aims to reduce the deleterious effects of an overly flexible diaphragm system.

Finally, it should be noted that these results were developed under the assumption that the URM walls behave elastically. That is, it is assumed that no failures such as pier rocking and bed joint sliding or diagonal shear cracking is developed in the typical perforated URM walls. Alternatively, it could also be assumed that as part of an overall rehabilitation scheme, appropriate strengthening treatments (or stiff PED's) will be applied to vulnerable URM walls to prevent such failures and therefore maintain essentially stiff elastic behavior.

ACKNOWLEDGMENTS

This study is supported by the Mid-America Earthquake Center under the National Science Foundation Grant EEC-9701785, Project ST-4.

REFERENCES

1. Abrams, D. P., "Performance of Rehabilitated URM Components," Project ST-6 (<http://mae.ce.uiuc.edu/TaskStatements/ST-6.html>), Mid America Earthquake Center, University of Illinois, Urbana-Champaign, IL, 2001.
2. Bracci, J. M. and Hueste, M. B. D., "Performance of Rehabilitated Floor and Roof Diaphragms," Project ST-8 (<http://mae.ce.uiuc.edu/TaskStatements/ST-8.htm>), Mid America Earthquake Center, Texas A&M University, College Station, TX, 2001.
3. Constantinou, M. C., Sigaher, A. N., "Energy Dissipation system Configurations for Improved Performance," *Proceedings of the 2000 Structures Congress & Exposition*, Philadelphia, PA, May 8-10, 2000.
4. Federal Emergency Management Agency (FEMA) Report 356, "Prestandard and Commentary for the Seismic Rehabilitation of Buildings," Washington, DC, November 2000.
5. French, S. and Olshansky, R., "Inventory of Essential Facilities in Mid-America," Final Report for Project SE-1, Mid-America Earthquake Center, October 2000.
6. Goodno, B. J., Craig, J.I., Dogan, T., and Towashiraporn, P., "Ductile Cladding Connection Systems for Seismic Design," Building and Fire Research Laboratory, NIST, Report GCR 98-758, October 1998.
7. Kim, S.-C. and White, D. W., "MDOF Response of Low Rise Buildings," draft report for Project ST-5, Mid-America Earthquake Center, School of Civil and Environmental Engineering, Georgia Institute of Technology, Atlanta, GA, 2001.
8. Moor, C., "Analytical and Experimental Evaluation of Advanced Cladding Connections," M.S.C.E. Thesis, School of Civil Engineering, Georgia Institute of Technology, Atlanta, GA, April 1992.
9. Park, J., Craig, J. I., and Goodno, B. J., "Simplified Nonlinear Design Model for URM In-Plane wall Response," Risk Mitigation for Regions of Moderate Seismicity, KEERC-MAEC Joint Seminar, Urbana-Champaign, IL, Aug. 5-8, 2001.
10. Pinelli, J.-P., Craig, J. I., Goodno, B. J., and Hsu, C. C., "Passive Control of Building Response Using Energy Dissipating Cladding Connections," *Earthquake Spectra*, Vol. 9, No. 3, 1993, pp.529-546.

11. Pinelli, J. P., Moor, C., Craig, J. I., and Goodno, B. J., "Testing of Energy Dissipating Cladding Connections," *Earthquake Engineering and Structural Dynamics*, Vol. 25, 1996, pp. 129-147.
12. Prakash, V., Powell, G. H., and Campbell, S., "DRAIN-2dx Base Program Description and User Guide," Version 1.10, Dept. of Civil Engineering, University of California Berkeley, November 1993.
13. Towashiraporn, P., Park, J., Craig, J. I. and Goodno, B. J., "Response Modification for URM Structures with Flexible Floor Diaphragms Using Passive Energy Dissipation," draft report for Project ST-4, Mid-America Earthquake Center, School of Civil and Environmental Engineering, Georgia Institute of Technology, Atlanta, GA, 2001.



KEERC-MAE Joint Seminar on
Risk Mitigation for Regions of Moderate Seismicity
University of Illinois at Urbana-Champaign, August 5-8, 2001



Sponsors: Korea Science and Technology Foundation, U.S. National Science Foundation, Brain Korea 21



Vertical Distribution of Equivalent Static Loads for Base Isolated Building Structures

Dong-Guen LEE¹

¹*Professor, Department of Architectural Engineering, Sungkyunkwan University,
Chunchun-Dong, Jangan-Gu, Suwon, Korea 440-746
email: dglee@yurim.skku.ac.kr*

ABSTRACT: It has been pointed out that the static lateral response procedure for a base isolated structure presented in UBC-97 somewhat overestimates the seismic story force. In this study the UBC-91 and UBC-97 static lateral load procedures for isolated structures are investigated, and a new formula is proposed for the vertical distribution of seismic load. The formula is derived by combining the fundamental mode shape of the isolated structure idealized as two degrees of freedom system and the fundamental mode shape of a fixed-based structure. The seismic story forces resulting from the proposed method are compared with those obtained from dynamic time history analysis and the code procedures. The results show that the proposed method provides conservative results compared with those from dynamic analysis and UBC-91 approach, and produces a more economic solution compared with the UBC-97 static lateral response procedure

KEYWORDS: base isolated structures, static lateral response procedure, vertical distribution of seismic loads, UBC-91, UBC-97.

INTRODUCTION

Seismic isolation mitigates earthquake-induced responses based on the concept of reducing the seismic demand by shifting the primary period of the structure rather than increasing the earthquake resistance capacity of the structure. In the United States, the Structural Engineers Association of Northern California (SEAONC) produced a document entitled Tentative Seismic Isolation Design Requirements [1] in 1986. This document was based on the basic theory of seismic isolation, and the earthquake loads were uniformly distributed along the height. In 1988 the Seismology Committee of the Structural Engineers Association of California (SEAOC) formed a subcommittee to make an isolation design document entitled General Requirements for the Design and Construction of Seismic Isolated Structures [2]. This was later adopted as an appendix to the seismic provisions in the 1991 Uniform Building Code (UBC-91) [3]. In UBC-94 [4], the vertical distribution of base shear was changed from an uniform one to a triangular one, which is generally used for fixed-base structures and produces very conservative load distribution. Similar concept has been continued in UBC-97 [5]. Some researchers, however, are concerned about the trend that the codes tend to be more conservative than those for conventional structures [6].

This paper presents a thorough investigation of the vertical load distribution of the static lateral response procedure specified in the UBC-91 and 97, and proposes a more rational formula for the distribution of seismic force based on the dynamics of a two-mass system. The proposed method may be applied, at least in preliminary analysis and design phase, to the linear isolation system that includes natural rubber isolators with moderate linear viscous damping.

VERTICAL LOAD DISTRIBUTION SPECIFIED IN UBC-91 AND 97

UBC-91 allowed the use of static analysis for a structure located farther than 15 km from an active fault, on soil profile types S1 and S2, in seismic zones 3 and 4 [3]. The distribution of the inertial forces on the structural system was based on the assumption that the super-structure acts like a rigid body and that the accelerations are the same at all floors. Based on this concept, the lateral force is distributed as follows :

$$F_x = \frac{w_x}{\sum w_i} \cdot V_s \quad (1)$$

where w_x and w_i are the weight at level x and i , respectively and V_s is the design lateral shear forces for the structure. This, however, neglects the flexibility of the super-structure and the participation of the higher modes, and therefore may not guarantee enough safety in some cases [7][8].

The UBC-97 seismic regulations for a seismic isolated structure are similar to those for structures without seismic isolation. The total lateral force above the isolation system V_s is distributed in accordance with the formula

$$F_x = \frac{w_x h_x}{\sum w_i h_i} \cdot V_s \quad (2)$$

where w_x is the weight at level x , and h_x is the height above isolation level. This leads to a triangular distribution of the lateral loads, which accounts for the possible higher mode contributions generated by nonlinearities in the isolators. Figure 1 schematically describes the behavior of an isolated structure subjected to an earthquake load and the idealized ones on which the UBC-91 and the later versions are based.

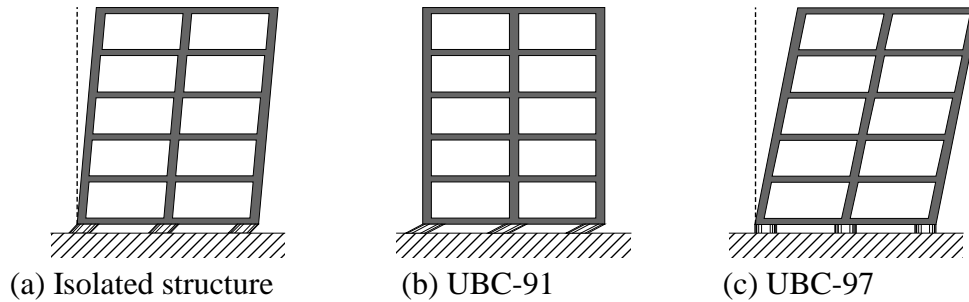


Figure 1 Schematic behavior of a base-isolated structure subjected to seismic loads

DISTRIBUTION OF SEISMIC LOADS

The proposed formula is based on the basic theory of structural dynamics of a two-mass model with linear seismic isolators as shown in Fig. 2. The procedure for obtaining the natural frequencies and mode shapes of such a system was derived by Kelly [6]. In the given structural model, m and m_b represent the mass of the super-structure and that of the base floor above the isolation system. The stiffness and damping of the structure are denoted by k_s and c_s , and those of the isolators are denoted by k_b and c_b , respectively. The equation of motion of the two-mass structure becomes

$$\mathbf{M}\ddot{\mathbf{v}} + \mathbf{C}\dot{\mathbf{v}} + \mathbf{K}\mathbf{v} = -\mathbf{M}\mathbf{r}u_g \quad (3)$$

where \mathbf{v} is relative displacement vector and \mathbf{r} is the influence vector in which each element is unity.

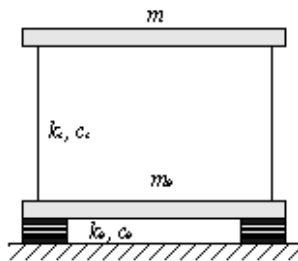


Figure 2 Idealized two-mass system with seismic isolation

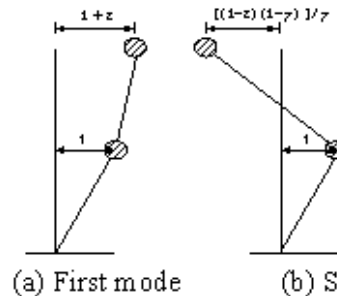


Figure 3 Mode shapes for the two-mass system

The solution of the eigenvalue problem leads to the following expressions for the natural frequencies and the mode shape vectors [1]:

$$\underline{\phi}_1 = \begin{pmatrix} 1 \\ 1 + \varepsilon \end{pmatrix} \quad \underline{\phi}_2 = \begin{pmatrix} 1 \\ \frac{1}{\gamma}(1 - \varepsilon)(1 - \gamma) \end{pmatrix} \quad \varepsilon = \left(\frac{\omega_b}{\omega_s}\right)^2 \quad (4)$$

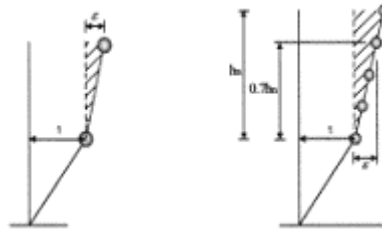
where the definition of each variable is given in Table 1. The above equations are obtained by neglecting the higher order terms of ε , the square of the frequency ratio, and the resultant mode shapes are plotted in Fig. 3.

Table 1 Parameters used in the formulation for the dynamic characteristics

Natural frequency of isolation system	$\omega_b = \left(\frac{k_b}{M}\right)^{\frac{1}{2}}$	Square of frequency ratio	$\varepsilon = \left(\frac{\omega_b}{\omega_s}\right)^2$
Natural frequency of super-structure	$\omega_s = \left(\frac{k_s}{m}\right)^{\frac{1}{2}}$	Mass ratio	$\gamma = \frac{m}{M}$

The derivation of the proposed method starts from the idea that the fundamental mode shape of an isolated structure may be simulated by combining the fundamental mode shape of the fixed-based structure, assumed as linear, and that of the equivalent two-mass system shown in

Fig. 3 (a). Figure 4 describes the combined mode shape of a general multi-story seismic isolated structure with the relative modal displacement at an effective height equal to the modal displacement at the top of the two-mass system. The effective height of a fixed-based structure corresponds to the height at which the lateral displacement is equal to that of the equivalent single degree of freedom system. The representative displacement of an equivalent single degree of freedom system, x_r , can be obtained as follows [9]:



(a) Fundamental mode of two-mass system

(b) Synthesized mode for isolated structure

Figure 4 Synthesis of fundamental mode shape for MDOF isolated structure from that of the two-mass system

$$x_r = \frac{\sum_i m_i x_i^2}{\sum_i m_i x_i} \quad (5)$$

where m_i is the mass of the i -th floor of a multi-story structure, and x_i is the maximum displacement of the i -th floor. For regular structures the effective height is generally taken to be $0.7 h_n$ for a shear wall structure and $0.6 h_n$ for a framed structure [10], where h_n is the total height of the structure. Priestley and Kowalsky [10] presented a formula for more precise

determination of effective height when mass or story heights vary significantly with height.

Based on this synthesized mode shape and with the effective height of αh_n the following formula is proposed for the seismic story force for a seismic isolated structure:

$$F_x = \frac{w_x (1 + \varepsilon h_x / \alpha h_n)}{\sum w_i (1 + \varepsilon h_i / \alpha h_n)} \cdot V_s \quad (6)$$

where α is generally taken to be 0.6 and 0.7 for framed and shear wall structures, respectively, and ε can be obtained from Eq. 4. Table 2 presents the relation between the ratio of the natural period of the super-structure and the isolated system described in Fig. 2, T_s / T_b , and the coefficient ε computed from Eq. 4 and from the mode shape vectors obtained from dynamic eigenvalue analysis. In the analysis the natural period of the isolation system, T_b , is fixed to 2 seconds. It can be noticed in the table that as the fundamental natural period of the super-structure decreases, i.e. as the structure becomes stiffer, the relative modal displacement, ε , also decreases. It can be observed, however, that the difference between the results of eigenvalue analysis and the simplified equation is negligible, especially when the period ratio is small (say less than 0.5). Therefore by using Eq. 4 the coefficient ε can be obtained accurately without carrying out eigenvalue analysis.

Suppose that the properties of the base-isolation system, such as mass of the super-structure, stiffness and damping of the isolators, etc., are predetermined, the seismic story force for general base-isolated multi-degree of freedom systems can be determined following the procedure summarized below:

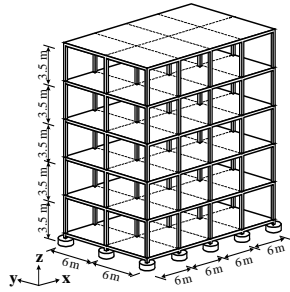
- 1) Determine the design lateral shear force V_s from code formula
- 2) Determine the natural frequency of the isolation system, $\omega_b = \sqrt{k_b / M}$
- 3) Compute the natural frequency of the super-structure from code formula
- 4) Compute the coefficient ε from Eq. 4
- 5) Determine effective height coefficient α
- 6) Obtain the seismic story force from the proposed formula, Eq. 6

Table 2 Variation of ε for various period ratios

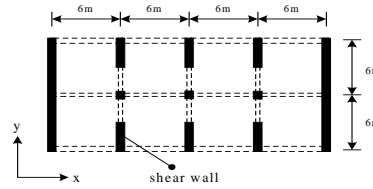
T_s / T_b	0.05	0.1	0.2	0.3	0.5	1.0	2.0
ε (approx.)	0.0025	0.010	0.040	0.090	0.250	1.000	4.000
ε (exact)	0.0025	0.009	0.040	0.091	0.255	1.049	4.319

VERIFICATION OF THE PROPOSED METHOD WITH THE RESULTS FROM DYNAMIC ANALYSIS

To compare the seismic force distribution computed from the proposed formula with those obtained from the code procedures and from dynamic analysis, a five-story reinforced concrete framed structure and a shear wall structure illustrated in Figs. 5 (a) and 5 (b) were analyzed. The floors were considered as rigid diaphragms with infinite in-plane stiffness.



(a) 5-story framed structure



(b) 5-story shear wall structure (plan)

Figure 5 Model structures with seismic isolation

Table 2 Design parameters of the model structures

	Period of isolation system, T_b (sec)	Period of super-structure, T_s (sec)	ε
Framed structure	1.523	0.625	0.168
Shear wall structure	1.523	0.367	0.058

Only three degrees of freedom in each nodal point in a floor. The representative height is taken to be $0.6 h_n$ for framed structures and $0.7 h_n$ for the shear wall structure, and 2 % of the critical damping was assumed for the super-structures. The seismic loads are enforced along the short (y) direction.

Table 2 lists the design parameters and their values used in the analysis. The periods are the effective ones at the design displacement obtained from the code formula. Many practical isolation systems involve higher damping than that inherent in the structure. To see the effect of isolator damping on the vertical distribution of the seismic force, two viscous damping coefficients of isolators, 5 % and 25 % of the critical damping, were considered in the analysis. The former may correspond to the damping of the natural rubber isolators, and the latter to the damping associated with lead-rubber isolators

Fundamental mode shape of the model structures

Figure 6 describes the fundamental mode shapes of the 5-story model structures both with and without base isolation obtained from eigenvalue analysis. The mode shapes were normalized so that the modal displacements at the top story were the same in both cases. The natural period of each mode and the corresponding effective mass coefficients $\bar{\mu}_i$, defined in the following equation, are given in Table 3:

$$\mu_i = \frac{(\phi_i^T \mathbf{M} \mathbf{r})^2}{\phi_i^T \mathbf{M} \phi_i}; \quad \bar{\mu}_i = \frac{\mu_i}{\sum_j m_j} \quad (7)$$

where ϕ_i is the i -th mode vector, \mathbf{M} is the mass matrix of the super-structure, and m_j is the lumped mass of the j -th story. These factors are independent of how the mode shape vectors are normalized. It can be noticed that the effective mass coefficients of the given isolated buildings are higher than 99 %, which indicates that the first mode dominates the dynamic behavior of the model structures.

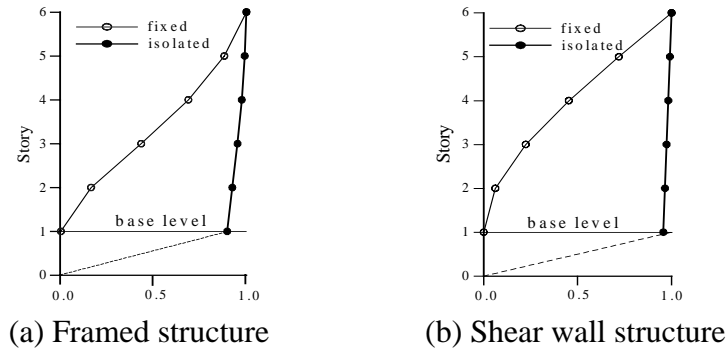


Figure 6 Fundamental mode shapes for isolated and fixed-based

Table 3 The natural periods and effective mass coefficient of the model structures in Y-direction

Structure		framed structure			shear wall structure		
Mode		1st	2nd	3rd	1st	2nd	3rd
Fixed-base structure	Period (sec)	0.43	0.13	0.06	0.07	0.01	0.00
	Effective mass coefficient (%)	81.27	11.07	4.62	67.07	20.53	7.26
Seismic isolated structure	Period (sec)	1.58	0.25	0.11	1.54	0.16	0.01
	Effective mass coefficient (%)	99.85	0.14	0.01	99.97	0.02	0.00

Figure 7 shows the fundamental mode shapes of the 5-story seismic isolated model structures obtained from the proposed method and the dynamic eigenvalue analysis. It can be seen that even though straight lines are used to predict the fundamental mode shapes in the proposed method, the mode shapes match well with those obtained from the eigenvalue analysis. This is especially true for the shear wall system.

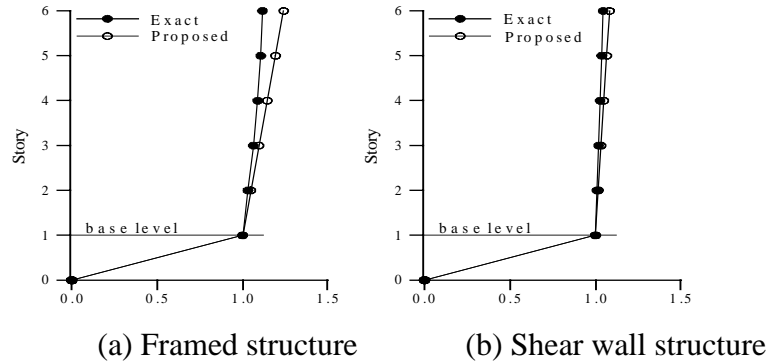


Figure 7 Fundamental mode shapes obtained from the proposed method and the dynamic eigenvalue analysis

Vertical distribution of seismic force in the 5-story structures

The example structures were first analyzed by direct integration method to obtain the vertical distribution of seismic force. For the dynamic analysis, El Centro (NS) was selected based on their frequency contents. As direct comparison of the base shear computed from the dynamic analysis and the static lateral response procedure is not appropriate, the peak ground acceleration of each vibration record was modified so that both records produce the same base shear with those obtained from the code procedures and the proposed method.

In Fig. 8 through Fig. 11 the results for vertical force distributions obtained from the proposed method and from UBC-91 and UBC-97 static lateral response procedures are compared with those computed by the dynamic time history analysis. In the figures β is the isolator damping ratio and B and B_D are the damping coefficients defined in the codes.

Figure 8 illustrates that for both ground excitations the slope of the vertical distribution of seismic force becomes larger in the order of UBC-97, proposed method, dynamic analysis, and UBC-91. Figure 9 shows that the cumulative story shears obtained from UBC-91 and UBC-97 form lower and upper bounds, respectively. The difference between the two methods decreases as the damping in the isolators increases, but compared with the result of the dynamic analysis, the UBC-91 approach is basically unsafe. In contrast, UBC-97 procedure results in triangular distribution of seismic force similar to the case of the fixed-based structure, which is too conservative compared with the result of the dynamic analysis. This conservatism may have originated from the concern that the high damping in isolator increases the effect of higher modes and consequently the seismic load in the super-structure. This may be true for the system with isolators having high hysteretic energy dissipation

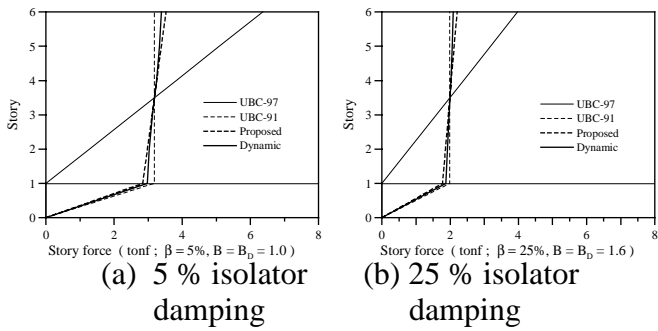


Figure 8 Vertical distribution of seismic story force in the framed structure

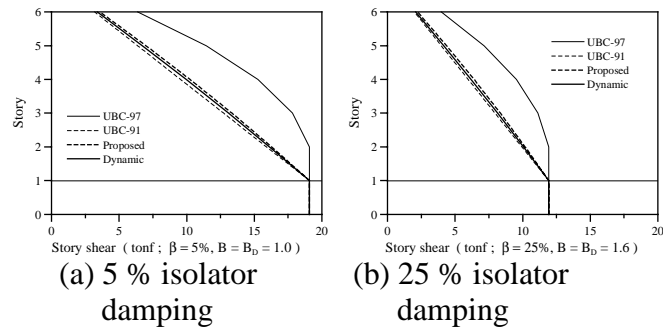


Figure 9 Story shear in the framed Structure

capacity, such as lead-rubber isolators. However the present study verifies that for low-rise seismic isolated building structures with moderate linear isolator damping, the UBC-97 approach results in overestimation of the seismic story force. It also can be noticed that the distribution of the seismic story force produced by the proposed method is slightly more slanted toward the result from the UBC-97 than that from the dynamic analysis. This leads to the more conservative cumulative story shear than that obtained from dynamic analysis. These observations demonstrate that the proposed method provides more economic solution than the code procedure for the vertical distribution of the seismic force while still maintaining a margin for safety.

The same procedures were repeated for the shear wall structure, and the results were presented in Figs. 10 and 11. In this case the representative height of $0.5 h_n$ was used taking into account the dynamic characteristics of the structure. Compared with the results for framed structure, the vertical distribution of the story forces obtained from the dynamic analysis and the proposed structure are closer to the result of UBC-91, which is a vertical line. Even in this case the story force and story shear distributions produced from the proposed method are slightly conservative than those from dynamic analysis.

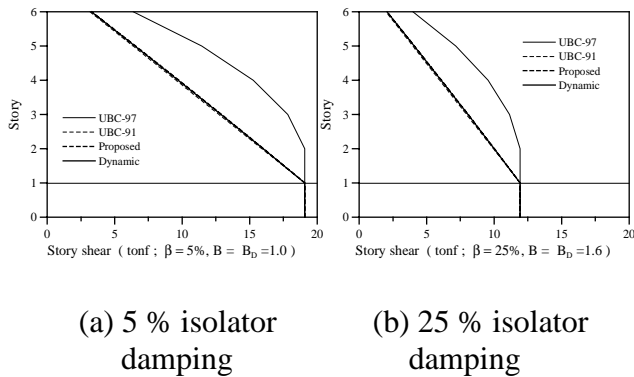


Figure 10 Vertical distribution of seismic story force in the framed structure

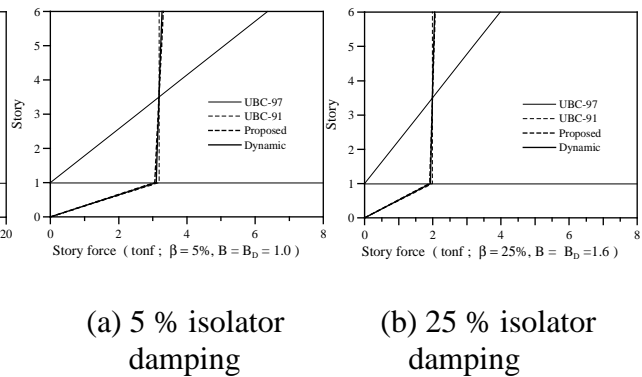


Figure 11 Story shear in the framed Structure

CONCLUSIONS

In this study the validity of the seismic force distribution formulae for seismic isolated structures regulated in UBC-91 and 97 are investigated, and a modified formula is proposed based on a dynamics of two-mass linear system. The following conclusions are drawn from the investigation of the seismic isolated 5-story framed and shear wall structures:

- (1) The UBC-91, in which the super-structure is regarded as a rigid body and the seismic load is distributed in accordance with the story mass, may underestimate the seismic load due to the negligence of the effect of building height. On the other hand UBC-97 disregarded the dynamic characteristics of the seismic isolated buildings and adopted the distribution formula for fixed-based structure, resulting in too conservative results compared with those of dynamic analysis.
- (2) The proposed formula provides slightly conservative seismic story force compared with the results from dynamic analysis, and results in a more economic design compared with the procedure of the UBC-97.
- (3) The proposed method and the code specified static lateral response procedure cannot be applicable for medium or high-rise structures in which the effect of the higher modes is not negligible.

REFERENCES

1. Structural Engineers Association of California, Recommended Lateral Design Requirements and Commentary, SEAOC Blue Book, 1985
2. Structural Engineers Association of California, General Requirements for the Design and Construction of Seismic-Isolated Structures, SEAOC Blue Book, 1989
3. Int. Conf. of Building Officials, "Earthquake Regulations for Seismic Isolated Structures", Uniform Building Code, Chapter 23, 1991
4. Int. Conf. of Building Officials, "Earthquake Regulations for Seismic Isolated Structures", Uniform Building Code, Appendix Chapter 16, 1994
5. Int. Conf. of Building Officials, "Earthquake Regulations for Seismic Isolated Structures", Uniform Building Code, Appendix Chapter 16, 1997
6. Kelly, J. M., "The Role of Damping in Seismic Isolation", Earthquake Engineering and Structural Dynamics, 28, 1999, 4-20
7. Kelly, J. M., Earthquake-Resistant Design with Rubber (2nd edn.), Springer, London, 1996
8. Naeim, F. and Kelly, J. M., Design of Seismic Isolated Structures, John Wiley & Sons Inc, New York, 1999

9. Lee, D. G., "Accurate and Simplified Models for Seismic Response Prediction of Steel Frame Structure", Ph. D. Thesis, Stanford Univ., 1984, 54-62
10. Priestley, M.J.N. and Kowalsky, M.J., "Direct Displacement-Based Seismic Design of Concrete Buildings", Bulletin of the New Zealand Society for Earthquake Engineering, 33, 4, 2000



KEERC-MAE Joint Seminar on
Risk Mitigation for Regions of Moderate Seismicity
University of Illinois at Urbana-Champaign, August 5-8, 2001



Sponsors: Korea Science and Technology Foundation, U.S. National Science Foundation, Brain Korea 21



Analytical Study on Inelastic Behavior and Ductility Capacity of Reinforced Concrete Bridge Columns Subjected to Seismic Load

Hyun Mock SHIN¹, and Tae-Hoon KIM²

¹ *Professor of Civil Engineering, Sungkyunkwan University
300 Chunchun-dong, Jangan-gu, Suwon, Kyonggi-do, 440-746, KOREA
email: hmshin@yurim.skku.ac.kr*

² *Ph.D. Candidate, Department of Civil Engineering, Sungkyunkwan University
300 Chunchun-dong, Jangan-gu, Suwon, Kyonggi-do, 440-746, KOREA
email: kth7love@nature.skku.ac.kr*

ABSTRACT: The purpose of this study is to find inelastic behavior and ductility capacity of reinforced concrete bridge columns subjected to seismic load. Material nonlinearity is taken into account by comprising tensile, compressive and shear models of cracked concrete and a model of reinforcing steel. The smeared crack approach is incorporated. In boundary plane at which each member with different thickness is connected, due to the abrupt change in his or her stiffness local discontinuous deformation can be taken into account by introducing interface element. Also an analytical model is developed to express the confining effects of lateral tie, which depend on the existence or nonexistence and the amounts of transverse confinement, etc. The proposed numerical method for inelastic behavior and ductility capacity of reinforced concrete bridge columns is verified by comparison with reliable experimental results.

KEYWORDS: inelastic behavior, ductility capacity, reinforced concrete bridge columns, seismic load, smeared crack, interface element, confining effects

INTRODUCTION

Many structural failures of reinforced concrete bridges during the recent earthquakes are due to the poor behavior of the structures in the inelastic range. The safeguards against intense earthquakes depend on reliable inelastic responses of the structural elements that provide mechanisms for the dissipation of the destructive earthquake energy. This suggests that structures in earthquake zones must be designed so that the energy from the loads may be dissipated by the post-elastic deformations in members; for this, the members must be designed for strength and also for ductility. However, the material characteristics of reinforced concrete are still not clearly describable with models and the design of reinforced concrete bridge columns depend heavily on empirical results [11, 14].

Finite element analysis with proper constitutive models can reliably trace the response of reinforced concrete bridge columns, however complex it is. The material models introduced in this paper are based on the multi-directional orthotropic models whose reference coordinates are set to the cracks. The analytical models of reinforced concrete element under the biaxial state of stress can be described using the smeared crack concept that the stress-strain relationship of reinforced concrete element is expressed using the corresponding average values. An interface element is developed to consider the local discontinuous deformations caused by abrupt changes in the section stiffness at the boundary plane connecting two components with different thicknesses. The finite element formulations include the simulation of the inelastic hysteretic behavior of the reinforced concrete structures and the material nonlinearity of reinforced concrete with the confining effect from the lateral reinforcement that increases the ductility and the energy absorption capacity.

A general purpose finite element analysis program implementing the reinforced concrete plane stress element and the interface element is developed. The program is built around the finite element analysis program shell named FEAP developed by Taylor [15]. Custom elements and nonlinear routines are easily adaptable in FEAP. Nonlinear analysis results for various reinforced concrete bridge columns subjected to given seismic loading show reasonable agreement with the recorded experimental data and this validates that the models may appropriately used as constitutive models for inelastic analyses of reinforced concrete bridge columns subjected to seismic load. The displacement ductility capacity is also computed for members and a seismic design method for reinforced concrete bridge columns considering the response modification factor is discussed.

NONLINEAR MATERIAL MODEL FOR REINFORCED CONCRETE [6, 7]

Reinforced concrete is highly nonlinear material. The nonlinear material model for the reinforced concrete is made up of models for concrete and a model for the reinforcing bars. Models for concrete may be divided into models for uncracked concrete and cracked concrete. The basic model adopted for crack representation is a non-orthogonal fixed crack approach of

the smeared crack concept, which is widely known to be a robust model for crack representation.

Model for Uncracked Concrete

The widely used elasto-plastic and fracture model for the biaxial state of stress proposed by Maekawa and Okamura [9] is used as the constitutive equation for the uncracked concrete. The nonlinearity and anisotropy of concrete are expressed independent of the loading history including the strain softening effects.

Model for Cracked Concrete

The cracked concrete may resist a certain amount of tensile stress normal to the cracked plane by the bond effect between the concrete and the reinforcing bars. A refined tension stiffness model is obtained by transforming the tensile stresses of concrete into the components in the direction normal to the crack and improved accuracy is expected, especially when the reinforcing ratios in orthogonal directions are significantly different and when the reinforcing bars are distributed only in one direction.

A modified elasto-plastic fracture model is used to describe the behavior of concrete in the direction of the crack plane. The model describes the degradation in compressive stiffness by modifying the fracture parameter in terms of the strain perpendicular to the crack plane.

The shear transfer model based on the Contact Surface Density Function [8] is used to consider the effect of shear stress transfer due to the aggregate interlock at the crack surface.

Model for the Reinforcing Bar in Concrete

The stress acting on the reinforcing bar embedded in concrete is not uniform and the value is maximum at locations where the bar is exposed to a crack plane. The constitutive equations for the bare bar may be used if the stress strain relation is in the elastic range. The post-yield constitutive law for the reinforcing bar in concrete considers the bond characteristics and the model is a bilinear model. Kato's model [4] for the bare bar under the reversed cyclic loading and the assumption of stress distribution denoted by a cosine curve are used in deriving the mechanical behaviors of reinforcing bars in concrete under the reversed cyclic loading.

MODELS AND ASSUMPTIONS FOR THE INTERFACE [6, 7]

The interface model for the boundary plane connecting two reinforced concrete elements with different sections is based on the discrete crack concept, which uses the relationships between the stress and the localized deformations. The model is one-dimensional and has no thickness; the relations between the normal force versus the normal displacement and the shear force versus the shear displacement are described.

Two-dimensional analysis necessarily assumes the stress distribution to be uniform in the direction of the element thickness. However, the stress distribution around the plane joining two elements with different thickness is of three-dimensional in nature and the assumption of uniformity is not valid. Because of this, the predicted deformation tends to be smaller than the actual response and this must be considered in the total deformation so that reliable structural behavior may be estimated. The strain-slip relation proposed by Shima et al. [13] is used as an analytical model for the pulling-out of reinforcing bars from the base caused by the tension in steel. The model describes a relation between the bar strain and the relative displacement of the bar to concrete. The relation is applicable to both elastic and plastic stress states for arbitrary loading, and for reinforcing bars with long embedded length and no slip at the free-end. The model for closure at joint plane considers the effect of the localized stress distribution. The shear slip model is derived from Li and Maekawa model [8] of the reinforced concrete plane stress element.

CONFINEMENT IN CONCRETE BY REINFORCEMENTS [6, 7]

The transverse reinforcements confine the compressed concrete in the core region and inhibit the buckling of the longitudinal reinforcing bars. In addition, the reinforcements also improve the ductility capacity of the unconfined concrete. As a result, this confinement increases the ultimate strength and strain of the reinforced concrete column and diverse stress-strain relationships have been proposed to depict this behavior [10, 12]. This study adopted a model proposed by Mander et al. [10]. The model described below modifies the compressive stress-strain model of the unconfined concrete to consider the confinement in concrete from the reinforcements. The equations consider the yield strength, the distribution type and the amount of the longitudinal and transverse reinforcing bars to compute the effective lateral confining stress and the ultimate compressive strength and strain of the confined concrete.

ANALYSIS PROGRAM BY FINITE ELEMENT METHOD [6, 7]

The proposed structural element library RCAHEST(Reinforced Concrete Analysis in Higher Evaluation System Technology) is built around the finite element analysis program FEAP [15] developed by Taylor. FEAP is characterized by modular architecture and by the facility of introducing any type of custom elements, input utilities and custom strategies and procedures. The FEAP will help alleviate many of the difficulties commonly encountered in maintaining the integrity of existing software components during the development of new research capabilities. FEAP permits users to add their own element modules to the program. Accompanying with the present study, we will attempt to implement such constitutive models for reinforced concrete, reinforced concrete plane stress element and interface element.

NUMERICAL EXAMPLES

Data from experiments by Ang et al. [2], Ishibashi and Yoshino [3], and Kawashima et al. [5] are used. Fig. 1 and 2 present geometric details of the tested specimens. The longitudinal

reinforcement ratio varies from 0.9 % to 3.8 %. The transverse reinforcement ratio varies from 0 to 1.02 %. The axial load ratio varies from 0 to 20 % and the aspect ratio ranges from 1.5 to 5.4.

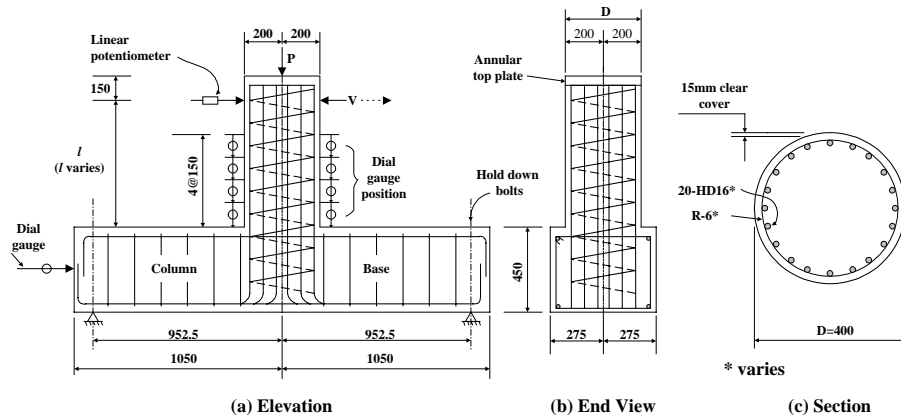


Figure 1 Geometric details of RC column specimens [2]

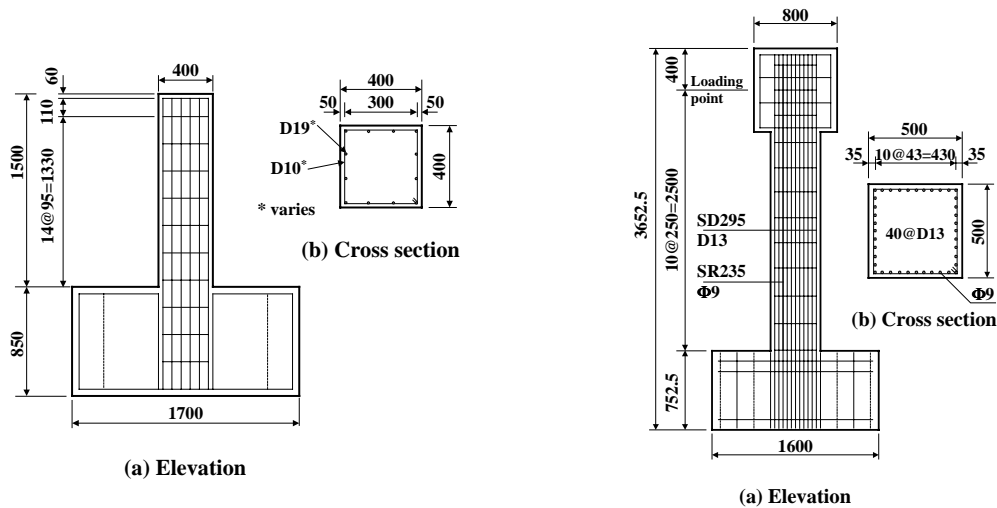


Figure 2 Geometric details of RC column specimens [3, 5]

Among the forty-seven specimens, Unit 4, Unit 5 and Unit 18 have very large yield displacements compared with similar others. Unit 21 failed prematurely. All other specimens have comparable values with analytical results and the comparative data are summarized on Table 1 and Table 2. In predicting the results of Unit series [2] involving primary shear failures, under a variety of reinforcement and loading conditions, the ratio of experimental to analytical ductility capacity had a mean value of 0.93 and a standard deviation of 34 percent. For other specimens [3, 5], the mean and standard deviation were 0.99 and 24 percent,

respectively. Inaccuracies, which may arise, shear failure mode is very brittle and it is difficult to decide ultimate displacement in experiments.

There are twice specimens (Unit 7, Unit 16, and Unit 23) as analytical ductility capacity, which is caused by both experimental error and analytical error. So it needs care to design columns under 2.0 of aspect ratio and over 3 % of longitudinal reinforcement ratio. The variations of the strength and the ductility ratios are shown in Fig. 3 where the experimental and analytical results reasonably agree. Both the experimental and analytical results show that the increase in transverse reinforcement ratio in reinforced concrete bridge columns yields higher ductility. The ductility of reinforced concrete bridge columns with transverse reinforcement after the yielding of longitudinal reinforcement may also be simulated by computation using finite elements. All the results support that the failure mode and ductility level of reinforced concrete bridge columns after yielding of longitudinal reinforcement can be estimated by the finite element analysis proposed in this paper. From these results, some tendencies are clearly identified again as follows.

- 1) The ductility tends to decrease when higher axial compressive force is applied.
- 2) The ductility is lower for larger longitudinal reinforcement ratio.
- 3) The ductility is higher for larger transverse reinforcement ratio.
- 4) The ductility is higher for larger aspect ratio.

The range of ductility capacity of single columns for experimental results is from 1.2 to 8.0. Thus it is unreasonable to uniformly adapt response modification factor of 3 as outlined in Standard Specifications for Highway Bridges [1]. The response modification factor must be expressed in an equation form that rationally considers the compressive axial force, the longitudinal reinforcement ratio, the transverse reinforcement ratio and the aspect ratio.

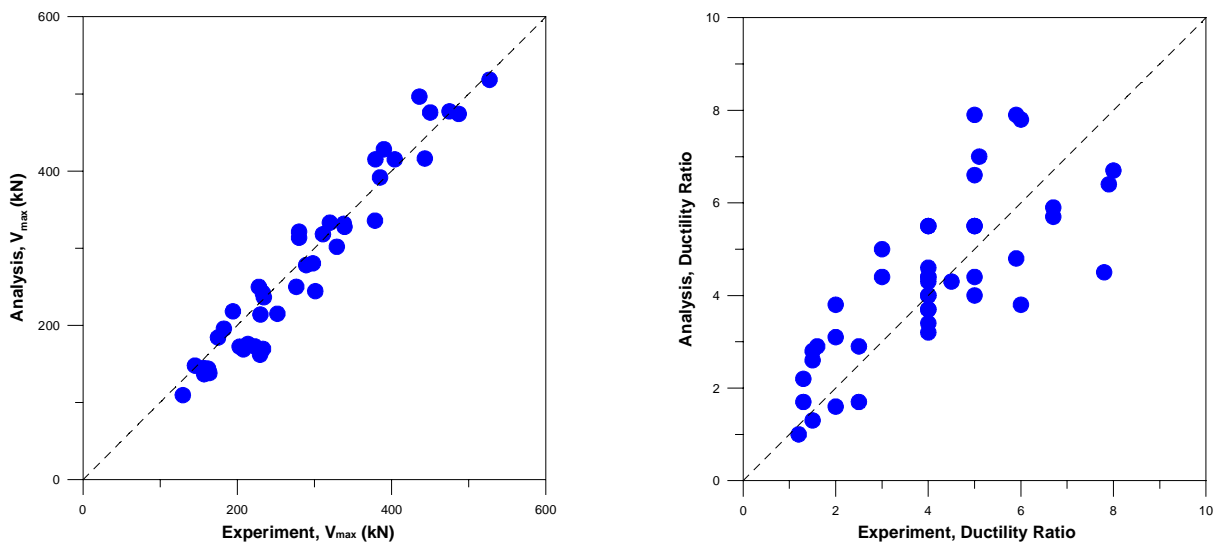


Figure 3 Comparison between analytical and experimental results of strength and ductility

Table 1 Experiment and analysis results for shear dominated RC columns

Specimen	Experiment				Analysis				Ratio of Experiment and Analysis Results			
	V_{\max} (kN)	δ_y (mm)	δ_u (mm)	μ	V_{\max} (kN)	δ_y (mm)	δ_u (mm)	μ	V_{\max}	δ_y	δ_u	μ
Unit 1	320.0	10.0	24.9	2.5	333.1	7.0	20.0	2.9	0.96	1.43	1.25	0.87
Unit 2	228.0	7.8	31.2	4.0	249.8	5.0	23.0	4.6	0.91	1.56	1.36	0.87
Unit 3	298.0	10.1	40.3	4.0	280.4	10.0	34.0	3.4	1.06	1.01	1.19	1.17
Unit 4	Very Large Yield Displacement				-	-	-	-	-	-	-	-
Unit 5	Very Large Yield Displacement				-	-	-	-	-	-	-	-
Unit 6	390.0	6.5	8.5	1.3	428.2	6.0	10.0	1.7	0.91	1.08	0.85	0.78
Unit 7	280.0	8.3	13.2	1.6	321.3	8.0	23.0	2.9	0.87	1.04	0.57	0.55
Unit 8	475.0	6.8	27.2	4.0	477.3	10.0	37.0	3.7	1.00	0.68	0.74	1.08
Unit 9	385.0	8.3	64.7	7.8	391.7	12.0	54.0	4.5	0.98	0.69	1.20	1.73
Unit 10	450.0	9.5	37.9	4.0	475.9	9.0	29.0	3.2	0.95	1.06	1.31	1.24
Unit 11	404.0	6.9	17.2	2.5	415.1	10.0	17.0	1.7	0.97	0.69	1.01	1.47
Unit 12	527.0	6.2	18.5	3.0	518.3	6.0	30.0	5.0	1.02	1.03	0.62	0.60
Unit 13	443.0	8.5	34.0	4.0	416.2	8.0	34.0	4.3	1.06	1.06	1.00	0.94
Unit 14	311.0	8.4	16.8	2.0	318.1	8.0	25.0	3.1	0.98	1.05	0.67	0.64
Unit 15	230.0	6.6	26.4	4.0	213.9	6.0	33.0	5.5	1.08	1.10	0.80	0.73
Unit 16	379.0	8.3	12.4	1.5	415.1	9.0	25.0	2.8	0.91	0.92	0.50	0.54
Unit 17	329.0	9.0	18.0	2.0	301.8	11.0	18.0	1.6	1.09	0.82	1.00	1.22
Unit 18	Very Large Yield Displacement				-	-	-	-	-	-	-	-
Unit 19	436.0	6.4	8.3	1.3	496.5	6.0	13.0	2.2	0.88	1.07	0.64	0.60
Unit 20	487.0	7.8	11.7	1.5	474.0	8.0	10.0	1.3	1.03	0.98	1.17	1.20
Unit 21	Failed Prematurely				-	-	-	-	-	-	-	-
Unit 22	280.0	8.8	13.2	1.5	313.6	8.0	21.0	2.6	0.89	1.10	0.63	0.57
Unit 23	339.0	8.5	16.9	2.0	327.7	8.0	30.0	3.8	1.03	1.06	0.56	0.53
Unit 24	338.0	8.1	32.2	4.0	331.6	8.0	32.0	4.0	1.02	1.01	1.01	0.99
Unit 25	233.0	5.1	6.1	1.2	242.0	4.0	4.0	1.0	0.96	1.28	1.53	1.20
Subtotal					Mean				0.98	1.03	0.93	0.93
					Standard Deviation				0.07	0.22	0.30	0.34

Table 2 Experiment and analysis results for flexure dominated RC columns

Specimen*	Experiment				Analysis				Ratio of Experiment and Analysis Results			
	V_{\max} (kN)	δ_y (mm)	δ_u (mm)	μ	V_{\max} (kN)	δ_y (mm)	δ_u (mm)	μ	V_{\max}	δ_y	δ_u	μ
P-10	161.8	12.41	83.10	6.7	141.6	14.3	82.0	5.7	1.14	0.87	1.01	1.17
P-11	162.1	12.39	83.17	6.7	143.8	14.3	84.0	5.9	1.13	0.87	0.99	1.14
P-13	156.3	12.34	96.95	7.9	144.6	14.3	91.0	6.4	1.08	0.86	1.07	1.23
P-56	175.0	14.63	58.31	4.0	184.2	16.3	60.0	3.7	0.95	0.90	0.97	1.09
P-57	182.6	16.08	64.33	4.0	195.6	18.0	80.0	4.4	0.93	0.89	0.80	0.90
P-58	194.4	20.13	60.31	3.0	218.1	18.1	80.0	4.4	0.89	1.11	0.75	0.68
I-1	129.4	6.9	55.2	8.0	109.5	8.3	56.0	6.7	1.18	0.83	0.99	1.19
I-2	203.0	11.0	44.0	4.0	172.3	10.0	55.0	5.5	1.18	1.10	0.80	0.73
I-3	276.5	13.0	58.5	4.5	249.9	12.0	52.0	4.3	1.11	1.08	1.13	1.04
I-4	233.4	11.0	55.0	5.0	169.4	10.0	55.0	5.5	1.38	1.10	1.00	0.91
I-5	207.9	11.0	44.0	4.0	168.8	10.0	44.0	4.4	1.23	1.10	1.00	0.91
I-6	213.8	10.5	52.5	5.0	175.8	10.0	66.0	6.6	1.22	1.05	0.80	0.76
I-7	229.5	10.4	52.0	5.0	161.9	10.0	55.0	5.5	1.42	1.04	0.95	0.91
I-8	252.0	10.5	52.5	5.0	215.0	10.0	44.0	4.4	1.17	1.05	1.19	1.14
I-9	145.1	10.0	60.0	6.0	147.8	9.0	70.0	7.8	0.98	1.11	0.86	0.77
I-10	163.8	9.0	45.0	5.0	138.2	8.0	63.0	7.9	1.19	1.13	0.71	0.63
I-11	156.9	9.1	54.0	5.9	136.7	8.0	63.0	7.9	1.15	1.14	0.86	0.75
IV-1	234.4	5.1	26.2	5.1	236.4	5.0	35.0	7.0	0.99	1.02	0.75	0.73
IV-2	289.3	4.6	27.1	5.9	278.0	6.3	30.0	4.8	1.04	0.73	0.90	1.24
IV-3	378.5	5.3	26.5	5.0	335.7	6.3	25.0	4.0	1.13	0.84	1.06	1.26
IV-4	222.6	8.1	32.8	4.0	172.7	10.0	40.0	4.0	1.29	0.81	0.82	1.01
IV-5	301.1	9.1	54.6	6.0	244.3	12.2	46.0	3.8	1.23	0.75	1.19	1.59
Subtotal					Mean				1.14	0.97	0.94	0.99
					Standard Deviation				0.14	0.14	0.14	0.24
Total					Mean				1.06	1.00	0.93	0.96
					Standard Deviation				0.13	0.18	0.23	0.29

* P-10 ~ P-58 = Kawashima et al. 1993; I-1 ~ IV-5 = Ishibashi and Yoshino 1988.

CONCLUSIONS

A method for analyzing the inelastic behavior and ductility capacity of reinforced concrete bridge columns subjected to seismic load is proposed. Analyses results by the proposed method show reasonable agreements with experimental data. The proposed method also predicts the load capacities, failure modes, crack patterns and load-deformation responses of reinforced concrete bridge columns with acceptable accuracy. From the results of the numerical simulations and comparisons with experimental data, the following conclusions are reached.

1. The proposed constitutive model and numerical analysis describe the inelastic behavior of the reinforced concrete bridge columns subjected to seismic load with acceptable accuracy and the method may be used in seismic design of reinforced concrete bridge columns.
2. Experimental and analytical values for yield and ultimate displacements and ductility capacity of the reinforced concrete bridge columns show reasonable agreement.
3. The included local discontinuous deformation at the boundary plane results in more accurate prediction of displacements and ductilities.
4. Further research is needed to determine the rational selection of the response modification factor to be used in the seismic design of reinforced concrete bridge columns.

ACKNOWLEDGMENTS

The study described in this paper was supported by the Korea Science and Engineering Foundation (KOSEF) through the Korea Earthquake Engineering Research Center (KEERC) under Grant No. 2000G0203. The authors wish to express their gratitude for the support received.

REFERENCES

1. American Association of State Highway and Transportation Officials (AASHTO), *Standard Specifications for Highway Bridges*, Sixteenth Edition, Washington, D.C., 1996.
2. Ang, B. G., Priestley, M. J. N., and Paulay, T., "Seismic Shear Strength of Circular Reinforced Concrete Columns," *ACI Structural Journal*, Vol. 86, No. 1, 1989, pp. 45-59.
3. Ishibashi, T., and Yoshino, S., "Study on Deformation Capacity of Reinforced Concrete Bridge Piers under Earthquake," *Journal of JSCE*, Vol. 8, No. 390, 1988, pp. 57-66, (in Japanese).

4. Kato, B., "Mechanical Properties of Steel under Load Cycles Idealizing Seismic Action," *CEB Bulletin D'Information*, No. 131, 1979, pp. 7-27.
5. Kawashima, K., Hasegawa, K., Nagashima, H., Koyama, T., and Yoshida, T., "Seismic Design Method of Reinforced Concrete Bridge Piers Based on Dynamic Strength and Ductility," Report of Public Works Research Institute, Ministry of Construction, Vol. 190, 1993, (in Japanese).
6. Kim, T. H. and Shin, H. M., "Analytical Approach to Evaluate the Inelastic Behaviors of Reinforced Concrete Structures under Seismic Loads," *Journal of the Earthquake Engineering Society of Korea*, EESK, Vol. 5, No. 2, 2001, pp. 113-124.
7. Kim, T. H., Lee, K. M., Yoon, C. Y., and Shin, H. M., "Inelastic Behavior and Ductility Capacity of Reinforced Concrete Bridge Piers under Earthquake. I: Theory and Formulation," *Journal of Structural Engineering*, ASCE, 2001, (Submitted for Publication).
8. Li, B., and Maekawa, K., "Contact Density Model for Stress Transfer across Cracks in Concrete," *Concrete Engineering*, JCI, Vol. 26, No. 1, 1988.
9. Maekawa, K., and Okamura, H., "The Deformational Behavior and Constitutive Equation of Concrete using Elasto-Plastic and Fracture Model," *Journal of the faculty of engineering*, University of Tokyo, Vol. 37, No. 2, 1983, pp. 253-328.
10. Mander, J. B., Priestley, M. J. N., and Park, R., "Theoretical Stress-Strain Model for Confined Concrete," *Journal of Structural Engineering*, ASCE, Vol. 114, No. 8, 1988, pp. 1804-1826.
11. Pincheira, J. A., Dtiwala, F. S., and D'Souza, J. T., "Seismic Analysis of Older Reinforced Concrete Columns," *Earthquake Spectra*, Vol. 15, No. 2, 1999, pp. 245-272.
12. Sheikh, S. A., and Uzumeri, S. M., "Strength and Ductility of Tied Concrete Columns," *Journal of Structural Engineering*, ASCE, Vol. 106, No. ST5, 1980, pp. 1079-1102.
13. Shima, H., Chou, L., and Okamura, H., "Micro and Macro Models for Bond Behavior in Reinforced Concrete," *Journal of the Faculty of Engineering*, University of Tokyo, Vol. 39, No. 2, 1987, pp. 133-194.
14. Watson, S., and Park, R., "Simulated Seismic Load Tests on Reinforced Concrete Columns," *Journal of Structural Engineering*, ASCE, Vol. 120, No. 6, 1994, pp. 1825-1849.
15. Zienkiewicz, O. C., and Taylor, R. L., *The Finite Element Method, Vol. 1 and 2*, Fourth Edition, McGraw Hill, New York, 1991.



KEERC-MAE Joint Seminar on
Risk Mitigation for Regions of Moderate Seismicity
University of Illinois at Urbana-Champaign, August 5-8, 2001



Sponsors: Korea Science and Technology Foundation, U.S. National Science Foundation, Brain Korea 21



Performance of Rehabilitated Reinforced Concrete Bridge Columns

Neil M. HAWKINS¹, and Joan Q. ZHONG²

¹ *Professor Emeritus and Interim Head, Department of Civil and Environmental Engineering,
University of Illinois at Urbana-Champaign
1114a Newmark Laboratory, 205 N. Mathews, Urbana, Illinois, USA
email: nmhawkin@uiuc.edu*

² *Former Pre-Doctoral Research Assistant, Department of Civil and Environmental
Engineering, University of Illinois at Urbana-Champaign
email: qunzhong@uiuc.edu*

ABSTRACT: Multi-column piers supporting existing bridges in the New Madrid Seismic Zone (NMSZ) are susceptible to damage in a repeat of the 1811-12 seismic events. Damage would include lap splice failures of the column reinforcement; shear failures of the columns, cap and foundation beams; beam bearing failures; and soil and foundation failures; as well as excessive displacements. This paper describes a methodology developed to characterize the generic vulnerability to seismic loading of multi-column pier supported existing bridges in the NMSZ and the reduction in that vulnerability if specific strategies are used to retrofit the columns of such bridges. The methodology involves five steps: identification of the characteristics of existing representative bridges in the NMSZ; structural and vulnerability assessments of both as-built and retrofitted representative multi-column bridge piers; prediction of the severity of structural damage likely to those piers under NMSZ synthetic earthquakes; expression of that damage in terms of fragility relationships; and mapping of how the retrofit costs relate to reductions in bridge replacement costs.

KEYWORDS: Concrete bridge columns, vulnerability assessments, retrofit strategies, bridge inventories, fragility relationships, damage estimates, retrofit costs.

INTRODUCTION

About 30 % of the total east-west highway traffic in the USA flows between Interstate 70 that connects Indianapolis with St. Louis and Interstate 40 that connects Nashville with Memphis and Little Rock. The NMSZ is centered between those two highways and a major event within that source is projected as having significant impact on both regional and national economies. Transportation disruptions would be one of the major causes of economic losses. The objective of the transportation networks research program (TNP) of the MAE Center was to improve methodologies for estimating those losses, particularly for highway systems, and to develop strategies for ameliorating those losses.

How to best retrofit bridge columns for seismic strengthening had been a major concern of the Illinois Department of Transportation (IDOT) since the early 1990s. The project (8) summarized here was initiated when the study of the highway inventory in Mid-America, as one of the first projects in the TNP (2), revealed many bridges supported on multi-column piers. The objectives were to define the reduction in highway system vulnerability that would result from a widespread program of bridge column wrapping and to develop rational, cost-effective and durable, retrofit methods for the multi-column bridge piers extant in the NMSZ.

In defining how to achieve the objectives it became clear that the major barrier was how to progress from the structural concerns for individual bridge, (a micro-level, site-specific problem), to system concerns, (the macro-level regional problem). In that transition there are issues of both aggregation and uncertainty that needed to be addressed. That barrier is one faced by highway planners any time funding is an issue for a system-wide bridge program.

In its first three years the MAE Center had a coordinated Transportation Networks Research Program. That program was split recently into a Network Vulnerability core research program and a Transportation Stakeholder Research Program. The research described in this paper was conducted as an integral part of the original TNP. The project was one connecting the research that has now evolved into the stakeholder program with the network research that is in the core program and focused originally on modeling transportation network vulnerability.

RESEARCH APPROACH

The approach utilized in this research is shown schematically in Figs. 1 and 2 for as-built and retrofitted multi-column piers, respectively. Step 1 was the development of an inventory of representative piers. Step 2 was the structural modeling of those piers and the subjecting of those models to a pushover analysis. In Step 3 the same models were subjected to a suite of synthetic ground motions typical of the motions expected as the result of a NMSZ event (7). Step 4 was determination of the damage to those models for the given suite of earthquakes and the expression of that damage in fragility terms. Step 5, Fig. 2, was the development of an appropriate retrofit strategy and Steps 6, 7 and 8 were the repetition of Steps 2, 3 and 4 for the retrofitted pier. Step 9 was then identification of the reduction in damage as a result of the application of the retrofit strategy.

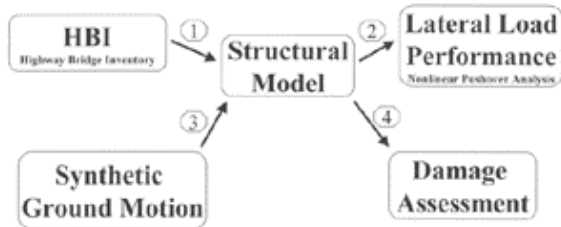


Figure 1 Methodology – Procedure for As-Built Pier

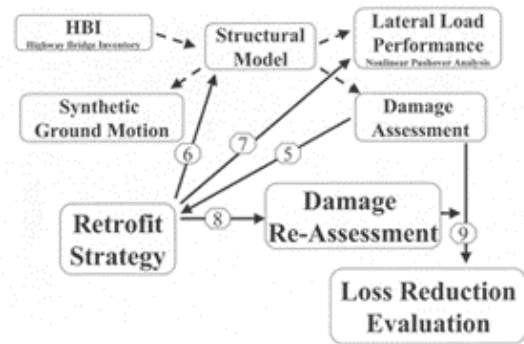


Figure 2 Methodology – Flow Diagram for Retrofitted Piers

Inventory

Because of the interest of IDOT in the project, IDOT provided access to their records for any state maintained bridges in Southern Illinois. As required by the Federal Highway Administration (FHWA), IDOT has an Earthquake Preparedness plan, (Ref. 4), that details how they will respond to the consequences of a seismic event within Illinois. A series of Priority Emergency Routes are specified for the vulnerable Southern Illinois area. The strategy of the state is to give top priority, for the limited retrofit monies available, to seismically strengthening the bridges on those routes. Accordingly, for this study the bridges on those routes were identified, numbered, and a random number generator used to select 10% of those bridges for further study. There are a total of 533 such bridges and therefore the properties of 53 bridges were examined in depth. First, the existing IDOT bridge inventory database was used to identify as many characteristics of each of the 53 bridges as possible. That inventory showed that about 5% of the bridges were culverts, 5% were single span structures and 90% were multiple span structures. Of that 90%, the decks of 50% and 40% of the bridges were supported on multi-column piers and wall piers, respectively. Columns were more common for overpasses and underpasses and wall piers for stream crossings. About 85% of the bridges were three spans or more in length. About 55% had skews of 20 degrees or less and only about 20% had skews greater than 40 degrees. The foregoing is standard information supplied by IDOT to FHWA and required for the National Bridge Inventory (NBI).

To determine details of the columns, the piers, the foundations, the soils at the site, and the bearings of the bridge, it was necessary to extract that information from the archived bridge drawings of IDOT. That information is not available from the NBI. The examination of the plans showed that the bridge cross-section at the typical multi-column pier had the form shown in Fig. 3. The concrete deck was supported on multiple beams sitting on steel bearings that rested on a cap beam connecting the column tops. The columns were connected at their bottoms by a crashwall that was supported on a foundation beam into which were embedded the tops of the piles supporting the pier. About 50% of the piers had three columns, about 40% had four, about 8% had two, and the remaining 2% had more than four columns. Column height to least width ratios ranged from 2.6 to 8.2 with an average value of 5.0. Column reinforcement ratios were typically 1% or less. Over 80% of the columns were rectangular and tapered, and for only about 10% of the piers were the soils sufficiently stiff that piles were not necessary.

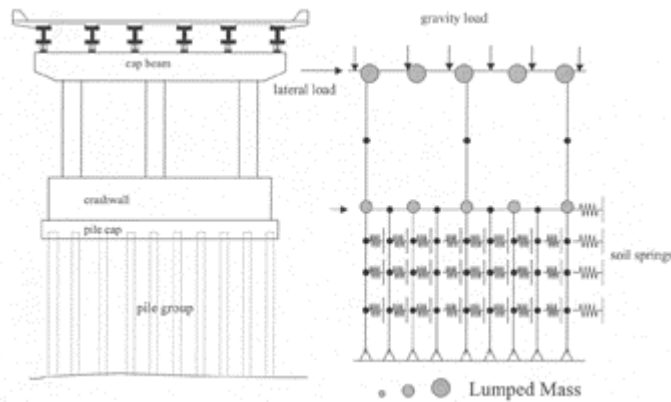


Figure 3 3-column Gent Model – Transverse Direction

Year built and bridge design types are compared in Fig. 4 for the NMSZ bridges listed in the NBI (2) and for the bridges examined in Southern Illinois. Clearly those characteristics are similar and therefore the Illinois data can be taken as representative of what is to be expected in the NMSZ as a whole. By contrast, data for the dominant bridge types in California (1) are also shown in Fig. 4. The concrete girders in California are typically built integrally with the pier and abutment supports and therefore the bridge characteristics in California differ markedly from those in the NMSZ.

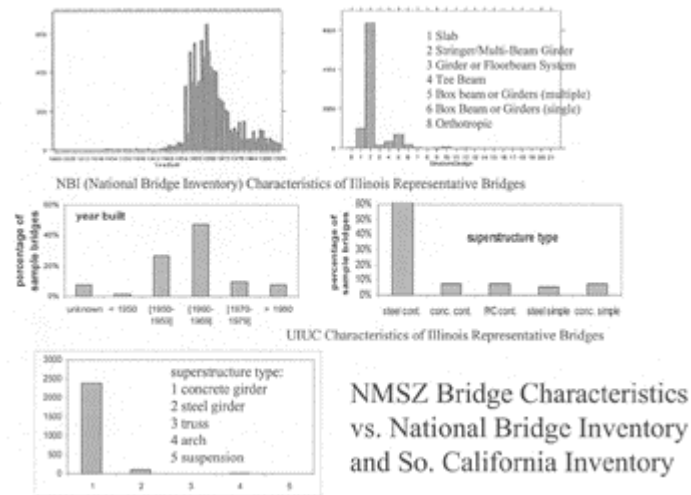


Figure 4 California Bridge Inventory Characteristics of Los Angeles, Venture, Orange and Riverside Counties

Structural Modeling

Structural models of the type shown in Fig. 3, excluding initially the lumped masses, were developed for each of the 26 bridge piers analyzed. The characteristics for each model were varied according to the details for each pier. Characteristics were expressed in terms of member strengths and ductility and included consideration of foundation flexibility effects. Each model was then first loaded laterally with a force applied at the cap beam level, (pushover analysis), and the initial stiffness, and the sequence for yielding and failure of the various elements of the pier were identified. The initial stiffness value was used to determine the fundamental period of the pier for dynamic analysis. Analyses were performed using the computer program Drain-2DX (6).

Earthquake Motions

For the events with both a 2% and 10% chance of occurrence in 50 years, the synthetic motions recommended in Ref.7 were used for dynamic analysis with appropriate adjustments for soil conditions and source distances. Dynamic analyses for each of the piers were performed using Drain-2DX, with the lumped masses of Fig. 3 included. The demand placed on each component of the pier was then compared with the capacity of that component for each of the motions and the probability of damage established. Probabilities were also calculated for a realistic range of component capacities given the likely range of the characteristics of the materials used in the component.

Damage Descriptors

Damage levels for a given earthquake for the range of strengths and earthquake motions studied were summarized using the descriptors of HAZUS (5), namely minor, moderate, major, and local failure/collapse. In applying those descriptors damage for ductile as well as brittle behavior was considered and a distinction made between damage to pier elements individually and to the pier as a whole.

Retrofit Strategy

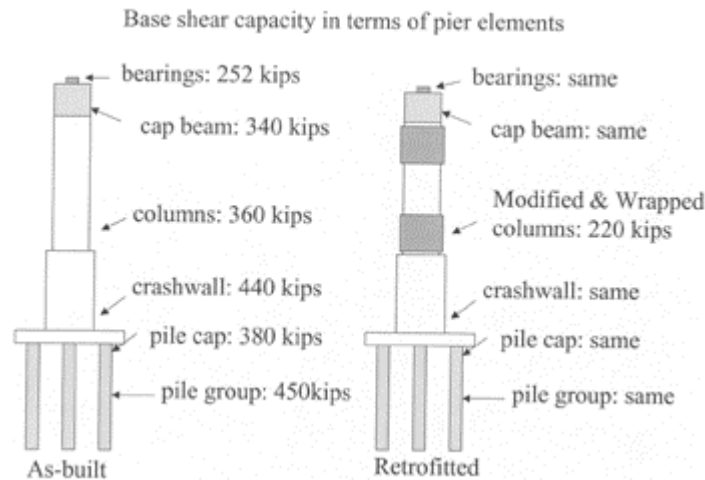


Figure 5 Retrofit Strategy

The retrofit strategy concluded to be the most cost-effective is illustrated in Fig. 5. The critical response of the bridges was generally in the transverse direction (the direction shown in Fig. 3) unless the skew was greater than about 30 degrees. However, for simplicity of illustration, the pier profile in the longitudinal direction is shown in Fig. 5. The retrofit strategy was basically to ensure weak column/ strong beam action in the transverse direction so that brittle elements of the pier were capacity protected. Shown on the left are the capacities of each element of a typical as-built pier. The least strength is associated with the bearings and the greatest strength with the piles. The bearings and cap beam are not practical locations in which to provide ductility. The best location is the columns. However, to achieve column ductility, the inadequate length lap splice at the base of the column needs to be protected against brittle failure by column wrapping. Thus, the optimum procedure is to cut sufficient of the dowel bars protruding out of the crashwall that the plastic hinge that forms at the base of the column has a capacity less than the least capacity of any other element of the pier (bearing and cap beam in Fig. 5). The column is then wrapped at its base and, if necessary, at the connection of its top to the cap beam.

Most piers in the NMSZ are located on soft soils and the use of steel jackets, as has been the practice in California, increases markedly the stiffness of the lightly reinforced NMSZ piers and increases markedly the seismic forces to be resisted by those piers. The use of steel jackets in soft soil conditions will usually also result in requiring retrofit of the foundation. However, the use of wraps made from prestressing strands, or advanced composites, does not stiffen the piers and can obviate the need for foundation retrofit.

In some cases it was also found that the stiffness of the pier became too small if too many dowel bars were cut in an attempt to capacity protect the bearings. The existing steel bearings then needed to be replaced with elastomeric bearings. Finally, 21% of the piers were on soil deposits that could liquefy under a major event or for which the drift of the as-built pier due to soil or column yielding was too large. In those cases the retrofit strategy of Fig. 5 becomes ineffective.

RESULTS

With the probabilities for damage of each pier established, it was assumed that all piers behaved independently during an earthquake and the results for events with a probability of occurrence of 2% and 10% in 50 years were constructed by assuming that damage to be normally distributed for the ten different motions used. Mean and standard distributions for the 2% and 10% events were determined

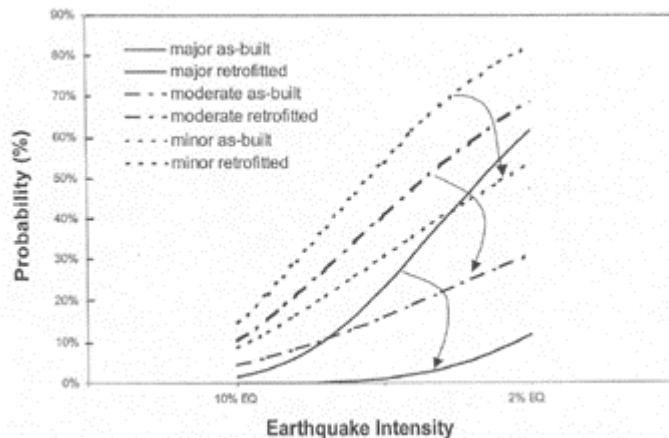


Figure 6 Effect of Retrofit on Vulnerability

Resulting pier vulnerability curves are shown in Fig. 6. The x-axis of Fig. 6 is the ground motion intensity for the 10 % and 2% events and the y-axis is the probability of a pier having damage exceeding the three different levels, minor, moderate and major, respectively. Relationships for both as-built and retrofitted piers are shown in Fig. 6. Although there are only two data points for each vulnerability for a given damage level, the relationships between levels are depicted as lognormal curves consistent with the methodology used to derive the vulnerability curves.

From Fig. 6 it can be seen that only minor or moderate damage occur in the 10% event. Further a program of column retrofit, as illustrated in Fig. 5, results in greater than a 50% reduction in the probability of both moderate and major damage for the 2% event.

To date IDOT has wrapped approximately 400 columns in the field using the Fig. 5 strategy. Wrapping has employed prestressing strand, e-glass and carbon fiber installations, with the costs of installation increasing in that same order. The average wrapping cost has been about 2% of the estimated replacement cost of the structure wrapped.

In a separate TNP study Hwang et al (3) have shown that for a typical as-built bridge in Memphis, the response for the bridge as a whole is very similar to the response for the most critical pier of the bridge. That bridge had the same form as the bridge of Fig. 3 with prestressed concrete girders replacing the steel girders.

CONCLUSIONS

The following conclusions were drawn from this study:

1. The bridge inventory characteristics found for priority emergency routes in Southern Illinois are typical of the bridge inventory characteristics for the New Madrid Seismic Zone as a whole. The majority of superstructures consist of concrete decks on continuous steel beams that are supported on bearings sitting on the top of concrete piers and abutments. Those characteristics differ markedly from the typical California bridge for which the concrete superstructure is integrally connected to the piers and abutments.
2. Multi-column piers exist on approximately 50% of the NMSZ bridges. Those bridges are primarily overpasses and underpasses. About 20% of those bridges are on foundations susceptible to liquefaction in a major event.
3. Wall piers exist on about 40% of the NMSZ bridges and about 70% of those bridges are over streams. The potential for liquefaction of their foundations is much higher than for bridges on multi-column piers.
4. There is likely to be significant damage to multi-column piers of existing bridges when the earthquake with 2% probability of occurrence in 50 years occurs. By contrast, the earthquake with 10% probability in 50 years would cause only minor damage.
5. A program of bridge pier wrapping would significantly reduce bridge losses in a major event and allow uninterrupted traffic flow on about 80% of the existing bridges with multi-column piers.
6. The cost of a multi-column bridge pier wrapping program is approximately 2% of the projected bridge repair/replacement costs following a major event. To be effective that program would have to also include column bar cutting and bearing modification.

ACKNOWLEDGMENTS

This research was performed as part of the Transportation Networks Research Program of the NSF sponsored Mid-America Earthquake Center headquartered at the University of Illinois at Urbana-Champaign. The assistance of the Office of Bridge and Structures of the Illinois Department of Transportation in the conduct of this research is gratefully acknowledged. Any opinions, findings, and conclusions or recommendations expressed in this paper are those of the authors and do not necessarily reflect the views of the MAE Center, the National Science Foundation or the Illinois Department of Transportation.

REFERENCES

1. Bosoz, N.I., A.S. Kiremidjian, S.A. King and K.H. Law, "Statistical Analysis of Bridge Damage data for the 1994 Northridge CA Earthquake", *Earthquake Spectra*, Vol. 15, No. 1, February 1999.
2. French, S.P and W.H. Bachman, "Transportation Facilities in Mid-America," *Proceedings of the 5th U.S. Conference on Lifeline Earthquake Engineering*, American Society of Civil Engineers (ASCE) Technical Council on Lifeline Earthquake Engineering (TCLEE) Seattle, WA, Report 99-387, August 1999.
3. Hwang, H., B.L. Jing, and Y-H. Chiu, " Seismic Fragility Analysis of Highway Bridges", *MAEC RR-4 Project Report*, Center for Earthquake Research and Information, The University of Memphis, , Nov. 30, 2000.
4. Illinois Department of Transportation, "Earthquake Preparedness Plan", Springfield, IL, 1998
5. NIBS for FEMA, " HAZUS Earthquake Loss Estimation Methodology Technical Manual", *National Institute of Building Science, Document No. 5201*, 1999.
6. Powell, G. H., and S. Campbell, "Drain-2DX Element Description and User Guide", *Report UCB/SEMM-94/08*, *Department of Civil Engineering, University of California, Berkeley*, 1994.
7. Wen, Y.K., and C-L. Wu, "Generation of Uniform Hazard Ground Motions for Mid-America Cities," *Proceedings of International Conference on Monte-Carlo Simulation*, Monte-Carlo, Monaco, June 18-21, 2000.
8. Zhong, Q., " Assessing the Effectiveness of Reducing Seismic Vulnerability by a Program of Bridge Pier Wrapping," *Ph. D. Thesis, University of Illinois at Urbana-Champaign*, June 2001.



KEERC-MAE Joint Seminar on
Risk Mitigation for Regions of Moderate Seismicity
University of Illinois at Urbana-Champaign, August 5-8, 2001



Sponsors: Korea Science and Technology Foundation, U.S. National Science Foundation, Brain Korea 21



Seismic Performance Evaluation of RC Bridge Piers with Limited Ductility by Pseudo Dynamic Test

Young S. CHUNG¹, and Jong H. PARK²

¹ *Professor of Civil Engineering, Chung-Ang University
456-756 Nae-Ri, Dedug-Myun, Ansung-City, Kyunggi-Do, Korea
email: chung47@cau.ac.kr*

² *Research Associate, Chung-Ang University
456-756 Nae-Ri, Dedug-Myun, Ansung-City, Kyunggi-Do, Korea
email: jongheob@chollian.net*

ABSTRACT: A number of bridges in the Kobe(1995) and Northridge(1996) earthquakes were collapsed or damaged, which gave us good lessons to evaluate a seismic capacity and to develop appropriate seismic design code for highway bridges in Korea. The objective of this study is to investigate the hysteretic behavior of reinforced concrete bridge piers, which have been widely used for railway and urban transportation facilities. Pseudo dynamic test was carried out to investigate the seismic performance of six(6) circular RC bridge piers subjected to artificial earthquake motions. Important test parameters are confinement steel ratio and input ground motion. The seismic behavior of circular RC bridge piers was evaluated through displacement ductility, energy absorption capacity, and capacity spectrum. It can be concluded that the limited ductility design concept should be more desirable for RC bridge piers in moderate or low seismicity region.

KEYWORDS: Pseudo Dynamic Test, RC Bridge Piers, Artificial Earthquake, Displacement Ductility, Energy Absorption Capacity, Capacity Spectrum

INTRODUCTION

Recently, it has been observed in the Korean Peninsula that the number of minor or low earthquake motions have been increased year by year. Furthermore, the collapse or near collapse of bridge superstructures during the 1995 Kobe earthquake and the 1996 Northridge earthquake stimulated the establishment of seismic design provisions for various infrastructures which could be appropriate for geological and topographical conditions in Korea. The objective of this pseudo dynamic test is to investigate the seismic performance of nonseismically designed circular reinforced concrete bridge piers, and then to study possible ways of ductility enhancement of concrete piers in the plastic hinge region. Considering that the Korean Peninsula is located in a moderate or low seismicity region, the seismic performance of limited ductile test specimens designed in accordance with Eurocode 8 have also been evaluated by the pseudo dynamic test.

DESCRIPTION OF EXPERIMENT

D10 deformed steel had been used as longitudinal steel in test specimens, of which confinement steels had been laterally used with D6 deformed steel. Yielding stress from the tensile coupon test was determined as 372MPa for D10 deformed steel and 343MPa for D6 deformed steel. A target compressive strength of concrete was $f_{ck} = 24\text{MPa}$ at 28 curing days. Circular solid RC piers of Hagal bridge, located in Kyung-Gi province, were adopted as a prototype of this test specimen. The bridge had been seismically designed in accordance with the provisions of KRBD(Korea Roadway Bridge Design) code.^[1] Two nonseismic and two seismic test specimens have been designed in accordance with the provisions of KRBD Code. Two test specimens were also designed in accordance with equation (1) for the limited ductile behavior of Eurocode 8.^[2]

$$\omega_{od,c} = 1.4\omega_{od,r} \quad \omega_{od,r} = 1.74 \frac{A_c}{A_{cc}} (0.009\mu_c + 0.17)\eta_k - 0.07 \geq \omega_{\omega,\min} \quad (1)$$

In equation (1), $\omega_{od,c}$ and $\omega_{od,r}$ are volumetric confinement steel ratio for circular and rectangular section, respectively. $\omega_{\omega,\min}$ is minimum volumetric confinement steel ratio, A_c is gross section area, A_{cc} is core concrete area, μ_c is required curvature ductility, and η_k is axial force ratio. Figure 1 shows detailed dimension of test specimens. Table 1 shows details of prototype and test specimen.

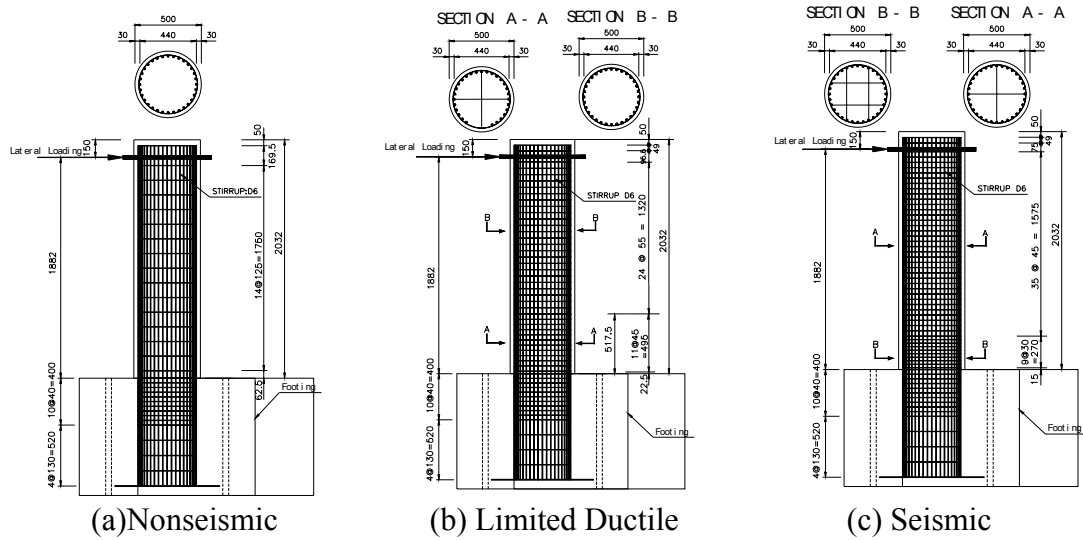
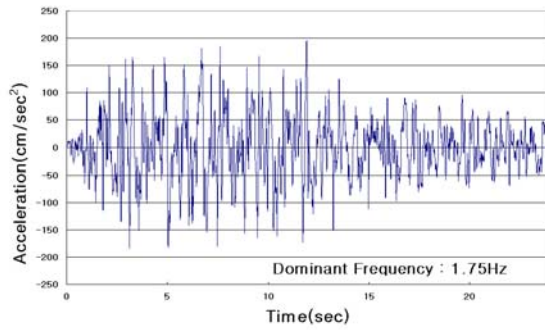


Figure 1 Detailed Dimension of Test Specimens

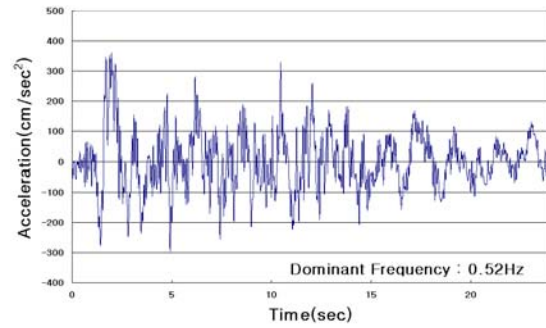
Table 1 Details of Prototype and Test Specimen

Classification		Prototype	Test Specimen		
			Nonseismic	Limited Ductile	Seismic
Longitudinal Steel		40@D29	32@D10		
Confinement Steel		D19	D6		
Volumetric Confinement Steel Ratio(%)		0.1614	0.03874	0.1076	0.1614
Longitudinal Steel Ratio(%)		1.1			
Space of Confinement Steel(mm)	PHR*	100	125	45	30
	NPHR**	150	125	55	45
Diameter(mm)		1,700	500		
Height(mm)		6,400	1,882		

* PHR: Plastic Hinge Region, ** NPHR: Nonplastic Hinge Region



(a) KHC(Korea Highway Cooperation)



(b) Kaihokus

Figure 2 Artificial Ground Acceleration

Figure 2 shows acceleration records of two input ground motions, which were used for this pseudo dynamic test. 0.20g and 0.36g are the PGA values for KHC artificial earthquake and Kaihokus artificial earthquake, respectively. These artificial earthquakes are based on rock soil condition and their duration is 24seconds. Dominant frequency is 1.75Hz for KHC artificial earthquake and 0.52Hz for Kaihokus artificial earthquake. Table 2 shows six(6) test specimens with input load. Six(6) test specimens are three for KHC(Korea Highway Cooperation) artificial earthquake and three for Kaihokus artificial earthquake of Japan. Important test parameters are input ground motion and confinement steel ratio. The applied scale factor between the prototype and the specimen is 3.4. PGA(Peak Ground Acceleration)values for input load 1 start from 0.154g and gradually increase to the failure PGA by approximate 0.1g. Sequential PGA values for two input loads are also shown in Table 2. The initial 0.154g value for each input load is determined in accordance with the seismic provisions of KRBD code.

Table 2 Six(6) Test Specimens with Input Load

Specimen Designation	Design Concept	Input Earthquake	Sequential Input Acceleration	
N-LP1	Nonseismic	KHC Artificial Earthquake	1	0.154g
L-LP1	Limited Ductile		2	0.220g
			3	0.300g
S-LP1	Seismic		4	0.400g
			5	0.500g
			6	0.600g
N-LP2	Nonseismic	Kaihokus Artificial Earthquake	1	0.154g
L-LP2	Limited Ductile		2	0.220g
S-LP2	Seismic		3	0.260g

EXPERIMENTAL PROGRAM

The pseudo dynamic test is similar to standard step-by-step nonlinear dynamic analysis procedures that the controlling computer software considers the response to be divided into a series of time step. Within each step the governing equation of motions are numerically solved for the incremental structural displacement. In the pseudo dynamic method, the ground motions as well as the structure's inertial and damping characteristic are specified numerically in a conventional dynamic analysis. However, the structure's restoring force is directly measured from the damaged specimen as the test progresses.^{[3][4]} Explicit Newmark β method was used as the algorithm of this pseudo dynamic test, as shown in Fig. 3. 1,000KN actuator was used for this pseudo dynamic test. Its maximum stroke is $\pm 250\text{mm}$. The applied axial force is $422\text{KN}(0.1f_{ck}A_g)$, which corresponds to the weight of bridge superstructure.

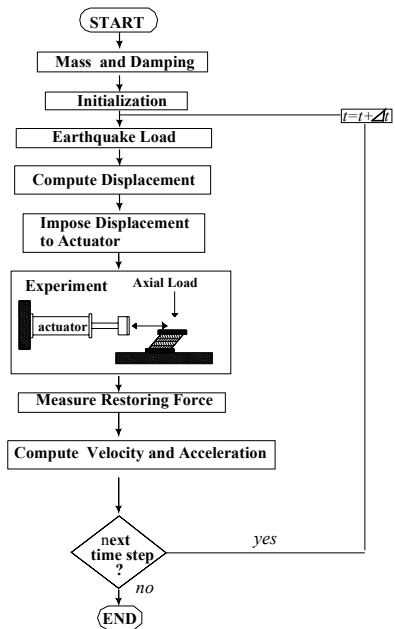


Figure 3 Explicit Newmark Algorithm

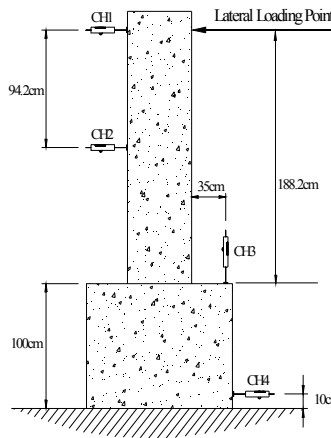


Fig. 4 LVDT Setup Photo 1 Pseudo Dynamic Test

During the pseudo dynamic test, lateral displacements were measured by 2 displacement transducers, which were located at 0.0cm, 94.2cm from the loading point of test column downward, as shown in Fig. 4. Steel strain gauges in the plastic hinge region were also used to measure the plastic strain of confinement and longitudinal steels. Photo 1 shows the pseudo dynamic test.

TEST RESULTS

Hysteretic Curve

Figure 5 shows the force-displacement relations of all test specimens by pseudo dynamic test. The hysteretic curves of seismic test specimens, L-LP1, L-LP2, S-LP1, and S-LP2, have by and large bigger energy absorption capacity than nonseismic test specimens, N-LP1 and N-LP2.

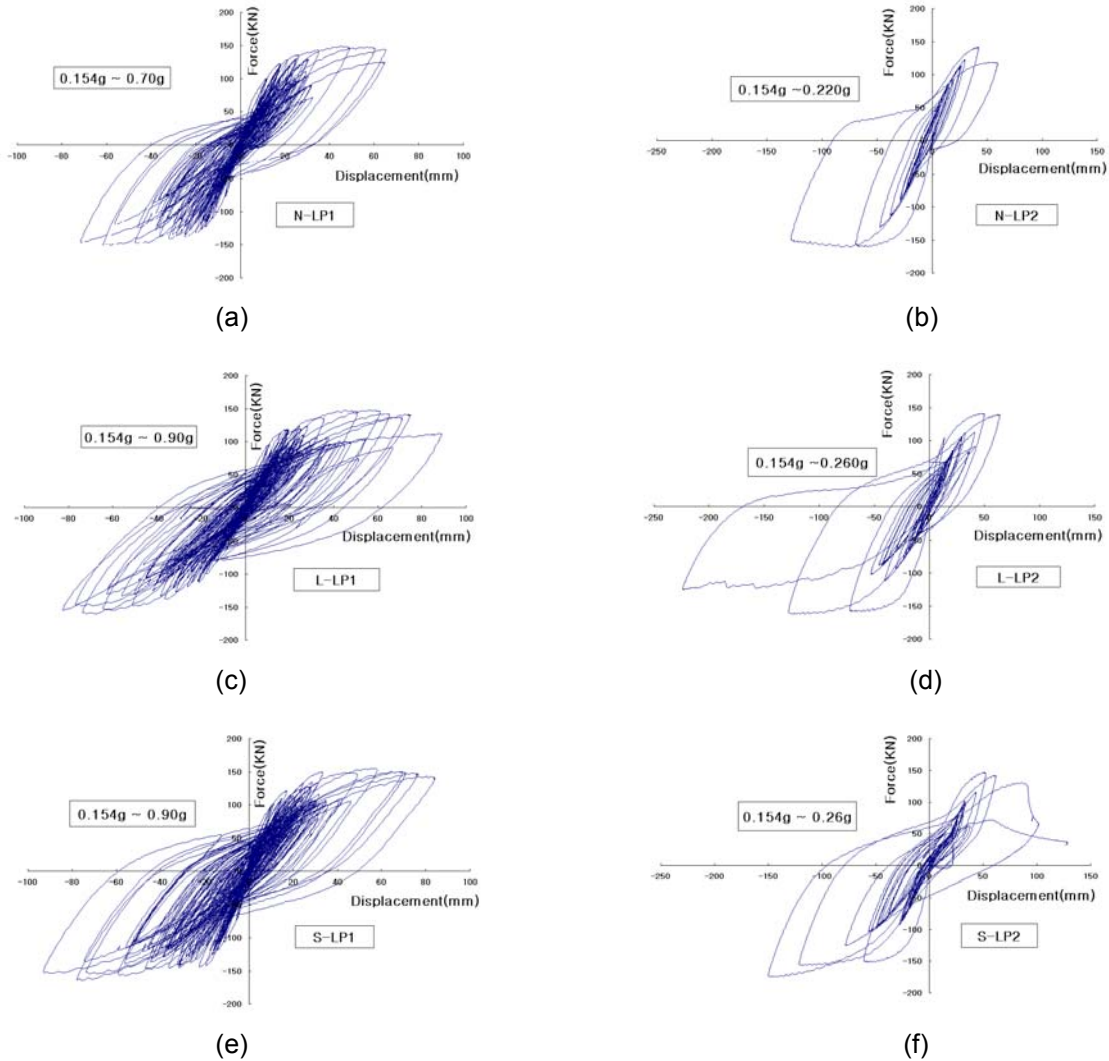


Figure 5 Force-Displacement Hysteresis Curve

It was also observed that all test specimens were failed in following sequence, such as cracking and spalling of cover concrete, breaking of the confinement steel, crushing of the core concrete, and then buckling of the longitudinal steel. All test specimens showed similar failure patterns. It is in particular noted from Fig. 5 (b), (d), (f) that nonseismic test specimen,

N-LP2, was severely damaged at 0.22g PGA acceleration, but L-LP2 and S-LP2 were damaged at 0.26g PGA acceleration.

Displacement Ductility

Seismic Performance of RC bridge piers can be evaluated as a displacement ductility. As shown in Fig. 6, the yield displacement can be calculated by extrapolating the straight line between the origin and $0.75V_i$ of the force-displacement envelope to the lateral load V_i , which correspond to the nominal flexural capacity of test specimen.^[5] As shown in Fig. 7, the ultimate displacement, Δ_u , defined as $\Delta_u = \text{Min} [\Delta_{\text{①}}, \Delta_{\text{②}}]$. $\Delta_{\text{①}}$ is the experienced maximum displacement when longitudinal or confinement steel is fractured but the strength on the descending branch of the force-displacement envelope curve is above $0.85V_{\text{max}}$. When the strength on the descending branch of the force-displacement envelope curve is dropped below $0.85V_{\text{max}}$, and longitudinal or confinement steel does not reach the failure state, $\Delta_{\text{②}}$ is the experienced maximum displacement just before $0.85V_{\text{max}}$. Displacement ductility, $\mu_{\Delta} = \Delta_u / \Delta_y$, and normalized displacement ductility values with respect to the displacement ductility of nonseismic test specimen are computed in Table 3.

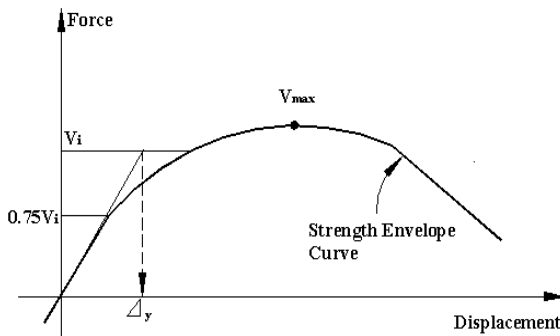


Figure 6 Definition of Yield Displacement

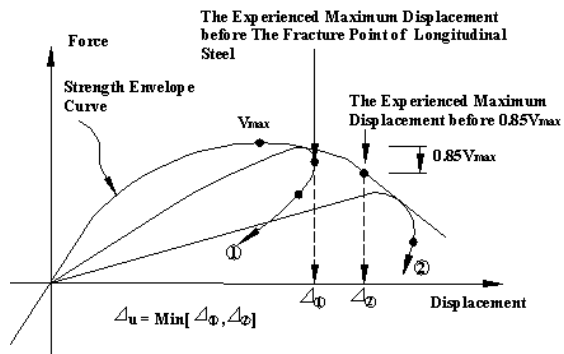


Figure 7 Definition of Ultimate Displacement

Table 3 Displacement Ductility

Classification	Displacement (mm)		Displacement Ductility $\mu_{\Delta} = \Delta_u / \Delta_y$	Normalized Displacement Ductility
	Yield	Ultimate		
N- LP1	11.66	73.34	6.3	1.0
L- LP1	11.17	82.64	7.4	1.2
S- LP1	10.19	92.97	9.1	1.5
N-LP2	16.45	111.35	6.8	1.0
L-LP2	15.69	127.95	8.2	1.2
S-LP2	14.59	141.10	9.7	1.4

Displacement ductility of limited ductile test specimen(L-LP1) was enhanced by 1.2 times by comparing with nonseismic test specimen N-LP1. As shown in Table 3, it can be obtained bigger ductility for L-LP1 and S-LP1, but lower ductility for N-LP1. Therefore, it is thought that limited ductile design concept should be more desirable for seismic preparedness of RC bridge piers in low or moderate seismicity region, in consideration of a good displacement ductility result for limited ductile test specimens.

Energy Analysis

For the measurement of energy capacity of all test specimens at a given PGA, cumulative input energy and dissipation energy have been analyzed. Cumulative input energy is defined as the cumulative workdone of the actuator, as shown in Fig. 8. The amount of dissipated energy in each load cycle has been calculated from the area of hysteresis loop between two consecutive displacement peaks, as shown in Fig. 9. As shown in Figs. 10 (a) and (b), it was obtained that cumulative input energy of limited ductile test specimens were enhanced by about 1.13 and 1.44 times as against those of nonseismic test specimens, respectively. Similarly, Figs. 11 (a) and (b) show that cumulative dissipation energy of limited ductile test specimens were enhanced by about 1.11 and 1.54 times as against those of nonseismic test specimens, respectively.

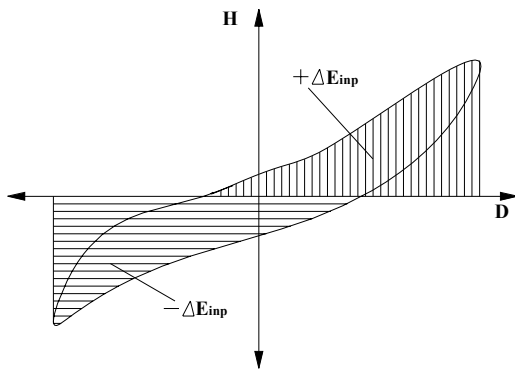


Figure 8 Definition of Input Energy

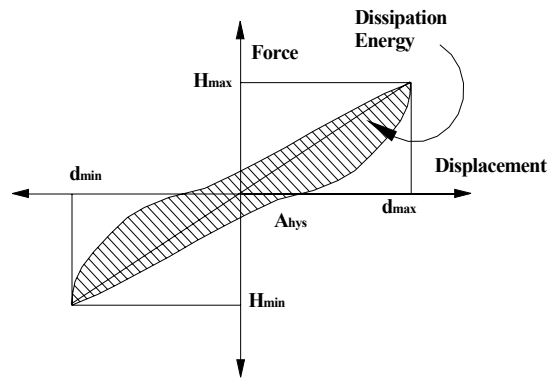
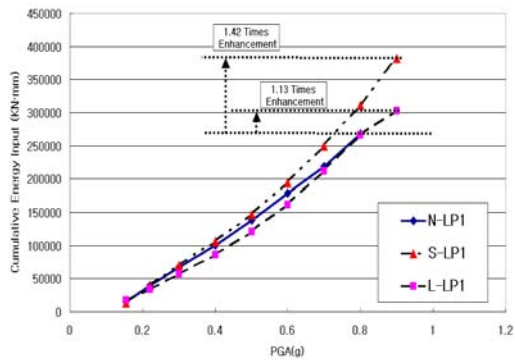
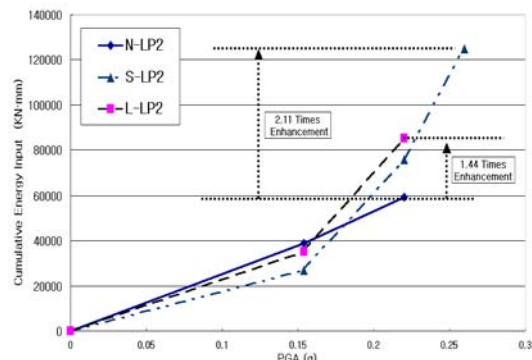


Figure 9 Definition of Dissipation Energy



(a) LP1



(b) LP2

Figure 10 Cumulative Input Energy

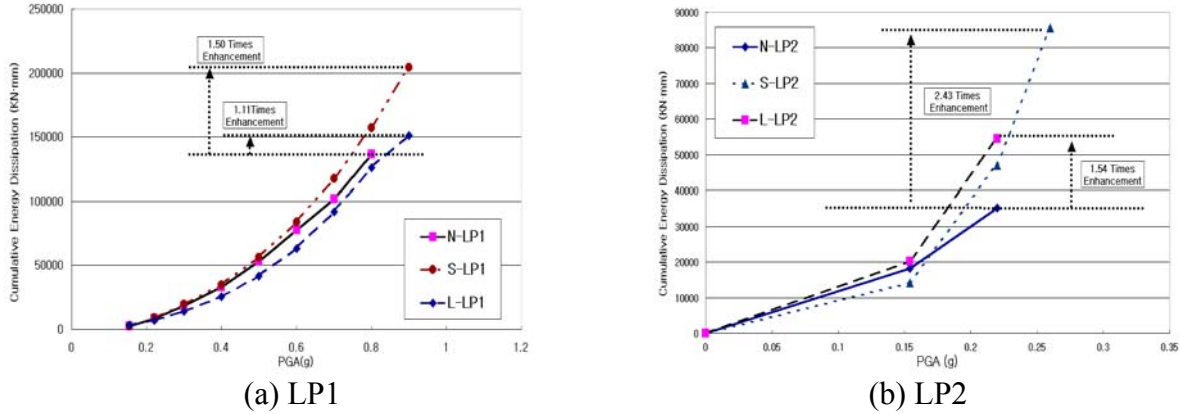


Figure 11 Cumulative Dissipation Energy

Capacity Spectrum

Seismic performance of test specimens was also evaluated through the capacity spectrum analysis of ATC40^[6]. As shown in Fig. 12, the capacity spectrum of all test specimens can be computed with the force and displacement values of prototype, of which considered the scale factor. Demand spectrum can be calculated to the function maintenance and the failure prevention level of KRBD code. Equivalent viscous damping ratio for demand spectrum can be calculated with the Takeda model of equation (2).

$$\xi_{eq} = 0.05 + (1 - (1 - \gamma) / (\sqrt{\mu} - \gamma\sqrt{\mu})) / \pi \quad (2)$$

In equation (2), $\gamma(=0.005)$ is the secant stiffness ratio after yielding, and μ is the displacement ductility.

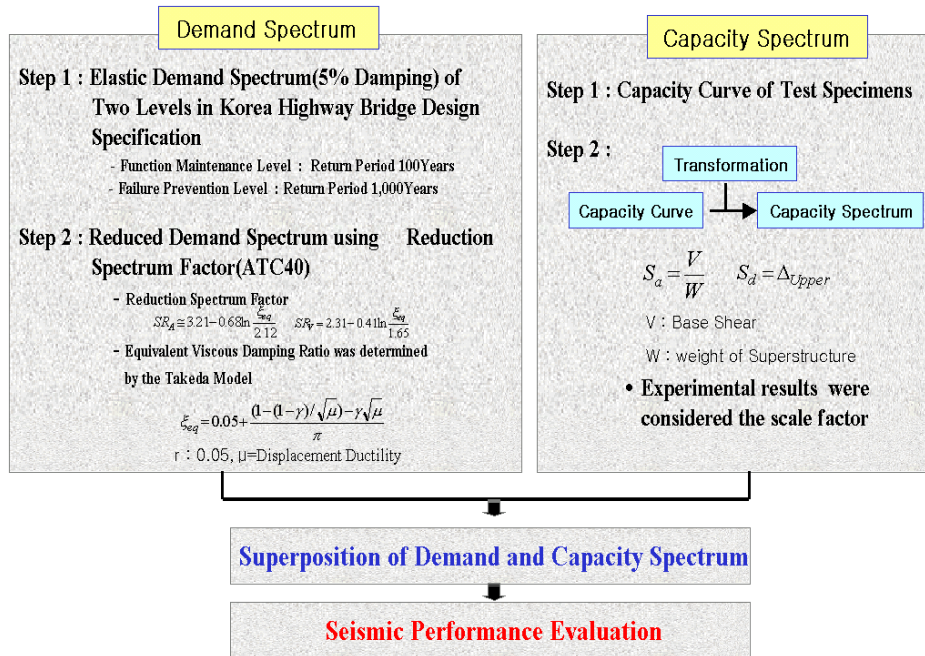
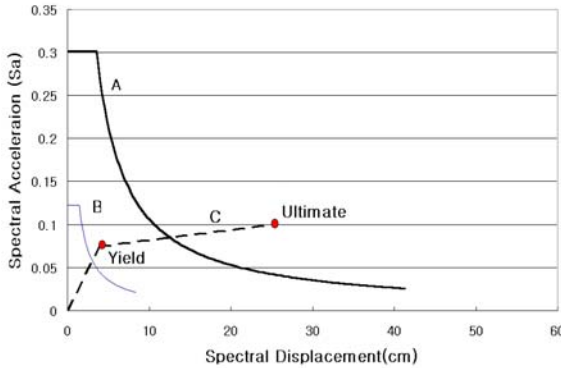
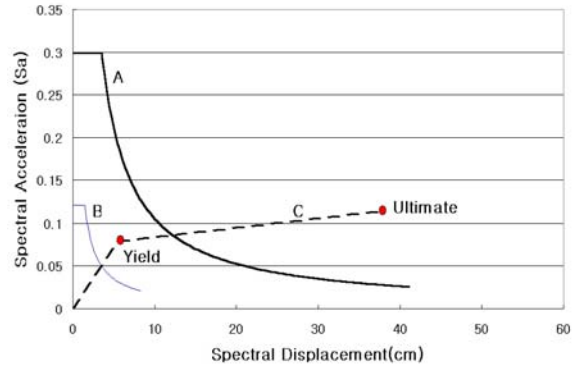


Figure 12 Capacity Spectrum Analysis of ATC 40

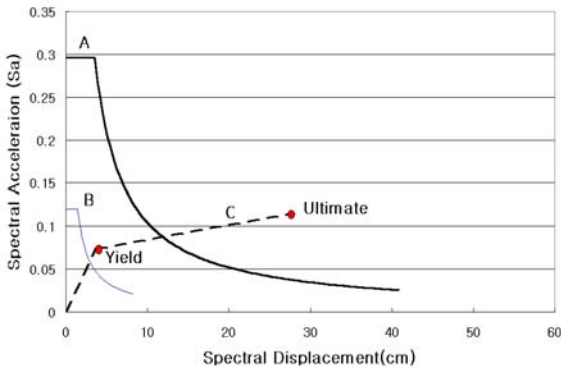
Capacity spectrums of all test specimens for 2 span continuous bridge piers were computed. Figure 13 shows that the results of capacity spectrum analysis satisfy both for the function maintenance and failure prevention level of KRBD code. Therefore, it can be said that even nonseismic test specimen, have quite good seismic resistance in moderate seismicity region.



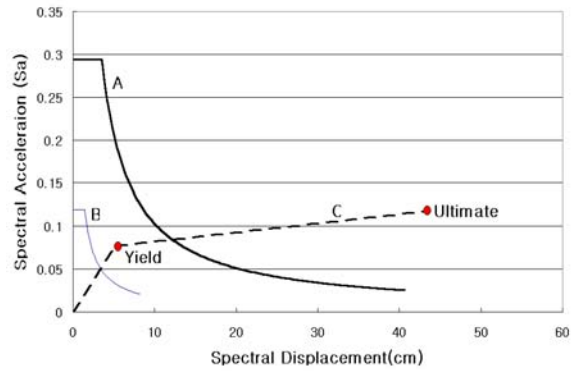
(a) N-LP1



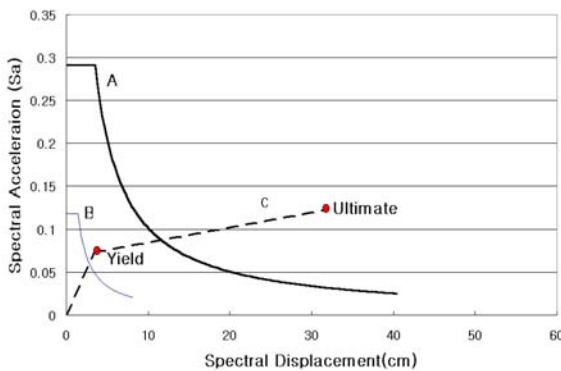
(b) N-LP2



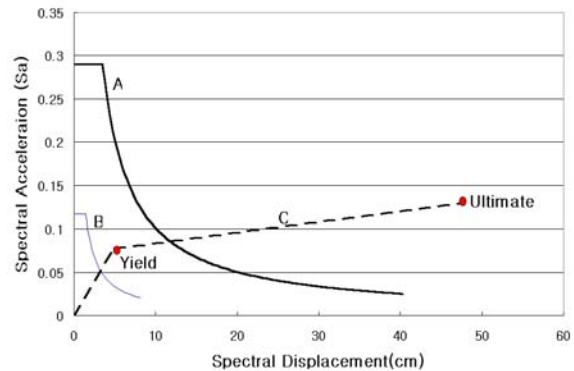
(c) L-LP1



(d) L-LP2



(e) S-LP1



(f) S-LP2

Curve A ————— : Failure Prevention Level of KRBD Code
 Curve B ————— : Function Maintenance Level of KRBD Code
 Curve C - - - - : Capacity Spectrum of 2 Span Continuous Bridge

Figure 13 Capacity Spectrum Analysis Results

CONCLUSIONS

Evaluating all test result through displacement ductility, energy analysis, and capacity spectrum of ATC40, it can be concluded that

- 1) Nonseismically designed RC bridge piers showed quite good seismic resistance under Korea Highway Cooperation artificial earthquake, but exhibited a notable damage at 0.22g of Kaihokus artificial earthquake.
- 2) However, further study will be needed to investigate the seismic performance of RC bridge piers with spliced longitudinal steels in the plastic hinge region.
- 3) Limited ductile specimens and seismic design specimens have shown similar seismic resistant capacity. Limited ductile design concept should be more desirable for RC bridge piers in moderate or low seismic region, like Korea.

ACKNOWLEDGMENTS

The authors gratefully acknowledge the partial support from the Korea Earthquake Engineering Research Center(Contract No. 1997G0402), The Ministry of Construction & Transportaion(Contract No. 970003-4) and the 1999-2000 Research Support Program of Chung-Ang University. The authors also thank Conclinic Co Ltd for providing experimental specimens.

REFERENCES

1. Ministry of Construction and Transportation, " Korea Roadway Bridge Design Code", 1996.
2. Commission of the European Communities, "Euroocde 8 - Structures in Seismic Regions Design(Part 2-Bridges)", *Draft Report*, March, 1994.
3. Christopher, R. T. and A. M. Stephen, "Hybrid Solution Techniques for Generalized Pseudo-Dynamic Testing", *Report No. UCB/EERC-87/09*, 1987.
4. Shing, P. B., A. M. Stephan, Pseudo-Dynamic Test Method for Seismic Performance Evaluation: Theory and Implementation, *Report No. UCB/EERC-83/12*, 1984.
5. Wehbe, N., D. S. Saiidi and B. Douglas, " Ductility of Rectangular Reinforced Concrete Bridge Columns with Moderate Confinement", *Technical Report NCEER-96-0003*, November, 1996.
6. ATC Applied Technology Council (ATC40), "Seismic Evaluation and Retrofit of Concrete Building", *California Seismic Safety Commission*, Report SSC 96-01, 1996.



KEERC-MAE Joint Seminar on
Risk Mitigation for Regions of Moderate Seismicity
University of Illinois at Urbana-Champaign, August 5-8, 2001



Sponsors: Korea Science and Technology Foundation, U.S. National Science Foundation, Brain Korea 21



Design Considerations on Seismic Isolation of Bridges in Low and Moderate Seismic Regions

Hyun-Moo KOH¹, Yong-Gil KIM² and Dong-Seok KIM³

¹ *Professor, School of Civil, Urban and Geosystem Engineering, Seoul National University(SNU), Korea*

² *Research Associate Ph.D, School of Civil, Urban and Geosystem Engineering, Seoul National University(SNU), Korea*

³ *Graduate student, School of Civil, Urban and Geosystem Engineering, Seoul National University(SNU), Korea*

ABSTRACT: This paper presents optimal design procedure and design considerations for seismic isolation of bridges in low and moderate seismicity region based on minimum life-cycle cost concept. The design procedure determines optimal reliability level of isolated bridges as the one that involves the highest net life-cycle benefit to the society, or the minimum life-cycle cost. A method of calculating minimum life-cycle cost of seismic-isolated bridges under specific acceleration level and soil condition is developed. Input ground motion is modeled as spectral density function compatible with response spectrum for combination of acceleration coefficient and site coefficient. Failure probability of critical structural components is calculated by spectrum analysis based on random vibration theory to simplify repetitive calculations in the minimization procedure. The results of example design and analysis show that seismic isolation is more cost-effective in low and moderate seismic region than in high seismic region.

KEYWORDS: cost effectiveness, life-cycle cost, stochastic linearization, failure probability, moderate seismic region, seismic-isolated bridges

INTRODUCTION

Seismic isolators are often used for bridges in a low and moderate seismicity region in order to reduce high construction cost usually caused by seismic performance requirements in such a region. However, the design codes and underlying design concept for isolators and isolated bridges usually follow those in a high seismicity region, which may not be appropriate to a low and moderate seismicity region. This paper addresses optimal design procedure and design considerations for seismic isolation of bridges in such a region based on life-cycle cost concept.

COST EFFECTIVENESS EVALUATION FOR SEISMIC-ISOLATED BRIDGE

Total life-cycle cost includes initial cost of construction and expected damage cost during the structure's life. Damage cost reduces with increasing of structural reliability. However, initial cost increases for more reliable and conservative structural design. There exists an optimal set of design variables that can minimize the total life-cycle cost. In order to apply this concept to seismic-isolated bridges, cost functions should be defined with appropriate design variables. To evaluate failure probability, a 2-DOF model of a seismic-isolated bridge is used to perform the repetitive calculations more easily in minimization procedure.

Stiffness of pier (k_1) and isolator (k_2) are selected as important design variables, because these two variables determine the natural period of seismic-isolated bridges. In addition, stiffness of pier k_1 is closely related with the cost of bridges. Expected value of cost function for seismic-isolated bridges is defined in Eq. [1]. The first two terms in the right hand side are initial cost function of pier and isolator, and the last term is expected damage cost function. Using the index of Eq. [2], cost effectiveness of seismic-isolated bridges relative to that of non-isolated bridges can be evaluated. The smaller index presents the higher cost effectiveness.

$$E[C_{iso}(k_1, k_2)] = C_p V_p(k_1) + C_{iso} V_{iso}(k_2) + C_d \bar{r}_d \cdot \bar{P}_f(k_1, k_2) \frac{V}{\lambda} (1 - e^{-\lambda t_{life}}) \quad [1]$$

$$E_{iso/non} = \frac{E[C_{iso}]_{\min}}{E[C_{non}]_{\min}} = \frac{V_p(k_1^{opt}) + r_{iso/p} V_{iso}(k_2^{opt}) + V_f \bar{r}_d \cdot \bar{P}_f(k_1^{opt}, k_2^{opt}) \frac{V}{\lambda} (1 - e^{-\lambda t_{life}})}{V_p(k_1^{opt}) + V_f P_f(k_1^{opt}) \frac{V}{\lambda} (1 - e^{-\lambda t_{life}})} \quad [2]$$

In order to reflect characteristics of ground motion such as acceleration scale and soil conditions, input ground motion is modeled as spectral density function compatible with response spectrum for combinations of acceleration and site coefficient specified in AASHTO code (AASHTO, 1997). The failure probability is calculated by crossing theory of spectrum analysis (Newland, 1993). Limit states are defined for the case of flexural failure of pier, local shear failure of isolator and unseating of superstructure, respectively, in terms of absolute or relative displacements. Ductility of pier is also considered in calculating failure probability. The nonlinear behavior of pier and its effects on failure probability are considered by stochastic linearization method (Lutes and Sarkani, 1997).

To investigate cost effectiveness of isolated bridges in low and moderate seismic region, cost effectiveness index defined in Eq. [2] is calculated according to different acceleration coefficients and soil conditions. Fig. 1 shows that cost effectiveness is dramatically increasing as the damage scale becomes larger and is better in the case of lower acceleration coefficients than in the case of higher acceleration coefficients. A larger damage scale means that the bridge is very important, and so a high level of reliability is required. At the site of soft soil condition such as soil type IV, while the increase in cost effectiveness is identical to the case of stiff soil condition for the case of lower acceleration coefficients, that for the case of higher acceleration coefficients is not so as the damage scale becomes larger. As a result, very important seismic-isolated bridges on stiff soil have higher cost effectiveness in low and moderate seismic region than in high seismic region. Such a trend of cost effectiveness is more clear in the case of soft soil.

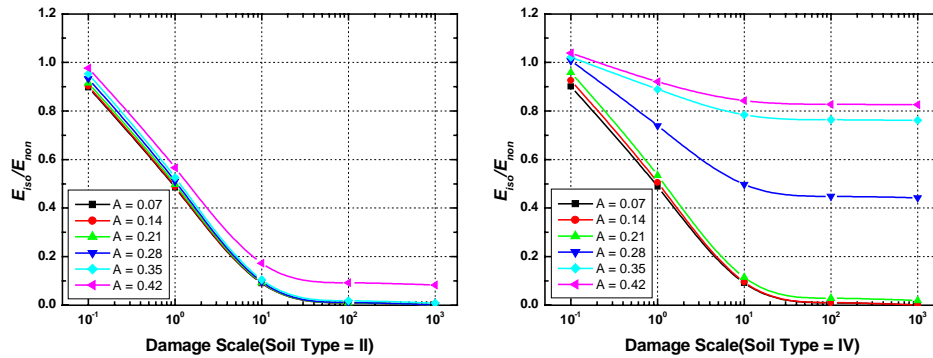


Figure 1 cost effectiveness of different acceleration coefficients according to damage scale

As shown in Fig. 2, cost effectiveness is very consistent regardless of soil types in the case of lower acceleration coefficients. Guide specifications for seismic isolation design of AASHTO (AASHTO, 1997) also specifies that site studies are recommended only when the acceleration coefficient exceeds 0.29. However, in the case of higher acceleration coefficients, soft soil condition reduces cost effectiveness of seismic isolation of bridges and the use of isolation under the soft soil condition sometimes can be economically inappropriate in high seismicity region.

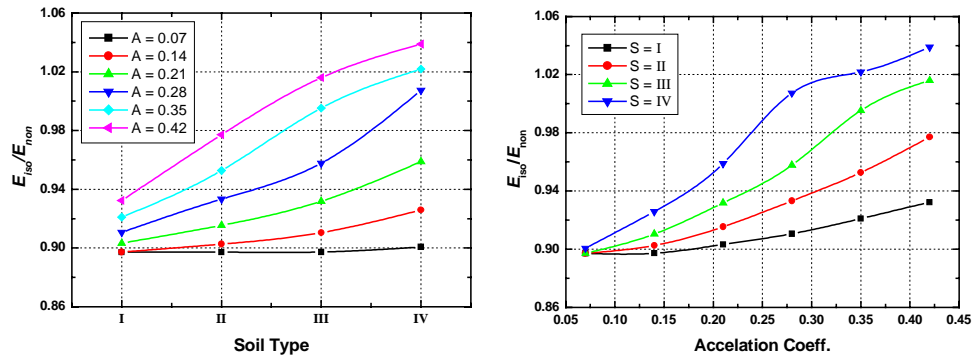


Figure 2 cost effectiveness according to soil types and acceleration coefficients

Fig. 3 shows optimal stiffness ratio of isolator and pier based on minimum total life-cycle cost. In low and moderate seismicity region, optimal ratio of isolator stiffness to pier stiffness is about 1/10, and corresponding period of isolated bridge is about three times longer that that of conventional bridge. In this case, it was found that the pier can be designed to behave elastically as the seismic force is greatly reduced by using more flexible isolator. This result is verified by experiment in Fig. 3 where elastic behavior of isolated pier on cyclic loading test is shown.

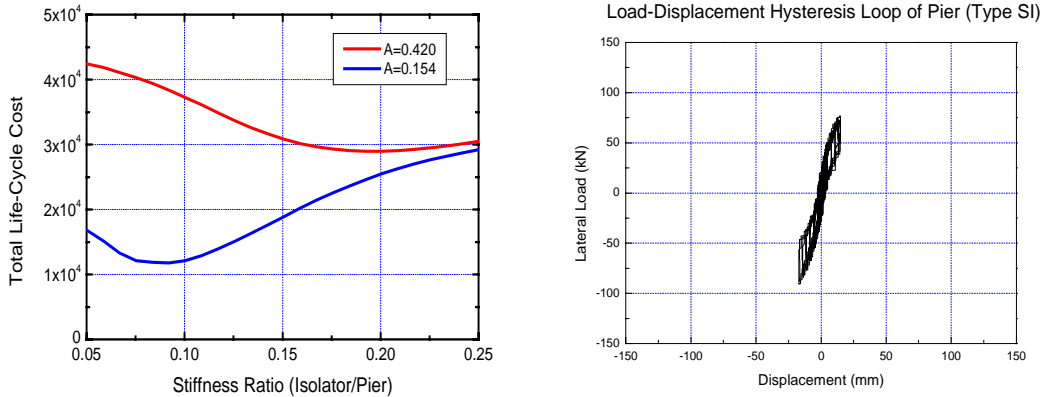


Figure 3 optimal stiffness ratio of isolator and pier & hysteretic behavior of isolated pier

CONCLUSIONS

The results of example design and analysis show that seismic isolation is more cost-effective in low and moderate seismicity region than in high seismicity region, and that optimal stiffness of isolators in such a region can be more flexible than in high seismicity region. This trend of cost effectiveness of seismic isolation is clear in the case of very important bridges.

REFERENCES

1. Wen, Y.K. and Ang, A.H-S, "Reliability and Cost-Effectiveness of Structures with Active Control", *Proceedings of the International Workshop on Intelligent Systems*, Elsevier Ltd., N.Y., 1992.
2. AASHTO, *Guide Specifications for Seismic Isolation Design*, Draft, AASHTO T-3 Task Group, 1997.
3. Newland, D.E., *An Introduction to Random Vibrations, Spectral and Wavelet Analysis*, John Wiley and Sons Inc. N.Y., 1993.
4. Lutes, L.D. and Sarkani, S., *Stochastic Analysis of Structural and Mechanical Vibrations*, Prentice Hall, Inc., New Jersey, 1997.
5. Koh, H.M. and Song, J., "Evaluation of Economical Efficiency for Seismic-Isolated Bridges Based on Minimum Life-Cycle Cost", *Journal of the Korean Society of Civil Engineers*, KSCE, 19(I-4) 1999.



KEERC-MAE Joint Seminar on
Risk Mitigation for Regions of Moderate Seismicity
University of Illinois at Urbana-Champaign, August 5-8, 2001



Sponsors: Korea Science and Technology Foundation, U.S. National Science Foundation, Brain Korea 21



Seismic Analysis of Major Bridges in Mid-America

Seung-II NAM¹ and Jamshid GHABOUSSI²

¹ *Research Assistant, Department of Civil Engineering, University of Illinois at Urbana-Champaign*

*3119 Newmark Laboratory, 205 N. Mathews, Urbana, Illinois, USA
email: s-nam1@uiuc.edu*

² *Professor, Department of Civil Engineering, University of Illinois at Urbana-Champaign*

*3118 Newmark Laboratory, 205 N. Mathews, Urbana, Illinois, USA
email: jghabous@uiuc.edu*

ABSTRACT: Seismic evaluations of major river crossing bridges in Mid-America requires special attention because of infrequent major destructive earthquake records and deep soft alluvial soil deposit. The soil-structure interaction effects are important in the seismic analysis of these structures, along with the effects of traveling waves. In this paper, current issues regarding distinct characteristics of Mid-America seismic zones and major bridges within the region, and a new method for representing soil-structure interaction effects under seismic excitations are proposed.

KEYWORDS: structural dynamics, seismic analysis, bridge, dynamic, soil-structure interaction

INTRODUCTION

There are numerous major river-crossing bridges in Mid-America region. These highway and railway links play a critically important role in the commerce and the general regional and national economy. Some of them are located within or near seismically active zone, such as the New Madrid seismic zone. In this region, the seismicity, the topography and the structural and geotechnical characteristics of bridges are different from those of West Coast which most researches have been focused on. Seismic retrofits of these bridges, many of which were designed and constructed without seismic consideration, are becoming an important issue. In fact, retrofits of almost all the major bridges in this region are now either being done or being planned. For this purpose, it is important to provide proper methods for the analysis of bridges under seismic excitations in order to detect vulnerabilities and retrofit measures while considering the special circumstances of Mid-America region.

Unlike small bridges or overpasses, major river-crossing bridges have complex dynamic characteristics and usually require full-scale three-dimensional finite element analysis. This analysis can produce satisfactory result when appropriate modeling is provided, yet more simplified method of analysis is necessary for practical purpose. The purpose of this paper is to address and discuss the issues about seismic performance analysis of major bridges in Mid-America region. The issues are classified into three areas here; (1) developments and applications of seismic input motions, (2) the effect of traveling seismic waves and (3) modeling and analysis of soil-foundation-bridge interactions. As a part of ongoing research by authors, a new method for representing soil-foundation-structure interactions is proposed.

SEISMIC CHARACTERISTICS IN MID-AMERICA REGION

The seismicity in Mid-America is different from other region, in any strong motion earthquake has not been recorded after the 1886 Charleston earthquake, but geological studies have reported that another major destructive earthquake is possible to occur with considerable probability. Due to infrequent seismic event, there is no actual strong motion record at hand for this region. Therefore, artificially generated earthquake time histories at the bedrock level reflecting the characteristics of the faults and the topography in the region are necessary.

In the New Madrid seismic zone, many lifeline structures are founded on deep soft alluvial soil deposit. The site amplification effects and liquefactions may be important issues for seismic evaluations of the structures. In order to obtain free field motions using artificial accelerograms, a nonlinear three-dimensional finite element model is preferred to conventional one-dimensional wave propagation models with equivalent linear method. Generally, seismic waves propagate through soil medium nonlinearly in three-dimensional manner and the vertical component of ground motions may play an important role in seismic analysis of major bridges with long spans.

EFFECT OF TRAVELING WAVES

In most cases of seismic analysis of a single structure, it has been assumed that the ground motion is a function of time only, not a function of space. This assumption will give satisfactory results for structures occupying relatively small areas. For bridges with long spans, however, the effect of spatial variation of ground motion becomes important. Generally, to implement the spatially varying ground motion to dynamic analysis of structures has been done by either deterministic or stochastic way. In deterministic ways of modeling, it has been often assumed that a seismic wave propagates with constant velocity without changing its shape [11,12]. Traveling waves tend to reduce the maximum displacements, in that peak values of input motions seldom occur simultaneously for all supports because of the phase difference of the wave at each support. The reduction of the displacement does not always mean the reduction of the response because differential motions of the structure are introduced and they result in the increase of internal forces. The quantitative nature of the decrease of displacements and the increase of internal forces depend upon the geometry and stiffness of the structures and the speed and the direction of the seismic wave. Although for simple structures under harmonic excitations two effects can be seen clear, for more complex situations such as long span bridges, the response becomes unpredictable and general tendency may not apply, e.g. the maximum displacement can be significantly increased under certain circumstances [3,12]. In stochastic implementations of traveling seismic waves, the variations of the shape of the ground motion are taken into account. In most cases, stochastic analyses are carried out in frequency domain in conjunction of response spectrum methods [2,10].

In time domain analysis, traveling seismic wave effects are often taken into account by using a ground motion time history moving along the ground surface. This one- or two-dimensional wave propagation does not consider three-dimensional nature of seismic wave propagations. For deep soil deposit with decreasing shear wave velocity from relatively rigid bedrock, the wave tends to propagate vertically with phase difference between each supporting point of the bridge. These phase shift and vertical propagation of seismic wave generally result in differential motion between supports and rocking motion at the base of bridge pier. For a more accurate seismic input to bridge model, a three-dimensional finite analysis should be used, where the input base motion propagates along the bedrock and through soil deposit.

MODELING OF SOIL-STRUCTURE INTERACTIONS

Most major river-crossing bridges in Mid-America are founded either on floating piles or caissons in deep alluvial soil deposit. Even if there have been a extensive researches on the detailed modeling and the behavior of pile foundations under dynamic loadings for many decades in the area of geotechnical engineering, the foundations of bridges are often simplified with equivalent springs and dashpots without rigorous consideration of dynamic interactions between piles and superstructures. In geotechnical studies, however, the behavior within piles has been a major concern and superstructures have been ignored or

oversimplified. Therefore, it is required that a model dealing the superstructure and the foundation with the same level of importance be developed.

Currently, roughly three classes of methods are available to model dynamic behavior of pile foundations; finite element models, boundary element models and Winkler-type foundation models. FE analysis is regarded as the most accurate method for the combined system of the superstructure, the foundation and the soil medium, if proper boundary conditions are provided. Recently, a simplified quasi-3D nonlinear FE model [5,6] and a full-scale 3D FE model using a plastic constitutive law for soil [1] were examined and it was shown nonlinearity and three-dimensionality of soil-structure interactions play an important role. The boundary element methods have advantages over finite element methods in that computational cost can be significantly reduced and radiation of waves can be precisely reproduced within linear range of soil behavior. Hybrid models have been reported [8,15], where FEM were used for structural components for representing nonlinear behavior and BEM for soil domain. Since BEMs and hybrid methods are based on the assumption that soil behaves linearly, they are not suitable for the situation of nonlinear wave propagating toward the foundation. As another alternative to the FEM approach, Winkler-type foundation models easily allow the nonlinear behavior of soil [4,13] and the time-domain. Generally, in Winkler-type models, radiation damping and p-y curves are considered to have significant effect on the response of nonlinear systems [16]. Due to the frequency-dependent nature of radiation damping, simple mass-spring models produce accurate results only in a certain range of the natural frequency of the system [17]. However, the frequency-dependence can be reproduced by using a series of masses-springs-dashpots [13].

NUMERICAL SIMULATION OF MAJOR BRIDGES

Unlike small bridges such as highway overpasses, major river-crossing bridges have to be modeled with special attention for seismic performance evaluations. Generally, the bridges have closely spaced natural frequencies and nonlinearities are abundant throughout the structure. When those natures are combined to the transient nature of earthquake motions, frequency domain analyses are not effective, and thus three-dimensional nonlinear analyses in time-domain are required. With a finite element model comprising the entire domain of soil-foundation-structure system, the three-dimensional nonlinear analysis can be performed in rigorous manner. The computational cost becomes the serious obstacle in the case of major bridges, mainly because of extensive mesh of soil domain with proper modeling of soil plasticity. Discrete parameter models using Winkler-type springs are widely accepted to represent the soil-foundation interactions since they can maintain the three-dimensionality and nonlinearity in time-domain and yet can significantly reduce the computational cost. However, it may be technically difficult to determine the value of discrete parameters used in these models and the performance of the models in a global structure has not been completely verified yet, especially for pile-to-pile interactions.

Proposed Model

In this section, a new method for developing a discrete parameter model is introduced. The study is in progress and the procedure is briefly described here. As the first step, a nonlinear finite element analysis, which consists of a bridge pier, its foundation and the soil medium around the foundation, is carried out with arbitrary dynamic loads. Time histories of the response at specific locations are sampled out of the result of the finite element analysis. Then, an arbitrary discrete parameter model with unknown parameter values is established. Series of dynamic analyses are performed to determine the parameters by using optimization search technique.

Genetic Algorithms are to be used for the optimization procedure because conventional optimization method is nearly impossible to be applied in this situation. The time history response from finite element analysis provides the reference data the discrete parameter model gradually resembles, and the reference value may have different forms. For instance, if proper experimental data are available, they can replace those of the finite element analysis. Nonlinearities are also parameterized to be determined in the procedure.

ACKNOWLEDGMENT

This research was funded by grant from the Mid-America Earthquake Center and the National Science Foundation. This support is gratefully acknowledged. Any findings, opinions and conclusions are solely those of the authors and do not represent those of the sponsors.

REFERENCES

1. Cai, Y. X., P. L. Gould and C. S. Desai, "Investigation of 3-D nonlinear seismic performance of pile-supported structures," Performance of Deep Foundations under Seismic Loading, ASCE Geotech. Special Publication No. 51, 1995, pp. 17-31.
2. Dumanoglu, A. A. and R. T. Severn, "Stochastic response of suspension bridges to earthquake forces," Earthquake Engineering and Structural Dynamics, Vol. 19, 1990, pp. 133-152.
3. Dusseau, R. A. and R. K. Wen, "Responses of a long span arch bridge to differential abutment motions," Proceedings of 3rd U.S. National Conference on Earthquake Engineering, EERI, 1986, pp. 2049-2060.
4. Ellassaly, M., A. Ghali and M. M. Elbadry, "Influence of soil conditions on the seismic behaviour of two cable-stayed bridges," Canadian Journal of Civil Engineering, Vol. 22, 1995, pp. 1021-1040.

5. Finn, W. D. L., T. Thavaraj and G. Wu, "Seismic analysis of pile foundations: State-of-art," Proceedings of 11th World Conference on Earthquake Engineering, 1996, Paper No. 2073.
6. Finn, W. D. L. and G. Wu, "Nonlinear seismic analysis of pile foundations," Proceedings of 11th World Conference on Earthquake Engineering, 1996, Paper No. 1414.
7. Goldberg, D. E., Genetic Algorithms in Search, Optimization, and Machine Learning, Addison-Wesley, 1989.
8. Guin, J and P. K. Banerjee, "Coupled soil-pile-structure interaction analysis under seismic excitation," Journal of Structural Engineering, ASCE, Vol 124, No. 4, 1998, pp. 434-444.
9. Hwang, H. M., Artificial acceleration time histories, Center for Earthquake Research and Information, University of Memphis, 1998.
10. Kiureghian, A. D. and A. Neuenhofer, "Response spectrum method for multiple-support seismic excitation," Earthquake Engineering and Structural dynamics, Vol 21, 1992, pp. 713-740.
11. Leger, P., I. M. Ide and P. Paultre, "Multiple support seismic analysis of large structures," Computers and Structures, Vol. 36, 1990, pp. 1153-1158.
12. Nazmy, A. S. and A. M. Abdel-Ghaffar, "Effect of ground motion spatial variability on the response of cable-stayed bridges," Earthquake Engineering and Structural Dynamics, Vol. 21, 1992, pp. 1-20.
13. Nogami, T., J. Otani, K. Konagai and H.-L. Chen, "Nonlinear soil-pile interaction model for dynamic lateral motion," Journal of Geotechnical Engineering, ASCE, Vol. 118, No. 1, 1992, pp. 89-106.
14. Nam, S.-I. et. al., "Analysis of soil-structure interaction of major river-crossing bridges," Proceedings of 12th World Conference on Earthquake Engineering, 2000, Paper No. 0496.
15. Pavlatos, G. D. and D. E. Beskos, "Dynamic elastoplastic analysis by BEM/FEM," Engineering Analysis with Boundary Elements, Vol. 14. 1994, pp. 51-63.
16. Wang, S. et. al., "Nonlinear seismic soil-pile-structure interaction," Earthquake Spectra, EERI, Vol. 14, No. 2. 1998, pp. 377-396.
17. Zheng, Z. and T. Takeda, "Effect of soil-structure interaction on seismic response of PC cable-stayed bridge," Soil dynamics and Earthquake Engineering, Vol. 14, 1995, 427-437.



KEERC-MAE Joint Seminar on
Risk Mitigation for Regions of Moderate Seismicity
University of Illinois at Urbana-Champaign, August 5-8, 2001



Sponsors: Korea Science and Technology Foundation, U.S. National Science Foundation, Brain Korea 21



Dynamic Behavior Analysis of Bridge Under Bi-directional Seismic Excitations

Sang-Hyo KIM¹, Ho-Seong MHA², Sang-Woo LEE³, and Jeong-Woon KANG⁴

¹ *Professor, Department of Civil Engineering, Yonsei University
Shinchon-dong, Seodaemoon-gu, Seoul 120-749, KOREA, email: sanghyo@yonsei.ac.kr*

² *Assistant Professor, Department of Civil Engineering, Hoseo University
Sechul-Li, Baebang-Myun, Asan, 336-759, KOREA, email: mhah@office.hoseo.ac.kr*

³ *Graduate Student, Department of Civil Engineering, Yonsei University
Shinchon-dong, Seodaemoon-gu, Seoul 120-749, KOREA, email: yah@str.yonsei.ac.kr*

⁴ *Engineer, Man Young Construction Engineering Consultants
Yeoksam-dong, Kangnam-gu, Seoul 135-080, KOREA, email: kajewoo@netian.com*

ABSTRACT: A dynamic analysis procedure for 2-dimensional bridge motions has been developed by using force-deformation model, which simulates the pier motion under biaxial bending due to the bi-directional seismic excitations. A three-dimensional mechanical model is utilized, which can consider the other phenomena such as pounding, rotation of the superstructure, abutment stiffness degradation, and foundation motions. The bi-directional seismic behaviors of the bridge are then examined by investigating the relative displacements of each superstructure to both ground and adjacent superstructures. It is found that the nonlinearity of pier due to the bi-axial bending affects the pier motions, but the dominant governing factors of the global bridge motions are the edge-pounding phenomenon and abutment stiffness degradation.

KEYWORDS: bridge, bi-axial bending, bi-directional seismic excitations, pounding, abutment stiffness degradation, bi-directional seismic behaviors.

INTRODUCTION

In many seismic analyses, the input excitations are generally applied to the structural systems in only one direction, in either the longitudinal or transverse direction. However, the ground motions are actually in 3-dimensional directions with random manner. Neglecting vertical component, seismic excitations can be described as bi-directional motions. For general aseismic design or analysis, each directional motions of the system are superimposed after being evaluated separately^[1]. For more realistic accurate prediction of the system dynamics, the seismic excitations with random directions should be applied^[2]. Also, 3-dimensional model capable of considering bi-directional response due to the bi-directional seismic excitations should be employed. The nonlinear pier motion upon the bi-axial bending and the pounding due to the rotational motion of the superstructures are of the most concern while many other components should also be considered. The analysis procedure is developed in this study for evaluating the responses of a bridge system by utilizing the nonlinear pier model with bi-axial bending behavior.

MODELING OF SYSTEMS

Bridge model

The bridge considered in this study is a simply supported three-span PSC girder bridge with span length of 30m as shown in Fig. 1. Bent type piers, shallow foundations, and seat-type abutments are used. The pier height is 12m and the abutment height is 6.5m. In this study, the total system is divided into four individual vibration units shown as dotted line in Fig. 1.

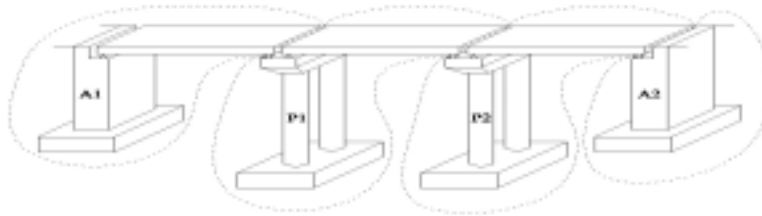


Figure 1 Bridge model

For better efficiency, a simplified mechanical model using the lumped mass system is proposed, which is depicted in Fig. 2. In the figure, u is the relative displacement to the ground, \ddot{u}_g is the ground acceleration, m , K , and C are the mass, stiffness, and damping constant of each element, d is the gap distances between adjacent vibration units, and S is the stiffness of the impact element. Superscripts T and R denote the transverse and rotational direction, respectively.

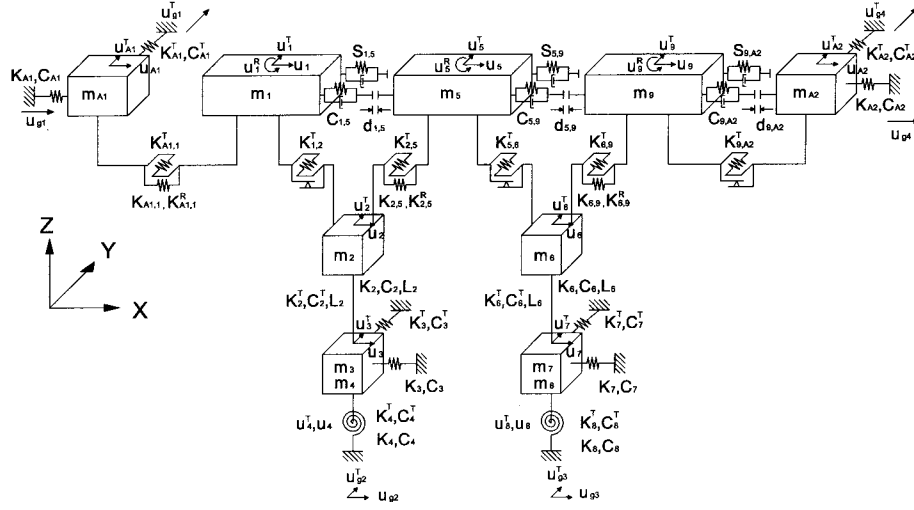


Figure 2 Simplified mechanical model of bridge

Nonlinear Pier Motions

In order to consider the bi-axial bending behaviors due to the bi-directional seismic excitations, a proper analysis model should be employed, while a simpler model is still needed to examine the global bridge motions. In this study, force-deformation model has been applied for its simplicity and relatively high accuracy [3].

The bi-directional hysteretic forces of a R/C pier in this model can be described with the following differential equations.

$$\begin{aligned} \dot{z}_x &= A\dot{u}_x - b|\dot{u}_x z_x|z_x - \gamma\dot{u}_x z_x^2 - b|\dot{u}_y z_y|z_x - \gamma\dot{u}_y z_x z_y \\ \dot{z}_y &= A\dot{u}_y - b|\dot{u}_y z_y|z_y - \gamma\dot{u}_y z_y^2 - b|\dot{u}_x z_x|z_y - \gamma\dot{u}_x z_y z_x \end{aligned} \quad (1)$$

where u_x , u_y and z_x , z_y are the displacements and hysteretic force components in the x- and y-directions. A , b , and γ are dimensionless quantities that control the shape and magnitude of the hysteresis loops. The total restoring force, which is the linear combination of linear restoring force and hysteretic force, is expressed as

$$\begin{Bmatrix} Q_x \\ Q_y \end{Bmatrix} = \alpha[K] \begin{Bmatrix} u_x \\ u_y \end{Bmatrix} + (1-\alpha)[K] \begin{Bmatrix} z_x \\ z_y \end{Bmatrix} \quad (2)$$

in which Q_x and Q_y are the total restoring forces, $[K]$ is the stiffness matrix, and α is the post-yielding stiffness ratio.

Bearings

The Bearing under bi-directional seismic excitations undergoes deformation due to the inertia force of superstructures. The deformation of bearings is generally ignored in bridge seismic analysis and the bearing is often modeled as a linear spring system with infinite stiffness.

However, the deformation of bearings should be considered to initiate the rotational motion of the superstructures in the bridge response analyses subjected to the bi-directional seismic excitations. The bearings are modeled with longitudinal, transverse, and rotational springs (i.e., $K_{2,5}$, $K_{2,5}^T$, and $K_{2,5}^R$) at the fixed supports and with only transverse springs (i.e., $K_{1,2}^T$) at the movable supports as shown in Fig. 2.

Pounding between Adjacent Superstructures

Under bi-directional seismic excitations, each unit with different transverse stiffness can cause rotational motions of the superstructures and also transverse deformations leading to pounding and opening between the superstructures as shown in Fig.3, particularly in bridge systems with stiff abutments. The pounding is described in this study by placing two spring-damper elements (impact elements) at the edges between the superstructures as shown in Fig. 2.

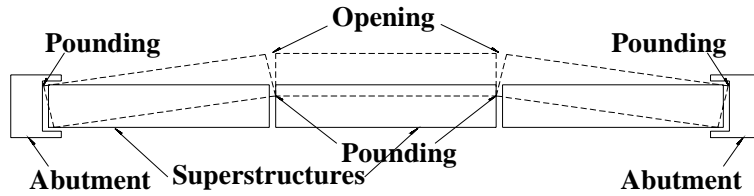


Figure 3 Pounding phenomena due to bi-directional seismic excitations

Foundation and Abutment Motions

Foundation is modeled as four DOFs system with translational and rotational springs (i.e., K_3 , K_3^T ; K_4 , K_4^T) and damping constants (i.e., C_3 , C_3^T ; C_4 , C_4^T) to consider ground conditions. The stiffness of foundation is determined according to Korean Standard Specification for Highway Bridges: Seismic Design (1996)^[1]. The abutment-backfill system is modeled as two DOFs system with nonlinear spring (i.e., K_{A1} , K_{A1}^T) and linear damping constants (i.e., C_{A1} , C_{A1}^T) to consider the abutment stiffness degradation. The nonlinear spring stiffness is obtained by using the formulation suggested by Siddharthan et al. (1996)^[4].

BI-DIRECTIONAL INPUT GROUND MOTIONS

The bi-directional seismic excitations can be simulated from two statistically independent seismic excitations by applying the vector sum of the two excitations. Each excitation is evaluated based on the well-known SIMQKE^[5]. An example of the planar time history of a simulated seismic excitation is shown in Fig. 4.

For more realistic combination of the input ground motions, real measured data are examined to determine the correlation between the excitations in both longitudinal and transverse directions^[6, 7, 8]. The result is shown in Fig. 5, and the applied peak ground accelerations (PGA) of bi-directional seismic excitations are tabulated in Table 1.

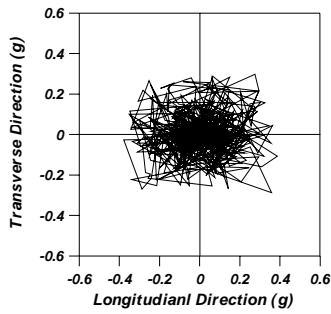


Fig. 4 Bi-directional input ground motion simulated

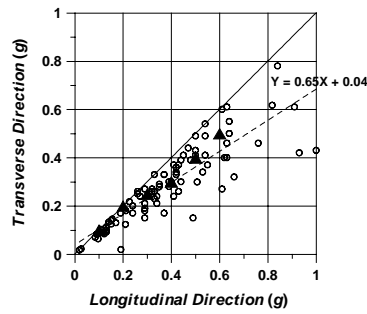


Fig. 5 Distribution of PGA recorded

Table 1 PGA of bi-directional seismic excitations

Combination	¹⁾ L-PGA	²⁾ T-PGA
1	0.1g	0.1g
2	0.2g	0.2g
3	0.3g	0.25g
4	0.4g	0.3g
5	0.5g	0.4g
6	0.6g	0.5g

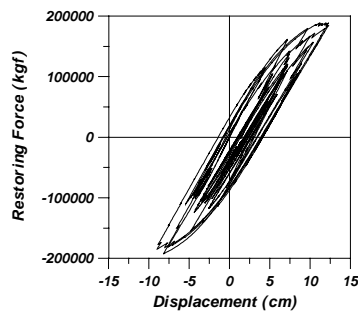
¹⁾ L-PGA=PGA in longitudinal direction

²⁾ T-PGA=PGA in transverse direction

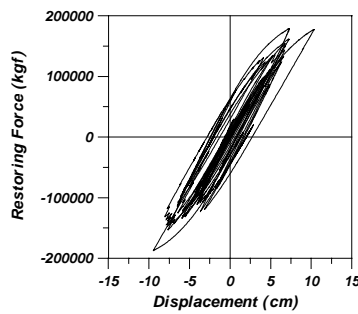
RESULTS AND OBSERVATIONS

The effects of pounding are examined, which is due to the 2-dimensional motions of the superstructure and also bi-axial bending of pier upon the global motions of the whole bridge system. The comparison made here are between two systems: one is under uni-directional seismic excitations; the other is under bi-directional seismic excitations.

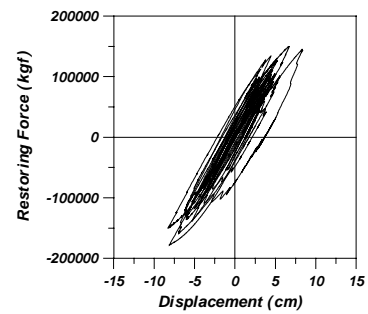
First, the hysteretic curves are generated to observe the differences of two systems (Fig. 6). The hysteretic curve of the longitudinal direction obtained from bi-directional analysis shows considerable difference from that obtained from uni-directional analysis (Fig. 6a and b).



(a) Longitudinal direction (uni-directional analysis)



(b) Longitudinal direction (bi-directional analysis)



(c) Transverse direction (bi-directional analysis)

Figure 6 Hysteretic curves (L-PGA=0.4g; T-PGA=0.3g)

Planar time histories are prepared to inspect the pier motions under bi-directional seismic excitations (Fig. 7). For both moderate and strong excitations, irregular motions can be easily observed showing that the bi-directional characteristics of excitations also reside in the bridge response.

The longitudinal responses are prepared to analyze the effect of the bi-directional motions of the system, and the corresponding time histories are depicted in Fig. 8. It can easily be seen

that two systems show different dynamic signatures. This is due to the bi-axial bending of the pier and the different pounding phenomena by introducing the rotational motions of the superstructures.

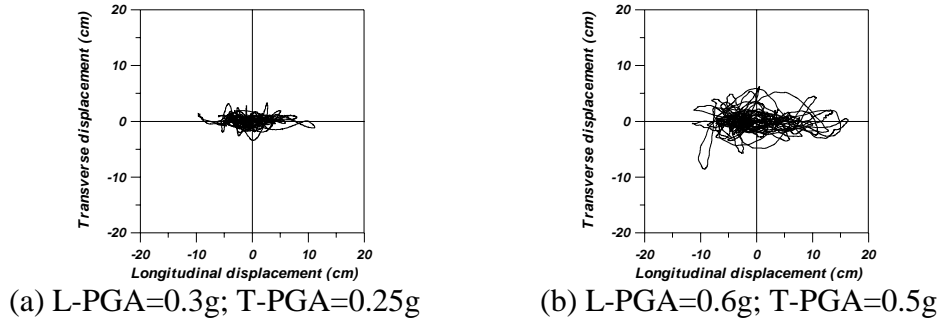


Figure 7 Planar time histories of relative displacements of pier unit (P1) to ground

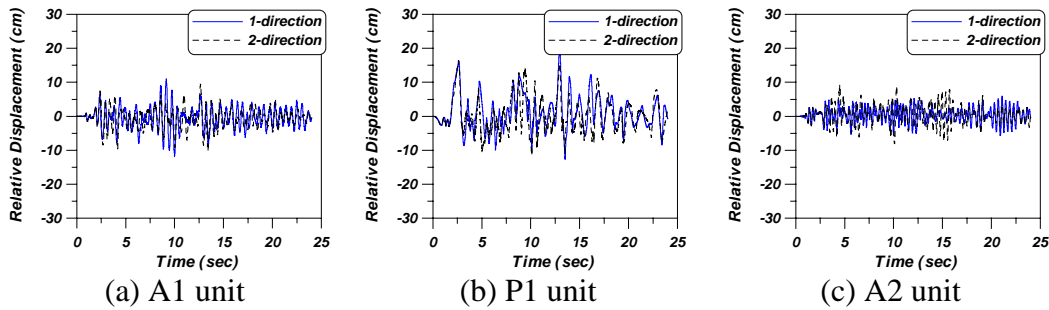


Figure 8 Time histories of relative displacements to ground (L-PGA=0.6g;T-PGA=0.5g)

In the seismic analysis of design purpose, the maximum values of the responses are of concern. The mean values and 90% extreme values of maximum relative displacements of each vibrating units to the ground are evaluated, and tabulated in Table 2. From results, it can be seen that A1 and P1 units do not show any significant differences for both analyses. However, the responses of P2 and A2 units are remarkably different, showing that the bi-directional analysis gives larger responses as the PGA increases. This may result from the rotational motions of the superstructures and edge-pounding phenomena. Time histories of rotational displacements of the three units are plotted in Fig. 9 and P2 unit shows much larger rotational motion compared to those of the other two units. This results from the fact that A1 and P1 units have the stronger rotational constraint than that of P2 unit.

Time histories of pounding forces are also obtained for comparison. As can be seen in Fig. 10, larger pounding force occurs in the case of bi-directional analysis. It is found that the most significant difference occurs in A2 unit. The stiffness degradation curves are compared for both models (Fig. 11). In bi-directional analysis, Stiffness of the A2 unit decreases dramatically compared to that of uni-directional analysis. From the results, response of A2 unit in bi-directional analysis is found to increase due to edge pounding and the rapid decrease of the stiffness.

The relative distances between adjacent vibration units are summarized in Table 3. The results are very similar to those of the relative displacements. The relative distances between A1 unit and P1 unit do not experience any notable changes due to bi-directional analysis. However, the relative distances between P2 unit and A2 unit as well as between P1 unit and P2 unit result in larger distances under higher PGA excitations.

Table 2 Simulated results of maximum relative displacements to ground (unit: cm)

PGA		A1 unit		P1 unit		P2 unit		A2 unit	
L-PGA	T-PGA	Uni-direction	¹⁾ Bi-direction	Uni-direction	Bi-direction	Uni-direction	Bi-direction	Uni-direction	Bi-direction
0.2g	0.2g	²⁾ 5.04 ³⁾ (6.75)	4.80 (6.71)	7.88 (9.28)	8.09 (9.67)	7.54 (9.31)	8.26 (10.48)	3.19 (4.44)	4.29 (6.80)
0.4g	0.3g	8.09 (11.65)	8.35 (11.58)	11.79 (13.81)	11.30 (13.90)	10.29 (12.75)	11.25 (13.99)	5.45 (7.56)	7.54 (9.36)
0.6g	0.5g	12.41 (15.25)	12.44 (16.54)	16.09 (20.76)	16.06 (19.16)	13.24 (15.32)	15.26 (19.20)	7.64 (10.27)	10.67 (13.32)

- ¹⁾ Vector summation of displacements in both longitudinal and transverse directions
- ²⁾ Mean value of maximum relative displacements
- ³⁾ 90% extreme value of Gumbel Type-I

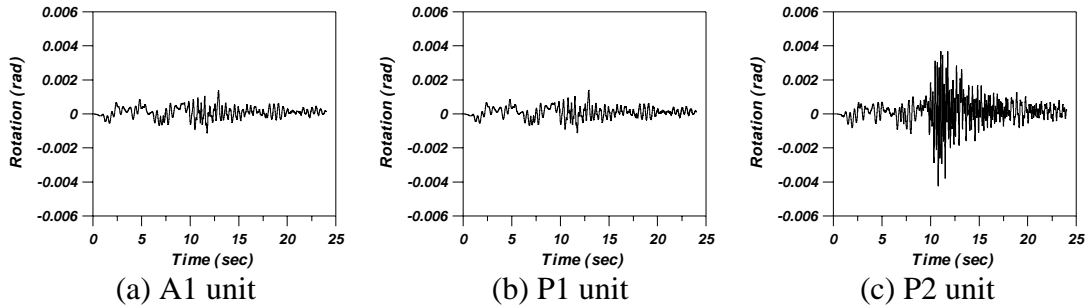


Figure 9 Time histories of rotations of superstructures (L-PGA=0.3g; T-PGA=0.25g)

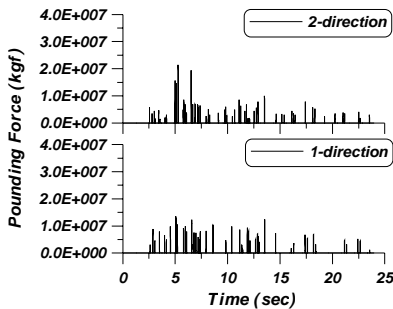


Fig. 10 Time histories of pounding forces between P2 and A2

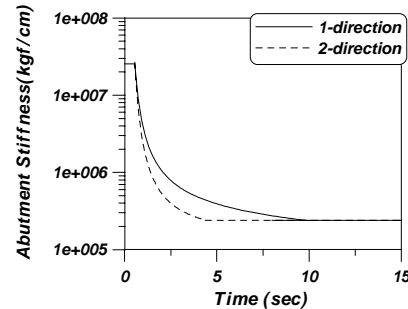


Fig. 11 Stiffness degradation curves of abutment (A2)

Table 3 Simulated results of maximum relative distances between adjacent vibration units (unit: cm)

PGA		A1 ~ P1		P1 ~ P2		P2 ~ A2	
L-PGA	T-PGA	Uni-direction	Bi-direction	Uni-direction	Bi-direction	Uni-direction	Bi-direction
0.2	0.2	¹⁾ 10.14 ²⁾ (12.47)	10.59 (12.91)	5.79 (9.16)	8.70 (12.05)	8.40 (10.64)	8.84 (11.98)
0.4	0.3	14.96 (17.97)	14.62 (17.57)	8.69 (11.76)	12.59 (16.20)	10.95 (13.10)	12.35 (16.43)
0.6	0.5	20.97 (29.03)	19.92 (27.84)	8.99 (10.64)	13.56 (18.12)	14.12 (18.24)	16.65 (21.86)

¹⁾ Mean value of maximum relative displacements

²⁾ 90% extreme value of Gumbel Type-I

CONCLUSIONS

In this study, the effects of bi-axial bending of pier and edge pounding due to rotational motion upon the global motions of the bridge system under bi-directional seismic excitations are examined. The following trends are observed:

- 1) The analysis tool developed in this study is found to be appropriate in evaluating the bridge responses under bi-directional seismic excitations.
- 2) The nonlinear bi-axial bending behaviors of bridge piers affect the global response of bridge system. However, the dominant governing factors are the edge-pounding phenomenon and abutment stiffness degradation due to rotation motions in the bi-directional models, especially under moderate seismic excitations.
- 3) Response of the A2 abutment unit, where the adjacent superstructure is not fixed, is significantly influenced by rotational motions. This is due to the considerable stiffness degradation in the bi-directional analysis compared to that in uni-directional analysis.

ACKNOWLEDGMENTS

This work is currently supported by the Brain Korea 21 Project and the Korea Science and Engineering Foundation (KOSEF) through the KEERC. Their continued financial assistance is gratefully acknowledged.

REFERENCES

1. Ministry of Construction and Transportation, *Korean Standard Specifications for Highway Bridge*, 1996
2. Dicleli, M. and Bruneau, M., “Quantitative Approach to Rapid Seismic Evaluation of Slab-on-Girder Steel Highway Bridges” *Journal of Structural Engineering*, Vol.222, No. 10, 1996, pp. 1160-1168
3. Kunnath, S.K., and Reinhorn, A.M., “Model for Inelastic Biaxial Bending Interaction of Reinforced Concrete Beam-Columns”, *ACI Structural Journal*, Vol. 87, No. 3, 1990, pp. 284-291
4. Siddharthan, R. V., El-Gamal, M., and Maragakis, E. A., “Stiffness of Abutments on Spread Footings with Cohesionless Backfill”, *Canadian Geotechnical Journal*, Vol. 34, 1997, pp. 686-697
5. Gasparini, D. A. and Vanmarcke, E. H., *Evaluation of Seismic Safety of Buildings Simulated Earthquake Motions Compatible with Prescribed Response Spectra*, Massachusetts Ins. of Technology, Report 2, 1976
6. Ministry of Construction, *Strong-Motion Acceleration Records from Public Works in Japan (No. 21)*, Technical Note of Public Works Research Institute, Vol. 64, 1995
7. Solnes, J., *Engineering Seismology and Earthquake Engineering*, Noordhoff International Publishing, 1974
8. Goltz, J. D., *The Northridge, California Earthquake of January 17, 1994, General Reconnaissance Report I & II*, NCEER-94-0005, 1994



KEERC-MAE Joint Seminar on
Risk Mitigation for Regions of Moderate Seismicity
University of Illinois at Urbana-Champaign, August 5-8, 2001



Sponsors: Korea Science and Technology Foundation, U.S. National Science Foundation, Brain Korea 21



Seismic Evaluation of a Steel Truss Railway Bridge

Douglas A. FOUTCH¹, and Seung-Yul YUN²

¹ *Professor, Civil Engineering, University of Illinois at Urbana-Champaign
3129 Newmark Laboratory, 205 N. Mathews, Urbana, Illinois, USA
email: d-foutch@uiuc.edu*

² *Research Associate, Civil Engineering, University of Illinois at Urbana-Champaign
3106 Newmark Laboratory, 205 N. Mathews, Urbana, Illinois, USA
email: syun@uiuc.edu*

ABSTRACT: Seismic evaluation of a railway bridge crossing the Mississippi River in Memphis, Tennessee, was conducted. Memphis is located in a region characterized by large but infrequent earthquakes. This is a historic bridge that was built in 1894 on deep soft soil. The main span of the bridge is 240 920 mm (790 feet) long and the tallest pier stands 4 024 mm (158 feet tall) above its caisson. The super structure of the bridge consists of trusses with built-up members. Linear and nonlinear analyses of the bridge have been conducted. The analyses of the bridge revealed that the superstructure of the bridge is very flexible transversely and that the bearings and the stone piers are the most vulnerable components under seismic loads. Failure mechanisms for the piers that were investigated include layers of stones that slide along a horizontal plane, overturning and separation between layers of stones, and overturning at the base with possible toe crushing. Different failure mechanisms governed for transverse and longitudinal directions of the bridge. An experimental investigation will be conducted to verify the analytical results.

KEY WORDS: seismic behavior of railway bridges, stone bridge piers, steel truss bridges, seismic fragility of bridges

INTRODUCTION

The railroads are a vital part of the transportation network in the United States. This is particularly true in mid-America. Corn, soybeans and other commodities are transported to markets across the country and to ports on the Atlantic seaboard, the Pacific Ocean and the Gulf of Mexico. In addition, many of the electrical power plants are coal fired. In many cases, dedicated rail lines run between the coalmines and the power plants.

This paper describes the preliminary investigation of a steel truss railway bridge that crosses the Mississippi River at Memphis, Tennessee. This is a region characterized by infrequent earthquakes of large magnitudes. In addition, the soils along the Mississippi River and its tributaries have a high potential for liquefaction. Another important characteristic of the region is that only a handful of railway (and highway) bridges cross the Mississippi River between St. Louis to the north and New Orleans to the south. As a result, if any of these bridges collapses or suffers major damage during an earthquake, this would cause a major disruption of commerce in the area. If one of these major bridges actually collapses, this could also disrupt the heavy barge traffic on the Mississippi.

DESCRIPTION OF THE BRIDGE

The bridge under investigation crosses the Mississippi River at Memphis, Tennessee, as shown in Figure 1. Construction of the bridge was completed in 1894. The bridge is owned and operated by the Burlington Northern-Santa Fe Railroad. Another railway bridge of similar design, length and alignment crosses the Mississippi a few meters away from the bridge being studied. It is owned and operated by the Illinois Central Railroad. A highway bridge also crosses the river in the same vicinity. It is conceivable that one of the bridges could collapse during an earthquake and bring down the other two bridges.

The main crossing segment of the bridge is composed of five steel truss spans supported by abutments at each end and four stone piers at intermediate locations. A plan and elevation view of the main crossing is shown in Figure 2. The five spans measure 116 967mm, 207 569mm, 207 569mm, 240 920mm and 68 829mm from east to west (left to right) in Figure 2. Long viaducts approach the main spans from both the east and west directions. These are composed of steel plate girder spans supported by trestles.

The piers supporting the main truss spans are stone piers with granite facades. The piers are made from slabs of limestone. Large caissons that extend to soft rock support the piers. When the piers were constructed, each layer of limestone was placed on a bed of concrete grout for seating and leveling purposes. Voids between individual limestone slabs at each level were also filled with grout. It is not known if the grout was considered to be a structural component that could be relied on for shear strength for the original design. Even if the grout was considered to be structural for design, it is unknown whether or not the grout plays an important part in the seismic resistance of the bridge today. An elevation and plan view of one of the piers is shown in Figure 3. Beginning at the west abutment that is labeled

Pier 0, Piers I through Pier IV measure 2 351mm (92.6 ft), 3 489 mm (135.8 ft), 4 024mm (158.4 ft) and 2 787mm (109.8 ft), respectively, from the top of the caisson to the pier top.

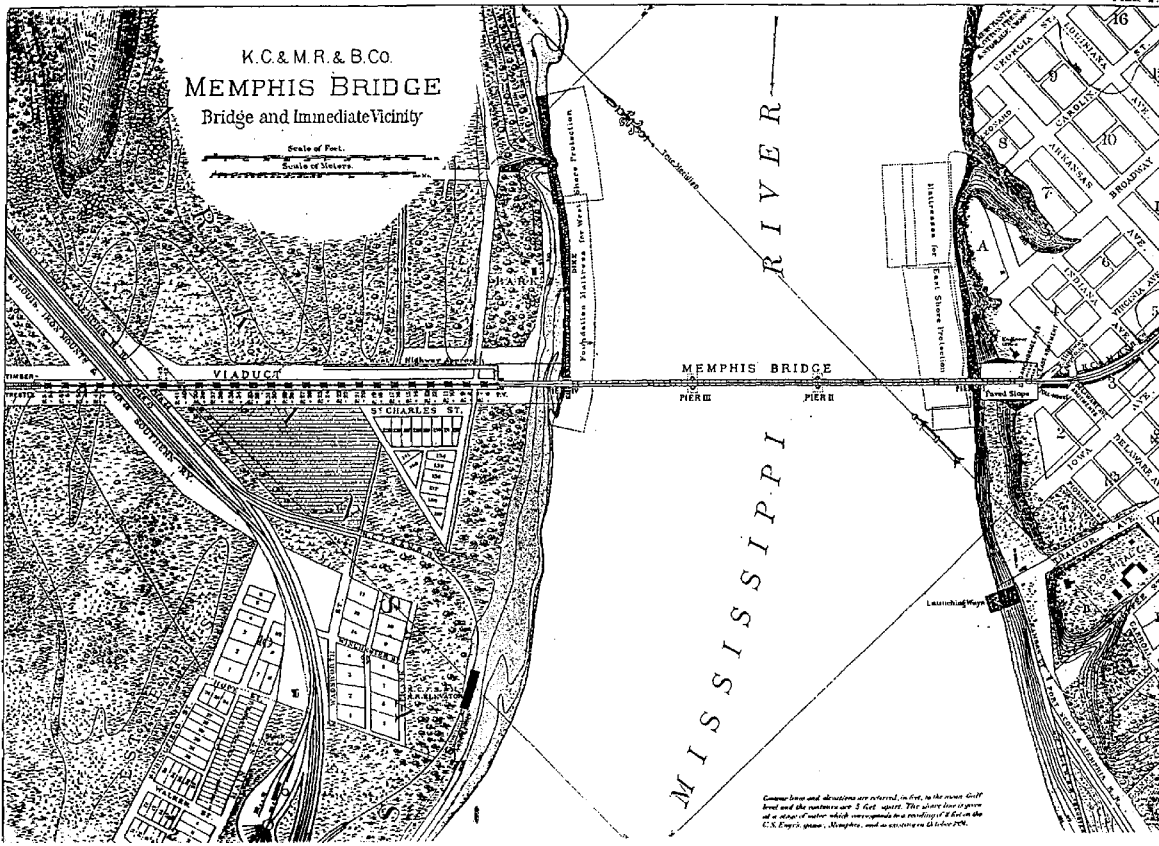


Figure 1 Location of Bridge

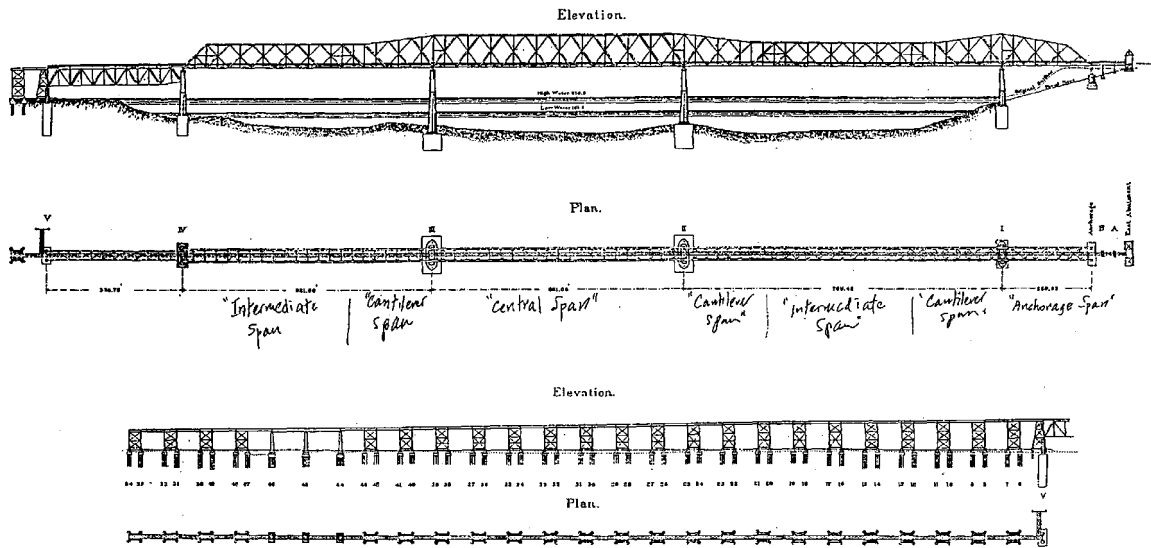


Figure 2 Plan and Elevation Views of the Steel Truss Bridge

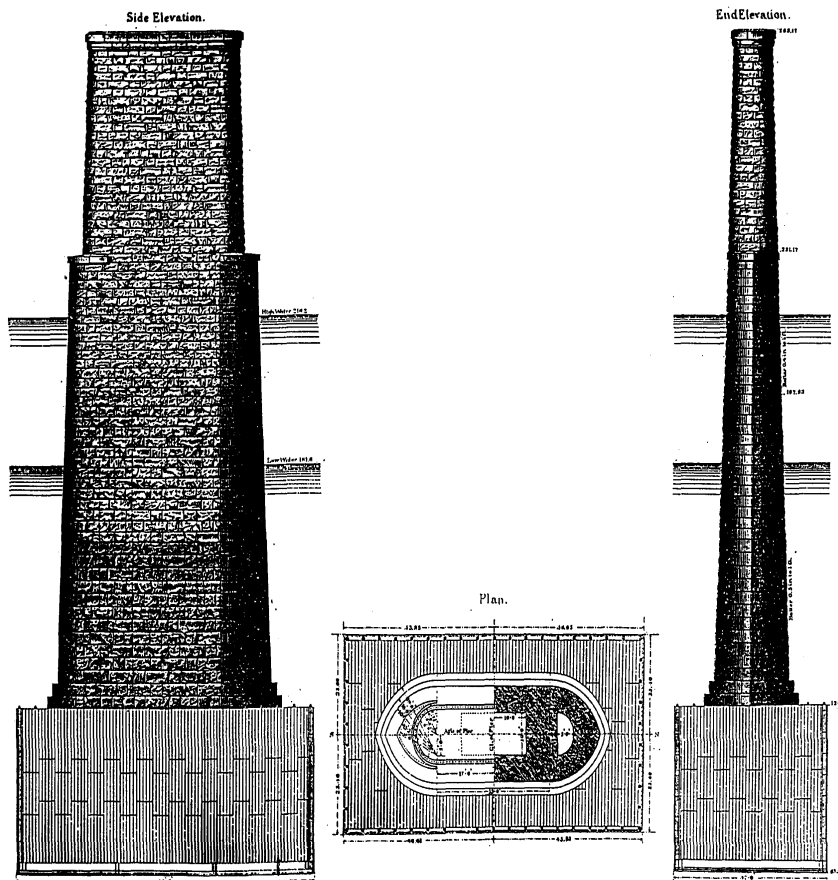


Figure 3 Plan and Elevation Views of Stone Piers

ANALYTICAL INVESTIGATION

A three dimensional analytical model of the bridge was developed. The natural frequencies and mode shapes for the bridge were calculated using the SAP 2000 computer program. Due to the nature of these long span truss bridges several of the lowest modes involve displacements of individual components of the bridge. The lowest mode was a transverse mode with a period of 3.05 seconds. The first vertical mode involving the whole truss was the fifth mode of the bridge with a period of 1.16 seconds. The lowest longitudinal mode was mode 6 with a period of 1.19 seconds.

The elastic response of the bridge was calculated for tri-axial ground motions (longitudinal, transverse and vertical) that are representative of those expected for an earthquake with a magnitude of 7.5 that occurs near the southern part of the New Madrid fault zone. This was considered to be a preliminary analysis to identify vulnerable parts of the bridge. A complete check of all of the superstructure members was not undertaken, but a cursory check revealed that the superstructure is not particularly vulnerable for ground motions of this amplitude. The most vulnerable components of the bridge are the bearings and the stone piers. Typical bearing details are shown in Figure 4.

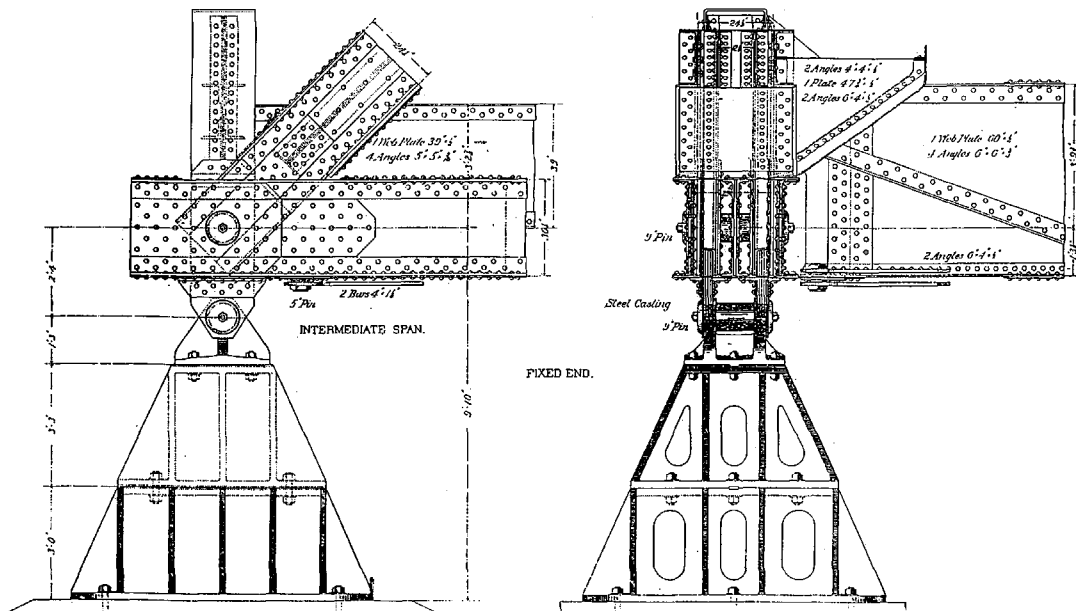


Figure 4 Typical bearing detail

A computer program capable of doing a detailed three-dimensional analysis with proper modeling of the stone piers is not available at this time. Each block of limestone would have to be modeled separately. Sliding along horizontal bed joints would have to be allowed for transverse response. As a pier deforms in the longitudinal direction of the bridge, layers of stone will separate along a horizontal joint when the calculated normal stress goes into

tension. However, the mortar cannot carry tension stress so the stone above the joint would not actually lift off. This would cause the stone above it to try to lift off as well, but with the same result. This phenomenon would progress up the pier until the response of the bridge changed direction. Crushing of the stones could also occur in conjunction with longitudinal response. The behavior is different in the transverse and longitudinal directions because of the difference in aspect ratios of the piers in each direction. Pictorial representations of these modes of response are given in Figure 5.

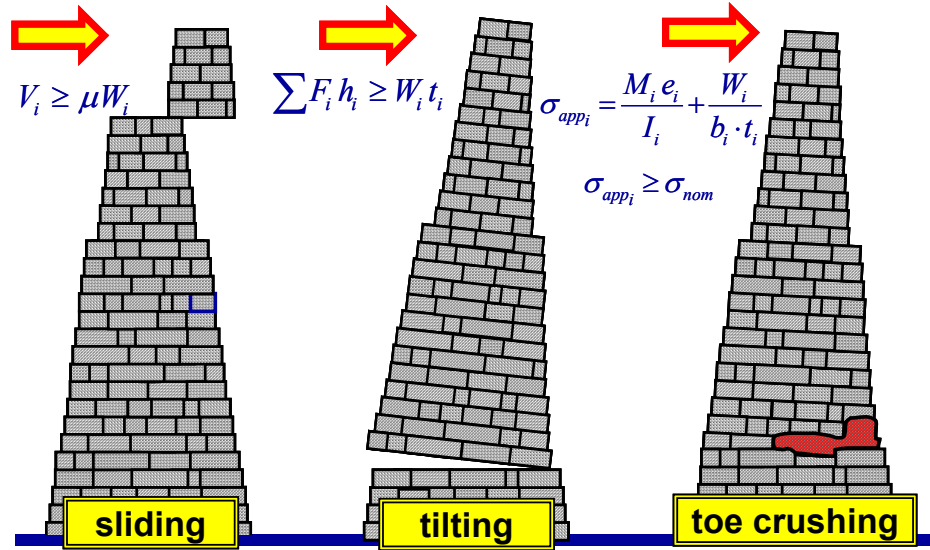


Figure 5 Failure mechanisms for stone piers

Two planar models of the bridge were developed using the Drain 2DX program, one each for the longitudinal and transverse directions. The piers were modeled using column elements with special connection elements. For the transverse direction sliding friction elements were used between column elements. For the longitudinal direction bilinear elastic elements were used that simulate the stone layers lifting off of the layer below. This is not how the pier would be expected to behave as described above. However, the results might be a crude predictor for the actual behavior. The hysteresis behavior for each connection spring is shown in Figure 6.

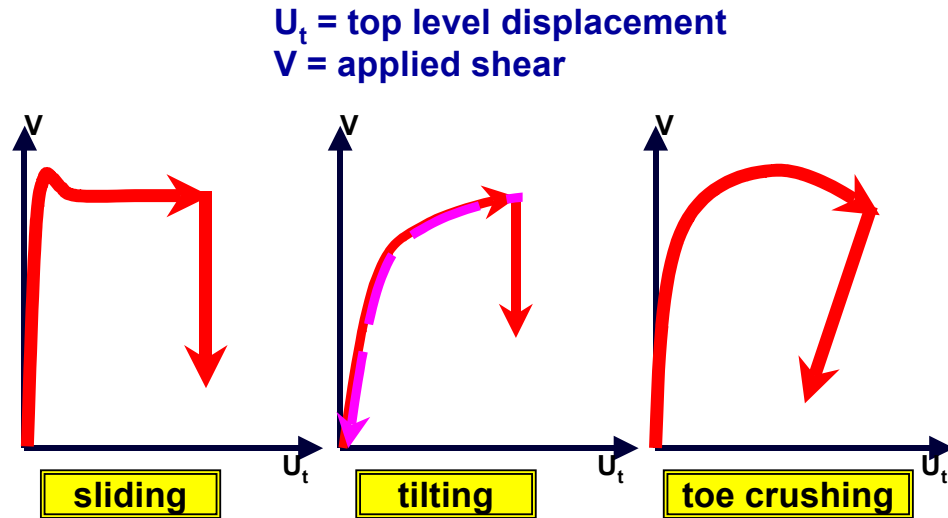


Figure 6 Hysteresis behavior for stone piers

A hazard curve for each direction of response was calculated based on the nonlinear analyses results. These are shown in Figure 7. The results show that longitudinal response is governed by tilting of the piers which initiates for an earthquake with a return period of 473 years. Sliding governs in the transverse direction with initiation occurring for an earthquake with a return period of about 1575 years.

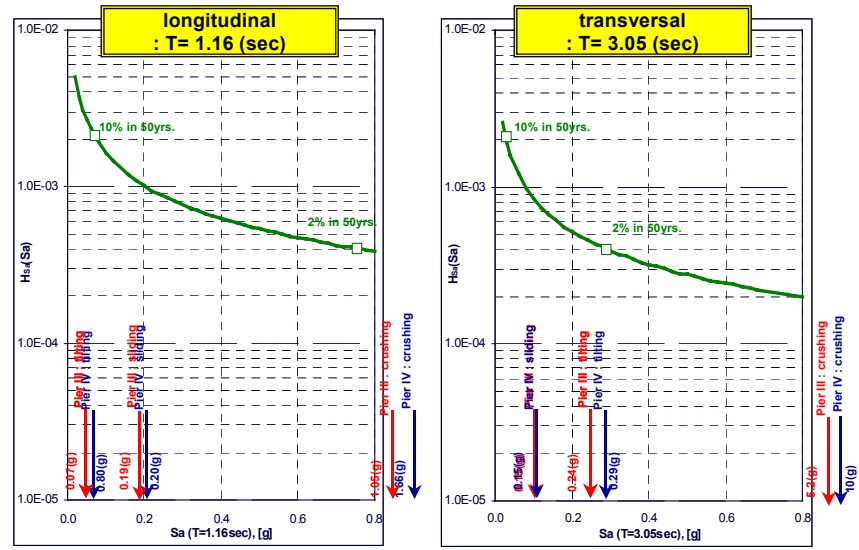


Figure 7 Hazard curve for stone piers

FUTURE RESEARCH

The analysis model using Drain 2DX is quite crude, so the accuracy of the analytical results is unknown. Shake table tests of four small models are planned for the near future. Two of these will be with grouted elements and two without. The two different configurations will model sliding behavior associated with transverse response and tilting behavior associated with longitudinal response. Half-scale concrete blocks will be used to model the stone slabs. A small steel single span superstructure carrying steel weights was constructed. This is not meant to be a model of the railway bridge. The purpose of the tests is to see if the analytical model is capable of accurately representing the behavior of sliding and tilting response. A schematic representation is given in Figure 8. Note that only uni-axial tests can be done using the UIUC shake table.

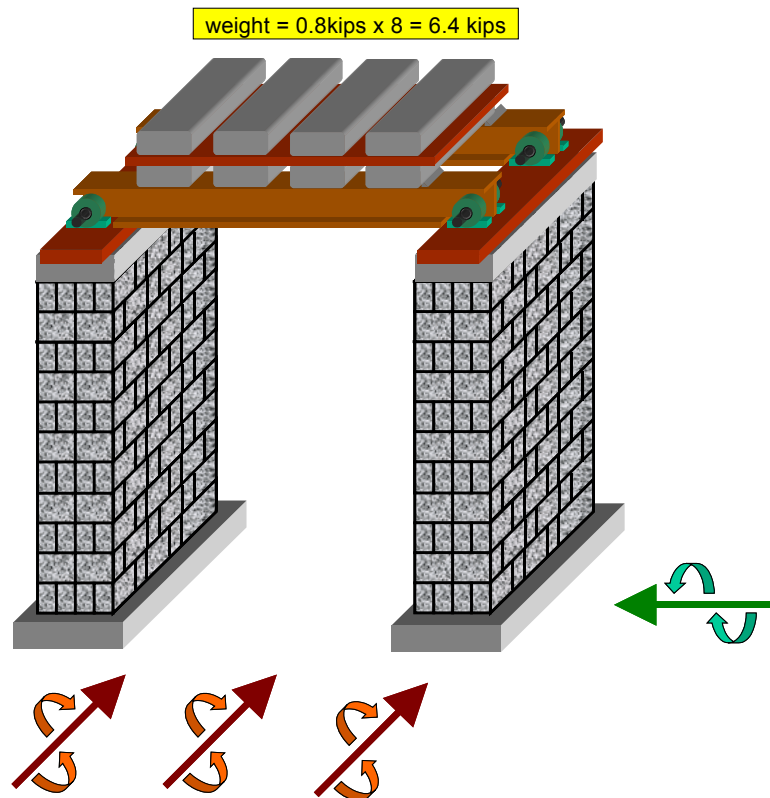


Figure 8 Schematic of model for shake table

CONCLUSIONS

The following conclusions may be gleaned from the analytical results:

- Preliminary result indicate at the bridge is very vulnerable to moderate seismic ground motion due to sliding and tilting of the stone piers in the transverse and longitudinal directions, respectively.
- Shake table tests are required to quantify the adequacy of the analytical models for the stone piers.

ACKNOWLEDGEMENTS

This research was sponsored by the Mid-America Earthquake Center through the National Science Foundation Grant EEC 9701785. All results, conclusions and findings are solely those of the authors and do not necessarily represent those of the sponsors.



KEERC-MAE Joint Seminar on
Risk Mitigation for Regions of Moderate Seismicity
University of Illinois at Urbana-Champaign, August 5-8, 2001



Sponsors: Korea Science and Technology Foundation, U.S. National Science



Seismic Responses of Geotechnical Port and Harbor Structures by the Shaking Table Test

Jae Ik HWANG¹, Sung Ryul KIM², Jae Hong KIM³, and Myoung Mo KIM⁴

¹ *Department of Civil Engineering, Seoul National University
San 56-1, Shillim-dong, Kwanak-gu, Seoul 151-742, KOREA
email: hwangman@gong.snu.ac.kr*

² *Department of Civil Engineering, Seoul National University
San 56-1, Shillim-dong, Kwanak-gu, Seoul 151-742, KOREA
email: yawnful@hananet.net*

³ *Department of Civil Engineering, Seoul National University
San 56-1, Shillim-dong, Kwanak-gu, Seoul 151-742, KOREA
email: narsis3638@hanmail.net*

⁴ *Department of Civil Engineering, Seoul National University
San 56-1, Shillim-dong, Kwanak-gu, Seoul 151-742, KOREA
email: geotech@gong.snu.ac.kr*

ABSTRACT: Shaking table model tests were performed to reproduce the dynamic behavior of a gravity quay wall and a pile-supported wharf as damaged by the Kobe earthquake in 1995. Using the scaling relations suggested by Scott and Iai (1989), the results of the model tests are compared with field measurements and with the results of previous model testing. The displacements of the gravity quay wall predicted by the current model tests are, at most, only one third of the measured displacements, while the displacements predicted by the model pile-supported wharf are about two thirds of the measured values. It is likely that model size contributed to this discrepancy.

KEYWORDS: shaking table tests, scaling relations, soil-structure interaction

INTRODUCTION

Shaking table tests have been used to estimate the dynamic behaviors of geotechnical structures qualitatively and quantitatively by taking into consideration soil-structure interactions, and appropriate analytical and numerical solutions. Shaking table tests suffer from a fundamental problem of scaling difference between the model and the prototype. Therefore, when using shaking table tests it is very important to choose reasonable scaling relationships between the model and the prototype.

Kagawa (1978) performed research on various geotechnical structures under dynamic loadings using force ratios, and Kokusho and Iwatate (1979) studied the dynamic nonlinear responses of soils using Buckingham's π theorem. Scott and Iai (1989) studied the soil-structure-fluid systems using basic equations, incorporating equilibria, constitutive law, strain definition etc., which govern the soil-structure-fluid system. From the results of such comparative studies, shaking table tests have attracted considerable attention in the study of soil-structure-fluid interactions.

Towata (1998) et al. performed small scale shaking table tests to analyze the interactions between gravity quay walls, backfill soils and foundations, and provided an qualitative understanding of dynamic behavior of quay walls. Iai (1999) simulated the dynamic behavior of gravity walls and pile supported wharfs in large-scale tests by considering scaling relations. In the present study, we analyzed the seismic responses of geotechnical port and harbour structures using shaking table model tests, whilst adopting scaling relations suggested by Scott and Iai. The results of our shaking table model tests were compared with those of shaking table tests carried out by Iai (1999) and observed prototype results (Sugano et al., 1996, Inagaki et al., 1996, Iai, 1997b).

SCALING RELATIONS

In shaking table model tests, the two important points are that the behavior of the model should mimic the prototype and that the fundamental laws of equilibrium and mass balance between the soil skeleton and pore water etc. should be satisfied both in the model and the prototype.

Scott and Iai studied soil-structure-fluid systems using governing equations incorporating equilibrium, constitutive law, strain definition etc. Major scaling factors from Scott and Iai for shaking table tests are shown in Table 1.

Saturated soil behavior is classified by two types (Whitman, 1985); (1) Soil is described to be of the cyclic mobility type, when soil deformation continues to increase during shaking but ceases to increase as soon as the shaking is stopped, and (2) to be of the strain softening type, when soil deformation continues to increase after shaking stops.

In the case of a cyclic mobility type, it is important to consider the scaling factor for strain (λ_ϵ) to understand the responses of the soil-structure system. When the shear wave velocities of model soils are known, the strain (λ_ϵ) scaling factor can be determined from equation (1) (Type I in Table 1). Otherwise, under the assumption that the shear elastic modulus is proportional to the square root of confining pressure, the strain-scaling factor (λ_ϵ) can be obtained from equation (2) (Type II in Table 1).

$$\lambda_\varepsilon = \lambda \left[\frac{(V_s)_m}{(V_s)_p} \right]^2 \quad (1)$$

$$\lambda_\varepsilon = \lambda^{0.5} \quad (2)$$

In the case of a strain softening type, the strain scaling factors cannot be introduced because of the large deformations involved. Therefore, the behaviors of the model can mimic the prototype only if the relative density of the model soils is lower than that of the prototype soils. In this case, the scaling factors of Type III shown in Table 1 can be applied.

Table 1 Major scaling factors for shaking table tests (Scott and Iai, 1989)

Quantity	Scaling factors (prototype/model)			
	Generalized scaling factor	Scaling factors in practice		
		Type I	Type II	Type III
		$\lambda_\rho = 1$	$\lambda_\varepsilon = \lambda^{0.5}, \lambda_\rho = 1$	$\lambda_\varepsilon = 1, \lambda_\rho = 1$
Length	λ	λ	λ	λ
Density	λ_ρ	1	1	1
Time	$(\lambda\lambda_\varepsilon)^{0.5}$	$(\lambda\lambda_\varepsilon)^{0.5}$	$\lambda^{0.75}$	$\lambda^{0.5}$
Acceleration	1	1	1	1
Velocity	$(\lambda\lambda_\varepsilon)^{0.5}$	$(\lambda\lambda_\varepsilon)^{0.5}$	$\lambda^{0.75}$	$\lambda^{0.5}$
Displacement	$\lambda\lambda_\varepsilon$	$\lambda\lambda_\varepsilon$	$\lambda^{1.5}$	λ
Stress	$\lambda\lambda_\rho$	λ	λ	λ
Strain	λ_ε	λ_ε	$\lambda^{0.5}$	1
Stiffness	$\lambda\lambda_\rho / \lambda_\varepsilon$	$\lambda / \lambda_\varepsilon$	$\lambda^{0.5}$	λ
Permeability	$(\lambda\lambda_\varepsilon)^{0.5} / \lambda_\rho$	$(\lambda\lambda_\varepsilon)^{0.5}$	$\lambda^{0.75}$	$\lambda^{0.5}$
Pore pressure	$\lambda\lambda_\rho$	λ	λ	λ
Flexural rigidity	$\lambda^5 \lambda_\rho / \lambda_\varepsilon$	$\lambda^5 / \lambda_\varepsilon$	$\lambda^{4.5}$	λ^5
Axial rigidity	$\lambda^3 \lambda_\rho / \lambda_\varepsilon$	$\lambda^3 / \lambda_\varepsilon$	$\lambda^{2.5}$	λ^3
Moment	$\lambda^4 \lambda_\rho$	λ^4	λ^4	λ^4
Shear force	$\lambda^3 \lambda_\rho$	λ^3	λ^3	λ^3
Axial force	$\lambda^3 \lambda_\rho$	λ^3	λ^3	λ^3

PROTOTYPES OF SHAKING TABLE MODEL TESTS

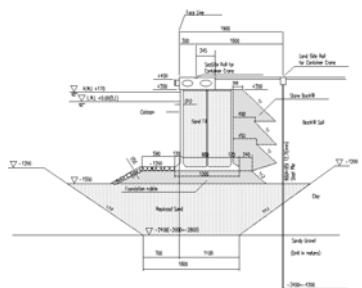
The Kobe earthquake of 1995 in Japan provided solid case history data on the dynamic behavior of geotechnical port and harbour structures (Sugano et al., 1996, Inagaki et al., 1996, Iai, 1997b). In this study, the prototypes of the shaking table model tests were a gravity quay wall and a pile-supported wharf in Kobe Port, which were severely damaged by the Kobe earthquake in 1995.

Gravity Quay Wall

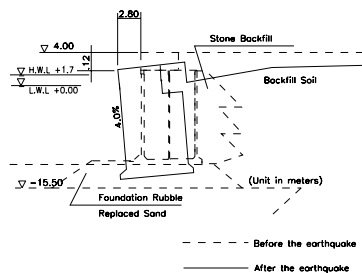
The first prototype of the shaking table test was the gravity quay wall located at Port Island, Kobe Port. Fig. 1 shows a cross section and the final deformation of a gravity quay wall after the earthquake at Port Island, Kobe Port. The geotechnical investigations were performed to evaluate the soil properties. Moreover, a cyclic triaxial test of undisturbed samples obtained using an in-situ freezing technique showed cyclic mobility behavior (Ichii et al., 1997). Fig. 1(b) shows the qualitative and quantitative deformations of the gravity quay wall, which was displaced about 2.8m towards the sea, had settled about 1.12m and had tilted about 4% toward the sea (Inagaki et al. 1996).

Pile-Supported Wharf

The second prototype of the shaking table test is a pile-supported wharf at Takahama Wharf in Kobe Port. Fig. 2 shows the cross section and the deformation/failure of the pile-supported wharf. As shown in Fig. 2, the wharf was constructed on a firm foundation deposit, which consisted of alternating layers of pleistocene clay and gravel; the SPT N-values ranged from 10 to 25 for the clay and 30 to 50 or higher for the gravel. An alluvial sand layer of thickness was ca. 2m with SPT N-values of ca. 15 was overlaid on the firm deposit. The concrete blocks of the retaining wall, were backfilled with decomposed granite with SPT N-values of about 10. As shown in Fig. 2, the deck of the wharf was displaced about 1.5 ~ 1.7m toward the sea. The steel piles buckled at the pile heads, except for the majority of the landward piles. The buckling was located close to the boundary between the layers of alluvial sand and pleistocene gravel and the level in which the thicknesses of the piles changed (Iai, 1997b).



(a) The cross section



(b) The final deformation

Figure 1 Gravity quay wall at Port Island, Kobe Port (Inagaki et al. 1996)

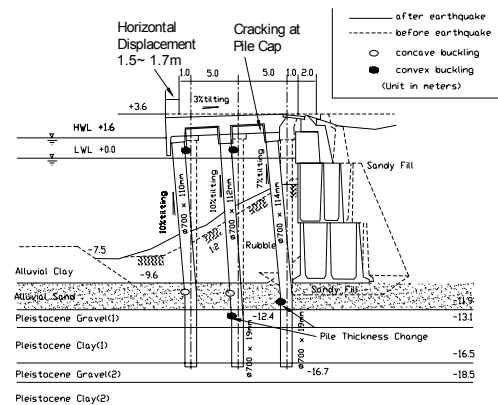


Figure 2 The cross section and the deformation /failure of a pile-supported wharf at Kobe Port (Iai, 1997)

CONDITIONS OF SHAKING TABLE MODEL TESTING

Gravity quay wall

In shaking table tests, the gravity quay wall was modeled at a scale of 1/56 of the prototype. The scaling factors of Type II in Table 1 were adopted, as shown in Table 2 because the prototype was of the cyclic mobility type.

Fig. 3 shows the cross section of gravity quay wall and the location of the measuring instruments. Eight pore pressuremeters (PP-1~PP-8), four accelerometers (A-1~A-4), and three LVDT's (D-1~D-3) were instrumented, as shown in Fig. 3.

The wall was made of concrete, of unit weight 2.44 t/m^3 . The soils were prepared with Jumunjin Standard Sands. The dense sand layer was densified by vibration with a harmonic wave of 20Hz, 0.4g for 4 minutes. The replaced sand and the reclaimed soil were prepared by vibrating with a harmonic wave of 20Hz, 0.4g for 60 seconds and for 30 seconds respectively. The relative densities of the replaced sand and the reclaimed soil were 65.83% and 41.91% respectively. Broken stones were used for the foundation rubble and stone backfill.

Table 2 Major scaling factors for shaking table tests for the gravity quay wall

Quantity	Scaling factors (prototype/model)	Scaling factors for 1/56 model
Length	λ	56.00
Time	$\lambda^{0.75}$	20.47
Acceleration	1	1.00
Displacement	$\lambda^{1.5}$	419.07
Stress/Pore pressure	λ	56.00

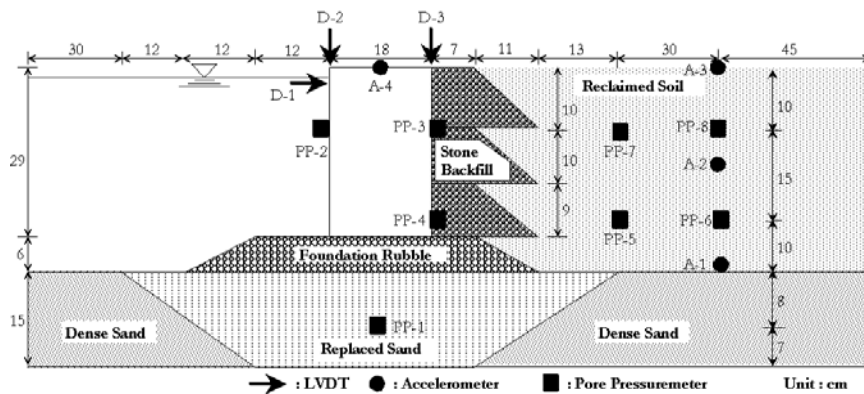


Figure 3 Cross section of gravity quay wall and location of measuring instruments

Pile-supported wharf

In the shaking table tests, the pile-supported wharf was modeled at a scale of 1/44 of the prototype, and the scaling factors of Type II in Table 1 were adopted. Table 3 shows the Major scaling factors for shaking table tests for the pile-supported wharf.

Fig. 4 shows the cross section of a model pile-supported wharf and the locations of the measuring instruments. Six pore pressuremeters (PP-1~PP-6), four accelerometers (A-1~A-4), and four LVDT's (D-1~D-4) were fitted as shown in Fig. 4.

The unit weight of the concrete block wall was 2.44 t/m^3 . The dense gravel layer was compacted firmly to fix the piles. Backfill soils were prepared by compacting with a harmonic wave of 20Hz, 0.4g for 30 seconds, to a relative density of 48.55%. Broken stones were used for the rubble dike and the stone backfill.

Table 3 Major scaling factors for shaking table tests for a pile-supported wharf

Quantity	Scaling factors (prototype/model)	Scaling factors for 1/44 model
Length	λ	44.00
Time	$\lambda^{0.75}$	17.08
Acceleration	1	1.00
Displacement	$\lambda^{1.5}$	291.86
Stress/Pore pressure	λ	44.00
Strain	$\lambda^{0.5}$	6.63
Flexural rigidity	$\lambda^{4.5}$	24862056.22
Axial rigidity	$\lambda^{2.5}$	12841.97

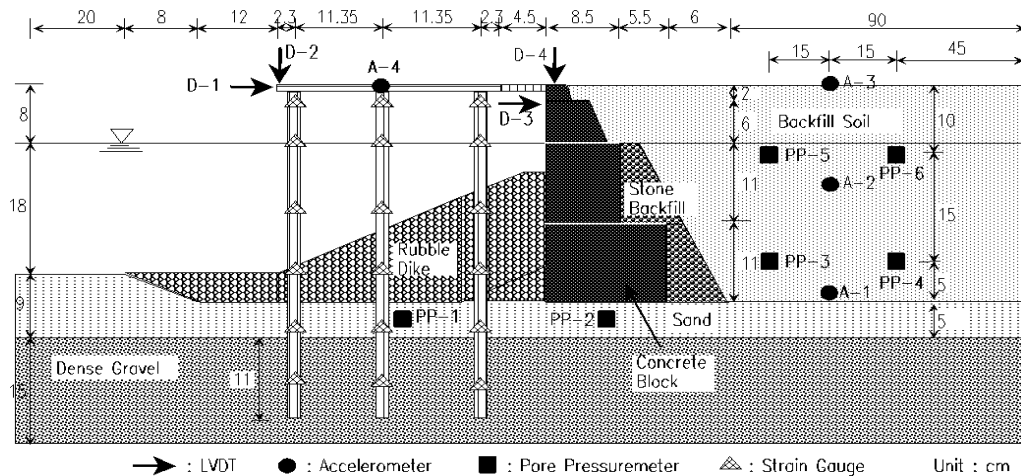


Figure 4 The cross section of a pile-supported wharf and the location of the measuring instruments

Input earthquake

Fig. 5 shows the time history of input earthquake, which is Kobe earthquake on the E-W direction (PGA=0.629g).

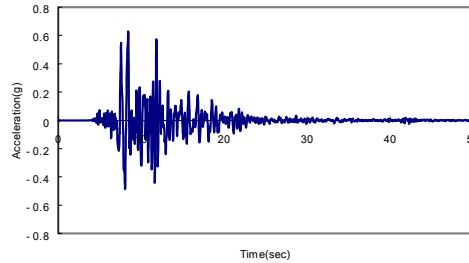


Figure 5 The time history of input earthquake(Kobe, JMA)

RESULTS AND DISCUSSIONS

The results of shaking table model tests are presented in terms of the prototype scale for comparison with the prototype results using the scaling relations suggested by Scott and Iai (1989).

Gravity Quay Wall

Fig. 6 shows the displacements of the model wall. The top of the model wall on the seaward side (D-1) was displaced horizontally 1.9m at maximum and 0.8m finally toward the sea. The top of the model wall on the seaward side (D-2) settled 0.38m finally. The top of the model wall on the landward side (D-3) settled 0.29m finally. The model wall was tilted about 0.91% towards the sea. The deformations of the model wall are a third to a fourth of those of the prototype. This inconsistency may be partly explained as followings. The deformation of the wall is greatly affected by interactions between the wall and the backfill soil. The model tests, however, did not simulate these interactions between the wall and the backfill soil due to a very short excitation period induced by the time scaling factor ($\lambda_t = \lambda^{0.75} = 17.08$). The deformation shape of the wall after shaking is shown in Fig. 7, moreover, the deformations of the model resemble those of the prototype in shape. The results of the shaking table model tests by Towata show that when the wall is heavy, the wall is deformed by being tilted towards the sea (1998). Therefore, the deformation shape obtained from the model test agrees with that obtained by Towata.

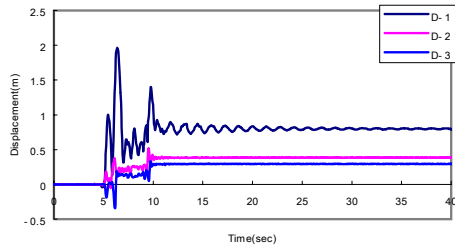


Figure 6 The displacements of the wall (scaled in terms of prototype) Pile-Supported Wharf

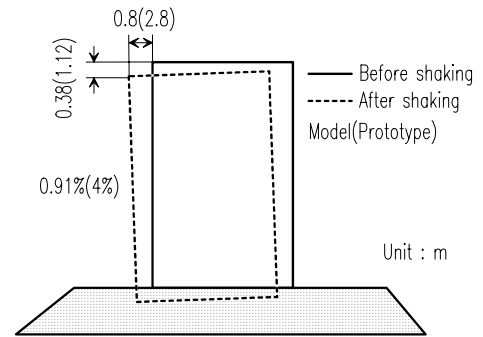


Figure 7 Deformation shape of the wall after shaking (scaled in terms of prototype)

Fig. 8 shows the displacements of the model pile-supported wharf. The top of the deck in seaside(on the seaward side?) (D-1) is displaced horizontally 3.99m at maximum and finally 1.05m towards the sea. From the model tests, the top of the deck on the seaward side (D-2) settled 0.05m, the top of the wall (D-3) was displaced horizontally 2.82m at maximum and 1.08m finally towards the sea, and the top of the wall (D-4) finally settled 0.65m. The displacements of the model deck were approximately two thirds of those of the prototype deck. This inconsistency, however, may be partly explained by the fact that the effects of pile yielding were not taken into account in the model tests.

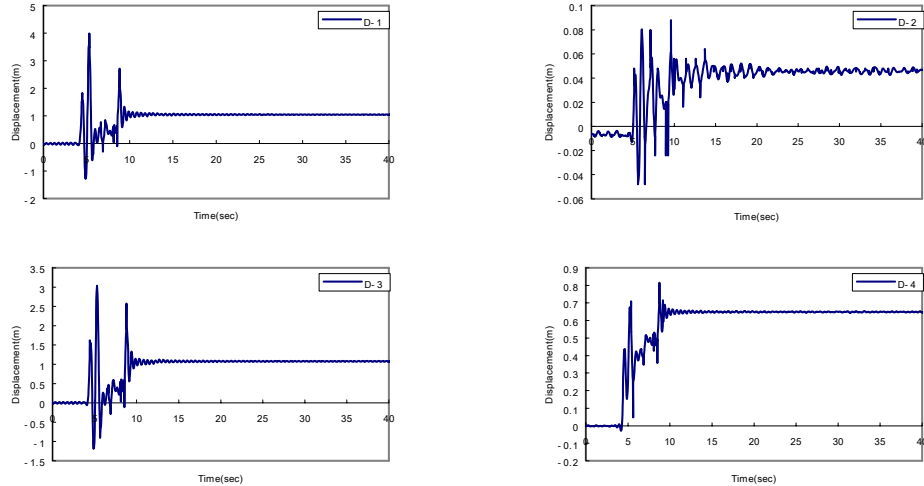


Figure 8 The displacements at the top of the deck and the wall (scaled in terms of prototype)

Fig. 9 shows the responses of the bending moments at piles 1, 2 and 3. These piles were located on the seaward side, the middle of the wall, and its landward side, respectively.

Fig. 15 shows the maximum and the final bending moments of the piles. As shown in Fig. 15(a), the buckling locations observed in the prototype piles coincide with the locations where the

maximum bending moments occurred, except for pile-2. The second measuring instrument at the bottom of pile-2 was considered to be broken, so its measured data are omitted from Figs. 14 and 15. The maximum bending moment at the pile head for piles-1 -2 had positive values, but pile-3 had a negative value, because earth pressure by the rubble dike was larger on pile 3 than the others. As shown in Fig. 10, the maximum and the final bending moments developed at the boundaries between the dense gravel and sand layer, where the prototype piles buckled.

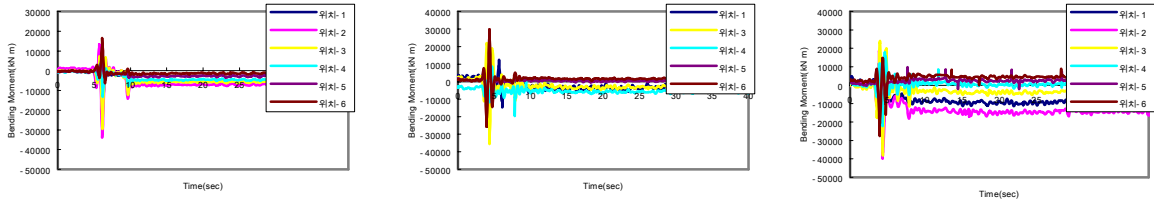
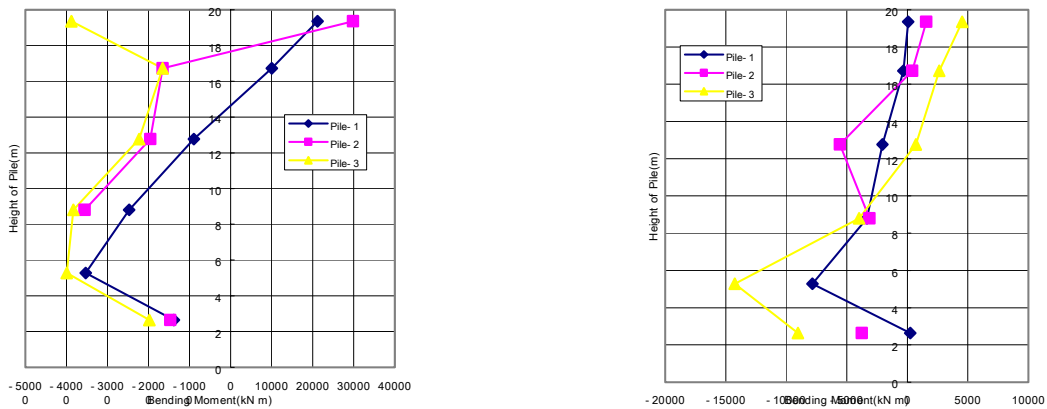


Figure 9 The responses of the bending moments at the piles (scaled in terms of prototype)



(a) The maximum bending moments (b) The final bending moments

Fig. 10 The maximum and the final bending moments of the piles (scaled in terms of prototype)

CONCLUSIONS

Shaking table tests were performed to reproduce the dynamic behavior of a gravity quay wall and a pile-supported wharf damaged by the Kobe earthquake in 1995. The scaling relations suggested by Scott and Iai (1989) were adopted in the model tests. The following conclusions were reached by comparing the test results with both field measurements and the results of the previous model tests.

1. In the case of the gravity quay wall, the displacements predicted by the current model tests were one third to one fourth those of the field measurements, which is very discouraging because the previously reported test results agreed well with each other. Scaling factors undoubtedly contributed to this large discrepancy. The length scaling factors of the current and the previous tests were 56 and 17, respectively. If the scaling factor becomes larger, the shaking period becomes smaller, which in turn affects the wall-backfill interactions, if they are not strictly time independent.
2. In the case of the pile-supported wharf, the current model test predicted the displacements to be two thirds that of the observed field values, while the previous model test's prediction were 50% of

actual. These discrepancies may have been caused by the use of non-yielding piles.

3. In the case of the pile-supported wharf, the buckling locations observed in the prototype piles were approximately the same as the maximum bending moment locations. These developed at the boundary between the dense gravel and the sand layer, where the prototype piles buckled. The maximum bending moments at the heads of the piles on the seaward side and in the middle of the piles of the wharf had positive values, while that of the piles on the landward side had negative values, which may have been caused by the larger earth pressures acting on the landward pile, caused by the rubble dike.

REFERENCES

1. S.Iai & T.Sugano, "Soil-structure interaction studies through shaking table tests", Proc. of The Second International Conference On Earthquake Geotechnical Engineering, Vol.3, 1999, pp. 927~940.
2. S. Iai, "Similitude for shaking table tests on soil-structure-fluid model in 1g gravitational field(closure)", Soils and Foundations, Vol.30(2), 1990, pp. 153~157.
3. A. Ghalandarzadeh, I. Towata, T. Orita, F. Yun, "Shaking table tests on seismic behavior of quay walls subjected to backfill liquefaction", Geotechnical Earthquake Engineering and Soil Dynamics III, Vol. 2, pp. 1046~1056.



KEERC-MAE Joint Seminar on
Risk Mitigation for Regions of Moderate Seismicity
University of Illinois at Urbana-Champaign, August 5-8, 2001



Sponsors: Korea Science and Technology Foundation, U.S. National Science Foundation, Brain Korea 21



Seismic Design and Analysis of Underground Structures, An Overview

Youssef M. A. Hashash¹, and John I-Chiang Yao²

¹ *Assistant Professor, Department of Civil and Environmental Engineering
University of Illinois at Urbana-Champaign
205 N. Mathews Avenue, MC-250, Urbana, Illinois, USA, 61801
email: hashash@uiuc.edu, (217) 333-6986*

² *Graduate Research Assistant, Department of Civil and Environmental Engineering
University of Illinois at Urbana-Champaign*

ABSTRACT: Underground facilities are integral parts of the infrastructure of modern society and are used for a wide range of applications, including subways and railways, highways, material storage, and sewage and water transport. The past 20 years have seen major progress in understanding of seismic response of underground structures. This paper presents an overview of “Seismic Design and Analysis of Underground Structures”, a report on the current state of seismic analysis and design for underground structures developed for the International Tunneling association. Seismic design loads for underground structures are characterized in terms of deformations and strains imposed by the surrounding ground. In contrast, surface structures are designed for inertial forces imposed by ground accelerations. Design methods have been developed to estimate seismic loads on underground structures. These methods include pseudo-static analysis whereby free-field motion is imposed on the underground structure as well as dynamic soil-structure interaction analysis. Free-field ground deformations and velocities due to a seismic event are estimated using site-specific response analysis that accounts for local geology. Historically, underground facilities have experienced a lower rate of damage than above-ground structures. However, failures of underground structures during recent earthquakes are reminders of the need to include seismic considerations in design details of underground structures.

KEYWORDS: underground structures, earthquakes, soil structure interaction, tunnels

INTRODUCTION

Underground structures have features that make their seismic behavior distinct from most surface structures, most notably (1) their complete enclosure in soil or rock and (2) their significant length (i.e., tunnels). The design of underground facilities to withstand seismic loading thus has aspects that are very different from the seismic design of surface structures.

This paper presents a short summary of Seismic Design and Analysis of Underground Structures [3], a report on the current state of knowledge in the area of seismic design and analysis for underground structures. The report updates the work prepared by St. John and Zahrah [14], which appeared in Tunneling and Underground Space Technology.

The report focuses on relatively large underground facilities commonly used in urban areas. This includes large-diameter tunnels, cut-and-cover structures and portal structures. The report focuses on methods of analysis of underground structures subjected to seismic motion, and provides examples of performance and damage to underground structures during recent major earthquakes. The report describes the overall philosophy used in the design of underground structures, and introduces basic concepts of seismic hazard analysis and methods used in developing design earthquake motion parameters. It describes how ground deformations are estimated and how they are transmitted to an underground structure, presenting methods used in the computation of strains, forces and moment in the structure. The report provides examples of the application of these methods for underground structures in Los Angeles, Boston, and the San Francisco Bay Area.

PERFORMANCE OF UNDERGROUND FACILITIES DURING SEISMIC EVENTS

The Daikai subway station collapse was the first collapse of an urban underground structure due to earthquake forces, rather than ground instability. Underground structures in the U.S. have experienced limited damage during the Loma Prieta and Northridge earthquakes, but the shaking levels have been much lower than the maximum anticipated events. Greater levels of damage can be expected during these maximum events. Station collapse and anticipated strong motions in major U.S. urban areas raise great concerns regarding the performance of underground structures. Several studies have documented earthquake damage to underground facilities. The following general observations can be made regarding the seismic performance of underground structures:

1. Underground structures suffer appreciably less damage than surface structures.
2. Reported damage decreases with increasing overburden depth.
3. Underground facilities constructed in soils can be expected to suffer more damage compared to openings constructed in competent rock.
4. Lined and grouted tunnels are safer than unlined tunnels in rock.
5. Tunnels are more stable under a symmetric load, which improves ground-lining interaction. Improving the tunnel lining by placing thicker and stiffer sections without stabilizing surrounding poor ground may result in excess seismic forces in the lining.

Backfilling with noncyclically-mobile material and rock-stabilizing measures may improve the safety and stability of shallow tunnels.

6. Damage may be related to peak ground acceleration and velocity based on the magnitude and epicentral distance of the affected earthquake.
7. Duration of strong-motion shaking during earthquakes is of utmost importance because it may cause fatigue failure and therefore large deformations.
8. High frequency motions may explain the local spalling of rock or concrete along planes of weakness. These frequencies, which rapidly attenuate with distance, may be expected mainly at small distances from the causative fault.
9. Ground motion may be amplified upon intersection with a tunnel if wavelengths are between one and four times the tunnel diameter.
10. Damage at and near tunnel portals may be significant due to slope instability.

ENGINEERING APPROACH TO SEISMIC ANALYSIS AND DESIGN

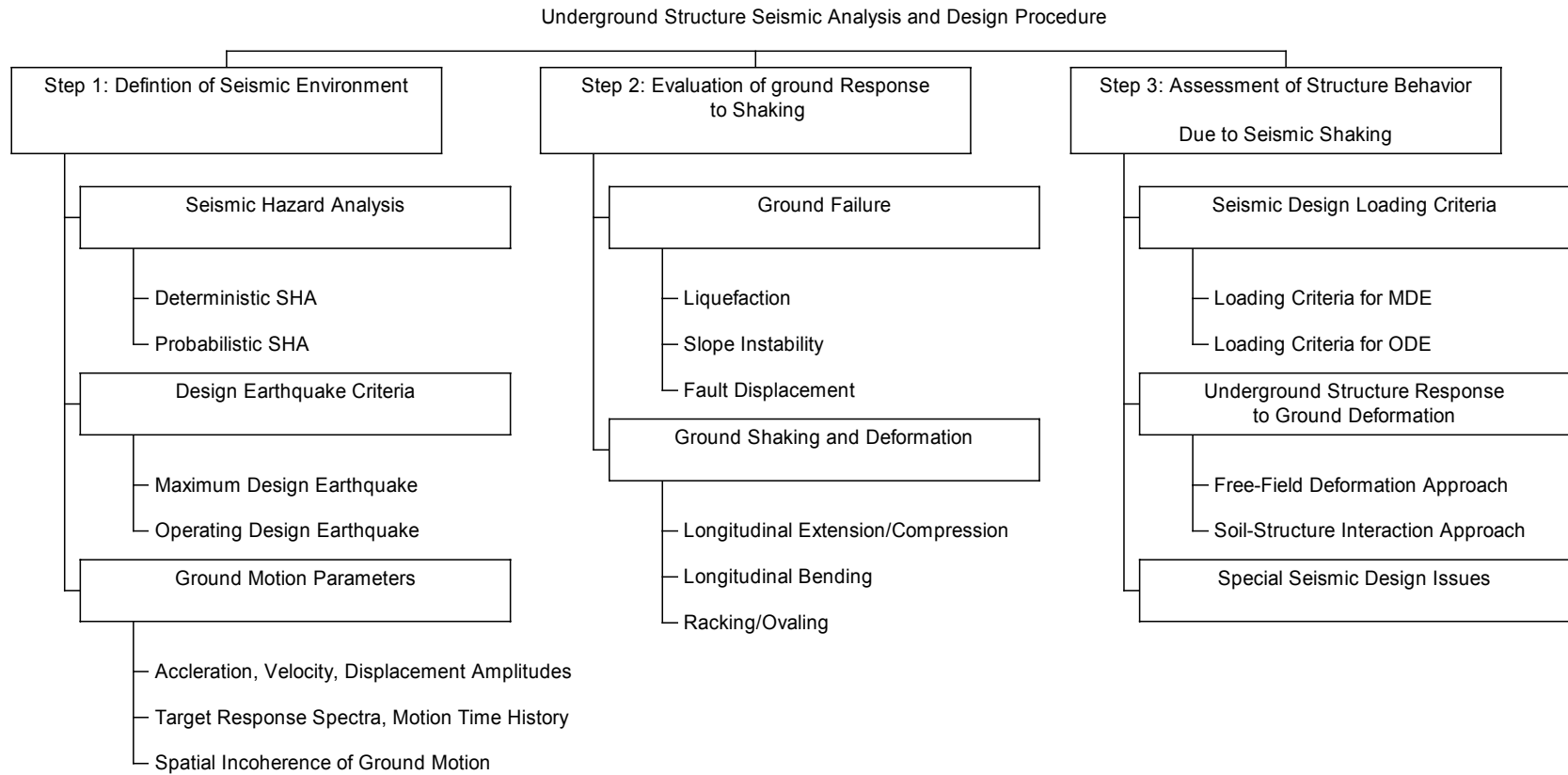
Earthquake effects on underground structures can be grouped into two categories: (1) ground shaking and (2) ground failure such as liquefaction, fault displacement, and slope instability. Ground shaking, which is the primary focus of this paper and the report [3], refers to the deformation of the ground produced by seismic waves propagating through the earth's crust. The major factors influencing shaking damage include: (1) the shape, dimensions, and depth of the structure; (2) the properties of the surrounding soil or rock; (3) the properties of the structure; and (4) the severity of the ground shaking [1][14].

Seismic design of underground structures is unique in several ways. For most underground structures, the inertia of the surrounding soil is large relative to the inertia of the structure. The focus of underground seismic design, therefore, is on the free-field deformation of the ground and its interaction with the structure. The emphasis on displacement is in stark contrast to the design of surface structures, which focuses on inertial effects of the structure itself.

The assessment of underground structure seismic response requires an understanding of the anticipated ground shaking as well as an evaluation of the response of the ground and the structure to such shaking. Table 1 summarizes a systematic approach for evaluating the seismic response of underground structures which consists of the following steps:

1. Definition of the seismic environment and development of the seismic parameters for analysis.
2. Evaluation of ground response to shaking, which includes ground failure and ground deformations.
3. Assessment of structure behavior due to seismic shaking including a) development of seismic design loading criteria, b) underground structure response to ground deformations, and c) special seismic design issues.

Table 1 Seismic Analysis Approach for Underground Structures



DEFINITION OF SEISMIC ENVIRONMENT

The goal of earthquake-resistant design for underground structures is to develop a facility that can withstand a given level of seismic motion with damage not exceeding a pre-defined acceptable level. The design level of shaking is typically defined by a design ground motion, which is characterized by the amplitudes and characteristics of expected ground motions and their expected return frequency [7]. A seismic hazard analysis is used to define the level of shaking and the design earthquake(s) for an underground facility. A seismic hazard analysis typically characterizes the potential for strong ground motions by examining the extent of active faulting in a region, the potential for fault motion, and the frequency with which the faults release stored energy. There are two methods of analysis: a) the deterministic seismic hazard analysis (DSHA) and b) the probabilistic seismic hazard analysis (PSHA). A probabilistic seismic hazard analysis provides a framework in which uncertainties in the size, location, and recurrence rate of earthquakes can be identified, quantified, and combined in a rational manner.

Once the seismic hazard at the site is characterized, the level of design earthquake or seismicity has to be defined. Current seismic design philosophy for many critical facilities requires dual (two-level) design criteria, with a higher design level earthquake aimed at life safety and a lower design level earthquake intended for economic risk exposure. The two design levels are commonly defined as "maximum design earthquake" (or "safety evaluation earthquake") and "operational design earthquake" (or "function evaluation earthquake"), and have been employed in many recent transportation tunnel projects, including the Los Angeles Metro, Taipei Metro, Seattle Metro, and Boston Central Artery/Third Harbor Tunnels.

Spatial Incoherence of Ground Motion

For long structures such as bridges or tunnels, different ground motions may be encountered by different parts of the structure and traveling wave effects must be considered [4]. The generation of ground motion time histories with appropriate spatial incoherence is a critical task if the designer is to compute differential strains and force buildup along a tunnel length. Hashash et. al. [2] show how the use of time histories with spatial incoherence affects the estimation of axial force development in a tunnel and can lead to significant longitudinal push-pull and other effects.

Wave Propagation and Site Specific Response Analysis

Ample strong ground motion data are generally not available at the depths of concern for underground structures, so the development of design ground motions needs to incorporate depth-dependent attenuation effects. Popular analytical procedures use one-dimensional site response techniques that ignore the effects of all but vertically propagating body waves. One method applies a deconvolution procedure to a surface input motion in order to evaluate the motion at depth. Linear, equivalent linear or non-linear one-dimensional wave propagation methods are commonly used to propagate waves through soft soil deposits

EVALUATION OF GROUND RESPONSE TO SHAKING

In the absence of ground failure that results in large permanent deformation, the design focus shifts to the transient ground deformation induced by seismic wave passage. The deformation can be quite complex due to the interaction of seismic waves with surficial soft deposits and the generation of surface waves. For engineering design purposes, these complex deformation modes are simplified into their primary modes. Underground structures can be assumed to undergo three primary modes of deformation during seismic shaking: (1) compression-extension (Figure 1 a), (2) longitudinal bending (Figure 1 c), and (3) ovaling/racking (Figure 1 e & f).

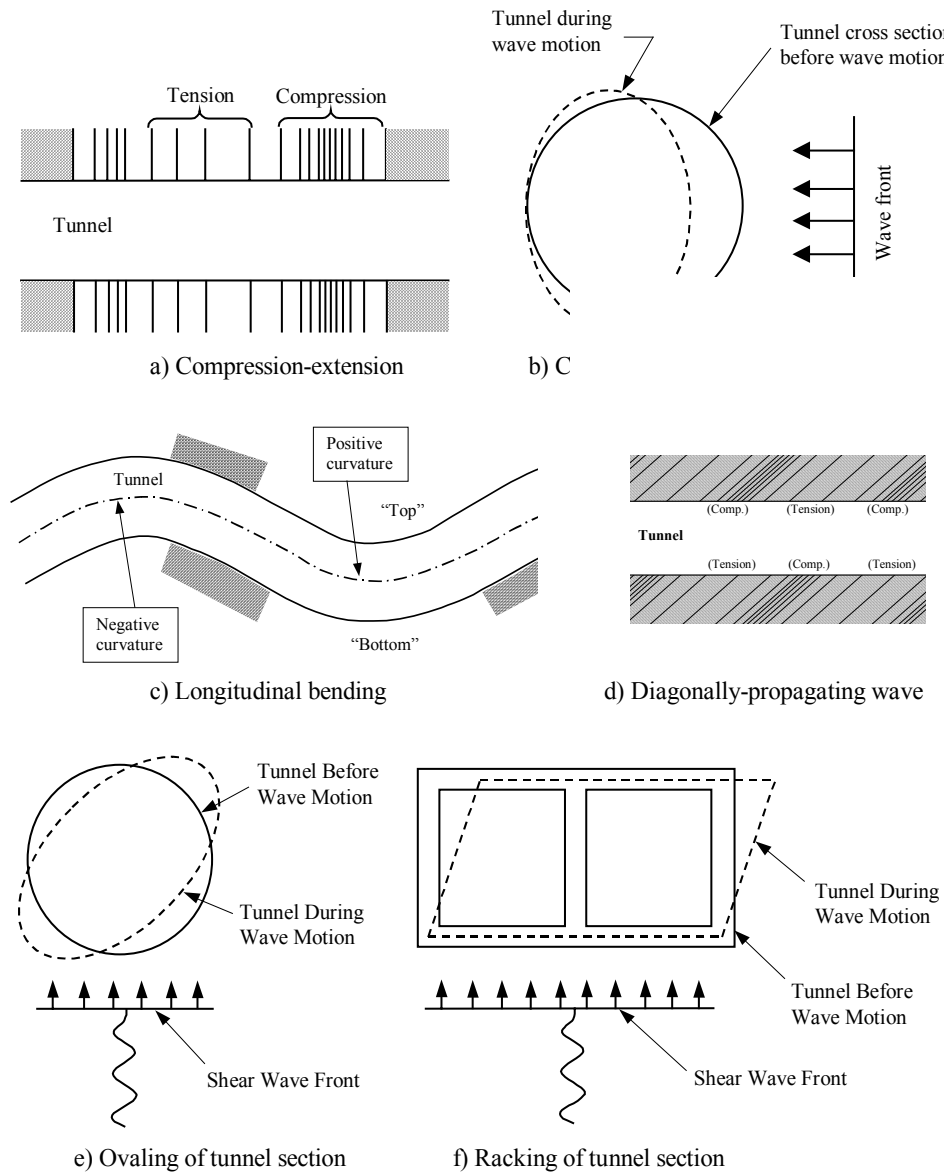


Figure 1 Deformation modes of tunnels due to seismic waves (after Owen and Scholl [9])

ASSESSMENT OF STRUCTURE BEHAVIOR DUE TO SEISMIC SHAKING

Underground Structure Response to Ground Deformation

This section introduces procedures used to compute deformations and forces corresponding to the three deformation modes (compression-extension, longitudinal bending and ovaling/racking).

Free Field Deformation Approach

The term “free-field deformations” describes ground strains caused by seismic waves in the absence of structures or excavations. These deformations ignore the interaction between the underground structure and the surrounding ground. The method is a simple and effective design tool when seismically induced ground distortions are small (i.e., low shaking intensity, very stiff ground, or the structure is flexible compared to the surrounding medium).

Simplified, closed-form solutions are useful for developing initial estimates of strains and deformations in a tunnel. St. John and Zahrah [14] used Newmark’s approach [8] to develop solutions for free-field axial and curvature strains due to compression, shear and Rayleigh waves. Combined axial and curvature deformations can be obtained by treating the tunnel as an elastic beam. Using beam theory, total free-field axial strains, are found by combining the longitudinal strains generated by axial and bending deformations [13]. These methods assume the seismic wave field to be that of plane waves with the same amplitudes at all locations along the tunnel, differing only in their arrival time. Wave scattering and complex three-dimensional wave propagation, which can lead to differences in wave amplitudes along the tunnel are neglected, although ground motion incoherence tends to increase the strains and stresses in the longitudinal direction.

Soil Structure Interaction Approach

The presence of an underground structure modifies the free field ground deformations. The soil structure interaction approach is necessary only for structures built in soft ground, as those in rock or stiff soils can be designed using free-field deformations. It should be further noted that increasing the structural stiffness, and therefore the strength capacity of the tunnel may not result in reduced forces – the structure may actually attract more force. Instead, a more flexible configuration with adequate ductile reinforcement or flexible joints may be more efficient [15]. The following paragraphs briefly describe procedures that model soil structure interaction.

In closed form elastic solutions, beam-on-elastic foundation solutions are used to model (quasi-static) soil-structure interaction effects. The solutions ignore dynamic (inertial) interaction effects. Under seismic loading, the cross-section of a tunnel will experience axial bending and shear strains due to free field axial, curvature, and shear deformations.

Wang [15] presented the maximum thrust and bending moment assuming full-slip conditions and maximum thrust assuming no-slip conditions for circular tunnels. Penzien and Wu [11]

developed similar closed-form elastic solutions for thrust, shear, and moment in the tunnel lining due to racking deformations. Penzien [12] provided an analytical procedure for evaluating racking deformations of rectangular and circular tunnels that supplemented the previous publication.

Shallow transportation tunnels are usually box shaped cut-and-cover structures. A box frame does not transmit static loads as efficiently as a circular lining, so the walls and slabs of the cut-and-cover frame need to be thicker, and therefore stiffer. The structural rigidity of box structures significantly reduces computed strains, often making it overly conservative to design these structures based on free-field strains [4]. Closed-form solutions are not available for rectangular tunnels. For ease of design, simple and practical procedures have been developed to account for dynamic soil-structure interaction effects [15].

A number of factors contribute to the soil-structure interaction effect, however the most important factor is the stiffness in simple shear of the structure relative to the ground it replaces, the flexibility ratio [15]. The racking deformations can be applied to an underground structure using the equivalent static load method. For deeply buried rectangular structures, most of the racking is generally attributable to shear forces developed at the exterior surface of the roof. The loading may then be simplified as a concentrated force acting at the roof-wall connection. For shallow rectangular tunnels, the shear force developed at the soil/roof interface decreases with decreasing overburden. The predominant external force that causes structure racking may gradually shift from shear force at the soil/roof interface to normal earth pressures developed along the side walls, so a triangular pressure distribution is applied to the model. The above discussion assumes homogeneous soil deposit. If the tunnel structure is at the interface between rigid and soft layers, the analyses has to account for the change in ground motion and shear deformation at the interface zone between the two soils.

Numerical Methods

The complex nature of the seismic soil-structure interaction problem for underground structures may require the use of numerical methods. This is especially true for cut-and-cover structures because of their greater vulnerability to seismic damage. Numerical analysis methods for underground structures include lumped mass/stiffness methods and finite element/difference methods. For analyzing axial and bending deformations, it is most appropriate to utilize three-dimensional models. In the lumped mass method, the tunnel is divided into a number of segments (masses/stiffness), which are connected by springs representing the axial, shear, and bending stiffness of the tunnel. The soil reactions are represented by horizontal, vertical, and axial springs [2], and the analysis is conducted as an equivalent static analysis. In finite difference or finite element models, the tunnel is discretized spatially, while the surrounding geologic medium is either discretized or represented by soil springs.

The ability of numerical analyses to improve on closed form solutions lies in the uncertainty of input data. If there is significant uncertainty in the input, refined analyses may be not of much value [14].

CONCLUSIONS

The material presented in this report describes the current state of knowledge for the design of underground structures. Many issues require further investigation to enhance our understanding of seismic response of underground structures and improve seismic design procedures. Some of these issues include:

1. Instrumentation of tunnels and underground structures to measure their response during ground shaking. This will be useful to understand the effect of spatial incoherency and directivity of the ground motion on tunnel response. Other instrumentation would be useful to measure differential movement between a tunnel and a portal structure, and to measure racking of rectangular structures such as subway stations.
2. Improved evaluation of the mechanism of the load transferred from the overburden soil to the ceiling slab of a cut and cover structure. Not all of the inertia force of the overburden soil is transferred to the ceiling slab, however, research into the evaluation of the soil block that provides inertia force has not yet been undertaken [5].
3. Research into the influence of high vertical accelerations on the generation of large compressive loads in tunnel linings and subway station columns. Large vertical forces may have been a factor in the collapse of the Daikai Subway station [5].
4. Development of improved numerical models to simulate the dynamic soil structure interaction problem of tunnels, as well as portal and subway structures. These models will be useful in studying the effect of high velocity pulses generated near fault sources on underground structures [2].
5. Evaluation of the significance of ground motion directivity and “fling effect” on tunnel response.
6. Evaluation of the significance of ground motion incoherence on the development of differential movement along the length of a tunnel [13].
7. Evaluation of the influence of underground structures on the local amplification or attenuation of propagated ground motion.
8. Research into the effects of repeated cyclic loading on underground tunnels [14].
9. Research into the application of non-conventional lining, bolting, and water insulation materials that can be used for seismic joints and enhance seismic performance of the tunnel.

REFERENCES

1. Dowding, C. H. and Rozen, A. (1978). “Damage to rock tunnels from earthquake shaking.” *Journal of the Geotechnical Engineering Division, ASCE*, Vol. 104, GT2, pp. 175-191.
2. Hashash, Y. M. A., Tseng, W. S., and Krimotat, A. (1998). “Seismic soil-structure interaction analysis for immersed tube tunnels retrofit.” *Geotechnical Earthquake Engineering and Soil Mechanics III*, ASCE Geotechnical Special Publication No. 75, Vol. 2, pp. 1380-1391.

3. Hashash, Y. M. A., Hook J. J., Schmidt, B., Yao, J. I. (2001). "Seismic Design and Analysis of Underground Structures," *Tunneling and Underground Space Technology* (in the process of publication). <http://cee.ce.uiuc.edu/hashash/ITASeisTunnelMay2001.pdf>
4. Hwang, R. N. and Lysmer, J. (1981). "Response of buried structures to traveling waves." *Journal of the Geotechnical Engineering Division, ASCE*, Vol. 107, No. GT2, pp. 183-200.
5. Iida, H., Hiroto, T., Yoshida, N., and Iwafuji, M. (1996). "Damage to Daikai Subway Station." *Soils and Foundations, Special Issue on Geotechnical Aspects of the January 17 1995 Hyogoken-Nambu Earthquake*, Japanese Geotechnical Society, January 1996, pp. 283-300.
6. Japanese Society of Civil Engineers (1975). *Specifications for Earthquake Resistant Design of Submerged Tunnels*.
7. Kramer, S. (1996). *Geotechnical Earthquake Engineering*. Prentice-Hall, Upper Saddle River, NJ, USA.
8. Newmark, N. M. (1968). "Problems in wave propagation in soil and rock." *Proceedings of the International Symposium on Wave Propagation and Dynamic Properties of Earth Materials*.
9. Owen, G. N. and Scholl, R. E. (1981). "Earthquake engineering of large underground structures." Report No. FHWA/RD-80/195, Federal Highway Administration and National Science Foundation.
10. Peck, R. B., Hendron, A. J., and Mohraz, B. (1972). "State of the art in soft ground tunneling." *Proceedings of the Rapid Excavation and Tunneling Conference*, American Institute of Mining, Metallurgical, and Petroleum Engineers, New York, pp. 259-286.
11. Penzien, J. and Wu, C. (1998). "Stresses in linings of bored tunnels." *International Journal of Earthquake Engineering and Structural Dynamics*, Vol. 27, pp. 283-300.
12. Penzien, J. (2000). "Seismically induced racking of tunnel linings." *International Journal of Earthquake Engineering and Structural Dynamics*, Vol. 29, pp. 683-691.
13. Power, M. S., Rosidi, D., and Kaneshiro, J. (1996). "Volume III Strawman: Screening, evaluation, and retrofit design of tunnels." Report Draft, National Center for Earthquake Engineering Research, Buffalo, New York.
14. St. John, C. M. and Zahrah, T. F. (1987). "Aseismic design of underground structures." *Tunneling and Underground Space Technology*, Vol. 2, No.2, pp. 165-197.
15. Wang, J.-N. (1993). *Seismic Design of Tunnels: A State-of-the-Art Approach*. Monograph 7, Parsons Brinckerhoff Quade & Douglas, Inc., New York.

16. Whitman, R. V. (1990). "Seismic design and behavior of gravity retaining walls." Design and Performance of Earth Retaining Structures, Cornell University, *ASCE Geotechnical Special Publication 25*, pp. 817-842.



KEERC-MAE Joint Seminar on
Risk Mitigation for Regions of Moderate Seismicity
University of Illinois at Urbana-Champaign, August 5-8, 2001



Sponsors: Korea Science and Technology Foundation, U.S. National Science Foundation, Brain Korea 21



Seismic Response Analysis of Jointed Pipeline Network

Moon K. KIM¹, and Woo Y. CHO²

¹ *Professor of Civil Engineering, Yonsei University
Applied Mechanics Laboratory, 134 Shinchon-dong, Seodaemun-gu, Seoul, KOREA
email: applymkk@yonsei.ac.kr*

² *Graduate Student, Department of Civil Engineering, Yonsei University
Applied Mechanics Laboratory, 134 Shinchon-dong, Seodaemun-gu, Seoul, KOREA
email: wooyeon@yonsei.ac.kr*

ABSTRACT: In this study, a modified ground strain model is developed to apply an equivalent earthquake load for the seismic analysis of buried pipelines. The ground strain can be obtained using the ratio of maximum ground velocity to wave propagation velocity. To reflect soil conditions and seismic characteristics, the wave propagation velocity is evaluated by a proposed dispersion curve based on wave energy distribution. In order to verify the developed ground strain model, the results of this study are compared with the observed ground strains of earthquake data. The results of the analyses are compared with those of a dynamic analysis and a response displacement method. Finally various parametric studies considering different properties of pipelines are performed.

KEYWORDS: ground strain, seismic analysis, buried pipeline, wave propagation velocity, beam theory, equivalent earthquake load

INTRODUCTION

Damage and disruption of buried pipelines caused by an earthquake may have severe effects on life since it may lead to loss of vital services, communications and transportation systems. These buried pipelines behave quite differently to the above-ground structures in many aspects. The buried pipeline is distributed over a wide range because of its function, and largely resisted by the surrounding soil. Because of these properties, the response of buried pipeline, according to the seismic wave propagation, can be summarized as follows. First, due to the property of line structure formation, wave phase is changed by earthquakes. This change of wave phase induces relative ground displacement: relative ground motion at each point of the line structure. Therefore, the relative ground movement between other points is responsible for inducing stresses at joints. Also, the large resistance by the surrounding soil causes the significant reduction of horizontal inertia forces, which comprise the main factor affecting the design of above-ground structure. These facts have already confirmed by experimental [1] and analytical [2] study. Using these facts, O'Rourke et al. [3] tried to analyze the behavior of buried pipeline using the theory of beam on elastic foundation and ground strain as seismic load. Recently, Mavridis and Pitilakis [4], Shakib et al. [5] analyzed the effect of interaction between ground and buried pipeline using the ground deformation and velocity of time-history curve based on actual earthquake records. In these previous studies, however, various types of earthquakes and ground characteristics have not been considered and an extensive analysis of complicated pipeline systems may be ineffective. In order to solve these ineffective problems, seismic loads are computed using modified ground strain. This modified ground strain use a dispersion curve of Rayleigh wave based on theory of wave propagation and the wave velocity produced by various types of earthquakes and ground characteristics. In addition, it is conducted to the earthquake analysis applied to the analysis model of buried pipeline

COMPUTATION OF GROUND STRAIN

As being seen in Figure 1(a), we can just use the linear ground strain for the quasistatic seismic loads. When the pipeline is located over the certain area like Figure 1(b) not in linear state, it is difficult to define a quasistatic seismic loads over the buried pipelines.

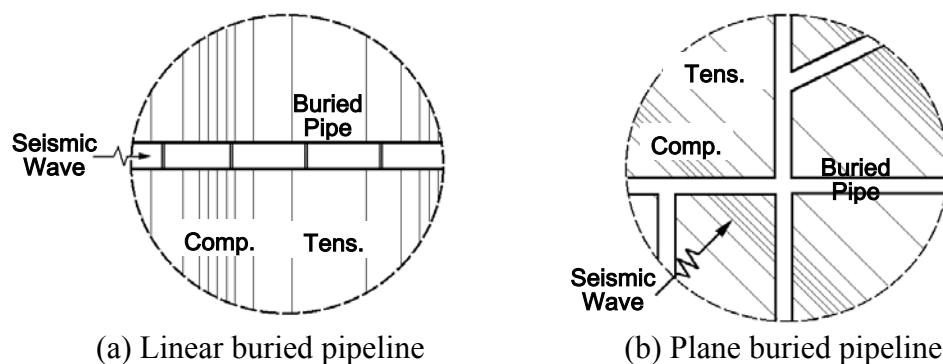


Figure 1 Incident seismic wave to buried pipeline

Therefore, the calculation of seismic force is the first thing to do based on the theory of wave propagation. Consider the elastic half-space and coordinate system shown in Figure 2.

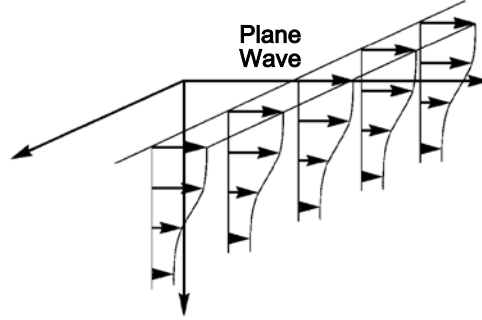


Figure 2 Typical plane wave in half-space

We assume that the motion of the material is described by the displacement field

$$\begin{aligned} u &= u(x, z, t), \\ v &= 0, \\ w &= w(x, z, t) \end{aligned} \quad (1)$$

Thus the motion is two-dimensional: it does not depend on the coordinate normal to the plane in Figure 1, and the component of the displacement normal to the plane is zero. Using the Helmholtz decomposition

$$\mathbf{u} = \nabla\Phi + \nabla \times \Psi \quad (2)$$

we can express the displacement components in terms of two scalar potentials:

$$\begin{aligned} u &= \frac{\partial\phi}{\partial x} + \frac{\partial\psi_2}{\partial z}, \\ w &= \frac{\partial\phi}{\partial z} - \frac{\partial\psi_2}{\partial x} \end{aligned} \quad (3)$$

where $\phi = \phi(x, z, t)$ and $\psi_2 = \psi_2(x, z, t)$. The scalar ψ_2 is the y component of the vector potential Ψ . Using potentials, the volumetric strain $\bar{\varepsilon}$ can be represented as eqn. (4) with displacements u and w .

$$\begin{aligned} \bar{\varepsilon} &= \varepsilon_{xx} + \varepsilon_{zz} \\ &= \frac{\partial u}{\partial x} + \frac{\partial w}{\partial z} = \frac{\partial}{\partial x} \left(\frac{\partial\phi}{\partial x} + \frac{\partial\psi_2}{\partial z} \right) + \frac{\partial}{\partial z} \left(\frac{\partial\phi}{\partial z} - \frac{\partial\psi_2}{\partial x} \right) \\ &= \frac{\partial^2\phi}{\partial x^2} + \frac{\partial^2\phi}{\partial z^2} = \nabla^2\phi \end{aligned} \quad (4)$$

where, the value related to the direction z is constant, so the volumetric strain in plane wave is same as the linear strain.

As earthquake wave propagates from the epicenter, axial ground strain according to the relative ground deformation occurs, at two points on the pipeline distant from each others. Since ground strain according to the wave propagation in earthquake inversely proportional to the wave propagation velocity and proportional to the ground velocity, maximum axial strain $(\varepsilon_g)_{\max}$ in the ground is expressed equation (5).

$$(\varepsilon_g)_{\max} = \frac{V_{\max}}{C} \quad (5)$$

where V_{\max} is maximum axial ground velocity and C is axial wave propagation velocity. Therefore, to predict the ground strain due to the earthquake wave propagation, calculation of maximum ground velocity and wave propagation velocity must proceed.

Maximum ground velocity according to the wave propagation can be obtained from the actual earthquake record or using the value presented from Newmark [6], maximum ground velocity can be obtained from maximum ground velocity at the base depot. Nevertheless, it is restricted by earthquake scale and ground condition. Therefore, present study, based on the total 350 kinds of earthquake record in Japan using the experimental equation reflects earthquake scale, depth of the epicenter, and ground condition as equation (6) presented by Kamiyama et al. [7], maximum ground velocity computed.

$$V_{\max}(M, D) = 2.879 \times 10^{0.153M} \times AMP, (D \leq 10^{0.014+0.218M}) \quad (6a)$$

$$V_{\max}(M, D) = 3.036 \times 10^{0.511M} \times D^{-1.64} \times AMP, (D > 10^{0.014+0.218M}) \quad (6b)$$

where V_{\max} is maximum ground velocity, unit is $10^{-2} m/s$, M is seismic intensity of Japanese Meteorological Association(JMA), D is depth of the epicenter, unit is km . And AMP in the equation (6) is increase coefficient depends on the ground condition and it is obtained from the standard penetration test (SPT) value (N)[7].

To predict ground strain according to the wave propagation, first of all, wave phase which mainly affects the ground motion must be decided. Generally criterion to the equation (7) target structure is affected by surface wave and the other cases are affected by body wave [8].

$$R/D > 1.5, M > 6.0 \quad (7a)$$

$$R/D > 1.5, 6.0 > M \geq 5.0 \quad (7b)$$

where R is distance from the epicenter, D is depth of epicenter. Since buried pipeline does not exist in deep situation, behavior of the buried pipeline is affected by the surface wave.

Effective wave velocity according to ground strain can be obtained modeling the surface wave expressed function of frequency and wavelength. Among the surface wave, Love wave moves like behavior of anti-plane and this generates bending deflection of the pipeline. It is known that bending deflection of the pipeline due to the earthquake is relatively small, so generally effect of bending is ignored [3]. Therefore, ground motion caused by wave propagation is governed by Rayleigh wave. Rayleigh wave which behaves like in-plane has vertical component and horizontal component. However, vertical component which induces bending deflection is not considered. Only horizontal component of the Rayleigh wave affects the axial behavior.

To compute this wave velocity of Rayleigh (C_R), considering semi-infinite domain with homogeneity and elasticity, wave propagation velocity (V_s) from characteristic equation of the Rayleigh wave like equation (8) is expressed with term of wave velocity and poisson's ratio as equation (9).

$$\left(2 - \frac{C_R^2}{V_s^2}\right)^2 - 4\left(1 - \frac{V_s^2}{V_p^2} \frac{C_R^2}{V_s^2}\right)^{1/2} \left(1 - \frac{C_R^2}{V_s^2}\right)^{1/2} = 0 \quad (8)$$

$$C_R = \frac{0.87 + 1.12\nu}{1 + \nu} V_s \quad (9)$$

As the real ground condition, in the case of the multi-layered semi-infinite ground wave propagation velocity of Rayleigh wave has dispersion feature changed with frequency and wavelength because medium deforms in the different layer. In the case of wave propagation velocity of Rayleigh wave, it is hard to understand the boundary condition between displacement and stress at each boundary face. It can not be computed theoretically. Therefore, dispersion curve of the Rayleigh wave at the multi-layered ground is suggested with approximate method like Figure 3. Figure 3(a) indicates wave propagation velocity of Rayleigh wave in the homogeneous semi-infinite media where wave velocity is 1.0 (regularized wave velocity) and Figure 3(b) indicates dispersion curve of the layer (shear wave velocity is 1.0, thickness is 1.0) on the half-space (shear wave velocity is 2.0). Since most of wave energy is contained in 1.0λ (one wave length) below the ground surface. Therefore wave propagation velocity (C_R) equals that of the upper layer if wave length is shorter than thickness of the upper layer (H). On the other hand, since wave propagation velocity is governed by the effect of wave propagation in the semi-infinite layer if wave length is longer than $30H$ (contains most of energy in the semi-infinite layer). When the wave length is $H \sim 30H$, wave propagation velocity is affected by both layer. Therefore dispersion curve of ground given by Figure 1(b) is expressed by equation (10).

$$\begin{aligned} C_{ph} &= 0.875V_H & \lambda &\geq 30H \\ &= (0.875V_H - \alpha_v V_L)(\log \lambda - \log H) / \log 30 + \alpha_v V_L & H &\leq \lambda \leq 30H \\ &= \alpha_v V_L & \lambda &\leq H \end{aligned} \quad (10)$$

where α_V is ratio of wave propagation velocity of Rayleigh wave in the homogeneous semi-infinite layer versus shear wave velocity, V_H is shear wave velocity in the semi-infinite layer, V_L is shear wave velocity in the surface layer. Boundary value used in equation (8) is value suggested by Mooney [8].

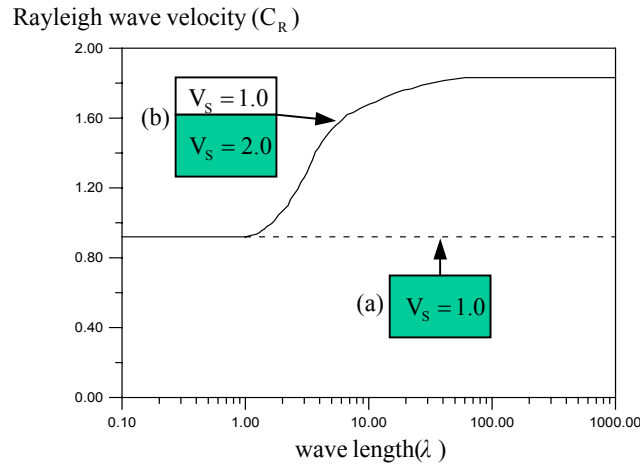


Figure 3 Dispersion curve of Rayleigh wave

VERIFICATION

The calculated equivalent seismic loads are applied to the cross type buried pipeline, shown in Figure 4, with respect to the rigid base of 500m/s , shear wave velocity and the buried pipes at a depth of 1.5m layered in ground having the surface layer of 30m depth and 90m/s shear wave velocity. Then the results are compared with the Lau's results [9] which are gained by dynamic analysis. The material properties of pipeline and ground layers are listed in Table 1.

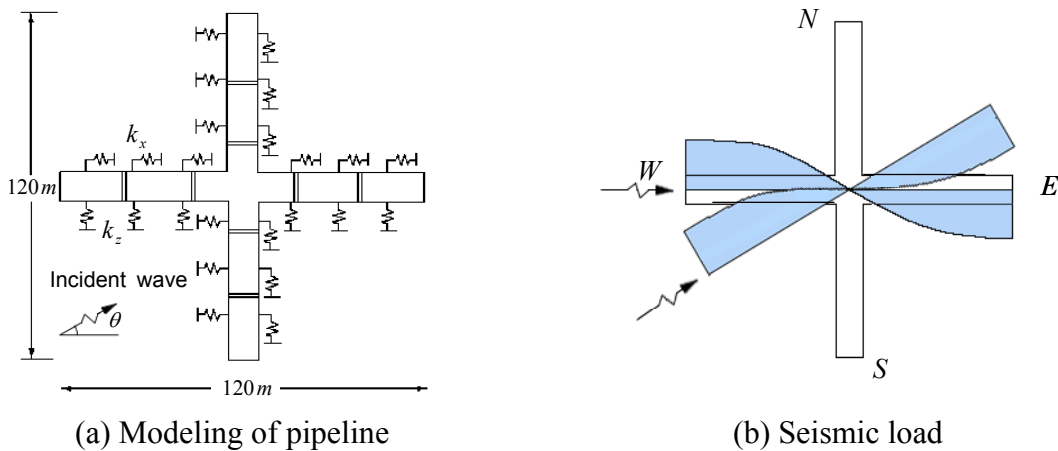
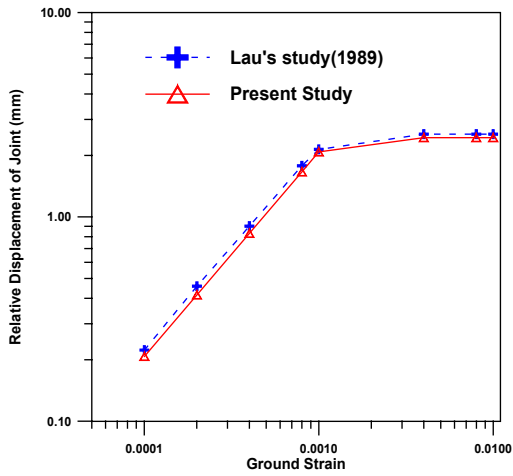


Figure 4 Cross-type buried pipelines

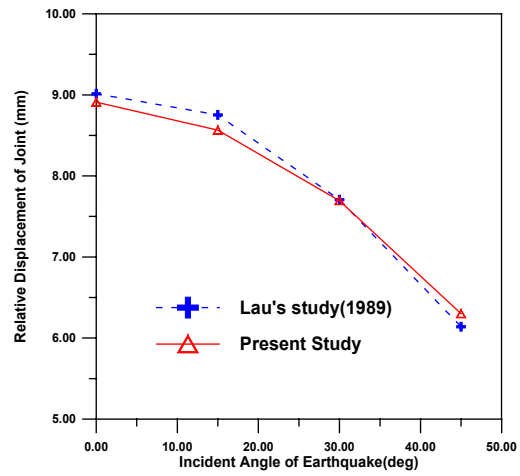
Table 1 Specification of pipeline and soil

	Properties	Values
Specification of pipe	Modulus of elasticity (<i>GPa</i>)	80.0
	Thickness (<i>mm</i>)	10.00
	Diameter (<i>mm</i>)	152.40
	Axial stiffness of joint (<i>N/m</i>)	18.22×10^2
	Elastic limit of joint displacement (<i>mm</i>)	25.40
	Rotational stiffness of joint (<i>N·m/rad</i>)	67.24×10^2
	Elastic limit of joint rotation (<i>rad</i>)	4.74×10^{-3}
Material properties of soil	Shear wave velocity of surface layer (<i>m/s</i>)	90.0
	Shear wave velocity of half-space (<i>m/s</i>)	500
	Axial stiffness of soil spring (<i>N/m²</i>)	72.00
	Lateral stiffness of soil spring (<i>N/m²</i>)	72.00
	Ultimate axial force of soil spring (<i>N/m</i>)	510.00
	Ultimate lateral force of soil spring (<i>N/m</i>)	2041.00

As the ground strain varies from 0.0001 to 0.01, with zero incident angle, the maximum relative displacements of joint increase. The results in Figure 5(a) show a maximum of 5% difference from Lau's results. Also, the results for the variance of the incident angle at the same ground strain (0.0004), as in Figure 5(b), show 2% difference. Therefore, the proposed procedure can consider various incident seismic wave and overcome the ineffectiveness indicated in the dynamic analysis, and can be applied to the expansion analysis of the pipeline network system.



(a) With ground strain ($\theta = 0$)



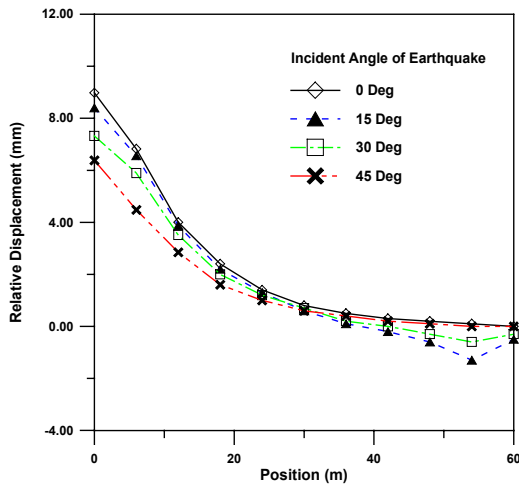
(b) With incident angle ($(\varepsilon_g)_{\max} = 0.0004$)

Figure 5 Comparison with Lau's results

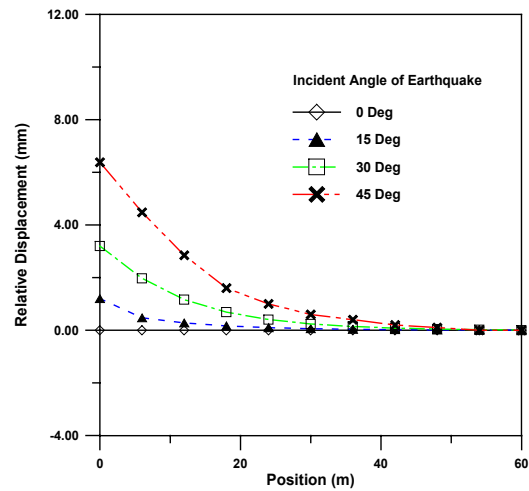
BEHAVIOR OF BURIED PIPELINES UNDER SEISMIC WAVES

The developed method is applied to the incident seismic wave analysis of cross type buried pipeline, shown in Figure 4. The dimensions of the buried pipelines and material properties of soil are presented in Table 1. For the ground strain, the value 0.001 is accepted. In earthquake, the most serious damage to the buried pipeline is usually occurred in large phase difference, so the 1/2 of phase length (λ) is considered as a seismic input for most severe condition for the buried pipeline.

Because the responses appear symmetrically with cross point, the results for the half part of the buried pipeline are presented. Referring to Figure 6, as the incident angle of seismic wave increase the tension displacement of E-W component joint decrease and that of N-S component joint increase because the variance of direction in seismic wave cause the load transferring.



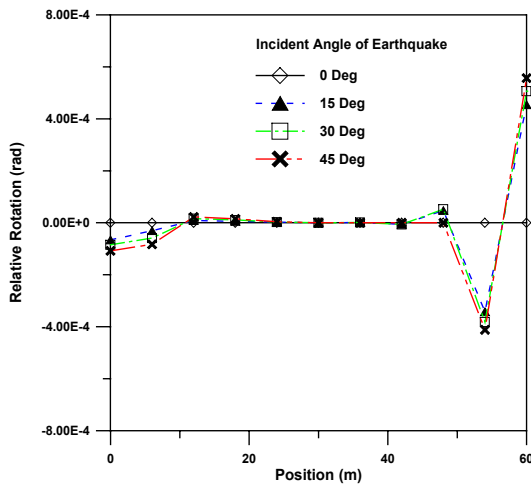
(a) E-W component



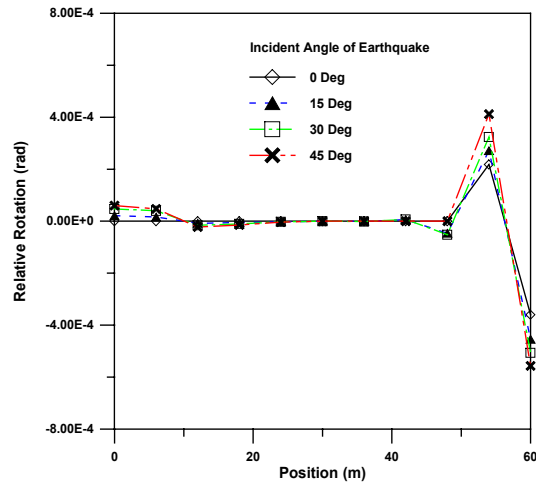
(b) N-S component

Figure 6 Relative displacement of joint

Also, in Figure 7(a), rotational displacement of E-W component joint near to the cross point of buried pipeline get increased as the incident angle approach to 45 degree. These components do not exceed the elastic limit of material in this ground strain (0.001) yet. However, it shows as the incident angle of seismic wave rotational displacement can cause a collapse of buried pipeline, so the consideration of rotation limit is required in design procedure.



(b) N-S component



(a) E-W component

Figure 7 Relative rotation of joint

CONCLUSIONS

In present study, ground strain generated by the progress of seismic wave considering the characteristics of the earthquake is estimated. Then the improved analysis methods that can be applied to it as loads to the model of earthquake analysis of buried pipes is proposed. The obtained results from the above procedure are the following.

With comparing the Lau's results by dynamic analysis, the propriety of earthquake analysis proposed this study was proved. Dynamic analysis can be supplemented by proposed procedure, due to the complexity of geometrical shape and the difficulty in calculation of the dynamic load. Also, it can be extended to the earthquake analysis of pipe network system.

The developed method is applied to the incident seismic wave analysis of cross type buried pipeline. From the results, it can be found that the variance of the incident angle of seismic wave causes the load transferring and rotational displacement can cause a collapse of buried pipeline, so the consideration of rotation limit is required in design procedure.

ACKNOWLEDGMENT

The authors gratefully acknowledge the partial support of the KEERC (Korea Earthquake Engineering Center) and Korea Ministry of Science and Technology (97-N2-01-01-A-02).

REFERENCES

1. Ariman, T. and Hamada, N., "Experimental investigations on seismic behavior of buried pipelines," *Lifeline Earthquake Engineering*, 1981, pp. 48-64.
2. Shinozuka, M., Kameda, H., and Koike, T., "Ground strain estimation for seismic risk analysis," *Journal of Engineering Mechanics, ASCE*, Vol. 109, No. 1, 1983, pp. 175-191.
3. O'Rourke, M.J., Pikul, R.R. and Wang, L.R.L., "Transverse seismic waves at pipeline junctions," *Journal of Technical Councils, ASCE*, Vol. 108, No. TC1, 1982, pp. 173-177.
4. Mavridis, G.A. and Pitilakis, K.D., "Axial and transverse seismic analysis of buried pipelines," *Proceedings of Eleventh World Conference on Earthquake Engineering*, 1996, pp. 109-116.
5. Shakib, H. and Shakib, N., "Analysis of buried pipelines to random ground motion in homogeneous medium," *Proceedings of Tenth European Conference on Earthquake Engineering*, 1995, pp. 2185-2190.
6. Newmark, M., *A Study of Vertical and Horizontal Earthquake Spectra*, Directorate of Licensing, U.S. Atomic Energy Commission, Washington, D.C., 1973.

7. Kamiyama, M. and O'Rourke, M.J., "A Simplified estimate of seismic soil strain for lifeline systems," *Proceedings of the Fourth U. S. Conference*, No. 6, 1995, pp. 192-199.
8. Mooney, H. M. and Bolt, B., "Dispersive Characteristics of the First Three Rayleigh Modes for a Single Surface Layer," *Bulletin of the Seismographic Society of America*, Vol. 56, No. 1, 1966, pp 43-67.
9. Lau, Y.C., *Elasto-Plastic Responses of Buried Pipeline Systems under Wave Propagation*, Ph.D. Thesis, Old Dominion University, 1989.



KEERC-MAE Joint Seminar on
Risk Mitigation for Regions of Moderate Seismicity
University of Illinois at Urbana-Champaign, August 5-8, 2001



Sponsors: Korea Science and Technology Foundation, U.S. National Science Foundation, Brain Korea 21



Key Parameters Governing the Performance of Soft Tunnel Coating for Seismic Isolation

Dae-Sang KIM¹

¹*Research Professor, Korea Earthquake Engineering Research Center,
Seoul National University, Korea
email: kds0660@gong.snu.ac.kr*

ABSTRACT: A method to cover up a tunnel lining with a soft and thin coating is discussed herein as a possible measure for mitigating seismic damage to tunnels. Long term earthquake observations at different tunnel sites within a variety of alluvial soil deposits have demonstrated that a circular tunnel is liable to deform in such a way that its two diagonal diameters crossing each other expand and contract alternately. Narrowing down vibration modes for discussion to this particular and the most important mode, any of the essential items of the soil-tunnel system, namely the soil, the coating and the tunnel lining, had only one degree of freedom, allowing the coating effect to be simply evaluated in terms of a limited number of key parameters.

KEYWORDS: Soft Coating, Seismic Isolation, Poisson's ratio, Constrained Modulus

INTRODUCTION

The damage to subway tunnels [1] used by the 1995 Hyogoken-Nambu earthquake has stimulated a sharp rise in research activities for possible measures to mitigate damage to underground structures. One of the possible measures discussed so far was to cover up a tunnel with a soft coating to minimize shear forces on tunnel-soil interface [2].

Long term earthquake observations at different tunnel sites within a variety of alluvial soil deposits have demonstrated that a circular tunnel is liable to deform in such a way that its two diagonal diameters crossing each other expand and contract alternately [3], which fact has been found to be linked with the motion of the surrounding soil at resonance. With keeping this fact in mind, Konagai [4] compared two extreme boundary conditions of soil-tunnel interface; the condition of fixed tangential strain and the shear stress-free condition. The former case suggests a firm bond between the tunnel lining and the soil, whereas the latter case is associated with an artificial slippery soil-tunnel interface. It has been shown in his simulations that reducing the shear stress on the soil-tunnel interface causes little difference when Poisson's ratio of the soil is close to 0.5.

The effect, however, depends on other ignored factors. Among those ignored, this paper takes into account the effect of expansion and contraction of soft coating materials that spread over tunnel linings.

MATHEMATICAL EXPRESSION OF SOIL-TUNNEL INTERACTION EFFECT

A multi-step method is often employed to isolate two primary causes of soil-structure interaction, that is, the inability of a structure to match the free-field deformation (kinematic interaction) and the effect of inertia force of the structure on the response of the surrounding soil (inertia interaction). When a hollow structure like a tunnel is concerned, the inertia interaction is often of less importance than the kinematic interaction. For this reason, it is usual in a practical design process that free-field ground displacement is applied through Winkler-type soil springs to a tunnel in order to evaluate stress patterns induced within its structure members.

In this discussion, it is noted that the motion of a soil deposit brought in resonance is, in general, the most responsible for the inclined elliptic vibration mode of a cylindrical hollow. Pinpointing the frequency for this particular vibration mode of the soil-tunnel system, thus, allows the interaction effect to be clearly described in terms of the uniquely determined soil stiffness for this mode. Hence, a soil deposit discussed in this chapter is a two-dimensional medium overlying stiff bedrock (Figure 1). The thickness H of this layer is thus one fourth of the stationary shear wavelength L , i.e.,

$$H \cong L / 4 = \pi v_s / 2\omega_0 \quad (1)$$

where, v_s = shear wave velocity of soil, $f_0 = \omega_0 / 2\pi$ = resonance frequency of the soil deposit. Needless to say, the tunnel diameter $2r_0$ should not be greater than the surface soil thickness H , and limits the discussion within this range of radius-thickness ratio r_0 / H as:

$$2 \frac{r_0}{H} = \frac{4}{\pi} s r_0 < 1 \quad \text{with } s = \omega_0 / v_s \quad (2)$$

The parameter $s r_0$ in Equation (2), referred to as the non-dimensional frequency, determines the soil stiffness for this particular mode.

In this multi step method, the soil-tunnel system is divided into two substructures - the inner substructure of the tunnel lining and the outer substructure of soil; the latter includes the thin tunnel coating. The motion of the cylindrical hollow, which is not affected by the presence of a tunnel lining, is first to be obtained. In this derivation, the presence of the thin flexible coating is ignored. Though its rigorous solution is available in a number of papers [5], radial and tangential displacements $u_{r,soil}$ and $u_{\theta,soil}$ are tentatively approximated by the static solutions for a cylindrical cavity inclusion in an unbounded medium under alternate shearing (Figure 1) [6]; the approximation yielding the simple description of $u_{r,soil}$ and $u_{\theta,soil}$ on the cavity wall as,

$$\begin{aligned} u_{r,soil} &\cong \hat{u}_{r,soil} \sin 2\theta \\ u_{\theta,soil} &\cong \hat{u}_{\theta,soil} \cos 2\theta \end{aligned} \quad (3a),(3b)$$

where, $\hat{u}_{r,soil} = \hat{u}_{\theta,soil} (= \hat{u}_{soil}) = 2\gamma r_0 (1 - \nu)$ (4)

and γ is the applied shear strain (Figure 1). It is noted in Equation (4) that $\hat{u}_{r,soil}$ and $\hat{u}_{\theta,soil}$ are identical to each other irrespective of Poisson's ratio. Thus, \hat{u}_{soil} is viewed as a representative displacement parameter of the soil.

The soil deformation, which is then applied to the tunnel lining through its thin coating, deforms forcibly the lining in the following manner:

$$\begin{aligned} u_{r,lining} &\cong \hat{u}_{r,lining} \sin 2\theta \\ u_{\theta,lining} &\cong \hat{u}_{\theta,lining} \cos 2\theta \end{aligned} \quad (5a),(5b)$$

The tunnel lining is assumed to be a flexible ring, whose motion follows the Bellnoulle-Euler hypothesis, and to be stiff enough in its tangential direction for the tangential strain $\epsilon_{\theta\theta,lining}$ to be kept zero. Thus, the lining's displacements $u_{r,lining}$ and $u_{\theta,lining}$ eventually satisfy the following equation at $r = r_0$:

$$\epsilon_{\theta\theta,lining} = \frac{1}{r} \frac{\partial u_{\theta,lining}}{\partial \theta} + \frac{u_{r,lining}}{r} = 0 \quad (6)$$

Substituting equation (5) into equation (6) yields:

$$\hat{u}_{r,lining} = 2\hat{u}_{\theta,lining} (= \hat{u}_{lining}) \quad \text{at } r = r_0 \quad (7)$$

Equation (7) implies that \hat{u}_{lining} is the only necessary index that describes the lining displacement.

Thus, the problem turns out to be deriving the transferring factor $\hat{u}_{lining} / \hat{u}_{soil}$ of the soil displacement to that of the lining and it is indispensable in this derivation to evaluate through the thin coating the stiffness of the outer substructure of soil. Though the presence of the upper free and lower fixed boundary conditions of the soil layer may affect the solution when the tunnel is close to either of these boundaries, the effects of these opposing boundaries are tentatively excluded, and the outer substructure of soil is eventually assumed to have an infinite extent. The assumption, by virtue of its mathematical convenience, allows the explicit description of the problem in the cylindrical coordinates. The derivation is not shown herein as it is obtained through a plane and conventional manipulation of Bessel functions [7, 8]; it is given in more detail in Ref. [9].

The transferring factor is finally given by:

$$TR = \frac{\hat{u}_{lining}}{\hat{u}_{soil}} = \frac{-\xi \cdot (2S_{rr} + 2S_{r\theta} + S_{\theta r} + S_{\theta\theta})}{\bar{G} - \xi \cdot (2S_{rr} + S_{r\theta} + S_{\theta r} + S_{\theta\theta})} \quad \text{with } \xi = \frac{G_s r_0^3}{18EI}, \quad \bar{G} = \frac{G_s}{G_c} \quad (8a)-$$

$$(8c)$$

where, EI = bending stiffness of the lining, G_s and G_c are the shear moduli of the soil and the coating material, respectively, and S_{rr} , $S_{r\theta}$, $S_{\theta r}$ and $S_{\theta\theta}$ are components of the stiffness matrix of the outer substructure of soil. The transferring factor $\hat{u}_{lining} / \hat{u}_{soil}$, which is denoted by TF hereafter, is a function of the following six non-dimensional parameters; (1) *radius-thickness ratio* r_0 / H , (2) *relative soil stiffness* ξ in Equation (8b), (3) *shear stiffness ratio* \bar{G} in Equation (8c), (4) *Poisson's ratio of soil* ν_s , (5) *Poisson's ratio of the coating material* ν_c and (6) *coating thickness - radius ratio* t / r_0 . In order for the coating effect to be objectively discussed in different soil-tunnel systems, a new index, reduction factor RF , is introduced; the index defined as the ratio between the transferring factors TF_{coat} and TF_{uncoat} for the cases with and without coating, respectively.

$$RF = \frac{TF_{coat}}{TF_{uncoat}} = \frac{\hat{u}_{lining,coat}}{\hat{u}_{lining,uncoat}} \quad (9)$$

EVALUATION OF COATING EFFECT

For the following parametric study, it is necessary to grasp possible ranges of the parameters in Equation (8a). Table I show some mechanical properties of possible coating materials discussed in a research project, in which the Public Works Research Institute (PWRI) [2] took the initiative. Possible variations of the parameters are set at those listed in Table II.

It is noted that Equation (8a) was obtained assuming a particular vibration mode for a soil-tunnel system. This implies that any of the essential items of the soil-tunnel system, namely the soil, the coating and the tunnel lining, has only one degree of freedom, allowing these items to be interpreted as three springs linked up in series (Figure 2). In this metaphor, the free-field ground motion is to be applied at the outermost end of the soil spring. The effect of the coating, namely the spring put in the middle, is thus more pronounced as this spring becomes softer in comparison with the others. Hence variations of coating effect, which appears as the reduction of RF with varying stiffness parameters ξ and \bar{G} , are shown in Figures 3 and 4 for different Poisson's ratios ($\nu_c = 0.45$ and $\nu_c = 0.47$, respectively) of the coating material. Either the increase of \bar{G} or the decrease of ξ yields the decrease of RF as expected. The RF value, however, seems to be rather insensitive to the change of ξ , and therefore, ξ is set at 1 in the following discussions. The coating effect becomes clearer as the Poisson's ratio of the coating material decreases; a further detailed discussion will be given later.

Figure 5 shows the variation of RF with \bar{G} and the radius-thickness ratio r_0/H . The variation of RF with respect to r_0/H is on a steep downward slant to the right when $r_0/H < 0.1$. Above this range of r_0/H , however, the RF value seems to be insensitive to the change of r_0/H . For this reason, r_0/H is set at 0.2 hereafter.

Setting ξ , r_0/H and ν_s at the abovementioned values, the reduction factor RF is plotted as a function of \bar{G} and ν_c in Figures 6 and 7 for two coating thickness-radius ratios of 0.1 and 0.2, respectively. These figures clearly show rather strong dependence on ν_c of the coating effect, that is to say, contraction and expansion of a coating material contribute greatly to a better seismic isolation effect. Paradoxically speaking, a flexible but incompressible coating material has little effect in reducing seismically induced forces. Decrease of ν_c for better seismic isolation, however, leads to a drastic reduction of the constrained modulus M_c of the coating material; M_c is given by:

$$M_c = 2G_c(1 - \nu_c)/(1 - 2\nu_c) \quad (10)$$

The reduction of M_c may be followed by a recognizable subsidence of the overburden soil. Figure 8 shows the variation of volumetric strain of a coating material having shear modulus of 200 kPa with respect to ν_c and the confining pressure described in terms of soil depth z . The static earth pressure coefficient is assumed as 0.5. Given an allowable limit of the volumetric strain, this figure provides a possible lower bound of Poisson's ratio of the coating material that can be used at a particular depth.

CONCLUSIONS

Soft and thin Coating of a tunnel lining has been intensively discussed for years by many researchers as a possible measure for mitigating damage to tunnels. It is noted in this discussion that a circular tunnel deforms during an earthquake in such a way that its diagonal diameters ($\theta = \pm 45^\circ$) alternately expand and contract; the fact clarified through long term earthquake observations. Based on this knowledge, the soil-coating-tunnel interaction for this particular vibration mode was investigated.

- (1) The transferring factor of the representative soil displacement to that of the lining was obtained as a function of six non-dimensional parameters.
- (2) Among these parameters, the Poisson's ratio ν_c of the coating material was found to be one of the most sensitive key parameters.
- (3) Reducing ν_c to an allowable lower bound, contraction and expansion of a coating material enhances greatly the seismic isolation effect.

REFERENCES

1. Iida, H., Hiroto, T., Yoshida, N. and M. Iwafuji, "Damage to Daikai Subway Station," Special Issue of Soils and Foundations, The Japanese Geotechnical Society, 1996, pp. 283-300.
2. Construction Ministry of Japan, "Research report of development of isolation materials for seismic design to underground structure," No.192, 1997.12.
3. Tamura, C. and Kato, K., "A Study on Deformation of Tunnels during Earthquakes," Recent Advances in Lifeline Earthquake Engineering in Japan, ASME, 1980, pp.151-158.
4. Konagai, K., "Diagonal expansion and contraction of a circular tunnel during earthquakes," Structural Eng./earthquake Eng., JSCE, Vol.15, No.1, 1998.4, pp.91-95.
5. Tamura C., K. Konagai and T. Suzuki, "Earthquake Response Analysis of Soft Soil Deposit on Undulating Bedrock," Report of the IIS, Univ. of Tokyo, Vol. 36, No. 5, (Serial No. 234), 1991, pp. 227-261.
6. Muir Wood, A.M, "The Circular Tunnel in Elastic Ground," Geotechnique, 25, No.1, 1975, pp.115-127.
7. Konagai, K., "Effect of Seismic Isolation for a Circular Tunnel Alternately Expanding and Contracting in its Diagonal Directions," Proc., 1st Colloquium on Vibration Reduction and Control, JSCE, pp.179-183, 1996.

8. Pao, Y.H. and Mow, C.C., "Diffraction of Elastic Waves and Dynamic Stress Concentrations," Crane Russak, New York, 1973.
9. Kim D.S., "Key parameters governing seismic isolation effect on underground structures," Doctoral Thesis, Department of Civil Engineering, University of Tokyo, 2000.

Table 1 Shear moduli and Poisson's ratios of possible coating materials

Coating material	Specific gravity	Shear modulus (kPa)	Poisson's ratio
Asphalt	1.114	500	0.4
Urethane	1.27	280	0.48
Silicone I	1.0	100	0.48
Silicone II	1.2	300	0.48
Silicone III	1.36	570	0.48
Liquid-type rubber	0.98	280	0.46
Solid-type rubber	0.591	580-1280	0.33-0.423

Table 2 Parameters for evaluation of isolation effect

<i>radius-thickness ratio</i> r_0 / H	0.05~0.25
<i>Relative soil stiffness</i> ξ	0.01~100
<i>Shear stiffness ratio</i> \bar{G}	1~1000
<i>Poisson's ratio of soil</i> ν_s	0.49
<i>Poisson's ratio of the coating material</i> ν_c	0.4~0.48
<i>coating thickness - radius ratio</i> t / r_0	0.05~0.2

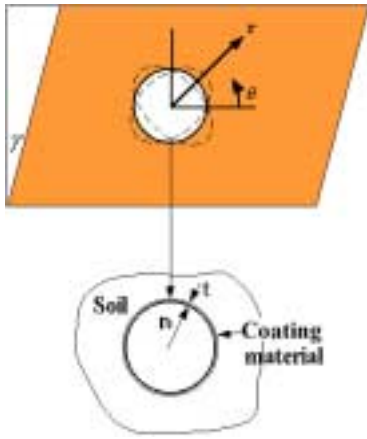


Figure 1 Cylindrical hollow in an unbounded medium under shearing

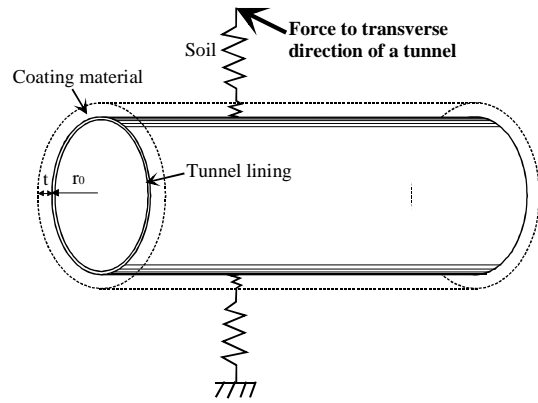


Figure 2 Schematic illustration of three springs in series

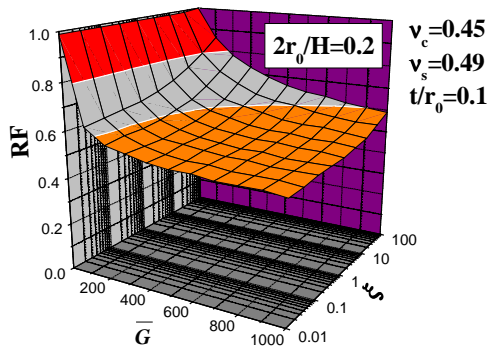


Figure 3 Variation of the reduction factor with \bar{G} and ξ in the case of $\nu_c = 0.45$

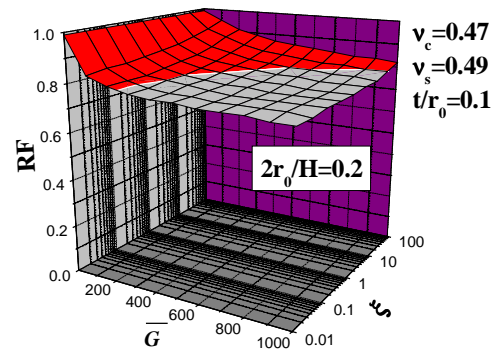


Figure 4 Variation of the reduction factor with \bar{G} and ξ in the case of $\nu_c = 0.47$

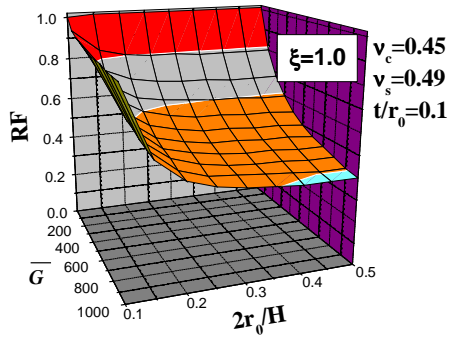


Figure 5 Variation of the reduction factor with \bar{G} and $2r_0/H$ in the case of $\nu_c = 0.45$

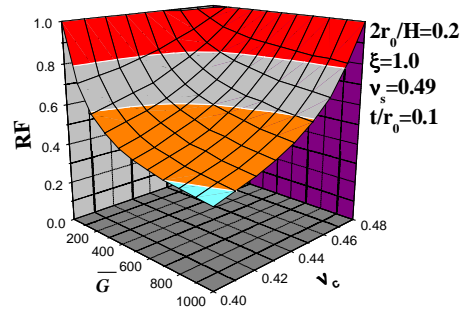


Figure 6 Variation of the reduction factor with \bar{G} and ν_c in the case of $t/r_0 = 0.1$

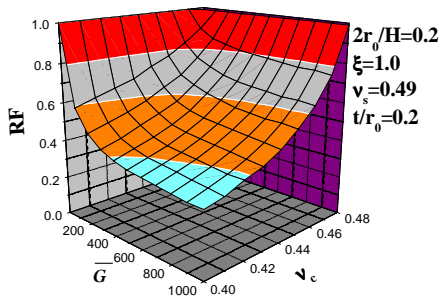


Figure 7 Variation of the reduction factor with \bar{G} and ν_c in the case of $t/r_0 = 0.2$

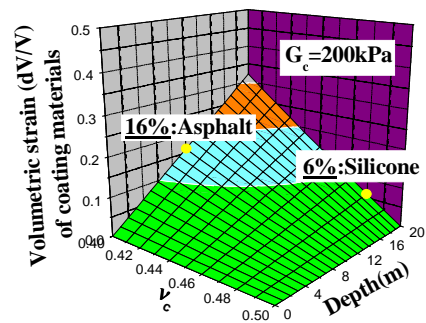


Figure 8 Variation of volumetric strain of coating materials



KEERC-MAE Joint Seminar on
Risk Mitigation for Regions of Moderate Seismicity
University of Illinois at Urbana-Champaign, August 5-8, 2001



Sponsors: Korea Science and Technology Foundation, U.S. National Science Foundation, Brain Korea 21



Scenario Analysis on Economic Impacts of Transportation Network Changes Under Unscheduled Events

Tschangho John KIM¹, Heejoo HAM², David BOYCE³ and Jong Sung LEE⁴

¹ *Professor of Urban and Regional Planning and of Civil Engineering,
University of Illinois at Urbana-Champaign
111 Temple Buell Hall, 611 Taft Drive, Champaign, Illinois, USA
email: t-kim7@uiuc.edu*

² *Research Associate, URS Corporation, Philadelphia*

³ *Professor of Civil and Mechanical Engineering, University of Illinois at Chicago*

⁴ *Ph.D student, Urban and Regional Planning, University of Illinois at Urbana-Champaign
111 Temple Buell Hall, 611 Taft Drive, Champaign, Illinois, USA, jonglee1@uiuc.edu*

ABSTRACT: The damages and losses caused by unscheduled events, especially earthquakes, have sudden and significant impacts not only on the region's economy where the event occurred but also on other regions. New Madrid Seismic Zone, located in the heart of the United States, may have great impacts on economic activities related to this area. Based on the Commodity Flow Survey (1993), a little more than 42% of total commodity flows in the US are related to the Midwest, including this New Madrid Seismic Zone. If a catastrophic earthquake occurs in this area, the indirect damages will spread far beyond the region, and will have sizable impacts in other regions.

This paper aims to estimate and evaluate the economic impacts from a catastrophic earthquake in regional and national contexts, emphasizing inter-industry relationship in conjunction with regional commodity flows as well as the assessment of seismic damages on transportation network. A model of interregional commodity flows, incorporating regional input-output relationships, and the corresponding transportation network flows is implemented for assessing economic impacts from an unexpected event.

Using the above analytical framework, the economic impacts from a catastrophic earthquake are estimated and evaluated based on hypothetical scenarios of the event, analyzing the magnitude and the extent of the direct and indirect impacts. Furthermore, the analytical results may be used to propose strategic managements of the recovery and reconstruction efforts after the event.

Paper to be presented at the 1st Meetings of the KEERC-MAE Seminar, August 6-8, 2001, Champaign, IL. This work was supported primarily by the Earthquake Engineering Research Centers Program of the National Science Foundation under Award Number EEC-9701785.

INTRODUCTION

The damages and losses caused by unscheduled events such as earthquakes, flood, and other major natural disasters, have sudden and significant impacts in region's economy where the event occurred. The impacts of the damages to production facilities and lifelines may spread cross boundaries of several regions via import-export relationships and would bring serious economic impacts on other regions. The economic impacts from unscheduled events stem not only from the damages and losses, but also from the recovery and reconstruction activities. To recover and reconstruct the facilities and lifelines damaged from unexpected events through investment or government financial aid, both direct and indirect economic impacts from the events need to be measured in regional and interregional context. Direct economic impact is the direct change of productions and demands due to the disruption of production facilities and lifelines from an unexpected event, and indirect economic impact is the change of other sectors by the change of a sector based on interindustry relationship.

The Midwest area including the New Madrid Seismic Zone located in the heart of the United States may have a great impact on economic activities related to this area since a little more than 42% of total commodity flows in the US are related to the Midwest. The Midwest economy, including Illinois, Indiana, Iowa, Kentucky, Michigan, Missouri, Ohio, Tennessee, and West Virginia, is probably best known as an economy mainly producing manufacturing goods and agricultural products. What is rarely known is that the inter-state trades within the Midwest are quiet large. According to the paper by Okuyama et al.(1998, 1999) and Kim et al. (1999) which analyzed the commodity flows based on the 1993 Commodity Flow Survey (CFS) data by the Bureau of Transportation Statistics, almost 40% of the outflows (exports) of the aggregated flows among the nine Midwest states go to other Midwest states while about 45% of the inflows (imports) are derived from the same region. The total volume of commodity trade among these nine states is \$417 billion, a value that exceeds trade in all commodities and services for the three members of NAFTA (US, Canada, and Mexico).

If a catastrophic earthquake occurs in the New Madrid Seismic Zone located near Memphis, Tennessee, where the largest earthquakes in the history of the United States took place during the winter of 1811-12, it could damage a transportation network and production facilities within the entire Midwest area. Since the Midwest area creates important economic activities for the commodity trade both inter-state and throughout the US, the indirect impacts from the event will spread far beyond the region through these import-export relationships and will

have sizable impacts in other regions. The analysis of commodity flows among the Midwest states and the estimation of interregional effects through the trade relationship are crucial to evaluate indirect impact from such an event.

This paper focuses on assessing the direct and indirect damages that an earthquake could cause in the New Madrid Seismic Zone located near Memphis, Tennessee, USA. To estimate and evaluate the economic impacts from a catastrophic earthquake in regional and national contexts, a model of interregional commodity flows, incorporating regional input-output relationships, and the corresponding transportation network flows is applied to highway and railway transportation networks. For such a model, this paper uses an interregional commodity flow model developed by Kim et al. (2001). The model integrates the conventional four step-process of transportation planning analysis: trip generation, trip distribution, mode choice and route choice into a single combined model with interregional input-output commodity flow model. Using the model, the economic impacts from a catastrophic earthquake are estimated and evaluated by analyzing the magnitude and the extent of the direct and indirect impacts based on hypothetical scenarios of an unexpected event.

INTERREGIONAL COMMODITY FLOW MODEL AND SOLUTION ALGORITHMS

The interregional commodity flow model considers a multi-state regional economic/input-output consisting of M industrial sectors and producing a like number of commodities, and distributed over R states, including the Rest-of-the-World. One of the classic commodity flow model was originally proposed by Wilson (1970a, 1970b) and Leontief and Strout(1963). This interregional commodity flow model can be integrated with a transportation network model to estimate the interregional and transportation network commodity flows by sector. The commodity flows can be represented by interregional flows between the subregions. These interregional, modal flows may be allocated to routes and links according to a simple least cost criterion, such as minimum distance traveled. Such a model can be formulated as a constrained optimization problem, solved by a partial linearization algorithm, and estimated with 1993 commodity flow data.

The model considers the transportation services and facilities of each mode like truck and railroad. This model minimizes the total costs subjected to several constrains with a material balance, conservations of interregional and route flows, and non-negativity for route flows. This model can be solved using the associated Lagrange multipliers and the algorithms like Evans algorithm applied for combined distribution and assignment model. We assume that exports and imports by commodity for each subregion are given by the regional models, and allocated to the subregional level for the period of analysis which we may take as one year. Our problem is to estimate the flows by sector/commodity between each pair of subregions, and allocate these flows to the transportation network.

Let f_a^w denote the total flow (tons) on link a of the $w \in W$ mode network over a cost (miles) of $d_a^w(f_a^w)$, link performance function by mode w , and let h_{ijr}^{mw} denote the flow (tons) of output of sector $m \in M$ from region $i \in I$ to region $j \in J$ on route $r \in R_{ij}$ by mode w . Also, let x_{ij}^{mw} denote the flow (\$) of the output of sector m from region i to region j by mode w . On the assumption that shippers prefer to hold their transportation costs as low as possible, subject to the dispersion of flows represented by the entropy constraint, we define the interregional commodity flow model developed by Kim et al. (2001) as follows:

$$\begin{aligned} \min_{\mathbf{h}, \mathbf{x}} \quad Z(\mathbf{h}, \mathbf{x}) = & \sum_{aw} \int_0^{f_a^w} d_a^w(\omega) d\omega + \sum_{mjw} \left(\frac{x_{ij}^{mw}}{g^m} \right) d_{ij}^w + \sum_m \frac{1}{\alpha^m g^m} \sum_{ijw} x_{ij}^{mw} \ln \left(\frac{x_{ij}^{mw}}{x_{ij}^m} \right) \\ & + \sum_m \frac{1}{\beta^m g^m} \sum_{ij} x_{ij}^m \ln \left(\frac{x_{ij}^m}{\bar{X}_i^m} \right) \end{aligned} \quad (1)$$

$$s.t. \quad \sum_i x_{ij}^m = \sum_n a^{mn} \sum_k x_{jk}^n + y_j^m \quad \text{for all } m, j \quad \text{Material balance} \quad (2)$$

$$\sum_w x_{ij}^{mw} = x_{ij}^m \quad \text{for all } m, i, j \quad \text{Conservation of OD flow} \quad (3)$$

$$\sum_r h_{ijr}^{mw} = \frac{x_{ij}^{mw}}{g^m} \quad \text{for all } m, i, j, w \quad \text{Conservation of route flow} \quad (4)$$

$$h_{ijr}^{mw} \geq 0 \quad \text{for all } m, r, i, j, w \quad \text{Non-negativity} \quad (5)$$

where the exogenous variables are:

a^{mn} = technical input-output coefficient representing the inputs from sector m required to make one unit of output of sector n

α^m = cost sensitivity parameter for sector m

β^m = cost sensitivity parameter for sector m

g^m = factor for converting sector m from dollars to tons (\$/ton)

\bar{X}_i^m = total estimated output of sector m in region i (\$)

y_j^m = final demand (consumption, investment and government expenditures) for sector m in region j (\$)

The endogenous variables are:

$d_a^w(f_a^w)$ = distance function of total flow on link a by mode w (miles)

d_{jj}^w = intraregional distance for region j by mode w (miles)

f_a^w = total flow on link a by mode w (tons)
 $= \sum_m \sum_{ijr} h_{ijr}^{mw} \phi_{ijr}^{aw}$

ϕ_{ijr}^{aw} = 1 if link a belongs to route r from region i to region j by mode w , and 0 otherwise

h_{ijr}^{mw} = flow of output of sector m from region i to region j on route r by mode w (tons)

x_{ij}^m = flow of the output of sector m from region i to region j (\$)

x_{ij}^{mw} = flow of the output of sector m from region i to region j by mode w (\$)

\mathbf{h} = vector of route flows

\mathbf{x} = vector of interregional flows

The total cost to be minimized in the system is constituted with summing the network assignment costs by mode, intraregional travel costs, origin-destination flow distribution costs, and origin-destination flow distribution costs by mode. Then the model estimates the commodity flows of links by mode, routes by mode, and origin-destination by mode for each sector as a result of the dispersion of commodity flows among regions and choices of minimum cost travel routes. Using Lagrange multipliers, the commodity flow form and the composite cost function are derived as follows:

$$x_{ij}^{mw} = \bar{X}_i^m \delta_i^m \varepsilon_j^m \exp(-\beta^m \tilde{c}_{ij}^m) \frac{\exp(-\alpha^m \mu_{ij}^{mw})}{\sum_w \exp(-\alpha^m \mu_{ij}^{mw})} \quad \forall mwij, i \neq j \quad (6)$$

where,

$$\delta_i^m = \exp(-\beta^m g^m \sum_l \gamma_l^l a_i^{lm} - 1.0) \quad \forall mi \quad (7)$$

$$\varepsilon_j^m = \exp(\beta^m g^m \gamma_j^m) \quad \forall mj \quad (8)$$

$$\tilde{c}_{ij}^m = -\frac{1}{\alpha^m} \ln \left\{ \sum_w \exp(-\alpha^m \mu_{ij}^{mw}) \right\} \quad \forall mij, i \neq j \quad (9)$$

γ_j^m = Lagrange multiplier

μ_{ij}^{mw} = Lagrange multiplier (equilibrium unit of shipment cost)

δ_i^m = balancing factor for sector m in subregion i

ϵ_j^m = balancing factor for sector m in subregion j

\tilde{c}_{ij}^m = composite cost of sector m from subregion i to subregion j

In this paper, Evans' (1976) algorithm is used to solve the model. Evans' algorithm includes both Wilson's (1970a, 1970b) iterative balancing method to generate the interregional commodity flows and the All-or-Nothing method to find the transportation network commodity flows in the subproblems. The convergence of Wilson's iterative balancing method can be judged by the relative error between the observed and estimated final demands for each sector and each subregion, or the relative change of balancing factors. In this paper, the former convergent criterion is used with 0.001 as the acceptance stopping value. The commodity flows estimated in the subproblem of the model are used to find an optimal solution in one dimensional line search in Evans' algorithm. The parameters in the model are estimated using the observed interregional commodity flows.

RESULTS OF COMMODITY FLOWS ESTIMATED BY THE MODEL

The model produced a variety of the estimated commodity flow results that include origin amounts (production) and destination amounts (attraction) of shipment, flow distributions (interregional and intraregional flows), shipments by mode, transportation network flows for highway and railway links, and total and mean shipment lengths. The commodity flows for sector 3 (Construction) and sector 13 (Services) are excluded from representing the results in the following tables and figures because they are assumed to produce and consume only locally. The total commodity flows by sector are compared between the observed and estimated in Table 1. Estimated share by sector for sectors 5, 6, 7, 9, and 12 have almost no difference to the observed shares.

Table 1 Total Commodity Flows by Sector (\$billion, %)

Sector	Observed		Estimated		Rate Diff*
	Flow	Share by sector	Flow	Share by sector	
1	121.56	2.86	264.06	6.73	-3.87
2	39.63	0.93	206.58	5.26	-4.33
4	814.65	19.15	521.08	13.28	5.87
5	460.67	10.83	398.59	10.16	0.67
6	185.17	4.35	153.48	3.91	0.44
7	211.04	4.96	149.12	3.80	1.16
8	338.85	7.97	200.02	5.10	2.87
9	323.37	7.60	340.31	8.67	-1.07
10	460.55	10.83	302.96	7.72	3.11
11	801.94	18.85	992.01	25.27	-6.42
12	496.67	11.68	396.77	10.11	1.57
Total	4254.09	100.00	3924.98	100.00	

Remark : * = Difference between the observed rate and the estimated rate

The model also estimated the commodity flows using two modes of transportation: highway and railway. As shown in Table 2, the mode share patterns between the observed and estimated are within the error margin less than 10% for most sectors.

Table 3 shows the commodity shipment results by mode between the Midwest region and other regions. The mode share rates from regions 6 and 7 (furthest from the Midwestern regions) to the Midwestern regions by railway are as high as 74% and 68%, respectively. Likewise, the share by railway to those regions from the Midwestern regions are 76% and 77%, respectively, indicating that the shipment modes are selected by the model based on the travel distance. In fact, the distance is the most important variable in the utility functions for mode choice as describe before. The longer distance commodities to be shipped, the higher shipment costs, and thus the choice has been the railway for shipping commodities for longer distance.

Table 2 US Commodity Flows by Mode by Sector

Sector	Highway				Railway			
	Flow (\$billion)	Flow Rate (%)	Mode Rate (%) ^a	Mode Rate (%) ^b	Flow (\$billion)	Flow Rate (%)	Mode Rate (%) ^a	Mode Rate (%) ^b
1	166.74	5.43	63.14	72.15	97.32	11.41	36.86	27.85
2	144.20	4.69	69.81	49.04	62.38	7.31	30.19	50.96
4	455.73	14.83	87.46	96.01	65.36	7.66	12.54	3.99
5	307.07	10.00	77.04	87.35	91.52	10.73	22.96	12.65
6	131.09	4.27	85.42	89.62	22.38	2.62	14.58	10.38
7	132.00	4.30	88.51	96.94	17.13	2.01	11.49	3.06
8	142.76	4.65	71.37	90.04	57.26	6.71	28.63	9.96
9	278.26	9.06	81.76	97.75	62.06	7.28	18.24	2.25
10	207.73	6.76	68.57	81.71	95.23	11.17	31.43	18.29
11	843.98	27.47	85.08	90.06	148.03	17.35	14.92	9.94
12	262.46	8.54	66.15	93.97	134.30	15.75	33.85	6.03
Total	3072.02	100.00	78.27	90.30	852.96	100.00	21.73	9.70

Remark : a = Mode rate for estimated commodity flow

b = Mode rate for observed commodity flow

Table 3 Commodity Flow by Mode between the Midwest (MW) and Other Region

From Region	To Region	Highway			Railway		
		Flow (\$billion)	Flow Rate (%)	Mode Rate (%)	Flow (\$billion)	Flow Rate (%)	Mode Rate (%)
1	MW	26.64	8.70	83.67	5.20	4.89	16.33
2	MW	94.24	30.77	85.23	16.33	15.36	14.77
3	MW	94.08	30.72	85.32	16.19	15.23	14.68
4	MW	42.15	13.76	80.49	10.21	9.61	19.51
5	MW	25.96	8.48	77.12	7.70	7.24	22.88
6	MW	2.27	0.74	25.96	6.49	6.10	74.04
7	MW	20.91	6.83	32.12	44.20	41.57	67.88
Total		306.26	100.00	74.23	106.33	100.00	25.77
MW	1	55.79	8.16	82.33	11.98	4.38	17.67
MW	2	204.16	29.84	87.21	29.94	10.96	12.79
MW	3	148.29	21.67	89.59	17.24	6.31	10.41
MW	4	120.92	17.67	80.45	29.38	10.75	19.55
MW	5	114.83	16.78	69.65	50.04	18.31	30.35
MW	6	9.77	1.43	24.08	30.80	11.27	75.92
MW	7	30.40	4.44	22.64	103.84	38.01	77.36
Total		684.16	100.00	71.46	273.20	100.00	28.54

MODEL APPLICATIONS

The model can be applied to analyze the economic impacts of an unexpected event, an earthquake, with hypothetical scenarios in the New Madrid Seismic Zone. If a transportation network is damaged from an earthquake, the model estimates interregional economic impacts on regional commodity flows in conjunction with inter-industry relationships. As the measure of the economic impacts, the paper considers various values such as the objective function value, the mean shipment length, and commodity flows estimated from the model. Five scenarios as in Figure 1 are analyzed and evaluated. It is assumed that the highway network sections related to the scenarios have been disrupted by a catastrophic earthquake event.

Scenario A : Section between Chicago, IL and Gary, IN on I-94

Scenario B : Section between Louisville, KY and Nashville, TN on I-65

Scenario C : Section between Little Rock, AR and Nashville, TN on I-40

Scenario D : Sections of Scenario B and Scenario C

Scenario E : Sections of Scenario A, Scenario B, and Scenario C

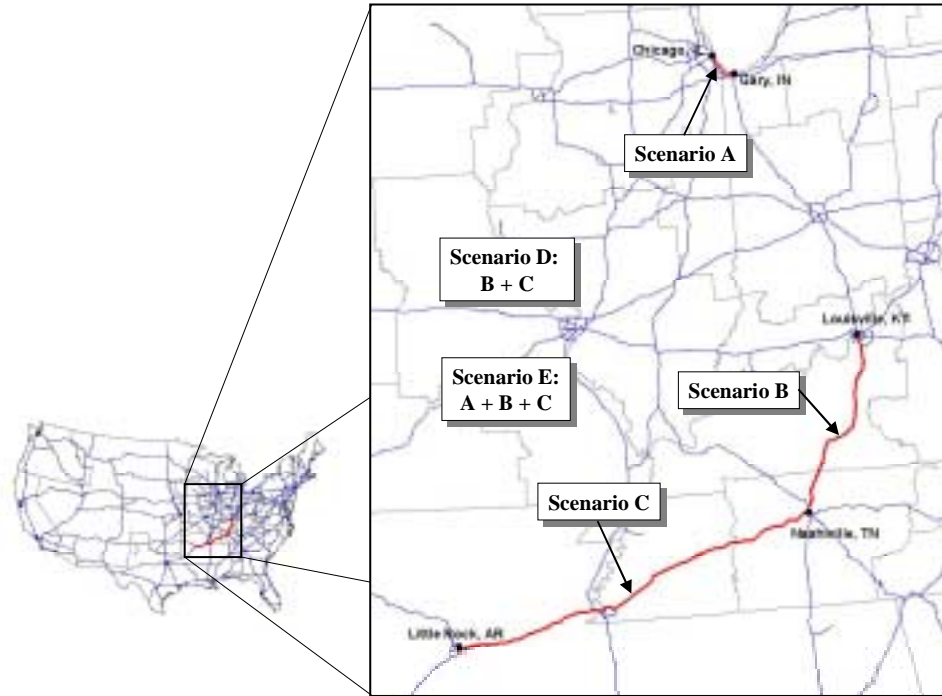


Figure 1 Locations of the Disrupted Highway Sections Analyzed with Scenarios

The interstate highway I-94 on Scenario A is located at a distance from the New Madrid Seismic Zone. The paper however considers it to evaluate the impacts due to the disruption of the section since the section is one of the important highway sections having a large shipment of commodity flows. The interstate highway I-65 on Scenario B and the interstate highway I-40 on Scenario C are located near New Madrid Seismic Zone within the Midwest region. Both Scenario D and Scenario E consider the worst situations due to the disruptions of more than two sections of the interstate highways.

The measures estimated from the model for the case *without* the event are compared with those for the cases *with* the events from the scenarios. Table 4 analyzes the changes of the objective function values and the mean shipment lengths. As shown in Table, the objective function values and the mean shipment lengths are increased consistently for all scenarios due to disruptions of transportation network sections. In scenario A, the objective function value is increased to \$3896.48 billions, a difference of \$12.17 billions, and the mean shipment lengths are also increased to \$519.64 billions in highway, a difference of \$15.17 billions, and \$1181.14 billions in railway, a difference of \$26.56 billions. The values measured on Scenario B and Scenario C are also increased due to an unexpected event, but the impacts on Scenario B and Scenario C are smaller than on Scenario A. Thus, it can be said that I-94 as considered in Scenario A involves more economic activities than I-65 in Scenario B and I-40 in Scenario C. The values measured on Scenario D and Scenario E are increased more than those of the previous scenarios due to the combination of the scenarios.

The changes of the objective function values are less than 1% as the range from 0.22% to 0.75%, but it cannot be said that the economic impacts are insignificant since they have

impacts on the whole system in the US. In addition, even if the mean shipment lengths are increased in the maximum 40 miles, the changes of the mean lengths are also significant when considered in the whole network system. In particular, these impacts should be evaluated with other changes related with the commodity flows compared in Table 5. These rates and values may be used as both the information to mitigate possible damages before an earthquake event and the strategies of recovery and reconstruction after the earthquake event.

Table 4 Changes of Objective Function Value and Mean Shipment Length by Mode for Scenarios

Scenario	List		Without Event	With Event	Difference	Rate(%)
A	Objective Function ($\times 10^3$)		3884.31	3896.48	12.17	0.31
	Mean Length (mile)	Highway	504.47	519.64	15.17	3.01
		Railway	1154.68	1181.24	26.56	2.30
B	Objective Function ($\times 10^3$)		3884.31	3893.00	8.69	0.22
	Mean Length (mile)	Highway	504.47	510.01	5.54	1.10
		Railway	1154.68	1162.26	7.58	0.66
C	Objective Function ($\times 10^3$)		3884.31	3894.17	9.87	0.25
	Mean Length (mile)	Highway	504.47	506.72	2.25	0.45
		Railway	1154.68	1155.30	0.62	0.05
D	Objective Function ($\times 10^3$)		3884.31	3901.29	16.98	0.44
	Mean Length (mile)	Highway	504.47	513.37	8.90	1.76
		Railway	1154.68	1165.86	11.18	0.97
E	Objective Function ($\times 10^3$)		3884.31	3913.43	29.12	0.75
	Mean Length (mile)	Highway	504.47	529.86	25.39	5.03
		Railway	1154.68	1194.62	39.94	3.46

The model estimated the commodity flows by considering two transportation networks for highway and railway. In particular, the model analyzes the flow generation, flow OD distribution, mode choice, and flow assignment together. Thus, with the specific conditions, the commodity flow results are very transferable. That is, when the highway shipment costs are increased highly due to the disruption of the highway sections, some commodity flows using the highway transfer to the railway with its lower shipment costs. In addition, under the same situation some commodity flows transfer to the intraregions rather than shipping to other regions. These phenomena in the model reflect the commodity flow patterns in the real world.

Table 5 Changes of Commodity Flows for Scenarios (\$billion)

Scenario	List of Commodity Flow	Without Event	With Event	Difference	Rate(%)
A	Interregional	2863.80	2856.59	-7.21	-0.25
	Intraregional	1061.19	1068.40	7.21	0.68
	Total Highway OD	3064.95	3061.82	-3.13	-0.10
	Total Railway OD	860.04	863.17	3.13	0.36
B	Interregional	2863.80	2857.97	-5.83	-0.20
	Intraregional	1061.19	1067.01	5.83	0.55
	Total Highway OD	3064.95	3063.14	-1.81	-0.06
	Total Railway OD	860.04	861.84	1.81	0.21
C	Interregional	2863.80	2852.42	-11.38	-0.40
	Intraregional	1061.19	1072.57	11.38	1.07
	Total Highway OD	3064.95	3055.94	-9.00	-0.29
	Total Railway OD	860.04	869.04	9.00	1.05
D	Interregional	2863.80	2846.45	-17.35	-0.61
	Intraregional	1061.19	1078.53	17.35	1.63
	Total Highway OD	3064.95	3054.40	-10.55	-0.34
	Total Railway OD	860.04	870.58	10.55	1.23
E	Interregional	2863.80	2839.10	-24.70	-0.86
	Intraregional	1061.19	1085.89	24.70	2.33
	Total Highway OD	3064.95	3051.26	-13.68	-0.45
	Total Railway OD	860.04	873.72	13.68	1.59

Table 5 shows the changes of the commodity flows due to the disruption of the transportation network section for each scenario. In Scenario A, the total interregional commodity flows without the event were \$2863.80 billions, but they are decreased to \$2856.59 billions with the event. The interregional commodity flows as much as \$7.21 billions are transferred to the intraregional commodity flows because of the increasing the shipment costs in highway due to the disruption of the highway network section. In addition, the total OD commodity flows by the highway mode are converted as much as \$3.13 billions to the railway mode for the same reason. Even though Scenario C has fewer impacts for the objective function value as well as the mean shipment length in Table 5 than Scenario A, both the interregional commodity flows (\$11.38 billions) and the total OD commodity flows (\$9.0 billions) by highway of Scenario C are converted more than Scenario A as shown in Table 5. As the worst case among five scenarios, Scenario E converts the most commodity flows to the intraregions and the railway mode as \$24.7 billions and \$13.68 billions, respectively.

REFERENCES

1. Brookshire, D.S., S.E. Chang, H. Cochrane, R.A. Olson, A. Rose and J. Steenson, (1997) Direct and indirect economic losses from earthquake damage, *Earthquake Spectra* 13(4), 683-701.
2. Chang, S.E., (1998) Direct economic impacts, Chapter 6 in Shinozuka, M., and Eguch, R.T. (eds.) *Engineering and Socioeconomic Impacts of Earthquakes: An Analysis of Electricity Lifeline Disruptions in the New Madrid Area*, Multidisciplinary Center for Earthquake Engineering Research, Buffalo, NY, 75-94.
3. Cho, S., P. Gordon, J.E. Moore, H.W. Richardson, M. Shinozuka and S. Chang, (1999) Integrating transportation network and regional economic models to estimate the costs of a large urban earthquake, *Paper presented at the RSAI meetings*, Montreal, Canada.
4. Cochrane, H. C. (1997) Forecasting the Economic Impact of a Midwest Earthquake, in Barclay G. Jones ed. *Perspectives on Mitigating the Impact of Earthquakes on the Economy*, National Center for Earthquake Engineering Research, 223-247.
5. Cole, S., (1998) Decision support for calamity preparedness: Socioeconomic and interregional impacts, Chapter 8 in Shinozuka, M., Rose, A. and Eguch, R.T. (eds.) *Engineering and Socioeconomic Impacts of Earthquakes: An Analysis of Electricity Lifeline Disruptions in the New Madrid Area*, Multidisciplinary Center for Earthquake Engineering Research, Buffalo, NY, 125-153.
6. Evans, S. P. (1976) Derivation and Analysis of Some Models for Combining Trip Distribution and Assignment, *Transportation Research*, 10, 37-57.
7. Kim, T. J., D. E. Boyce, H. Ham, and Y. Okuyama (1999) Implementation of an Integrated Transportation Network and Input-Out Model for Assessing Economic Impacts of Unexpected Events : A Solution Algorithm and Issues, paper presented at the *Annual Meetings of the North American Regional Science Association*, May 7-8, Ithaca, N.Y.
8. Kim, Tschangho J., H. Ham, and D.E. Boyce (2001) Implementation of a Combined Trip Generation, Mode Choice, Flow Distribution and Route Choice Model for Interregional Commodity Flows.
9. Leontief, W. W. and A. Strout (1963) Multiregional Input-Output Analysis, in T. Barna (ed.) *Structural Interdependence and Economic Development*, Macmillan, London.
10. Miyazawa, K. (1976) *Input-output Analysis and the Structure of Income Distribution*, New York, NY, Springer-Verlag.
11. Okuyama, Y., G. J.D. Hewings, and M. Sonis (1997) Economic Impacts of an Unscheduled Event: Interregional Analysis Based on Miyazawa's Framework, *Journal of Applied Regional Science*, 2, 79-93.

12. Okuyama, Y., G. J.D. Hewings, T. J. Kim, D. E. Boyce, H. Ham, and J. Sohn (1998) Economic Impacts of an Earthquake in the New Madrid Seismic Zone: A Multiregional Analysis, paper presented at the 45th North American Meetings of Regional Science Association International, Nov. 11-14, Santa Fe, N.M.
13. Okuyama, Y., G. J.D. Hewings, T. J. Kim, D. E. Boyce, H. Ham, and J. Sohn (1999) Economic Impacts of an Earthquake in the New Madrid Seismic Zone: An Overview, paper presented at the Annual Meetings of the North American Regional Science Association, May 7-8, Ithaca, N.Y.
14. Rose, A. and J. Benavides (1998) Regional Economic Impacts, in Masanobu Shinozuka, Adam Rose, and Ronald T. Eguchi (eds.) *Engineering and Socioeconomic Impacts of Earthquakes*. Multidisciplinary Center for Earthquake Engineering Research, Buffalo, 95-123.
15. Rose, A., J. Benavides, S. E. Chang, P. Szczesniak, and D. Lim (1997) The Regional Economic Impact of an Earthquake: Direct and Indirect Effects of Electricity Lifeline Disruptions. *Journal of Regional Science*, 37 (3), 437-458.
16. Wilson, A. G. (1970a) Interregional Commodity Flows: Entropy Maximizing Procedures, *Geographical Analysis*, 2, 255-282.
17. Wilson, A.G. (1970b) *Entropy in Urban and Regional Modelling*. London, Pion.



KEERC-MAE Joint Seminar on
Risk Mitigation for Regions of Moderate Seismicity
University of Illinois at Urbana-Champaign, August 5-8, 2001



Sponsors: Korea Science and Technology Foundation, U.S. National Science Foundation, Brain Korea 21



Evaluation of Dynamic Pile Group Effect by Shaking Table Tests

S. R. KIM¹, I. S. HA², and M. M. KIM³

¹ *Graduate Student, Seoul National University, Seoul, South Korea
email: yawndful@hananet.net*

² *Graduate Student, Seoul National University, Seoul, South Korea
email: molafrog@snu.ac.kr*

³ *Professor, Seoul National University, Seoul, South Korea
email: geotech@gong.snu.ac.kr*

ABSTRACT: We performed shaking table tests on model pile groups to investigate the mechanics of dynamic pile-soil interactions, and to evaluate the dynamic pile group effect. Tests are executed on a single pile and group piles(3×3) varying the pile spacing from three to eight times the pile diameter. A mass was located on top of the piles to simulate a superstructure. Dynamic p-y curves of the single pile and the group piles were obtained from the tests and compared with the backbone slopes of API cyclic p-y curves. From these comparisons, dynamic pile group effects were evaluated in terms of pile depth, shaking frequency, and shaking intensity.

KEYWORDS: Dynamic pile group effects, Shaking table tests, dynamic pile-soil interaction, dynamic p-y curve

INTRODUCTION

The group piles under dynamic loads are believed to exhibit some softening behavior due to pile-soil interactions. This group pile effect is a function of the characteristics of shakings, soils, piles, and pile arrangements.

Finn & Gohl(1992) investigated the influence of pile spacing on the pile group effect using shaking table tests on a single pile and 2×2 group piles embedded in a dense sand layer. They analyzed the test results using SPASM8(Matlock et al., 1979), and noted that the dynamic pile group effect is expected to be negligible when the center-to-center pile spacing is larger than 6D(six times the pile diameter).

Dou & Byrne(1996) adopted the hydraulic similitude technique to run a shaking table test on a single pile in dense sands and obtained the experimental p-y curves from the moment distribution curves using simple beam theory, from which they observed that the API p-y curves underestimate soil resistance at shallow depths in the case of strong shakings.

In this research, 1-g shaking table tests were performed on a single pile and group piles(3×3) embedded in dense sands, to evaluate the dynamic pile group effect. To this end, experimental p-y curves were obtained from the test results using simple beam theory, and compared with API p-y curves.

SHAKING TABLE TEST PROGRAMS

A test box was made of 2.0cm thick plexi-glass, of length 1.5m, width 1.0m and depth 0.7m. The minimum distance between the sidewall of the test box and the pile shaft was 63D, so that friction between the walls and the soils was negligible. 5.5cm thick sponges were attached to the inside faces of the box to reduce the rigid boundary effects, and sandpaper was attached to the bottom of the box to prevent slip between soils and the bottom of the test box.

Hollow aluminum pipes were used as model piles. The physical properties of the model piles were: outer diameter 14mm, thickness 1mm, and length 70cm. The flexural rigidity (EI) of the pipes was $6.19 \times 10^5 \text{ N}\cdot\text{cm}^2$, and their elastic modulus(E) 70Gpa. The embedded pile length was 60cm on average.

Pile tips were inserted in the test box to prevent rotation and translation. Piles were bolted to the pile cap, which was designed to arrange the center-to-center pile spacing to 3, 6, or 8 pile diameters. A mass was placed on top of piles to simulate the inertial force caused by a superstructure. In the case of a single pile, the weight of the lumped mass was 0.86kg and therefore, for 3×3 group piles, the total superstructure weight was 7.7kg(0.86kg×9 piles).

In total, 36 strain gauges, 4 accelerometers, and 2 LVDTs were instrumented, as shown in Figure 1. Strain gauges were attached to the outside of the piles to obtain the time varying

moment distribution curves along the pile shafts. The strain gauge wires were fed through holes to the pile interior. In the case of group piles, three selected piles were instrumented. Instrumented piles had 6 pairs of strain gauges placed at a depth of 0, 5, 10, 17.5, 25 and 40 cm from the ground surface. In this paper, discussions are made upon the data obtained from the center pile.

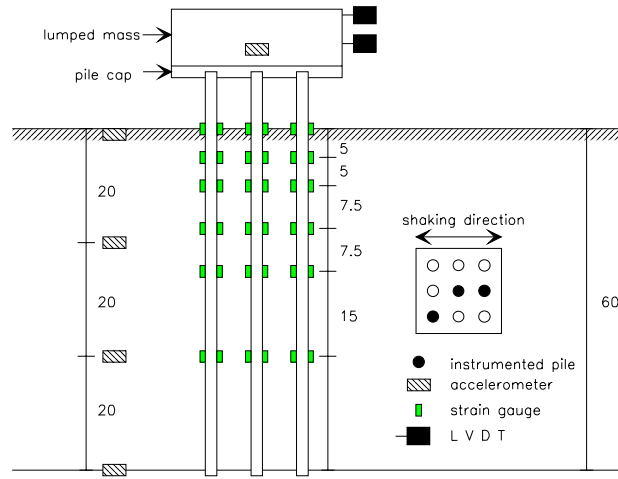


Figure 1 Schematic drawing of test set-up

The accelerometers were installed at the center of gravity of the superstructure mass to measure the inertial force acting on the piles, and at various depths in the free field to measure the ground acceleration response. Two LVDTs were installed to measure the lateral displacement and rotation of the superstructure mass.

The average particle size of the model sands (D_{50}) used was 0.58mm (with a coefficient of uniformity (c_u) of 1.68) and the maximum and the minimum dry densities of the sand are 1.66 ton/m^3 and 1.33 ton/m^3 , respectively. Dense sand ground was formed by vibration compaction. The piles were positioned according to the desired center-to-center pile spacing, which were fixed to the pile cap to prevent relative displacement during vibration. Model grounds were compacted using a sine wave of frequency 20Hz and amplitude 0.4g for 4 minutes after the sands were poured into the box. The compaction process was repeated 7 times, and each time, the same weight of sands were poured into the test box. The relative density of the sand ground was 70% in average. After each test, ground settlement was measured, and the residual density of the ground was recalculated. The change in the density of the ground before and after testing was minimal.

The center-to-center pile spacings of 3x3 pile groups were 3D, 6D and 8D. The frequency of the input acceleration varied from 5 to 20Hz, and the amplitude of the peak acceleration from 0.1g to 0.4g.

EXPERIMENTAL P-Y CURVES

Experimental p-y curves at a set times was obtained from moment distribution curves along the pile shafts, using simple beam theory. Pile deflection y_{pile} was obtained by double integration of the moment distribution curve, and soil resistance p by double differentiation, as shown in Equation 1.

$$y_{pile} = \iint \frac{M(z)}{EI} dz, \quad p = \frac{d^2 M(z)}{dz^2} \quad (1)$$

where EI=flexural rigidity, M(z)=bending moment at the depth of z.

Measured bending moments were only determined at certain discrete locations so that a curve-fitting technique was necessary to obtain the continuous data of pile deflection and soil resistance. In this research, the cubic spline fitting method of Yan & Dou (1991) was used. The noises in moment data were removed by bandpass filtering. The following constraints were imposed on the fitting process, the absence of translation or rotation at the pile tip, and that the soil resistance at the soil surface is zero. By doubly integrating and differentiating the fitted curves, p and the y_{pile} were obtained.

The y of the p-y curve represents the relative displacement between soil and pile. Therefore, the soil displacement around the pile y_{soil} must be subtracted from y_{pile} to obtain y. Values for y_{soil} can be obtained by doubly integrating to acceleration data at each depth in the free field. The determine value of y_{soil} was, however, almost the same as the input displacement of the shaking table, thus y_{soil} was neglected in this study.

TEST RESULTS

The Experimental p-y Curves of A Single Pile

Figure 2 shows experimental p-y curves at depths of 5cm, 10cm and 17.5cm. The frequency of the input accelerations was 5Hz, and the amplitude of these accelerations varied from 0.2g to 0.4g. The experimental p-y curves were obtained from the oscillation cycle, when the amplitude of the input acceleration stabilized. In the same figure, the backbone slopes of API recommended cyclic p-y curves are shown, these were computed using a peak friction angle of 38° and the soil modulus parameter k of 61,000 kN/m³, as recommended for dry dense sands. It can be seen that the API p-y curves are in relatively good agreement with the experimental curves for all depths for low to mid acceleration levels (0.2g-0.3g). In the case of 0.4g peak acceleration, however, the cyclic curves were softer than those deduced from the experiments. It was noticed in the experimental curves that the hysteresis loop became larger as the peak input acceleration increased or the soil depth became shallower, which may reflect higher energy dissipation under these conditions.

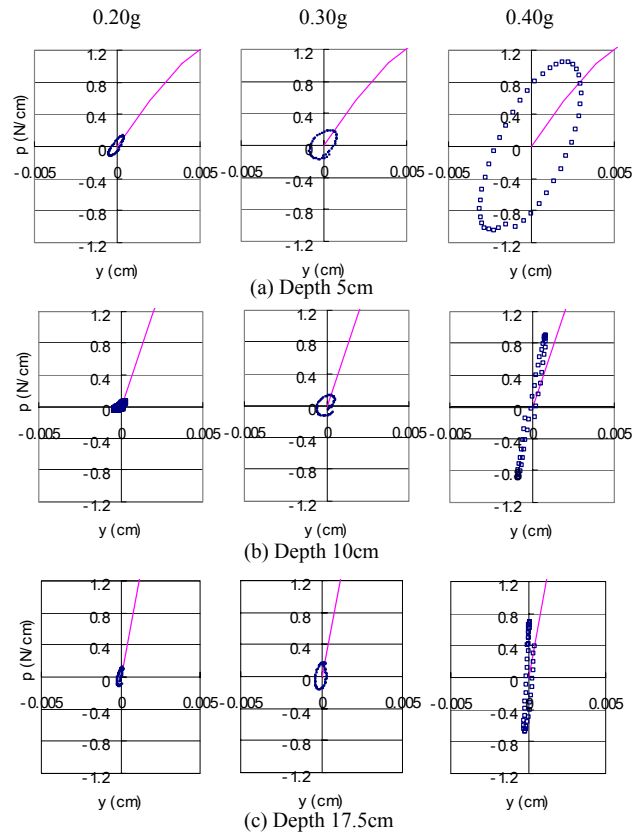


Figure 2 Experimental p-y curves of a single pile (input frequency: 5Hz)

The Experimental p-y Curves of Group Piles

The influence of the amplitude of input accelerations

Figure 3 shows the experimental p-y curves of group piles at various levels of peak input accelerations at depths of 5cm, 10cm and 17.5cm. The center-to-center pile spacing was $3D$, and the frequency of the input acceleration was 5Hz. At shallow pile depth with a 5cm ($3.5 \times$ pile diameter), the group pile effect was apparent even under conditions of relatively low acceleration (0.2g). The experimental p-y curves became softer than the API curves which represent the behavior of single piles. At the depth of 10cm, the group pile effect was apparent for during tests conducted at medium to high levels of acceleration (0.3g-0.4g), while it appeared only at high acceleration levels (0.4g) at a depth of 17.5cm ($14.5 \times$ pile diameter).

Brown et al.(1988) suggested the p multiplier factor concept to obtain the p - y curve of group piles from the p - y curve of a single pile. Table 1 shows p multiplier factors obtained from the p - y curves in Figure 3. The p multiplier factors were determined by dividing the slope of an experimental p - y curve by the backbone slope of the API p - y curve. The maximum value of the p multiplier factors was set as one; a multiplier factor of less than one means that the group piles behaves in a softer manner than a single pile. As the peak input acceleration were increased, or the soil depth decreased, the p multiplier factor decreased due to incremental pile group effects.

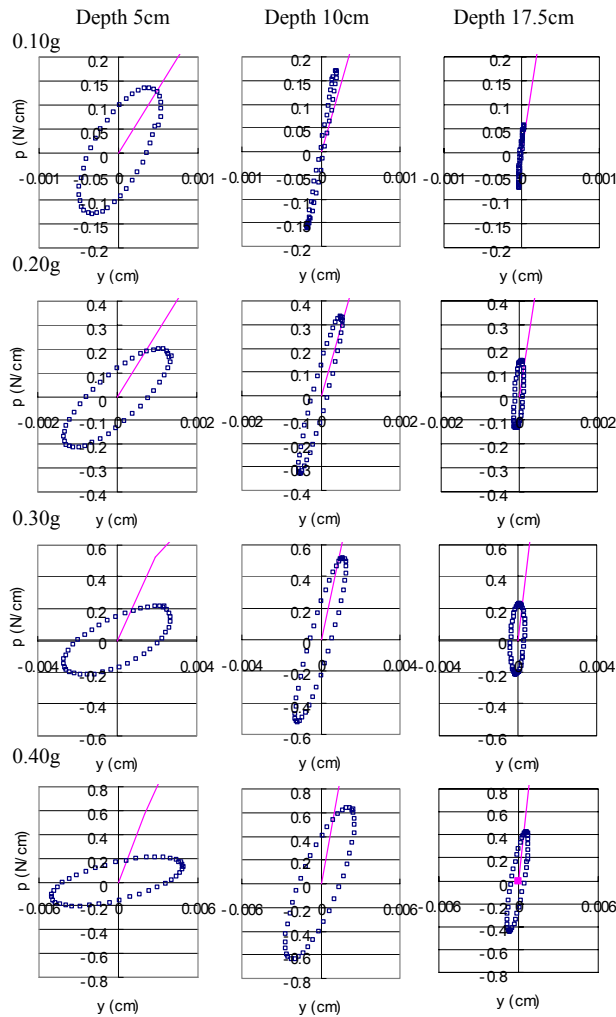


Figure 3 Experimental p - y curves of group piles for various levels of peak accelerations ($s=3D$, input exciting frequency: 5Hz)

Table 1 p multiplier factors

Amplitude of Input accelerations	P multiplier factor		
	Depth 5cm	Depth 10cm	Depth 17.5cm
0.1g	1.00	1.00	1.00
0.2g	0.54	1.00	1.00
0.3g	0.32	0.70	1.00
0.4g	0.20	0.44	0.60

The influence of the frequency of input accelerations

Figure 4 shows the p-y curves for various frequencies of input accelerations. The amplitude of the peak base acceleration was 0.20g, and the frequency of the input acceleration varied from 5Hz to 20Hz. It was observed that the maximum pile deflections(y) and the maximum soil reactions(p) increased as the acceleration frequency increased toward the natural frequency of the pile-soil system which was estimated to be around 20Hz by sweep testing.

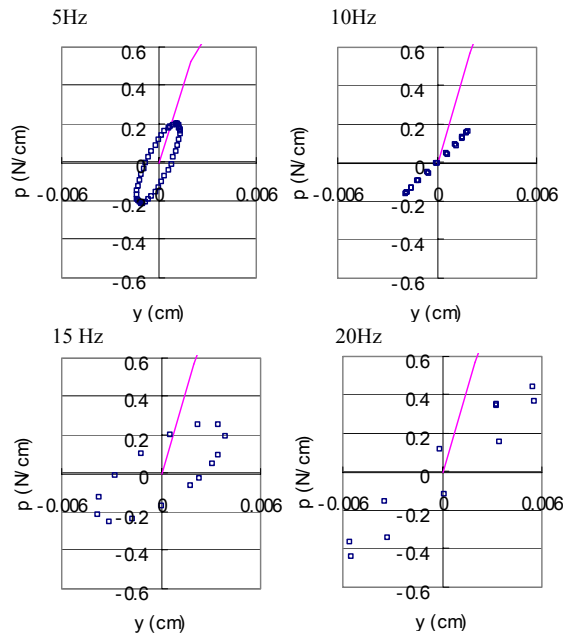


Figure 4 Experimental p-y curves of group piles for different input acceleration frequencies (s=3D, Depth: 5cm, peak acceleration: 0.20g)

The influence of the center-to-center pile spacing

Figure 5 shows the p-y curves (measured at center piles) for different center-to-center pile spacings. The amplitude and the frequency of input acceleration were 0.4g and 5Hz, respectively. At a pile spacing of 3D, the group effect was clearly observed from the softened experimental p-y curves compared with the backbone slope of the API cyclic p-y curves. At pile spacings of 6D and 8D, however, the group pile effects did not appear. Therefore, it could be said that group piles with larger pile spacings than 6D do not experience the group pile effect.

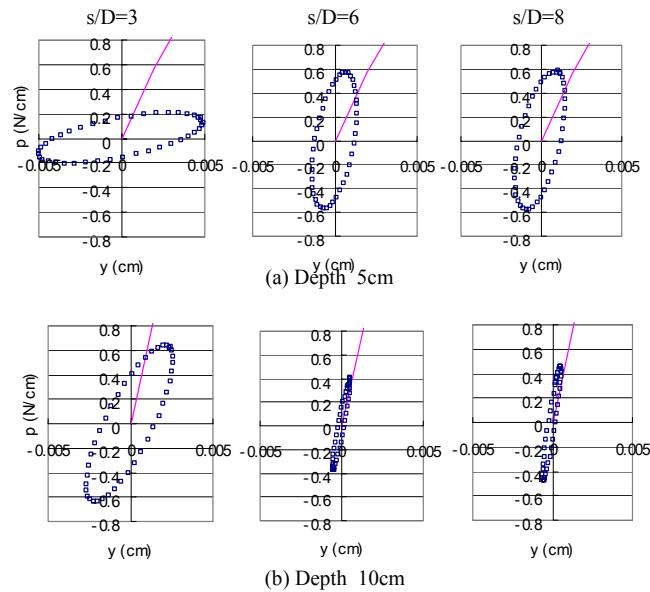


Figure 5 Experimental p-y curves of group piles (input acceleration: 5Hz, 0.40g)

APPLICATION OF EXPERIMENTAL P-Y CURVES

The nonlinear response of a pile to lateral loading can be computed in terms of moment, shear, and deflection using the finite difference program LPILE (Reese & Wang, 1997). Figure 6 shows the predicted pile bending moment distribution along the length of the pile for tests under 0.3g and 0.4g peak base accelerations. It may be seen that the API recommended p-y curves underestimated the bending moments for both tests by a significant amount. In the same figure, the bending moment distribution calculated using the LPILE program using modified API p-y curves which were constructed by multiplying the p-multipliers to the original API p-y curves are shown, where it is seen to agree well with the measured values.

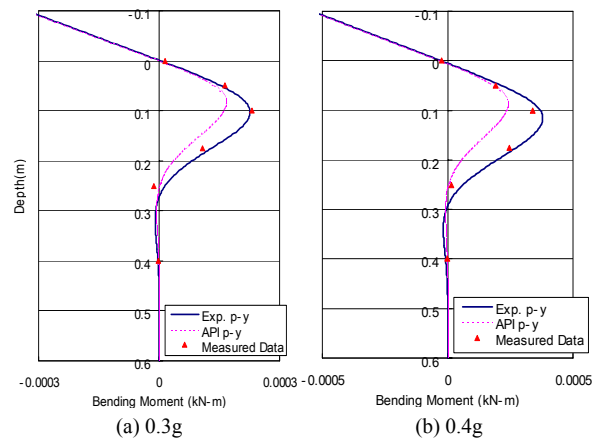


Figure 6 Computed and measured bending moments ($s=3D$, input acceleration: 5Hz)

CONCLUSIONS

The following conclusions were drawn by comparing the shaking table test results on single and group piles with the results calculated using the API recommended procedures.

1. The backbone slopes of API cyclic p-y curves of a single pile subjected to a dynamic loading are in a good agreement with the experimental p-y curves of a single pile for all depths at low to mid acceleration levels (0.2g-0.3g). However, at high acceleration levels (0.4g), the API p-y curves were estimated to be softer than the experimental p-y curves.
2. At shallow pile depth ($3.5 \times$ pile diameter), the group pile effect appears clearly even under conditions of relatively low acceleration (0.2g). As a result, the experimental p-y curves of the group piles become softer than the API p-y curves. At a depth of 7 pile diameters, the group effect appears at high acceleration levels (0.3g-0.4g), and at increased depth ($14.5 \times$ pile diameters) it appears only at high acceleration levels (0.4g).
3. The magnitudes of the maximum pile deflections and the maximum soil reactions of piles increase rapidly as the shaking frequency approached the natural frequency of the pile-soil system.
4. For center-to-center pile spacings of 6 pile diameters or larger, no group pile effects were observed.

5. It was found that the response of group piles, in terms of bending moments under dynamic lateral loading, was significantly underestimated if the API recommended p-y curves were used in the calculation, while the bending moments, which were calculated along the pile length, using modified API p-y curves constructed by multiplying p-y multipliers to the original API p-y curves, agree well with the measured values. Thus, it is recommended to use the concept of p-multipliers in the process of API p-y curve construction to include pile group effects.

REFERENCES

1. Brown D.A., Morrison C. & Reese L.C. 1988. Lateral Load Behavior of Pile Group in Sand. *Journal of Geotechnical Engineering* 114(11): 1261-1276.
2. Dou H. & Byrne P.M. 1996. Dynamic Response of Single Piles and Soil-Pile Interaction. *Canadian Geotechnical Journal* 33: 80-96.
3. Finn W.D. & Gohl W.B. 1992. Response of Model Pile Groups to Strong Shaking. In Prakash S.(ed.), *Piles under Dynamic Loads*: 27-55. ASCE.
4. Matlock H., Foo S., Tsai C. & Lam I. 1979. *SPASM 8 – A Dynamic Beam-Column Program for Seismic Pile Analysis with Support Motion*. Fugro Inc.
5. Reese L.C. & Wang S.T. 1997. *LPILE^{PLUS} 3.0 for Windows User's Manual*. Ensoft Inc.
6. Ting J.M. 1987. Full Scale Cyclic Dynamic Lateral Pile Response. *Journal of Geotechnical Engineering* 113(1): 30-45.



KEERC-MAE Joint Seminar on
Risk Mitigation for Regions of Moderate Seismicity
University of Illinois at Urbana-Champaign, August 5-8, 2001



Sponsors: Korea Science and Technology Foundation, U.S. National Science Foundation, Brain Korea 21



Non-Linear Wave Propagation in the Mississippi Embayment

Youssef M. A. HASHASH¹ and Duhee PARK²

¹ *Assistant Professor, University of Illinois at Urbana-Champaign,
205 N. Mathews Avenue, Urbana, Illinois, USA
email: hashash@uiuc.edu*

² *Graduate Research Assistant, University of Illinois at Urbana-Champaign,
2216 Newmark Laboratory, 205 N. Mathews Avenue, Urbana, Illinois, USA
email: dpark1@uiuc.edu*

ABSTRACT : This paper summarizes the development of a new non-linear one-dimensional site response analysis model for vertical propagation of horizontal shear waves in deep soil deposits. The new soil model accounts for the influence of large confining pressures on strain dependent modulus degradation and damping of soil. In addition, new formulation is introduced for the viscous damping matrix. Details of the new model, DEEPSOIL, can be found in [1].

The new model is used to estimate ground motion amplification and attenuation for three soil columns 100 m, 500 m and 1000 m thick, representative of soil thickness variability within the Mississippi Embayment. The new model shows that some high frequency components of ground motion, usually filtered out using conventional wave propagation methods, are transmitted through these deep deposits. Spectral amplification factors of deep deposits are greater than unity and can be as large as 5 in the longer period range of 2-10 sec. Preliminary evaluation of model results show that computed surface response spectra in the period range of 0.5-2 sec are larger than the 1997 NEHRP recommended design response spectrum.

KEY WORDS: Site response, deep deposit, frequency content, nonlinear, amplification, confining pressure, viscous damping

INTRODUCTION

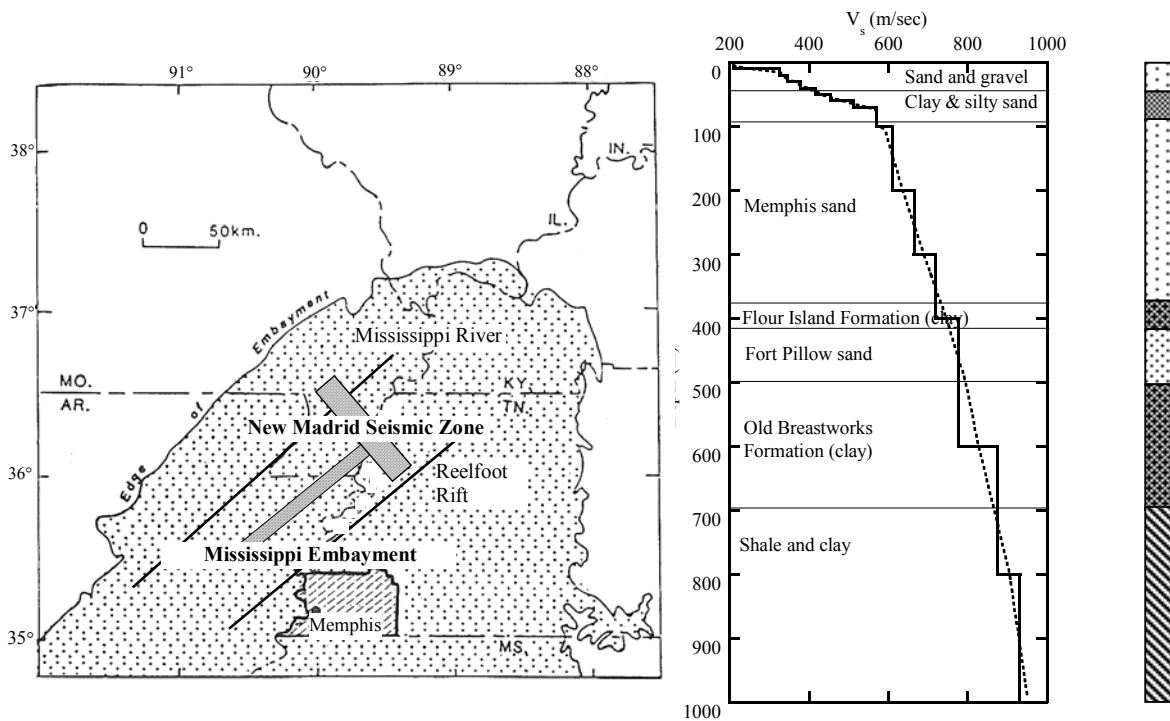
Earthquakes in the New Madrid Seismic Zone (NMSZ) are characterized as low probability, high consequence events. Estimate of ground motion characteristics in the NMSZ is required to assess the seismic vulnerability of structures and the susceptibility of soils to liquefaction. The presence of very deep (up to 1000 m) unconsolidated deposits in the Mississippi Embayment has an important, though poorly understood effect on the propagation of seismic waves.

In the absence of strong motion records, numerical models can be used to develop an understanding of wave propagation characteristics of the Mississippi Embayment. This paper proposes a new one-dimensional, non-linear wave propagation model to account for the effect of very high confining pressures encountered in the Embayment. The model development is based in part on recent data regarding cyclic response of soils under high confining pressures. A series of analyses are presented to illustrate the influence of deep deposits on the amplitude and frequency content of propagated weak and strong ground motions.

THE MISSISSIPPI EMBAYMENT AND NEW MADRID SEISMIC ZONE

The Mississippi Embayment is a syncline or a trough-like depression that plunges southward along an axis that approximates the course of the Mississippi River. The Paleozoic rock forms the bedrock floor of the Mississippi Embayment and is located about 1000 m below Memphis and Shelby County, which is near the central part of the Mississippi Embayment. The presence of thick unconsolidated deposits adds significant uncertainty regarding the nature of seismic ground motion propagation and attenuation in the Embayment. The effect of soil deposits on propagated ground motion is well documented in other parts of the world (e.g. Mexico City, [2]). However, limited information is available regarding wave propagation through very thick deposits (up to 1000 m) such as those found in the Mississippi Embayment.

The geologic layers can be considered nearly horizontal. Analysis of wave propagation through these deposits is approximated as one-dimensional vertical propagation of horizontal shear waves. Three profiles, 1000 m, 500 m, and 100 m deep, shown in **Figure 1**, are selected to represent the range of soil depths encountered in the Embayment ([3],[4]). The 1000 m profile is representative of conditions in the Memphis, Shelby County area while the 100 m profile represents conditions south of the St. Louis Area. The selected shear wave velocity profile is based on a combination of surface information and a few deep wells as compiled by Romero et al. [5]. The density of the soil (ρ) in the columns is assumed to be 1.98 kg/m^3 .



V_s and soil profile at Memphis, TN

Figure 1 Mississippi Embayment and shear wave velocity profiles used in the analysis

ONE-DIMENSIONAL WAVE PROPAGATION IN SOIL DEPOSITS

One-dimensional site response analysis is used to solve the problem of vertical propagation of horizontal shear waves (SH waves) through a horizontally layered soil deposit. Horizontal soil layer behavior is approximated as a Kelvin-Voigt solid whereby constant elastic shear moduli and viscous damping characterize soil properties. Solution of wave propagation equations is performed in the frequency domain. Seed, Idriss and co-workers introduced the equivalent linear approximation method to capture non-linear cyclic response of soil. Modulus degradation and damping curves are then used to obtain revised values of shear modulus and damping.

The equivalent linear approach is computationally easy to use and implement. However, it does not capture the full range of cyclic behavior of soil, including modulus degradation due to number of loading cycles, permanent (residual) straining of soil and excess pore pressure generation. Non-linear analysis is used to capture these important aspects of soil behavior. In this approach, equations of motion and equilibrium are solved in discrete time increments in the time domain. A constitutive model is used to represent soil behavior.

In this approach, equations of motion and equilibrium are solved in discrete time increments in the time domain. The required mass, damping and stiffness matrices M , C , K in this non-linear model are assembled from the incremental properties of the layers, which in turn are obtained from a constitutive model that describes the non-linear behavior of the soil.

NON-LINEAR PRESSURE DEPENDENT CYCLIC SOIL MODEL

The constitutive model used in the analysis is based on modified hyperbolic model [6]. In this model, there is no coupling between confining pressure and shear stiffness. The model is extended in this paper to capture the influence of confining pressure on modulus degradation and damping.

Effect of Confining Pressure on Shear Modulus and Damping

Laird and Stokoe [7] performed resonant column and torsional shear tests at strain levels up to 10^{-3} and confining pressures up to 3.5 MPa using remolded sand specimens, as well as undisturbed specimens of sand, silty sand, silt, lean clay, and fat clay. Low and high amplitude cyclic torsional shear and resonant column tests were used to determine the effect of strain amplitude and confinement on shear modulus and damping curves. In this paper, only results from remolded sand specimens (washed mortar sand) are used. Figure 2 plots the extrapolated modulus degradation curve to an effective stress of 10000 kPa (equivalent to a depth of 1000 m, with the water table at ground surface).

A new formulation for the reference strain is introduced to capture the influence of confining pressure on modulus degradation and damping ratio. Figure 2 shows that using the new formulation; the model can capture the variation in shear modulus measured in laboratory experiments by Laird and Stokoe [7].

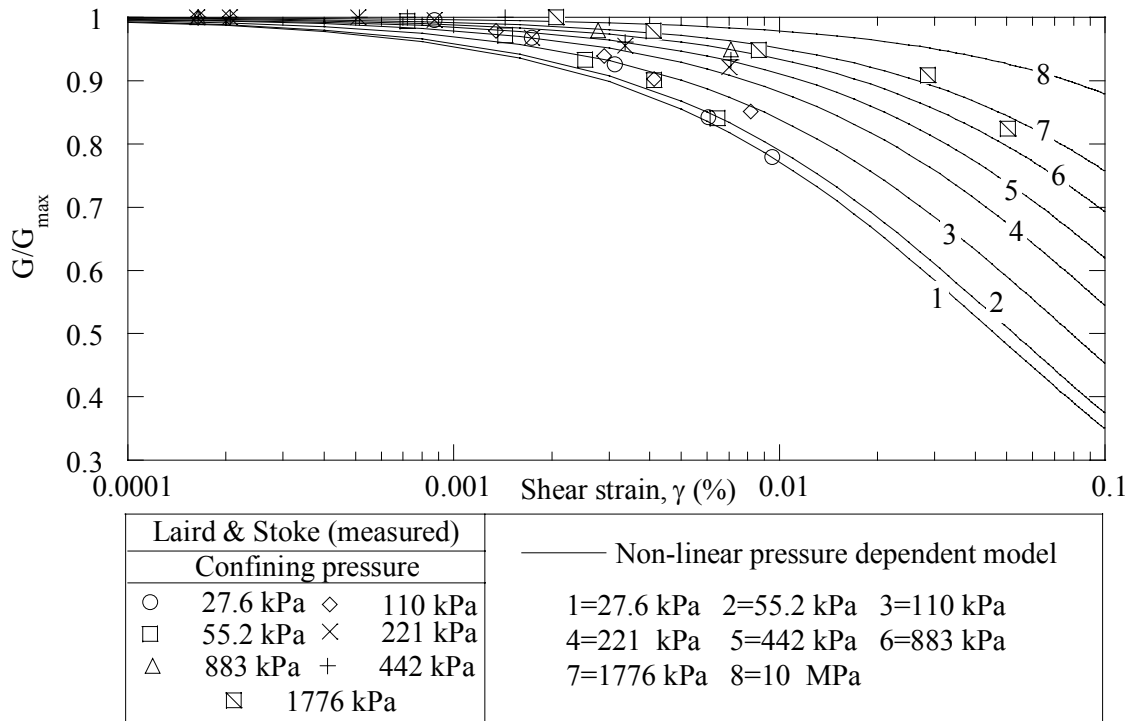


Figure 2 Influence of confining pressure on normalized shear modulus degradation curves in the proposed nonlinear model. Data of Laird and Stokoe shown for comparison

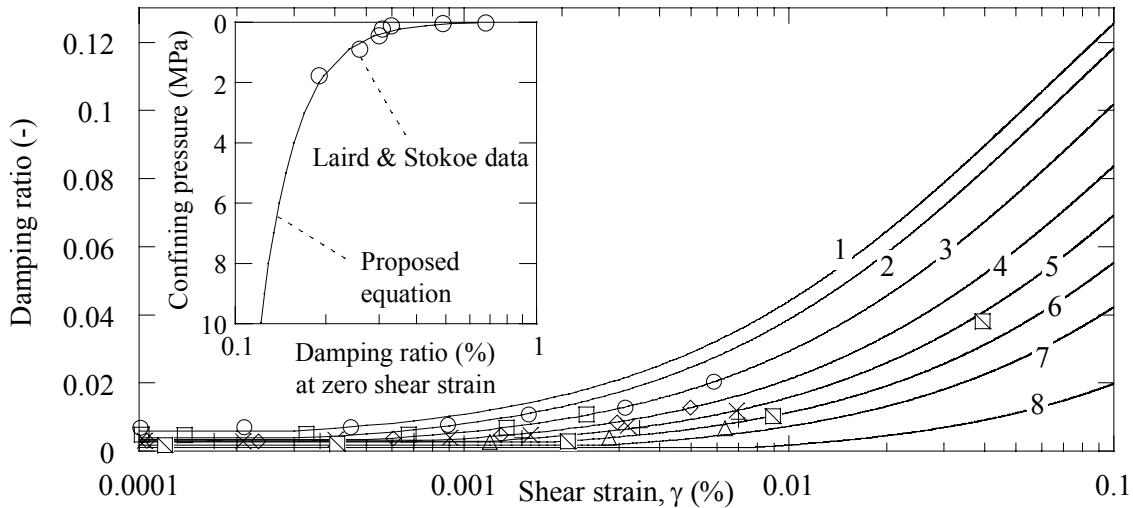


Figure 3 Influence of confining pressure on damping ratio curves in proposed nonlinear model. Data of Laird and Stokoe shown for comparison. Legend shown in Figure 2

Hysteretic damping of the soil model defined by Matasovic [8] can capture damping at strains larger than 10^{-4} to 10^{-2} %, depending on the value of reference strain. However, the hyperbolic model is nearly linear at small strains (less than 10^{-4} to 10^{-2} %) with practically no damping, which can cause unrealistic resonance during wave propagation. The model described by Matasovic [6] incorporates additional damping to the dynamic equation in the form of [C] matrix, using the values of the equivalent damping ratio ξ obtained from the damping ratio curves at small strains (**Figure 3**).

Laird & Stokoe data show a dependency of very small strain soil damping on confining pressure. A new pressure dependent small strain damping is proposed in this paper to describe the dependency of zero strain equivalent damping ratio on confining pressure.

Figure 3 shows a comparison between the small strain damping and Laird & Stokoe data. Figure 3 includes plots of the total damping ratio equal to hysteretic plus small strain damping. The proposed equation captures measured damping at very small strains, as shown in the inset. Total damping curves fall within range of measured data but do not provide an exact fit.

Effect of Viscous Damping Formulation

In a non-linear soil model, soil damping is captured through hysteretic loading-unloading cycles in the soil model. The use of the damping matrix [C] may become unnecessary. The damping matrix may be used as a mathematical convenience or to include damping at very small strains where response of many constitutive models is nearly linear elastic.

[C] is assumed to be independent of strain level and therefore, the effect of hysteretic damping induced by nonlinear soil behavior can be separated from (but added to) viscous damping. The [C] matrix is a combination of the mass matrix and the stiffness matrix. In conventional site response analysis, small strain viscous damping effects are assumed proportional only to the stiffness of the soil layers and that only 1st mode determines the damping matrix. While it is a reasonable assumption in short soil columns, it cannot be applied to thick columns resulting in over-estimation of the damping matrix. It can seriously underestimate the response by filtering out a significant portion of high frequency component.

INFLUENCE OF CONFINING PRESSURE AND NEW VISCOUS DAMPING FORMULATION

The influence of confining pressure on 1-D site response is demonstrated through comparisons of analyses using non-linear, confining pressure-dependent (NLPD) and independent (NLPI) soil models. The difference between the two models can be observed by examining the surface response spectra shown in Figure 4. For a soil thickness of 1000 m, the influence of the confining pressure is very pronounced. Short period spectral accelerations are much larger for the NLPD model compared to the NLPI model. For both models, motion amplification is computed at a period of about $T=5.0$ seconds which corresponds to the theoretical characteristic site period for the 1000 m soil column. Similar observations can be made for the 500 m column. For the 100 m column, response spectra are also similar for $T>0.9$ sec. However, for shorter periods the NLPD model spectral acceleration is larger than that of the NLPI model. The influence of pressure-dependent behavior is still significant for the 100 m thick column.

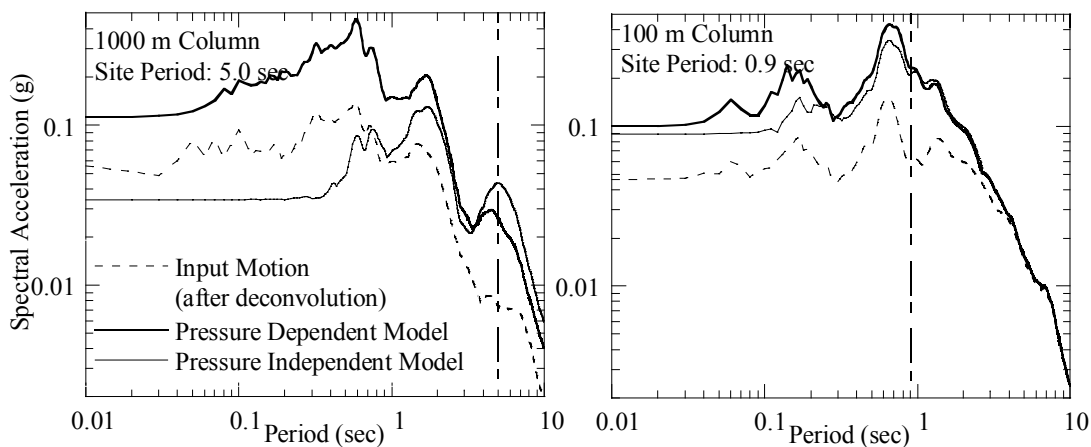


Figure 4 Comparison of surface response spectra, with 5% damping using pressure dependent and pressure independent soil models. Input time series is recordings at Yerba Buena Island during Loma Prieta Earthquake. Note the overall higher spectral acceleration in the pressure dependent model analyses (dark solid lines) compared to pressure independent analyses (light solid lines)

VERIFICATION OF THE MODEL

The new model was verified using ground motion records at Treasure Island-Yerba Buena during the Loma Prieta earthquake (1989). Verification was also done using several records in the Mississippi Embayment during the Warm Springs Earthquake (1999). The computed responses agreed well with those recorded.

RANGE OF COMPUTED SPECTRAL AMPLIFICATION FACTORS IN EMBAYMENT

A measure of the effect of deep soil deposits on propagated ground motion is the spectral amplification factor. The spectral amplification factor is defined as the ratio of surface spectral acceleration to input motion spectral acceleration for a given period or frequency. 13 Input ground motion time series have been selected to include a range of earthquake events at rock outcrop and synthetic time series using the program SMSIM [8] and parameters for the NMSZ (Frankel et al., 1996). The peak accelerations, a_{max} , range from 0.0073 g to 1.16 g. Three soil columns, 100 m, 500 m and 1000 m thick, shown in Figure 1 are used in the analyses. The non-linear, confining pressure-dependent (NLPD) soil model proposed in this paper is used in most analyses.

Figure 5 plots Fourier amplitude spectral amplification factors for the 1000 m soil column analyses. The plots include spectra for thirteen time series selected for the parameter study, using the NLPD model. It is not possible to distinguish individual spectra in these plots. However, it is possible to establish ranges of amplification factors that can be interpreted from these analyses. Most time series results fall within a well-defined band. The amplification factor has a peak at approximately 0.2 Hz, which corresponds to the characteristic site period. Other peaks are observed that correspond to higher order natural frequencies of the soil column. A gray trend line is sketched through the data, which shows the general change of amplification factor with frequency. In the frequency range 0.1 to 4 Hz the amplification factor is greater than unity and can be up to a value of 5. At higher frequencies, the amplification factor is less than one. This interpretation represents the general trend, but as Figure 5 shows, there are numerous exceptions.

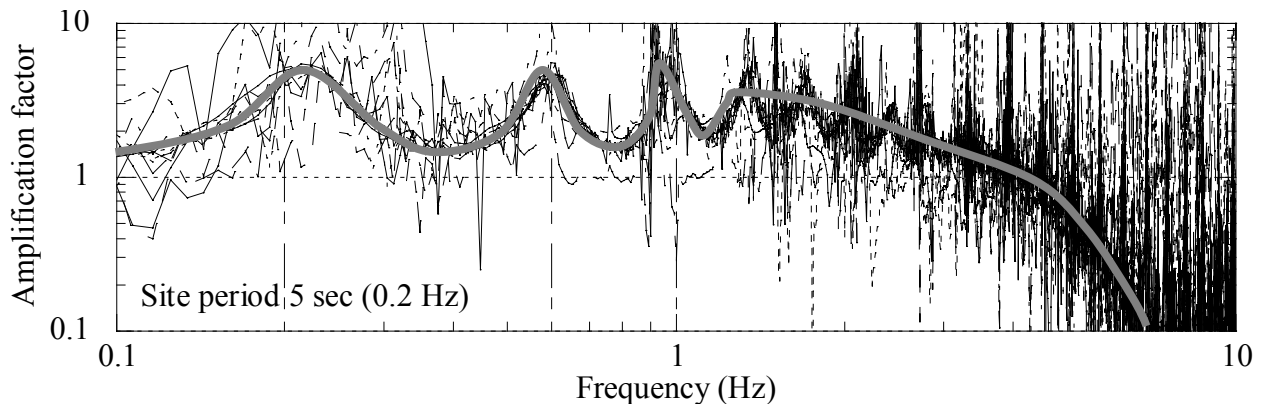


Figure 5 Ratio of computed surface to input Fourier amplitude spectra for all ground motions using pressure dependent model and 1000 m soil column. The gray line shows the general trend for the data sets. The peaks correspond to the site natural frequencies

Figure 6 plots Fourier amplitude spectral amplification factors for the 500 m soil column analyses. The plot shows that the amplification factor has peaks at the deposit natural frequencies. The amplification factor exceeds unity over a frequency range of 0.1 to 5 Hz. Higher frequency amplification factors are generally less than unity.

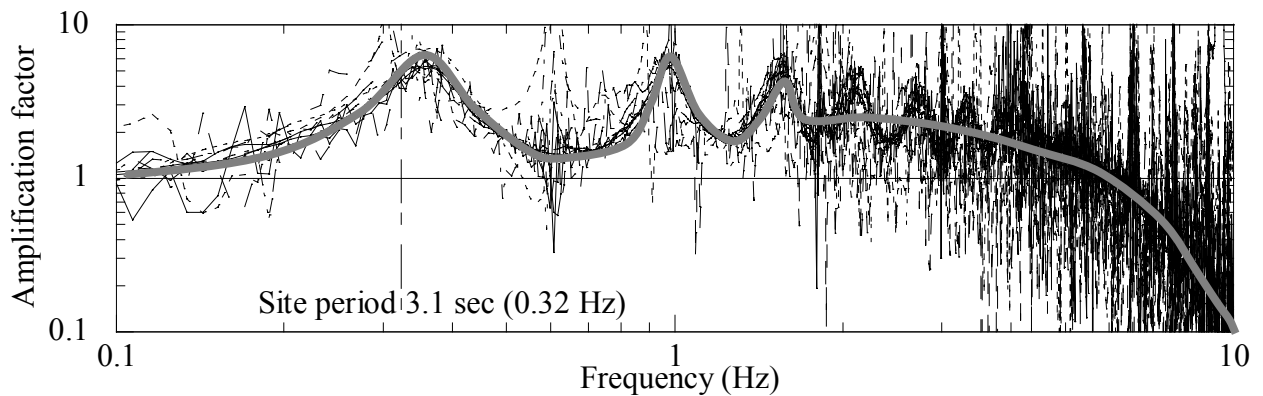


Figure 6 Ratio of computed surface to input Fourier amplitude spectra for all ground motions using pressure dependent model and 500 m soil column. The gray line shows the general trend for the data sets. The peaks correspond to the site natural frequencies

Figure 7 plots Fourier amplitude spectral amplification factors for the 100 m soil column analyses. The plot shows that there is significantly less amplification of ground motion at low frequency (long periods) compared to 1000 m and 500 m soil columns. The plot shows that greater amplification of high frequency components is computed compared to deeper soil profiles.

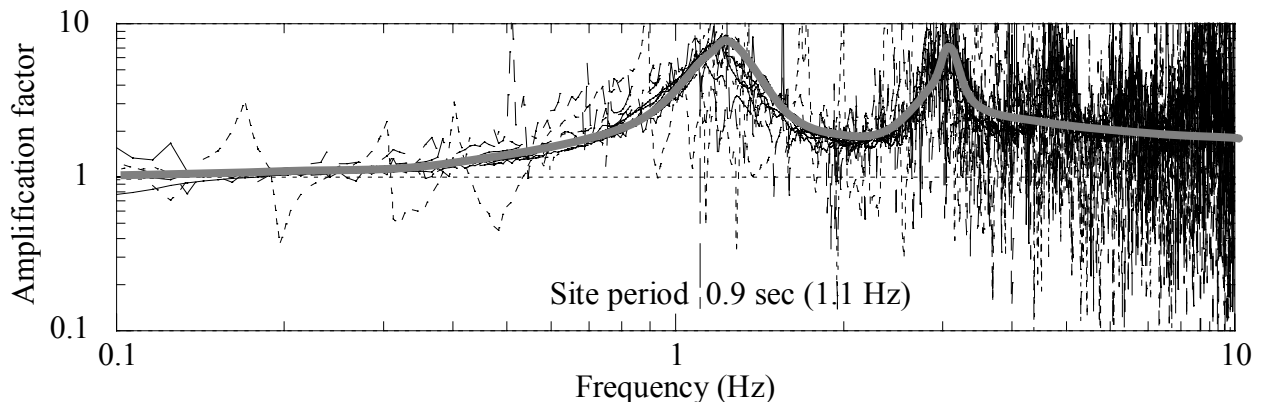


Figure 7 Ratio of computed surface to input Fourier amplitude spectra for all ground motions using pressure dependent model and 100m soil column. The gray line shows the general trend for the data sets. The peaks correspond to the site natural frequencies

Amplification factor plots show that for deeper soil columns there is greater amplification of low frequency (long period) components. The analyses for the three soil columns show that amplification factors at short periods/high frequency generally increase with decreasing soil deposit thickness. The fundamental frequency of the site and higher order natural frequencies influence the amplification factor. The deposit natural frequencies are related to the shear wave velocity of the site. It is necessary to obtain more extensive measurements of shear wave velocity profiles at depth at various locations within the Embayment.

COMPARISON WITH SELECTED NEHRP RESPONSE SPECTRUM FOR NMSZ

Response spectra from the present analyses (NLPD only) are compared with response spectra proposed in the NEHRP Recommended Provisions of 1997 (FEMA 302). The NEHRP response spectrum is developed for Site Class D (Stiff Soil). The soil column defined in **Figure 1** and used in the analyses falls within the NEHRP Site Class D. NEHRP spectral accelerations are obtained from Maps 13 & 14, Maximum Considered Earthquake Ground Motion for the New Madrid Area. Maximum values of spectral parameters in NMSZ $S_a(0.2 \text{ sec})=3.69 \text{ g}$ and $S_a(1 \text{ sec})=1.23 \text{ g}$ at the B-C boundary are used.

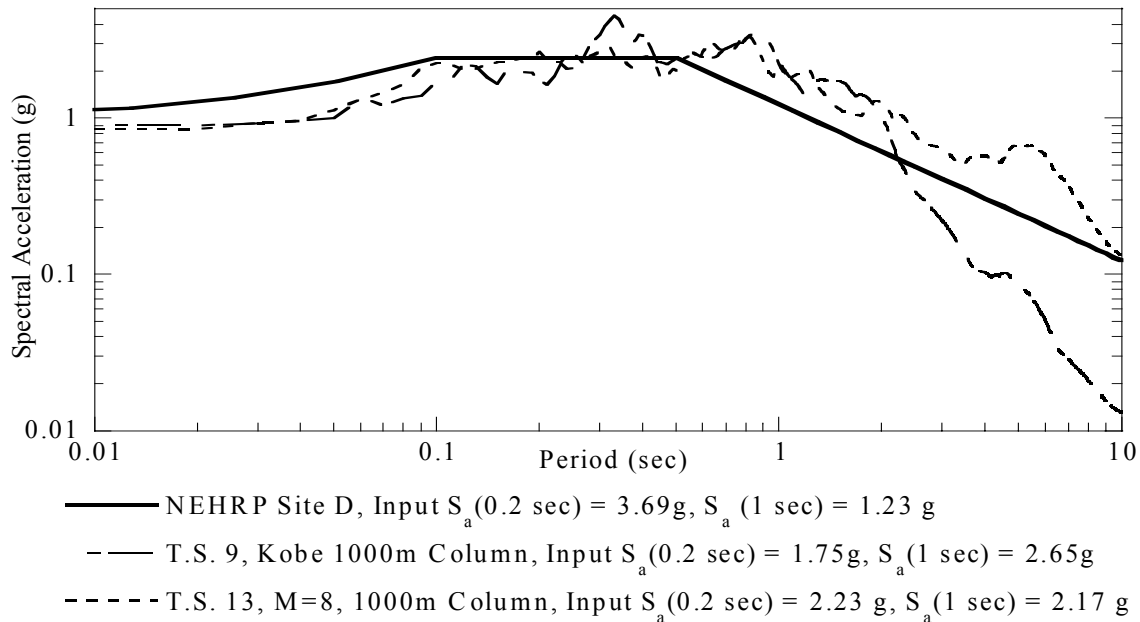


Figure 8 Comparison of computed surface response spectra with the maximum NEHRP recommended spectrum for the NMSZ. At periods greater than 0.7 sec, computed spectra exceed NEHRP spectra

Figure 8 shows a plot of surface response spectrum for NEHRP Site Class D and for a 1000 m soil column using the proposed model and input motion from Kobe earthquake (station JMA NS) and synthetic ground motion from SMSIM ($M = 8$, $R = 20 \text{ km}$). Both of the time series have spectral parameters less than those used in developing NEHRP spectrum. The computed response in the proposed model gives spectral accelerations larger than those for NEHRP Site Class D at periods longer than 0.3 sec. A detailed study is planned to re-examine NEHRP spectral values systematically within the Mississippi Embayment using the new proposed model to represent the underlying soil column.

CONCLUSIONS AND FUTURE WORK

Analyses presented in this paper show the importance of the influence of confining pressure on seismic site response analysis. The analyses show that:

- Significant portions of high frequency components of ground motion are propagated through deep soil deposits.
- Propagation of seismic waves through very deep deposits result in the development of long period ground motion.
- Spectral amplitudes of propagated ground motions are higher than what would be obtained using conventional wave propagation analyses. Therefore estimates of ground motion that are derived from paleo-liquefaction features should consider the higher propagated ground motions.

The paper presents preliminary results of ongoing model development. Further work is underway to improve model calibration.

ACKNOWLEDGEMENTS

This work was supported primarily by the Earthquake Engineering Research Centers Program of the National Science Foundation under Award Number EEC-9701785; the Mid-America Earthquake Center. The authors gratefully acknowledge this support.

REFERENCES

1. Hashash, Y.M.A., and Park, D. (2001), "Non-linear one-dimensional seismic ground motion propagation in the Mississippi Embayment," Engineering Geology
2. Stone, W. C., Yokel, F. Y., Celebi, M., Hanks, T. and Leyendecker, E. V. (1987). "Engineering aspects of the September 19,1985 Mexico earthquake." NBS Building Science Series 165, National Bureau of Standards, Washington, D.C., 207 p.
3. Ng, K. W., Chang, T. S., and Hwang H. (1989). "Subsurface conditions of Memphis and Shelby County." Technical Report NCEER-89-0021, National Center for Earthquake Engineering Research, State University of New York at Buffalo, Buffalo, NY.
4. VanArsdale, R. B., Williams, R. A., Schweig III, E. S., Shedlock, K. M., Kanter, L. R. and King, K. W. (1994). "Preliminary seismic reflection study of Crowley's Ridge, Northeast Arkansas." U.S. Geological Survey Professional Paper 1538-A-C, United States Government Printing Office, Washington.
5. Romero, S. and Hebel, G. and Rix, G. J., (2001), "Recommended reference profile for Memphis, Tennessee." <http://mae.ce.uiuc.edu/Research/GT-1/RRP.htm>. Engineering Geology.
6. Matasovic, N. (1993). "Seismic response of composite horizontally-layered soil deposits." Ph. D. Thesis, Department of civil engineering, University of California at Los Angeles.

7. Laird, J. P. and Stokoe, K. H. (1993). "Dynamic properties of remolded and undisturbed soil samples test at high confining pressure." Geotechnical Engineering Report GR93-6, Electrical Power Research Institute.
8. Boore, D. M. (2000). "SMSIM – Fortran programs for simulating ground motions from earthquakes: Version 1.87." User Manual, V 1.0, U.S. Geological Survey Open-File Report 96-80-A, 73 pp.



KEERC-MAE Joint Seminar on
Risk Mitigation for Regions of Moderate Seismicity
University of Illinois at Urbana-Champaign, August 5-8, 2001



Sponsors: Korea Science and Technology Foundation, U.S. National Science Foundation, Brain Korea 21



Shaking Table Test of Small-Scale Model of a Concrete Gravity Dam

Jin Ho LEE¹ and Jae Kwan KIM²

¹ *Graduate Student, School of Civil, Urban and Geosystem Engineering,
Seoul National University
San 56-1, Shillim-dong, Kwanak-ku, Seoul, Korea
email: ohnij2@snu.ac.kr*

² *Associate Professor, School of Civil, Urban and Geosystem Engineering,
Seoul National University
San 56-1, Shillim-dong, Kwanak-ku, Seoul, Korea
email: jkwankim@plaza.snu.ac.kr*

ABSTRACT: A series of shaking table tests was conducted with small-scale models of concrete dams. The models were cast using plaster-based material. The tests were conducted at various height water levels and with different kinds of reservoir bottom conditions. It is observed that the effects of the fluid-structures interactions can not be ignored. Also, the reservoir bottom absorption and the sediments may have effects on the response of concrete dams to earthquake. The damage pattern due to strong ground motion was examined.

KEYWORDS: Shaking table test, small-scale model, concrete gravity dam, fluid-structure interactions, seismic design, sediments, seismic performance

INTRODUCTION

The safety of concrete gravity dams to earthquake is an issue of increasing concern because of the hazard presented by a large reservoir which is proportional to the increasing population downstream of the dam. And it has become a major factor in the planning of new dams and in the safety evaluations of existing dams. But all linear and nonlinear earthquake analysis of concrete dams are based on numerous assumptions, each of which has a limited range of validity. As a result, dam model tests were conducted for the purpose of verification of analysis and examination of non-linear behavior of the concrete dams.

Several experimental studies were done using shaking table in which the dam models were constructed using a plaster-based material or other material [1-4]. Another research has been completed using models tested in centrifuges [5].

In this study, a series of shaking table tests was performed. The dam models were cast using plaster-based material. The effects of the water level of reservoir and absorption of the reservoir bottom were investigated. The non-linear behavior of the dam models was examined while increasing the level of input motion intensity.

EXPERIMENTAL SET-UP AND PROCEDURE

Two-dimensional models of Hap-Cheon Dam in Korea and Pine Flat Dam in California were constructed. The choice of model material greatly depends on the scaling requirements. Because the concrete gravity dams is massive structures, the modeling of the dams requires large reductions in the geometry and material properties. A set of scale factors for the most common physical quantities of a linear earthquake analysis problem is listed in Table 1. These factors have been derived from a dimensional analysis. In this dimensional analysis, length, Young's modulus and accelerations due to gravity were chosen as fundamental physical quantities of length, force and time, respectively. The scale factors for length, Young's modulus and acceleration due to gravity were chosen as 100, 100 and 1, respectively. Because the scale factors of material properties such as Yong's modulus and strength are very large, a weak model material should be used.

Plaster is a versatile material in the sense that it can yield a band of strengths for varying water to plaster ratios. At very large water to plaster ratios, very low strengths can be achieved. Because of the large proportion of water, a water-absorbing material such as the diatomite must be used to keep the mix consistent. And lead powder can be used for the improvement the density of material. 100 mm × 200 mm cylindrical specimens were cast and tested for compressive strength and Young's modulus of elasticity. Uniaxial stress-strain curves for the model material in compression are shown in figure 1. Tensile strength was determined by split cylindrical tests on specimens of the same size. The ingredients of the model material are given in Table 2. The properties of dam concrete and the average properties of model material are given in Table 3.

Table 1 The scale factors for dam model

Physical quantity	Scale factor	Physical quantity	Scale factor
Force	$S_E S_L^2 = 1000000$	Stress	$S_E = 100$
Pressure	$S_E = 100$	Strain	1
Acceleration (due to gravity)	$S_g = 1$	Mass density	$\frac{S_E}{S_L S_g} = 1$
Velocity	$\sqrt{S_L S_g} = 10$	Ultimate strength	$S_E = 100$
Displacement or linear dimension	$S_L = 100$	Time	$\sqrt{\frac{S_L}{S_g}} = 10$
Young's modulus	$S_E = 100$	Frequency	$\sqrt{\frac{S_g}{S_L}} = \frac{1}{10}$

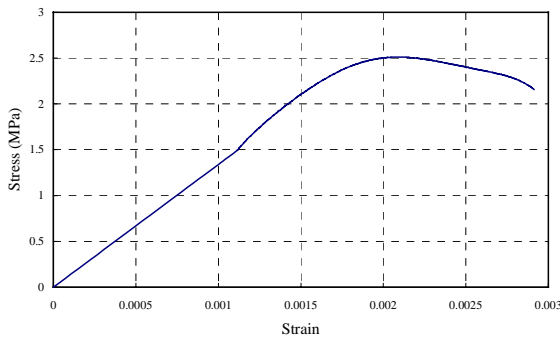
Two types of model were constructed. One is a model of Hap-Cheon Dam in Korea and the other is a model of Pine Flat Dam in California. The Pine Flat Dam model is modified to have vertical upstream face. A slab representing the foundation was cast with the model to provide the flexibility of the base of the dam. The detailed ingredients and the properties of the foundation model material are given in Table 2 and 3, respectively. The complete configurations of the models are shown in Figure 2.

Table 2 Ingredient ratios of model materials (parts by weight to one part of plaster)

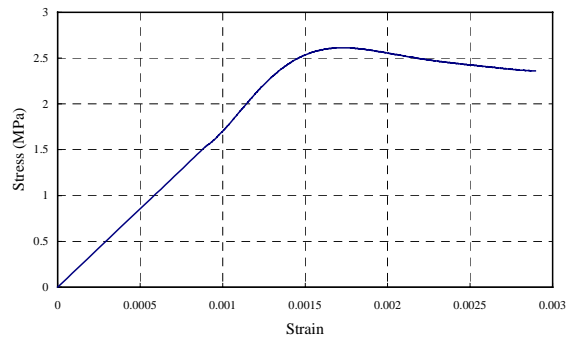
	Ingredients	Hap-Cheon Dam model	Pine Flat Dam model
Dam body	Diatomite	1.784 kg	1.638 kg
	Water	4.208 kg	3.704 kg
	Lead powder	6.994 kg	7.751 kg
Foundation	Diatomite	1.784 kg	1.089 kg
	Water	4.208 kg	2.658 kg
	Lead Powder	6.994 kg	-
Reservoir bottom	Diatomite	0.862 kg	1.089 kg
	Water	2.205 kg	2.658 kg
	Lead powder	-	-

Table 3 Properties of materials

		Hap-Cheon Dam		Pine Flat Dam	
		Prototype	Model	Prototype	Model
Dam body	Mass density	2300 kg/m^3	1714 kg/m^3	2480 kg/m^3	1921 kg/m^3
	Young's modulus	19.62 GPa	1495.6 MPa	22.39 GPa	1656.8 MPa
	Ultimate compressive strength	11.77 MPa	2593.3 kPa	22.41 MPa	2644.6 kPa
	Ultimate tensile strength	1.77 MPa	204.0 kPa	2.24 MPa	308.1 kPa
Foundation	Young's modulus	54.17 GPa	1495.6 MPa	68.90 GPa	419.82 MPa
Reservoir bottom	Young's modulus	54.17 GPa	552.24 MPa	68.90 GPa	419.82 MPa



(a) Hap-Cheon Dam model



(b) Pine Flat Dam model

Figure 1 The stress-strain curve for the dam model material

A rectangular steel tank of $0.320 \text{ m} \times 1.700 \text{ m}$ cross section was used to simulate the reservoir effects (e.g. hydrostatic and dynamic pressure). The end of the tank was sealed by a flexible rubber membrane that was in contact with the upstream face of the dam model. The strength and stiffness of membrane can be negligible, so the reservoir static and dynamic pressures were properly applied to the model. If the reservoir is of finite length (in the upstream direction), the pressure increase not more than 0.5 % if $L/H > 2$ (L = the length and H = the depth of the reservoir) and the effects of length are negligible for $L/H > 3$ [6]. In this study, the tank is 4.0m length, so the effects due to finite length of the reservoir can be negligible. In addition, a damper consisting of aluminum chip was used to weaken the effects of the reflective waves. To simulate the reservoir bottom absorption of compressive waves, a plaster-based material was cast in the tank. The detailed ingredients and the properties of the material are given in Table 2 and 3, respectively.

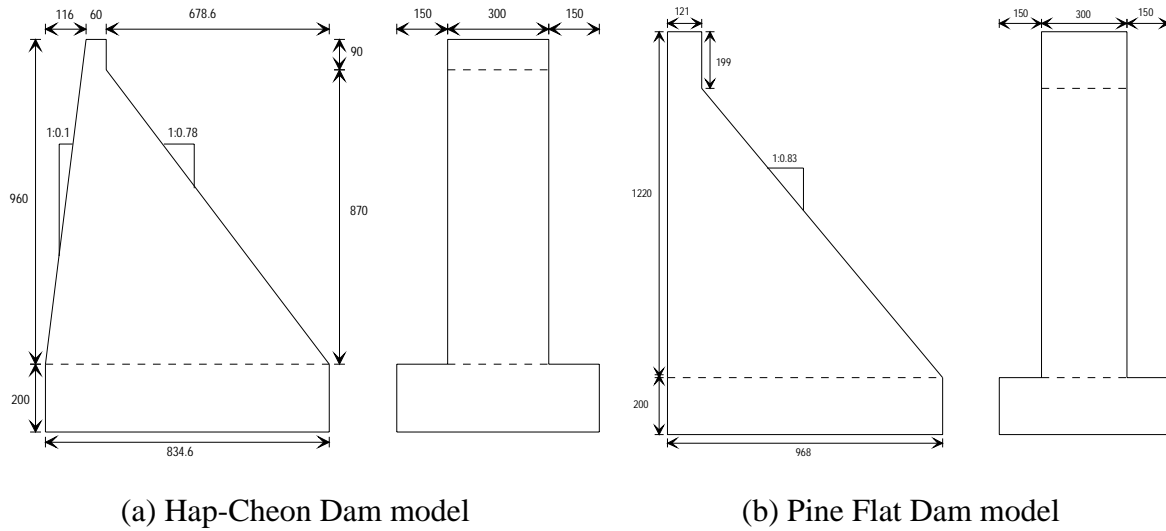


Figure 2 The detailed configuration of the dam model

The dam model and the tank were mounted on the $4\text{ m} \times 4\text{ m}$ 6 DOF shaking table in Korea Institute of Machinery and Materials (KIMM) using H beam of 6 m length. The maximum capacity of the table is 30 ton and the maximum acceleration is 1.5 g in the horizontal direction and 1.0 g in the vertical direction. The maximum reproducible frequency of the table is 50 Hz . The complete set-up is shown in Figure 3.



Figure 3 The complete set-up

The accelerations, displacements and strains on the dam model were measured and hydrodynamic pressures and wave heights of the reservoir. Also, the accelerations of the shaking table were measured. The instrumentation locations of the Hap-Cheon Dam model are shown in Figure 4. The instrumentation of the Pine Flat Dam model was similar.

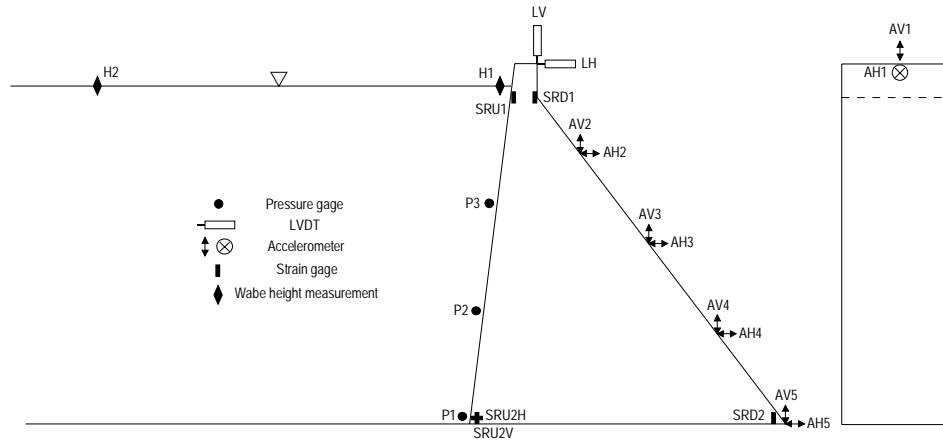


Figure 4 The instrumentation of the Hap-Cheon Dam model

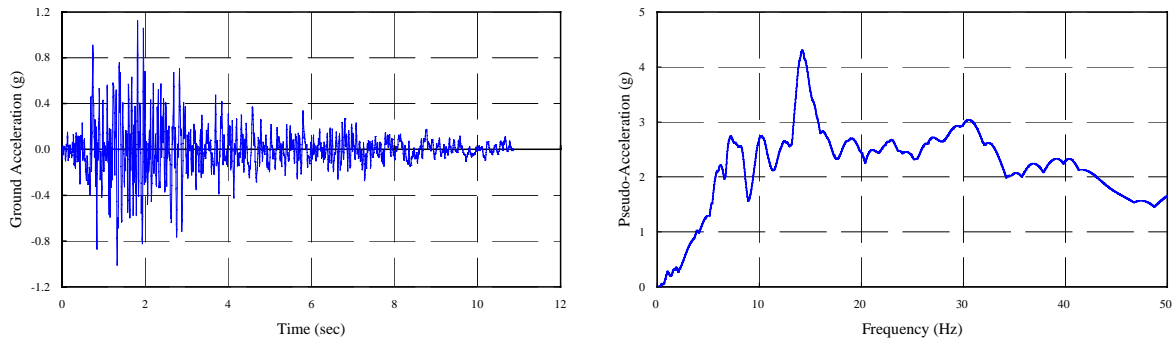
Two kinds of test were conducted: exploratory test and fragility test. The objective of the exploratory test is to identify the dynamic characteristics of the model under various conditions. The objective of fragility test is to investigate the response of the dam models to the strong earthquake motion.

In the exploratory test, the model was shaken by unidirectional table motion in horizontal direction, unidirectional motion in vertical direction and bidirectional motion in horizontal and vertical direction. Three different types of excitations were employed: random vibration, Taft earthquake (1952) and Kobe earthquake (1995). Response spectra and time histories of two earthquake records in the horizontal direction are shown in Figure 5.

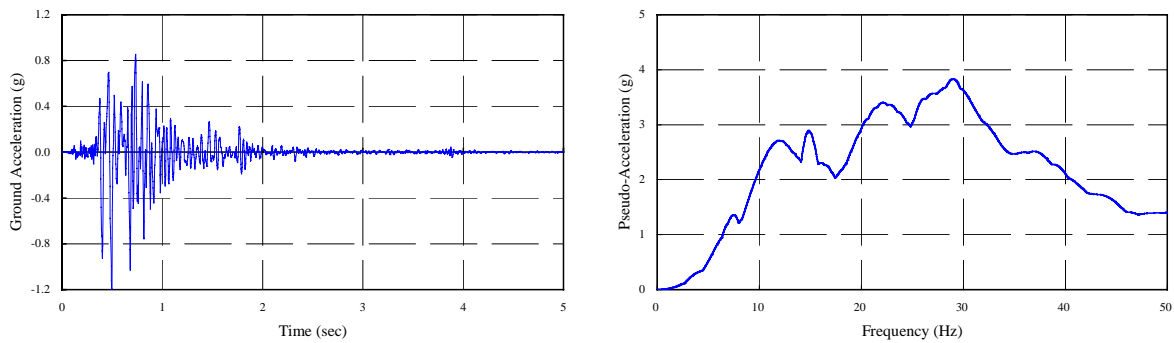
To examine the effects of the fluid-structure interactions, the tests were conducted with and without the reservoir effects. When the reservoir effects were considered, the tank was filled with water to a full reservoir level (0.90 m height of the water for the Hap-Cheon Dam model and 1.10 m for the Pine Flat Dam model) and a half reservoir level.

The tests were conducted under various boundary conditions of reservoir bottom. The reservoir bottom was supposed to be rigid and the tests were conducted with a steel plate laid on the reservoir bottom of plaster-based material (steel bed). To take into the consideration of the absorption effects of the reservoir bottom, the tests were conducted without the steel plate (plaster bed). The tests were conducted with kaolinite laid on the reservoir bottom to investigate the effects of the sediments (mud bed). The effects of reflective waves were investigated through the tests without the aluminum chip damper (mud bed without damper).

The fragility test is done to investigate the response of the dam models to the strong earthquake motion and the damage pattern. The model was shaken by unidirectional motion in horizontal direction and the Taft earthquake was employed as input motion. The intensity of excitation was increased from 0.1 g with 0.1 g increments.



(a) Taft earthquake



(b) Kobe earthquake

Figure 5 The time histories and response spectra of input motion

TEST RESULTS

Figure 6 is a transfer functions at the crest in horizontal direction. The Welch method is employed to obtain those curves in Figure 6 by taking average of the transfer functions obtained from original data set. The natural frequencies and damping values were identified from the test results and summarized in Table 4. The natural frequencies were decreased and the damping ratios were increased due to the effects of the fluid-structure interactions. And the natural frequencies and damping ratios were changed slightly according to the boundary conditions of the reservoir bottom. The reservoir bottom absorption and the sediments may have important effects on the response of concrete dams to earthquakes. The removal of the damper increased the natural frequency and decreased the damping ratio. It can be concluded that the effects of the reflective waves cannot be negligible.

Table 4 Natural frequencies and damping ratios

Conditions	Natural frequency	Damping ratio
Dry Dam	16.41 Hz	0.867 %
Full Reservoir with Steel Bed	14.94 Hz	1.495 %
Full Reservoir with Plaster Bed	14.94 Hz	1.572 %
Full Reservoir with Mud Bed	14.64 Hz	1.534 %
Full Reservoir without Damper	14.65 Hz	0.901 %

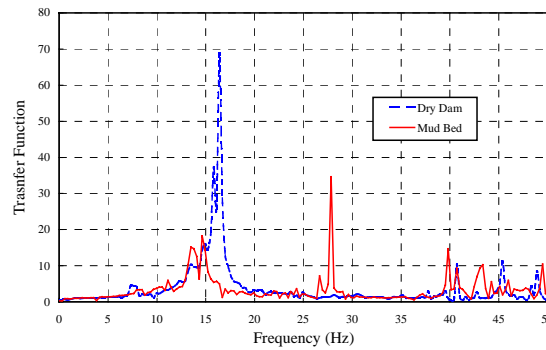


Figure 6 The transfer functions at the crest of Hap-Cheon Dam model

The flexibility of the dam model influenced the hydrodynamic pressure. The distribution of hydrodynamic pressure is presented in Figure 7. The distribution differs from the rigid dam case [6].

The intensity of excitation was increased from 0.1 g with 0.1 g increments. It was not until an input of 0.9 g peak acceleration was applied that the crack appeared on the Hap-Cheon Dam model and 0.8 g on the Pine Flat Dam model. Two type of crack propagation were observed (Figure 8).

CONCLUSIONS

A series of shaking table tests was conducted on small-scale models of concrete dams. The model were cast using plaster-based material. The test were conducted under various conditions of water level and reservoir bottom. It is observed that the effects of the fluid-structures interactions can not be ignored. Also, the reservoir bottom absorption and the sediments may have effects on the response of concrete dams to earthquake. The damage pattern due to strong ground motion were examined.

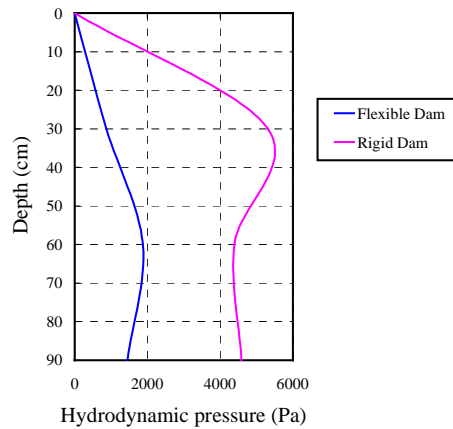


Figure 7 The distribution of hydrodynamic pressure of Hap-Cheon Dam model



(a) Hap-Cheon Dam model



(b) Pine Flat Dam model

Figure 8 The crack propagation of dam models

ACKNOWLEDGMENT

This research was performed by the Natural Hazards Prevention Research Project, one of the Critical Technology-21 Programs, funded by the Ministry of Science and Technology of Korea. This study was supported partly by the fund of Korea Science and Engineering Foundation (KOSEF) through the Korea Earthquake Engineering Research Center (KEERC). And this work was supported by the Brain Korea 21 Project in 2001. Their kind support is duly acknowledged.

REFERENCES

1. Niwa, A. and R. W. Clough, "non-linear Seismic Response of Arch Dams," *Earthquake Engineering and Structural Dynamics*, Vol. 10, 1982, pp.267-281.
2. Donlon, W. P. and J. F. Hall, "Shaking Table Study of Concrete Gravity Dam Monoliths," *Earthquake Engineering and Structural Dynamics*, Vol. 20, 1991, pp.769-786.
3. Mir, R. A. and C. A. Taylor, "An Experimental Investigation into Earthquake Induced Failure of Medium to Low Height Concrete Gravity Dams," *Earthquake Engineering and Structural Dynamics*, Vol. 24, 1995, pp.373-393.
4. Hariss, D. W. , N. Snorteland, T. Dolen and F. Travers, "Shaking Table 2-D Models of a Concrete Gravity Dam," *Earthquake Engineering and Structural Dynamics*, Vol. 29, 2000, pp.769-787.
5. Plizari, G. and V. E. Saouma, "Centrifuge Modeling and Analysis of Concrete Gravity Dams," *Journal of Structural Engineering*, ASCE, Vol. 121, 1995, pp.1471-1479.
6. Chopra, A. K., "Hydrodynamic Pressure in Dams during Earthquakes," *Journal of Engineering Mechanics Division*, ASCE, Vol. 93, No. EM6, Proc. Paper 5695, 1967, pp.205-223.



KEERC-MAE Joint Seminar on
Risk Mitigation for Regions of Moderate Seismicity
University of Illinois at Urbana-Champaign, August 5-8, 2001



Sponsors: Korea Science and Technology Foundation, U.S. National Science Foundation, Brain Korea 21



Simplified Nonlinear Design Model for URM In-plane Wall Response

Joonam PARK¹, James I. CRAIG², and Barry J. GOODNO³

¹ *Graduate Research Assistant of Civil Engineering, Georgia Institute of Technology
790 Atlantic Drive, Atlanta, Georgia, USA
email: joonam.park@ce.gatech.edu*

² *Professor of Aerospace Engineering, Georgia Institute of Technology
270 Ferst Drive, Atlanta, Georgia, USA
email: james.craig@ae.gatech.edu*

³ *Professor of Civil Engineering, Georgia Institute of Technology
790 Atlantic Drive, Atlanta, Georgia, USA
email: bgoodno@ce.gatech.edu*

ABSTRACT: The nonlinear in-plane behavior of unreinforced masonry (URM) walls is quite complicated and difficult to predict. While high fidelity computational models can be developed on a brick-by-brick basis using interface elements between them, such models require considerable computational resources and are unwieldy to use for design studies. Therefore, there is a need to develop a rational but much simpler lumped-parameter model that can reasonably describe the nonlinear in-plane response of URM walls as efficiently as possible. Basic nonlinear properties for solid URM walls can be obtained using semi-empirical equations such as those in FEMA 356^{*}. A simple in-plane model for a general perforated wall is developed by decomposing the wall into multiple regions and modeling each region by a single nonlinear spring. These springs are then assembled into a 2-D parallel-series lumped parameter model. To account for less than fully fixed boundary conditions of these regions, both an “effective height” and an “effective end stiffness” approach are used. An additional factor based on overall wall aspect ratio is applied to reflect the degree of in-plane bending action in the wall. DRAIN-2dx is used as the computational tool and the simple zero-length nonlinear spring (Type 04) is used for the wall models.

^{*} “Prestandard and Commentary for the Seismic Rehabilitation of Buildings,” Federal Emergency Management Agency, Washington, DC., Report FEMA-356, November 2000.

KEYWORDS: unreinforced masonry, in-plane wall, nonlinear behavior, seismic behavior, simplified model, perforated wall, lumped parameter model.

INTRODUCTION

The structural behavior of unreinforced masonry (URM) is much more complex than that of other common construction materials such as steel or reinforced concrete [1,5,9]. Masonry is essentially a two-phase material and its properties are therefore dependent upon the properties of its constituents, the brick and the mortar. The presence of multiple wythes and the influence of the mortar joint as a plane of weakness are significant features which have no counterpart in the behavior of reinforced concrete. While the behavior of URM at low stress levels is essentially linearly elastic, it quickly becomes highly nonlinear once cracking develops along mortar joints and/or through bricks.

For the analysis of URM structures under earthquake excitation, the most refined approach is to individually model the brick units with continuum elements and the mortar joints with interface elements [2,3,6]. However, for the analysis of an entire masonry structure, the modeling of every mortar joint can quickly become impractical, especially in design studies where multiple configurations and/or loadings need to be considered. Simplified methods are needed for design purposes, but to be effective, these must be developed and carefully calibrated with refined models. One such approach is described in this paper.

APPROACH

Computer-based numerical methods for structural analysis are capable of achieving very high levels of fidelity for many applications, but this almost always requires substantial amounts of computing power, and more importantly, solution times can increase dramatically. For design applications where alternative configurations must be studied and a range of parameter values considered, the use of such high fidelity analysis models can become unwieldy and far too time-consuming to be practical. In such cases, one approach is to consider simpler analytical models that provide less fidelity but still capture the essential behavioral features [6,7]. These will be called “*design models*” to differentiate them from the higher fidelity “*nominal models*” to which they are usually calibrated. Design models offer computational simplicity and, more importantly, speed but do not provide the same level of detail as a nominal model would. Good design models simulate the most important features of the nominal model but at a significant saving in computational time and effort. This two-level approach to handling complexity in design analysis is common in many areas of engineering, and the particular terminology used here is widespread in control engineering.

Since the present study is trying to assess the improvement in performance of URM essential facilities in Mid-America, rather than for a particular building, it is important to be able to apply URM wall models to a wide range of building configurations in a computationally efficient manner. For this reason, use of simpler design models for the bulk of the study is preferable to use of more costly nominal models. Nominal models are more appropriate for

evaluation of the final configurations and designs developed for a single building using the design models.

High fidelity nominal models for URM buildings are characterized by large numbers of degrees of freedom and nonlinear material behavior, both of which greatly increase the model complexity. Since the nonlinear response is an essential and defining characteristic of URM behavior [6,9], reduction in the number of degrees of freedom provides the only practical basis for developing suitable design models. In this paper, only the in-plane loading and response of URM walls are considered, and the design models will reflect this simplification. In the larger study, design models for other components of URM buildings such as foundations, walls (out-of-plane behavior) and floor and roof diaphragms, incorporating only a few degrees of freedom with lumped masses and nonlinear spring behavior have been developed but will not be discussed.

The first simplification for in-plane URM wall response is to consider only the critical regions of the wall that will capture the dominant failure modes of the structure. A further simplification can be achieved by ignoring individual mortar and bricks and treating masonry as a homogenous material. In this approach, the behavior of the masonry system is represented by an equivalent continuum [6]. We extend this approach and consider a URM wall containing one or more openings for doors and windows (e.g., a perforated wall) to be made up of a number of wall segments or “components,” each of which maintains the integrity of the brick-mortar bond internal to it and therefore behaves largely in a linear elastic manner. Cracks are assumed to develop between these components and the relative motion can involve opening/closing, crushing, or sliding. A simple nonlinear spring element with limited degrees of freedom is then used for the masonry component model. The spring reflects the initial elastic behavior of the component as well as the nonlinear behavior associated with the inter-component interactions across the cracks.

The essential nonlinear behavior of URM is modeled in the present study starting at the component level. If the components are carefully chosen, it should be possible to model the nonlinear behavior for each component in a relatively simple manner, using for example, bilinear inelastic spring models with or without hysteretic behavior, or simple gap opening/closing models. The model for an entire wall can then be constructed by combining the constituent component models in parallel and series combinations, as appropriate to the particular modeling approach used. The resulting “composite” model is capable of developing much more complex behavior than any of the individual components, but yet the overall modeling and analysis process is kept at a relatively simple conceptual level.

COMPOSITE IN-PLANE MODEL FOR GENERAL URM WALLS

Solid Wall Properties

For a general understanding of the in-plane behavior of a masonry wall, it is important to begin with the behavior of a solid wall. When subjected to in-plane loading, a solid URM wall

behaves elastically under the initial loading, and a simple plane stress model is generally adequate to describe this behavior. Out-of-plane behavior under elastic in-plane loading is usually not of concern owing to relatively large wall thickness. As the in-plane loading is increased, either flexural or shear cracking—or a combination of both—will occur, resulting in deflections that are nonlinear with respect to the applied forces.

There are four kinds of in-plane failure modes for the solid URM wall. The type of failure mode is determined primarily based on the masonry strength, wall aspect ratio, and the vertical compressive stress. A suitable design model for in-plane wall behavior should be capable of representing each of these kinds of failures, depending on the particular design conditions encountered. These failure mechanisms are:

- *Rocking failure*: As horizontal load or displacement demand increases, bed joints crack in tension, and shear is carried by the compressed masonry; final failure leads to overturning of the wall.
- *Bed-joint sliding*: Due to the formation of horizontal tensile cracks in the bed-joints, subjected to reversed seismic action, potential sliding planes can form along the cracked bed joints; this failure mode is possible for low levels of vertical load and/or low friction coefficients.
- *Diagonal tension cracking*: Peak resistance is governed by the formation and development of inclined diagonal cracks, which may follow the path of bed- and head-joints or may go through the bricks, depending on the relative strength of mortar joints, brick-mortar interface, and bricks.
- *Toe crushing*: When the strength, as limited by toe compression stress, is less than the strength determined by rocking, the wall undergoes a sudden failure due to the crushing of the toe.

The in-plane force-deflection behavior of unreinforced masonry shear walls is linearly elastic before net flexural tension stresses at the wall heel exceed tensile strengths, or diagonal tension, or bed-joint sliding shear stresses exceed shear strengths. FEMA 356 provides formulas for calculation of the in-plane linear elastic stiffness, k , of a URM wall as follows.

$$k = \begin{cases} \frac{1}{\frac{h_{eff}^3}{3E_m I_g} + \frac{h_{eff}}{A_v G_m}} & \rightarrow \text{for a cantilevered shear wall} \\ \frac{1}{\frac{h_{eff}^3}{12E_m I_g} + \frac{h_{eff}}{A_v G_m}} & \rightarrow \text{for a fixed-fixed shear wall} \end{cases} \quad (1)$$

where h_{eff} is the wall height, A_v is the shear area, I_g is the moment of inertia for the gross section, E_m is the masonry elastic modulus, and G_m is the masonry shear modulus.

These are simple flexure and shear stiffness expressions, however, the strength of the wall is different for each failure mode and must be determined separately. FEMA 356 provides design formulas for the strength of each failure mode of a solid wall under an in-plane force applied along its top. FEMA 356 also notes that unreinforced masonry walls and piers should be considered as deformation-controlled components if their expected lateral strength, limited by bed-joint sliding, shear stress, or rocking, is less than the lower bound lateral strength limited by diagonal tension or toe compressive stress. Otherwise, these components should be considered as force-controlled components.

Each of the above failure modes has associated with it a characteristic type of hysteresis that must be incorporated into any design model. Figure 1 shows the idealizations of the hysteresis behavior for each failure mode as synthesized using simple multiparameter geometrical rules.

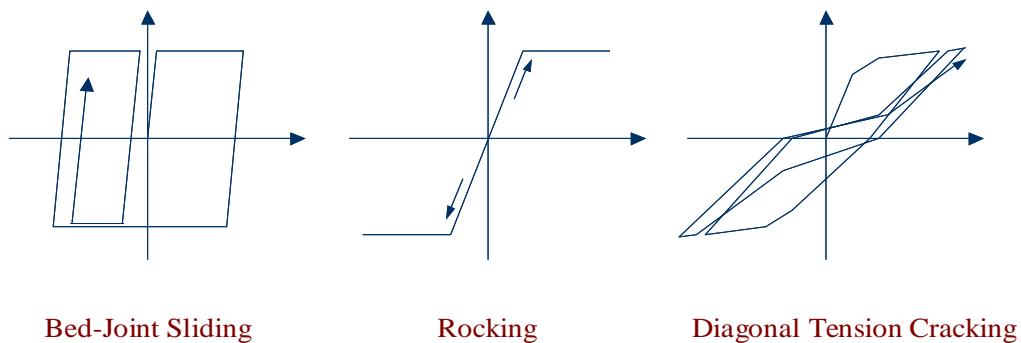


Figure 1 Idealization of hysteresis behavior of each failure mode

Modeling of a Perforated Wall

In reality, few masonry walls exist as a solid wall configuration. Rather, a general masonry wall has one or more major openings, such as doors and windows, which may comprise more than 10% of the wall area, and it is important to be able to accurately model such walls. Under initial levels of in-plane loading, such a wall will develop an elastic stress distribution pattern that depends on the number, size, shape and relative arrangement of the perforations. As the loading is increased, the elastic stresses will increase until one or more of the failure modes described above develops in some region of the wall. If sufficient post-failure strength can be achieved, additional regions will also experience one or more of the failure modes. While this process is quite complicated and detailed computational models can be very large and time-consuming to execute, it nonetheless can form the basis for a simpler design model.

The anticipated failure zones, as identified by simple elastic behavior (which is relatively easily modeled using commonly available plane stress computational analysis tools), or perhaps by experience and simple heuristics, can be used to define certain regions of the wall that do not fail and continue to exhibit linearly elastic behavior. These regions typically include some of the masonry piers and many of the lintels and spandrel sections. The in-plane force-deformation behavior of these regions, which we will now refer to as wall components, can usually be adequately modeled using classical bending and shear deformation

formulations. The failure modes, failure strengths, and the hysteretic behavior for each wall component can be determined based on the provisions in FEMA-356 as noted above. These characteristics can readily be incorporated into attributes for nonlinear spring elements whose initial elastic behavior models the elastic properties of the component itself. Finally, these nonlinear springs can be assembled into a parallel and series arrangement that approximates the topology of the wall components themselves. In this manner, a “composite” wall model consisting of the parallel- and series-connected nonlinear springs can be created.

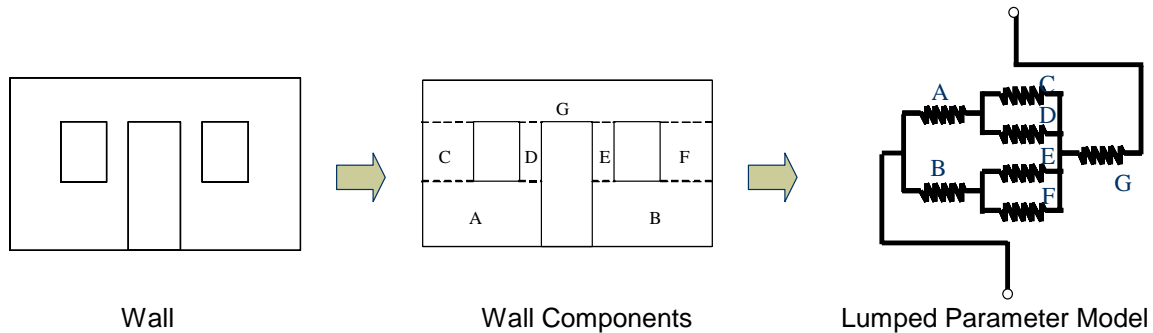


Figure 2 Decomposing and modeling of a perforated wall

The single-story perforated wall shown in Figure 2 is a simple example to illustrate the methodology. The wall includes a door and two symmetrically arranged window openings. These perforations effectively break up the single wall into a number of segments such as the two relatively thin (high aspect ratio) piers on either side of the door (D, E) as well as the two piers with much lower aspect ratios on the outer sides of the windows (C, F, adjoining the wall ends). In addition, the lintels (or spandrel, G) and the regions below the windows (A, B) define additional wall segments. A simple spring composite model can then be developed based on the decomposition of the wall as shown the third part of the figure.

Model Calibration

The elastic stiffness of the perforated wall in Figure 2 calculated using the simplified spring model is considerably stiffer than it should be compared to plane stress FEM analysis results. In addition, the elastic stiffness of a perforated wall calculated by several other simplified methods tends to be much higher than the actual stiffness as well [5,7]. Therefore, some kind of adjustment is needed to provide an adequate lumped parameter design model.

Effective Height Method and Effective Stiffness Method

One source for the discrepancy in initial elastic stiffnesses is quickly apparent when the in-plane deformations of the URM wall computed from a plane stress FEM analysis are examined (Figure 3). It is obvious from the deformation patterns at the upper and lower ends of the piers that the assumption of fixed (clamped) ends for these piers is not accurate. The end rotation cannot be assumed to be fixed as is implied in the equations from FEMA-356. In fact, the pier boundary conditions are neither fixed nor free as assumed in the FEMA-356 formulas. We will address this issue by either (a) introducing the concept of an “effective height” or (b) by incorporating an “effective (rotational end) stiffness” for the piers to account

for the non-ideal end conditions, while allowing use of the classical beam bending and shear deformation formulas in FEMA-356.

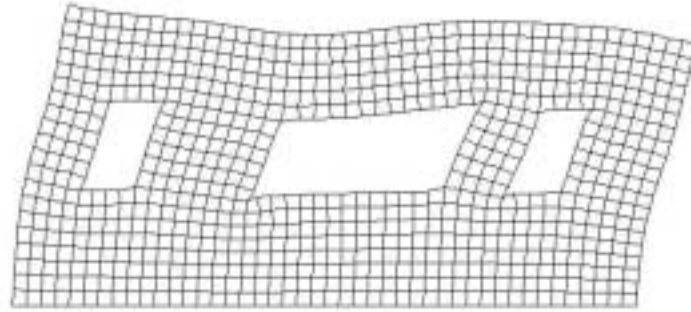


Figure 3 Example FEM Plane Stress Analysis of a Perforated URM Wall

Figure 4(a) shows a single-story URM pier taken out of a URM wall with openings. The most direct approach is to model the rotational flexibility at the ends using rotational springs as shown in Figure 4(b). The objective is then to estimate the effective rotational stiffness, k_p , at each end of the pier. The effective height approach accounts for the added rotational flexibility by increasing the pier height (e.g., beam length) by a factor, r , while maintaining the ideal fixed end conditions. This approach is illustrated in Figure 4(c) for a pier whose physical height is H_p but whose ends are not ideally fixed to the upper and lower spandrel/lintel components. The increased height will result in a stiffness reduction that, if correctly computed, will equal the reduction due to less than fixed end conditions. Since this increased pier height is not real, but is used simply to compute a more accurate stiffness, we will refer to it as an “effective height.”

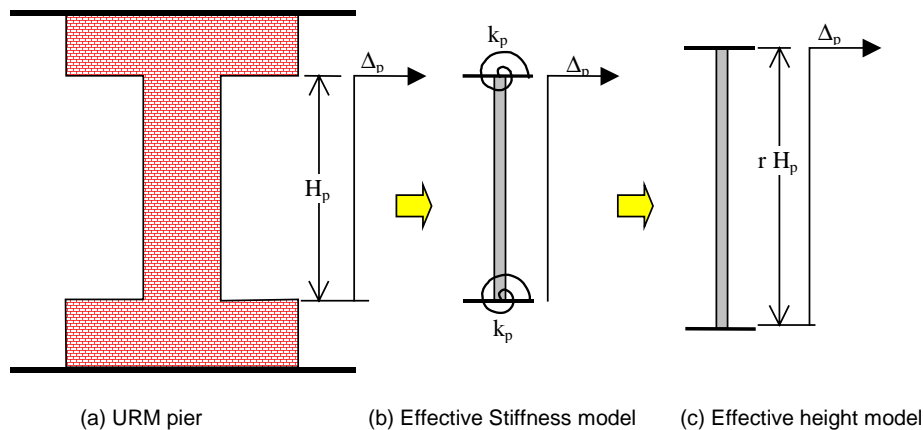


Figure 4 Formulations for Effective Height and Effective Stiffness of URM Pier

As can be seen in Eq. (2), the effective height, $r H_p$, of the pier is determined so that the in-plane deflection per unit load (e.g., the flexibility) of a pier of this height with fixed ends is equivalent to the deflection of a pier of height, H_p , but with assumed end rotational stiffnesses, k_p . As a result,

$$\Delta p = \frac{H_p^3}{12EI} + \frac{1.2H_p}{GA} + \frac{H_p^2}{2k_p} = \frac{(rH_p)^3}{12EI} + \frac{1.2H_p}{GA} \quad (2)$$

where Δp is the horizontal displacement measured from the top to the bottom of the pier, H_p is the height of the pier, and k_p is the effective rotational stiffness of the pier joint area. Note that the effective height factor, r , is not applied to the shear term in the pier deflection calculation because the flexibility of the joint area at the pier ends doesn't affect the shear deformation of the pier. At this point, the issue is how to calculate the effective height factor or the effective stiffness for each masonry pier based on the particular configuration of the perforated URM wall.

The effect of different end conditions (k_p values) at the top and bottom of the pier can be approximated by breaking the pier into two half-height piers cantilevered from the ends and pinned together in the middle as illustrated in Figure 5. Ideally, the pin joint should be located at the inflection point, so using half-heights for each segment is an approximation, but it greatly simplifies the formulation.

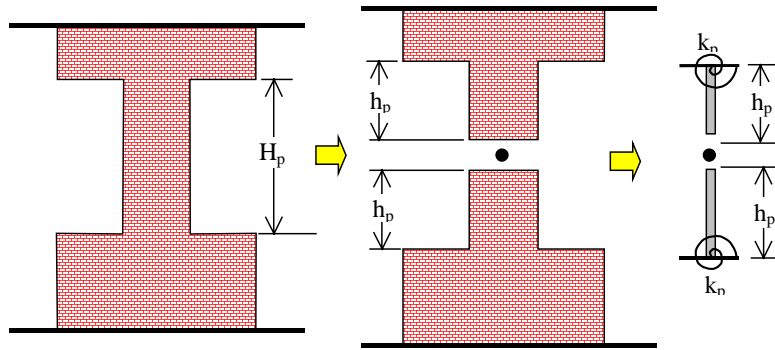


Figure 5 Decomposition of Pier into Two Half-Height Components

An appropriate pier model is now a cantilevered pier, and Eq. (2) can be modified to represent a cantilevered pier as follows:

$$\Delta p = \frac{h_p^3}{3EI} + \frac{1.2h_p}{GA} + \frac{h_p^2}{k_p} = \frac{(rh_p)^3}{3EI} + \frac{1.2h_p}{GA} \quad (3)$$

Pier End Conditions

Accurate estimation of the pier end conditions is difficult to achieve. The depth of the spandrel or lintel components compared to the pier width is obviously an important parameter, but the effect of their widths (e.g., lengths in the horizontal direction) is not so clear. Also, the pier height to width ratio (aspect ratio) is probably important. But the pier ends are not always so well-defined because the openings on either side of the pier may be of different heights. In this case a parameter that reflects this asymmetry must be defined. Pareto optimization can provide a means to identify the most important parameters on the basis of their quantitative

effect on the computed result (in this case the pier stiffness), but in this case, the various geometric variables are interdependent and difficult to separate clearly. As a result, after applying engineering judgment and using trial and error calculations, the following three parameters were defined to represent the different kinds of pier end conditions (Figure 6).

1. W_p/h_p - the aspect ratio of the pier
2. H_b/W_p - the ratio of the depth of the spandrel component to the pier width.
3. α - a factor that determines the asymmetry of the pier end ($0 \leq \alpha \leq 1$).

The first two parameters are measures of the pier and spandrel geometries, respectively. The third parameter defines the asymmetry of the end region and is simply the fraction of the spandrel height eliminated by the opening on one side of the pier. The range of values is $0 \leq \alpha \leq 1$, and $\alpha=0$ corresponds to a symmetric end while $\alpha=1$ represents a corner pier or a configuration with a pier adjacent to a doorway. The parameters have all been defined so that practical values are between 0 and 10. In addition, when the parameters are equal to 0, the effective height factor should be approximately unity.

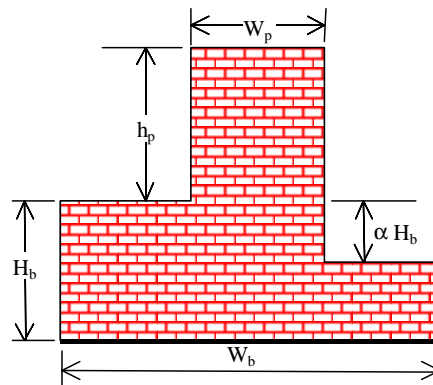


Figure 6 Definition of Parameters Defining the Pier End Condition

Reference Solution

The “exact” solution for this problem is considered to be a plane stress analysis, and in this study it is performed for URM wall configurations shown in Figure 6 using ABAQUS. Values of 495,000 ksi and 0.2 are used for the elastic modulus and Poisson’s ratio for masonry material. The structural thickness is set to unity (1.0 inch), and a unit shear force (1.0 lb) is applied horizontally at the top of the pier. The shear force is distributed over the top edge of the pier to avoid stress concentration at a single node. A standard 4-node linear element is used, and the size of the mesh is set so that either the height or the width of the pier, which ever is smaller, is always divided into more than four elements. The relative horizontal displacement between the top and the bottom of the pier is computed from average nodal displacements across each pier end (the pier bottom is defined by h_p).

Regression Analysis

The pier effective height factor, r , is determined using multivariate polynomial regression analysis (i.e., a “response surface”). However, for the case of 3 parameters, this would yield

up to 9 regression coefficients (for quadratic polynomials) and would lead to an unnecessarily complicated formulation. A simpler solution (ignoring interaction terms and using exponentials instead of polynomials) is sought, and the approach taken is to define nominal values for each of the parameters and then fix two of them while varying the third in order to compute the regression for the r factor. Under the assumption that the parameters are largely independent of each other, the r factor for the pier is the product of the three r factors from each separate regression analysis as shown in Eq. (4). For all cases, the overall width of the wall segment (W_b) is set to six times that of the pier width (W_p) in order to minimize flexure of the bottom masonry spandrel (which is fixed across the lower base).

$$r = \left[1.005 + 0.19 \left(\frac{H_b}{W_p} \right)^{\frac{1}{5}} \right] \times \left[1 + 0.1\alpha^{\frac{1}{4}} \right] \times \left[0.803 + 0.281 \left(\frac{W_p}{h_p} \right)^{\frac{7}{10}} \right] \quad (4)$$

Similarly, the effective stiffness coefficient, ξ , which is defined as $EI/(k_p W_p)$, can be expressed in terms of each variable using the simple exponential regression results for each case. Note that in the effective stiffness method, the parameter W_p/h_p does not need to be included because the height of the pier does not affect the stiffness of the pier end. One of two equations is normalized and multiplied to the other equation to establish the general expression of ξ in terms of two variables.

$$\xi = \left[0.4 \left(\frac{Hb}{Wp} \right)^{\frac{1}{5}} \right] \times \left[1 + 0.714\alpha^{\frac{1}{4}} \right] \quad (5)$$

Again, it is noted that these equation are established on the assumption that the finite element analysis gives the correct result, and it is also noted that each parameter must be in the range for which the regression analysis is generated.

Consideration of Bending Effect

Both methods are based on a simple shear model that assumes the horizontal displacements of each component are due to the corresponding shear force. However, there will also be in-plane bending action in the wall, and the effect will become larger as the wall aspect ratio increases (wall height/length). An additional bending deflection must be added so that:

$$\Delta_{top} = \Delta_{eff} + \Delta_b \quad (6)$$

where Δ_{top} is the displacement at the top of the wall, Δ_{eff} is the displacement obtained from either the effective height method or the effective stiffness method, and Δ_b is the displacement from the beam bending effect in the wall. The displacement due to the beam effect of the wall, Δ_b , can be estimated as follows.

$$\Delta_b = \frac{H^3}{3EI} \quad (7)$$

where H is total height of the wall and I is the moment of inertia of the section of the wall. However, since this equation is for the case of a solid wall (no openings), a correction factor for the effect of the openings has to be considered.

$$\Delta_{top} = \Delta_{eff} + \Delta_b = \Delta_{eff} + \rho \frac{H^3}{3EI} \quad (8)$$

where ρ is the correction factor for the opening effect. This correction factor can be determined in a same way as it is done for the effective height and stiffness factors. First, a wall is chosen such that the top displacement due to the lateral load at the top is dominated by bending rather than shear effects (an aspect ratio larger than 4). The relationship between the opening ratio, η_p , and the factor is established by performing a regression analysis yielding:

$$\rho = 1 + 0.0035\eta_p + 0.0004\eta_p^2 \quad (9)$$

where η_p is the ratio of the area of the openings to the area of the overall wall (%).

EXAMPLE

As an example, we will consider a wall (Figure 7) from the full-scale URM structure being tested in Project ST-11 at the Mid America Earthquake Center [8]. Figure 7 also shows the simplified nonlinear lumped parameter model developed according to the methods presented in this paper with the lateral load vertically distributed for static equivalent loading in based on FEMA 356. The spring model is implemented in DRAIN-2dx [4] using the Type 04 spring element.

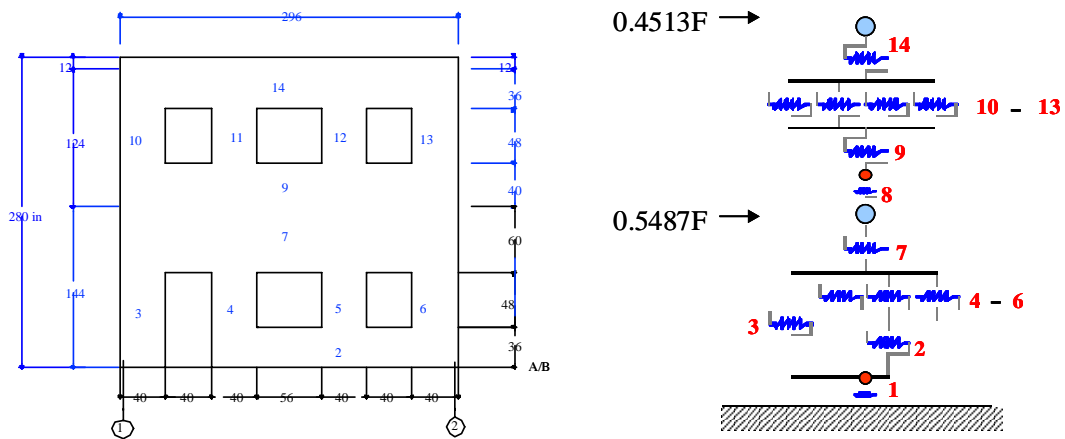


Figure 7 Modeling of the Example Wall

The behavior of the wall model is examined under a monotonic loading such that the capacity of the wall can be illustrated. As shown in Figure 8, inner piers at the second floor fail first (point A), followed by failure of the outer piers at the second floor (point B).

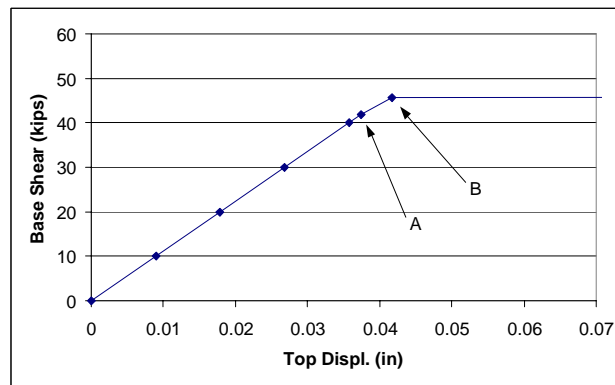


Figure 8 Behavior of the wall under the monotonic loading

ACKNOWLEDGMENT

This study is supported by the Mid-America Earthquake Center under the National Science Foundation Grant EEC-9701785, Project ST-4.

REFERENCES

1. Bruneau, M. (1994) "Seismic Evaluation of Unreinforced Masonry Buildings—A State-of-the-Art Report", Canadian Journal of Civil Engineering, V 21 N 3, June, pp. 512-539.
2. Lourenco, P. B. (1996) "Computational Strategies for Masonry Structures", Delft University Press.
3. Magenes, G. & Calvi, G. (1997) "In-Plane Seismic Response of Brick Masonry Walls", Earthquake Eng Struct Dyn V 26 N 11, November, John Wiley & Sons Ltd Chichester England, p1091-1112.
4. Prakash, V. & Powell, G. H. (1993) "DRAIN-2DX Base Program Design Documentation", Report UCB/SEMM-93/16, University of California at Berkeley.
5. Schneider, R. & Dickey, W.L. (1987), "Reinforced Masonry Design", Prentice Hall, Second Edition, pp.400-417.
6. Shing, P.B. & Klingner, R.E. (1998) "Nonlinear Analysis of Masonry Structures", Elsevier Science Ltd.
7. Tena-Colunga, A. & Abrams, D. P. (1992) "Response of an Unreinforced Masonry Building During the Loma Prieta Earthquake", National Science Foundation, Research Grant NSF BCS 90-03654.
8. Yi, T., Leon, R., & Kahn, L. F. (2001) "Large-scale Test of Low-rise Building System", <http://www.maec.gatech.edu/st11/>, Mid-America Earthquake Center.
9. Zhuge, Y., Thambiratnam, D., & Corderoy, J (1998) "Nonlinear Dynamic Analysis of Unreinforced Masonry", Journal of Structural Engineering, March.



KEERC-MAE Joint Seminar on
Risk Mitigation for Regions of Moderate Seismicity
University of Illinois at Urbana-Champaign, August 5-8, 2001



Sponsors: Korea Science and Technology Foundation, U.S. National Science Foundation, Brain Korea 21



Cost Effectiveness Evaluation and Optimal Design of Seismically Isolated Bridges

Daegi HAHM¹, Hyun-Moo KOH², Junho SONG³

¹ *PhD Candidate, School of Civil, Urban and Geosystem Engineering,
Seoul National University(SNU), Korea*

² *Professor, School of Civil, Urban and Geosystem Engineering,
Seoul National University(SNU), Korea*

³ *PhD Candidate, Department of Civil Engineering,
University of California at Berkeley, USA*

ABSTRACT: A method of optimal design and cost effectiveness of seismically isolated bridges is developed based on minimum life cycle cost concept. Input ground motion is modeled as spectral density function compatible with response spectrum for combination of acceleration coefficient and site coefficient. Failure probability is calculated by spectral analysis method based on random vibration theories. Ductility of piers is considered by evaluating equivalent linear pier stiffness based on stochastic linearization method. Stiffness of pier and isolator are adopted as optimal design variables and cost functions are defined using them. The exemplifying designs and analyses show that the presented method helps to design seismically isolated bridges optimally based on life cycle concept and to evaluate their cost effectiveness in various kinds of acceleration and soil conditions at ease.

KEYWORDS: seismically isolated bridges, cost effectiveness, life-cycle cost, statistical linearization, failure probability

INTRODUCTION

Infrastructures should be designed optimally so as to minimize their social cost during life cycle. The minimized life cycle cost can be used in evaluating cost effectiveness of a specific structural system.

There are numerous researches being developed on optimal design and cost effectiveness evaluation methods based on the life cycle concept. These approaches have been applied to various kinds of structural systems such as buildings and bridges. The methods are also being applied to vibration control system such as active control [1] and seismically isolated bridges [2].

Seismic isolation is a relatively new technology for seismic design of bridges and is being equipped in recent constructions. However, the methods for optimal design and cost effectiveness evaluation are not developed sufficiently. In the previous research [3], a method was developed to satisfy this necessity but the stiffness of pier was assumed to be linear in the spectral analysis and it was not able to consider ductility of pier and its effect on life cycle cost. In designs of non-isolated bridges, ductility of pier is so important factor that nonlinear behavior of pier should be considered in calculating failure probability.

Stochastic linearization method is applied in evaluating equivalent linear stiffness of pier. As a result, the method of optimal design and cost effectiveness evaluation considering ductility of pier is presented in this study. According to exemplifying designs and analyses based on the method, properties of optimal seismic design and cost effectiveness in various conditions are studied.

LIFE-CYCLE COST CONCEPT FOR SEISMICALLY ISOLATED BRIDGES

Total life cycle cost of an infrastructure consists of initial construction cost and expected damage cost during its life cycle. Seismic isolation for bridges reduces initial cost of pier because seismic isolator enables smaller pier to sustain equivalent seismic ground motion by period shift of the structural system. However, initial cost increases at the same time due to cost of the isolation. Expected damage cost also change with the combination of pier stiffness and isolator stiffness (Figure 1).

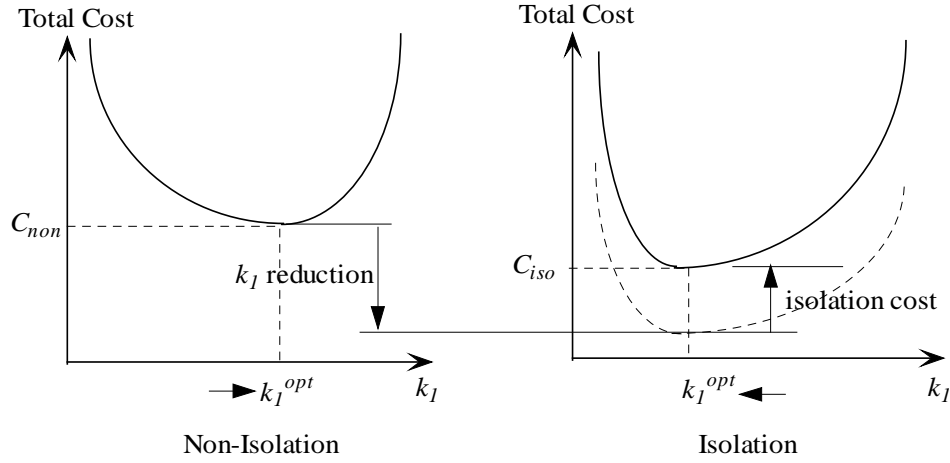


Figure 1 Life Cycle Cost Concept for Seismically Isolated Bridges

Expected value of cost function for seismically isolated bridges is defined as follows.

$$E[C_{iso}(k_1, k_2)] = C_p V_p(k_1) + C_{iso} V_{iso}(k_2) + C_d \vec{r}_d \cdot \vec{P}_f(k_1, k_2) \frac{\nu}{\lambda} (1 - e^{-\lambda t_{life}}) \quad (1)$$

where k_1 is stiffness of pier, k_2 is stiffness of isolator, C_p is initial cost of pier per unit volume, V_p is volume of pier, C_{iso} is initial cost of isolation, V_{iso} is volume of isolator, C_d is assumed damage scale of the bridge, \vec{r}_d is vector of damage cost ratios of limit states, $\vec{P}_f(k_1, k_2)$ is vector of conditional probability of each limit state given occurrence of earthquake, ν is occurrence rate of earthquake, λ is discount rate and t_{life} is life cycle of the bridge [1]. We are able to design seismically isolated bridges optimally by finding the combination of stiffness of pier and stiffness of isolator (k_1, k_2) minimizing the expected value of cost function shown in Eq. 1. Moreover, cost effectiveness of isolated bridge relative to non-isolated bridge can be evaluated by comparing the value of minimized cost with that of non-isolated.

Failure probability $\vec{P}_f(k_1, k_2)$ of the cost function defined in Eq. 1 is calculated by spectrum analysis based on random vibration theories in order to make repetitive calculations easy during cost minimization procedure. Therefore, input ground motion is modeled as spectral density function compatible with response spectrum for combinations of acceleration coefficient and site coefficient [3, 4].

STATISTICAL LINEARIZATION

Ductility of Pier

Piers designed according to most seismic design codes have additional capacity even after their yielding – namely, ductility. Ductility of piers is an important seismic capacity of bridges, particularly of non-isolated bridges. Therefore, ductility of pier should be considered in calculating failure probability of piers and in evaluating cost effectiveness because piers of isolated and non-isolated bridge have different nonlinear behavior [5]. In this study, mechanical property of piers is modeled as bilinear hysteretic curve as shown in Figure 2.

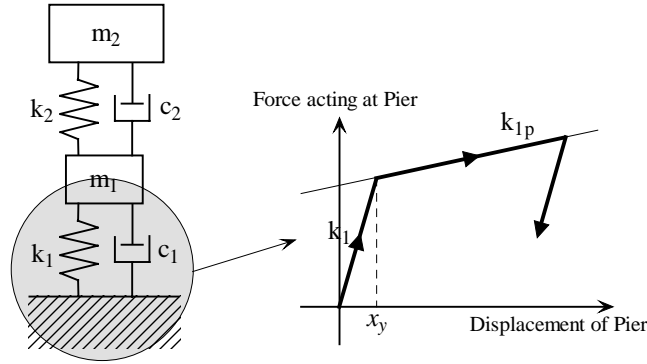


Figure 2 Bilinear Modeling of Pier

Statistical Linearization

To consider the presented bilinear model of piers in spectrum analysis for failure probability, statistical linearization method is applied. The method finds out equivalent linear coefficients a_1 , a_2 in Eq.4 minimizing the mean squared error from a given nonlinear function in Eq. 3. (C_1+a_2) and $(k_{1p}+a_1)$ replace C_1 and k_1 of Eq. 1 in spectrum analysis.

$$m_1 \ddot{u}_1(t) + C_1 \dot{u}_1(t) + k_{1p} u_1(t) + g[\{u_1(t)\}] = F(t) \quad (3)$$

$$m_1 \ddot{u}_1(t) + (C_1 + a_2) \dot{u}_1(t) + (k_{1p} + a_1) u_1(t) = F(t) \quad (4)$$

where k_{1p} is post-yielding stiffness of pier, a_1 and a_2 are coefficient minimizing the mean squared error, $g[\{u_1(t)\}]$ is nonlinear function describing elastoplastic behavior and $F(t)$ is force acting at pier. Error to be minimized is defined as follows.

$$\hat{E}(t) \equiv a_2 \dot{u}_1(t) + k_{1p} u_1(t) - g[\{u_1(t)\}] \quad (5)$$

The coefficients a_1 and a_2 can be obtained by the following equations based on several assumptions [6]

$$a_1 = k_1 \left[1 - \frac{8}{\pi} \int \left(\frac{1}{z^3} + \frac{u_y^2}{2\sigma_{u_1}^2 z} \right) \sqrt{z-1} \exp\left(\frac{-u_y^2 z^2}{2\sigma_{u_1}^2} \right) dz \right] \quad (6)$$

$$a_2 = \sqrt{\frac{2}{\pi}} \frac{k_1 u_y}{\omega_a \sigma_{u_1}} \left[1 - \Phi\left(\frac{u_y}{\sigma_{u_1}} \right) \right] \quad (7)$$

where u_y is yielding displacement of pier, σ_{u_1} is standard deviation of u_1 , ω_a is average frequency of displacement and $\Phi(\cdot)$ is the cumulative distribution function for a standardized Gaussian Random variable.

Failure Probability Calculation

Transfer function of each displacement can be derived from the equation of motion in Eq. 1 and spectral density functions are obtained using the transfer functions and the input ground motion model cited in previous chapter. Integration of spectral density function of responses leads to standard deviation, and the rate crossing over predetermined limit states can be calculated by the following equation assuming the input motion is subject to Gaussian distribution [7].

$$\nu_u = \frac{1}{2\pi} \frac{\sigma_{\dot{u}}}{\sigma_u} \exp\left(-\frac{u_{lim}^2}{2\sigma_u^2} \right) \quad (8)$$

where ν_u is crossing rate of response u , $\sigma_{\dot{u}}$ is standard deviation of time rate of u , σ_u is standard deviation of u and u_{lim} is limit state defined on u . On the assumption that occurrence of failure is subject to Poisson distribution, conditional failure probability given an earthquake is calculated with duration time of earthquake (t_d) as follows.

$$P_{f_u/eq} = 1 - \exp(-\nu_u t_d) \quad (9)$$

The results of exemplifying analyses show that the failure probability with respect to the design variables, pier stiffness and isolator stiffness (Figure 3). As ductility of pier affects differently according to conditions, ductility of piers should be considered in calculating failure probability for cost effectiveness evaluation by special methods such as statistical linearization.

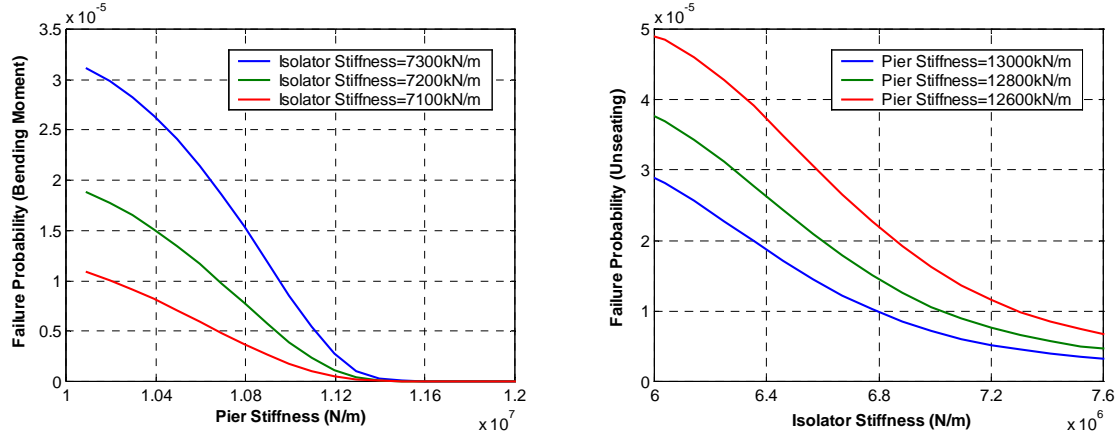


Figure 3 Failure Probability of Non-Isolated Pier

COST EFFECTIVENESS EVALUATION

In order to evaluate cost effectiveness of seismically isolated bridges relative to non-isolated bridges, cost effectiveness index is defined as follows [1].

$$E_{iso/non} = \frac{E[C_{iso}]_{min}}{E[C_{non}]_{min}} = \frac{V_p(k_1^{opt}) + r_{iso/p} V_{iso}(k_2^{opt}) + V_f \bar{r}_d \cdot \bar{P}_f(k_1^{opt}, k_2^{opt}) \frac{V}{\lambda} (1 - e^{-\lambda t_{ijc}})}{V_p(k_1^{opt}) + V_f P_f(k_1^{opt}) \frac{V}{\lambda} (1 - e^{-\lambda t_{ijc}})} \quad (10)$$

where k_1^{opt}, k_2^{opt} are optimal stiffness of pier and isolator minimizing each life cycle cost, $r_{iso/p}$ is ratio of cost of isolator to that of pier with the equal volume and V_f is assumed damage scale regulated in the unit of pier volume with initial cost equal to assumed damage cost.

Cost Effectiveness indices were evaluated changing acceleration coefficients (Figure 4). At the sites of relatively stiff soil condition (soil type II), cost effectiveness becomes higher with decrease of acceleration coefficient value, but the difference is not so significant. If the soil is soft (soil type IV), cost effectiveness of isolation decreases as acceleration coefficient increases at almost all assumed damage scales. We can also see that a soft soil condition leads to decrease of cost effectiveness of isolation in high seismic region.

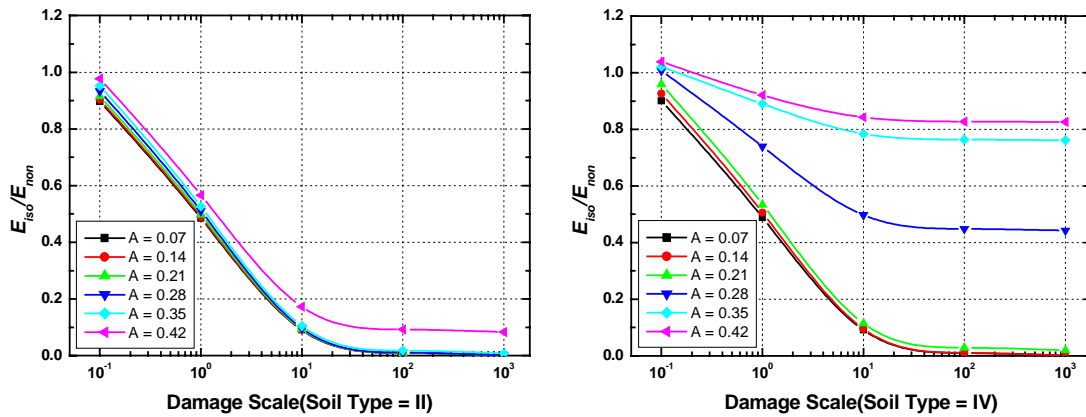


Figure 4 Cost Effectiveness with Acceleration Coefficients and Soil Type

CONCLUSIONS

A method of optimal design minimizing life cycle cost and cost effectiveness evaluation for seismically isolated bridges are developed based on life cycle cost concept. The method calculates failure probability using spectrum analysis to perform the repetitive process easily but is able to consider ductility of piers by statistical linearization method. Seismically isolated bridges are more cost-effective in stiff soil regions than in soft soil region. If damage scale is assumed big, that is, the bridge is very important and requires high reliability, cost effectiveness of seismic isolation system is higher than that of small damage scale region.

The method presented in this study is expected to help decision-maker to decide whether isolation will be adopted for the given conditions or not. In case that isolation is adopted, the method also helps to design system of the bridge optimally from cost-effectiveness point of view. If sufficient information about initial cost and detail information of damage is supplemented to the presented method, more well-founded and concise evaluation of cost effectiveness will be feasible.

REFERENCES

1. Wen, Y.K. and Ang, A.H-S., 1992, "Reliability and Cost-Effectiveness of Structures with Active Control," Proceedings of the International Workshop on Intelligent Systems, Elsevier Ltd., N.Y.
2. Parducci, A. and Materazzi, L.A., 1995, "A Wide Spread Criterion for Estimating the Expected Benefits Deriving from the Application of Seismic Isolation," Proceedings of 10th European Conference on Earthquake Engineering, Balkema, Rotterdam.

3. Koh, H.M. and Song, J., 1999, "Evaluation of Economical Efficiency for Seismic-Isolated Bridges Based on Minimum Life-Cycle Cost," *Journal of the Korean Society of Civil Engineers*, KSCE, 19(I-4).
4. AASHTO, 1997, *Guide Specifications for Seismic Isolation Design*, Draft, AASHTO T-3 Task Group.
5. Kim, D.S., 1999, *Response Modification Factors for Seismically isolated Bridges in Low and Moderate Seismic Region*, M.S. Thesis, Seoul National University, Seoul, Korea.
6. Lutes, L.D. and Sarkani,S., 1997, *Stochastic Analysis of Structural and Mechanical Vibrations*, Prentice Hall, Inc., NJ.
7. Newland, D.E., 1993, *An Introduction to Random Vibrations, Spectral and Wavelet Analysis*, John Wiley and Sons Inc., N.Y.



KEERC-MAE Joint Seminar on
Risk Mitigation for Regions of Moderate Seismicity
University of Illinois at Urbana-Champaign, August 5-8, 2001



Sponsors: Korea Science and Technology Foundation, U.S. National Science Foundation, Brain Korea 21



Fatigue Strength of Stud Shear Connection in Full-Depth Precast Concrete Deck Bridge

HyungKeun RYU¹, SungPil CHANG²

¹ *Ph. D. candidate, School of Civil, Urban & Geosystems Eng.,
Seoul National University, Korea
email: ryu99@snu.ac.kr*

² *Professor, Dr-Ing, School of Civil, Urban & Geosystems Eng.,
Seoul National University, Korea
email: changsp@plaza.snu.ac.kr*

ABSTRACT: In full depth precast deck bridge, mechanical behavior of the stud shear connection is different from that of stud shear connection in cast in place (CIP) bridge. The different structural characteristics of precast deck bridge from cast in place bridge are shear pocket which is filled with non shrinkage mortar to connect slab with girder and bedding layer which is needed to lay slab on girder stably. Thus, in order to evaluate the static and fatigue strength of stud shear connection in precast deck bridge, consideration of structural characteristics of precast deck bridge is essential. In this paper, push tests were conducted in order to estimate fatigue strength of stud shear connection in full depth precast deck bridge considering of structural characteristics, bedding layer thickness and non shrinkage mortar which is filling material of shear pocket and then S-N curve equation was proposed.

KEYWORDS: precast deck bridge, stud shear connection, fatigue strength, S-N curve equation

INTRODUCTION

The type of concrete and steel composite bridge is very useful and efficient because concrete is strong against compressive force and steel is strong against tensile force. Thus, the application of this type is expected to increase.

This type of bridge has composite action by shear connector. Thus the shear connector is a very important element because it allow composite act by connecting concrete slab and steel girder. For this reason, many researchers have studied about the shear connector for a long time. Especially, stud shear connector is recognized as efficient connector and many researches have been progressed about that. However, most current studies are about the stud shear connector of cast in place bridge and only a few studies are about that of precast concrete deck bridge.

Nowadays, increasing traffic volume and overload truck have done damaged to bridge deck. Accordingly, rapid replacement and rehabilitation of deck are essential. Precast deck bridge meets the demand of those operations and it is a very efficient and economical structural system. In precast deck bridge, mechanical behavior of the stud shear connector is different from that of stud shear connector in cast in place(CIP) bridge. Therefore, on the precast deck bridge, the research of the stud shear connector is essential. Figure 1 is a general type of precast deck bridge.

The different structural characteristics of the precast deck bridge from cast in place bridge are shear pocket which is filled with non-shrinkage mortar to connect slab with girder and bedding layer which is needed to lay slab on girder stably. Figure 2 shows different characteristics of precast deck bridge from the CIP bridge.

For this reason, it is not reasonable to apply the general design strength equation of shear connector in CIP bridge for the shear connector in precast deck bridge. Since general strength equation of shear connector which is used in design is developed for shear connector in CIP composite bridge.

Kim[4] had carried out static push tests about precast deck bridge which have parameters that are strength of non shrinkage mortar, diameter of stud shank and thickness of bedding layer. Consequently, from the results of experiments, he suggested the following equation of ultimate strength.

$$Q_u = \alpha (0.36A_{sh} + 18.71) \quad (1)$$

$$\alpha = 1 - 0.0086 (b_h - 20) \quad (2)$$

where Q_u : the ultimate strength of shear connection in precast deck bridge(kN), A_{sh} : the area of stud shear connector(mm^2), α : the decrease coefficient of ultimate strength of shear connection considered bedding thickness, b_h : bedding layer thickness(mm).

However fatigue strength of stud shear connection considering of bedding layer thickness was not studied. Therefore, in this paper, push tests were conducted in order to estimate fatigue

strength of stud shear connection in full depth precast deck bridge considering of structural characteristics, bedding layer thickness and non shrinkage mortar which is filling material of shear pocket and then S-N curve equation was proposed.

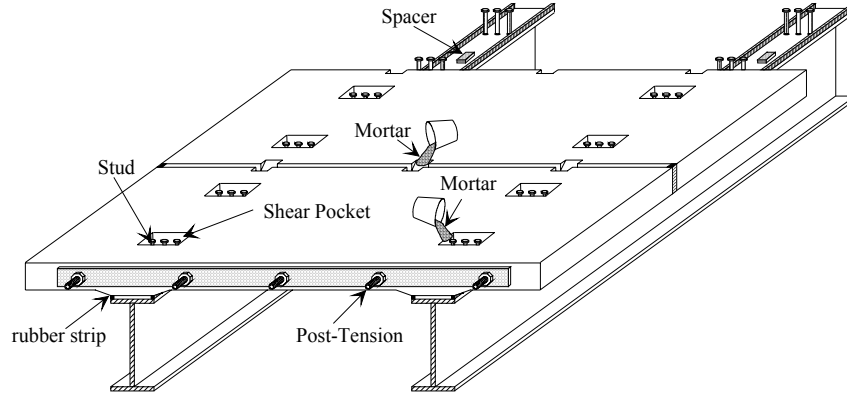
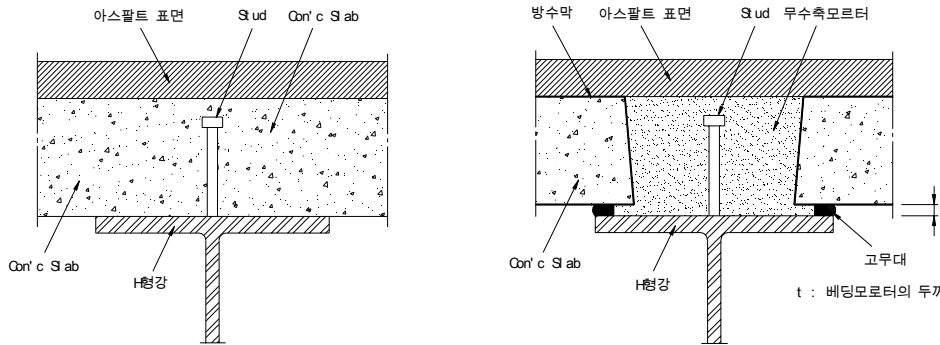


Figure 1 Precast Concrete Deck composite bridge



(a) CIP concrete deck (b) precast concrete deck

Figure 2 The comparison with stud shear connector

PUSH TESTS

Test Specimen

To examine the behavior of shear connection, push tests were executed and Figure 3 shows push tests specimen that was used in this study.

The length and width of the precast concrete deck used in push-out test are determined to be 60cm and 70cm respectively referring to a standard push-out test specimen suggested by Eurocode 4[2] and the thickness is determined to be 22cm by minimum thickness rule of Korean Highway Standard Specification(1996).

Also, to consider loading redistribution, the shear connection was arranged in two rows and to describe real behavior of bridge, thickness of deck and diameter of stud shank were determined to be 22cm, 19mm respectively which were used in real composite bridge.

To prevent split failure of concrete deck, the width of precast deck was enlarged and as real composite bridge, the failure had been shear failure of stud shear connector.

Since the direction of concrete casting affects the strength of shear connection a lot, the direction of casting in deck with concrete and shear pocket with non-shrinkage mortar was same as the direction of real casting in precast deck composite bridge.

To prevent stress concentration between steel girder and precast concrete deck and consider effect of haunch, steel girder was set on the non shrinkage mortar layer, that is called bedding layer. And to eliminate effect of bond and friction, in interface between girder and slab, oil was applied. Therefore, conservative test results had been derived.

Also, to prevent deformation of steel girder, the thickness and width of upper flange in girder was limited.

Generally, connecting plate and bolts, etc to connect girder and girder projected into flange of steel girder. In precast deck bridge, because hardening concrete deck was already set on the girder, these projections should be considered in construction. Therefore before the precast deck was set, bedding layer was made on the steel girder that was manufactured using spacer and rubber strip were set on the girder and shear pocket filled with non shrinkage mortar. Also the bedding layer play a role to prevent vibration occurred in live loading and crushing of concrete. Accordingly, there should be bedding layer in precast deck bridge. However for this reason, it is considered that loading mechanism of shear connection change. Therefore, in precast deck bridge, it is necessary for bedding layer and because bedding layer is structural characteristics of precast deck bridge, the fatigue push-out tests with parameter that is bedding layer thickness were conducted and then, from the results, S-N curve was derived.

The diameters of shear connector in push-out tests were all 19mm and compressive strength of non shrinkage mortar were mean 48.9MPa. And fatigue tests were conducted on bedding layer thickness, respectively, 20mm, 30mm, 40mm.

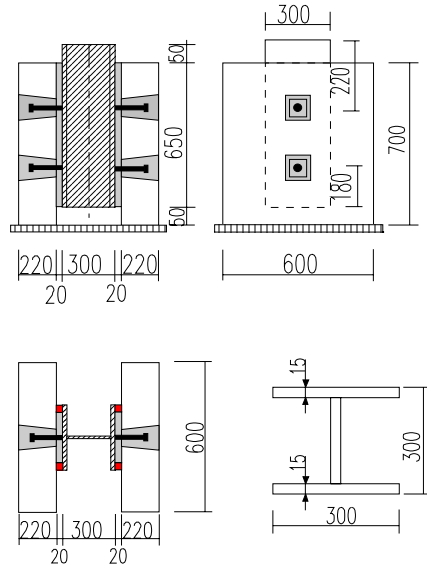


Figure 3 The dimension of push-out specimens

Material Properties

It is important to know about material properties using the tests. Thus, the compressive strength of non-shrinkage mortar, Young's modulus and tensile strength of shear connector were determined by experiments as this.

The experiment of compressive strength of non shrinkage mortar was conducted following KS L 5105(test methods of compressive strength of hydraulic cement mortar) and after standard cylinder specimen was made, for 28 days, it was cured in the air.

As a result of compressive strength test, the strength was mean 48.9MPa. Besides, to seek relationship between compressive strength and Young's modulus, tests about 100mm×200mm cylinder specimens were done.[1] As a result of test, the relation of compressive strength and Young's modulus in non shrinkage mortar was as equation (3).

$$E_m = 3280\sqrt{\sigma_m} \quad (3)$$

where E_m is Young's modulus of non shrinkage mortar(MPa) and σ_m is compressive strength of non shrinkage mortar using 100mm×200mm cylinder specimen.(MPa)

To determine the tensile strength of stud, tension tests were executed by KS B 0802 and from the tests results, the tensile strength of stud shear connector was mean 503MPa.

Tests Procedure

The process of fatigue push-out tests with precast deck specimen is as follows.

The loading force applied by hydraulic repetitive applying load tester of MTS is capable of loading maximum 500kN and the shape of cyclic load was sine wave.

The shear stress ranges applied by one side loading whose minimum loading was fixed to 4.9kN and maximum loading only varied.

The shear stress ranges applied by each load, 108MPa, 125MPa, 151MPa chosen by referring to current researches and S-N curve equations. The shear stress ranges were determined by dividing into stud shank four areas after maximum value minus minimum value. So, the shear stress range per shear connector is 27MPa, 31.3MPa, 37.8MPa.

The loading velocity was determined to be 5Hz that less affects displacement considered characteristic of test specimen.

The Table 1 shows test variables. And the measurement contents in this test were applied loading magnitude, relative slip between steel girder and concrete slab and number of cyclic load in failure.

The applied loading magnitude is measured by load cell within test equipment and controlled by test management S/W within PC. The relative slip of shear connector is measured by LVDT(Large Vertical Deformation Tester) while the load applies slowly until maximum value of cyclic load in each step after applied cyclic load stopped and it is continued until failure of specimen Figure 4 shows adhesive position of LVDT. Also, to observe the strain of shear connector, strain gauges were adhered to stud shank of each specimen. The number of measurement times are basically 0, 1000, 10,000, 50,000, 100,000 but contents were measured as often as possible to check bond between steel and concrete, crack occurrence and crack propagation. The relative slip was measured with four 1/100mm LVDT installed on the left, right, front and back of H shape section and the measured value was averaged. The number of cyclic loading was measured to be the cumulative record number in failure.

Table 1 Fatigue Tests

Specimen	Compressive Strength Of Mortar(MPa)	Maximum Load(kN)	Minimum Load(kN)	Stress Range(MPa)
F2a	48.9	31.85	1.255	26.975
F2b	48.9	36.75	1.255	31.3
F2c	48.9	44.10	1.255	37.8
F3b	48.9	36.75	1.255	31.3
F3c	48.9	44.10	1.255	37.8
F4a	48.9	31.85	1.255	26.975
F4b	48.9	36.75	1.255	31.3
F4c	48.9	44.10	1.255	37.8

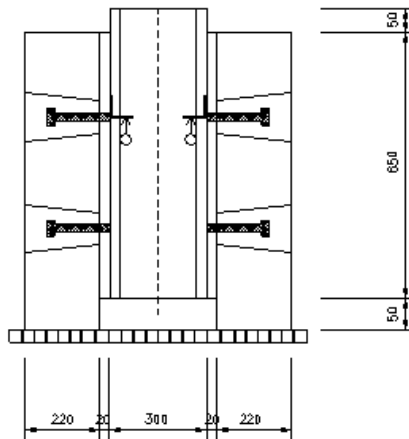


Fig
Figure 4 Adhere position of LVDT

RESULTS OF TESTS

Failure Modes

In this study, weld failure modes of shear connector in push-out tests were all W-mode[2,5] irrelevant to the bedding layer thickness and shear stress ranges.

Figure 5 shows examples of weld failure section in push-out tests.

Because W mode was occurred in all shear connectors, It was confirmed that fracture was occurred in weld-collar/shank interface. Fatigue crack might occur at the end of stud shank

and propagated horizontally. By propagation of fatigue crack, the area of stud was reduced and thus the stiffness of stud shear connection was weakened. Then, when the area of stud shank that was not resisted maximum load of cyclic load was reduced, immediately brittle failure was occurred. It was known that dark and smooth failure surfaces were fatigue failure surfaces and light and rough surfaces were brittle failure surfaces. From these facts, it was confirmed that most of failure surface of stud shear connection was fatigue failure surface. Also, as shown in Figure 6, after fatigue failure of shear connector, split crack or failure did not occur in the bedding layer, its depth of 20mm, 30mm, 40mm. Maybe it means bedding layer less affects the fatigue strength of stud shear connector in this test ranges.

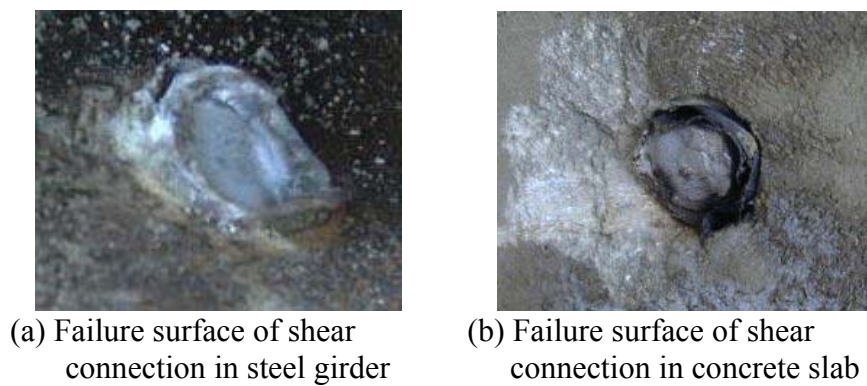


Fig
Figure 5 Fatigue failure surface of shear connection



Figure 6 The cross of bedding layer after fatigue failure of shear connector

Relative Slip

Relative slip history curve for bedding layer thickness and each shear stress ranges is shown like Figure 7. In comparison between (a) and (b), the relative slip history curve measured by LVDT is similar to the relative slip history curve measured with strain gauge adhered to stud shank. Accordingly, the relative slip measured by LVDT can describe deformation of shear connector well.

(a) Relative slip measured by LVDT (b) Strain of stud shank measured by strain gage

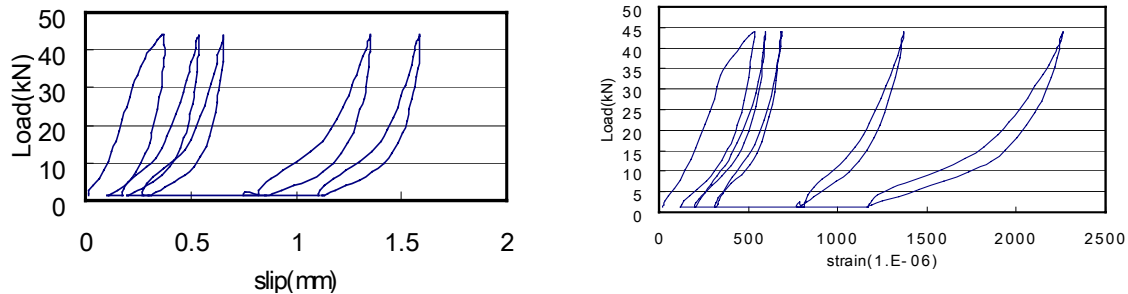


Figure 7 The history curve of relative slip in F4c

Residual Slip Curve

The residual slip curve according to the bedding layer thickness and applied shear stress ranges was shown as Figure 8 and 9. For same bedding layer thickness, the higher shear stress ranges applied, the more residual slips occurred. Thus, it supports the general fact that as shear stress ranges expand, fatigue life reduces.

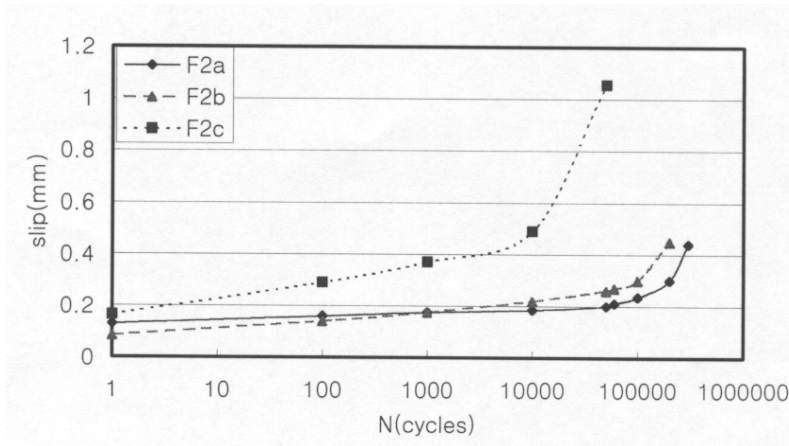
However in case of F4b, residual slip increase most rapidly. It disagrees the fact that as shear stress ranges increase, fatigue life decrease. It seems the reason that there is already an initial crack in shear connector, thus it was judged that this results should be excluded. And for same applied shear stress ranges, there wouldn't be any particular tendency. From this, it is considered that bedding layer thickness less affects fatigue crack propagation.

On the contrary, magnitude of initial crack or residual slip more affects fatigue crack propagation.

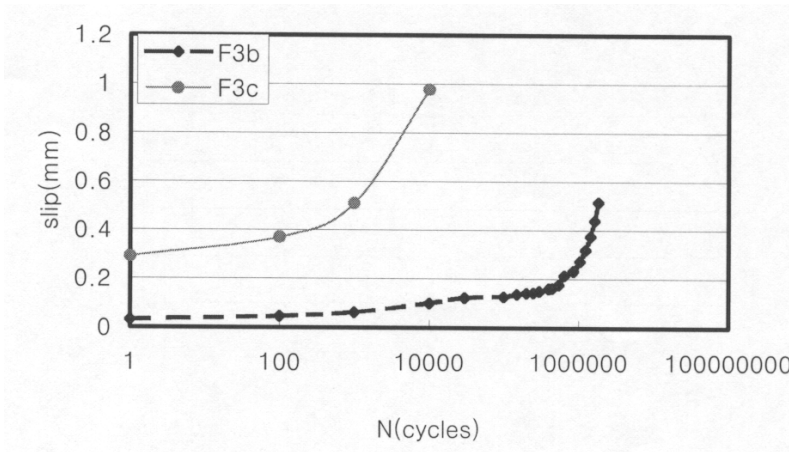
As mentioned above, relative slip measured by LVDT described indirectly deformation of the stud shear connection thus relative slip progress increasing number of cyclic loading is considered same as crack propagation of shear connection.

Therefore, as shown in the Figure 8 and 9, large initial relative slip curve inclined more rapidly and thus it was confirmed that the initial crack occurred in faults of manufacture, welding flaw, carriage and storage were important factors that determined the fatigue life of shear connector.

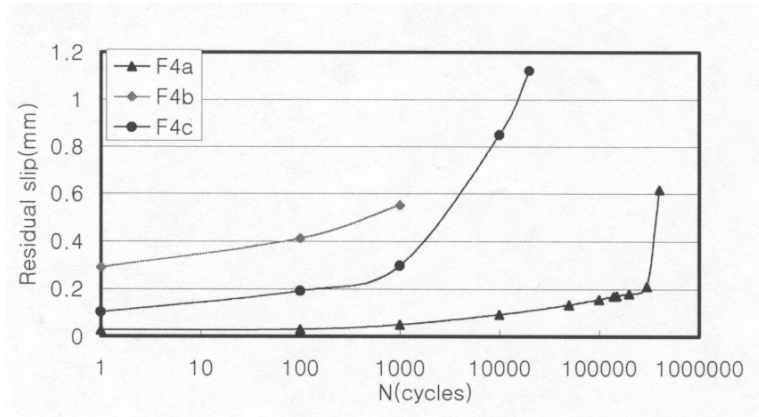
Consequently, also considering of current study, it is supposed that the strength of non shrinkage mortar and bedding layer thickness less affect fatigue life of shear connection in precast deck bridge and shear stress ranges are main factor that affect fatigue life of shear connection. And it is also supposed that initial flaw or some faults affect fatigue life much as factors in general fatigue problems.



(a) Bedding layer thickness, 20mm

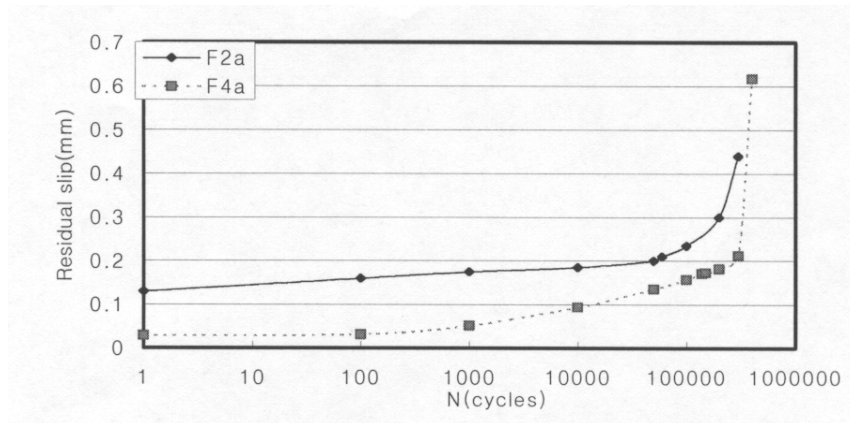


(b) Bedding layer thickness, 30mm

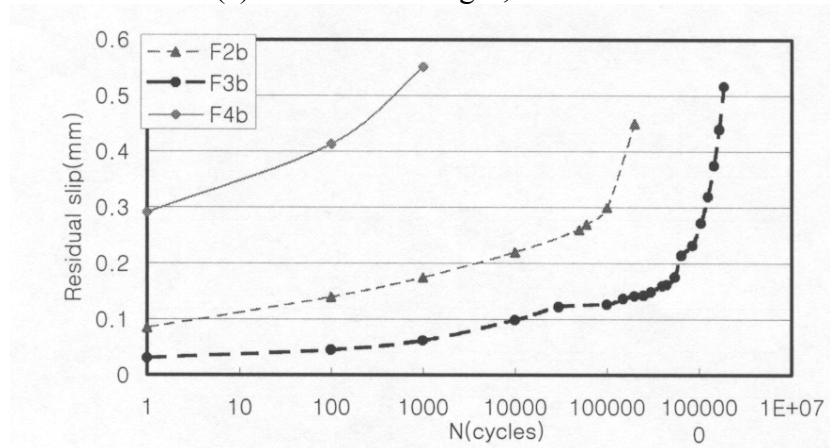


(c) Bedding layer thickness, 40mm

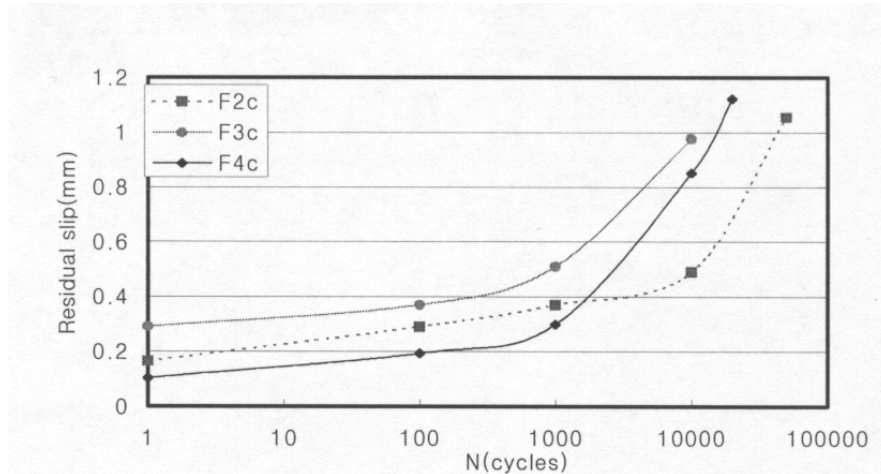
Figure 8 Residual slip curve to number of cyclic load in bedding layer thickness



(a) Shear stress ranges, 108MPa



(b) Shear stress ranges, 125MPa



(c) Shear stress ranges, 151Mpa

Figure 9 Residual slip curve to number of cyclic load in shear stress ranges

THE SHEAR STRESS DISTRIBUTION

As the number of cyclic load increases, strain history of shear connection measured by strain gauges adhered to four connectors, that were right upward, right downward, left upward and left downward is shown like Figure 10. In Figure 10, it is shown that strain histories of right or left upward and downward have tendency to gather. It is likely to show the fact of stress redistribution between shear connection. Because in strain history of right up and downward, the upward strain is larger than the downward one in early loading stage but as the number of cyclic load increases, the upward strain becomes same as the downward strain and in the late stage, in contrast, the downward strain is larger than the upward strain.

As the number of cyclic load increase, applied shear stress decrease in damaged shear connection but stress increases more in shear connection not damaged.

Therefore, from the results, it was confirmed that the applied shear stress was redistributed among shear connections arranged in a row.

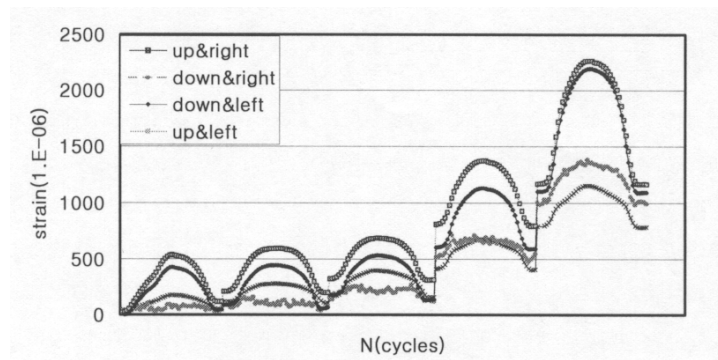


Figure 10 The strain distribution of shear connection to number of cyclic load

S-N CURVE

From the results of fatigue push-out tests, whose experimental variables were bedding layer thickness, the effect of bedding layer thickness on fatigue life of shear connection was not shown clearly. Therefore, the data of fatigue tests were adjusted without consideration of bedding layer thickness and the strength of non-shrinkage mortar. Then from that, the S-N curve equation of stud shear connector was obtained in precast concrete deck bridge.

Figure 11 shows the derived S-N curve. In this Figure, one is the mean S-N curve equation (4) and the other is S-N curve equation (5) that has reliability of 95% low limit. In order to apply the design, S-N curve equation that has reliability of 95% low limit is more conservative.

$$\text{Log } N = 10.226 - 0.1519R, r=0.83 \quad (4)$$

$$\text{Log } N = 9.432 - 0.1519R \quad (5)$$

where N is the number of cyclic load, R is the horizontal shear stress ranges

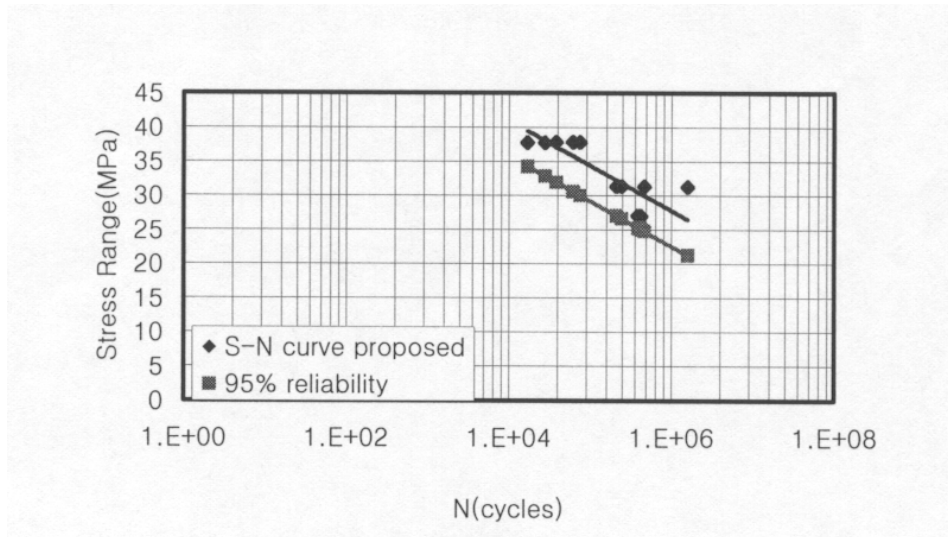


Figure 11 Suggested S-N curve equation and 95% reliability equation

CONCLUSION

The weld failure modes of shear connector in push-out tests were all W-mode irrelevant to the bedding layer thickness and shear stress ranges. And for same bedding layer thickness, the higher shear stress ranges applied, the more residual slips occurred but for same applied shear stress ranges, there wouldn't be any particular tendency. From this, it is considered that bedding layer thickness less affects fatigue crack propagation.

Consequently, also considering of current study, it is supposed that the strength of non shrinkage mortar and bedding layer thickness less affect fatigue life of shear connection in precast deck bridge and shear stress ranges are main factor that affect fatigue life of shear connection in this test ranges.

Therefore, the data of fatigue tests were adjusted without consideration of bedding layer thickness and the strength of non-shrinkage mortar. Then from that, the S-N curve equation of stud shear connector was obtained in precast concrete deck bridge.

REFERENCES

1. ChangSu, Shim, etc, "Shear stiffness of Shear connections in Full-Depth Precast Concrete Deck Bridge", *Journal of Korea Society of Steel Construction*, Vol. 10, No.4, 1998, pp. 749-758.
2. Hallam, M.W., "The behavior of stud shear connector under repeated loading", *Research report No. R281, University of Sydney*, 1978.
3. ENV 1994-1-1: 1992 Eurocode 4, *Design of Composite Steel and Concrete Structures Part 1.1, General rules and rules for buildings*, 1994.
4. JongHee Kim, "Static and Fatigue Behavior of Stud Shear Connector in Precast Concrete Bridge," *Ph.D. Thesis, Dept. of Civil Engineering, Seoul National University*, 2000.
5. Lo, K.K., "Fatigue testing of stud connector", M.Eng.Sc. thesis, Univ. of Melbourne, 1978.



KEERC-MAE Joint Seminar on
Risk Mitigation for Regions of Moderate Seismicity
University of Illinois at Urbana-Champaign, August 5-8, 2001



Sponsors: Korea Science and Technology Foundation, U.S. National Science Foundation, Brain Korea 21



Nonlinear Embankment Contribution to the Seismic Response of Short Bridges

Mehmet INEL¹ and Mark ASCHHEIM²

¹ *Research Assistant, Department Civil and Environmental Engineering, University of Illinois at Urbana-Champaign
1241 Newmark Laboratory, 205 N. Mathews, Urbana, Illinois, USA
email: inel@uiuc.edu*

² *Assistant Professor of Civil and Environmental Engineering, University of Illinois at Urbana-Champaign
2118 Newmark Laboratory, 205 N. Mathews, Urbana, Illinois, USA
email: aschheim@uiuc.edu*

ABSTRACT: Analysis of the recorded response of two “short” bridges indicates that the flexibility of the bridge embankment has a significant effect on the displacement demands sustained by substructure columns during earthquakes. This paper presents a MDOF model to estimate the displacement response of such bridges in the skew direction accounting for embankment flexibility, using nonlinear models of embankment fill soils. The model is calibrated to existing data available for two California bridges. Comparison of displacement demands computed by nonlinear dynamic analysis illustrates that the MDOF model described in this paper is more successful than conventional models for estimating seismic displacement demands of substructure columns in “short” bridges.

KEYWORDS: embankment flexibility, seismic displacement demands, short bridges.

INTRODUCTION

Current practice (e.g. ATC-32 [2] and Caltrans [3]) neglects the influence of the embankments in the design of bridges to resist seismic actions. However, recent studies [9, 10, 11, 13, 14, 15, 16, 17] have shown that the decks of “short” bridges are relatively stiff, and displacements in transverse direction are dominated by the response of embankments. This difference becomes significant in the performance-based design of bridges when damage to the substructure columns must be evaluated. This paper presents a MDOF model to estimate the displacement response of bridges that lack intermediate joints for thermal movement, termed “short” bridges, accounting for embankment flexibility. An “equivalent” SDOF model was also developed, and is discussed in detail by Inel (2001). The models are calibrated to existing data available for two California bridges. Displacement demands computed using the proposed model are compared with results obtained using conventional models for seven recorded responses.

RECORDED RESPONSE

The recorded response of two instrumented bridges to seven earthquakes (Table 1) is used to calibrate the proposed model.

Table 1 List of Recorded Motions at MRO and PSO

Record ID	Location	Earthquake	Date	Magnitude (M_L)	Free Field Peak Acceleration (g)
79_m0	MRO	Imperial Valley	79/10/15	6.4	0.300
86_m0	PSO	Cape Mendocino	86/11/21	5.1	0.246
86_a1	PSO	Cape Mendocino	86/11/21	5.1	0.135
87_m0	PSO	Cape Mendocino	87/07/31	5.5	0.096
92_m0	PSO	Cape Mendocino/Petrolia	92/04/25	6.4	0.472
92_a1	PSO	Cape Mendocino/Petrolia	92/04/26	6.2	0.415
92_a2	PSO	Cape Mendocino/Petrolia	92/04/26	6.4	0.206

The Meloland Road Overcrossing (MRO), located near El Centro, California, is a two-span, non-skew, reinforced concrete box-girder bridge with equal continuous spans of 31.7 meters supported on two monolithic abutments and a single central column (Fig. 1a). The abutments and central column are supported on timber piles. The bridge was subjected to the 1979 Imperial Valley earthquake, having magnitude (M_L) of 6.4. During the earthquake, 26 channels recorded the response of the bridge superstructure, abutment, embankment, and nearby free-field (Fig. 1b). No damage to the bridge was observed.

The Painter Street Overcrossing (PSO) is a two-span, prestressed concrete box-girder bridge located on U.S. Highway 101 in Rio Dell, California. It has two unbalanced spans of 44.5 and 36.3 meters, and is supported on two abutments and a two-column central bent (Fig. 2a). Both

abutments and the central bent are skewed at an angle of 39 degrees. The east abutment is monolithic while the west abutment has an expansion joint for longitudinal movement. The abutments and bent columns rest on driven concrete friction piles. The response of this overpass was recorded on 20 data channels (Fig. 2b) during nine earthquakes of magnitude (M_L) 4.4 to 6.4; six of these were large enough that they were selected for use in the present study.

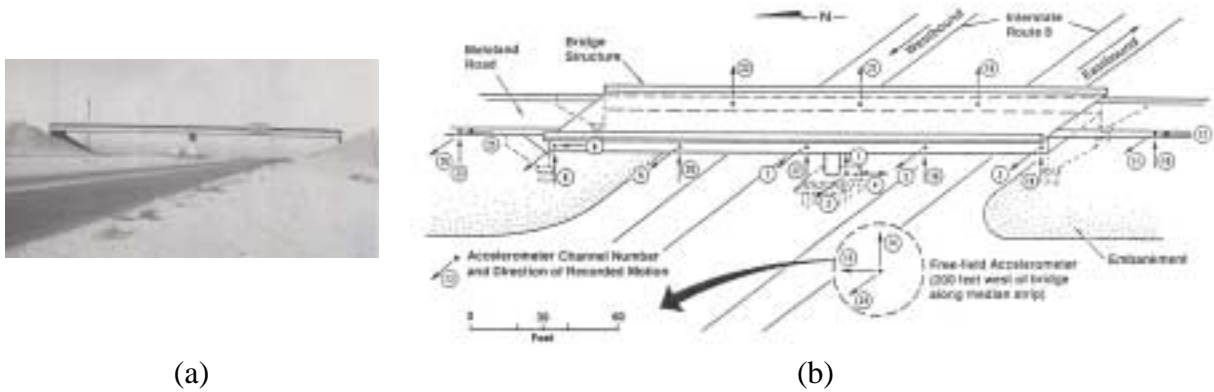


Figure 1 (a) Meloland Road Overcrossing (MRO) bridge photo (Wilson and Tan (1990)); (b) CSMIP instrumentation array of MRO (Werner et al. (1987))

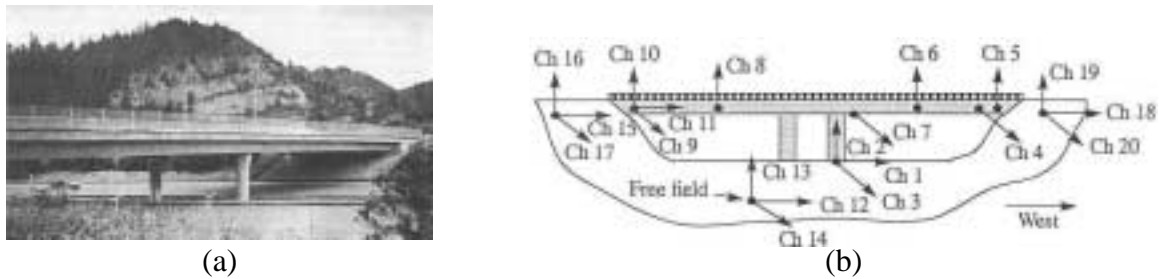


Figure 2 Painter Street Overcrossing (PSO) bridge photo and CSMIP instrumentation array (McCallen et al. (1994))

Empirical Observations of Recorded Bridge Response

Previous studies of MRO and PSO determined that: the bridge superstructure, abutments and embankment soil are a strongly coupled system when subjected to an earthquake [4, 5, 8, 9, 10, 11, 13, 14, 15, 16, 17], significant nonlinear global behavior of the entire bridge system can occur due to localized nonlinear behavior of embankment soil [9, 10, 11, 13, 14, 15, 16, 17], the deck of these bridges is relatively stiff and deformations in transverse direction are dominated by the response of approach embankment for moderate and strong shaking [9, 14,

15, 17], and overall bridge system natural periods of vibration are sensitive to both the stiffness and the inertia of approach embankment soil [9, 11, 14, 15, 17].

Inel (2001) used a statistically-based technique called Principal Component Analysis (PCA) [1] to identify the nonlinear response “mode” shapes from the recorded response of seven earthquake motions (Table 1). Displacement response in the skew direction was used for the skewed PSO to obtain the PCA modes. The PCA mode shapes indicate that the deck remains nearly rigid for the cases with high PGA, while in-plane deck deformations are more prominent for the cases with low PGA. This implies that the bent column deformation demands are dominated by the response of the embankments, particularly for stronger motions. These observations are consistent with the idea that the embankments appear to be relatively stiff for small shaking intensities and soften considerably at higher shaking intensities. The PCA mode shapes for three of the seven records are shown in Fig. 3a (MRO) and Fig. 3b (PSO).

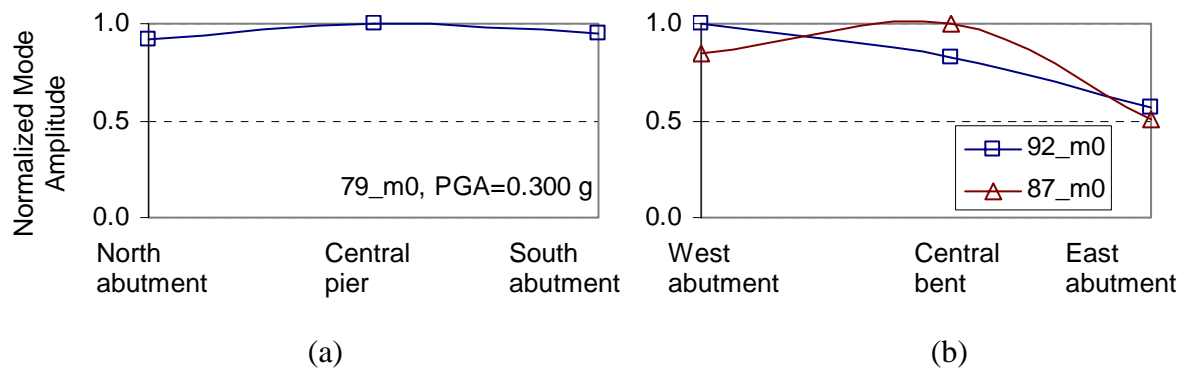


Figure 3 (a) First PCA Mode Shape of recorded response (a) MRO and (b) PSO subjected to the 87_m0 and 92_m0 events

MODELING OF THE BRIDGE COMPONENTS

A generic 2D idealization of a “short” bridge is shown in Fig. 4. The model represents the mass and stiffness of the deck, column bent, and abutments or approach embankments. The bridge is modeled along the skew coordinates such that model axes X and Y are in the skew directions of the bridge.

The reinforced concrete deck is modeled as a “stick beam” using elastic beam-column elements. Mass is lumped at each node along the deck. Three-fourths of the gross moment of inertia is used to account for cracking for the reinforced concrete decks, and the full gross moment of inertia is used for prestressed decks, per ATC-32 recommendations.

The column bent is represented by a bilinear spring in the bent direction attached to the deck node at the deck level. The bilinear spring properties may be obtained by pushover analysis of the bent substructure, to determine the capacity curve of the bent. The gross moment of inertia

of the bent cap and 50% of the gross moment of inertia of the columns are used, per ATC-32 recommendations.

ATC-32 provides recommendations for modeling abutment flexibility in the longitudinal direction that match Caltrans' practice. Suggestions that fall short of explicit recommendations are made for modeling abutments in the transverse direction. Based on these recommendations and practices known to have been used for modeling transverse abutment flexibility prior to ATC-32, an interpretation of the ATC-32 recommendations was established (Fig. 5). This "interpreted" approach is compared with the model developed in this study for embankment flexibility.

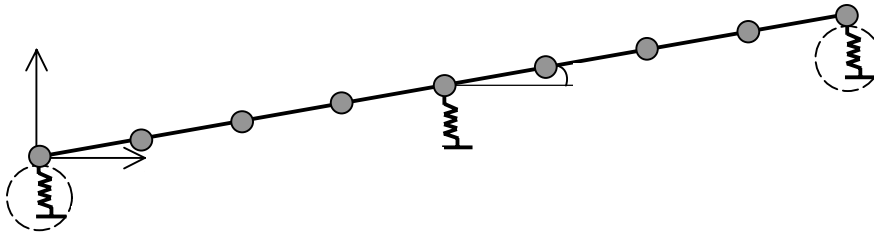


Figure 4 2D idealization of MDOF analytic bridge model, representing resistance to transverse deformations of bridge deck in plan of the deck

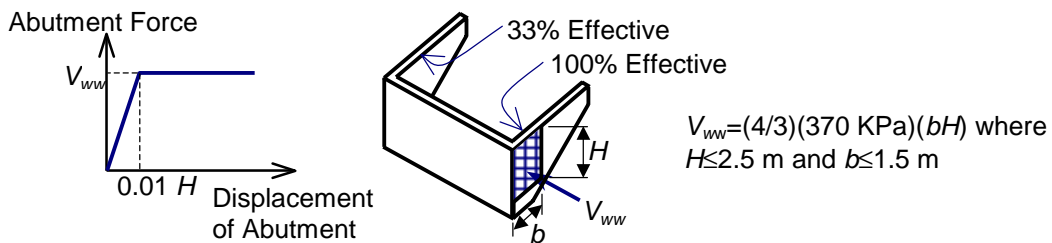


Figure 5 The interpreted ATC-32 approach for abutment stiffness in transverse direction

In the "interpreted" approach the transverse stiffness of the abutment is calculated based on the contribution of the wingwalls and piles. The effective wingwall width is limited to 1.5 m (5 ft). An average soil pressure capacity of 370 KPa (7.7 ksf) is assumed over a 2.5-m (8-ft) height of the wingwall and the typical standard pile capacity of 180 kN (40 kips) per pile is applied to all piles supporting the abutment. The wingwall that develops passive pressure under transverse response is assumed to be fully effective, whereas the "active" wall is assumed to contribute an additional resistance equal to 1/3 of the passive wall contribution. The full soil resistance is assumed to be mobilized at 1 percent of the 2.5-m height; ATC-32 recommends values ranging from 0.6 to 2 percent. The resistance calculated this way was applied in the skew direction of the bridge.

Modeling of Approach Embankment

The proposed approach embankment model is shown in Fig. 6. This model is refined from “soil-slice” model developed by Wissawapaisal and Aschheim (2000) to improve layer discretization and to include bridge skew. The soil slice is assumed to have a uniform thickness given by L' . The engineering properties of the fill soils are used to determine the mechanical properties of the plane strain slice. The slice is divided into horizontal layers. In this study, half of the mass tributary to each layer is distributed to the top of the layer and the other half is distributed to the bottom of the layer. The abutment backwall is assumed to be rigid, since it is stiff in-plane relative to the fill soils. The mass of all layers within L' is included. Simple shear deformation of embankment soil layers is represented using shear springs placed between the masses at the top and bottom of each layer.

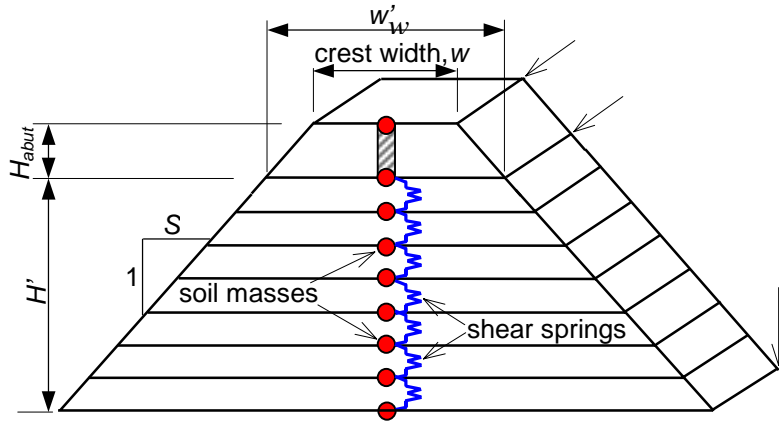


Figure 6 A generic embankment cross-section (the cut is in the transverse direction)

The cross section of Fig. 6 is a transverse cut. Equivalent load-deformation response can be obtained whether the cross section is modeled in the transverse or skew directions. For simplicity, the transverse direction is used to develop the load-deformation response of the embankment, and simple trigonometric relationships are applied to determine the component of resistance in the skew direction. Values of L' are in the longitudinal direction. The component of longitudinal resistance in the skew direction was neglected in the coordinate transformations.

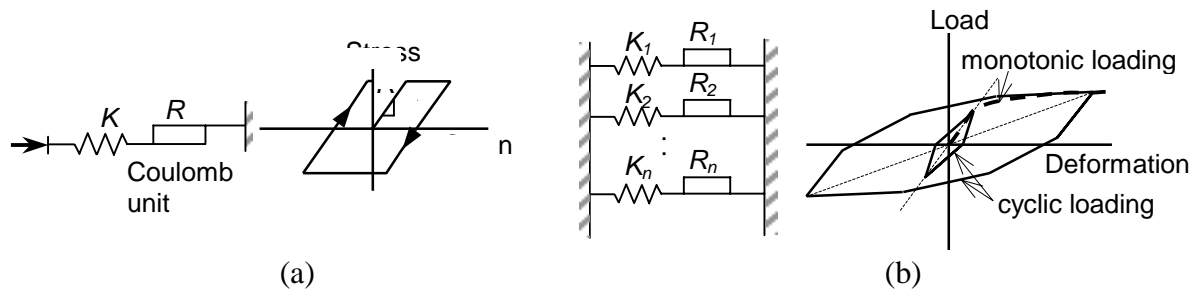


Figure 7 (a) Iwan spring and its stress-strain relationship, and (b) the use of Iwan springs in parallel to represent nonlinear hysteretic soil behavior by Taylor et al. (1978)

The approach embankment model is based on several assumptions: (1) shear deformations are the only deformations considered within each layer, (2) the layers between the top of the embankment and the base of the pile cap are assumed to be rigid, based on the large in-plane shear stiffness of the reinforced concrete back wall of the abutment, (3) the loosely compacted soil between abutment wing-walls moves with abutment, generating negligible additional resistance or damping, and (4) soil-pile interaction is not explicitly modeled.

The stiffness and strength of each layer of embankment soil is estimated based on expected engineering properties of the fill. Soil softening behavior is based on established modulus degradation relationships and modeled using parallel elements (Fig. 7), as suggested by Iwan (1973) and Taylor et al. (1978).

CALIBRATION OF THE REFINED MDOF MODEL

Models of the MRO and PSO were used to calibrate the proposed model to the recorded response of these bridges. The ground motions were applied to bridge models in the skew direction (Table 1). The relative displacement and absolute acceleration of the central pier response history and PCA mode shapes for a range of embankment length, L' (from 1 m to 20 m), were obtained and compared with the recorded response and the PCA mode shapes computed from the recorded data, to determine values of the effective embankment length that give the best matches to the recorded response. Several criteria were used to establish the lengths that result in the “best” computed responses. The first and most important criterion is the goodness of relative displacement history of the central pier, especially in the highest amplitudes of response to a given recorded input motion. Second is the general trend in the relative displacement and absolute acceleration histories of the central pier, in regard to both amplitude and frequency. Third is that the dominant PCA mode shape obtained for the computed data should be similar to the one obtained for the recorded data. The three criteria led to a range of “acceptable” embankment lengths, L' , rather than a single value. Three different embankment lengths L_1 , L_2 , and L_3 were identified: L_2 is the “best” value of L'

determined empirically, and L_1 and L_3 are the smallest and largest values of embankment length that give “acceptable” response, respectively.

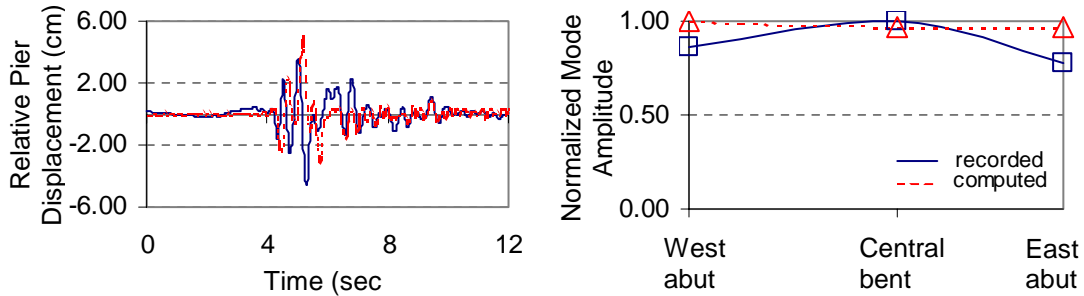


Figure 8 Response comparisons of PSO subjected to 1992 Cape Mendocino main event (PGA=0.472g) for the effective embankment thickness, $L'=L_2=8$ m

Fig. 8 provides an example comparison of the recorded and computed displacement histories and PCA mode shapes for the 1992 main event of Cape Mendocino earthquake. Values of L_1 , L_2 , and L_3 in Fig. 9a do not show a trend with PGA. Peak pier displacement values are relatively stable for L_1 , L_2 , and L_3 (Fig. 9b). Fig. 10 shows that the proposed model can accurately estimate the recorded displacements using the L_2 values of embankment length.

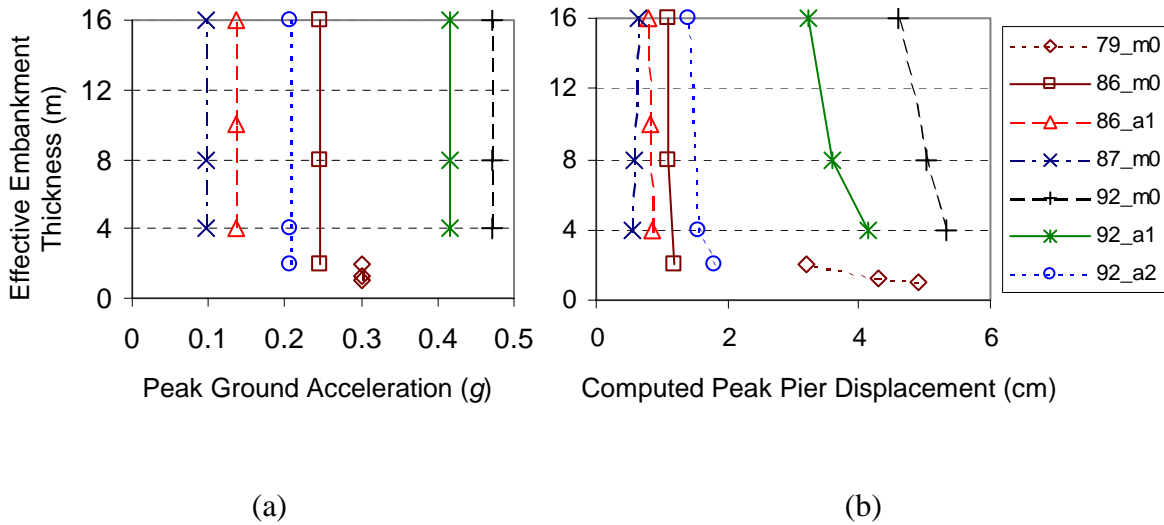


Figure 9 Ranges of identified approach-embankment effective width, L' versus (a) PGA, and (b) computed peak pier displacements

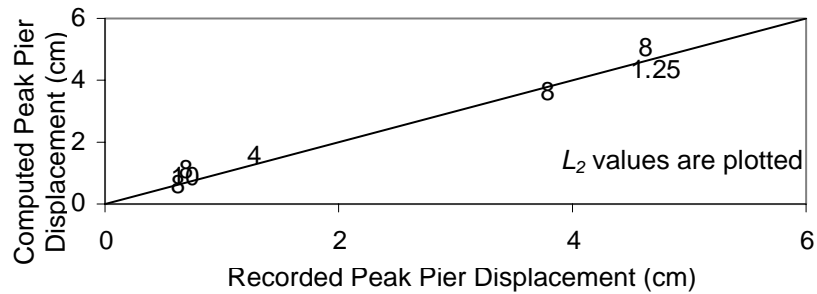


Figure 10 Accuracy of the proposed model for pier displacement demands using L_2

COMPARISON OF THE PROPOSED MODEL TO CONVENTIONAL PRACTICE

Peak displacement demands computed by the proposed model using $L' = L_2$ and conventional practice are compared in Fig. 11. Springs representing embankment flexibility in the proposed model were replaced with either bilinear springs for the “interpreted” ATC-32 abutment model or with pin supports. Fig. 11 plots the ratio of computed to recorded peak displacement demands versus PGA of recorded motions and versus recorded peak displacement demands. The pinned model increasingly underestimates displacements as the peak recorded displacement increases. The ATC-32 model exhibits a similar trend, but overestimates peak displacements. The accuracy of the proposed model tends to be independent of PGA and peak displacement. The computed results are summarized in Table 2; the proposed model is seen to be more accurate and have less variance than the other two models.

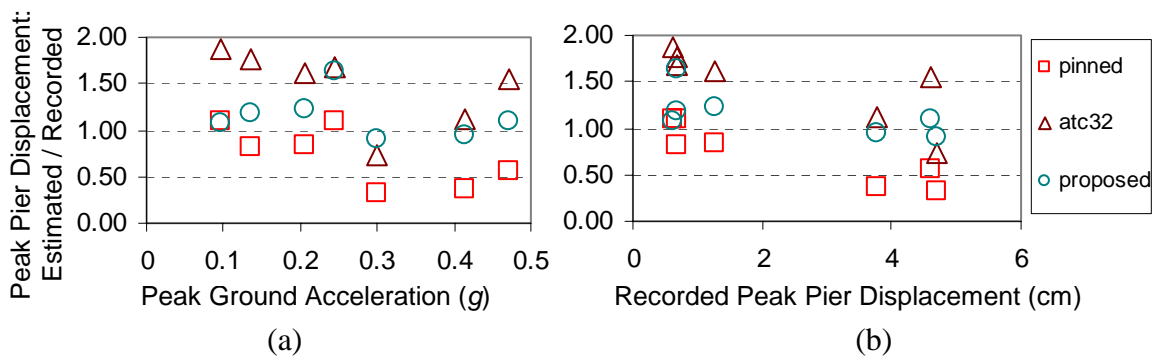


Figure 11 The ratio of the estimated and recorded peak pier displacements (relative to the ground) using conventional and proposed models versus (a) PGA and (b) recorded peak pier displacements

Table 2 Comparison of displacement estimates using conventional and proposed models

Record ID	PGA (g)	Δ_{Recorded} (cm)	$\Delta_{\text{Estimated}} / \Delta_{\text{Recorded}}$		
			Pinned	ATC-32	Proposed
79_m0	0.300	4.7	0.32	0.73	0.91
86_m0	0.246	0.68	1.10	1.68	1.62
86_a1	0.135	0.69	0.83	1.76	1.18
87_m0	0.096	0.61	1.10	1.87	1.07
92_m0	0.472	4.62	0.55	1.55	1.09
92_a1	0.415	3.77	0.38	1.12	0.96
92_a2	0.206	1.26	0.84	1.60	1.23
Average			0.73	1.47	1.15
Standard deviation			0.32	0.40	0.24

SUMMARY AND CONCLUDING REMARKS

Empirical observations and analyses of the recorded response of two instrumented bridges indicate that the deck remains nearly rigid for strong excitations, while in-plane deck deformations are more prominent for smaller excitations. The analyses show that the flexibility of the bridge embankment has a significant effect on the displacement demands sustained by the substructure columns of short bridges, particularly for strong excitations. These observations are consistent with the idea that the embankments are relatively stiff for small shaking intensities and soften considerably as shaking intensities increase.

Nonlinear MDOF and “equivalent” SDOF models to account for embankment flexibility were developed by Inel (2001). The MDOF model reported here was refined from the “soil slice” model developed by Wissawapaisal and Aschheim (2000) to improve layer discretization and to include bridge skew for estimating the seismic displacement response of “short” bridges in the skew direction. The model is calibrated to the recorded response of two bridges. Nonlinear dynamic analyses illustrate that the proposed model is more successful than conventional practice (pinned and the “interpreted” ATC-32 models) in estimating displacement demands of “short” bridges. The conventional models were prone to either significantly overestimate or underestimate displacement responses relative to the recorded response.

ACKNOWLEDGMENTS

The authors appreciate the efforts of Vladimir Grazier of the California Division of Mines and Geology for preparing a supplemental release of data for the Meloland Road Overcrossing. Support was provided to the first author from Pamukkale University of Denizli, Turkey. This work was supported in part by the Earthquake Engineering Research Centers Program of the National Science Foundation under Award Number EEC-9701785.

REFERENCES

1. Aschheim, M., Black, E., and Cuesta, I. 2001, "Principal Component Analysis and Peak Displacement Estimates of MDOF Systems Responding to Seismic Excitations," submitted to *Engineering Structures*.
2. ATC-32 (1996), *Improved Seismic Design Criteria for California Bridges: Provisional Recommendations*, Applied Technology Council, Redwood City, California.
3. Caltrans SDC (1999), *Caltrans Seismic Design Criteria Version 1.1*, California Department of Transportation, Sacramento, California, July.
4. Douglas, B. M., Maragakis, E. A., Vrontinos, S., and Douglas, B. J. 1990, "Analytical Studies of the Static and Dynamic Response of the Meloland Road Overcrossing," *Proceedings of Fourth U.S. National Conference on Earthquake Engineering*, Vol. 1, Palm Springs, CA, May 20 - May 24, pp. 987-996.
5. Goel, R. K., and Chopra, A. K. 1997, "Evaluation Of Bridge Abutment Capacity and Stiffness during Earthquakes," *Earthquake Spectra*, Vol. 13, No. 1, pp. 1-23.
6. Inel, M., 2001, *Design Strategies for the Performance Based Seismic Design of Short Bridges*, Ph.D. Dissertation, University of Illinois at Urbana-Champaign (in preparation).
7. Iwan, W. D. 1973, "A Model for the Dynamic Analysis of Deteriorating Structures," *Proceedings of the 5th World Conference on Earthquake Engineering*, Paper No. 222, pp. 1782-1791.
8. Maroney, B., Romstad, K., and Chajes, M., 1990, "Interpretation of Rio Dell Freeway Response During Six Recorded Earthquake Events," *Proceedings of Fourth U.S. National Conference on Earthquake Engineering*, Vol. 1, Palm Springs, CA, May 20 - May 24, pp. 1007-1016.
9. McCallen, D. B., and Romstad, K. M. 1994, "Dynamic Analyses of a Skewed Short-Span, Box-Girder Overpass," *Earthquake Spectra*, Vol. 10, No. 4, pp. 729-755.

10. Price, T. E., and Eberhard, M. O. 1998, "Efficient Procedure for Modeling the Transverse Seismic Response of Bridge Embankments," *6th US. National Conference on Earthquake Engineering*, Seattle, Washington, May 31 - June 04.
11. Sweet, J., and Morrill, K. B. 1993, "Nonlinear Soil-Structure Interaction Simulation of the Painter Street Overcrossing," *Proceedings of the 2nd Annual Seismic Research Workshop*, CA, March 16-18.
12. Taylor, P. W., and Larkin, T. J. 1978, "Seismic Site Response of Nonlinear Soil Media," *Journal of Geotechnical Engineering*, Vol. 104, No. GT3, pp. 369-383.
13. Werner, S. D., Beck, J. L., and Levine, M. B. 1987, "Seismic Response Evaluation of Meloland Road Overpass Using 1979 Imperial Valley Earthquake Records," *Earthquake Engineering and Structural Dynamics*, Vol. 15, pp. 249-274.
14. Werner, S. D., Beck, J. L., and Nisar, A., 1990, "Dynamic Tests and Seismic Excitation of a Bridge Structure," *Proceedings of Fourth U.S. National Conference on Earthquake Engineering*, Vol. 1, Palm Springs, CA, USA, May 20 - May 24, pp. 1037-1046.
15. Werner, S. D. 1993, *Study of Caltrans' Seismic Evaluation Procedures for Short Bridge Overcrossing Structures*, Dames & Moore, Inc., Oakland, CA, August.
16. Wilson, J. C., and Tan, B. S. 1990, "Bridge Abutments: Assessing Their Influence on Earthquake Response of Meloland Road Overpass," *Journal of Engineering Mechanics, ASCE*, Vol. 116, No. 8, pp. 1838-1856.
17. Wissawapaisal, C., and Aschheim, M. 2000, *Modeling the Transverse Response of Short Bridges Subjected to Earthquakes*, CD Release 00-05, Mid-America Earthquake Center, University of Illinois, Urbana, September.



KEERC-MAE Joint Seminar on
Risk Mitigation for Regions of Moderate Seismicity
University of Illinois at Urbana-Champaign, August 5-8, 2001



Sponsors: Korea Science and Technology Foundation, U.S. National Science Foundation, Brain Korea 21



Seismic Assessment of Existing Unreinforced Masonry Buildings

Sang-Cheol Kim¹, and Donald W. White²

¹ *Graduate Student, School of Civil and Environmental Eng., Georgia Institute of Technology
790 Atlantic Drive, Atlanta, Georgia, USA
email: sckim@cruella.ce.gatech.edu*

² *Associate Professor, School of Civil and Environmental Eng., Georgia Institute of
Technology
790 Atlantic Drive, Atlanta, Georgia, USA
email: don.white@ce.gatech.edu*

ABSTRACT: FEMA 356 provides a variety of equations and requirements pertaining to seismic assessment of existing unreinforced masonry buildings. Typically, these types of structures have significant diaphragm flexibility. This paper evaluates, provides clarification and suggestions for potential improvement to several of the provisions in FEMA 356, and comments on further research needs with emphasis on linear static procedures and methods accounting for the flexibility of wood floor diaphragms. Specifically, the paper addresses the calculation of diaphragm deflections, fundamental period, and categorization of structures based on torsional coupling.

KEYWORDS: flexible diaphragms, wood diaphragms, diaphragm deflections, torsional coupling, categorization of diaphragms, period, low rise buildings, structural analysis, seismic response,

INTRODUCTION

The *Prestandard and Commentary for the Seismic Rehabilitation of Buildings*, FEMA 356 [1], is a recently completed comprehensive reference for performance-based seismic rehabilitation of buildings. This document addresses issues of diaphragm flexibility which are often key in the assessment of existing unreinforced masonry building structures. However, the state of knowledge regarding the seismic behavior of these types of structures, particularly the potential positive and negative influences of diaphragm flexibility on the structural response, is still limited. This paper evaluates, provides clarification, and suggests potential improvements to a few important provisions in FEMA 356 pertaining to the consideration of diaphragm flexibility. Further research needs are also discussed. Particular emphasis is placed upon a few key provisions pertaining to linear static procedures and wood floor diaphragms. Specifically, the paper addresses the calculation of diaphragm deflections, fundamental period, and categorization of structures based on torsional coupling.

DIAPHRAGM DEFLECTION FORMULAS

With the exception of plywood diaphragms, for which a more detailed formula based on APA research [6] is specified, FEMA 273 [2] provides the following formula for calculation of deflections due to lateral loading in all wood diaphragms:

$$\Delta_d = \frac{vL^4}{G_{d_FEMA273} b^3} \quad (1)$$

where v is the shear in units of force per unit length at the ends of the diaphragm span, L is the span length of the diaphragm, b is the diaphragm width, and $G_{d_FEMA273}$ is the diaphragm stiffness parameter associated with this equation. Values of $G_{d_FEMA273}$ are specified in FEMA 273 for a wide range of diaphragm types. The derivation of Eq. 1 is outlined in [7]. Unfortunately, there is a significant error in this derivation. The derivation is based on the simple Euler-Bernoulli beam theory equation

$$\Delta_d = \frac{5wL^4}{384EI} \quad (2)$$

in which shear deformations are assumed to be negligible, and where w is an equivalent uniformly distributed load, L is the diaphragm span, and EI is the diaphragm flexural rigidity. After substitution of $w = W/L = 2vb/L$ and $I = tb^3/12$, where W is the total lateral load transmitted by the diaphragm, and t is the diaphragm equivalent thickness (in concept, this is the approach taken in [7]), this equation can be expressed as

$$\Delta_d = \frac{vL^3}{(3.2Et)b^2} = \frac{vL^3}{G_{d_FEMA273} b^2} \quad (3)$$

where $\bar{G}_{d_FEMA273}$ is an appropriate stiffness term associated with this “corrected” equation, which would of course be different than the reported values in FEMA 273. The form of Eq. 1 results from an error in the substitution of the terms as explained in the development of Eq. 3. It is important to emphasize that neither of these equations should be taken too literally. In other words, Eq. 1 (or alternatively Eq. 3) is applied to estimate the deflections in a wide variety of diaphragm types, many of which are either dominated by shearing deformations or in which, strictly speaking, beam theory does not apply. The values of $G_{d_FEMA273}$ have been estimated based on limited test data and expert judgment. Nevertheless, the form of Eq. 1 developed in [7] is derived erroneously, and to the knowledge of the authors, has no rational basis, causes problems when this equation is applied to diaphragms with small aspect ratios L/b . These problems will be explained subsequently, after discussion of a new equation for calculation of diaphragm deflections, specified in FEMA 356 [1].

FEMA 356 gives the following equation for calculation of deflections in non-plywood diaphragms:

$$\Delta_d = \frac{vL}{2G_{d_FEMA356}} \quad (4)$$

where $G_{d_FEMA356}$ is an appropriate diaphragm stiffness for use with this equation, specified in FEMA 356. Equation 4 is based on a shear deformable beam theory model in which the shear deformations are assumed to dominate the response of the system to the extent such that the contributions of chord flexibilities, etc. to the diaphragm deflections may be neglected. In other words, in Eq. 4, the flexural rigidity EI is assumed to be infinite (e.g., the chords are assumed to be rigid). This is in contrast to Eq. 3, in which the shear flexibility of the diaphragm is assumed to be zero, and thus the diaphragm deflections are assumed to come entirely from bending deformations. In the view of the authors, Eq. 4 is a more appropriate equation for calculation of wood diaphragm deflections, since as noted earlier, shear deformations are typically the major contributor to the flexibility of these systems.

Reference 5 reports recent test results for several representative wood floor diaphragms. It is interesting to consider how the initial and recommended design secant stiffness values from these tests compare to current $G_{d_FEMA356}$ values. Table 1 shows these comparisons.

With the exception of their tongue and groove single straight-sheathed diaphragm test, the secant stiffnesses in [5] are significantly higher than the stiffnesses specified in FEMA 356. Furthermore, as would be expected, the diaphragm initial stiffnesses are significantly higher than the recommended design secant stiffness values.

Peralta et al. [5] calculate their recommended secant stiffness values based on a bilinear representation of the experimental backbone curves, with the second branch of the bilinear representation set as a tangent to the backbone curves at large diaphragm displacements (the experimental backbone curves were approximately linear in this range), and with the first “secant” branch of the bilinear representation being set to obtain equal area under the

experimental and bilinear backbone curves. All sources of deformation (shear and flexural deformations of the floor system, deformation of the anchorages at the diaphragm boundaries, etc.) are included within the stiffness values derived from the Texas A&M tests. The reader is referred to [5] for details of the diaphragm characteristics and test results.

Table 1 Comparison of FEMA 356 [1] Expected and Experimental [5] Stiffness Values for Wood Diaphragms

Diaphragm Designation and Type		$G_{d_FEMA356}$ kN/cm (kips/in)	G_{di}^1 kN/cm (kips/in)	$G_{d_secant}^2$ kN/cm (kips/in)	Δ_y / L^3
1A: Single Straight Sheathed (1x4 in. tongue and groove decking w/ 2x10 in. joists)		3.5 (2)	5.8 (3.3)	2.4 (1.4)	0.0020
2: Single Straight Sheathed (1x6 in. boards w/ 2x10 in. joists)		3.5 (2)	18.0 (10)	9.0 (6)	0.0022
2B and 2C: Wood Structural Panel Overlay on Straight Sheathing	Unblocked, Unchorded	8.7 (5)	52.0 (30)	40.7 (24)	0.0008
	Blocked, Unchorded	12.2 (7)	116.8 (67)	57.8 (33)	0.0008

1. G_{di} = approximate initial tangent stiffness of back-bone curve from experiment [5]
2. G_{d_secant} = secant stiffness of first branch of a bilinear representation of the back-bone curve, determined as defined within the text [5]
3. Δ_y/L = diaphragm "yield deflection" divided the diaphragm span length, where yield is defined at the transition to the second branch of the bilinear representation of the backbone curve [5]

One additional observation regarding the data in Table 1 should be considered by the engineer in applying the FEMA 356 equations. FEMA 356 does not distinguish between different types of straight-sheathed diaphragms. The Texas A&M study illustrates the fact that the stiffness properties of diaphragms categorized as the same type in FEMA 356 may be significantly different. The 1x4 in. tongue and groove and 1x6 in. board single straight-sheathed diaphragms tested in [5] have secant stiffness values of $G_{d_secant} = 2.4$ kN/cm and 9.0 kN/cm respectively, compared to a recommended value of 3.5 kN/cm in FEMA 356.

Depending on one's perspective, it may be argued that the recommended FEMA 356 values are a reasonable coarse approximation of the broad range of diaphragm stiffnesses which may exist for this type of diaphragm in practice, or alternatively, it may be argued that the FEMA 356 equation predictions may be inaccurate by close to an order of magnitude relative to the physical response.

As noted previously, there are problems associated with the usage of the FEMA 273 equation (Eq. 1) for calculation of non-plywood wood diaphragm deflections. Figure 2 illustrates these problems and highlights a number of other issues by showing representative plots of the diaphragm stiffness, quantified as the end shear $V = vb$ divided by the mid-span displacement Δ_d , versus L/b for different formulas and different values of the associated diaphragm stiffness terms G_d . Figure 3 is a repeat of Fig. 2, but with emphasis on low stiffness values. These

figures focus on different predictions for straight-sheathed diaphragms, although an upper-bound prediction of the stiffness for a comparable plywood diaphragm is shown for comparison purposes.

Figures 2 and 3 show that the FEMA 273 Eq. 1 predicts substantially larger diaphragm stiffness than the other equations for diaphragms with aspect ratios of two or less. In fact, at approximately an aspect ratio of one, which is certainly a practical case, Eq. 1 with the FEMA 273 specified value of $G_{d_FEMA273} = 350 \text{ kN/cm}$ for a single straight-sheathed diaphragm predicts that such a diaphragm is even stiffer than the corresponding upper-bound estimate of the stiffness of a comparable 1.27 cm (0.5 in.) thick plywood diaphragm. The upper-bound estimate of the plywood diaphragm stiffness is obtained by assuming rigid chords, zero nail slip, and zero chord-splice slip, such that the only contribution to the diaphragm flexibility is the shear deformation of the plywood panels themselves. The source of this flaw in the FEMA 273 equations appears to be the error in the development of Eq. 1 discussed previously, combined with the fact that the values of $G_{d_FEMA273}$ were set in large part by considering diaphragm experimental tests that were focused on L/b values in the vicinity of three and larger [3].

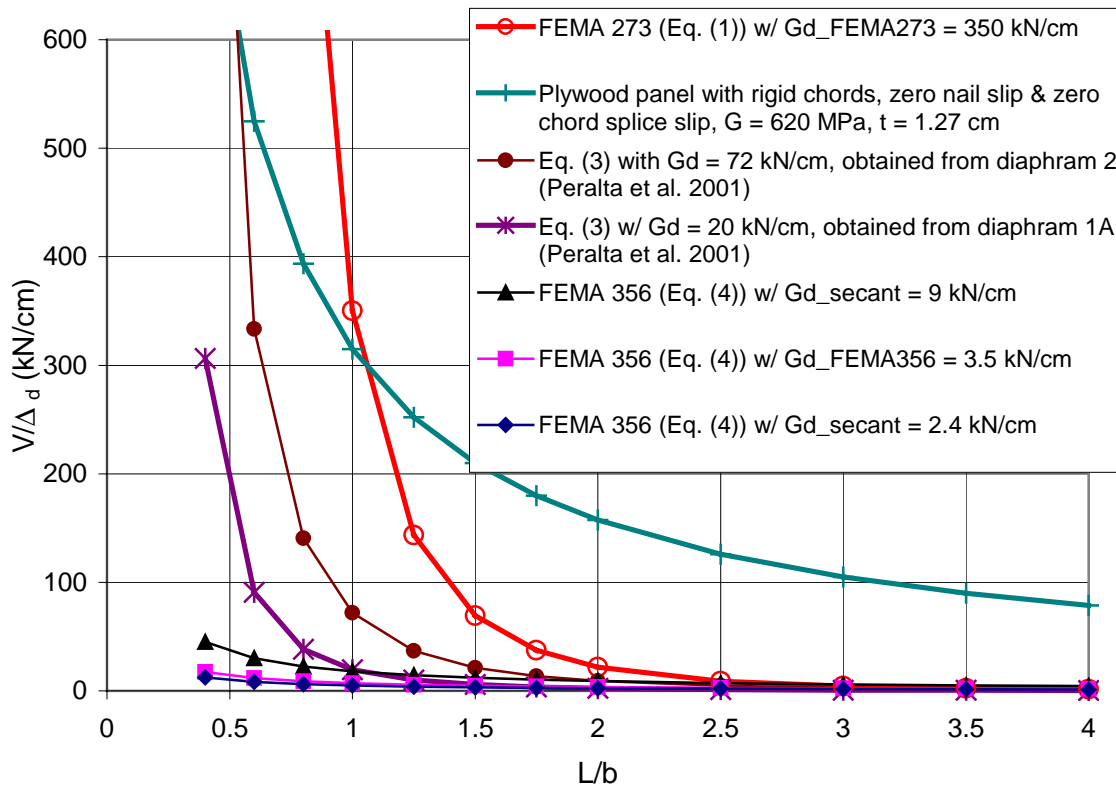


Figure 2 Various predicted diaphragm stiffnesses ($V/\Delta d$) versus aspect ratio L/b for straight sheathed diaphragms and comparison to an upper-bound estimate of the stiffness for a comparable plywood diaphragm.

It is interesting to note that Eq. 3 also predicts a diaphragm stiffness larger than that based on the upper-bound equation for the plywood diaphragm when L/b is less than about 0.5 and $\bar{G}_d = 72 \text{ kN/cm}$ is computed based on the secant stiffness from test 2 (1x6 in. straight sheathing boards on 2x10 in. joists). The source this erroneous prediction is the use of Euler-Bernoulli beam theory in the development of Eq. 3. Obviously, the assumption of negligible shear deformations does not apply for diaphragms with such small aspect ratios, and in fact, its applicability for diaphragms with aspect ratios significantly smaller than $L/b = 2$, which is the aspect ratio of all the diaphragms tested in [5], is suspect. It can be seen from Fig. 3 that Eq. 3 with a value of $\bar{G}_d = 20 \text{ kN/cm}$, obtained from the secant stiffness of diaphragm 1A [5], predicts a higher stiffness than that predicted by Eq. 4 with $G_{d_secant} = 9 \text{ kN/cm}$ (based on diaphragm 2), at approximately $L/b = 1$.

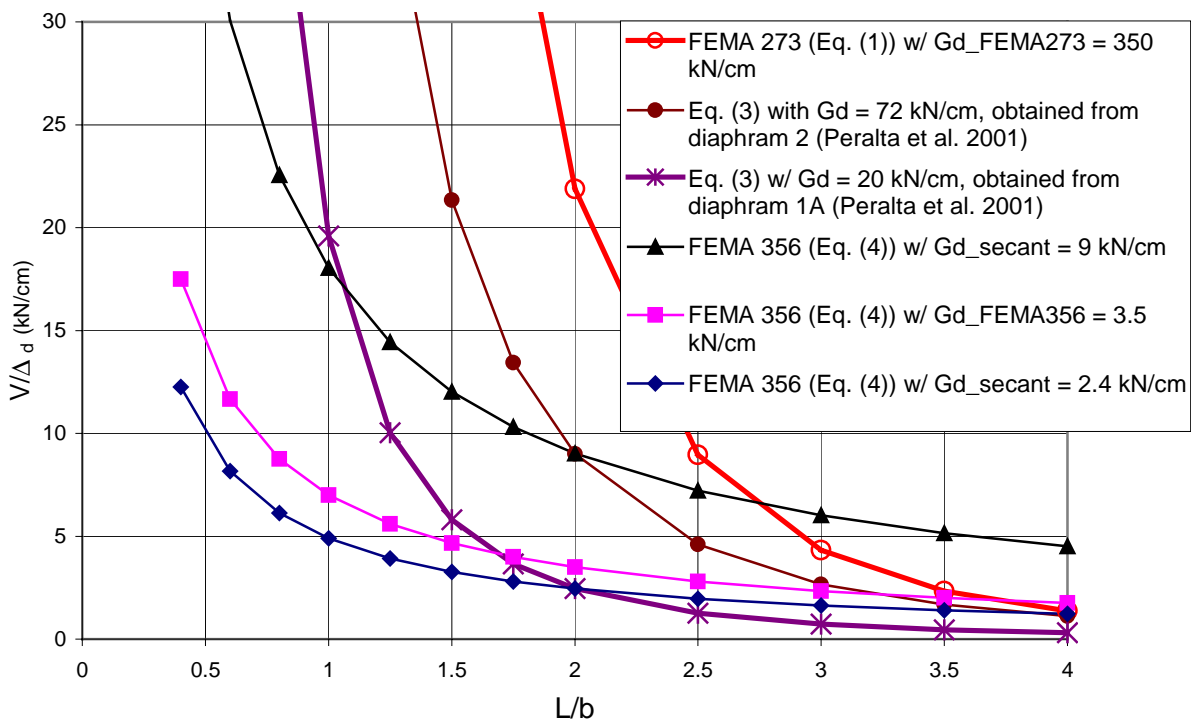


Figure 3 Various predicted diaphragm stiffnesses (V/Δ_d) versus aspect ratio L/b for straight sheathed diaphragms.

The new FEMA 356 equation (Eq. 4) is believed to provide the best estimate of the stiffness for diaphragms with aspect ratios less than about three. Figure 3 shows the predictions obtained by this equation using the corresponding G_{d_secant} values obtained from tests 2 (9 kN/cm) and 1A (2.4 kN/cm) reported in [5], as well as based on the specified value of $G_{d_FEMA356} = 3.5 \text{ kN/cm}$ specified in FEMA 356. Nevertheless, the test data for verification of how the diaphragm stiffnesses actually vary for different L/b ratios is extremely limited.

The engineer should be cautioned about the use of Eq. 4 particularly for diaphragms with aspect ratios larger than about three. Note that the predictions by Eqs. 3 and 4 shown in Fig. 3

are the same for curves corresponding to the two diaphragms tested in [5] at $L/b = 2$. This is of course because the tests in [5] have an aspect ratio of $L/b = 2$, and the G_{d_secant} and \bar{G}_d values were back-calculated to fit the test results. Also, note that Eq. 3 predicts a much sharper drop than Eq. 4 in the stiffness for increasing values of L/b greater than two. This larger drop in stiffness is interpreted by the authors as an over-conservative for the diaphragms considered, since the diaphragm deformations are interpreted to be predominately shear in their nature. However, for diaphragms with larger shear stiffnesses and larger aspect ratios, Eq. 4 may overpredict the diaphragm stiffness.

Lastly, it is apparent that for diaphragms with low stiffness such as those considered in Fig. 3, the associated out-of-plane wall deformations may provide substantial contribution to the diaphragm stiffness. Consideration of these contributions may be merited at least for low to possibly moderate earthquake excitations. However, if the out-of-plane wall drifts are larger than some limit, the current FEMA 356 approach of neglecting out-of-plane wall stiffnesses altogether is likely to be merited.

FEMA 273 and 356 currently do not provide any limits on wall out-of-plane deformations for various conditions such as collapse prevention or immediate occupancy. Such limits, or alternative checks to ensure the integrity of the out-of-plane walls, need to be defined. Issues which need to be considered in establishing these limits include the potential effects of combined in-plane and out-of-plane lateral and vertical seismic excitation of the wall elements. The tests by [5] and other test data indicate that wood floor diaphragms may be able to sustain extensive deformations themselves, at least for a small number of cycles, without substantial loss in resistance.

APPROXIMATE PERIOD CALCULATION

FEMA 356 provides the following equation for approximate calculation of the fundamental period in one-story buildings with single-span flexible diaphragms:

$$T = (0.1\Delta_w + 0.078\Delta_d)^{0.5} \quad (5)$$

where Δ_w and Δ_d are the in-plane wall and diaphragm displacements in inches, "due to a lateral load in the direction under consideration, equal to the weight of the diaphragm." For one-story buildings with multiple-span diaphragms, use of this equation is permitted with a lateral load equal to the weight tributary to the diaphragm span under consideration, applied to calculate a separate period for each diaphragm span¹. The period that maximizes the pseudo lateral load is then used for design of all walls and diaphragm spans within the building. However for unreinforced masonry buildings with single-span flexible diaphragms, six stories or less in height, use of the following simpler formula is permitted

¹ In the view of the authors, the application of Eq. 5 in the context of single-span diaphragms also should be based on the weight tributary to the diaphragm, not just on the diaphragm weight itself.

$$T = (0.078\Delta_d)^{0.5} \quad (6)$$

where Δ_d is the maximum diaphragm displacement in inches, due to a lateral load in the direction under consideration, equal to the weight tributary to the diaphragm.

FEMA 356 suggests that the diaphragm displacement Δ_d should be based on the likely distribution of the inertial forces, and suggests a parabolic distribution with a maximum magnitude of $1.5F_d/L$, where F_d is the total inertial load applied to the diaphragm, for the equivalent static loading. However, for diaphragms dominated by shear flexibility, as implied by Eq. 4, the authors find that the lumping of one-half of the total diaphragm inertial load at the center of the diaphragm overestimates the diaphragm displacements and underestimates the diaphragm stiffness by only 11 percent. In light of the other approximations involved with estimating the diaphragm stiffness and deflections, this approximation seems merited. Use of lumped masses also facilitates the use of more sophisticated three-dimensional lumped parameter modeling approaches for the structural analysis described in [4].

It is important for the engineer to understand the origin of Eqs. 5 and 6 for proper interpretation of their applicability to general structures. Equation 6 is obtained approximately by considering a Ritz analysis for the free vibration of a simply-supported beam with uniformly distributed mass along its length, based on Euler-Bernoulli beam theory (a coefficient of 0.081 is obtained based on this model). Also, in the limit of a rigid diaphragm ($\Delta_d = 0$), the remaining portion of Eq. 5 is obtained by applying the lumped diaphragm inertial loading at the top of the wall in a Rayleigh-Ritz approach. The summation in Eq. 5 then gives a coarse approximation of the fundamental period of the three degree-of-freedom system composed of a Euler-Bernoulli beam of uniformly distributed mass, simply-supported on flexible transverse springs (representing the wall flexibilities). Equation 6 is effectively a prediction of the diaphragm natural period for the case of rigid structural walls. It should be noted that if the natural period of the diaphragm is calculated based on lumping of the mass at the diaphragm mid-span, a Ritz analysis predicts a coefficient of 0.1 instead of 0.078 in Eqs. 5 and 6. This is obtained as:

$$T = 2\pi\sqrt{\frac{m}{k}} = 2\pi\sqrt{\frac{m}{(mg/\Delta_d)}} \cong (0.1\Delta_d)^{0.5} \quad (7)$$

Kim and White [4] consider the effect of lack of symmetry in the response of flexible diaphragm structures. In general, the above approximate period formulas tend to give accurate estimates of the periods obtained by Ritz analysis for symmetric structures. However, for unsymmetric structures, the fundamental period is often underestimated based on the above formulas. Nevertheless, accurate calculation of the period by Ritz analysis for unsymmetric structures does not necessarily lead to accuracy in the assessment of such structure by equivalent static procedures.

CATEGORIZATION OF DIAPHRAGMS BASED ON TORSIONAL COUPLING

FEMA 356 gives provisions for categorizing diaphragms as either rigid, stiff or flexible. If a diaphragm is considered as flexible, there are implications that coupling between wall elements of the structural system may be neglected to a large extent. The FEMA 356 procedures for calculation of the fundamental period for such structures is addressed in the previous section. If a diaphragm is considered rigid, then coupling between the wall elements is generally accounted for based on the relative wall stiffnesses. The response of a structure with stiff diaphragms is obviously between these two extremes. FEMA 356 does not provide any direct guidance for seismic assessment of buildings with stiff diaphragms.

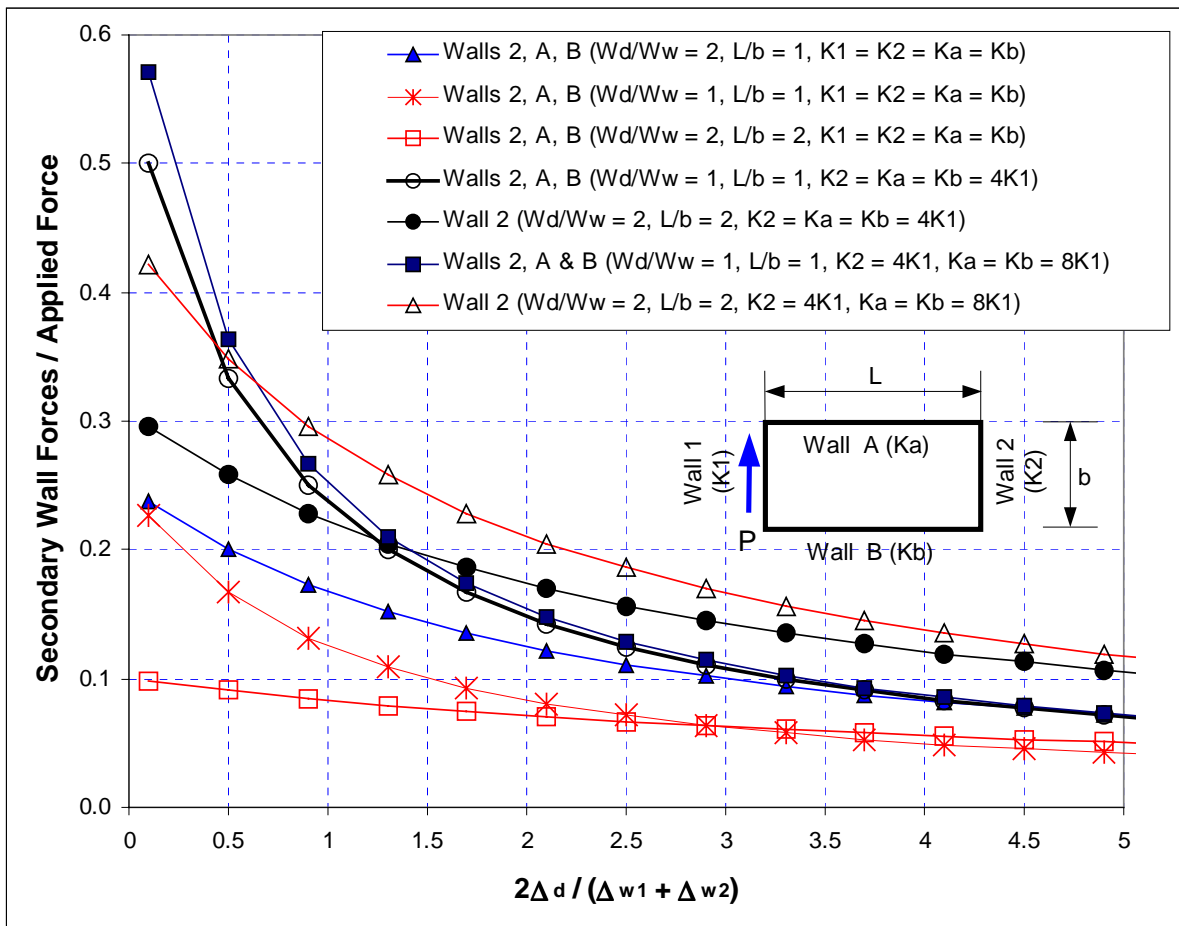


Figure 4 Distribution of inertial force from one wall to other walls as a function of the diaphragm and wall stiffness characteristics.

The above categorization of diaphragms in FEMA 356 is based on the ratio between the diaphragm displacements associated with out-of-plane wall deformation Δ_d and the average in-plane wall displacements at the sides of the diaphragm in the direction under consideration $(\Delta_{w1} + \Delta_{w2})/2$. If this ratio is greater than two, the diaphragm is assumed to be flexible, and if it is less than 0.5, the diaphragm is assumed to be rigid. The lateral forces applied to the

diaphragm and to the walls in the calculation of these deflections are to be consistent with the distribution of mass within the system.

Figure 4 shows an example plot from on-going research [4] in which the influence of diaphragm characteristics on the seismic performance of unreinforced masonry buildings is being studied in detail. This figure focuses on an inertial loading from one wall (wall 1) of a simple one-story single-diaphragm structural configuration, and how this force distributes to the other walls of the building. The influence of the relative weight associated with the diaphragm and the out-of-plane walls, W_d , versus the weight associated with the excitation of each of the in-plane walls, W_w , is considered in addition to the aspect ratio of the diaphragm L/b and the relative wall stiffnesses. In short, the figure shows that substantial torsional coupling can exist even for diaphragms that are presently classified as flexible. Damage to wall 1 and the associated inelastic deformations will only increase the torsional coupling. The detailed assessment of the implications of this figure are under investigation by the authors.

REFERENCES

1. American Society of Civil Engineers (ASCE), "Prestandard and Commentary for the Seismic Rehabilitation of Buildings," Publication No. 356, Federal Emergency Management Agency, Washington, D.C., 2000.
2. Applied Technology Council (ATC), "NEHRP Guidelines for the Seismic Rehabilitation of Building," Publication No. 273, Federal Emergency Management Agency, Washington, D.C., 1997.
3. Coil, J. (1999), personal communication.
4. Kim, S.C. and White, D.W. "MDOF Response of Low-Rise Buildings," ST-5 project final report, Mid-America Earthquake Center, National Science Foundation, Georgia Institute of Tech., 2001 (in preparation).
5. Peralta, D. F., Bracci, J. M. and Hueste M. B. D. "Seismic Performance of Rehabilitated Floor and Roof Diaphragms", ST-8 project final report, Mid-America Earthquake Center, National Science Foundation, Texas A&M Univ., 2001 (in review).
6. Tissell, J.R. and Elliott, J.R., "Diaphragms and Shear Walls," American Plywood Association (APA), 1997, 55 pp.
7. Tissell, J.R. and Rose, J.D., "Roof Diaphragms for Manufactured Homes," American Plywood Association (APA), Rep. No. 146, 1993, 30 pp.



KEERC-MAE Joint Seminar on
Risk Mitigation for Regions of Moderate Seismicity
University of Illinois at Urbana-Champaign, August 5-8, 2001



Sponsors: Korea Science and Technology Foundation, U.S. National Science Foundation, Brain Korea 21



Structural Damage Assessment from Model Data Using a System Identification Algorithm with a Regularization Technique

Joo Sung KANG¹, Inho YEO² and Hae Sun LEE³

¹*Graduate Student, Seoul National University
School of Civil, Urban and Geosystem Eng., Shillim-dong, Kwanak-gu, Seoul 151-742, Korea
email: jskang94@plaza1.snu.ac.kr*

²*Senior Researcher, Highway Management Corporation
Research Institute, Ichon 467-860, Korea
email: ihyeo@himan.co.kr*

³*Associate Professor, Seoul National University
School of Civil, Urban and Geosystem Eng., Shillim-dong, Kwanak-gu, Seoul 151-742, Korea
email: chslee@plaza.snu.ac.kr*

ABSTRACT: The parameter estimation scheme for System Identification (SI) has been developed by many researchers for more than three decades. It is achieved by comparing the measured responses of a real structure and the calculated responses of a mathematical model. Generally the dynamic test is applied to a large structure for diagnosis of the system. Modal parameter estimation is formulated as a minimization problem the discrepancy between the real measurement data and the predictions of a mathematical model of the structure. It is usually difficult to measure at all of the degrees of freedom and to collect data from all of the modes. Furthermore, the measurement data always include a considerable measuring errors. Inverse problem for parameter estimation is sever ill-posedness problem because of the sparseness of measurement data and the measuring error. Tikhonov norm for the change of the stiffness is used as the regularization function. Geometric Mean Scheme (GMS) is employed to determine a regularization factor.

KEYWORDS: System Identification, model data, ill-posedness, regularization, GMS

INTRODUCTION

Structural damage often causes a loss of stiffness in one or more elements of a structure that affects its modal responses such as modal frequencies and mode shapes. Many methods have been developed to detect the location and severity of damage based on these changes. In this study, system identification (SI) based on the minimization of least square errors between measured mode shape vector and calculated mode shape vector is employed.

To solve nonlinear optimization problem, the recursive quadratic programming (RQP) and the Fletcher active set strategy are employed [1]. In RQP, sensitivity of calculated mode shape vector with respect to the system parameters is required. Current proposed algorithms to calculate sensitivity of mode shape vector, such as the modal method, the modified modal method, and the Nelson's method [6] are valid only when the mode shape vector is normalized with respect to mass matrix. Unless fully measured mode shape vector is available due to economic or physical restriction, normalization of measured mode shape vector cannot be obtained. So an algorithm to calculate sensitivity of the mode shape vector which is normalized with respect to an arbitrary matrix is developed.

It is known that SI is typically ill-posed inverse problem which suffers from severe numerical instabilities, such as non-existence, non-uniqueness, and discontinuity of solution. A regularization technique [2,3] is adopted to overcome such numerical instabilities. As a regularization function, Tikhonov norm which is difference between a baseline stiffness property and an assumed stiffness property is used. A regularization factor plays the most important role for estimation of both numerically and physically meaningful solution [2,3]. GMS proposed by Park [8] is used to determine an appropriate regularization factor.

In real situation, measurement data suffer from the measurement noises. When the measurement data are polluted with noise, it is very difficult to distinguish whether the damage is caused either by real damage or by noise in measurement data. Since measurement noise is inevitable in the real situation, the estimated system parameters from SI may be easily meaningless in the damage detection and assessment. To overcome this drawbacks, data perturbation scheme proposed by Hjelmstad and Shin [5] and statistical approach proposed by Yeo [9] are incorporated with SI for damage detection and assessment.

PARAMETER ESTIMATION

In this study damage is defined as the reduction of a system parameters from its baseline value which is assumed as a priori information. System parameters are estimated by the output error estimator using modal data such as Eq. (1).

$$\underset{\mathbf{x}}{\text{Minimize}} \quad \Pi(\mathbf{x}) = \frac{1}{2} \sum_{i=1}^{nmd} \left\| \mathbf{f}_i - \hat{\mathbf{f}}_i \right\|^2 \quad \text{subject to} \quad \mathbf{R}(\mathbf{x}) \geq 0 \quad (1)$$

where \mathbf{x} , \mathbf{f}_i , $\hat{\mathbf{f}}_i$, nmd , $\mathbf{R}(\mathbf{x})$ are system parameter vector, calculated mode shape vector of i -th mode, measured mode shape vector of i -th mode, the total number of the measured modes and constraints of system parameters, respectively.

REGULARIZATION

The parameter estimation with the output error estimator is typically ill-posed inverse problem. Ill-posed problems suffer from three instabilities: nonexistence of solution, non-uniqueness of solution and/or discontinuity of solution when measured data is polluted by noise [2]. So far, many authors have attempted to overcome an instability problem by imposing upper and lower constraints on the system parameters. However, Neuman [6] and Hjelmstad [4] have shown that constraints are not sufficient to guarantee a meaningful solution.

In this study it is utilized regularization technique in order to overcome ill-posedness in optimization processing. The following regularization function is used for the current identification of a structure.

$$\Pi_R = \frac{\beta}{2} \left\| \mathbf{x} - \mathbf{x}_0 \right\|_T^2 \quad (2)$$

where β and \mathbf{x}_0 denote the regularization factor and the system parameters representing baseline stiffness properties of a structure, respectively. $\| \cdot \|_T$ is the Tikhonov norm of a matrix.

The regularization effect in parameter estimation process is determined by the regularization factor. Some rigorous methods to find an optimal regularization factor have been proposed for linear inverse problems. The geometric mean scheme (GMS) proposed by Park is adopted to determine the optimal regularization factor [8]. In the GMS, the optimal regularization factor is defined as the geometric mean between the maximum singular value and the minimum singular value of the Gauss-Newton hessian matrix of the error function given in Eq. (1).

$$\beta = \sqrt{S_{\max} \cdot S_{\min}} \quad (3)$$

where β , S_{\max} , S_{\min} denote regularization factor, maximum singular value and minimum singular value which is not zero, respectively.

By adding the regularization function to the error function, the regularized output error estimator is defined as follows :

$$\text{Minimize}_{\mathbf{x}} \quad \Pi = \frac{1}{2} \sum_{i=1}^{nmd} \left\| \mathbf{f}_i(\mathbf{x}) - \hat{\mathbf{f}}_i \right\|^2 + \frac{\mathbf{b}}{2} \left\| \mathbf{x} - \mathbf{x}_0 \right\|^2 \quad \text{subject to} \quad \mathbf{R}(\mathbf{x}) \leq 0 \quad (4)$$

SENSITIVITY

To solve the constrained nonlinear optimization problem expressed by Eq. (4), the recursive quadratic programming (RQP) and the Fletcher active set strategy are employed [1]. In RQP we need the sensitivity of the Eq. (1) with respect to system parameters. The sensitivity is shown in Eq. (5)

$$\Pi_{,x} = \sum_{i=1}^{nmd} \left\| \mathbf{f}_i - \hat{\mathbf{f}}_i \right\| \cdot \mathbf{f}_{i,x} \quad (5)$$

where the subscript $(\cdot)_{,x}$ denotes the partial derivative with respect to a system parameter.

In case where the mode shape vector is normalized by mass matrix of the structural system, several methods to calculate the sensitivity are already proposed, such as the modal method, the modified modal method, and the Nelson's method [6] and so on. When the mode shape vector is normalized by mass matrix, the sensitivity matrix of the vector is as follows:

$$\mathbf{f}_{j,x} = - \sum_{i \neq j}^{nmd} \frac{\mathbf{f}_i^T \mathbf{K}_{,x} \mathbf{f}_j}{(\ddot{\omega}_i - \ddot{\omega}_j) \mathbf{f}_i^T \mathbf{M} \mathbf{f}_i} \mathbf{f}_i \quad (i \neq j) \quad (6)$$

where $\ddot{\omega}$, \mathbf{M} , and $\mathbf{K}_{,x}$ denote eigen value, the mass matrix, and the sensitivity matrix of the stiffness matrix of a structural system with respect to a system parameter, respectively. However, in the system identification where the partially measured mode shape is used to determine design variables we cannot use the sensitivity of the normalized mode shape by the mass matrix.

If we assume that $\bar{\mathbf{f}}$ is normalized by arbitrary matrix \mathbf{C} , then we can express its sensitivity $\bar{\mathbf{f}}_{,x}$ as follows:

$$\bar{\mathbf{f}}_{j,x} = \frac{1}{\mathbf{f}_i^T \mathbf{C} \mathbf{f}_i} \left(\mathbf{f}_{j,x} \sqrt{\mathbf{f}_i^T \mathbf{C} \mathbf{f}_i} - \mathbf{f}_j \frac{\mathbf{f}_i^T \mathbf{C} \mathbf{f}_{i,x}}{\sqrt{\mathbf{f}_i^T \mathbf{C} \mathbf{f}_i}} \right) \quad (7)$$

If we substitute m_c for $\sqrt{\mathbf{f}_i^T \mathbf{C} \mathbf{f}_i}$, the Eq. (5) can be represented as the following equation.

$$\bar{\mathbf{f}}_{i,x} = \frac{1}{m_c} \mathbf{f}_{i,x} - \frac{1}{m_c^3} (\mathbf{f}_i^T \mathbf{C} \mathbf{f}_{i,x}) \mathbf{f}_i \quad (8)$$

MEASURED DATA PERTURBATION SCHEME

If a sufficient number of measured data sets are available for the same measurement condition, the effect of measurement noise on identification results may be reduced by averaging the measured data. In real situations, however, only limited sets of noisy measurement data are available. Therefore, it is usually difficult to determine whether the changes of the system parameters are caused by measurement noise or by actual damage.

The data perturbation method, which has been proposed by Hjelmstad and Shin [5] for a numerical simulation study, is employed. In the data perturbation method, a series of the system identification is performed with generated data sets around a given set of measured displacements by perturbing the given data with a small magnitude. As a result, the identified system parameters are interpreted statistically with their distributions.

To obtain samples of a system parameter for its statistical distribution, the measured data perturbation iteration is performed with the following perturbed measurement data.

$$(\bar{u}_j)_i^k = (\bar{u}_j)_i (1 + \eta_j^k) \quad (9)$$

where $(\bar{u}_j)_i^k$ and η_j^k are a perturbed displacement for load case i and a random number, respectively, for the j -th component of the measured displacement at the k -th iteration.

DAMAGE SEVERITY

After mean and standard deviation are evaluated using the measured data perturbation scheme, it is the next progression to determine which member is damaged. Because baseline value of the system parameter is a prior knowledge, it is possible to define damage by comparing the estimated mean value of a member with its baseline value. When any estimated system parameter value is less than its baseline value, it is regarded that the system parameter encounters damage. According to the statistical interpretation proposed by Yeo [9], we can calculate the damage severity as follows :

$$S_D = \frac{x_0 - \bar{x}}{x_0} \times 100(\%) \quad (10)$$

where x_0 and \bar{x} are the baseline value and the estimated mean value of a design system parameter.

EXAMPLE

The numerical example structure is 2-story frame structure as shown in Fig. 1. Since the axial rigidity can be neglected in a frame structure, the only flexural rigidity EI of each member is selected as the system parameter. The damage is assumed that the rotational rigidity of support 11 is lost perfectly

by any severe load. It is assumed that the damage is reflected as the reduction of the flexural stiffness of the member connected to the support.

Fig. 1 and Fig. 2 show the geometry condition and boundary conditions and the finite element model of the structure, respectively. It is assumed that the structure is made of steel. Therefore Young's modulus of each element is assumed uniformly 206Gpa. A cross-section of each element is 0.02 m \times 0.02 m rectangle. Moment of inertia from the neutral axis is $1.33 \times 10^{-8} \text{ m}^4$. 5% proportional random noise for each mode shape is added to the noise-free mode shape vector. The baseline values of all the system parameters are 2746.67 N·m², and which is used as the initial values for design parameters. A posteriori information used as the measurement is modal displacement including horizontal and vertical displacement, and rotational displacement at nodes 3,5,13 and 15. The total number of degrees of freedom of the structure is 48, and the number of measured degrees of freedom is 12. First three modes are used in the ROEE in Eq. (4).

Fig. 3 represents the estimation result as the normalized values of system parameters. The figure shows that system parameters of several members is reduced than their baseline values. However only the three members (5, 9, 10) are assessed as damaged members using the statistical approach of Yeo [9]. Their damage severities are shown in Fig. 4. The two members are just ones connected with the hinged support and the other member is the side bay member. Maybe the reason that the member 5 is assessed to a damaged member is the sparseness of measurement data in parameter estimation.

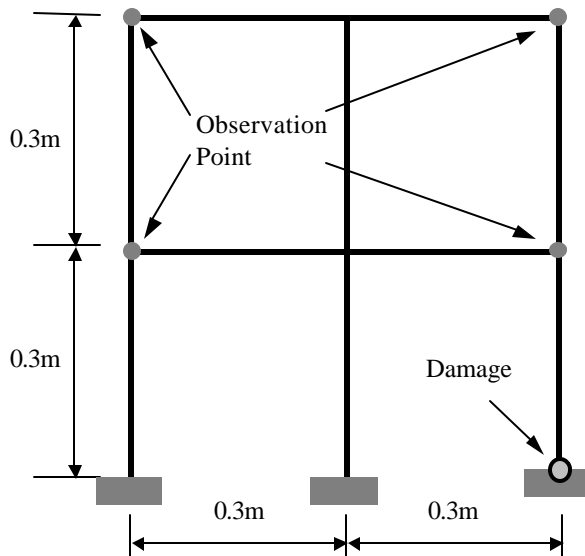


Fig. 1 Geometry and boundary condition

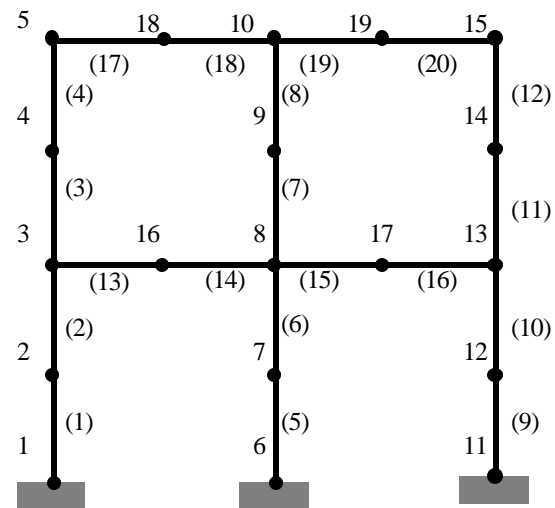


Fig. 2 FEM modeling

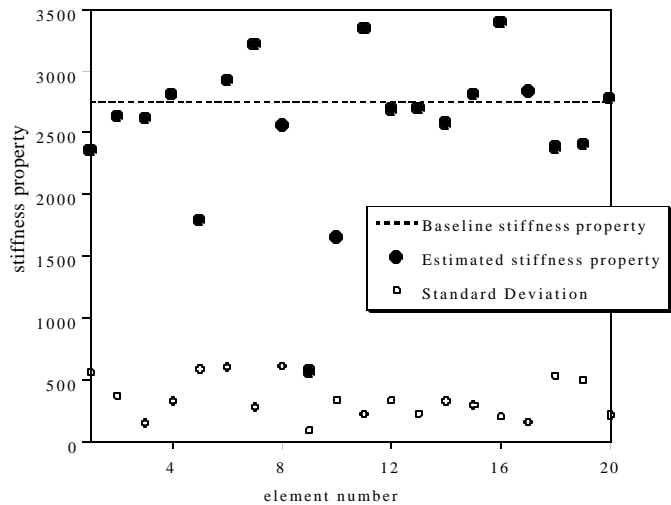


Fig. 3 Estimated result

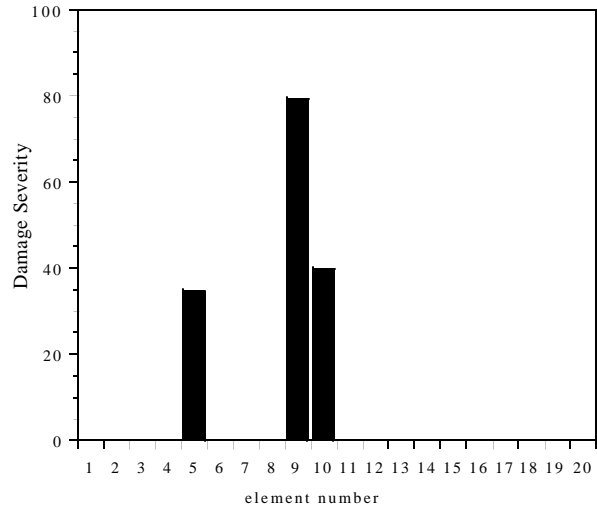


Fig. 4 Damage severity

CONCLUSION

The damage detection and assessment algorithm using mode shape vector is proposed. The Tikhonov regularization technique is employed to alleviate the ill-posedness of the inverse problem in SI. The GMS is utilized to determine the optimal regularization factor. The method to calculate the sensitivity matrix of the mode shape vector, which is normalized by an arbitrary matrix, is presented. Data perturbation scheme is used to assess the structural damage statistically. Statistical approach is used to determine damaged members and assess the damage severity.

In spite of successful detection of the deterioration of the frame is assessed as the reduction of flexural rigidity of the member connected to the support but the proposed algorithm still has many problems. Because the system identification scheme using modal data contains drawbacks caused by insensitiveness of lower mode shape to changes of structural properties, proposed algorithm needs to higher mode shape to distinguish the mode shape by changes of structural properties but it can't be obtained in real situation. So it is needed to update proposed algorithm to overcome these problems.

REFERENCE

1. Banan, M.R. and Hjelmstad, K.D. (1993), "Identification of structural systems from measured response," Structural Research Series NO. 579, Dept. of Civil Eng. Univ. of Illinois at Urbana-Champaign, May

2. Bui, H.D. (1994), "Inverse problems in the mechanics of materials: An introduction", CRC Press, Boca Raton
3. Groetsch, C.W. (1984). "The theory of Tikhonov regularization for Fredholm equations of the first kind", Pitman Advanced Publishing, Boston
4. Hjelmstad, K.D. (1996). "On the uniqueness of modal parameter estimation." J. of Sound and Vibration 192(2), 581-598
5. Hjelmstad, K.D., and Shin, S.B. (1997). "Damage Detection and Assessment of Structures from static response." J. of Engineering Mechanics, ASCE, 123(6), 568-576
6. Nelson, R.B. (1976). "Simplified Calculation of Eigenvector Derivatives," AIAA Journal, Vol. 14, Sept. 1976, pp. 1201-1205
7. Neuman, S. P., and Yakowitz S. (1979). "A statistical approach to the inverse problem of aquifer Hydrology." Water Resources Research, 15(4), 845-860
8. Park, H.W., Shin, S.B. and Lee, H.S., "Determination of Optimal Regularization Factor for System Identification of Linear Elastic Continua with the Tikhonov Function," International Journal for Numerical Methods in Engineering, Vol. 51, No.10, 2001, pp.1211-1230.
9. Yeo, I.H., Shin, S.B., Lee, H.S., Chang, S.P., "Statistical Damage Assessment of Framed Structures from Static Responses," Journal of Engineering Mechanics, ASCE, Vol. 126, No. 4, pp. 414-421, 2000



KEERC-MAE Joint Seminar on
Risk Mitigation for Regions of Moderate Seismicity
University of Illinois at Urbana-Champaign, August 5-8, 2001



Sponsors: Korea Science and Technology Foundation, U.S. National Science Foundation, Brain Korea 21



Utility Software for Earthquake Engineering

Erich M. BRETZ ¹, Mehmet INEL ², Edgar BLACK ³, Mark A. ASCHHEIM ⁴, and Daniel P. ABRAMS ⁵

¹ *Research Assistant, Department of Civil and Environmental Engineering, University of Illinois at Urbana-Champaign
1241 Newmark Laboratory, 205 N. Matthews, Urbana, Illinois, USA
email: ebretz@uiuc.edu*

² *Research Assistant, Department of Civil and Environmental Engineering, University of Illinois at Urbana-Champaign
1241 Newmark Laboratory, 205 N. Matthews, Urbana, Illinois, USA
email: inel@uiuc.edu*

³ *Research Assistant, Department of Civil and Environmental Engineering, University of Illinois at Urbana-Champaign
1241 Newmark Laboratory, 205 N. Matthews, Urbana, Illinois, USA*

⁴ *Assistant Professor of Civil and Environmental Engineering, University of Illinois at Urbana-Champaign
2118 Newmark Laboratory, 205 N. Matthews, Urbana, Illinois, USA
email: aschheim@uiuc.edu*

⁵ *Hanson Engineers Professor of Civil and Environmental Engineering and
Director of Mid-America Earthquake Center, University of Illinois at Urbana-Champaign
1245 Newmark Laboratory, 205 N. Matthews, Urbana, Illinois, USA
email: d-abrams@uiuc.edu*

ABSTRACT: Utility Software for Earthquake Engineering (USEE) is a Windows-based program that provides an easy-to-use graphic interface for performing simple computer simulations of the response of structures subjected to earthquake ground shaking. The interface also provides access to data and products of the Mid-America Earthquake Center. The current version of USEE features a nonlinear single-degree-of-freedom (SDOF) computation engine that provides for several kinds of analyses including SDOF response, response spectra, and the approximate response of multistory buildings using an equivalent SDOF model. Linear, bilinear, and stiffness-degrading load-deformation models are implemented for use in these analyses. Base input waveforms are chosen from a catalog of recorded ground motions, synthetic ground motions [1], and pulse excitations; users may add accelerograms of their choosing. Response data is summarized on screen and may be saved as ASCII text files for subsequent processing; graphics may be copied to other Windows applications. This paper describes the current version and developments to be incorporated in Version 2.

KEYWORDS: inelastic response spectra, elastic response spectra, nonlinear response, SDOF oscillator, equivalent SDOF oscillator, dynamic response computation, flag hysteresis, effective height

INTRODUCTION

The objective of project ST-18 of the Mid America Earthquake Center is to develop an easy to use graphical interface to compute nonlinear response and to provide access to products of the Mid America Earthquake Center. USEE was designed to leverage existing user knowledge of graphic interfaces, invoke “wizards” to guide users through sequences of data input screens, provide cut and paste compatibility with other Windows software, and provide a shell interface that can easily be expanded to provide access to future products of the Mid America Earthquake Center. This paper describes current program capabilities, computational approaches, and program validation, as well as features being implemented in Version 2. The software and manual can be obtained from <http://mae.ce.uiuc.edu/>; a complete report is also available [2].

PROGRAM CAPABILITIES

The program provides capabilities for three types of dynamic analyses. In each analysis, the user is guided through a series of data input screens and the result of the computation is displayed in the final screen. Each type of analysis relies on a common engine to compute the response of a single-degree-of-freedom oscillator. Three load deformation models are available in USEE: linear, bilinear, and stiffness-degrading. The base input may be selected from a catalog of recorded ground motions, synthetic ground motions, and pulse excitations [2].

COMPUTATIONAL ISSUES

SDOF Response Computation

Response during each time interval is computed using the linear acceleration method [3]. In this method, the response acceleration is assumed to vary linearly during the time step, and the properties of the oscillator are assumed to be invariant. The assumption of invariant oscillator properties introduces an error related to the overshooting of the yield point of the oscillator if yield is reached during a time step.

Overshoot Tolerance and Variable Time Step

To minimize the amount of “overshoot,” a user-specified overshoot tolerance must be satisfied during any time step in which a change in stiffness occurs. If the user-specified tolerance is not satisfied, then the solution for the time step is discarded and USEE repeats the calculation at the beginning of the time step with a smaller time increment, equal to 1/10 of the initial time step. The reduced time step is used for all subsequent steps until a change in stiffness is encountered. If the convergence tolerance is satisfied for the reduced time step, the program continues, but reverts to the original time step for subsequent calculations. If convergence is not satisfied with the reduced time step, the solution for the last time step (using the reduced time step) is discarded and a new time step equal to 1/10 of the previous time step is used. This process of reducing time steps is recursively applied until the specified tolerance is satisfied [2].

Constant Ductility Computation

In computing constant ductility spectra, USEE determines the yield strength coefficient, C_y , which causes ductility, μ , to be equal to a specified value. Several properties of the strength-ductility relationship, such as the potential existence of multiple solutions or no solutions for a given period, require that a special solution strategy be employed, as described in [4]. The solution strategy may involve a large number of SDOF analyses, and an efficient algorithm reduces computation time. If relatively few SDOF analyses are done, the possibility of missing an unrecognized higher strength solution exists. Thus, a two-phase solution procedure is employed. The first phase identifies the region in which a solution is to be obtained by applying a “check-reject” test to determine if a higher-strength region is likely to contain a solution. This process is applied to narrow the bounds on the solution. Once the initial bounds are narrowed sufficiently, the second phase is begun. In this phase, a bisection approach is applied to determine a solution as rapidly as possible, within the bounds determined by the first phase.

VALIDATION

SDOF Response

To validate the accuracy of the USEE computations, response was computed for selected examples that are presented in *Dynamics of Structures* [5]. Results were also compared with solutions obtained using the programs NONSPEC [6] and NONLIN [7]. The same load-deformation models, damping, and excitation are used for each analysis case. These consist of SDOF systems having elastic-perfectly plastic response, subjected to the 1940 NS El Centro record that is used in *Dynamics of Structures*. The analysis cases and the results obtained are summarized in Table 1.

Table 1 Validation of SDOF code

		T (sec)	ζ %	Fy / W	Peak Displacement, cm			
					USEE	Ref [5]	NONSPEC	NONLIN
Linear	1	0.5	2	----	6.83	6.78	6.83	7.11
	2	1.0	2	----	15.16	15.16	15.16	15.57
	3	2.0	2	----	18.98	18.97	18.98	19.63
	4	2.0	0	----	25.19	25.17	25.20	26.29
Bilinear	1	0.5	0	0.170	4.35	4.34	4.35	4.35
	2	0.5	5	0.125	4.70	5.26	4.70	4.95
	3	0.5	5	0.250	4.55	4.45	4.55	4.57
	4	0.5	5	0.500	4.50	4.11	4.50	4.45
	5	0.5	5	1.000	5.72	5.72	5.72	5.83

Review of Table 1 reveals that USEE agrees very closely with NONSPEC, but differs noticeably in some cases from the results reported in *Dynamics of Structures* or computed using NONLIN.

Single-Degree-of-Freedom Analogies of Multistory Buildings

Using an equivalent SDOF model, it is possible to estimate the displacement response of multistory buildings. Figure 1 compares the roof displacement response of a 12-story moment-resistant frame computed using DRAIN-2DX [8] with the estimate obtained from the *Multistory Building Approximation* module of USEE. In both cases, the El Centro record is used, scaled by a factor of 2.

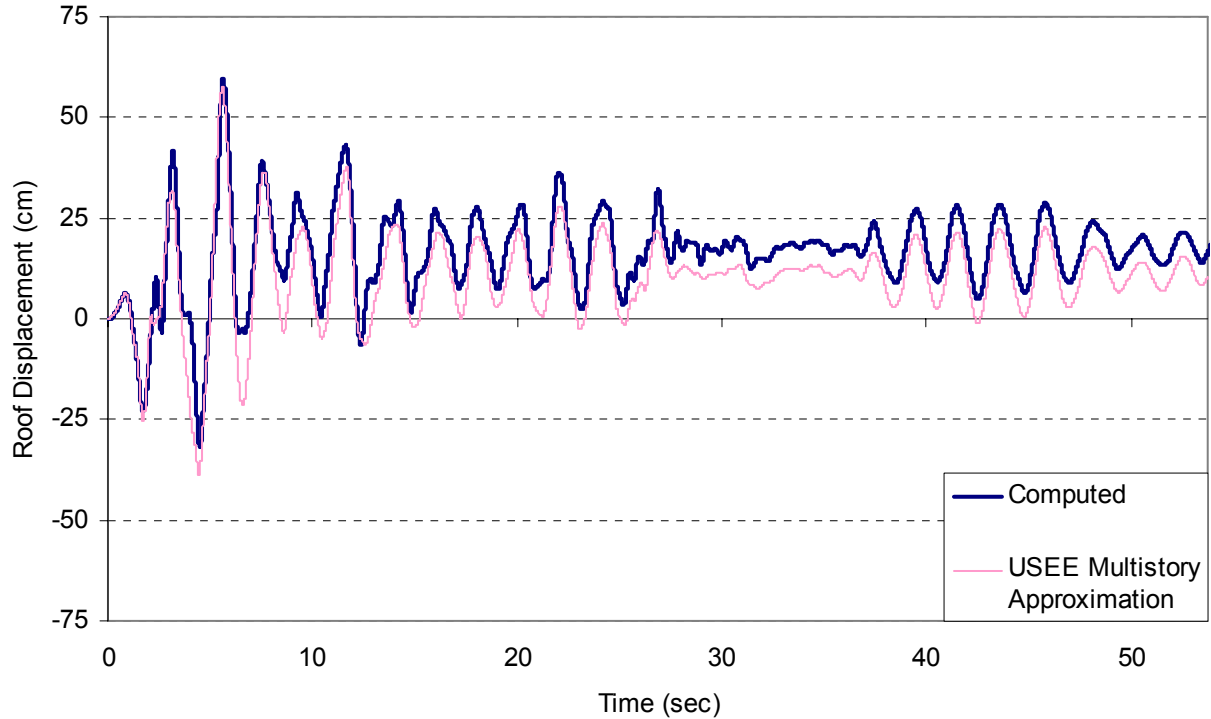


Figure 1 Displacement history of a 12-story building frame subjected to 1940 El Centro record (amplitude scaled by a factor of 2)

It may be observed that the displacements are nearly identical in amplitude and phase, presumably differing only due to the contributions of higher modes. While the roof displacement response is estimated well, higher modes often must be considered to estimate the story shears and overturning moments with accuracy.

Constant Ductility Spectra

Constant ductility response spectra computed with USEE, BISPEC [9], and PCNSPEC were compared for five ground motions packaged in USEE. Figure 2 shows the response spectra computed for the El Centro record for $\mu=2$. The solutions obtained using the three programs were nearly identical in all cases. In a few instances, PCNSPEC missed the highest strength solution.

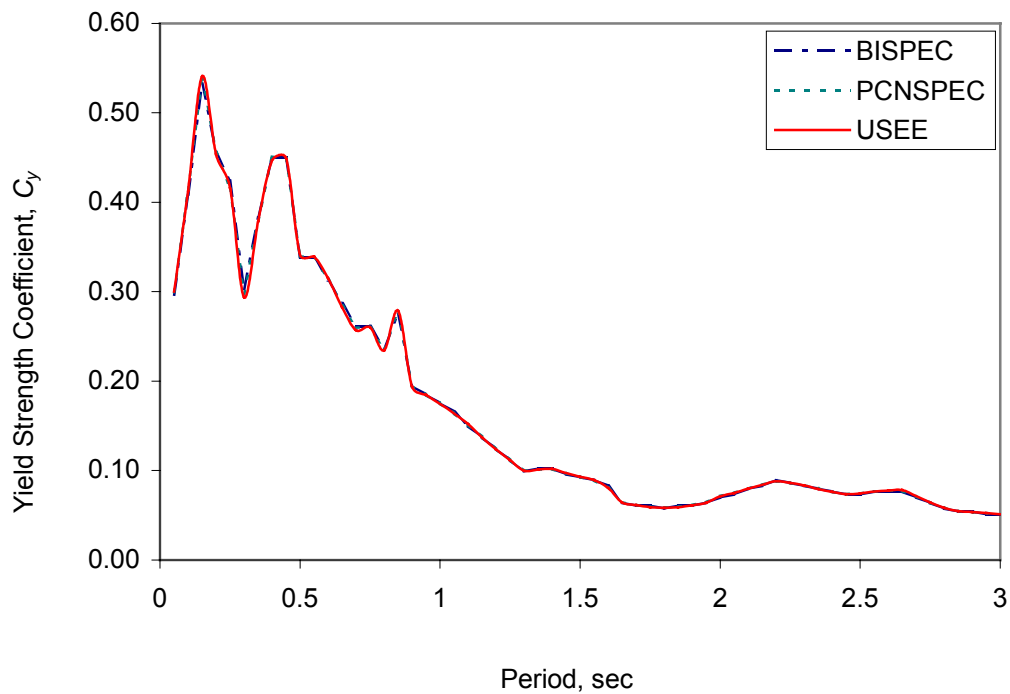


Figure 2 Constant ductility response spectrum for $\mu = 2$ for the El Centro record

The clock times required to obtain constant ductility response spectra for $\mu=2$ and $\mu=8$ for 5 records are shown in Figure 3. A complete description of these records may be found in the USEE manual [2]. The differences in computation time may be the result of many factors including the efficiency of the algorithms for the forward computation, the efficiency of algorithms used for constant ductility iterations, overhead associated with graphical interfaces, and other implementation-specific details.

For the foregoing reasons, one can not conclude from Figure 3 that the constant ductility algorithm implemented in USEE is necessarily more efficient than those implemented in other software programs. It is clear, however, that the combination of the constant ductility algorithm, the efficiency of the forward computation, and other implementation-specific details work together to result in relatively fast computations using USEE.

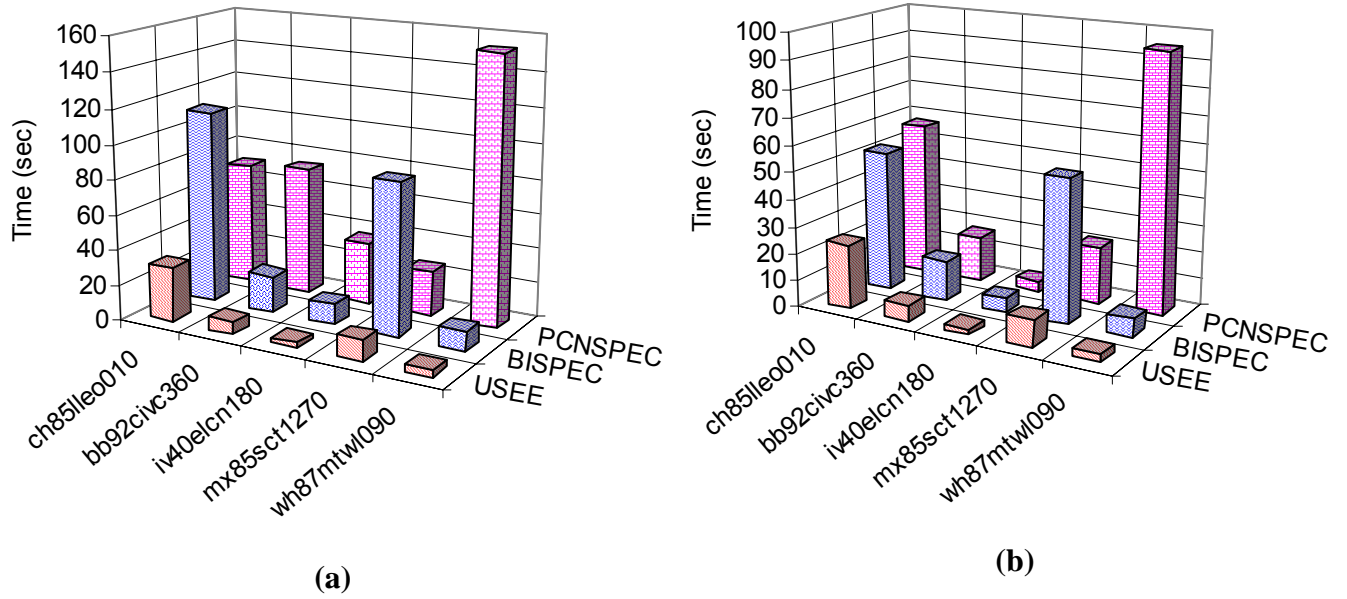


Figure 3 Clock time required to compute response spectra for (a) $\mu=2$ and (b) $\mu=8$ using different software programs and ground motion records

FUTURE CAPABILITIES

Work is presently directed at developing enhancements to the SDOF computation engine and the addition of a nonlinear site response module. The two major enhancements to the SDOF computation response computation are the treatment of second-order effects and the addition of a flag hysteresis model.

Treatment of Second-order Effects

For elastic structures, the presence of second-order effects (P-delta) often has little effect on the dynamic response of the structure. Conversely, in inelastic structures, particularly when the presence of P-delta effects causes the post-yield stiffness to become negative, response amplitudes may be substantially larger.

In a subsequent release of USEE, the user will be able specify P-delta effects in the form of the stability coefficient, θ , or a new parameter termed the effective height of the oscillator. The stability coefficient is defined as the ratio of geometric stiffness, k_g , to lateral stiffness, k_e [10]. The effective height of an oscillator is defined as follows:

$$h_{eff} = \frac{D}{D+L} h \quad (1)$$

where D = dead load, L = live load, and h = height of the oscillator as shown in Figure 4.

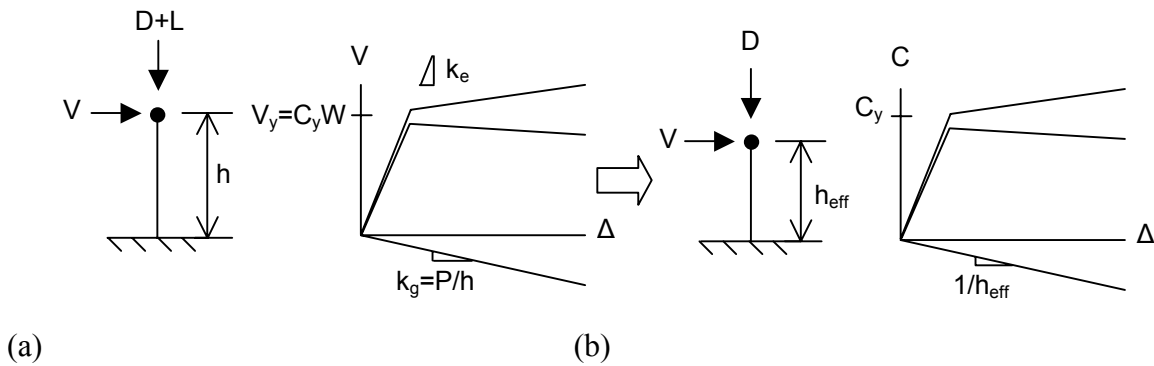


Figure 4 SDOF oscillators and their bilinear load-deformation response when the treatment of P-Delta effects causes a reduction in stiffness equal to (a) the geometric stiffness and (b) h_{eff}

Flag Hysteresis

The behavior of prestressed reinforced concrete shear walls may be modeled with a “flag” hysteresis shown in Figure 5. “Yield” of such a wall system is reached when gaps begin to open along horizontal joints of the wall under lateral loading. A bilinear elastic hysteresis may be used to approximately describe the behavior of the nonlinear elastic shear wall (Fig 5a).

The use of mild steel allows yielding of the steel to occur. The yielding of steel is manifested as a “flag” hysteretic model (Fig 5b). The height of the “flag” is specified as a percent, β , of the elastic range F_y . Users specify the value of β to reflect the desired behavior of the oscillator.

Additional Modules

Site Response

USEE will be linked to code developed in project GT-2B “Non-Linear Site Response Analysis for Deep Deposits in the New Madrid Seismic Zone.” In this project, a computer program, DEEPSOIL, provides for nonlinear site response analysis. DEEPSOIL is a nonlinear wave propagation program that allows for input of depth dependent dynamic soil properties.

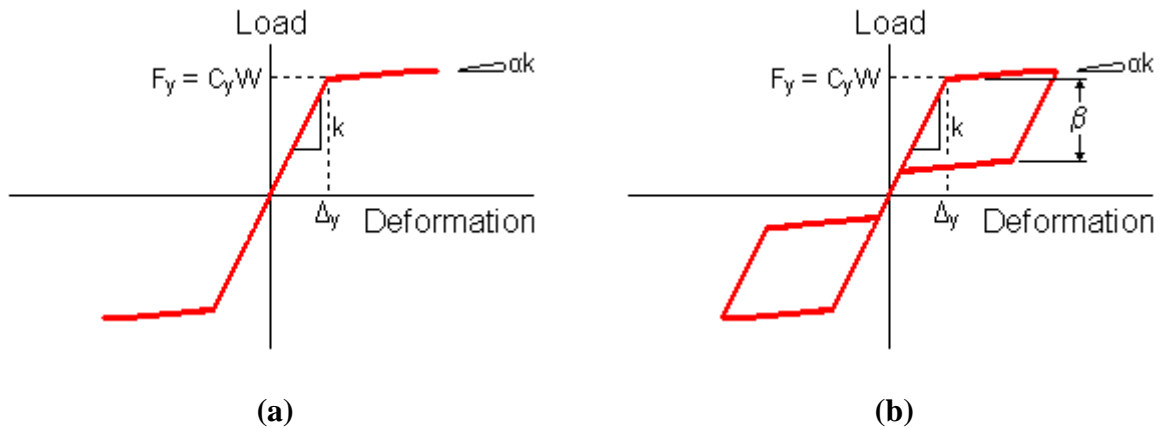


Figure 5 (a) Bilinear Elastic Hysteresis (b) Flag Hysteresis

CONCLUSIONS

USEE's visual interface allows students, practicing engineers, and researchers to quickly simulate nonlinear dynamic response and to understand the influence of parameter variations on response characteristics. The results of the USEE's SDOF computation agree well with the results obtained in NONSPEC, NONLIN, and *Dynamics of Structures*. The "equivalent" SDOF model, based on the first mode shape, can be useful for estimating the roof displacement history and peak displacement response. The algorithm for computing constant ductility that is implemented in USEE is at least as accurate as BISPEC and PCNSPEC and the computation is relatively fast.

ACKNOWLEDGMENTS

Synthetic ground motions distributed with USEE were developed by Y.K. Wen and Chiun-Lin Wu as part of project RR-1 of the Mid-America Earthquake Center. Previous work by Mahin and Lin (1983), which utilized an algorithm developed by Professor R. Klingner of the University of Texas at Austin, Abrams (1985), and Boroschek and Mahin (1991) was relied upon in the development of this software. We are grateful as well to students in courses at Texas A&M and the University of Illinois who have provided many useful comments and suggestions. This work was supported primarily by the Earthquake Engineering Research Centers Program of the National Science Foundation under Award Number EEC-9701785.

REFERENCES

1. Wen, Y.K. and Chiun-Lin Wu, Project RR-1 of the Mid America Earthquake Center.
2. Inel, M., Black, E., Bretz, E., Aschheim, M., and Abrams, D., "Utility Software for Earthquake Engineering," Mid America Earthquake Center. Available for download from <http://mae.ce.uiuc.edu/>, 2001.
3. Newmark, N.M., "A Method of Computation for Structural Dynamics," *Journal of the Engineering Mechanics Division*, ASCE, Vol. 85, No. EM 3, July 1959.
4. Inel, M., Aschheim, M.A., and D.P. Abrams (under review), "An Algorithm for Computing Isoductile Response Spectra", *Journal of Earthquake Engineering*.
5. Chopra, A., *Dynamics of Structures. Theory and Applications to Earthquake Engineering*, Prentice-Hall, Inc., New Jersey, 1995.
6. Boroschek, R.L., and Mahin, S.A., *PCNSPEC Manual, A Modified Version of NONSPEC*, 1991 (unpublished).
7. Charney, F., *Nonlinear Dynamic Time History Analysis of Single Degree of Freedom Systems (NONLIN), Version 6.01*, Advanced Structural Concepts, Inc., Golden, Colorado, and Schnabel Engineering, Denver, Colorado under a contract with Federal Emergency Management Agency, 1998. Also available from <http://www.fema.gov/emi/nonlin.htm>.
8. Prakash, V., Powell, G.H., and Campbell, S., 1993, *Drain-2DX Base Program Description and User Guide*, Report No. UCB/SEMM-93/18, Structural Engineering Mechanical and Materials, Berkeley, California, 1993.
9. Hachem, M.M., BISPEC Version 1.1.2, University of California, Berkeley, 2000. Available from <http://www.ce.berkeley.edu/~hachem/bispec/index.html>.
10. Bernal, Dionisio, "Amplification Factors for Inelastic Dynamic p- Δ Effects in Earthquake Analysis," *Earthquake Engineering and Structural Dynamics*, Vol. 15, 1987, pp. 635.



KEERC-MAE Joint Seminar on
Risk Mitigation for Regions of Moderate Seismicity
University of Illinois at Urbana-Champaign, August 5-8, 2001



Sponsors: Korea Science and Technology Foundation, U.S. National Science Foundation, Brain Korea 21



Displacement Based Seismic Design of Asymmetric-Plan Buildings

Bong-Ho CHO¹ and Sung-Gul HONG²

¹ *Graduate Student, Department of Architecture, Seoul National University
Shinlim-Dong, Kwank-Gu, Seoul, Korea
email: cho525@snu.ac.kr*

² *Assistant Professor, Department of Architecture, Seoul National University
Shinlim-Dong, Kwank-Gu, Seoul, Korea
email: sglhong@snu.ac.kr*

ABSTRACT: Displacement based seismic design concepts are extended to design of asymmetric-plan buildings. This study proposes methods for proportioning of strength and stiffness of walls, determination of target displacement and calculation of design base shear by the direct displacement based design procedure. An eccentricity of stiffness is used as a main parameter in elastic domain and an eccentricity of strength in inelastic domain. In order to ensure the desirable performance of asymmetric structural wall buildings at different design levels, torsional mechanism and ductility capacity of each wall should be reasonably considered in the design procedure. According to the proposed design procedure, base shears for example asymmetric-plan building in Korea zone I and UBC zone III are calculated and an optimal strategy for strength proportioning is discussed.

KEYWORDS: Torsional Design, Torsional Mechanism, Displacement Based Design, Structural Walls, Constant Yield Curvature Assumption.

INTRODUCTION

It is well known that asymmetric-plan buildings are vulnerable during earthquakes. To reduce vulnerability, current seismic code provisions restrict excessive ductility demand of members due to torsion. These code provisions are mainly based on elastic behavior and enable us to proportion strength of walls with assumption that stiffness depends only on wall length (Fig. 1(a)). However, according to the displacement based design proposed by Priestley and Kowalsky [4,5], the yield curvature of a cantilever wall is dependent on wall length (Fig. 1(b)) and the assumption of constant stiffness for walls of equal length leads to significant errors.

Contrary to current code provisions based on the constant stiffness assumption for cantilever walls, Paulay [2,3] identified torsional plastic mechanisms based on the constant curvature assumption and determined system ductility capacity of asymmetric-plan buildings by classifying asymmetric building systems into torsionally restrained and unrestrained systems.

This paper proposes displacement based seismic design method for asymmetric-plan wall buildings. The proposal involves methods for proportioning of stiffness and strength of walls, determination of target displacement and calculation of design base shear by the direct displacement based design procedure. The design method is composed of following three steps. In the initial step, strengths of walls are proportioned. Once the strength ratio among the walls is proportioned, the eccentricity of stiffness and strength, the torsional and lateral stiffness are determined based on the constant yield curvature assumption. The center of stiffness or strength can be used as main design parameters depending on elastic or inelastic behavior. In the next step, the target displacement of system is determined. A Target displacement is limited by the member whose displacement capacity is reached first. In the final step, the total base shear of system is calculated by the direct displacement method and then the base shear of each cantilever wall is distributed.

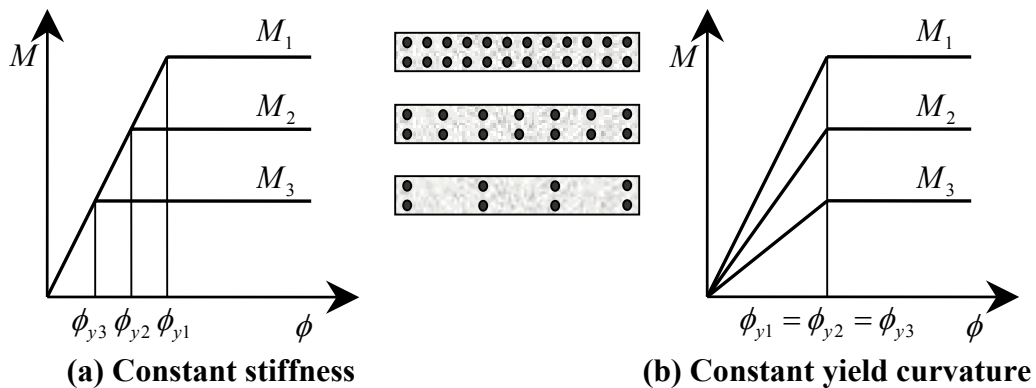


Fig. 1 Stiffness-strength relationship for cantilever walls of equal length

STRENGTH PROPORTIONING

As an initial step to the displacement based design for asymmetric-plan buildings, an appropriate strength ratio among walls is selected. For given geometric properties such as center of mass, dimensions of system, lengths and locations of walls, design parameters involving the eccentricities of strength and stiffness, the lateral and torsional stiffness are found. Based on the constant yield curvature assumption, the determination of strength ratio leads to the determination of other design parameters. According to the design strategy for locating C.V. or C.S., three methods are proposed and detailed procedures of each method for the model in Fig. 2 are described.

Table 1 Strength proportioning methods

Method	Torsional provisions of codes	Method I	Method II	Method III
Design strategy	Locate C.V. between C.S. and C.M.	Locate C.S. at target location	Locate C.V. at target location	Locate C.V. by target rotation
Behavior	Elastic behavior	Elastic behavior	Inelastic behavior	
Application	Force based design	Displacement based design		
Assumption	Constant stiffness	Constant yield curvature		

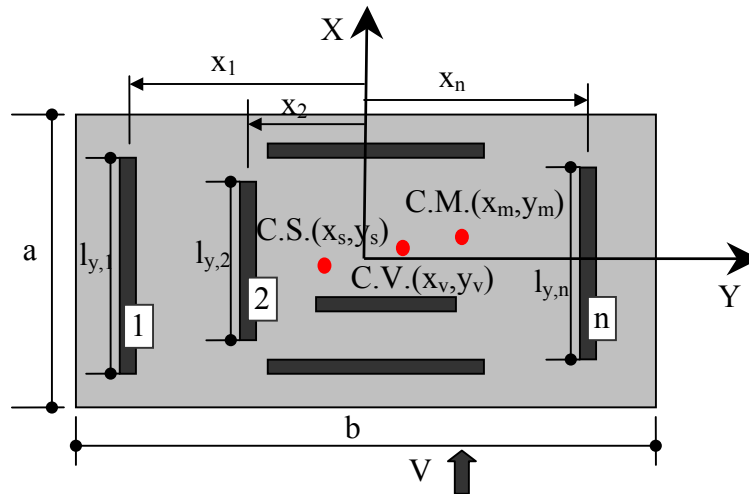


Fig. 2 Model of asymmetric-plan building

Method I – Locating center of stiffness at target location

If zero eccentricity of stiffness in the asymmetric-plan building (Fig.2) is intended, the following procedures to coincide the center of stiffness (C.S.) with the center of mass (C.M.) can be used.

Step 1 Select initial strength ratio of each wall

Strengths of walls in y-direction (loading direction) are distributed proportionally to the square of each wall length. The stiffness of each wall is calculated by dividing the strength by its yield displacement that is inversely proportional to the wall length. For convenience, the total sum of strength and stiffness of walls in y-direction are assumed to be a unit.

$$V_{y,i} = \frac{\alpha l_{y,i}^2}{\sum V'_{y,i}} = \frac{\alpha l_{y,i}^2}{\sum \alpha l_{y,i}^2} = \frac{l_{y,i}^2}{\sum l_{y,i}^2} \quad (1)$$

$$K_{y,i} = \frac{V_{y,i}/(\beta/l_{y,i})}{\sum K'_{y,i}} = \frac{V_{y,i}l_{y,i}/\beta}{\sum V_{y,i}l_{y,i}/\beta} = \frac{V_{y,i}l_{y,i}}{\sum V_{y,i}l_{y,i}} \quad (2)$$

where $\beta/l_{y,i}$ = the yield displacement and α, β = constants. Note that V and K denote the ratios of strength and stiffness and V' and K' the absolute values of strength and stiffness. The stiffness ratio of walls in x-direction (transverse direction) is obtained by assuming that base shears in x and y directions are same.

$$K_{x,i} = \frac{l_{x,i}^3 \sum l_{y,i}^2}{\sum l_{y,i}^3 \sum l_{x,i}^2} \quad (3)$$

Step 2 Find the centers of stiffness and strength

$$(x_s, y_s) = \left(\frac{\sum x_i K_{y,i}}{\sum K_{y,i}}, \frac{\sum y_i K_{x,i}}{\sum K_{x,i}} \right) \quad (4)$$

$$(x_v, y_v) = \left(\frac{\sum x_i V_{y,i}}{\sum V_{y,i}}, \frac{\sum y_i V_{x,i}}{\sum V_{x,i}} \right) \quad (5)$$

Step 3 Calculate normalized eccentricity of stiffness

$$\xi = (x_s - x_m) / b \quad (6)$$

Step 4 Calculate torsional stiffness of system and required additional strength ratio

$$K_T = \sum K_{y,i} (x_i - x_s)^2 + \sum K_{x,i} (y_i - y_s)^2 \quad (7)$$

$$V_{y,i}^T = \frac{K_{y,i} (x_i - x_s) \xi b}{K_T} = \frac{K_{y,i} (x_i - x_s) \xi}{\rho^2 b} \quad (8)$$

where the normalized radius of gyration of stiffness is calculated by eq. (9)

$$\rho = \frac{1}{b} \sqrt{K_T / \sum K_{y,i}} = \frac{\sqrt{K_T}}{b} \quad (9)$$

Step 5 Update strength and stiffness ratios

New strength ratio is obtained by adding required strength ratio ($V_{y,i}^T$) to resist torsion to the assumed strength in the k-th step.

$$V_{y,i}^{k+1} = V_{y,i}^k + V_{y,i}^T \quad (10)$$

New stiffness ratio is also updated by eq. (2)

Step 7 Repeat Step 2 to Step 6 until the eccentricity of stiffness reaches zero.

Non-zero eccentricity of stiffness can allow us an appropriate reinforcement ratio distribution among the walls when there is an excessive eccentricity of stiffness after the first iteration. To achieve this proportionality, the center of mass is assumed to be at the target center of stiffness.

Method II – Locating center of strength at target location

If zero eccentricity of strength in the asymmetric-plan building (Fig.2) is intended, the following procedures to coincide the center of strength (C.V.) with the center of mass (C.M.) can be used.

Step 1 Try an initial strength ratio among walls

Distribute the strength ratio of walls in y-direction (loading direction) by eq.(1).

Step 2 Determine complementary strength ratio for zero eccentricity of strength

A complementary strength ratio is necessary to render the eccentricity of strength zero. They are assumed by eq. (11).

$$V_{y,i}^T = pl_i^2 \quad (\text{when } x_i < x_v) \quad (11\text{-a})$$

$$V_{y,i}^T = ql_i^2 \quad (\text{when } x_i > x_v) \quad (11\text{-b})$$

In order to find constants p and q , the following two conditions are necessary. The additional strength $V_{y,i}^T$ should satisfy eq. (12) to keep the sum of strengths unchanged and the center of modified strength must coincide with C.M. by eq. (13)

$$\sum pl_i^2 + \sum ql_i^2 = 0 \quad (12)$$

$$\sum x_i V_{y,i}^{k+1} = \sum x_i (V_{y,i}^k + V_{y,i}^T) = x_m \quad (13)$$

Step 3 Modify the strength ratio

The eccentricity of strength can be shifted by modification of the initial strength ratio.

$$V_{y,i}^{k+1} = V_{y,i}^k + V_{y,i}^T \quad (14)$$

Method III – Locating center of strength by pre-determined target rotation

This method is applicable to torsionally restrained systems [8] where target rotation is restrained by transverse walls which remain elastic. This method determines the target location of C.V. that is calculated from the torsional stiffness and the target rotation angle.

Step 1 Choose target rotation by graphical method

In the first step, the target rotation angle θ can be selected between θ_1 and θ_2 that are limited by displacement capacity of walls. The target rotation angle resulting in the smallest base shear is chosen as an optimum rotation angle. The system damping value by eq. (17) is used as a criterion for magnitude of base shear.

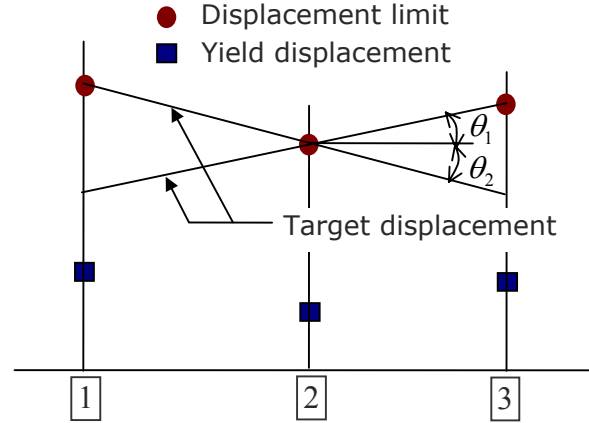


Fig. 3 Target rotation angle

Step 2 Calculate target eccentricity of strength

Torsional stiffness is calculated from the elastic stiffness of transverse walls.

$$K_T = \sum \frac{V_{x,i}}{\Delta_{x,i}} (y_i - y_s)^2 \quad (15)$$

where $\Delta_{x,i}$ is the yield displacement of wall in the transverse direction. The target eccentricity of strength is calculated by equilibrium condition.

$$e_v = \frac{K_T \theta}{\sum V_{y,i}} \quad (16)$$

Step 3 Proportion strength ratio among the walls by Method II

Assume C.M. at the target C.V. and distribute strength by Method II.

TARGET DISPLACEMENT

After the strength ratio is allocated, the base shear is determined by the direct displacement based design procedure. The selection of target displacement is the first step to the displacement based design. The target displacement of an isolated cantilever wall is determined by the capacity of plastic hinge rotation or code-specified drift limits [1]. When a system consists of a group of walls, C.M. is considered as a reference point of the target

displacement. The target displacement at C.M. is determined by a step-by-step procedure. As displacement demand increases, the walls yield and the system properties change. The lateral stiffness, the torsional stiffness and the eccentricity of stiffness are revised at each step and the target displacement is determined when one of walls reaches the displacement limit.

DESIGN BASE SHEAR

The base shear corresponding to the target displacement is calculated by the design displacement spectrum. The system damping in an equivalent S.D.O.F system is derived from the effective damping of each wall, where a weighted mean average is appropriate, given by eq. (17).

$$\xi_e = \sum_i^n V_{y,i} \xi_{y,i} \quad (17)$$

The displacement spectrum is modified by the system damping and the effective period corresponding to the target displacement is determined from the spectrum. Finally, the design base shear is calculated from the effective period and the stiffness. The base shear is distributed to each wall according to the determined strength ratio.

DESIGN EXAMPLE

Design base shear forces of an example wall building shown in Fig. 4 are calculated by the proposed design methods and Table 2 shows the results. Base shear forces for one example asymmetric building vary to the extent of 48% according to the strength proportioning methods. For implementation of method I, two cases are demonstrated depending on different target location of C.S. In Case 1, C.S. is located at $X=-1$ and the ratio of amounts of uniformly distributed reinforcements of each wall ($A_{s,i}$) to the sum of them of all walls ($\sum A_{s,i}$) is calculated as (0.23, 0.352, 0.418). In this case the reinforcement ratio of wall 3 is twice larger than that of wall 1. When 10% eccentricity of stiffness is allowed, C.S. moves to the location at $X=-1.72$ by Case 2, which results in $A_{s,i}$ to $\sum A_{s,i}$ ratio as (0.28, 0.344, 0.376).

Displacement profiles of system and members by Method II and III are shown in Fig. 5. Numbers 1, 2 and 3 denote the identification number of walls and A, B and C indicate each step when any walls yield. Line B in Method II, line C in Method III respectively indicate the target displacement and the rotation angle. In Method II, wall 3 does not yield at the target displacement, meanwhile in Method III, the displacement capacity of all walls contributes to the displacement capacity of system. As a result, the target displacement by Method III is largest and base shear is smallest. Therefore, the strength distribution by Method III is considered as an optimal method.

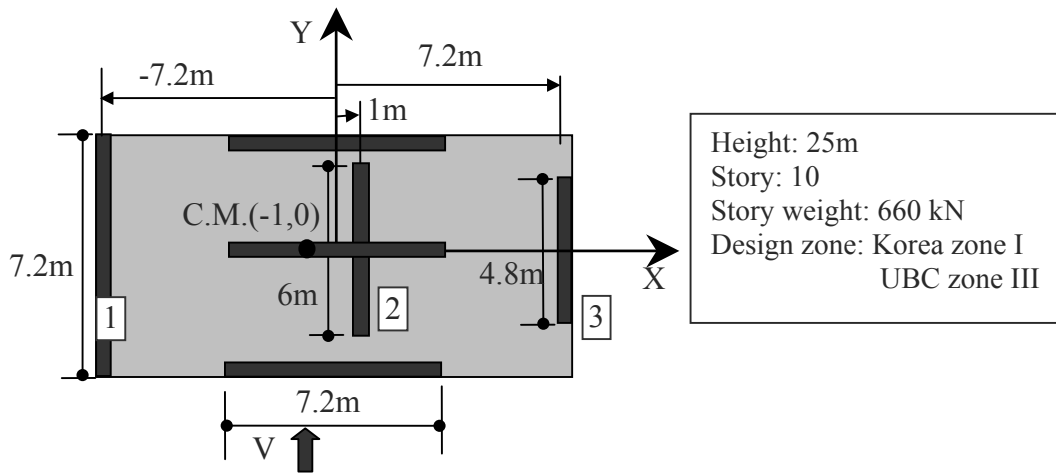
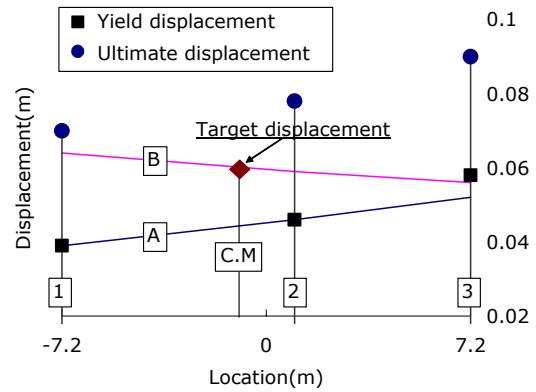
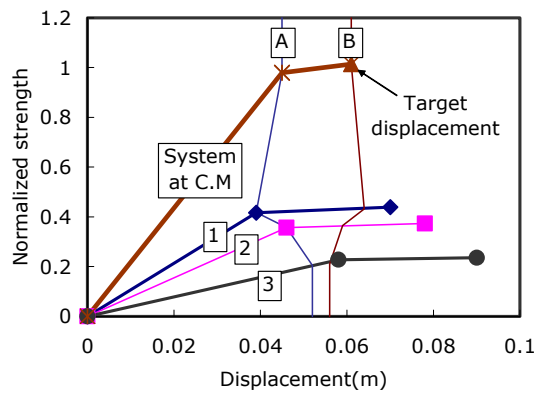


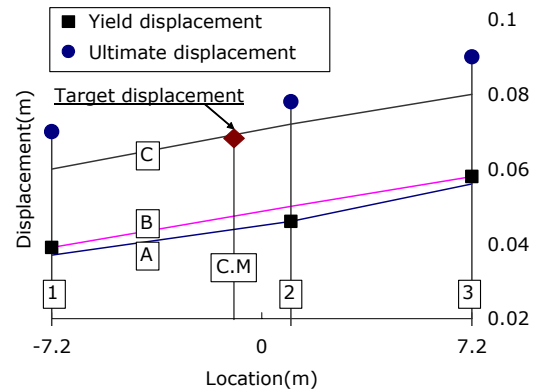
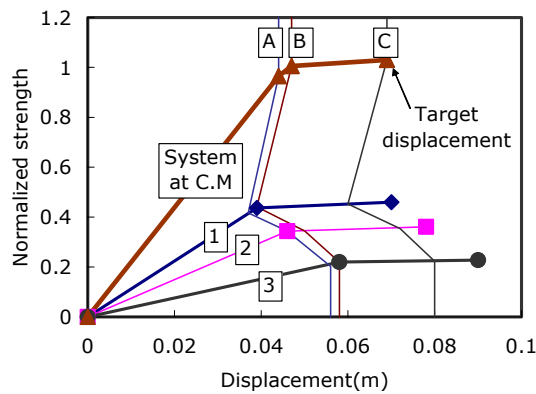
Fig. 4 Example model

Table 2 Design result

Method	Method I (Case 1)	Method I (Case 2)	Method II	Method III
Design strategy	Locate C.S. at C.M.	Locate C.S. at X=-1.72	Locate C.V. at C.M.	Locate C.V. at X=-1.217
C.S.	X=-1	X=-1.72	X=-1.857	X=-2.072
C.V.	X=-0.113	X=-0.842	X=-1	X=-1.217
Strength ratio	0.348,0.371,0.281	0.409,0.348,0.243	0.416,0.356,0.228	0.437,0.344,0.22
$A_{s,i}$ to $\sum A_{s,i}$ ratio	0.23,0.352,0.418	0.28,0.344,0.376	0.289,0.356,0.356	0.306,0.35,0.347
Target displacements (C.M./members)	0.053 / 0.064,0.049,0.038	0.059 / 0.064,0.057,0.053	0.061 / 0.064,0.059,0.056	0.069 / 0.06,0.072,0.08
Design force (Korea/UBC)	642.7kN / 3549kN	587.1kN/ 3393kN	576.8kN / 3362kN	433kN / 2718kN



(a) Method II



(b) Method III

Fig. 5 Displacement profile by Method II and III

CONCLUSION

Based on the constant yield curvature assumption, displacement based design method of asymmetric-plan buildings is proposed. This method determined strength ratio by locating C.S. and C.M. according to the design strategy. Method I focus on elastic behavior and Method II and III focus on inelastic behavior. By the displacement based design method, target displacement and base shear are determined. Base shear forces for the example asymmetric building vary considerably according to the strength proportioning methods. The difference results from extent of utilizing ductility capacity of each wall. Judging from the design results, Method III can utilize ductility capacities of walls most effectively and is considered as an optimal method for seismic design of asymmetric building in inelastic range. The proposed design procedure that considers torsional mechanism and ductility capacity of each wall is appropriate for performance based design of asymmetric-plan buildings.

ACKNOWLEDGMENTS

This work was supported by grant No. 1999-1-310-002-3 from the Basic Research Program of the Korea Science & Engineering Foundation. Financial support by the Brain Korea 21 Project is also gratefully acknowledged. Opinions, findings and conclusions in this paper are those of the authors and do not necessarily represent those of the sponsors.

REFERENCES

1. Hong, S. G and B. H. Cho “Direct-Displacement-Based Seismic Design and Evaluation of R/C Structural Walls,” *Proceedings of EESK Conference*, Vol. 5, Spring 2001, pp. 231-238
2. Paulay, T. “Torsional Mechanisms in Ductile Building Systems,” *Earthquake Engng. struct. Dyn.* Vol. 27, 1998, pp.1101-1121
3. Paulay, T. “A Simple Displacement Compatibility-Based Seismic Design Strategy for Reinforced Concrete Buildings,” *12th World Conference on Earthquake Engineering*, 2000, Paper 0062
4. Priestley, M. J. N. and M. J. Kowalsky, “Aspects of Drift and Ductility Capacity of Rectangular Cantilever Structural Walls,” *Bulletin, New Zealand National Society for Earthquake Engineering*, Vol. 31, 1998, pp.73-85
5. Priestley, M. J. N. and M. J. Kowalsky, “Direct Displacement-Based Seismic Design of Concrete Buildings,” *Bulletin, New Zealand National Society for Earthquake Engineering*, Vol. 33, 2000, pp.421-444



KEERC-MAE Joint Seminar on
Risk Mitigation for Regions of Moderate Seismicity
University of Illinois at Urbana-Champaign, August 5-8, 2001



Sponsors: Korea Science and Technology Foundation, U.S. National Science Foundation, Brain Korea 21



Seismic Rehabilitation of Unreinforced Masonry Shear Walls

Ömer O. ERBAY¹, and Daniel P. ABRAMS²

¹ *Doctoral Student, Department of Civil and Environmental Engineering, University of Illinois at Urbana-Champaign
1241 Newmark Laboratory, 205 N. Mathews, Urbana, Illinois, USA
email: erbay@uiuc.edu*

² *Hanson Engineers Professor of Civil and Environmental Engineering, University of Illinois at Urbana-Champaign
1241 Newmark Laboratory, 205 N. Mathews, Urbana, Illinois, USA
email: d-abrams@uiuc.edu*

ABSTRACT: This paper summarizes the results of three full-scale brick masonry shear wall tests. As part of this testing program, two plain and one rehabilitated shear walls were tested. Based on the behavior of the plain walls, the third wall was rehabilitated by the center-core technique. The experimental results are presented and discussed in the scope of FEMA 356, seismic rehabilitation guidelines. The walls were constructed using reclaimed solid clay bricks (units compressive strength of 28 MPa (4050 psi)) and Type S mortar (cement:lime:sand ratio of 1:3½:4½). Aspect ratio, height-to-length, was held constant at approximately 0.5 for each wall. The walls were tested under harmonic deformation cycles at quasi-static loading rates. The deformation level was progressively increased in each test until there was a significant loss in the force carrying capacity of the walls. The results showed that unreinforced masonry walls can behave during earthquakes with a substantial amount of inelastic deformation and energy dissipation. The center-core rehabilitation technique enhanced the sliding shear capacity of the walls through dowel action. The strain history of the embedded reinforcing bars suggested that walls rehabilitated with this method can be treated as reinforced masonry walls.

KEYWORDS: unreinforced brick masonry, shear strength, ductility, performance based design, center-core, rehabilitation, old construction.

INTRODUCTION

Today regions where earthquakes occur with low probability but high consequence, are gaining more attention due to increased seismic risk. The risk results from the concentration of buildings and infrastructure built before the legislation of seismic codes [9], as is the case in New Madrid seismic zone.

In terms of the building population, the main threat comes from the old existing buildings. To reduce future economical as well as human life losses these buildings need to be evaluated and if necessary, they should be rehabilitated to ensure acceptable performance level. The recent seismic rehabilitation pre-standard, FEMA 356, addresses this issue in the perspective of performance-based engineering concepts. This approach requires a rational understanding of the performance characteristics of both the buildings and the components that form these buildings. Similar information is needed for different rehabilitation measures. The later information is essential in designing cost effective as well as reliable rehabilitation schemes. The purpose of this paper is to address these issues for old unreinforced masonry shear walls (URM). The experimental results of two non-rehabilitated and a rehabilitated URM shear walls are presented in view of the performance parameters given in the FEMA 356 document.

TEST SETUP AND MATERIAL PROPERTIES

Figure 1 shows the schematic drawing of the loading rig together with a typical test wall. The loading rig consists of a post-tensioned concrete masonry reaction wall, a concrete foundation pad (305x1524x5180 mm, (12x60x204 in)), a concrete loading beam (457x457x4290 mm, (18x18x169 in)), a pair of horizontal 490 kN (110 kip) capacity servo-hydraulic actuators and a pair of vertical 400 kN (90 kip) hydraulic jacks.

The vertical stress was maintained constant throughout each test and was set equal to 0.62 MPa (90 psi) for the first wall and 0.90 MPa (130psi) for the second and the third walls. The test specimens were intended to emulate a cantilevered wall fixed at the foundation level and free at the centerline of the top concrete beam.

Horizontal loads were applied at the center of the top concrete beam, which was 1980 mm (78 in) above the concrete foundation surface. The horizontal actuators were operated in deformation-controlled mode, applying three equivalent harmonic displacement cycles at quasi-static rates. The amplitude of these deformation cycles was gradually increased until a significant loss in the load carrying capacity of the wall was achieved. The horizontal displacements were measured at the same level where the horizontal forces were applied. A fixed reference column outside the loading rig served as the datum for these measurements.

The reinforcement amount is selected based on the minimum requirements given in UBC 1997, sec 2108.2.5.2, [11]. In view of this document, four 16 mm (#5) conventional reinforcing bars were selected as the vertical reinforcement. With this reinforcement configuration the wall had a vertical reinforcement ratio, ρ_{sv} , of 0.01 %. The bars were placed at the center of each core and strain gauged at the base of the wall.

Sand-Polyester (also known as Orthophthalic Polyester Resin–Sand) mix was used for grouting purposes. The mix had a sand-to-polyester volumetric ratio of 1.5:1.0. At the later stage of the mixing procedure, the catalyst DDM-9 (10 cc per 1 liter of mix (2.5 cubic inches per 1 gallon of mix)) was added to accelerate the setting time. Cylinder tests showed that the grout mix had an average compressive strength of 85.6 MPa (12.4 ksi) and an average compressive elastic modulus of 6190 MPa (897ksi).

WALL BEHAVIOR UNDER CYCLIC LOADING

Plain Wall Behavior

Non-rehabilitated walls were tested under two different vertical compressive stresses, 0.62 MPa (90 psi) and 0.90 MPa (130 psi). In general, the response was similar for both walls. The initial behavior was liner-elastic till the initiation of a flexural crack at the base joint level. This crack, with increasing drift amplitudes, was further developed and joined with the crack that was forming from the other side of the wall. As the crack fully developed along the base, the walls started to slide along that joint. After that point the lateral load carrying capacity of the walls was limited by the amount of surface friction between the wall base and the concrete foundation. The limiting state was reached when the deterioration at the toe region reached a level at which the out-of-plane stability of the walls was altered and they moved out-of-plane.

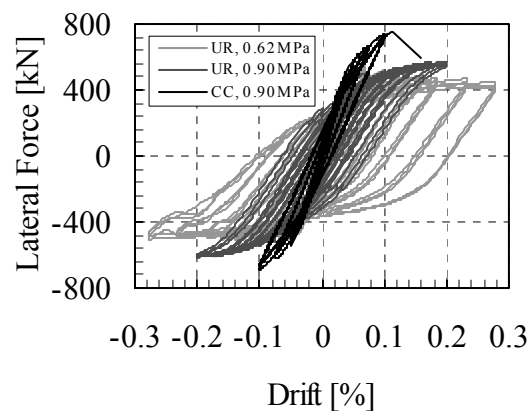


Figure 2 Measured Force-Deflection Curves for Masonry Wall Specimens

The first plain wall specimen, 1S, had a constant vertical compressive stress of 0.62 MPa (90 psi). The behavior was linear-elastic up to a drift level of 0.04 % at which a flexural crack took place at the base joint. The lateral load was approximately 74 % of the ultimate lateral load capacity of the specimen. At approximately 0.1 % drift, the wall started to slide causing unrecoverable deformations along the wall base. Figure 2 shows the full force-displacement response history of the wall. As can be seen, sliding shear response becomes more dominant, more dissipated energy within loops, with increasing drift levels. Other than providing a good energy dissipation mechanism, the sliding shear behavior greatly enhanced the deformation capacity of the wall. Lateral drifts as large as seven times the initial flexural cracking drift, were observed without loss of lateral load capacity. High post-cracking strength is due to the friction acting along the base joint and therefore suggest that the vertical compressive load plays a significant role on ductility. The limit state was reached at a drift level of 0.3%. The limit state mode can be stated as toe-crushing together with an out-of-plane failure.

The second wall, 2S, had a vertical compressive stress of 0.90 MPa (130psi). The general response behavior was very similar to the first specimen except that the higher vertical compressive stress level resulted in higher lateral load capacity, Figure 2. The initial flexural crack occurred at approximately 0.04 % drift, corresponding to a lateral load level of approximately 65 % of the ultimate lateral strength. At approximately 0.13 % drift level, the sliding started at the base of the wall. After this point, the amount of sliding increased with increasing load levels. One interesting observation was that the amount of sliding was also increased with the repetition of deformation cycles even at the same load level. This indicates that the roughness of the sliding surface was deteriorated in each deformation cycle. At approximately 0.2% drift level the wall reached its limit state. The mode of failure can be represented as toe-crushing together with out-of-plane failure. The ultimate drift level is approximately five times the drift level at the initial flexural cracking.

Rehabilitated Wall Behavior

The center-core rehabilitation technique was selected to improve the sliding shear strength and the flexural capacity of the wall specimens. The vertical compressive stress was set equal to 0.90 MPa (130 psi), the same value for the second plain wall. Initial cracking drift level was similar to plain walls. The load corresponding to this drift level was approximately 66 % of the maximum attained load level during the test. The outer reinforcing bars yielded at approximately 0.06 % drift level, indicating that the cores were able to develop the full yield strength of the reinforcing bars, Figure 3. This suggests that the behavior of the specimen can be represented by that of a reinforced masonry wall. A horizontal offset can be seen in the strain history of the East corner reinforcement. This is due to relative sliding of the core to the surrounding masonry beyond 0.07 % drift level. Similar observation can be made for the West corner reinforcement but in the vertical direction. This indicates a permanent plastic deformation in the bar.

The sliding shear capacity was improved due to the presence of the cores. They acted as shear keys and reacted the shear developed at the base through dowel action. Moreover, the presence of the vertical reinforcement resulted in smaller flexural cracks that further enhanced the sliding shear capacity through better particle interlock mechanism. Though the energy dissipation characteristics of sliding shear behavior was not observed in this specimen, energy was dissipated due to yielding of the reinforcing bars. The ultimate drift reached was 0.113% at which the loading beam lost bond with the specimen.

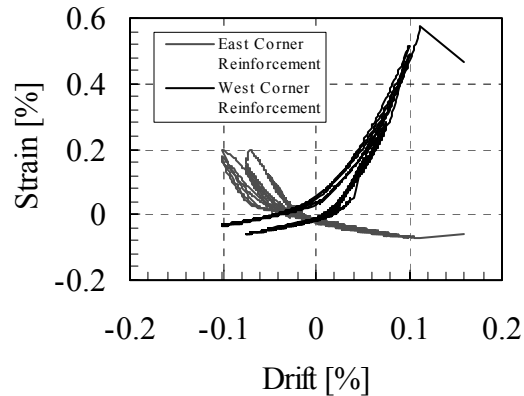


Figure 3 Strain Variation at Corner Reinforcements in Specimen 3S

PERFORMANCE PARAMETERS PER FEMA 356

The recent performance-based seismic rehabilitation pre-standards, FEMA 356, offers four different analyses methods to evaluate the seismic vulnerability of buildings before and after rehabilitation. In each method, an assembly of components and elements model the building's structural system. In this modular idealization approach, the performance of the overall system as well as the performance of the individual components that form the system can be analyzed together and the performance objectives can be ensured both at the global and at the local levels.

The acceptance criteria of the system and the component are defined in terms of performance parameters for each performance objectives. The FEMA 356 document provides two options to determine these performance parameters for each system and component type: 1) using the information and the mathematical relationships provided in the document for different systems and components, 2) testing a representative system or component and using the results of that experiment. Even though the second option is costly and time consuming, it can be sometimes superior to the first option, which may be over conservative for complex system or component behavior.

In light of these discussions the results of this current experimental investigations can be utilized in two ways: 1) to estimate the performance parameters of URM shear wall type components, 2) to verify the mathematical relationships that are provided in the FEMA 356 document to estimate the performance parameters of URM shear wall components.

In the FEMA 356 document, the term “performance parameters” typically refers to three variables: strength, deformation capacity and stiffness. Each variable plays an important role in the performance characteristics of a component. Table 1 summarizes the estimates of these performance parameters for tested shear walls.

Table 1 Summary of Test Results

Wall ID	Aspect Ratio, h/L	Vertical Comp. Stress MPa (ksi)	Initial Lateral Stiffness kN/mm (kip/in)	Maximum Attained Shear Strength KN (kip)	Maximum Drift Level %	Brief Response History
1S	0.52	0.62 (90)	718 (4094)	543 (122)	0.279	Flex. Crack → Base Sliding → Toe Crushing + Out-Of-Plane Failure
2S	0.52	0.90 (130)	692 (3950)	615 (138)	0.200	Flex. Crack → Base Sliding → Toe Crushing + Out-Of-Plane Failure
3S	0.52	0.90 (130)	735 (4190)	753 (169)	0.113	Flex. Crack → Yielding → Contact Failure of the Top Beam

As can be seen from the table, the initial lateral stiffnesses are very close for all three walls. Even though the third wall was reinforced and grouted with a stiffer material than the surrounding masonry, the presence of the cores didn't change the stiffness of the plain wall significantly. This may be attributable to low vertical-steel-ratio of 0.01 %. All experimentally computed stiffness values are tend to be higher than the values computed by the mathematical relationships provided in the FEMA 356 document. Based on these relationships, the initial stiffnesses can be computed as 493 kN/mm (2810 kip/in) and 385 kN/mm (2194 kip/in) for plain and rehabilitated walls, respectively. The difference in the theoretical and the experimental stiffness may be attributable to the influence of the test setup, which may not ideally simulate cantilever boundary conditions.

Investigations on the strength performance parameter revealed that the shear capacity of the plain walls was highly influenced by the vertical compressive stress level. Higher shear capacities were recorded for higher vertical stress levels. This observation is directly attributable to the external equilibrium of the applied forces, [1]. The shear capacity of the walls was also enhanced by the application of the center-core rehabilitation technique. The presence of the reinforced cores improved the flexural as well as the sliding shear capacity of the walls. The theoretical estimates per FEMA 356 yields 414 kN (93 kip), 568 kN (127 kip) and 754 kN (169 kip) for 1S, 2S and 3S, respectively. The limit state modes were estimated as toe-crushing for both plain walls. In view of these results, it is possible to say that the shear capacity as well as the failure mode of the walls are well represented by the theoretical relationships provided in the FEMA 356 document. It should be noted that the direct comparison of the results of the rehabilitated wall may not be accurate since, this wall didn't reach its ultimate capacity due to premature bond failure of the loading beam.

Unlike the strength performance parameter, the overall deformation capacity of the walls was reduced as the vertical compressive stress level increased. The increase in vertical compressive stress level was compensated by an increase in the compressive stress intensity at the toe region. This redistribution and rescaling of the base stresses resulted toe-crushing at an earlier drift level. Comparison of the plain and the rehabilitated wall may not yield realistic results owing to the fact that the bond between the loading beam and the rehabilitated wall failed at a lower drift level than the plain wall was pushed to. However, the fact that the reinforcing bars yielded, suggests a ductile behavior.

The FEMA 356 document provides a procedure through which one may determine deformation limits and ductility factors (m factors) for different performance objectives and generate idealized non-linear backbone curves. The m factors are utilized in the Linear Static Procedure (LSP) analysis. They are used to amplify the capacity of a component to consider the available ductility and nonlinearity in that component. The non-linear backbone curve is utilized in the Nonlinear Static Procedure (NSP) analysis. The details of these analysis procedures are beyond the scope of this paper. More information can be found in [3, 6, 7].

Table 2 Deformation Performance Parameters for the Plain Walls

Wall ID	Acceptance Criteria			m Factors		
	Performance Objective			Performance Objective		
	IO %	LS %	CP %	IO %	LS %	CP %
1S	0.04	0.21	0.28	1.0	4.8	6.4
2S	0.04	0.15	0.20	1.0	3.5	4.7

The results of the plain wall tests were investigated to determine the deformation parameters for different performance objectives. Table 2 presents these parameters together with the suggested ones in the FEMA 356 document. The steps followed to obtain the deformation parameters of the first wall are provided to illustrate the procedure. The procedure starts with the determination of the envelope curve as shown in Figure 4a. This curve passes through the intersection points of the 2nd cycle of the (i-1)th deformation step and the 1st cycle of the (i)th deformation step for all deformation steps. After determining the envelope curve

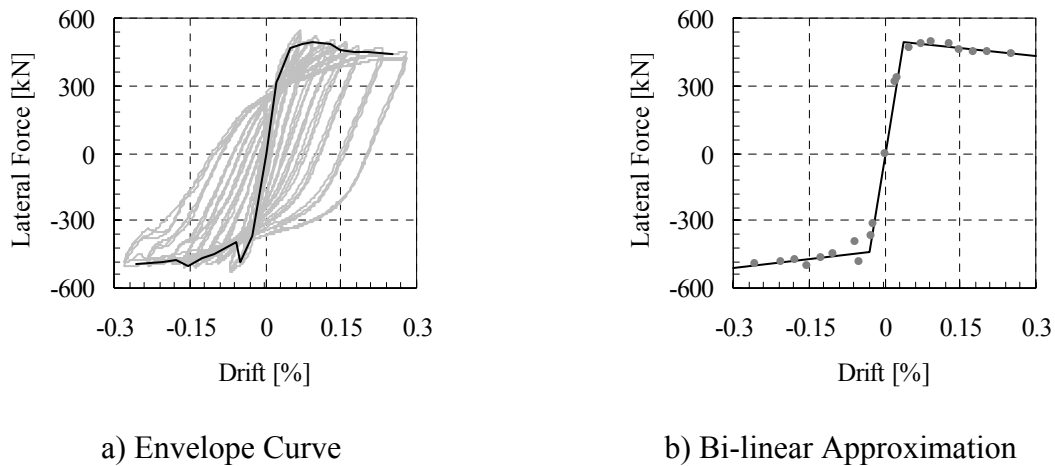
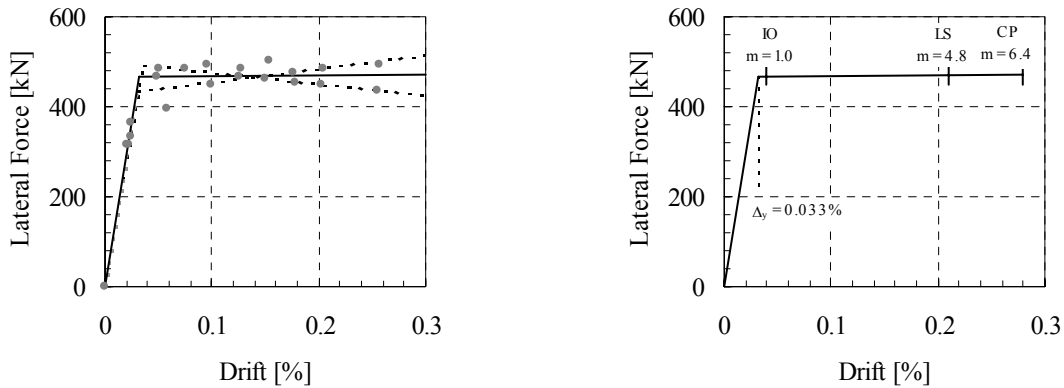


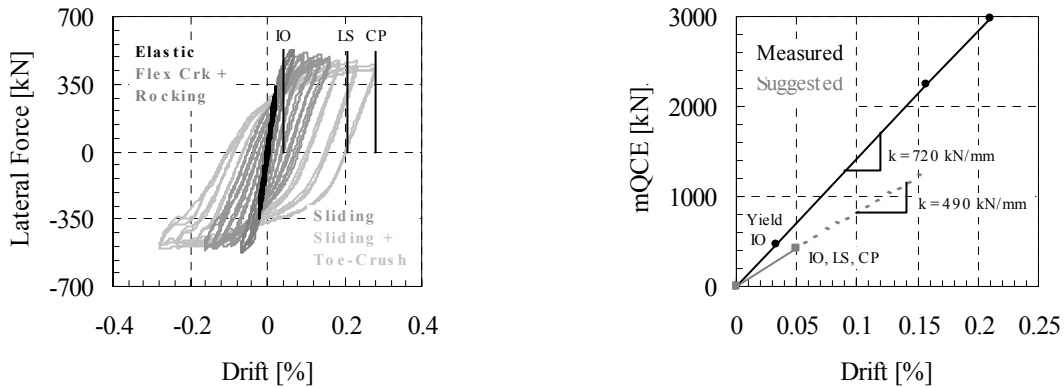
Figure 4 Envelope Curve Derivation

points, a piecewise linear approximation is fitted to that data as shown in Figure 4b. The final idealized non-linear backbone curve is determined by averaging the backbone curves at the positive and the negative quadrants as shown in Figure 5a. Figure 5b shows the final idealized non-linear backbone curve together with the computed m factors for different



a) Average Idealized Non-linear Curve b) Idealized Non-linear Backbone Curve

Figure 5 Derivation of the Idealized Non-linear Backbone Curve



a) Drift Levels Associated with Different Performance Objectives b) Comparison of m Factors for Toe-Crushing Limit State Mode

Figure 6 The Meaning of the Deformation Performance Parameters

performance objectives. The drift level at which the first visible damage occurred on the test wall was assigned as the drift limit to the Immediate Occupancy (IO) performance objective. This corresponds to 0.04 % drift at which the first flexural crack started to develop at the base of the wall. The ultimate drift level was assigned as the drift limit for the Collapse Prevention performance objective. This corresponds to 0.28 % drift at which the toe-region was crushed

and the wall failed in the out-of-plane direction. The 75 % of the Collapse Prevention drift level is assigned to the drift level of the Life Safety performance objective. Figure 6a shows these drift levels on the hysteresis curve. It can be seen that the drift limits approach to the ultimate deformation level as the severity of the performance objective increases.

Figure 6b compares the performance parameters obtained from the test results to the ones that are suggested in the FEMA 356 document. The comparison is presented in perspective of the LSP analysis. Currently, in the FEMA 356 document, the toe-crushing is regarded as a force-controlled limit state mode and a unity is assigned to the associated m factor. This results same shear strength and deformation capacity for all performance objectives in the LSP analysis. However, based on the results obtained from the wall experiment suggests m factors that are different from unity. The effect of this difference can be seen as higher shear strengths and deformation capacities as shown in Figure 6b.

CONCLUSIONS

This paper has presented the test results of three clay-brick masonry shear walls. The walls were constructed with reclaimed bricks and were tested under harmonic deformation cycles at quasi-static loading rates. The results are presented from a perspective of recent performance-based seismic rehabilitation pre-standards, FEMA 356.

Results showed that unreinforced masonry walls can behave during earthquakes with a substantial amount of inelastic deformation capacity and energy dissipation. The walls possessed higher post-cracking strength than their strength at initial cracking (as high as 50% was observed). Similarly, deformation capacities were larger than the initial cracking deformation capacity, (more than a factor of five was observed). Both performance parameters were highly influenced by the vertical compressive stress level. Higher stress levels resulted in higher lateral strength but lower deformation capacities.

The behavior of the plain walls with Type S mortar was dominated by sliding shear behavior, for which the lateral strength was limited by the amount of friction developed at the wall base. The center-core rehabilitation technique enhanced (improvement of as much as 20% was observed) the sliding shear capacity through dowel action. In addition, smaller flexural cracks were observed with the center-core technique. The strain history of the embedded reinforcing bars suggested that walls rehabilitated with this method can be treated as reinforced masonry walls.

The deformation and strength limit states presented in this study were representative of single wall behavior and might underestimate the wall behavior in an actual building in which, surrounding members enhance the response by confining and restraining the wall.

ACKNOWLEDGMENTS

Research on rehabilitation of unreinforced masonry shear walls was done as part of project ST-6 of the Mid-America Earthquake Center. This work is supported primarily by the Earthquake Engineering Research Centers Program of the National Science Foundation under Award Number EEC-9701785. Author would like to thank Mr. Shaun Franklin, Mr. Jaret Lynch and the Newmark Civil Engineering Laboratory technical staff for their assistance in this research.

REFERENCES

1. Abrams, D. P., "Strength and Behavior of Unreinforced Masonry Elements," *Proceedings of Tenth World Conference in Earthquake Engineering*, Balkema, Rotterdam, 1992, pp. 3475-3480.
2. Abrams, D. P., "Seismic Rehabilitation Methods for Unreinforced Masonry Walls," *Third Multilateral Workshop on Development of Earthquake and Tsunami Disaster Mitigation Technologies and Their Integration for the Asia-Pacific Region*, Manila, Philippines, Nov. 2000.
3. Abrams, D. P., "Performance Based Engineering Concepts for Unreinforced Masonry Building Structures," *Submitted for Publication in Journal of Progress in Structural Engineering and Materials*, Wiley Interscience.
4. Breiholz, D. C., "Center-core Strengthening System for Seismic Hazard Reduction of Unreinforced Masonry Bearing Wall Buildings," *Proceedings of 12th World Conference on Earthquake Engineering*, Auckland, New Zealand, Jan. 2000, PS3-6H, 135.
5. Erbay, O. O., Abrams, D. P., "Seismic Rehabilitation of Unreinforced Masonry Shear Walls," *Proceedings of the 9th Canadian Masonry Symposium*, Fredericton, New Brunswick, Canada, June 2001.
6. FEMA-273, "NEHRP Guidelines for the Seismic Rehabilitation of Buildings," *Federal Emergency Management Agency*, Washington D. C., Oct. 1997.
7. FEMA-356, "NEHRP Guidelines for the Seismic Rehabilitation of Buildings," *Federal Emergency Management Agency*, Washington D. C., Dec. 2000.
8. Lizundia, B., W. T. Holmes, M. Longstreth, A. Kren and D. P. Abrams, "Development of Procedures to Enhance the Performance of Rehabilitated URM Buildings," *National Institute of Standards and Technology report prepared by Rutherford and Chekene Engineers*, San Francisco, March 1997.
9. FEMA 366, "Estimated Annualized Earthquake Losses for the United States," *Federal Emergency Management Agency*, Washington D. C., Feb. 2001.

10. UBC, "Uniform Building Code," *International Conference of Building Officials*, Vol. 2, 1997, pp203-235.



KEERC-MAE Joint Seminar on
Risk Mitigation for Regions of Moderate Seismicity
University of Illinois at Urbana-Champaign, August 5-8, 2001



Sponsors: Korea Science and Technology Foundation, U.S. National Science Foundation, Brain Korea 21



Ductility Confinement of RC Shear Walls

Su Min KANG¹, and Honggun PARK²

¹ *Grad. Student, Department of Architectural Engineering, Seoul National University
San 56-1, Shinlim-Dong, Kwanak-Gu, Seoul, Korea
email: ksm@snu.ac.kr*

² *Assist. Professor, Department of Architectural Engineering, Seoul National University
San 56-1, Shinlim-Dong, Kwanak-Gu, Seoul, Korea
email: hgpark@gong.snu.ac.kr*

ABSTRACT: Experimental studies were performed to investigate variations in the ductility of shear walls with the length of the boundary confinement. Five specimens modeling the compressive zone with different confinement area were tested against eccentric vertical load. Through the experimental and numerical studies, the strength, ductility, and failure mode of the compression zone were investigated. Also, nonlinear numerical analyses for the overall cross-sections of the shear walls were performed to investigate variations of the stress and strain distribution, and the length of compression zone. On the basis of the experimental and numerical studies, a design method was developed to determine the confined area and the corresponding reinforcement required for a given ductility demand of curvature.

KEYWORDS: Confinement, Ductility, Reinforced Concrete, Seismic Design, Shear Wall

INTRODUCTION

Recently, for assuring the seismic performance and economical design of members, it is a general tendency to adopt advanced design methods such as the capacity spectrum method and the displacement based design which require ductility design for individual structural members. To implement such ductility design methods, it is necessary to estimate the ductility of shear walls accurately.

The seismic provisions in ACI 318-99 require that the lateral confinement is extended at least from the extreme fiber to the half of the compression zone, and that the details of the confinement follow those used for column design. However, the provisions are empirical and are not based on the behavioral characteristics of the confined shear walls. Therefore, it is necessary to develop a design method that can be used to more accurately estimate the strength and ductility of shear walls, and to determine the reinforcement details for the lateral confinement.

EXPERIMENTAL STUDY

Fig. 1 shows the moment-curvature relationship for the plastic hinge region of a high-rise shear wall. As shown in the figure, the ductility of shear wall with no boundary confinement is directly proportional to the maximum compressive strain causing crushing failure of concrete. Therefore to accurately assess the ductility of shear wall, it is necessary to precisely determine the compressive strain at the failure. However, for the shear walls with boundary confinement, the confined and unconfined zones coexist in the cross sections, and therefore it is unclear when the failure occurs and where the failure is initiated from.

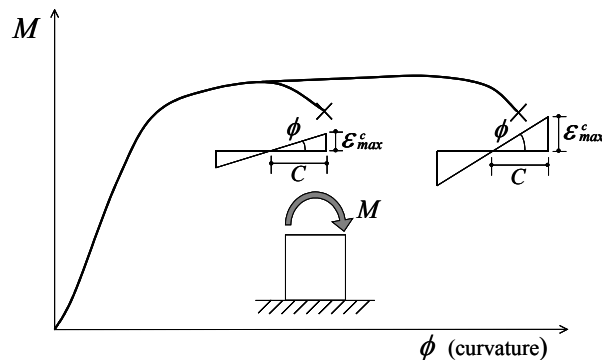


Figure 1 Variation of Curvature Ductility with Ultimate Compressive Strain

The objective of the experimental study is to investigate variations of the strength and ductility with the length of boundary confinement, and the profile of the stress and strain profiles along the cross sections.

The specimen and test set-up are shown in Fig. 2. Only the compression zone of the cross section was tested because the overall cross section of a high-rise shear wall was too large to test. The specimen was subjected to an eccentric compressive load. The eccentricity of the

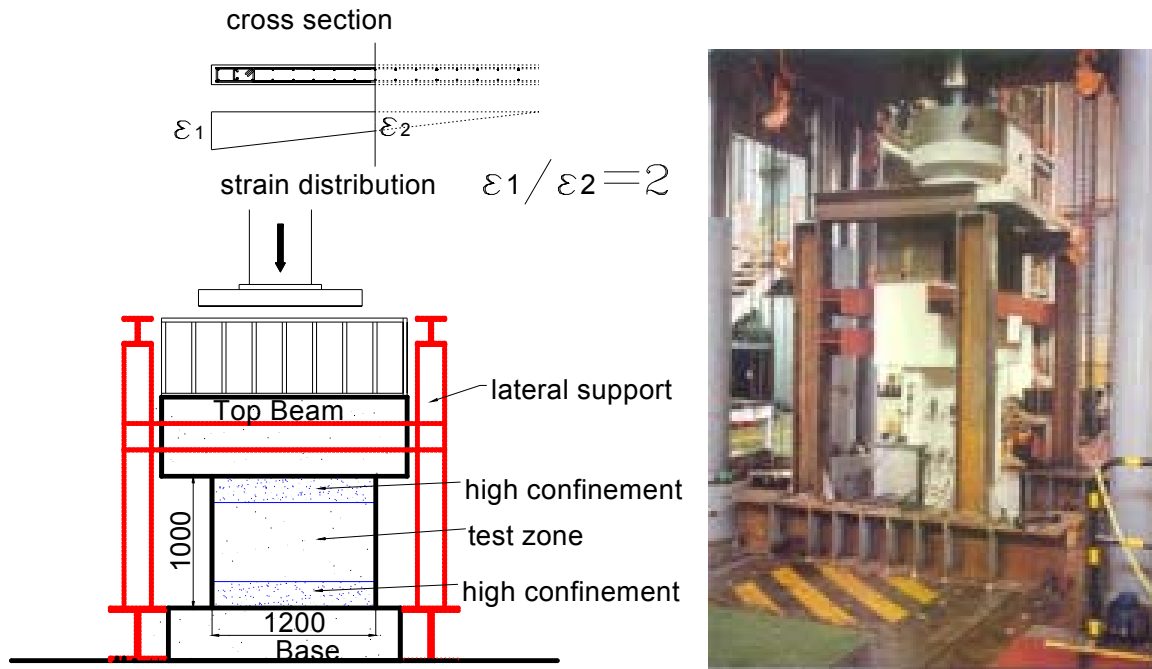


Figure 2 Test Set-up for Compression zone

compressive force was adjusted so that the ratio of the maximum to the minimum strains at the edges of the cross-section was approximately 2:1 for specimens W1, W2 and W3, and 1:0 for the W4 and W5.

Fig. 3 shows the cross sections of the specimens with different confinement lengths and strain distributions. The material properties are presented in Table 1. The vertical spacing of the ties used for the confinement was 50mm.

Table 1 Properties of Specimens

Specimen	f'_c (MPa)	Vertical Reinforcement		Reinforcement for Confinement				Ultimate Strain	
		r_v	f_y (MPa)	r_x	r_y	$r_s=r_x+r_y$	f_y (MPa)	Left End	Right End
W1	34	0.007	334	-	-	-	-	0.00193	0.0011
W2	34	0.007	334	0.0284	0.0170	0.0454	321	0.00246	0.00105
W3	29	0.007	334	0.0284	0.0136	0.0420	321	0.00344	0.00102
W4	30	0.007	334	0.0284	0.0170	0.0454	321	0.00198	0.00008
W5	28	0.007	334	0.0284	0.0136	0.0420	321	0.01031	0.00024

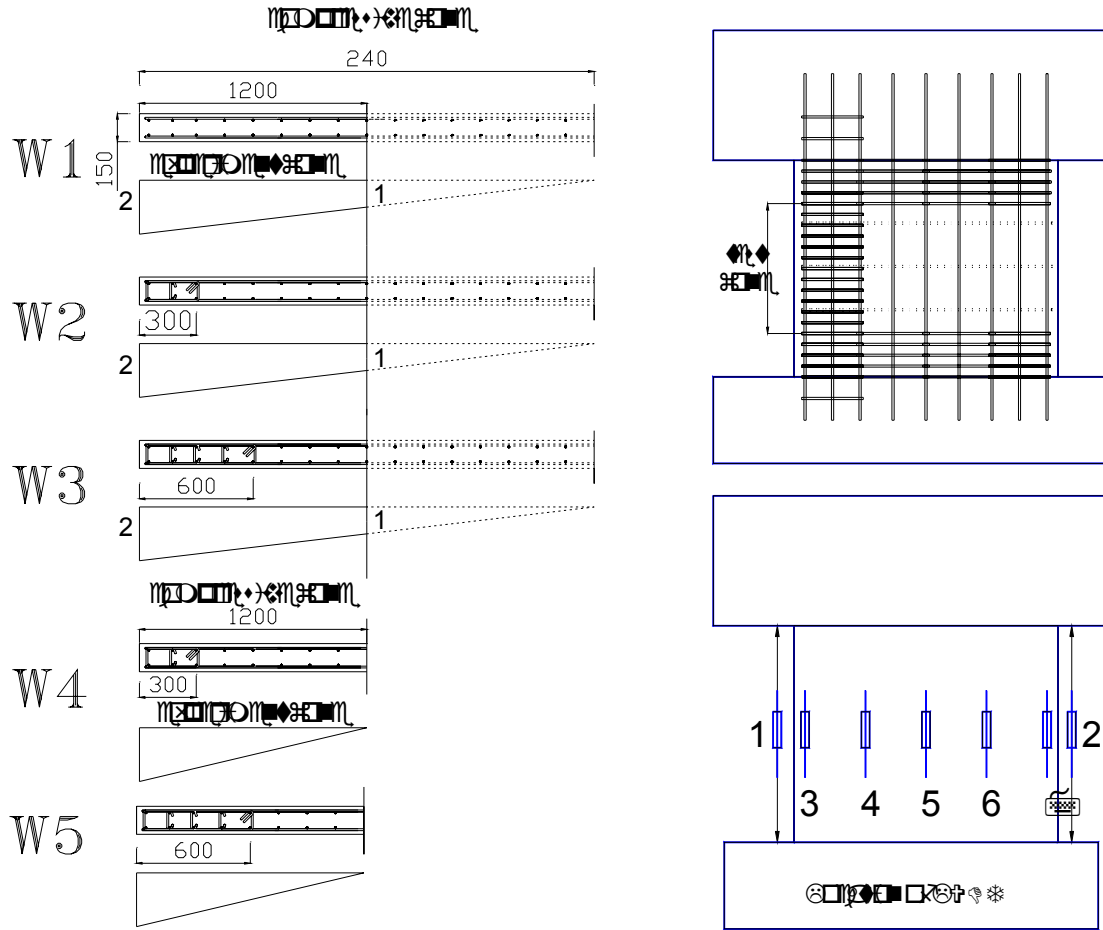


Figure 3 Specimens and Location of LVDT

The relationship of the compressive load and vertical strain measured by LVDT 1 and 2, are shown in Fig. 4. W1 with no boundary confinement failed in a brittle manner, and the maximum strain at failure was 0.0019, which was approximately equivalent to the ultimate strain corresponding to the cylinder strength. W2 and W4 with small confined area also show very low ductility, as was observed in W1. W3 with relatively large boundary confinement shows improved strength and ductility, but the ultimate strain was at most 0.0034. W5 with the large boundary confinement and the steep strain gradient shows sufficient ductility. Fig. 5 shows the strain history measured at LVDT 3-7. The load-strain curves shown in the figure can be classified into two types according to their behavior after the maximum load is reached; softening curves with strain increases and unloading curves with strain decreases. The softening curve indicates that crushing of concrete initiating the failure of the specimen occurs. In the figures, it can be seen that the failures were initiated in the unconfined zone just outside the confined zone.

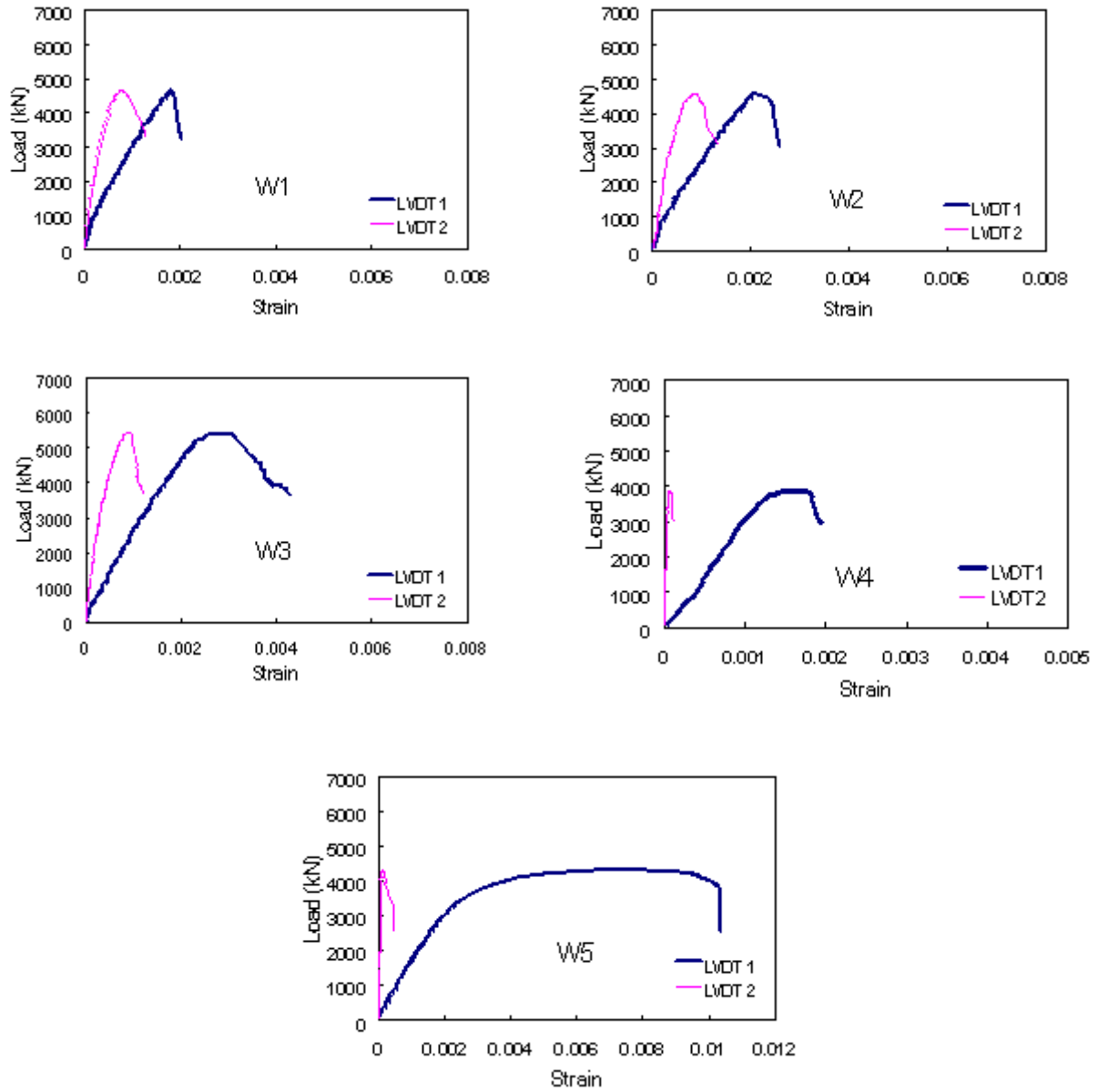


Figure 4 Load vs. Vertical Strains Measured at LVDT 1 and 2

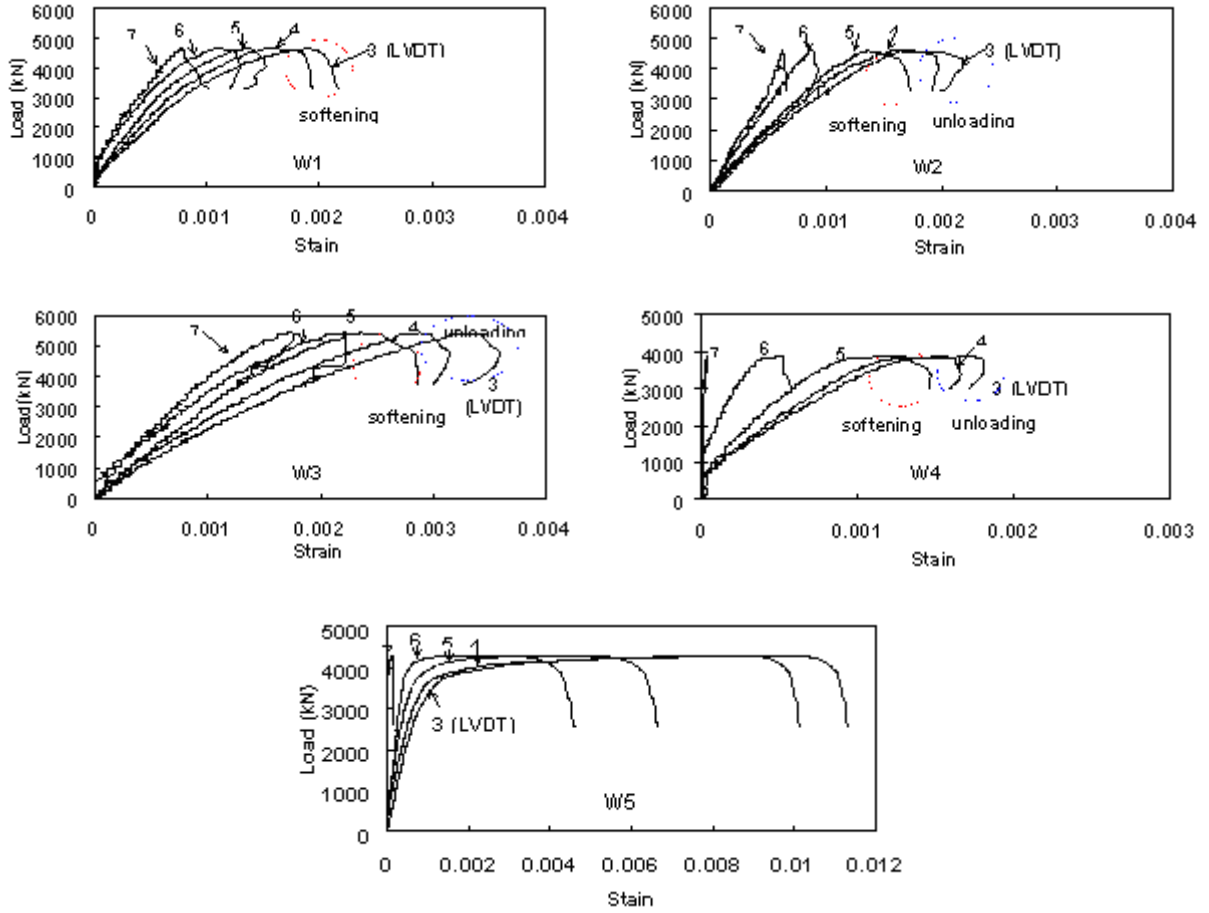


Figure 5 Load vs. Vertical Strains Measured at LVDT 3-7

ANALYSIS OF EXPERIMENTAL RESULTS

The stress-strain model for confined concrete developed by Mander [1] was used to predict the strength and ductility of the specimens. The stress-strain relationship is defined as

$$f_c = \frac{f_{cc} x r}{r - 1 + x^r} \quad \text{where} \quad x = \frac{\varepsilon_c}{\varepsilon_{cc}}, \quad r = \frac{E_c}{E_c - E_{sec}}, \quad \varepsilon_{cc} = \varepsilon_{co} [1 + 5(\frac{f'_{cc}}{f'_{co}} - 1)] \quad (1)$$

f'_{cc} = compressive strength of confined concrete

$f'_{co}, \varepsilon_{co}$ = unconfined concrete strength and corresponding strain

For the numerical analysis, the specimen was divided into two regions: (a) unconfined region, (b) confined region (Fig. 6). The load was calculated by integrating the stresses corresponding to the strain distribution along the cross section. In Fig. 7, the relation between load and maximum compressive strain are compared with the test results.

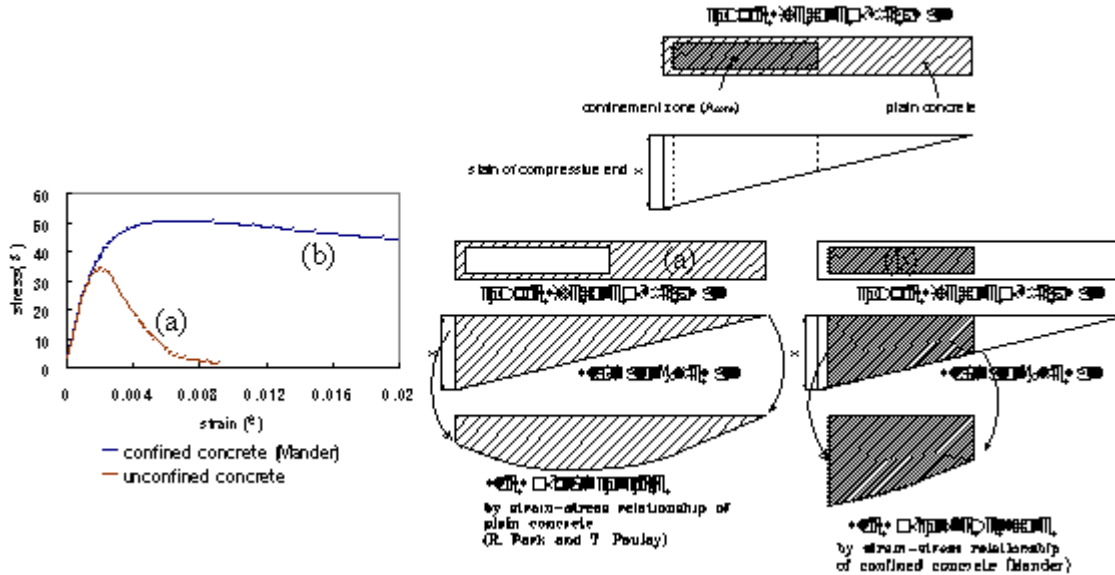


Figure 6 Zoning of Cross Section for Numerical Analysis

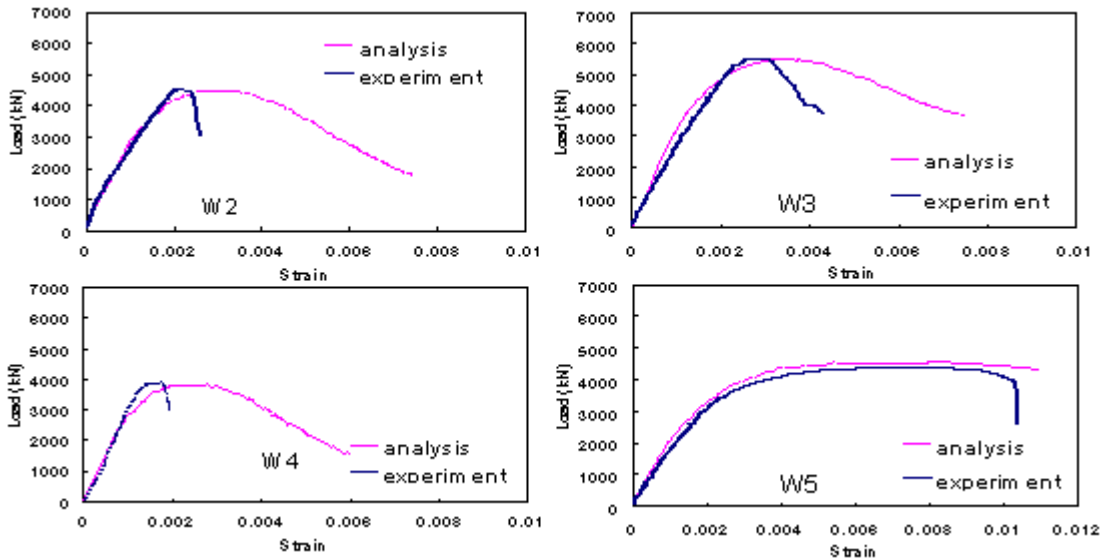


Figure 7 Comparison of Experimental and Numerical Results

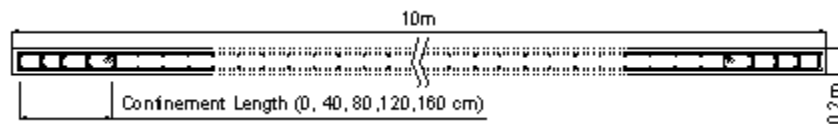
The numerical analyses estimate well the behavior of the specimens until the maximum load is reached. At the maximum load, the specimens show the brittle failure while the numerical analyses present ductile behaviors. Before the maximum load is reached, the stress increase of the confined zone compensates the softening stress of the unconfined zone. After the maximum load is reached, the instability due to the softening behavior of the unconfined region cause the brittle failure over the entire cross section. Therefore, it can be recognized that the compression zone with limited confinement maintains the ductile behavior until the maximum load is reached.

NUMERICAL STUDY

Nonlinear numerical analyses were conducted for the cross-sections of shear walls. For the analyses, Ucfyber [2] was used. Similar to the numerical analyses for the specimens, the shear wall was divided into the confined and unconfined regions, where different stress-strain relations of concrete were applied. The variations of the moment-curvature curve with the length of the boundary confinement are shown in Fig. 8. The numerical results obtained at the maximum load are summarized in Table 2.

As expected, the boundary confinement has an effect on the ductility rather than the strength of the shear walls. As the confinement length increases, the curvature capacity representing the cross-sectional ductility increases remarkably. The reason is that the confinement increases the strength as well as the ductility of the confined zone, and therefore, the confinement not only enhances the ductility of the confined zone but also reduces the length of compression zone itself (Fig. 9).

Through extensive numerical studies, it was found that for typical and economically designed



$$(f'_c=24 \text{ MPa}, f_y=320 \text{ MPa}, r_s=0.042, r_v=0.0039, P=0.2A_g f'_c)$$

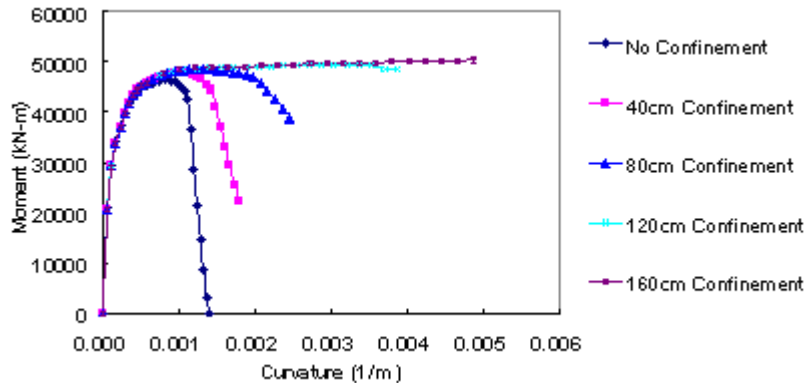


Figure 8 Variations of Moment-Curvature Relations with Confinement Area

Table 2 Summaries of Numerical Results at Failure

Confinement Length (cm)	Strength (kNm)	Curvature ($10^{-4} \cdot 1/m$)	Length of Compression Zone (m)	Ultimate Compressive Strain	Maximum Compressive Strain in the Unconfined Zone	Confinement Ratio against Compression zone (%)	Actual Confinement Ratio against Compression zone
0	46200	9.77	2.94	0.00300	0.00300	-	-
40	47600	13.0	2.74	0.00356	0.00302	13.6	14.6
80	48700	17.9	2.52	0.00451	0.00301	27.2	31.7
120	49600	37.3	2.26	0.00843	0.00358	40.8	53.1
160*	50500	49.1	2.04	0.01	0.00166	54.4	78.4

(* : Moment increases continuously during analysis.)

shear walls, the maximum compressive strains in the unconfined region corresponding to the maximum load are 0.003-0.0036. Once the maximum compressive strain is reached, the strength enhancement of the confined region cannot compensate the strength reduction of the unconfined region. Therefore, the length of the compression zone begins to increase and the moment-carrying capacity decreases. Based on the experimental results for the compression zone, it is conservatively assumed that the ductility of shear wall is maintained until the maximum moment is reached. Generally, the ductility design of shear walls with no lateral confinement is based on the maximum compressive strain at the extreme fiber. On the other hand, the ductility design of the shear walls with boundary confinement should be based on the maximum compressive strain of the unconfined region, which is approximately 0.003.

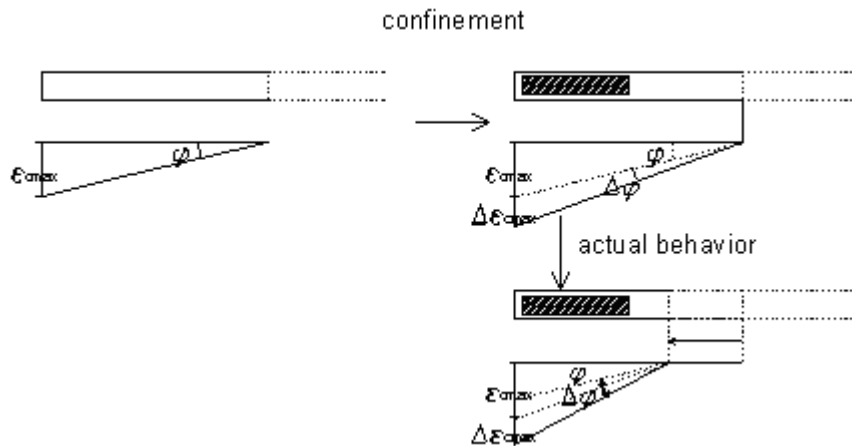


Figure 9 Curvature Enhancement due to Increase of Ultimate Strain and Decrease of Compressive Area

DEVELOPMENT OF DUCTILITY DESIGN METHOD

In the ductility design of shear wall, it is necessary to determine the confinement area and the reinforcement ratio of ties for a given ductility demand of curvature. For the shear wall with boundary confinement, the stress-strain relations over the cross-section are so complicated that it is difficult to derive an effective design method. In this study, several assumptions were used to derive a simplified but sufficiently accurate design method (see Fig. 10): 1) At the ultimate load, the maximum strain of unconfined zone is 0.003; 2) The stress distributions of the confined and unconfined regions can be idealized with the conventional rectangular stress blocks; 3) The representative stress of the confined region corresponds to the strain obtained in the middle of the stress block; and 4) All the reinforcement yield before the ultimate load is reached.

The design procedure is summarized as follows:

- 1) The length or area of the confined region, $A_{\text{confinement}}$ is assumed.
- 2) For the given curvature demand, the strain distribution and the length of the compression zone are determined based on the maximum strain of the unconfined region, 0.003 (Fig. 10).
- 3) The average strain of the confined region is calculated with the strain distribution.
- 4) The required average stress of the confined zone can be calculated by using the equilibrium with the applied moment and axial force (Eq. 2).
- 5) In the figures showing the series of the confined stress-strain curves for various reinforcement ratios, the required reinforcement ratio (r_s) can be calculated.
- 6) If the reinforcement ratio is too high, repeat the procedure with a new $A_{\text{confinement}}$

Since the confined stress can be expressed with the confined strain as presented in Eq. 2. The demand for the confined stress can be presented as a continuous curve in Fig. 11. The intersection points of the demand curve and the capacity curves corresponding to various reinforcement ratios are the performance points. A variety of confinement design can be obtained at once.

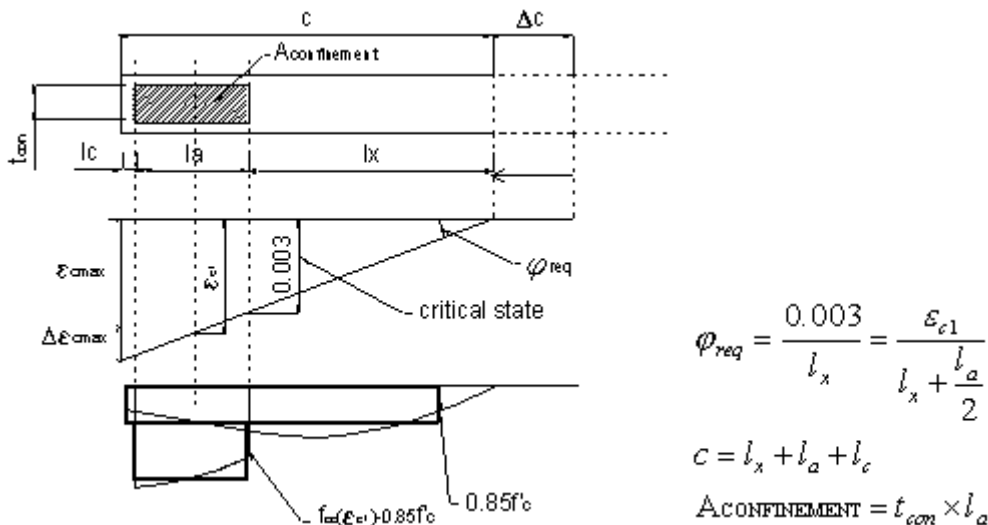


Figure 10 Idealization of Stress and Strain at Failure

$$f_{cc}(\varepsilon_{c1}) = 0.85f'_c + \frac{\varphi_{req}(P + (l - 2c)t\rho_v - 0.85f'_c t c)}{2(\varepsilon_{c1} - 0.003)t_{con}} \quad (2)$$

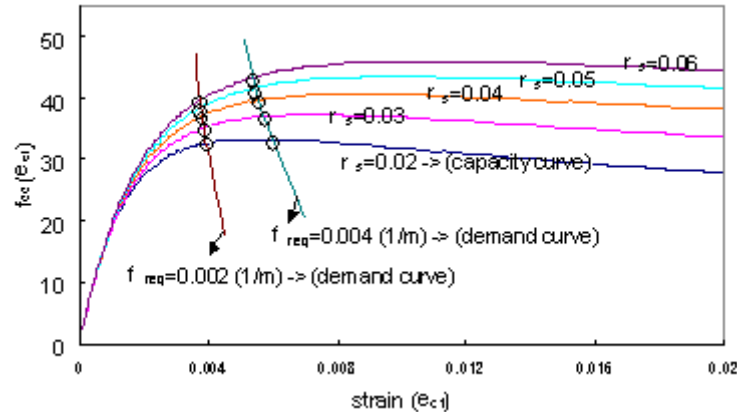


Figure 11 Demand and Capacity Curves of Confined Stress-Strain

CONCLUSIONS

Experimental and numerical studies were performed to investigate the behavior of shear walls with boundary confinement. The major findings of this study are summarized as follows:-

1. According to the experiment, in the shear wall with no boundary confinement, crushing failure occurs so abruptly on the entire cross section that the ductility is much less than that generally expected. The maximum compressive strain at failure is equivalent to the ultimate strain corresponding to the cylinder strength. Therefore, the current ductility design method requiring lateral confinement, only in the region where the compressive strain exceeds 0.004 or more, does not assure the ductility of shear walls.
2. The failure of the compressive zone with boundary confinement occurs in a brittle manner once the maximum load is reached. Therefore the ductility of shear wall with boundary confinement is effective up to the maximum moment.
3. The brittle failure is initiated by concrete crushing of the unconfined region. The ultimate strain of the unconfined region is approximately 0.003.
4. As the confinement length increases, the curvature capacity representing the cross-sectional ductility increases remarkably. The reason is that the confinement not only enhances the ductility of the confined zone but also reduces the length of compression zone itself.

Based on the experimental and numerical studies, a design method was developed to determine the confined area and/or the lateral reinforcement for a given ductility demand of curvature. Also, for an economical and simple design, a graphical method using demand and capacity curves was developed.

ACKNOWLEDGMENTS

The research presented herein has been carried out by the financial assistance of the Brain Korea 21 and grant No. 1999-1-310-002-3 from the Basic Research Program of the Korea Science & Engineering Foundation, and the authors are sincerely grateful to the authorities for their support.

REFERENCES

1. Mander, J. B., Priestley, M. J. N., and Park, R.(1988) "Theoretical Stress-Strain Model For Confined Concrete" *J. Struct. Engrg.*, ASCE, 114(8), 1804-1826.
2. Charles Chadwell, <Ucfyber - Cross Section Analysis Software>, University of California, Berkeley 1999, <http://nisee.berkeley.ed>.
3. Honggun Park, and Su Min Kang "Earthquake-Resistance of Slender Shear Wall with No Boundary Confinement", *Journal of Korea Concrete Institute*, KCI, 12(5), 2000.



KEERC-MAE Joint Seminar on
Risk Mitigation for Regions of Moderate Seismicity
University of Illinois at Urbana-Champaign, August 5-8, 2001



Sponsors: Korea Science and Technology Foundation, U.S. National Science Foundation, Brain Korea 21



Flexural Behavior of Retrofitted Masonry Piers

Jaret M. LYNCH¹, and Daniel P. ABRAMS²

¹ *Research Associate, Department of Civil Engineering, University of Illinois at Urbana-Champaign*

1241 Newmark Laboratory, 205 N. Mathews, Urbana, Illinois, USA

email: jmlynch1@uiuc.edu

² *Hanson Engineers Professor of Civil and Environmental Engineering and Director of Mid-America Earthquake Center, University of Illinois at Urbana-Champaign*

1245 Newmark Laboratory, 205 N. Mathews, Urbana, Illinois, USA

email: d-abrams@uiuc.edu

ABSTRACT: Current rehabilitation techniques for unreinforced masonry piers are presented. Measured behavior of rehabilitated and non-rehabilitated piers governed by flexural mechanisms is summarized. The effectiveness of each rehabilitation is quantified in the context of the FEMA linear static procedure and performance based design. The accuracy of the FEMA 356 procedure for estimating linear static behavior of structural masonry components is examined.

KEYWORDS: URM, rehabilitation, pier, LSP, Center Core, FRP, Shotcrete, Surface Coating, performance-based design

INTRODUCTION

Unreinforced masonry structures are often damaged or destroyed as a result of seismic excitation. A number of non-structural and structural deficiencies may be retrofitted using prescriptive techniques. For example, parapet walls should be braced at specified intervals and connections between floor diaphragm and walls should be of an approved type. Should the stakeholder require an enhanced level of functionality after an earthquake or more complicated structural problems exist, performance based design may be used to arrive at an acceptable solution.

Performance based design calls for the assignment of acceptance criteria corresponding to the desired structural performance level. Assuming that damage of a masonry pier or system may be correlated to the deformation it undergoes, these acceptance criteria take the form of drift limits. At present, these drift limits for rehabilitated masonry components have been based largely on engineering judgment. One goal of current experimental testing of masonry is to evaluate the accuracy of these existing drift limits and suggest updated parameters for use with the FEMA linear static procedure and other methods of analysis.

IMPLEMENTATION OF REHABILITATION METHODS

Research of the Mid-America Earthquake Center Project ST-6 has investigated flexural mechanisms governing the behavior of URM walls. Eight piers were subjected to in-plane displacement reversals applied to their top, while the loading rig frame shown in Figure 1 maintained a constant amount of vertical compressive force. Non-rehabilitated piers were tested in addition to piers rehabilitated using the methods described in the previous section. The plain walls provided a basis for comparison with the rehabilitated piers and allowed researchers to determine the influence vertical compressive stress has on the flexural behavior of piers. All of the test piers were constructed to the same dimensions out of reclaimed bricks and had a height to width ratio equal to 1.77.

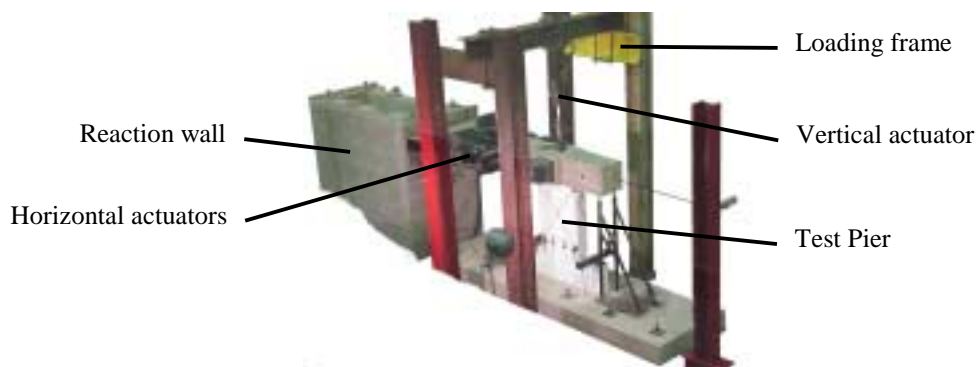


Fig. 1 Test pier in loading frame

The techniques used to rehabilitate URM structural elements vary widely throughout the world based on the availability of native materials, knowledge-level of craftsmen and engineers, as well as other social and economical factors. The methods presented herein are the best estimate of current practice in the United States, and their implementation follows the suggestions set forth in a report developed by the U.S. National Institute of Standards and Technology [2].

Fiber Reinforced Polymer (FRP)

Strips of this composite were adhered to the surface of the pier in areas of expected tension cracking. The glass fibers were oriented perpendicular to the potential plane of fracture. Additional bands of FRP were placed around the pier to provide anchorage to the primary vertical strips and confinement of the masonry. This rehabilitation benefits from its compactness; however, the appearance of the wall is altered in the process.

Shotcrete

This popular method of seismic rehabilitation consists of steel reinforcement covered by a layer of sprayed on concrete. The steel rebar is anchored to the masonry pier at regular intervals with the goal being to induce composite action of the masonry and rehabilitation.

Ferro-cement Surface Coating

Ferro-cement surface coatings make use of a hardware mesh (most often steel) that is mechanically anchored to the existing masonry. A thin layer of mortar is troweled on through the mesh such that the steel reinforcement is sufficiently covered. This rehabilitation is able to be applied to irregularly shaped surfaces and also provides an aesthetic finish to the wall.

Center Core

Center Core is a proprietary technique that embeds reinforcing bars within an unreinforced masonry wall. Cores are drilled in an existing masonry wall in which a reinforcing bar is placed and epoxy grout later pumped into the cavity. Center Core may be used while the building is in operation and does not affect the aesthetics of the masonry surface.

MEASURED BEHAVIOR OF REHABILITATED PIERS

The measured force-deflection relationships for each of the rehabilitated test piers are shown in Figure 2. The control specimen having no rehabilitation is included for comparison in each of the graphs. The relative amount of energy dissipation may be inferred from the area enclosed by the force-deflection curves. Each rehabilitated pier exhibits an initially linear force-deflection relationship. Effective yield strength may be estimated from these plots as well as the maximum drift and secondary stiffness.

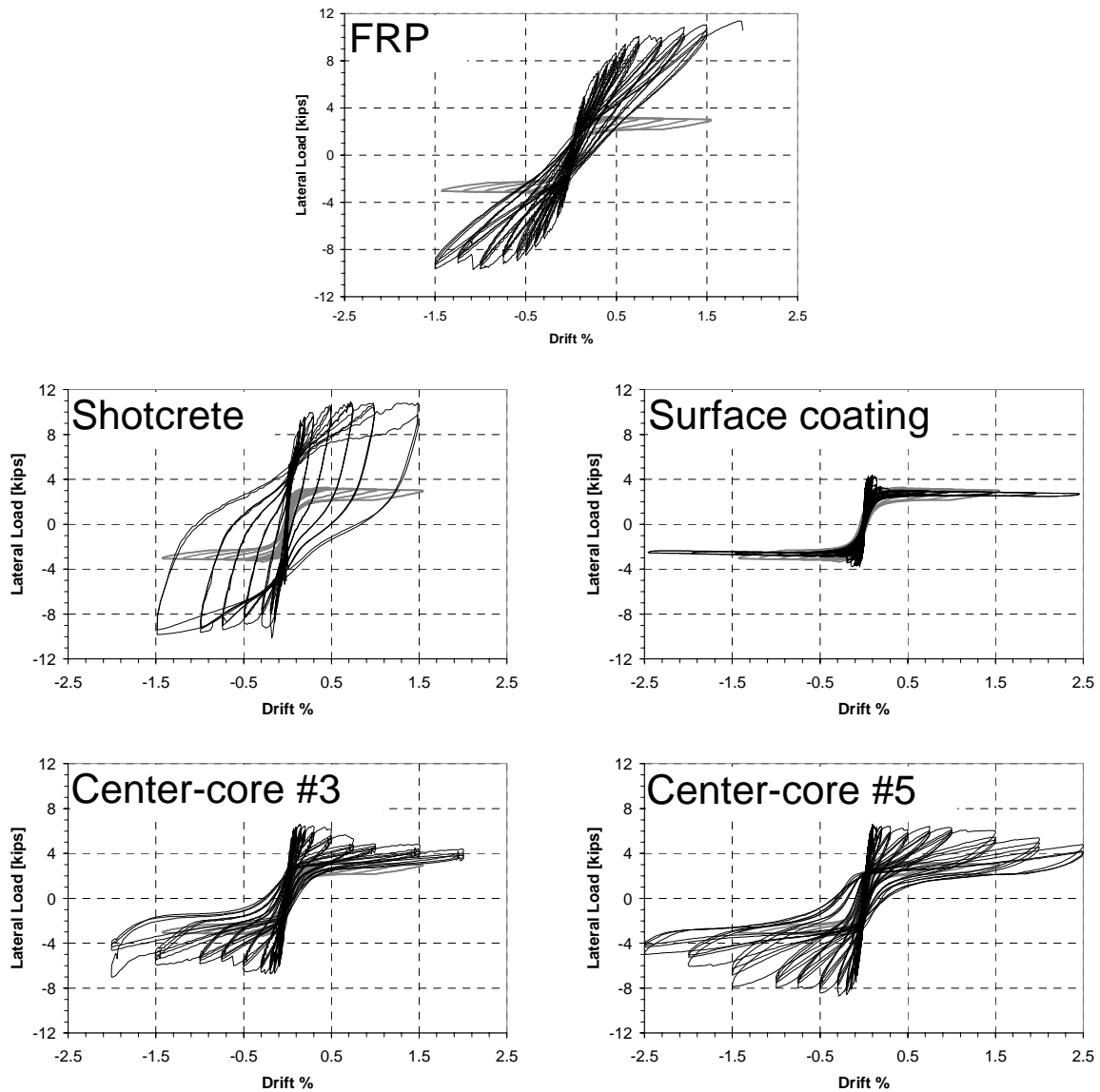


Fig. 2 Force-deflection relationships for rehabilitated piers

Using the framework of the FEMA 356 Seismic Rehabilitation Prestandard, [1] the measured force-deflection behavior of each pier is distilled into an approximate bilinear curve. Structural performance levels are assigned to the bilinear curve as specified in Section 2.8.3 of FEMA 356 and the corresponding m-factors (deformation capacities) are calculated.

A comparison may be drawn between the measured behavior and that which is predicted by the LSP of Section 7.4 of [1]. The accompanying set of m-factors, Table 7-3 of [1] is to be used in the absence of an experimental testing program (as is most often the case). The FEMA prediction incorporates an “educated guess” of the m-factor for each structural performance level along with a mechanics based calculation of the initial stiffness and yield strength of the pier (QCE). Figure 3 presents these comparisons for each of the rehabilitated test piers.

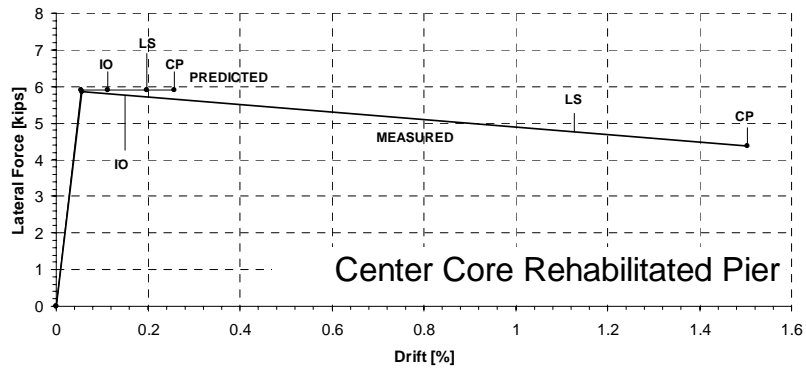
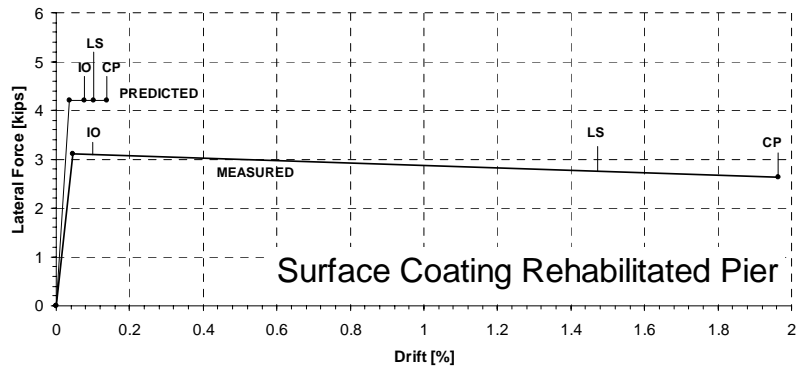
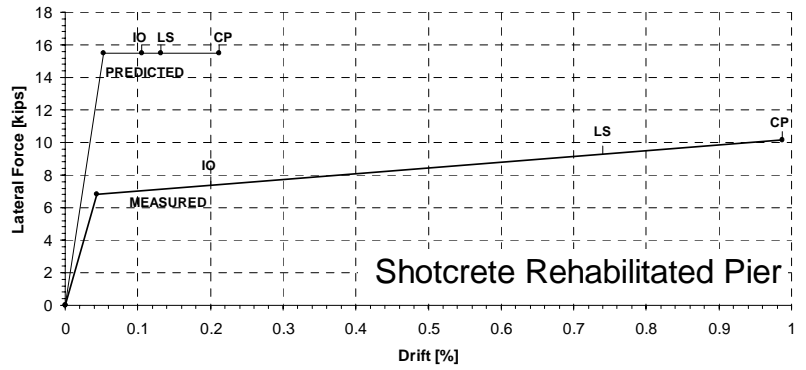
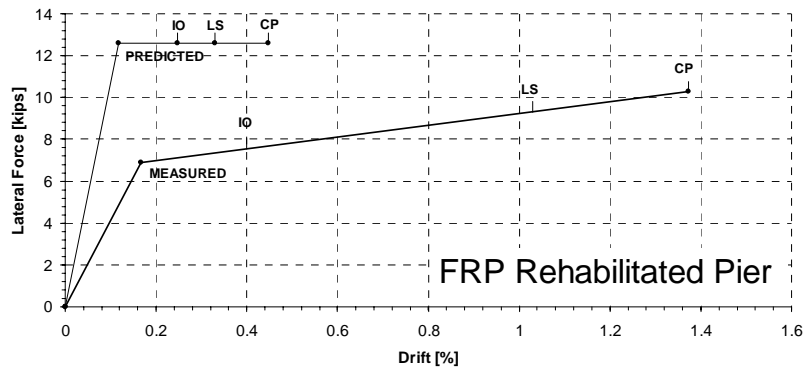


Fig. 3 Comparison of bilinear force-deflection relationships

The overall accuracy of the FEMA predicted m-factor, and mechanics based strength and stiffness may be determined by comparison with the measured flexural behavior of the piers. Figure 4 shows the predicted and measured LSP capacity (mQ_{CE}) for the Life Safety Performance Objective.

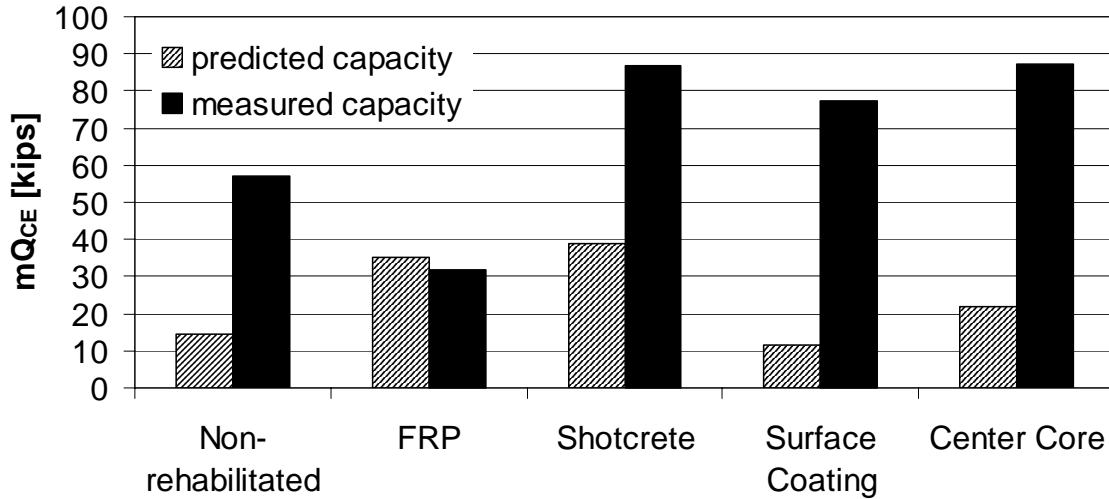


Fig. 4 Accuracy of FEMA predicted LSP behavior

The measured strength and deformation capacity of each rehabilitated pier is shown in Figures 5 and 6 respectively. The efficacy of each rehabilitation is evaluated by comparing the product of the deformation capacity and the expected yield strength of each pier (mQ_{CE}). A comparison of the measured mQ_{CE} for the rehabilitated piers is shown in Figure 7.

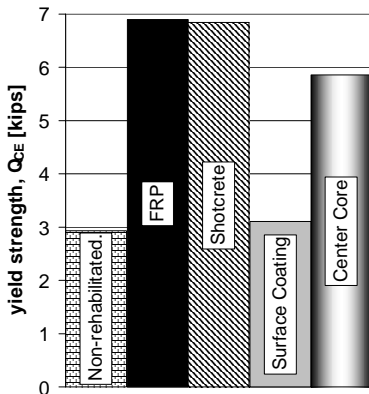


Fig. 5 Strength of rehabilitated piers

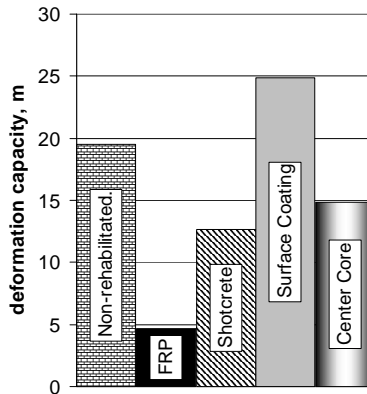


Fig. 6 Deformation capacity of rehabilitated piers

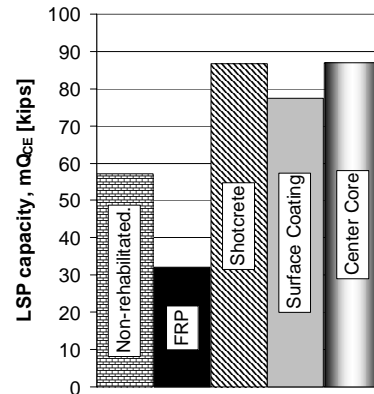


Fig. 7 LSP capacity of rehabilitated piers

CONCLUDING REMARKS

The lateral force-deflection relationships included in Figure 2 show a wide range of flexural behavior caused by the presence of the rehabilitations. The plain wall used for a benchmark shows the typical nonlinear-elastic behavior of a rocking pier. Damage in the rocking mode is limited to the area of the bed joint crack. Rocking is observed to be a stable mechanism capable of in-plane drifts up to 2.5%. The FRP rehabilitated specimen softened as the load increased to a point at which the composite fully delaminated from the surface of the masonry. This caused an abrupt loss of capacity. The shotcrete rehabilitated specimen behaved as a reinforced concrete pier with no evidence of composite action with the masonry. Large amounts of energy were dissipated as the rebars yielded repeatedly. The plastic deformation of the rebar caused the pier to tilt out of plane, thus stopping the test. The surface-coating rehabilitated pier exhibited a similar force-deflection relationship to that of the plain wall with the exception of a slight increase in strength of the initial linear portion of the force-deflection curve. Once the steel hardware mesh fractured, the rocking behavior returned and provided large deformation capacity. The Center Core rehabilitated pier benefited from the presence of the reinforcing bars; however, an embedment length of 40 bar diameters was not sufficient to anchor the core. The core proceeded to slip in its cavity such that the rebar did not yield.

Strength and stiffness estimates for rehabilitated masonry piers may be accurately calculated if the stress-strain behaviors of the constituent materials are known. However, the deformation capacity of the rehabilitated pier is more difficult to predict. This is evident upon examination of Figure 3, in which the estimated and measured strengths are of the same order of magnitude, but the deformation capacity predicted is less than one-tenth the measured quantity. The FEMA suggested m-factors do a reasonably good job even though they are many times smaller than the measured deformation capacity of the piers. This is because the overestimate of the strength balances the underestimate of the ductility.

The effectiveness of each rehabilitation may be determined from examination of Figures 5 through 7. Strength enhancements of a factor of two are noted for each of the rehabilitation methods except surface coating. The deformation capacity was diminished for each of the rehabilitation methods except surface coating. FRP showed the greatest reduction of deformation capacity. The combined effects of strength and ductility are shown in Figure 7. It is interesting to recognize that the shotcrete, surface coating and Center Core rehabilitated piers all have similar effectiveness (approximately 30% increase compared to non-rehabilitated wall). Also of note is the reduction of effectiveness with FRP. The FRP rehabilitated pier attained only 50% of the LSP capacity of the plain wall. This leads to the conclusion that the best approach to rehabilitation of URM piers and walls may be to do nothing to structural elements expected to behave in a rocking mode and induce rocking if possible in other cases. If rehabilitation is necessary, shotcrete or Center Core should be the methods of choice.

ACKNOWLEDGMENTS

Project ST-6 of the Mid-America Earthquake Center is supported primarily by the Earthquake Engineering Research Centers Program of the National Science Foundation under Award Number EEC-9701785. Gratitude is extended to Mr. Shaun Franklin for executing the majority of the testing program. Appreciation is offered to Omer Erbay, Dr. Grzegorz Banas and Dr. John Nichols for their contribution of knowledge to this project.

REFERENCES

1. FEMA-356, "Prestandard and Commentary for the Seismic Rehabilitation of Buildings," Federal Emergency Management Agency, Washington D.C., Dec. 2000.
2. Lizundia, B., W.T. Holmes, M. Longstreth, A. Kren and D. P. Abrams, "Development of Procedures to Enhance the Performance of Rehabilitated URM Buildings," National Institute of Standards and Technology report prepared by Rutherford and Chekene Engineers, San Francisco, March 1997.



KEERC-MAE Joint Seminar on
Risk Mitigation for Regions of Moderate Seismicity
University of Illinois at Urbana-Champaign, August 5-8, 2001



Sponsors: Korea Science and Technology Foundation, U.S. National Science Foundation, Brain Korea 21



Unified Constitutive Model for RC Planar Members Under Cyclic Load

Honggun PARK¹, and Jae Yo KIM²

¹ *Assistant Professor, Department of Architectural Engineering, Seoul National University
San 56-1 Shinlim-Dong Kwanak-Gu, Seoul, Korea
email: hgpark@gong.snu.ac.kr*

² *Graduate Student, Department of Architectural Engineering, Seoul National University
San 56-1 Shinlim-Dong Kwanak-Gu, Seoul, Korea
email: beholder@snu.ac.kr*

ABSTRACT: A constitutive model unifying plasticity and crack damage models was developed to address the cyclic behavior of reinforced concrete planar members. The stress of concrete in tension-compression was conceptually defined by the sum of the compressive stress of the intact concrete and the tensile stresses developed by tensile cracking. The plasticity model with multiple failure criteria was used to describe the isotropic damage of compressive crushing affected by the anisotropic damage of tensile cracks. The multiple fixed crack damage model was used to describe the tensile stress-strain relationship of multi-directional cracks. The unified model can describe the behavioral characteristics of reinforced concrete in cyclic tension-compression conditions, i.e. multi-directional crack orientations, progressively rotating crack damage, and compressive crushing of concrete. The proposed constitutive model was implemented to finite element analysis, and it was verified by a comparison with existing experimental results from a reinforced concrete shear panel and shear walls under cyclic load conditions.

KEYWORDS: Cyclic Load, Plasticity, Reinforced Concrete, Multiple Fixed Crack Model, Unified Constitutive Model, Multiple Failure Criteria

INTRODUCTION

Plasticity models using multiple failure criteria have been broadly studied to describe the behavior of reinforced concrete members. Since the multiple failure criteria makes it possible to present the combined behavior of the isotropic damage of compressive crushing and the anisotropic damage of tensile cracking, the plasticity models can accurately describe the post-cracking behavior of reinforced concrete in tension-compression. However, the scopes of most previous studies have been limited to the behavior of reinforced concrete members under monotonic load conditions.

Several researchers have attempted to extend the applicability of the plasticity model to the unloading/reloading characteristics of plain concrete under repeated/cyclic uniaxial load conditions (Cachim et al. [2], Chen and Buyukozturk [3], Fardis et al. [4]). However, the cyclic behavior of reinforced concrete members is significantly affected by the anisotropic damage caused by tensile cracking, tension softening/stiffening behavior, and the behavior of the reinforcing steel. Therefore, the plasticity model, which is applicable to reinforced concrete members under cyclic load conditions, should address such behavioral characteristics.

In reinforced concrete subjected to cyclic loading, under loading, the current crack orientation presenting the overall anisotropic crack damage can rotate because tensile cracking occurs successively. On the other hand, under unloading/reloading, the crack orientation should be fixed because no further crack damage occurs. Therefore, the fixed or rotating crack models using the assumption that the crack orientation is always fixed or rotated during loading and unloading are inappropriate to describe the cyclic behavior of reinforced concrete.

In this study, a plasticity model was attempted to describe the cyclic behavior of reinforced concrete affected by multiple tensile cracks. The new concepts related to the material model were introduced to overcome the disadvantages of the fixed and rotating crack models.

MATERIAL MODEL

The plasticity model, previously developed by Park and Klingner [9], was modified to present the cyclic behavior of reinforced concrete. In the plasticity model, more than two independent failure criteria of compressive crushing and tensile cracking should be satisfied:

$$f_1 = f_2 = f_3 = \dots = f_k = 0, \quad (1)$$

where subscript '1' indicates compressive crushing, and the other subscripts are related to tensile cracking. Total plastic strain is the sum of the individual plastic strains related to the corresponding failure criteria.

$$\underline{\varepsilon}_p = \sum_i^k \underline{\varepsilon}_{pi} \quad (2)$$

For compressive crushing, the Drucker-Prager failure criterion is used:

$$f_1 = g_1(\sigma, J_2) - \alpha \bar{\sigma}_1(\hat{\varepsilon}_{p1}) = 0, \text{ where } g_1(\sigma, J_2) = A_1\sigma + A_2\sqrt{3J_2} + A_3. \quad (3)$$

The yield surface function $\bar{\sigma}_1(\hat{\varepsilon}_{p1})$, shown in Figure 1, as presented by Park and Klingner [9]. In the figure, $\hat{\varepsilon}_{p1}$ = the equivalent plastic strain; G_c = the fracture energy of compressive crushing; and h = the effective length corresponding to a Gauss point. In Eq. 3, the constants A_1 , A_2 , and A_3 can be calculated in accordance with the existing data from Kupfer et al. [6] (Park and Klingner, [9]). α is the strength reduction factor to describe the early crushing of concrete occurring due to the coexisting tensile crack (Vecchio and Collins [12]).

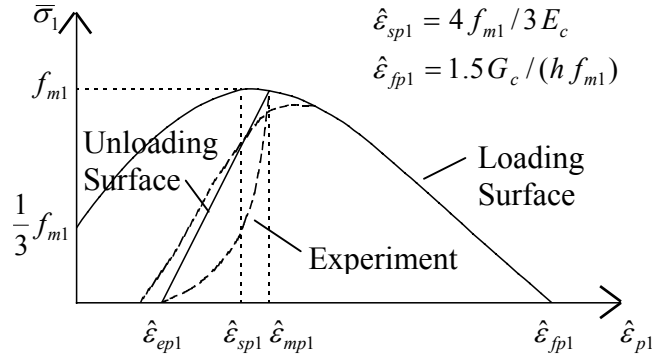


Figure 1 Yield Surface Function for the Crushing Failure Criterion

To describe the degraded stiffness, the unloading/reloading surface is implemented in addition to the loading surface. Based on results reported by Karsan and Jirsa [5], the path of the unloading/reloading surface is simplified as shown in Figure 1, and the permanent plastic strain $\hat{\varepsilon}_{ep}$ is defined as

$$\frac{\hat{\varepsilon}_{ep1}}{\hat{\varepsilon}_{sp1}} = 0.145 \left(\frac{\hat{\varepsilon}_{mp1}}{\hat{\varepsilon}_{sp1}} \right)^2 + 0.13 \left(\frac{\hat{\varepsilon}_{mp1}}{\hat{\varepsilon}_{sp1}} \right) \quad (4)$$

The proposed constitutive model uses the multiple fixed crack orientations to overcome the disadvantages of the fixed and rotating crack models in describing the behavior of reinforced concrete in cyclic tension-compression conditions. The multiple fixed crack orientations are equally spaced, and in each orientation, the failure surface of tensile cracking is introduced:

$$f_i = g_i(\underline{\sigma}) - \bar{\sigma}_i(\hat{\varepsilon}_{pi}) = 0 \quad \text{for } \hat{\varepsilon}_{pi} > 0 \quad i = 2, 3, \dots, k \quad (5a)$$

$$f_i = g_i(\underline{\sigma}) - \bar{\sigma}_i(\hat{\varepsilon}_{pi}) \leq 0 \quad \text{for } \hat{\varepsilon}_{pi} = 0 \quad i = 2, 3, \dots, k \quad (5b)$$

$g_i(\underline{\sigma})$ is σ_{θ_i} , the normal stress component in the i th reference orientation. $\bar{\sigma}_i$ is the failure surface function defined by the tensile plastic strain $\hat{\varepsilon}_{pi}$ as shown in Figure 2 (a).

The failure surface function $\bar{\sigma}_i(\hat{\varepsilon}_{pi})$ can be defined with an uniaxial stress-plastic strain curve of the concrete in tension. However, with this failure surface function, even though a tensile crack exists in a reference orientation, new tensile cracking can occur independently in the adjacent orientation when the stress approaches the tensile cracking stress. This is not true because tensile cracking produces nonlocal damage to the concrete in the adjacent orientation.

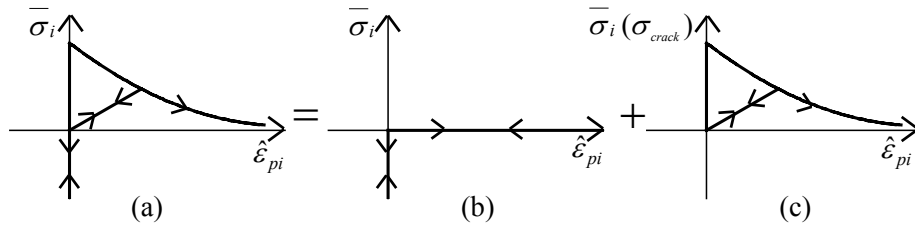


Figure 2 Idealization of the Tensile Stress-Strain Relation in the Fixed Crack Orientation

To overcome this shortcoming, the following modification is made. In a reference orientation, the tensile stress-strain relation shown in Figure 2 (a) is separated into the plastic flow with $\bar{\sigma}_i = 0$ (Figure 2 (b)) and the tensile stress that is a function of the plastic strain (Figure 2 (c)). Through this modeling, the stress of the concrete is conceptually defined by the sum of the compressive stress of the concrete affected by the plastic flow and the tensile stresses induced by tensile cracking:

$$\underline{\sigma} = \underline{\sigma}_c + \sum^m \underline{\sigma}_{crack} \quad (6)$$

where m = total number of reference orientations with active tensile cracks.

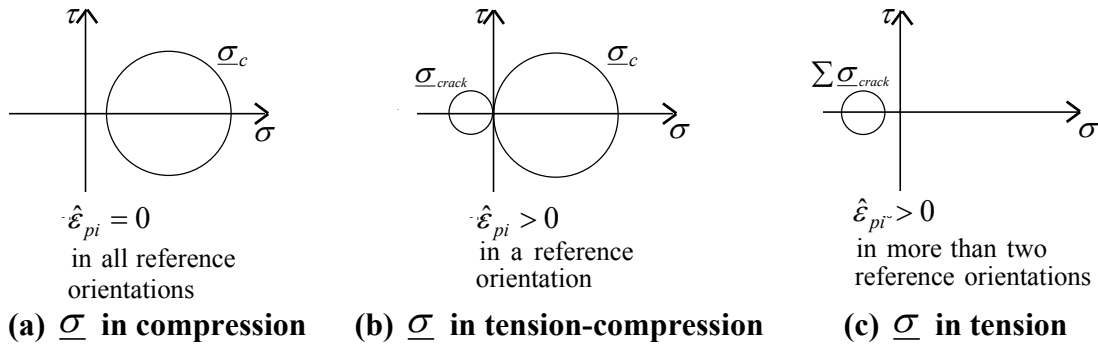


Figure 3 Variations of Concrete Stress with Plastic Tensile Strain $\hat{\varepsilon}_{pi}$

The compressive stress $\underline{\sigma}_c$ is affected by the failure criteria of the compressive crushing and tensile cracking shown in Eqs. 3 and 5. Since the multiple reference orientations of tensile cracking are used and $\bar{\sigma}_i$ in the reference orientations is assigned to zero, any normal stress in the reference orientations can not be in tension. Therefore, $\underline{\sigma}_c$ is kept approximately in uniaxial or multiaxial compression. As shown in Figure 3, if in a reference orientation $\hat{\varepsilon}_{pi} > 0$, which indicates that a tensile crack opens, $\underline{\sigma}_c$ is kept in uniaxial compression (Figure 3 (b)). If $\hat{\varepsilon}_{pi} > 0$ in more than two reference orientations, $\underline{\sigma}_c = 0$ (Figure 3 (c)). If in all the reference orientations $\hat{\varepsilon}_{pi} = 0$ i.e. if there are no active cracks, $\underline{\sigma}_c$ is in uniaxial or biaxial compression (Figure 3 (a)).

An active crack is defined in a reference orientation with $\hat{\varepsilon}_{pi} > 0$. Under further loading, the crack orientation can rotate to the adjacent reference orientations where the normal stress develops plastic strain $\hat{\varepsilon}_{pi}$. On the other hand, under unloading/reloading, the crack orientation is fixed to the current reference orientation with the active crack because the plastic strains representing tensile crack damages do not develop in the adjacent orientations. Therefore, by using the concepts of the multiple fixed crack model and the plastic flow of tensile cracking, it is possible to describe the behavioral characteristics of tensile cracks: the rotating damage under loading and the fixed damage under unloading/reloading.

Tensile stress $\underline{\sigma}_{crack}$ is defined in the reference orientations with active tensile cracks, $\hat{\varepsilon}_{pi} > 0$. The tensile stress-strain curve is defined as shown in Figure 4:

$$\sigma_{crack} = E \hat{\varepsilon}_{pi} \quad \text{for } \hat{\varepsilon}_{pi} < \varepsilon_{et}, \text{ and} \quad (7a)$$

$$\sigma_{crack} = f_t \exp\left(-\varepsilon_{ft} / (\hat{\varepsilon}_{pi} - \varepsilon_{et})\right) \quad \text{for } \hat{\varepsilon}_{pi} > \varepsilon_{et}, \quad (7b)$$

where $\varepsilon_{et} = f_t / E$; $\varepsilon_{ft} = G_t / hf_t$; and G_t = the fracture energy of tensile cracking. To describe the nonlocal damage caused by tensile cracking, it is assumed that the reference orientations within $\pi/4$ from the initial crack orientation have the same maximum plastic strain representing the tensile crack damage.

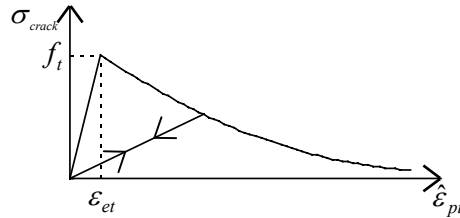


Figure 4 Tensile Stress-Strain Relation

As shown in Figure 5, the post-cracking stress of reinforced concrete is composed of tension softening, bond, and reinforcing steel stresses (Park and Klingner [9]). The tension softening stress is defined by Eq. 7 in the each crack direction. The bond stress σ_{bond} is considered in the orientation of each reinforcement layer. The maximum bond stress, f_{bond} , was suggested by Park and Klingner [9].

$$f_{bond} = 30f_t\rho \leq 0.6f_t \quad (8)$$

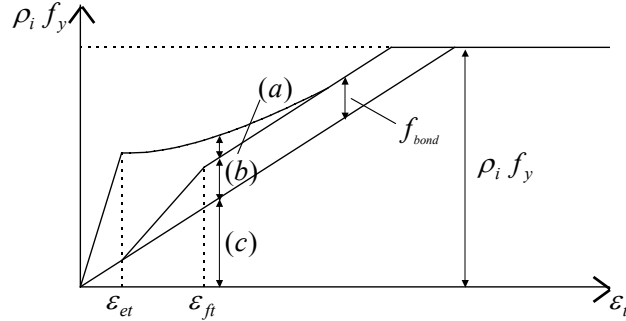


Figure 5 Tensile Stress-Strain Relation of Reinforced Concrete : (a) Tension Softening; (b) Bond Stress; and (c) Reinforcing Steel

Consequently, the total stress of the concrete including the bond stress is defined by the sum of the compressive stress, the tensile stress, and the bond stress.

$$\underline{\sigma} = \underline{\sigma}_c + \sum_i^m \underline{\sigma}_{crack} + \sum_i^n \underline{\sigma}_{bond} \quad (9)$$

where n = total number of reinforcing steel layers

The shear stiffness degradation along the cracks is also important for describing the shear transfer mechanism. In sufficient shear transfer is usually observed as a pinching effect during cyclic loading. In this study, shear stiffness degradation is considered in the reference orientations with the active tensile cracks. The shear transfer stress and strain relation developed by Okamura and Maekawa [8] is used to develop the reduced shear stiffness G_r . The tangent shear stiffness can be obtained:

$$G_r = f_{st} \frac{4\beta}{\epsilon_{pi}(1 + \beta^2)^2} \leq G \quad (10)$$

where $f_{st} = 38.5(f'_c)^{1/3}$ in MPa and $\beta = \frac{2\gamma_{pi}}{\epsilon_{pi}}$. f_{st} is the shear transfer strength. ϵ_{pi} and γ_{pi}

are the normal and the shear plastic strains in the i th reference orientation representing the current crack orientation.

FINITE ELEMENT IMPLEMENTATION

In nonlinear finite-element analyses, it is necessary to obtain the current stresses satisfying all the failure criteria in Eqs. 3 and 5 for given total strains or strain increments. In this numerical program, a typical elastic-predictor-plastic-corrector algorithm is applied for the purpose.

Reinforced concrete members are modeled by four-node rectangular elements for planar finite-element analyses. The reinforcing steel can be idealized either as two-dimensional rectangular elements with smeared properties or as discrete line elements. For the material model of reinforcing steel, a cyclic model developed by Brown and Jirsa [1] is used, and perfect bond between concrete and reinforcing steel is assumed. For nonlinear computations, a simplified displacement-control method introduced by Ramm [10] is used.

VERIFICATIONS

In order to verify the validity of the proposed model, the numerical results were compared with two experiments. Stevens et al. [11] tested shear panels in cyclic compression-tension. The SE8 geometry is shown in Figure 6, and the material properties and reinforcement ratios are summarized in Table 1. SE8 was anisotropically reinforced by reinforcing ratios of 3% in the X direction and 1% in the Y direction, and was subjected to reversed cyclic pure shear.

Table 1 Material Properties and Reinforcement (Stevens et al., 1991))

Specimen	Concrete Compressive Strength (f_c'), Mpa	Reinforcement			
		X-direction		Y-direction	
		Yield Stress (f_y), MPa	Reinforcement Ratio (ρ), percent	Yield Stress (f_y), MPa	Reinforcement Ratio (ρ), percent
SE8	37.0	492	2.94	479	0.98

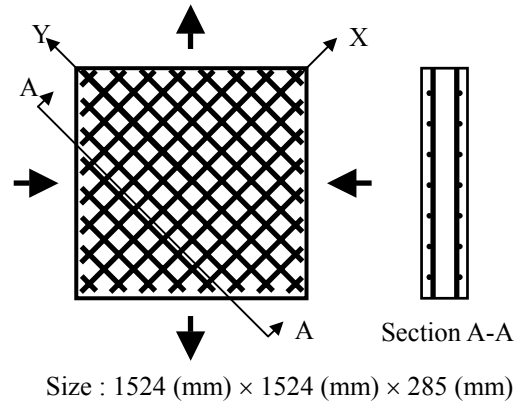
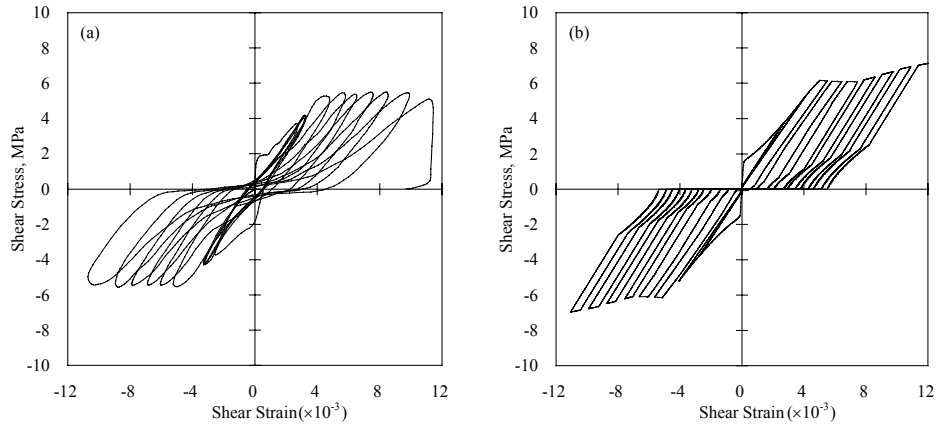


Figure 6 Shear Panel tested by Stevens et al. (1991)

The shear stress-strain response of the specimen is shown in Figure 7. The response displays the highly pinched hysteresis loops that are the characteristics of shear-dominated behaviors. For the early cycles, before any yielding occurs, the hysteresis loops are quite stable. However, after the reinforcing steel in Y direction yields, large strain increments are accumulated on each successive cycle. The compressive strength of the concrete decreases due to the large tensile cracks, and eventually the panel fails by concrete crushing.



**Figure 7 Shear Stress-Strain Response of SE8 :
(a) Experiment ; and (b) Numerical Analysis**

In Figure 7, the numerical response exhibits the same trend as the experimental data for the shear strain-stress. However, numerical analyses do not accurately describe the unloading/reloading curves. This is because the material model uses simplified unloading/reloading relations in the compressive and tensile stress-strain curves and does not describe the transition relations occurring during crack opening and closing. Furthermore, the numerical analysis overestimates the strength of the panel. Stevens et al. [11] reported that the strength reduction factor, developed by Vecchio and Collins [12], overestimates the compressive strength of the concrete in cyclic tension-compression.

Table 2 Material Properties of PCA Wall Specimens (Oesterle et al., 1976)

Specimen	Concrete Compressive Strength, MPa	Yield stress of Reinforcement			Reinforcement Ratio		
		Boundary Elements, MPa	Vertical Web Reinforcement, MPa	Horizontal Web Reinforcement, MPa	Boundary Elements, percent	Vertical Web Reinforcement, percent	Horizontal Web Reinforcement, percent
B1	53.0	449.6	520.6	520.6	1.11	0.29	0.31
B2	53.6	410.3	532.3	532.3	3.67	0.29	0.63

During the 1970s, a series of shear walls were tested at the Portland Cement Association. Wall B1 and B2 tested by Oesterle et al. [7] and the finite element model is shown in Figure 8. The material properties are summarized in Table 2.

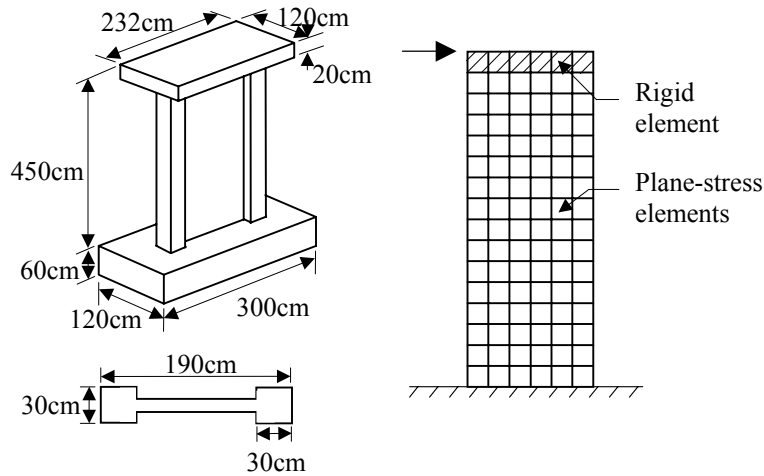
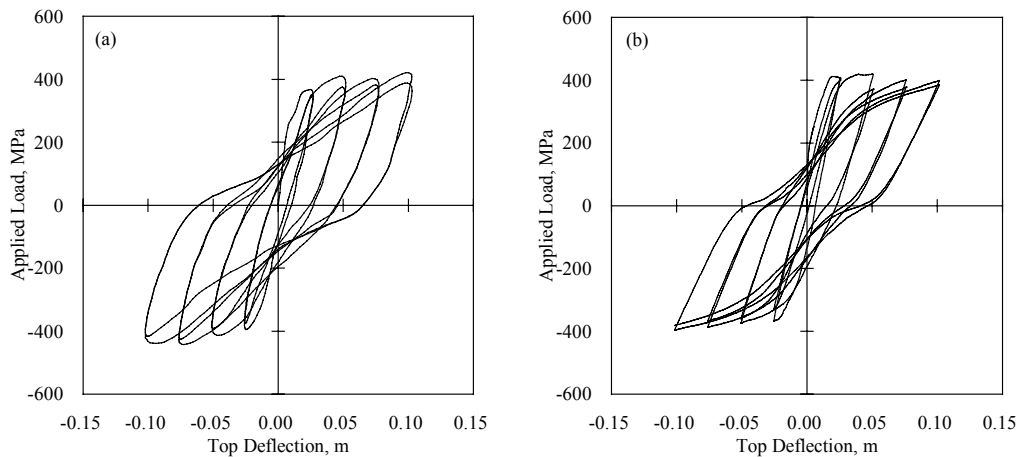


Figure 8 Shear Walls Tested by Oesterle et al. (1976)

The behaviors of the specimens that failed in flexure (Wall B1) and shear (Wall B2) are shown in Figure 9 (a) and 10 (a), respectively. The overall responses of the two walls are similar. Both walls experiences yielding of the longitudinal reinforcement in the boundary elements at a displacement level less than 3cm. Subsequently, wall stiffness degrades when the walls are subjected to displacement cycles beyond yielding. Wall B2 with the larger amount of longitudinal boundary reinforcement presents the more pinched hysteresis loops. This is because the amount of web reinforcement is relatively small.



**Figure 9 Load versus Top Deflection Curve for Wall B1 :
(a) Experiment ; and (b) Numerical Response**

As shown in Figure 9 (b) and 10 (b), the numerical hysteretic responses exhibits the same trends as the experiments. After yielding, the lateral stiffness of both numerical results degrade as the number of cycles increase. As expected in walls susceptible to shear failure, the numerical analysis satisfactorily displays the pinched hysteresis curves for Wall B2. The reduced tangent stiffness in Eq. 10 has a major effect on describing the pinched behavior.

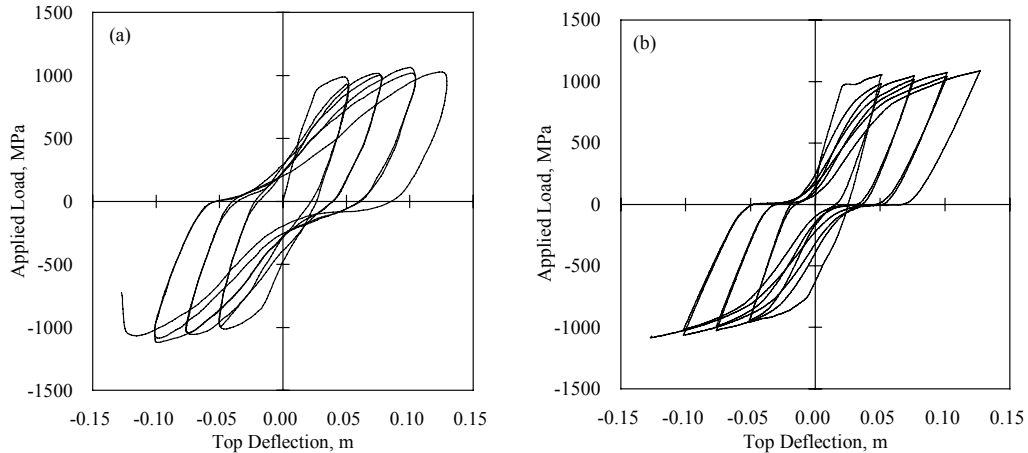


**Figure 10 Load versus Top Deflection Curve for Wall B2 :
(a) Experiment and (b) Numerical Response**

CONCLUSIONS

A material model for reinforced concrete in cyclic tension-compression needs to describe multi-directional tensile cracks and the compressive behavior affected by non-local anisotropic damage caused by tensile cracks. In this study, a constitutive model unifying the plasticity and crack damage models was developed to describe the cyclic behavior of reinforced concrete.

The stress of concrete was conceptually defined with the sum of the compressive stress of the concrete and the tensile stress induced by tensile cracking. The concepts of the multiple fixed crack orientations and the plastic flow of tensile cracking were introduced to describe the cyclic behavior of concrete affected by the anisotropic damage caused by multi-directional and non-orthogonal tensile cracks. Using these concepts, it is possible to describe the damage history characteristics of reinforced concrete under cyclic loading: rotating crack damage under loading and fixed crack damage under unloading/reloading. In addition, shear stiffness degradation was used to describe the stiffness reduction of the shear transfer along tensile cracks i.e. the pinched behavior during cyclic loading. The validity of the proposed material model was verified with the experimental results of shear panels and walls.

ACKNOWLEDGMENTS

The research presented herein has been carried out by the financial assistance of the Major Field in Brain Korea 21 and grant No. 1999-1-310-002-3 from the Basic Research Program of the Korea Science & Engineering Foundation, and the authors are sincerely grateful to the authorities for their support.

REFERENCES

1. Brown, R. H. and Jirsa, J. O., "Reinforced Concrete Beams under Load Reversals", *ACI Structural Journal*, Vol.68, No.5, 1971, pp.380-390.
2. Cachim, P. B., Figueiras, J. A., and Pereira, P. A. A., "Model for Concrete under Cyclic Actions", *Computational Modelling of Concrete Structures*, Balkema, Rotterdam, Vol.1, 1998, pp.643-651.
3. Chen, E. S. And Buyukozturk, O., "Constitutive Model for Concrete in Cyclic Compression", *J. Eng. Mech.*, ASCE, Vol.111, 1985, pp.794-814.
4. Fardis, M. N., Alibe, B., and Tassoulas, L., "Monotonic and Cyclic Constitutive Law for Concrete", *J. Struct. Engrg.*, ASCE, Vol.109, 1983, pp.516-536.
5. Karsan, P. and Jirsa, J. O., "Behavior of Concrete under Compressive Loadings", *J. Struct. Engrg.*, ASCE, Vol.95, No.12, 1969, pp.2543-2563.
6. Kupfer, H. B., Hildorf, H. K., and Rusch, H., "Behavior of Concrete under Biaxial Stresses", *ACI Structural Journal*, Vol.66, No.8, 1969, pp.656-666.
7. Oesterle, R. G., Fiorato, A. E., Johal, L. S., Carpenter, L. S., Russell, H. G., and Corley, W. G., "Earthquake-Resistant Structural Walls-Tests of Isolated Walls", *Report to the National Science Foundation, Construction Technology Laboratories*, PCA, Skokie, Illinois, Nov. 1976, pp.315.
8. Okamura, H. and Maekawa, K., "Nonlinear Analysis and Constitutive Models of Reinforced Concrete", Gihodo-Shuppan Co., Tokyo, 1991.
9. Park, H. and Klingner, R. E., "Nonlinear Analysis of RC Members Using Plasticity with Multiple Failure Criteria", *J. Struct. Engrg.*, ASCE, Vol.123, No.5, 1997, pp.643-651.
10. Ramm, E., "Strategies for Tracing the Nonlinear Response near Limit Points", *Nonlinear Finite Element Analysis in Structural Mechanics*, W. Wundelich, E. Stein, and K. J. Bathe, eds., Springer-Verlag KG, Berlin, Germany, 1981, pp.63-89.

11. Stevens, N. J., Uzumeri, S. M., and Collins, M. P., "Reinforced Concrete Subjected to Reversed Cyclic Shear-Experiments and Constitutive model", *ACI Structural Journal*, Vol.88, No.2, 1991, pp.135-146.
12. Vecchio, F. J. and Collins, M. P., "The Modified Compression-Field Theory for Reinforced Concrete Elements Subjected to Shear", *ACI Structural Journal*, Vol.83, No.2, 1986, pp.219-231.



KEERC-MAE Joint Seminar on
Risk Mitigation for Regions of Moderate Seismicity
University of Illinois at Urbana-Champaign, August 5-8, 2001



Sponsors: Korea Science and Technology Foundation, U.S. National Science



Dynamic Stability of Unreinforced Masonry Bearing Walls

Can C. SIMSIR¹, Mark A. ASCHHEIM², and Daniel P. ABRAMS³

¹ *Research Assistant, Ph.D. Candidate, University of Illinois at Urbana-Champaign
1241 Newmark Laboratory, 205 N. Mathews, Urbana, Illinois, USA
email: simsir@uiuc.edu*

² *Assistant Professor of Civil and Environmental Engineering, University of Illinois at
Urbana-Champaign
2118 Newmark Laboratory, 205 N. Mathews, Urbana, Illinois, USA
email: aschheim@uiuc.edu*

³ *Hanson Engineers Professor of Civil and Environmental Engineering, University of Illinois
at Urbana-Champaign
1241 Newmark Laboratory, 205 N. Mathews, Urbana, Illinois, USA
email: d-abrams@uiuc.edu*

ABSTRACT: This paper describes an ongoing study of the effects of diaphragm flexibility on the response of unreinforced masonry (URM) buildings. In this study, an idealized low-rise masonry building was tested on a shake table. The building was constructed to allow the stiffness of the diaphragm to be modified. Excitation of the structure caused relative displacements of the diaphragm mass and masonry walls. Different diaphragm stiffnesses and various earthquake ground motions were used. The bearing walls remained stable while supporting gravity loads. Midheight cracking and collapse of the walls occurred only under reduced gravity loads and augmented wall mass. Results from this experimental study as well as an analytical method to determine the dynamic stability of the out-of-plane bearing walls are reported.

KEYWORDS: Unreinforced masonry, dynamic testing, out-of-plane bearing wall, diaphragm flexibility, dynamic stability

INTRODUCTION

Engineers have been concerned that earthquakes may cause the collapse of load bearing masonry walls responding out of plane, especially for buildings having relatively flexible floor diaphragms. This concern is particularly relevant to the Central and Eastern United States, where unreinforced masonry (URM) buildings are common and were usually designed and constructed with little or no consideration for seismic actions. Large magnitude earthquakes have occurred in the past in this region. Although future large earthquakes are expected to occur infrequently, the low rate of attenuation of seismic waves increases the portion of the Central and Eastern United States that is susceptible to damage.

Laboratory tests of URM walls responding out of plane have been performed in the past, in both quasi-static and dynamic studies. In the quasi-static out-of-plane tests by Yokel and Dickers [16], the main objective was to study the effects of wind load. Lateral load was applied as a distributed pressure by means of inflated air bags. Clay brick as well as concrete block specimens were tested. Base and Baker [5], West et al. [14], Yokel and Fattal [17], and West et al. [15] carried out similar tests on wall panels that were simply supported at the top and bottom, and loaded axially at the top. These researchers all reported failures due to cracking at the mid-height of the walls.

The ABK Joint Venture [1] [2] performed tests on reinforced and unreinforced masonry walls loaded dynamically out of plane. The unreinforced clay brick and concrete block masonry walls had different height-to-thickness ratios. A constant axial load was applied by a mass suspended from the top of the wall. Controlled displacement histories were applied dynamically by separate servo-hydraulic actuators at the top and bottom of each wall. Displacement histories applied at the top of the wall were amplified to simulate the effects of the floor diaphragm flexibility. Most of the URM walls cracked horizontally approximately at their mid-heights and near the base well before failure, with collapse occurring as the mid-height cracks opened substantially, leading to instability. Based on these tests, Kariotis et al. [12] and Adham [3] identified allowable wall height-to-thickness ratios as a function of the overburden ratio (superimposed weight over wall weight) and peak input velocities at the top and base of the wall.

Bariola et al. [4] reported a series of dynamic tests on clay brick parapet URM walls conducted on a shake table. These walls were cantilevered from their bases. No axial load was applied (other than the self-weight of the wall). The wall height-to-thickness ratio was not found to have a clear influence on the peak ground acceleration required to cause instability. For walls of the same height-to-thickness ratio but with different thicknesses, the thicker walls required higher base accelerations for failure. Failure occurred due to instability of the wall rocking about its base. Lam et al. [13] also performed shake table tests on a clay brick URM cantilever wall. Similar mode of failure was observed, and simplified analytical methods were suggested to estimate the response history.

Doherty [6] carried out shake table tests on clay brick URM walls supported at the top and bottom by a rigid frame. Specimens were axially loaded, initially concentrically. The axial

load was forced to shift its position during the test producing eccentric loading of the walls, which failed at mid-height. Floor diaphragm flexibility was not represented in these tests.

Seismic provisions for the rehabilitation of existing buildings in FEMA 273 [7] and FEMA 356 [9] provide permissible height-to-thickness ratios for URM walls based on the potential for out-of-plane failure. The tabulated values are based on the work done by ABK, but are tabulated as a function of design spectral acceleration rather than as originally put forth. For the empirical design of new structures, IBC 2000 [10] requires the height-to-thickness ratio to not exceed 18 for URM bearing walls.

This paper summarizes work in progress at the University of Illinois. The research focuses on the out-of-plane response of URM walls to which inertial loads are applied as both the diaphragm and the table accelerate. Described are the test specimens, test results, and comparisons of the results with simulations of the response. The mid-height cracking and mid-height failures observed in previous out-of-plane dynamic tests of URM walls did not develop in these tests; explanations for this difference are offered.

SPECIMEN DESCRIPTION

An idealized model masonry building was constructed on the shake table at the University of Illinois (Figure 1). The test set-up was built to investigate the response of out-of-plane wall component as an integral part of the building system. The masonry walls are identified as “out-of-plane” or “in-plane” based on their orientation relative to the direction the shake table is excited. The out-of-plane walls support the gravity load of the diaphragm mass, while the in-plane walls resist to the inertial forces from the diaphragm mass.

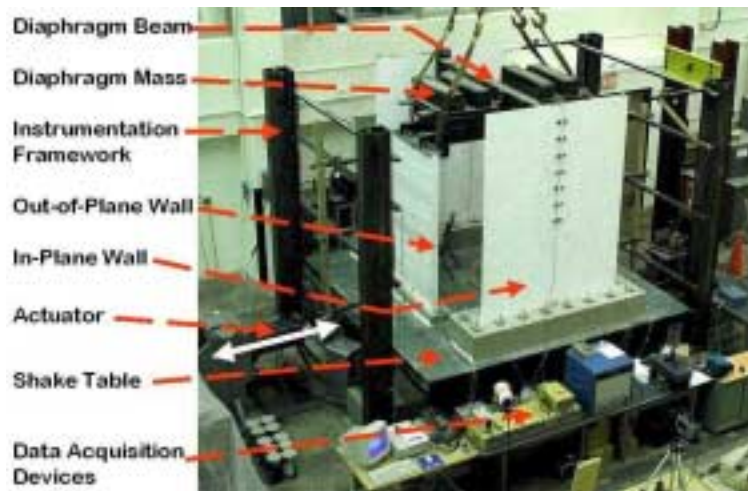


Figure 1 Specimen on shake table

The walls were built from half-scale hollow concrete blocks with each block having dimensions 194x92x92 mm ($7\frac{5}{8} \times 3\frac{5}{8} \times 3\frac{5}{8}$ inch). Measured strengths of the concrete blocks and other materials are given in Table 1.

Table 1 Material strengths

Material	Compressive Strength, MPa (psi)	Tensile Strength, MPa (psi)
Unit concrete block	12.76 (1850)	
Type O mortar	1.59 (230)	
Masonry prism (with Type O mortar)	10.55 (1530)	0.083 (12)
Masonry prism (with Type S mortar)	11.31 (1640)	
Grout	31.16 (4520)	

The two out-of-plane wall panels are 1016-mm (40-inch) long, 2032-mm (80-inch) tall, and 92-mm ($3\frac{5}{8}$ inch) thick (single wythe). These dimensions result in a height-to-thickness ratio of 20, the largest permissible value for existing construction in FEMA 273 [7] and FEMA 356 [9]. Type O mortar was used for the ungrouted out-of-plane walls, to mimic the weak materials in many existing unreinforced masonry (URM) buildings in the Central and Eastern United States.

The two in-plane walls are 1829-mm (72-inch) long, 2540-mm (100-inch) tall, and 92-mm ($3\frac{5}{8}$ inch) thick (single wythe). Based on masonry strength design, they are adequately reinforced with vertical and horizontal steel reinforcing bars to withstand an acceleration of the diaphragm mass (2950 kg or 6.50 kips) of 5 g. The in-plane walls are grouted and are mortared to reinforced concrete footings anchored to the shake table. Type S mortar was used for the in-plane walls. These walls simply provide a load path for inertial shear forces and are not the main object of the current investigation.

The weight of the diaphragm is supported on the out-of-plane walls by means of stringers that bear on the walls on a pin connection. The mass of 2950 kg (6.50 kips) was selected to develop an axial stress representative of a 3-story building. The pin connection uses ball bearings that are mounted onto a steel plate that is anchored by steel shear studs to the out-of-plane wall. Only the top course of the out-of-plane wall is grouted, to anchor the shear studs. The pin connection allows rotation at the top of the wall with respect to the diaphragm, while keeping the gravity load applied concentrically on the wall.

The floor diaphragm is represented by an A36 steel tube spanning 2540 mm (100-in.) between pins attached to the two in-plane walls. Both stiff and flexible diaphragms were represented by mounting different tube cross sections between the pins. The stiff diaphragm used a 305x102x6.4 mm (12x4x0.25 inch) tube and the flexible diaphragm used a 203x51x4.76 mm (8x2x0.19 inch) tube, both in weak-axis bending. The stiff diaphragm had 9 times the lateral stiffness of the flexible one. From free vibration tests, the structure was determined to have a natural period of 0.16 seconds with the stiff diaphragm, and 0.37 seconds with the flexible diaphragm. The flexible beam could correspond to a single straight sheathed wood diaphragm in a 6.1 m x 21.3 m (20 ft x 70 ft) rectangular building, based on an equation offered in FEMA273 [7]:

$$\Delta = vL^4 / (G_d b^3) \quad (1)$$

where Δ is diaphragm deflection, v is maximum shear per unit length in the direction under consideration, L is diaphragm span between shear walls, b is diaphragm width, and G_d is diaphragm shear stiffness.

The diaphragm beam was connected to the in-plane walls by ball bearings mounted on a steel plate; the steel plate was anchored to the wall. The steel plate allowed the elevation of the diaphragm beam to be changed, to accommodate out-of-plane walls with different heights. The hinged connection allowed for rotation and vertical displacement but prevented transverse displacement of the diaphragm beam with respect to the in-plane walls. Inertial forces associated with the diaphragm mass were transmitted to the in-plane walls through the diaphragm beam. Slotted holes on the beam allowed for vertical movement of the mass relative to the beam to accommodate rocking of the out-of-plane walls.

TESTS

A total of 22 ground motion excitations were applied. For each, the name of the ground motion record, the peak table acceleration, the type of diaphragm on the specimen, and the maximum measured displacement at the top of the out-of-plane wall relative to the table are given in Table 2.

Before and after each ground motion excitation, low amplitude frequency sweep tests were performed to determine the natural period of the structure. These tests often showed the natural period of the structure increased after a ground motion excitation, indicating damage to the specimen. The range of fundamental periods observed over different runs is shown in Figure 2, together with the pseudo-acceleration response spectra of the Nahanni and Big Bear Earthquakes. The spectra shown were computed for viscous damping equal to 1.4% of critical damping, which is representative of the damping values determined from the decay of the low amplitude responses measured in the frequency sweep tests.

Ground acceleration histories from 1985 Nahanni Earthquake (Northwest Territories, Canada) and 1992 Big Bear Earthquake (California) were utilized as input functions to the uniaxial shake table. The Nahanni motion came from an intra-plate earthquake and may have frequency characteristics representative of a future earthquake in Central and Eastern United States. The selection of Big Bear as input ground motion is based on its ability to amplify the response — the effective period of vibration increases as nonlinearities develop, and increasing spectral accelerations result for the stiff specimen with the Big Bear record, while reduced acceleration demands are computed for the flexible specimen (Figure 2). The reduced accelerations correspond to increased spectral displacements.

For the 21st and 22nd test runs, lead bricks were bolted along the height of one of the out-of-plane walls, approximately tripling its mass. Furthermore, the gravity load carried by both walls was reduced from 2950 kg (6.50 kips) to 1590 kg (3.50 kips) by removing some of the diaphragm mass.

Table 2 Shake table runs

Run Number	Record Name	Peak Table Acceleration, g	Diaphragm Type	Peak Displacement at the Top of the Out-of-Plane Wall Relative to the Base of the Wall, mm (inches)
1	Nahanni	0.057	Stiff	0.97 (0.038)
2	Nahanni	0.109	Stiff	1.70 (0.067)
3	Nahanni	0.149	Stiff	4.06 (0.16)
4	Nahanni	0.186	Stiff	5.33 (0.21)
5	Nahanni	0.267	Stiff	5.84 (0.23)
6	Nahanni	0.283	Stiff	5.84 (0.23)
7	Nahanni	0.339	Stiff	7.11 (0.28)
8	Nahanni	0.501	Stiff	7.87 (0.31)
9	Nahanni	0.674	Stiff	11.94 (0.47)
10	Nahanni	0.909	Stiff	15.24 (0.60)
11	Nahanni	0.248	Stiff	3.56 (0.14)
12	Nahanni	1.177	Stiff	14.22 (0.56)
13	Big Bear	0.374	Stiff	5.33 (0.21)
14	Big Bear	0.618	Stiff	9.40 (0.37)
15	Big Bear	recording error	Stiff	19.81 (0.78)
16	Big Bear	1.197	Stiff	18.54 (0.73)
17	Big Bear	0.134	Flexible	11.94 (0.47)
18	Big Bear	0.372	Flexible	33.02 (1.30)
19	Big Bear	0.616	Flexible	45.97 (1.81)
20	Big Bear	1.085	Flexible	65.53 (2.58)
21(*)	Big Bear	0.122	Flexible	13.97 (0.55)
22(*)	Big Bear	0.364	Flexible	wall collapsed

(*): Tests with reduced gravity load and augmented wall mass

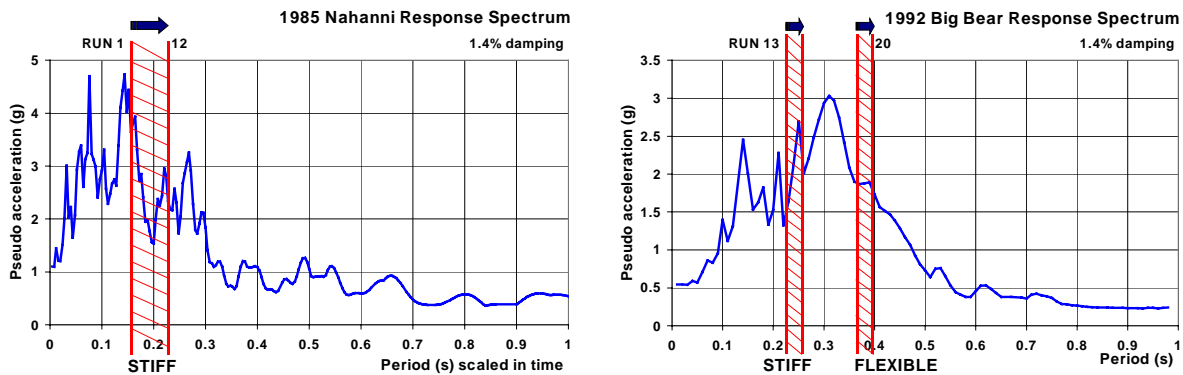


Figure 2 Shift in natural periods for stiff and flexible specimens subjected to 1985 Nahanni and 1992 Big Bear Earthquakes

TEST RESULTS

The specimen was visually examined after each test. Horizontal cracks at the base of the out-of-plane walls were observed for the first time after the 7th test run. These cracks, located in the mortar between the bottom course of block and the concrete footings, became more pronounced in the subsequent runs. No cracks or failures occurred above the base of the out-of-plane walls until run number 22. The in-plane walls sustained diagonal shear cracks during the 15th run. Strain gauges indicated that a few of the steel reinforcing bars inside the in-plane

walls exceeded the yield strain during this run. Strains in the flexible steel diaphragm beam exceeded yield at mid-span during the 20th run.

Displacements at the top and mid-height of the out-of-plane wall, relative to the table, are plotted in Figure 3 for the 20th run. In this and the other runs, the mid-height displacements were in phase with and approximately one-half of the displacements measured at the top of the out-of-plane wall, indicating nearly rigid-body rocking of the wall about its base after rocking began in the 7th run. The largest wall displacement response was obtained in the 20th run, in which the diaphragm was flexible. The out-of-plane walls displaced as much as 65.5 mm (2.58 inch), corresponding to a 3.2% story drift. The walls had a residual drift of 2.5 mm (0.1 inch) after run number 20.

Except for cracking at the base, the walls were undamaged even to drifts of 3.2%. FEMA 306 [8] relates damage due to out-of-plane flexural response of URM walls to FEMA 273 [7] performance levels. According to this relation, the slight damage observed in the test specimen would correspond to an Immediate Occupancy performance level, even though such large story drifts would imply Life Safety or Collapse Prevention demand levels, according to FEMA 273 [7] and FEMA 356 [9].

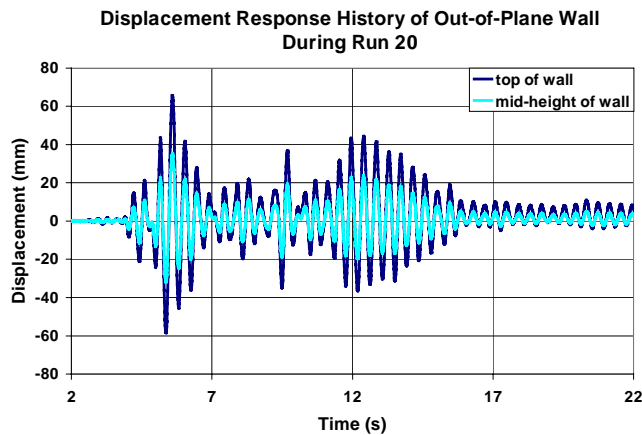


Figure 3 Displacement response history from Run 20

The effect of diaphragm flexibility on the out-of-plane displacement response is apparent in Figure 4, which plots the peak displacements at the top of the out-of-plane wall for each run. As an example, Runs 14 and 19 indicate that the peak displacement of the flexible diaphragm specimen (46.0 mm) is approximately five times larger than that of the stiff diaphragm specimen (9.4 mm), for the same ground motion record (1992 Big Bear, with PGA=0.62g). This results from the difference in spectral displacements associated with the periods of vibration of the flexible- and stiff-diaphragm structures.

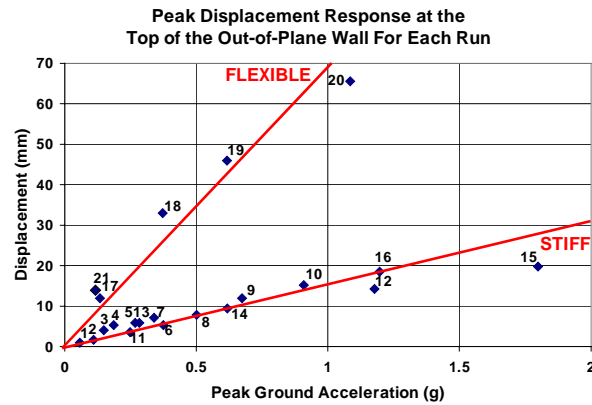
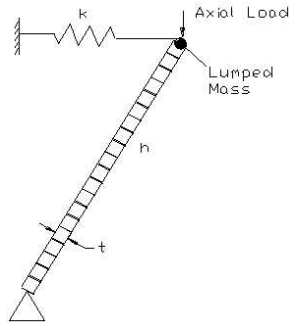


Figure 4 Peak displacement response from all runs

During the 22nd test run, the out-of-plane wall with the augmented mass collapsed due to the formation of horizontal cracks on the wall. These cracks were located in the mortar below the top course, below the bottom course, and two thirds of the wall height from the bottom. Although the other out-of-plane wall did not collapse, it also produced a horizontal crack at two thirds of its height from the bottom.

ESTIMATING PEAK DISPLACEMENTS

The response of the structure was estimated using an “equivalent” SDOF model. The spring in Figure 5 incorporates the stiffnesses of the diaphragm and the in-plane wall, assuming they are two separate springs connected in series. The diaphragm mass and half of the wall mass are lumped at the end of the spring for convenience. The wall is idealized as a rigid body, rocking about its base, even at small excitation amplitudes. Second-order (P-Delta) effects associated with the diaphragm weight may be considered in this model, but were not included in the present calculations. Response was computed using the program USEE (Inel et al. [10]). A linear elastic model was used for the stiff specimen because the diaphragm remained elastic. A bilinear model was used for the flexible specimen, because the diaphragm beam yielded in some runs. Mass, stiffness, strength, and damping characteristic of measured values were used



in the ESDOF model.

Figure 5 Equivalent SDOF model

Estimated peak displacements from the equivalent SDOF analysis are compared with the measured values in Figure 6.

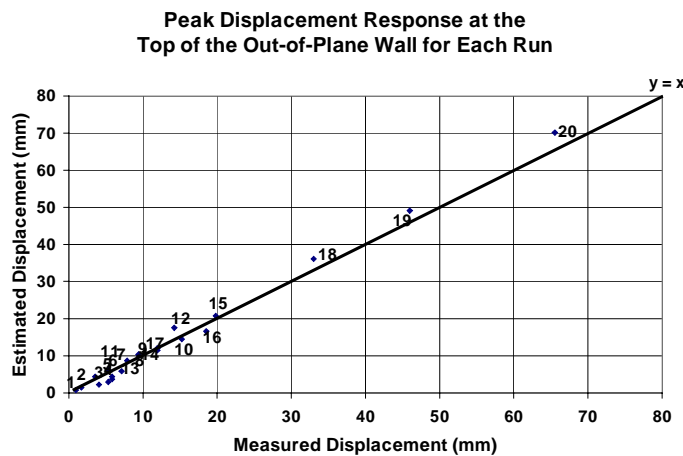


Figure 6 Correlation between measured and computed response

CONCLUSIONS

An ongoing shake table study is investigating effects of diaphragm flexibility on the out of plane response of unreinforced masonry (URM) walls. Analytical work is still in progress. The following results have been obtained:

1. The present test series utilized stiff and flexible diaphragms to excite the out-of-plane walls on a shake table. Unlike previous tests that used different setups for loading the walls, no mid-height collapses resulted with the present setup, except when the axial load was reduced and wall mass was significantly increased by supplementary mass.
2. At peak drifts as large as 3.2%, only minor cracks at the base of the wall were apparent, due to rocking of the walls at their bases. Residual drifts were negligible (0.13%). The

observed damage corresponds to Immediate Occupancy performance. To reach Life Safety and Collapse Prevention demand levels, more substantial damage such as spalling of mortar and offsets at the cracks would have to occur. Such damage was not observed in the present tests even beyond the drift (2.5%), associated with the Collapse Prevention performance level in FEMA 306 [8].

3. Diaphragm flexibility significantly increases the out-of-plane displacement response. This is consistent with the increase in spectral displacement associated with an increase in period resulting from the flexibility of the diaphragm.
4. Peak displacements were estimated with reasonable accuracy using a simple equivalent SDOF system subjected to the measured table excitations. The ESDOF system requires knowledge of the floor mass, viscous damping ratio, and the stiffnesses of the diaphragm and in-plane walls.
5. Based on observed out-of-plane wall failures in past earthquakes, it appears that adequate anchorage of URM walls to the diaphragm is critical to preventing collapse. The out-of-plane performance of walls subjected simultaneously to significant in-plane shear was not assessed in the present tests.
6. URM walls appear to be more susceptible to out-of-plane failure under reduced gravity loads and augmented wall mass.

Tests were performed on a specimen having capable connections that prevented sliding or pullout of the diaphragm relative to the masonry walls. The unreinforced out-of-plane walls were discrete, free-standing elements; that is, not built integrally with the orthogonal reinforced masonry in-plane walls.

ACKNOWLEDGMENTS

This work was supported primarily by the Earthquake Engineering Research Centers Program of the National Science Foundation through the Mid-America Earthquake Center under Award Number EEC-9701785. The collaborative engagement of researchers at the Construction Engineering Research Laboratory (CERL) of the Engineer Research and Development Center, U.S. Army Corps of Engineers is appreciated.

REFERENCES

1. ABK, "Methodology for Mitigation of Seismic Hazards in Existing Unreinforced Masonry Buildings: Wall Testing, Out-of-Plane", Topical Report 04, El Segundo, California, 1981.
2. ABK, "Methodology for Mitigation of Seismic Hazards in Existing Unreinforced Masonry Buildings: The Methodology", Topical Report 08, El Segundo, California, 1984.
3. Adham, S. A., "Static and Dynamic Out of Plane Response of Brick Masonry Walls", *Proceedings of the 7th International Brick Masonry Conference*, Melbourne, 1985, pp.1218-1224.
4. Bariola, J., J. F. Ginocchio, and D. Quinn, "Out of Plane Seismic Response of Brick Walls", *Proceedings of the 5th North American Masonry Conference*, University of Illinois at Urbana-Champaign, 1990, pp.429-439.
5. Base, G. D., and L. R. Baker, "Fundamental Properties of Structural Brickwork", *Journal of the Australian Ceramic Society*, No. 1, Vol. 9, 1973, pp.1-7.
6. Doherty, K. T., "An Investigation of the Weak Links in the Seismic Load Path of Unreinforced Masonry Buildings", Thesis for the Degree of Doctor of Philosophy, The University of Adelaide, Australia, 2000.
7. FEMA 273, NEHRP Guidelines for the Seismic Rehabilitation of Buildings, Report No. FEMA 273, Federal Emergency Management Agency, Washington, D.C., 1997.
8. FEMA 306, Evaluation of Earthquake Damaged Concrete and Masonry Wall Buildings, Report No. FEMA 306, Federal Emergency Management Agency, Washington, D.C., 1999.
9. FEMA 356, Prestandard and Commentary for the Seismic Rehabilitation of Buildings, Report No. FEMA 356, Federal Emergency Management Agency, Washington, D.C., 2000.
10. IBC, International Building Code, International Conference of Building Officials, Whittier, California, 2000.
11. Inel, M., E. Black, M. A. Aschheim, and D. P. Abrams, Utility Software for Earthquake Engineering, Mid-America Earthquake Center, University of Illinois, Urbana, 2001. Available for download from <http://mae.ce.uiuc.edu/>

12. Kariotis, J. C., R. D. Ewing, A. W. Johnson, and S. A. Adham, "Methodology for Mitigation of Earthquake Hazards in Unreinforced Brick Masonry Buildings", *Proceedings of the 7th International Brick Masonry Conference*, Melbourne, 1985, pp.1339-1350.
13. Lam, N. T. K., J. L. Wilson, and G. L. Hutchinson, "The Seismic Resistance of Unreinforced Masonry Cantilever Walls in Low Seismicity Areas", *Bulletin of the New Zealand National Society for Earthquake Engineering*, Vol. 28, No. 3, 1995, pp.179-195.
14. West, W. H., H. R. Hodgkinson, and W. F. Webb, "The Resistance of Brick Walls to Lateral Loading", *Proceedings of the British Ceramic Society*, No. 21, 1973, pp.141-164.
15. West, W. H., H. R. Hodgkinson, and B. A. Haseltine, "The Resistance of Brickwork to Lateral Loading – Part 1 – Experimental Methods and Results of Tests on Small Specimens and Full Sized Walls", *The Structural Engineer*, No. 10, Vol. 55, 1977, pp.411-421.
16. Yokel, F. Y., and R. D. Dickers, "Strength of Loadbearing Masonry Walls", *Journal of Structural Engineering, American Society of Civil Engineers*, Vol. 120, No. ST5, 1971, pp.1593-1608.
17. Yokel, F. Y., and G. Fattal, "Failure Hypothesis for Masonry Shear Walls", *Journal of Structural Engineering, American Society of Civil Engineers*, Vol. 120, No. ST3, 1976, pp.515-532.

Resolutions of KEERC-MAE Center Joint Seminar on Risk Mitigation for Regions of Moderate Seismicity

August 7, 2001

Researchers from the Korea Earthquake Engineering Research Center (KEERC) and the Mid-America Earthquake (MAE) Center met together on the campus of the University of Illinois at Urbana-Champaign at the first joint KEERC-MAE seminar on August 5 through 8, 2001. Sponsors for the seminar on *Risk Mitigation for Regions of Moderate Seismicity* included the Korea Science and Engineering Foundation, Brain Korea 21, and the U.S. National Science Foundation. A total of 43 technical papers were presented on response and seismic design of buildings, bridges and lifelines and earthquake ground motions.

Whereas Korea and the eastern and central United States are each subjected to moderate levels of seismic risk resulting from intraplate earthquakes, and both the KEERC and the MAE Center have a mission to reduce the potential loss of life and property due to earthquakes, an excellent potential exists for future collaboration between these two centers on the infrequent, high consequence earthquakes common to their respective regions. From the 27 research papers presented by faculty researchers, in addition to 16 student presentations, the following technical themes were found in common for research of the two centers:

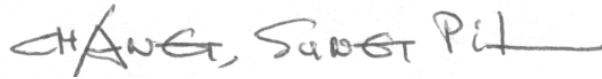
- Improved basic understanding of source mechanisms for intraplate earthquakes and resulting path and site effects.
- Development of new methods and approaches to assess and mitigate risk for regions of moderate seismicity.
- New analysis tools for estimating seismic response of structures.
- New engineering design methods for moderate earthquakes.
- Cost-effective rehabilitation methods for existing construction.
- Improved methods for modeling fragility of vulnerable construction.
- Further understanding of seismic behavior for structural components.
- New response modification technologies.
- Further understanding of soil-foundation-structure interaction.
- Improved methods for estimating response of underground structures.
- Improved understanding of societal aspects of risk mitigation.

The objective of the joint seminar was to explore areas of potential collaboration between the KEERC and the MAE Center as expressed under a recently signed Memorandum of Understanding with the Asian-Pacific Network of Centers for Earthquake Engineering Research (ANCER). The joint seminar followed, in concept, the guiding principle of ANCER to leverage and coordinate limited resources in respective countries towards the development and implementation, on a cooperative basis, of innovative engineering

methods and new enabling technologies needed to design, construct, maintain, manage and renew the built environment for reduced seismic hazards. In this vein, the joint seminar was intended to develop synergies needed to facilitate joint research projects that are of a scope and magnitude such that they cannot be easily carried out by individual centers. Therefore, be it resolved that the KEERC and the MAE Center will:

1. Encourage and support collaboration of individual researchers from the KEERC and the MAE Center on the technical themes itemized above.
2. Agree to continue the formal collaboration established with this event by holding an annual joint seminar alternating at the location of each center. Consistent with the scope of ANCER, future joint seminars will be focused towards an assessment of the state-of-the-art of a special subject of mutual interest or towards development of future research plans on subject areas of potential importance.
3. Continue research collaboration through the exchange of research plans, the exchange of data and information, the networking of experimental facilities, the exchange of research personnel, and cooperative research projects.

These resolutions are based on consensus agreement of seminar participants at the conclusion of the seminar on August 7, 2001.



Sung-Pil Chang
Director, Korean Earthquake Engineering Research Center



Daniel P. Abrams
Director, Mid-America Earthquake Center



KEERC-MAE Joint Seminar on
Risk Mitigation for Regions of Moderate Seismicity
University of Illinois at Urbana-Champaign, August 5-8, 2001



Sponsors: Korea Science and Technology Foundation, U.S. National Science Foundation, Brain Korea 21



List of Attendees

KEERC Participants

Sung Pil Chang

Director

Korean Earthquake Engineering Research Center

Seoul National University

Civil Engineering

Shillim 9-dong, Kwanak-gu, Seoul, KOREA 151-744

Tel: +82-2-880-8780-3

changsp@plaza.snu.ac.kr

Chang Eob Baag

Seoul National University

Geoscience

baagce@plaza.snu.ac.kr

Young Soo Chung

Chungang University

Civil Engineering

Chung47@cau.ac.kr

Sung Gul Hong

Seoul National University

Architectural Engineering

sglhong@snu.ac.kr

Dae Sang Kim

KEERC

Civil Engineering

kds0660@gong.snu.ac.kr

Jae Kwan Kim

Seoul National University

Civil Engineering

jkwankim@plaza.snu.ac.kr

Moon Kyum Kim

Yonsei University

Civil Engineering

applymkk@yonsei.ac.kr

Myoung Mo Kim
Seoul National University
Civil Engineering
geotech@gong.snu.ac.kr

Sang Hyo Kim
Yonsei University
Civil Engineering
sanghyo@yonsei.ac.kr

Hyun Moo Koh
Seoul National University
Civil Engineering
khm@gong.snu.ac.kr

Dong Guen Lee
Sungkyunkwan University
Architectural Engineering
dglee@yurim.skku.ac.kr

Hae Sung Lee
Seoul National University
Civil Engineering
chslee@plaza.snu.ac.kr

Jae Hoon Lee
Yeongnam University
Civil Engineering
jholee@yu.ac.kr

Hong Gun Park
Seoul National University
Architectural Engineering
hgpark@gong.snu.ac.kr

Hyun Mock Shin
Sungkyunkwan University
Civil Engineering
hms Shin@yurim.skku.ac.kr

Chang Ho Park
Brain Korea 21
Seoul National University
Phone: +82-2-880-1830

KEERC Student Participants

Bong Ho Cho

Seoul National University
BK21
Architectural Engineering
Cho525@snu.ac.kr

Daegi Hahm

Seoul National University
BK21
Civil Engineering
hahmdae@sel.snu.ac.kr

Ik Soo Ha

Seoul National University
BK21
Civil Engineering
molafrog@snu.ac.kr

Joo Sung Kang

Seoul National University
BK21
Civil Engineering
River75@snu.ac.kr

Su Min Kang

Seoul National University
BK21
Architectural Engineering
ksm@snu.ac.kr

Jae Yo Kim

Seoul National University
BK21
Architectural Engineering
beholder@snu.ac.kr

Jin Ho Lee

Seoul National University
BK21
Civil Engineering
ohnij2@snu.ac.kr

Hyung Geun Ryu

Seoul National University
BK21
Civil Engineering
ryu99@snu.ac.kr

MAE Participants

Dan Abrams

Director, MAE Center
University of Illinois
1245 Newmark Lab
205 N. Mathews Ave
Urbana, IL 61801
PH: 217-333-0565
d-abrams@uiuc.edu

Jim Craig

Georgia Institute of Technology
School of Aerospace Engineering
Knight 321-5
Atlanta, GA 30319
PH: 404-894-3042
James.craig@ae.gatech.edu

Amr Elnashai

Associate Director, MAE Center
University of Illinois
Civil Engineering
2129E Newmark Lab
Tel: 265-5497
aelnash@staff.uiuc.edu

Douglas Foutch

University of Illinois
Civil & Environmental Engineering
3129B Newmark Lab
205 N. Mathews Ave
Urbana, IL 61801
PH: 217-333-6359
d-foutch@uiuc.edu

Jamshid Ghaboussi

University of Illinois
Civil & Environmental Engineering
3118 Newmark Lab
205 N. Mathews Ave
Urbana, IL 61801
PH: 217-333-6939
jghabous@uiuc.edu

Youssef Hashash

University of Illinois
Civil & Environmental Engineering
2230C Newmark Lab
205 N. Mathews Ave
Urbana, IL 61801
PH: 217-333-6986
hashash@uiuc.edu

Neil Hawkins

University of Illinois
Interim Head of Dept., Civil & Environmental Engineering
2129E Newmark Lab
205 N. Mathews Ave
Urbana, IL 61801
PH: 217-333-3815
nmhawkin@uiuc.edu

Robert Herrmann

Saint Louis University
Earth & Atmospheric Sciences
221 North Grand Blvd.
St. Louis, MO 63103
PH: 314-977-3120 FAX: 314-977-3117
rbh@eas.slu.edu

Charitini Kadianaki

Imperial College
London, UK
Civil Engineering South Kensington Campus
charitini.kadianaki@ic.ac.uk

T. John Kim

University of Illinois
Urbana & Regional Planning
111 Temple Buell
Champaign, IL 61820
PH: 217-244-5369
t-kim7@uiuc.edu

Jim LaFave

University of Illinois
Civil & Environmental Engineering
3108 Newmark Lab
205 N. Mathews Ave
Urbana, IL 61801
PH: 217-333-8064
jlafave@staff.uiuc.edu

Jong Sung Lee

University of Illinois
Urbana & Regional Planning
111 Temple Buell
Champaign, IL 61820
PH: 217-244-6465
jonglee1@uiuc.edu

Yi-Kwei Wen

University of Illinois
Civil & Environmental Engineering
3129E Newmark Lab
205 N. Mathews Ave
Urbana, IL 61801
PH: 217-333-1328
y-wen@uiuc.edu

Donald White

Georgia Institute of Technology
Civil & Environmental Engineering
790 Atlantic Drive
Atlanta, GA 30332-0355
PH: 404-894-5839
donald.white@ce.gatech.edu

MAE Student Participants**Erich Bretz**

University of Illinois
1235 Newmark Lab
205 N. Mathews Ave
Urbana, IL 61801
PH: 217-344-0970
ebretz@uiuc.edu

Omer Erbay

University of Illinois
1235 Newmark Lab
205 N. Mathews Ave
Urbana, IL 61801
PH: 217-333-5963
erbay@uiuc.edu

Mehmet Inel

University of Illinois
1235 Newmark Lab
205 N. Mathews Ave
Urbana, IL 61801
PH: 217-344-5432
inel@uiuc.edu

Sang-Cheol Kim

Georgia Institute of Technology

595 McAfee St, NW, #38

Atlanta, GA 30313

PH: 404-873-6271

gt0180d@prism.gatech.edu

Jaret Lynch

University of Illinois

1235 Newmark Lab

205 N. Mathews Ave

Urbana, IL 61801

PH: 217-265-0585

jmlynch@uiuc.edu

Duhee Park

University of Illinois

2216 Newmark Lab

205 N. Mathews Ave

Urbana, IL 61801

PH: 217-333-6942

dpark1@uiuc.edu

Joonam Park

Georgia Institute of Technology

350385 Georgia Tech Station

Atlanta, GA 30332

PH: 404-385-0827

gt0385a@prism.gatech.edu

Can Simsir

University of Illinois

1235 Newmark Lab

205 N. Mathews Ave

Urbana, IL 61801

PH: 217-333-5963

simsir@uiuc.edu